



Terms and Conditions of Use of Digitised Theses from Trinity College Library Dublin

Copyright statement

All material supplied by Trinity College Library is protected by copyright (under the Copyright and Related Rights Act, 2000 as amended) and other relevant Intellectual Property Rights. By accessing and using a Digitised Thesis from Trinity College Library you acknowledge that all Intellectual Property Rights in any Works supplied are the sole and exclusive property of the copyright and/or other IPR holder. Specific copyright holders may not be explicitly identified. Use of materials from other sources within a thesis should not be construed as a claim over them.

A non-exclusive, non-transferable licence is hereby granted to those using or reproducing, in whole or in part, the material for valid purposes, providing the copyright owners are acknowledged using the normal conventions. Where specific permission to use material is required, this is identified and such permission must be sought from the copyright holder or agency cited.

Liability statement

By using a Digitised Thesis, I accept that Trinity College Dublin bears no legal responsibility for the accuracy, legality or comprehensiveness of materials contained within the thesis, and that Trinity College Dublin accepts no liability for indirect, consequential, or incidental, damages or losses arising from use of the thesis for whatever reason. Information located in a thesis may be subject to specific use constraints, details of which may not be explicitly described. It is the responsibility of potential and actual users to be aware of such constraints and to abide by them. By making use of material from a digitised thesis, you accept these copyright and disclaimer provisions. Where it is brought to the attention of Trinity College Library that there may be a breach of copyright or other restraint, it is the policy to withdraw or take down access to a thesis while the issue is being resolved.

Access Agreement

By using a Digitised Thesis from Trinity College Library you are bound by the following Terms & Conditions. Please read them carefully.

I have read and I understand the following statement: All material supplied via a Digitised Thesis from Trinity College Library is protected by copyright and other intellectual property rights, and duplication or sale of all or part of any of a thesis is not permitted, except that material may be duplicated by you for your research use or for educational purposes in electronic or print form providing the copyright owners are acknowledged using the normal conventions. You must obtain permission for any other use. Electronic or print copies may not be offered, whether for sale or otherwise to anyone. This copy has been supplied on the understanding that it is copyright material and that no quotation from the thesis may be published without proper acknowledgement.

The Earthquake-Resistance of Flush End-Plate Joints

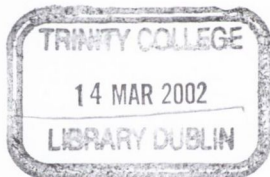
A Thesis Submitted to the University of Dublin in Partial Fulfilment of the Requirements
for the Degree of Doctor of Philosophy in the Faculty of Engineering

by

Andrew William Thomson B.A., B.A.I.

October 2001

Department of Civil, Structural and Environmental Engineering
University of Dublin
Trinity College
Dublin



THESIS 6660

Declaration

The author hereby declares that this thesis, in whole or in part, has not been submitted to any other university as an exercise for a degree. Except where reference has been given in the text, it is entirely the author's own work.

The author confirms that the Library may lend or copy this thesis upon request, for academic purposes.

A handwritten signature in blue ink that reads "Andrew Thomson". The signature is written in a cursive style with a horizontal line underneath it.

Andrew W. Thomson

October 2001

To the memory of my father

James Alexander Thomson

Acknowledgements

I would like to express my sincere gratitude to my supervisor, Dr. Brian Broderick, for his help and support. His advice and encouragement has been extremely valuable throughout the course of my studies.

Thanks are due to the technicians in the Department of Civil, Structural and Environmental Engineering in Trinity College Dublin for their help and expertise over the last number of years. In particular, I would like to thank the Chief Technician, Chris O'Donovan for his advice and cooperation. Sincere thanks are also due to George Jones, Gerard McGranaghan and Dave McAuley for their experimental assistance.

I would like to thank my fellow postgraduate students in the department for their friendship and support. I would especially like to thank Cathy, Bryan, and Quentin. Their presence has helped make the last few years a truly enjoyable experience.

I would also like to thank some of my other friends who have helped me in different ways during the course of this work. Thanks are especially due to Susan, Tom, Brian, Joe, John and all the others for putting up with me. I would also like to thank the other Monday night die-hards and all my other friends of DUSAC who never let me forget that it was possible to do research and have fun at the same time!

I would especially like to thank my family, Ann and Ian for their support and understanding during the last few years. Without them, I would never have gotten this far and I owe them everything.

Finally, this thesis is dedicated to the memory of my father, James Alexander Thomson. Without his inspiration, this would never have been started and could not have been finished.

Summary

This thesis investigates the applicability of flush end-plate joints to frames in low-to-moderate seismic zones. Although a great deal of research has been carried out on the use of semi-rigid joints in frames, most of this has concentrated on the monotonic, rather than the cyclic or dynamic response of the joints. In addition, the majority of research has examined angle and extended end-plates. Flush end-plate joints are advocated for use in the wind-moment design method in the United Kingdom and considerable design guidance is available. In order to ensure a ductile response, careful selection of design details, such as the end-plate thickness, bolt size and spacing amongst others, is necessary. Although the available guidance already considers these criteria as part of the ductility requirements, it is uncertain whether sufficient rotation capacity for seismic engineering applications is always provided.

Monotonic and cyclic tests were carried out on beam-to-column sub-assemblages employing a range of joint details. In order to carry out this experimental work, a new computer-based control system for the testing of structural elements was developed. By using servo-hydraulic actuators, this system is capable of imposing various different displacement loading patterns on test specimens.

Both monotonic and cyclic tests were performed and the resulting moment-rotation characteristics of the specimens are examined for initial stiffness, ductility, moment capacity and stability under cyclic loads. A total of twenty-two beam-to-column sub-assemblages were tested in three test series. The first series was used to calibrate and test the experimental control system, and therefore problems were expected with these specimens. The second and third test series consisted of a range of specimens designed with various end-plate thicknesses, column sizes and bolts. These experimental results are compared to the design characteristics determined from Eurocode 3. It is observed that the design characteristics over-estimate the initial stiffness of the joint and under-predict the resistance capacity.

The specimen details are varied to provide different types of joint failure mode as defined in BS 5950 and Eurocode 3. These failure modes are based on a notional T-stub, and the ratio of the flexural resistance of this T-stub to the axial resistance of the bolts. Mode 1 joints are subject to formation of plastic hinges in the T-stub at the bolt line and the beam, or column, web line, while the bolts remain elastic. Mode 2 joints form plastic hinges at the web line followed by yielding of the bolts, while mode 3 joints are subject to yielding of the bolts only, while the T-stub plate remains elastic.

Based on these experimental results, a prediction model for the moment-rotation response of flush end-plates is developed. This model was developed using a moment-curvature relationship to predict the force-displacement curve of a notional T-stub. This force displacement relationship is translated into the moment-rotation curve for the joint. The effects of column web deformations are also included. These resulting moment-rotation relationships are compared to the experimental results and the design characteristics. It is observed that the proposed model gives a much better prediction for those joints employing thinner end-plates. This is due to the relative importance of the different components of the joint. The prediction model displays a much better correlation with the initial stiffness and the moment capacity of the joint than is observed for the Eurocode 3 design method.

In order to investigate the viability of flush end-plate joints in areas of low-to-moderate seismic risk, a number of design cases studies are investigated. Four moment-resisting frames are designed using the wind-moment method and then evaluated for seismic resistance. The joints employed in these frames were varied to examine the effect of employing joints with different failure modes. The frames were also evaluated using three different joint models. These were the Eurocode 3 design model; the Eurocode 3 model employing a modified stiffness expression; and the proposed model. As the wind-moment method is a semi-rigid design method and the joints employed were partial strength, it is observed that the joint moment capacity is the critical factor in the seismic design ground acceleration. It was observed that the proposed model predicted higher critical seismic resistances for all of the joints employed in the study than either of the other two models. It was also observed that the joint ductility directly affected the seismic resistance of the frame. It was concluded that flush end-plate joints are viable for use in the earthquake-resistant design of low-to-medium rise buildings in areas of low-to-moderate seismicity.

Table of Contents

TITLE PAGE	i
DECLARATION	ii
DEDICATION	iii
ACKNOWLEDGEMENTS	iv
SUMMARY	v
TABLE OF CONTENTS	vii
LIST OF FIGURES	xiii
LIST OF TABLES	xviii
1. INTRODUCTION	1
1.1 INTRODUCTION	2
1.2 SCOPE OF RESEARCH STUDY	5
1.3 ORGANISATION OF THESIS	7
2. LITERATURE REVIEW OF SEMI-RIGID JOINTS AND FRAMES	9
2.1 INTRODUCTION	10
2.2 JOINT DEFINITION	11
2.3 CLASSIFICATION OF STEEL FRAMES	14
2.4 CLASSIFICATION OF STRUCTURAL STEEL JOINTS	16
2.4.1 CLASSIFICATION BY STIFFNESS	17
2.4.2 CLASSIFICATION BY STRENGTH	18
2.4.3 CLASSIFICATION BY ROTATION, OR DUCTILITY, CAPACITY	19
2.5 DISCUSSION OF JOINT FAILURE MODES	20

2.6	STRAIN-RATE EFFECTS ON STEEL MEMBERS AND JOINTS	27
2.7	EXPERIMENTAL STUDIES ON JOINT AND FRAME BEHAVIOUR	31
2.7.1	BEAM-TO-COLUMN SUB-ASSEMBLAGE TESTS	31
2.7.2	FULL-SCALE SEMI-RIGID FRAME EXPERIMENTS	34
2.8	METHODS OF JOINT MODELLING	36
2.8.1	MATHEMATICAL MODELS	36
2.8.1.1	<i>Experimental Curve Fitting Models</i>	36
2.8.1.2	<i>Simplified Analytical Models</i>	43
2.8.2	FINITE ELEMENT BASED MODELS	48
2.8.3	MECHANICAL ANALOGUE MODELS	54
2.8.4	CONCLUSIONS ON MODELLING TECHNIQUES	60
2.9	CONCLUSIONS	61
3.	TEST PROCEDURES AND SOFTWARE	63
3.1	INTRODUCTION	64
3.2	RECOMMENDED TESTING PROCEDURES	65
3.2.1	DEFINITION OF FORCE AND DISPLACEMENT	65
3.2.2	COMPLETE TESTING METHOD	66
3.2.3	SHORT TESTING METHOD	67
3.3	STRUCTURAL TESTING CONTROL SOFTWARE	68
3.3.1	BASIC SCANNING PROGRAM	69
3.3.2	SHAKEDOWN TESTING PROGRAM	71
3.3.3	CONSTANT AMPLITUDE CYCLIC WAVEFORM PROGRAM	76
3.3.4	STRUCTURAL ELEMENT CYCLIC LOADING PROGRAM	81
3.4	CONTROL SYSTEM INTEGRATION	86
3.4.1	SERVO-HYDRAULIC ACTUATOR COMMAND PROCESS	88
3.4.2	SIGNAL CONDITIONING PRINCIPLES	89
3.4.3	COMPUTER INTEGRATION AND CONTROL	92
3.5	CONTROL SYSTEM ACCURACY	93
3.5.1	TEST SYSTEM ACCURACY	93
3.5.1	WIREBALL-REINFORCED CONCRETE BEAM-COLUMN MEMBERS	95

3.6	CONCLUSIONS	98
4.	EXPERIMENTAL SET-UP AND SYSTEM VERIFICATION	100
4.1	INTRODUCTION	101
4.2	EXPERIMENTAL PROCEDURES AND SPECIMENS	101
4.3	EXPERIMENTAL EVALUATION PARAMETERS	103
4.3.1	DUCTILITY	105
4.3.2	RESISTANCE AND RIGIDITY RATIOS	105
4.4	EXPERIMENTAL SPECIMENS AND DESIGN CALCULATIONS	106
4.4.1	TEST SERIES ONE	108
4.4.2	TEST SERIES TWO	112
4.4.3	TEST SERIES THREE	117
4.5	TEST SERIES ONE EXPERIMENTAL RESULTS	120
4.5.1	EXPERIMENTAL RESULTS & OBSERVATIONS: SPECIMEN 1.1	122
4.5.2	EXPERIMENTAL RESULTS & OBSERVATIONS: SPECIMEN 1.2	124
4.5.3	EXPERIMENTAL RESULTS & OBSERVATIONS: SPECIMEN 1.3	127
4.5.4	EXPERIMENTAL RESULTS & OBSERVATIONS: SPECIMEN 1.4	127
4.5.5	EXPERIMENTAL RESULTS & OBSERVATIONS: SPECIMEN 1.5	130
4.5.6	EXPERIMENTAL RESULTS & OBSERVATIONS: SPECIMEN 1.6	131
4.5.7	TEST SERIES ONE CONCLUSIONS	133
4.6	CONCLUSIONS	136
5.	EXPERIMENTAL OBSERVATIONS AND RESULTS	139
5.1	INTRODUCTION	140
5.2	TEST SERIES TWO EXPERIMENTAL RESULTS	140
5.2.1	EXPERIMENTAL RESULTS & OBSERVATIONS: SPECIMEN 2.1	142
5.2.2	EXPERIMENTAL RESULTS & OBSERVATIONS: SPECIMEN 2.2	144
5.2.3	EXPERIMENTAL RESULTS & OBSERVATIONS: SPECIMEN 2.3	146
5.2.4	EXPERIMENTAL RESULTS & OBSERVATIONS: SPECIMEN 2.4	147
5.2.5	EXPERIMENTAL RESULTS & OBSERVATIONS: SPECIMEN 2.5	151
5.2.6	EXPERIMENTAL RESULTS & OBSERVATIONS: SPECIMEN 2.6	152

5.2.7	EXPERIMENTAL RESULTS & OBSERVATIONS: SPECIMEN 2.7	154
5.2.8	EXPERIMENTAL RESULTS & OBSERVATIONS: SPECIMEN 2.8	155
5.2.9	TEST SERIES TWO CONCLUSIONS	157
5.2.9.1	<i>Eurocode 3 Design Model</i>	157
5.2.9.2	<i>Improved Joint Behaviour</i>	158
5.2.9.3	<i>Bolt Pre-loading</i>	159
5.3	TEST SERIES THREE EXPERIMENTAL RESULTS	160
5.3.1	EXPERIMENTAL RESULTS & OBSERVATIONS: SPECIMEN 3.1	161
5.3.2	EXPERIMENTAL RESULTS & OBSERVATIONS: SPECIMEN 3.2	165
5.3.3	EXPERIMENTAL RESULTS & OBSERVATIONS: SPECIMEN 3.3	167
5.3.4	EXPERIMENTAL RESULTS & OBSERVATIONS: SPECIMEN 3.4	169
5.3.5	EXPERIMENTAL RESULTS & OBSERVATIONS: SPECIMEN 3.5	171
5.3.6	EXPERIMENTAL RESULTS & OBSERVATIONS: SPECIMEN 3.6	174
5.3.7	EXPERIMENTAL RESULTS & OBSERVATIONS: SPECIMEN 3.7	175
5.3.8	EXPERIMENTAL RESULTS & OBSERVATIONS: SPECIMEN 3.8	177
5.3.9	TEST SERIES THREE CONCLUSIONS	179
5.3.9.1	<i>Eurocode 3 Design Comparison & Failure Modes</i>	180
5.3.9.2	<i>Loading Rate Effects</i>	181
5.3.9.3	<i>Improved Joint Behaviour</i>	182
5.4	EXPERIMENTAL CONCLUSIONS & RECOMMENDATIONS	183
5.4.1	EUROCODE 3: ANNEX J DESIGN IMPLICATIONS	183
5.4.2	BOLT PRE-LOAD	183
5.4.3	CYCLIC EVALUATION PARAMETERS	184
5.4.4	STIFFNESS HARDENING	185
5.4.5	IMPROVED JOINT BEHAVIOUR	185
5.4.6	FAILURE MODES	186
5.4.7	DUCTILITY	187
5.4.8	RECOMMENDATIONS	188
5.5	CONCLUSIONS	189
6.	PREDICTION MODELLING OF JOINT RESPONSE	190
6.1	INTRODUCTION	191
6.2	PROPOSED JOINT MODEL	191
6.2.1	T-STUB MODELLING TECHNIQUE	193

6.2.1.1	<i>Basis of Approach</i>	193
6.2.1.2	<i>Material Model</i>	193
6.2.1.3	<i>Moment-Curvature Relationship</i>	194
6.2.1.4	<i>Failure Modes</i>	196
6.2.1.5	<i>Ultimate plastic displacement for a mode 1 failure mechanism</i>	197
6.2.1.6	<i>Ultimate plastic displacement for a mode 2 failure mechanism</i>	200
6.2.1.7	<i>Ultimate plastic displacement for a mode 3 failure mechanism</i>	208
6.2.1.8	<i>Prediction of the force-displacement curve</i>	209
6.2.1.9	<i>Proposed Change to the T-stub model</i>	215
6.2.2	COLUMN WEB MODELLING	219
6.2.2.1	<i>Column Web in Shear</i>	219
6.2.2.2	<i>Column Web in Tension</i>	220
6.2.2.3	<i>Column Web in Compression</i>	221
6.2.3	NON-LINEAR MOMENT-ROTATION MODELLING OF FULL JOINT	221
6.3	MODEL VALIDATION	224
6.4	CONCLUSIONS	231
7.	SEISMIC DESIGN CASES STUDIES	233
7.1	INTRODUCTION	234
7.2	BASIS OF THE WIND-MOMENT DESIGN METHOD	234
7.3	SEISMIC DESIGN	236
7.3.1	SEISMIC DESIGN SPECTRUM	236
7.3.2	DETERMINATION OF DESIGN GROUND ACCELERATION	240
7.4	DESIGN CASE STUDIES	241
7.4.1	CASE STUDY ONE: TWO STOREY, ONE BAY FRAME	242
7.4.2	CASE STUDY TWO: FOUR STOREY, ONE BAY FRAME	245
7.4.3	CASE STUDY THREE: FOUR STOREY, FOUR BAY FRAME	247
7.4.4	CASE STUDY FOUR: SEVEN STOREY, TWO BAY FRAME	250
7.5	CONCLUSIONS	254
8.	CONCLUSIONS	257
8.1	SUMMARY OF RESEARCH STUDY	258

8.2	PRINCIPAL CONCLUSIONS	260
8.2.1	EXPERIMENTAL CONTROL SYSTEMS	260
8.2.2	CYCLIC BEHAVIOUR OF FLUSH END-PLATE JOINTS	260
8.2.3	IMPROVEMENT OF JOINT BEHAVIOUR	261
8.2.4	EUROCODE 3: ANNEX J DESIGN CHARACTERISTICS	262
8.2.5	JOINT RESPONSE MODELLING	262
8.2.6	SEISMIC DESIGN OF FRAMES	263
8.3	SUGGESTIONS FOR FURTHER RESEARCH	264
8.3.1	EXPERIMENTAL WORK	264
8.3.2	IMPROVEMENTS IN THE PREDICTION OF JOINT RESPONSE	265
8.3.3	SEISMIC FRAME DESIGN	265
	REFERENCES	266
	APPENDIX A: MATERIAL PROPERTIES	277
A.1	STEEL TENSILE TEST RESULTS	278
A.2	BOLT TENSILE TEST RESULTS	284
	APPENDIX B: STRAIN GAUGE RESULTS	286
B.1	TEST SERIES TWO	287
B.2	TEST SERIES THREE	292
	APPENDIX C: SAMPLE CALCULATIONS FOR PROPOSED JOINT	
	RESPONSE MODEL	301
	APPENDIX D: FRAME DESIGN SPECIFICATIONS	312
D.1	CASE STUDY 1	313
D.1	CASE STUDY 2	317
D.1	CASE STUDY 3	318
D.1	CASE STUDY 4	319

List of Figures

Figure 1.1: Typical Wind-Moment Joint (Flush End-plate)	2
Figure 2.1: Illustrated definition of joint and connection	11
Figure 2.2: Sources of joint deformability	13
Figure 2.3: Structural properties of a joint	14
Figure 2.4: Stiffness Classification Boundaries	17
Figure 2.5: Strength Classification Boundaries	19
Figure 2.6: Component Ductility	21
Figure 2.7: Equivalent Tee-Stub for a flush end-plate joint	23
Figure 2.8: Yield line patterns for equivalent tee-stubs (Eurocode 3, 1998)	24
Figure 2.9: Failure Modes of equivalent Tee-stubs	25
Figure 2.10: Graphical representation of failure mechanisms (Eurocode 3, 1998)	26
Figure 2.11: Influence of strain-rate effects on properties of steel (Gioncu, 2000)	28
Figure 2.12: Bi-linear Curve Approximation	37
Figure 2.13: Tri-linear Curve Approximation	38
Figure 2.14: Multi-linear Curve Approximation	38
Figure 2.15: Non-linear Curve Approximation	39
Figure 2.16: Standardised Moment-Rotation Function	40
Figure 2.17: Tri-linearised Moment-Rotation Loops	42
Figure 2.18: Cyclic Moment-Rotation Curve Model	43
Figure 2.19: Deformation of Flush End-Plate Joint (Johnson & Law, 1981)	45
Figure 2.20: Load-Deflection Behaviour (Patel & Chen, 1984)	49
Figure 2.21: Orthotropic Surface Results for Double Angle Joints	50
Figure 2.22: Modelling of Bolts with Bar Elements (Patel & Chen, 1985)	51
Figure 2.23: Typical 2D mesh for End-plate Joint Analysis (Krishnamurthy, 1980)	52
Figure 2.24: Finite Element Mesh for Beam-to-Beam Joint (Choi & Chung, 1996)	53
Figure 2.25: Finite element model of flush end-plate joint (Tucker (2002))	54
Figure 2.26: Modelling of bolts (Tucker (2002))	54
Figure 2.27: Mechanical Model of Double Angle Web Joints	55
Figure 2.28: Mechanical Model of a Full Welded Joint (Tschemmerneegg, 1988)	56
Figure 2.29: Mechanical Model of a Bolted Joint (Huber & Tschemmerneegg, 1998)	57
Figure 2.30: Joint modelled using Line Elements (Driscoll, 1987)	58
Figure 2.31: Type of Joint to be modelled and Model Geometry (Calado & Ferreira, 1995)	58

Figure 2.32: T-Stub Model (Kennedy & Hafez, 1984)	59
Figure 3.1: Force-Displacement Curve	66
Figure 3.2: Cyclic displacement waveform for ECCS procedures	67
Figure 3.3: Method for determining cyclic parameters using the short testing procedure	68
Figure 3.4: Program Code for All Loading Program Inputs	70
Figure 3.5: Imposed Waveform for Shakedown Test Program	73
Figure 3.6: User Interface for Shakedown Testing Program	73
Figure 3.7: Program Code for Shakedown Test Program	74
Figure 3.8: Program Code for Waveform Generator for shakedown test.vi sub-routine	75
Figure 3.9: User Interface for Constant Amplitude Waveform Program	77
Figure 3.10: Code Diagram for Constant Amplitude Waveform Program	78
Figure 3.11: Program code for Waveform Generator for Constant Amplitude.vi sub-routine	80
Figure 3.12: User interface for Structural Element Cyclic Loading program	82
Figure 3.13: Code for Structural Element Cyclic Loading Program	83
Figure 3.14: Program Code for Waveform generator for Full Test.vi	84
Figure 3.15: Program code for Construct Array.vi sub-routine	85
Figure 3.16: Flowchart detailing system integration	87
Figure 3.17: Separated actuator command console with signal conditioning unit	88
Figure 3.18: Integrated actuator command console	89
Figure 3.19: Actuator Control System with Computer Control	92
Figure 3.20: Comparison of intended displacement with external displacement transducer	94
Figure 3.21: Difference between internal displacement transducer and intended displacement	94
Figure 3.22: Difference between intended displacement and internal actuator displacement transducer measurement for Test 2.6 (Cyclic)	95
Figure 3.23: Force-Displacement response for specimen C.B.6.1 (Ryan, 2001)	96
Figure 3.24: Force-displacement response for specimen C.B.6.2 (Ryan, 2001)	97
Figure 3.25: Force-displacement response for specimen C.B.6.3 (Ryan, 2001)	97
Figure 4.1: Schematic Diagram of Experimental Specimen Set-up	102
Figure 4.2: Experimental Set-up (specimen 2.5)	102
Figure 4.3: Cyclic Parameters for a single cycle	104
Figure 4.4: Cyclic Area Parameters for a single cycle	104
Figure 4.5: End-Plate Dimensions for Test Series One	109

Figure 4.6: Eurocode 3: Annex J Design Moment-Rotation Characteristics	111
Figure 4.7: Measurement device locations in test series one	111
Figure 4.8: End-Plate Dimensions for Test Series Two	113
Figure 4.9: Predicted Moment-Rotation Relationship for Test Series Two	115
Figure 4.10: Measurement device locations in test series two	116
Figure 4.11: Eurocode 3: Annex J predictions for Test series 3	119
Figure 4.12: Measurement device locations in test series three	119
Figure 4.13: Moment-Rotation Relationship for Specimen 1.1	122
Figure 4.14: Moment-rotation hysteresis curve for Specimen 1.2	124
Figure 4.15: Final Deformed Joint for Specimen 1.2	125
Figure 4.16: Low cycle fatigue tearing of specimen 1.2 end-plate	125
Figure 4.17: Cyclic evaluation parameters for specimen 1.2	126
Figure 4.18: Moment-Rotation Curve for Specimen 1.4	128
Figure 4.19: Final Deformed Shape of Specimen 1.4	128
Figure 4.20: Cyclic Evaluation Parameters for Specimen 1.4	129
Figure 4.21: Moment-Rotation Curve for Specimen 1.5	131
Figure 4.22: Moment-Rotation Curve for Specimen 1.6	132
Figure 4.23: Cyclic Evaluation Parameters for Specimen 1.6	132
Figure 5.1: Failure mode interaction diagram for specimens 2.1 and 2.2	141
Figure 5.2: Moment-Rotation response for Specimen 2.1	143
Figure 5.3: Resistance Ratio for Specimen 2.1	143
Figure 5.4: Moment-Rotation Relationship for Specimen 2.2	144
Figure 5.5: Experimental evaluation parameters for specimen 2.2	145
Figure 5.6: Moment-Rotation characteristics for specimen 2.3	146
Figure 5.7: Example of applied filter for specimen 2.3	147
Figure 5.8: Moment-Rotation characteristics for specimen 2.4	148
Figure 5.9: Constant Amplitude Moment-Rotation characteristics for specimen 2.4	149
Figure 5.10: Resistance ratio for constant amplitude cycles for specimen 2.4	149
Figure 5.11: Cyclic evaluation parameters for specimen 2.4	150
Figure 5.12: Final deformed shape of specimen 2.4	151
Figure 5.13: Moment-rotation response for specimen 2.5	152
Figure 5.14: Moment-Rotation response for specimen 2.6	153
Figure 5.15: Cyclic evaluation parameters for Specimen 2.6	154
Figure 5.16: Moment-Rotation characteristics for specimen 2.7	155
Figure 5.17: Moment-Rotation response for specimen 2.8	156
Figure 5.18: Moment-Rotation relationship for Specimen 3.1	162

Figure 5.19: Underside of specimen 3.1 (post-test)	162
Figure 5.20: Beam strain gauge results (specimen 3.1)	163
Figure 5.21: Comparison of measured load and displacement (specimen 3.1)	164
Figure 5.22: Deformed shape of specimen 3.1	165
Figure 5.23: Moment-rotation relationship for specimen 3.2	166
Figure 5.24: Cyclic evaluation parameters for specimen 3.2	166
Figure 5.25: Moment-Rotation relationship for specimen 3.3	167
Figure 5.26: Underside of specimen 3.3 showing yield pattern	168
Figure 5.27: Cyclic evaluation parameters for specimen 3.3	169
Figure 5.28: Moment-Rotation relationship for specimen 3.4	170
Figure 5.29: Cyclic evaluation parameters for specimen 3.4	171
Figure 5.30: Moment-rotation relationship for specimen 3.5	172
Figure 5.31: Final deformed shape of specimen 3.5	172
Figure 5.32: Cyclic evaluation parameters for specimen 3.5	173
Figure 5.33: Moment-rotation relationship for specimen 3.6	174
Figure 5.34: Cyclic evaluation parameters for specimen 3.6	175
Figure 5.35: Moment-rotation relationship for specimen 3.7	176
Figure 5.36: Cyclic evaluation parameters for specimen 3.7	177
Figure 5.37: Moment-rotation relationship for specimen 3.8	178
Figure 5.38: Strain gauge #2 result from specimen 3.8	178
Figure 5.39: Cyclic evaluation parameters from specimen 3.8	179
Figure 5.40: Comparison of yield and ultimate rotation values	187
Figure 5.41: Comparison of partial ductility capacities	188
Figure 6.1: Graphical representation of model	192
Figure 6.2: σ - ϵ relationship	194
Figure 6.3: Moment-curvature diagrams for a mode 1 failure mechanism	197
Figure 6.4: Plastic rotation for a mode 2 failure mechanism	201
Figure 6.5: Moment-curvature diagrams for a mode 2: case 2 failure mechanism	203
Figure 6.6: Moment-curvature diagrams for a mode 2: case 3 failure mechanism	205
Figure 6.7: Moment-curvature diagrams for mode 2: case 4 failure mechanism	207
Figure 6.8: Quadrilinear modelling of the force-displacement curve	210
Figure 6.9: Typical moment-rotation for extended and flush end-plate joints	216
Figure 6.10: Equivalent length and breadth for cantilever approximation (Brown et al, 2001)	217
Figure 6.11: Equivalent plastic strains of end-plate (Tucker, 2002)	219
Figure 6.12: Column web effective widths	220

Figure 6.13: Coupling between T-stub force-displacement curves	223
Figure 6.14: Prediction and experimental curves for specimens 2.1, 2.2 and 2.4	225
Figure 6.15: Prediction and experimental curves for specimens 2.5	226
Figure 6.16: Prediction and experimental curves for specimens 3.1 and 3.2	227
Figure 6.17: Prediction and experimental curves for specimens 3.3 and 3.4	228
Figure 6.18: Prediction and experimental curves for specimens 3.5 and 3.6	228
Figure 6.19: Prediction and experimental curves for specimens 3.7 and 3.8	229
Figure 6.20: EC3: Annex J, predicted curve and experimental data for specimen 3.2	230
Figure 6.21: EC3: Annex J, predicted curve and experimental data for specimen 3.7	231
Figure 7.1: Elastic Response Spectrum (CEN, 2000)	237
Figure 7.2: Equivalent Seismic Forces	240
Figure 7.3: Case study 1 – 2-Storey, 1-bay frame	243
Figure 7.4: Case Study 2 – 4-Storey, 1-bay frame	246
Figure 7.5: Case Study 3 – 4-Storey, 4-bay frame	248
Figure 7.6: Case Study 4 – 7-Storey, 2-bay frame	251

List of Tables

Table 2.1: List of components for flush end-plate connections	12
Table 2.2: Eurocode 3 frame model type	15
Table 4.1: Description of experimental specimens	107
Table 4.2: Joint Properties for Test Series One	110
Table 4.3: Design Parameters for Test Series One	110
Table 4.4: Joint Properties for Test Series Two	113
Table 4.5: Predicted Design Parameters for Test Series Two	114
Table 4.6: Specimen properties for test series three	118
Table 4.7: Predicted Design Parameters for Test Series Two	118
Table 4.8: Specimen Experimental Properties for Test Series One	121
Table 4.9: Comparison between Experimental Results and Eurocode 3 Predictions	134
Table 5.1: Specimen Experimental Properties for Test Series Two	141
Table 5.2: Comparison between Experimental Results and Eurocode 3 Prediction Model	157
Table 5.3: Specimen Experimental Properties for Test Series Three	160
Table 5.4: Comparison between experimental results and Eurocode 3 design calculations	181
Table 6.1: Suggested material properties for Grade 43 steel (Faella et al, 1999)	194
Table 6.2: Parameters depending on material properties	211
Table 6.3: Comparison between predicted experimental joint characteristics	224
Table 7.1: Recommendations for design using the Wind-Moment Method	236
Table 7.2: Parameters for Type 2 response spectrum (CEN, 2000)	238
Table 7.3: Behaviour Factors and Structure ductility classes	239
Table 7.4: Joint Failure Mode and Behaviour factors	239
Table 7.5: Summary of design loadcases	241
Table 7.6: Design Ground Acceleration (g) for Case Study 1	243
Table 7.7: Joint details for Case Study 2	245
Table 7.8: Design Ground Acceleration (g) for Case Study 2	245
Table 7.9: Joint details for Case Study 3	249
Table 7.10: Design Ground Acceleration (g) for Case Study 3	249
Table 7.11: Joint details for Case Study 4	252
Table 7.12: Design Ground Acceleration (g) for Case Study 4	253
Table 7.13: Summary of critical design ground accelerations	255

Chapter 1

Introduction

1.1 Introduction

In the design of joints for moment-resisting steel frame buildings, it is common to assume that the joints are either fully rigid (continuous construction) or perfect hinges (simple construction). For design in seismic regions, rigid joints are preferred either for moment resistance or because semi-rigidly connected frames are considered too flexible. Towards this end, most earthquake-resistant designs specify full-strength heavily welded beam-column joints, with the result that the advantages of semi-rigid joints, such as lower construction costs and simpler fabrication procedures, cannot be realised. In recent years it has been noted that semi-rigid joints may be used to great advantage in frames situated in areas of low to medium seismic risk, and the wind-moment joints advocated for use in the United Kingdom would seem well-suited to this application. These joints, illustrated in Figure 1.1, are usually characterised as semi-rigid, partial-strength joints that yield in a controlled and ductile manner. To ensure this ductile response, careful selection of design details such as end-plate thickness and bolt size is essential.

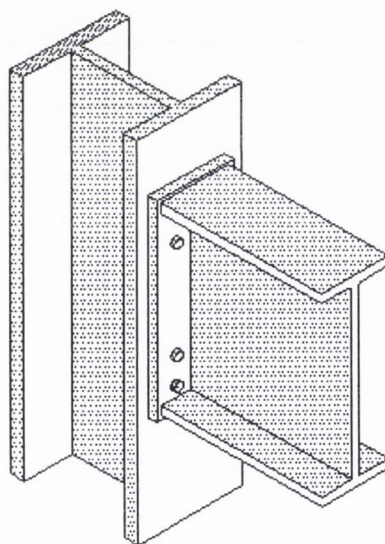


Figure 1.1: Typical wind-moment joint (flush end-plate)

In earthquake regions, as elsewhere, steel frames may be designed as moment-resisting or braced. While the design of more complex building structures may involve the use of structural cores and hybrid construction, the majority of designs are executed by considering idealised collections of plane frames. In comparison with braced structures, the greatest disadvantage associated with moment-resisting frames is the large interstorey deflections experienced under service load conditions. Eurocode 8 (CEN, 2000), for instance, limits allowable interstorey drift to 1.5% of storey height, and this becomes the controlling criterion in many designs.

Nevertheless, moment-resisting frames are often favoured in design because of the freedom they offer the internal arrangement of the building. In seismic design, such frames are especially attractive as, with correct detailing, they may possess high global ductility capacities. This ductility allows the seismic energy input during an earthquake to be dissipated through repeated inelastic cyclic deformations, justifying the use of large seismic force reduction factors. This is achieved by following the capacity design approach, in which the relative strengths of connected frame elements are controlled to ensure a desired pattern of inelastic behaviour. Specifically, the resistances of energy-dissipative elements are designed to be lower than those of connected elements in which seismic energy is not intended to be dissipated. In moment-resisting frames, it is usual for the dissipative zones to take the form of plastic hinges in beams, while elastic conditions are maintained in columns and joints. However, there is no reason in principle why joint elements cannot be considered as potential dissipative zones, unlike columns where inelastic frame stability problems can arise.

The wind-moment design approach is a well established method for the design of unbraced steel frames. The method relies on the rotational stiffness of the joints to resist any horizontal loading, such as wind-loading, and assumes that the joints are pinned when considering vertical loads such as gravity loading. This 'simple' design approach is allowed for in BS 5950 (BSI, 1990) and Eurocode 3 (CEN, 1993). Now recognised as a form of semi-continuous design, the wind-moment method allows the economic benefits offered by the use of semi-rigid joints to be realised. Frames designed using such joints have been shown to be practical and economical when the wind-moment method is used within recommended limits.

In earthquake engineering, the use of spectral design accelerations and force reduction (or 'behaviour') factors allows earthquake-resistant designs to be verified using simplified sets of equivalent static forces. Consequently, the design process commonly reduces to the provision of a structural system with adequate lateral resistance and stiffness.

Many of the same issues are encountered when designing for wind loads. When semi-continuous construction is employed, the use of standard details can be beneficial: joint stiffness and moment capacity can be readily evaluated from design tables, while sufficient ductility can be assumed. This ductility is guaranteed by following a procedure similar to the capacity design approach favoured in earthquake-resistant design. One or more components of the joint are selected as the yielding locations, while all others are required to remain elastic, irrespective of the level of response. Typically, weld failure is prevented because it is considered a brittle response mode, while column shear panel or end plate yielding is encouraged.

For earthquake resistance in moment-resisting frames, steel joints must be sufficiently stiff (for serviceability requirements), strong (for ultimate limit state requirements), ductile (when energy dissipation is required) and display a symmetrical response under cyclic loading conditions.

Stiffness:

Although the primary need for adequate joint stiffness is to limit interstorey displacements, it also has implications for the natural vibration period of the structure. An accurate estimate of this period is necessary if design seismic forces are to be evaluated accurately. Conventional column design procedures also rely upon reasonable estimates of joint stiffness. For static load conditions, improved stiffness can be achieved through the use of thicker end plates and column flanges, the addition of column web stiffeners, or the use of deeper beams. However, during strong ground motion, cyclic inelastic joint response will display continuously varying stiffness characteristics and not all of these approaches may remain valid.

Strength:

The yield and ultimate moment resistances required from a joint will depend on the seismic action and force reduction factors employed in a given design. Adequate resistance is provided by the conventional approach of employing deeper beams and larger joint elements. Whenever a joint is selected to be a dissipative zone, the capacity design approach requires an accurate and reliable upper bound estimate of joint resistance, as well as the lower bound normally required. A conservatively low estimate of resistance will not therefore suffice. In this context, it may be useful to identify those components of the joint whose resistance can be determined accurately, and to ensure that these become the controlling features of joint behaviour.

Ductility:

In earthquake-resistant design, the ductility capacity of a structure or member must be sufficient for the seismic force reduction factor employed. As with the wind-moment method, designers are not required to quantify the ductility capacity of individual members, instead standard design details are available which, when followed, are deemed to provide a known level of ductility. These details are normally stipulated in terms of semi-empirical rules, based on experimentally demonstrated cyclic response characteristics. Typically, test specimens are required to repeatedly display the same resistance in three or more cycles of the same amplitude.

While high levels of ductility capacity are always attractive, the ductility demand on a dissipative structural element will vary with both peak ground motion and yield resistance.

Hence, in regions with low or moderate design seismic actions, or in designs where small force reduction factors are employed, less ductility will be required.

In addition to determining the location of the plastic hinges in moment-resisting frames based on the above parameters, it is also possible to pre-determine the failure mode of the joints in that frame. Therefore, a frame that is designed to allow the joints to yield, and hence control the failure of that frame, may still possess varying levels of global ductility. BS 5950 and Eurocode 3 both define three standard failure modes for joints that may be represented by bolted T-stubs. Based on the failure mode of the joint, the frame may provide higher or lower levels of seismic resistance. Therefore, a moment-resisting frame should not only be designed to incorporate the location of the yield points but also the manner of the joint failure.

1.2 Scope of Research Study

Despite the advantages of pre-determining the joint failure mode in a frame, very little work has been done in this area. The majority of work in the area of joint failure in frame systems has concentrated on the pre-determination of the hinge location in the frame. While having the joint yield holds advantages, these may be negated by the type of failure mode. In addition, much of the work in this area has concentrated on the joint failure mode under monotonic testing. It is possible that continuous load reversals and fatigue may adversely affect the joint behaviour. The principal areas in which work is needed are explained below.

1. Eurocode 3: Annex J provides a design model for the use of semi-rigid partial strength joints under monotonic loads. This design model is capable of producing a moment-rotation behaviour curve for a large number of joint typologies including extended and flush endplates, top and seat angles and web angle joints which may be represented using equivalent T-stubs. The Eurocode 3 design model is able to determine the joint failure mode based on the ratio of flexural resistance of the T-stub to axial resistance of the bolts. These failure modes have been shown to be accurate for monotonic loading and are widely accepted in practice. However, no work has been done to determine if these modes continue to be valid under cyclic or dynamic loads.
2. As the Eurocode 3 design model is intended to be used with a wide range of joint details and joint types, some simplification must be accepted. However, previous work has raised doubts over the accuracy of the design moment-rotation behaviour for both extended and flush end-plate joints produced with this method. The design moment-rotation characteristics must be compared to experimental results with regard to the rotation capacity, moment resistance and stiffness of the joint.

3. The Eurocode 3 design model also lacks the means to predict the failure rotation of a joint. Simplified rules are presented to determine if the joint possesses adequate rotational capacity for use in a global frame analysis. For use under monotonic loads, this would normally be adequate. However, under seismic loads, the rotational demand on a joint and hence the structure may be much higher. Based on this, an accurate model of the joint ductility capacity is required if these joints are to be used in areas of seismic activity. Although Eurocode 8 already provides this to some extent by the use of behaviour factors, a model capable of producing available ductility for a particular joint would remove some of the uncertainty in the use of these factors.
4. As stated above, it is possible to control the failure behaviour of a frame by pre-determining the location of plastic hinges. However, if the joints are chosen as the location of the plastic hinges, which will happen if partial strength semi-rigid joints are employed, the failure mode of the joint could affect the global behaviour of the frame under cyclic and seismic conditions. There have been no studies done on how this joint failure mode will affect the seismic design forces acting on a frame, and hence the maximum ground acceleration for the frame.

To advance the level of knowledge in these areas, a combined experimental and analytical programme of research has been undertaken. The joints in this study were confined to flush end-plate joints with two bolt rows. To assess the moment-rotation characteristics of these joints under cyclic loading, an extensive series of experiments were carried out. In order to facilitate this work, a new control system was developed for the servo-hydraulic actuators available. A total of twenty-two specimens were tested under both monotonic and cyclic loads, employing different joint details. These details included the beam and column sections, the end-plate thickness, the bolt size and the bolt grade. Combinations of the various joint details were used to control the failure mode of the joints which were then evaluated for resistance and rotational capacity. These experimental results were first compared to the Eurocode 3 design model results for both the moment-rotation characteristics and the failure modes. A prediction model was then developed, the results from which were also compared with the experimental results. The final part of the study was to perform a small series of seismic design frame analyses to determine the affects the joint failure modes would have on the maximum ground acceleration that the frames could withstand. These frames are analysed using the Eurocode 3 joint characteristics as well as those from the new prediction model. The presentation of this work is outlined in the following section.

1.3 Organisation of Thesis

Chapter 2 presents a comprehensive literature review on the behaviour of semi-rigid joints and frames. Frame definitions are first outlined, followed by methods of classifying joints based on their stiffness and strength. A proposed classification method based on rotational capacity is also presented. The failure modes for the joints is then set out as defined in Eurocode 3. As earthquakes involve sudden load reversals and changes in the strain rates, a discussion of the effects of these on steel and joints is presented. Thereafter, a limited review of previous experimental work on semi-rigid joints and frames is presented, followed by a comprehensive review of modelling techniques for joint behaviour. These techniques range from simple mathematical models to highly complex finite element solutions. Using this review, the optimum model for the joint type under consideration could be chosen.

In Chapter 3, a new computer-based test control system developed as part of this study is presented. The software used for this system was a graphical programming language called LabVIEW which has been developed specially for use in laboratory studies. This software provides commands to the data acquisition hardware that controls the hydraulic test system. Three separate programs were developed to facilitate a wide range of applications. The first is a “Shakedown test Program”. This program imposes a small displacement wave on the specimens and records data obtained from measurement devices. This allows the user to check that everything is working correctly before executing a full test. The second program developed was the “Constant Amplitude Test Program”. This program was designed to impose a set number of constant amplitude displacement cycles on a specimen. The first of these cycles can also be considered as a monotonic test if the displacement amplitude is large enough. The third program is the “Structural Cyclic Test Program”. This program was developed to impose an increasing amplitude displacement wave on the specimen. All of these programs are capable of simultaneously controlling the actuator system while reading from multiple measurement devices. The program code is set out in Chapter 3 and the integration of the computer into the test system is explained. Tests carried out to investigate the accuracy of the system are also presented. The versatility of the system is demonstrated with a short discussion of the testing of some reinforced concrete specimens.

Chapter 4 is the first of two experimental chapters in the thesis. The experimental procedures and parameters employed are fully explained in this chapter. The experiments in this study were divided into three separate test series. The details of the experimental specimens are presented for all three series, along with the design moment-rotation characteristics from Eurocode 3: Annex J. This is followed by the experimental results from the first test series. Not all of these experiments were successful and, therefore the results are not considered to be fully reliable. The moment-rotation characteristics of each specimen are presented and the results discussed in terms of

resistance capacity, resistance drop and failure mode. The results are also compared to the design characteristics and the discrepancies are discussed.

The second experimental chapter is Chapter 5 in which the results from the second and third test series are presented. Again, the results are discussed in terms of moment resistance capacity, rotational capacity, and failure mode. The Eurocode 3 design calculations are compared to these results, showing similar discrepancies to those observed in the first test series. The joint behaviour for all three experimental series is summarised in terms of failure mode, ductility and cyclic evaluation parameters such as the resistance drop. The implications of the differences between the experimental results and the design characteristics are discussed and a number of recommendations are made with regard to the use of flush end-plates with Eurocode 3: Annex J.

In Chapter 6, a moment-rotation prediction model is presented. This is a T-stub model for flush end-plates similar to those tested as part of this study. The model was developed using a force-displacement curve model developed for extended end-plate joints combined with a second model for the column web behaviour under compression, tension and shear. The assumptions and approximations required for the model are listed and explained. The formula required to calculate the moment-rotation curve are presented fully. Results from the prediction model are then compared to the experimental results. The discrepancies between the model and experimental results are discussed and the accuracy of the prediction results is shown.

Chapter 8 presents a small study carried out on the behaviour of frames with different joint failure modes. These frames are all designed using the wind-moment method and the joints details selected accordingly. Linear pushover analyses are carried out on these frames using both the Eurocode 3 design calculations and the new prediction model results. The results from these analyses are compared with each other and with the results of a pushover analysis of a rigidly jointed frame. Recommendations on design behaviour factors and joint failure modes are given.

In the final chapter, a summary of the work is presented along with the principal conclusions. The areas in which further research is required are identified.

Chapter 2

Literature Review of Semi-Rigid Joints and Frames

2.1 Introduction

In the last three decades, a large body of research has been produced with regard to the behaviour of frames and the influence of the beam-to-column joints. As this study concentrates on the non-linear response of flush end-plate joints under cyclic loads, it is important that a clear understanding of the joint behaviour under static loads is obtained. To this end, this chapter begins by defining the difference between a joint and a connection. These two terms are often used interchangeably by engineers involved in both research and practice.

The classification of frames is presented. Frames are classified as either braced or unbraced, and sway or non-sway based on the lateral stiffness and the influence of second order effects. Methods of classifying the behaviour of joints are then presented. These joint methods commonly refer to the strength or the stiffness of the joint compared to the connected members. A third classification method, recently proposed, is also presented, although it has not been finalised as yet. Based on the frame classification and the joint classification, the type of analytical model to be used for a particular frame may be determined.

This is followed by a discussion of the static failure modes of certain types of joints. These joints encompass top- and seat-angles, extended end-plate, flush end-plate, welded and any other type that may be designed using the guidelines set out in Eurocode 3: Annex J employing a tee-stub model. A review of research carried out of the effects of increased strain rate is then presented. As cyclic loading is often used to approximate earthquake loading, an understanding of how the sudden and dramatic load reversals would affect the response is highly important. This review covers work directly related to the behaviour of steel joints as well as the material properties.

The next section presents conclusions from some of the experimental work carried out into semi-rigid joints. This section begins with a review of beam-to-column sub-assemblages experiments. The second part is concerned with full scale tests carried out on frames that employ semi-rigid joints. It should be noted that this study is not exhaustive and is intended only to give a broad outline, due to the volume of research available. These types of tests are important to gain accurate responses for the modelling of joints. Numerous modelling techniques are presented in the final section. These range from simple curve fitting techniques to highly complex finite element programs. These techniques are discussed and conclusions are drawn on the usefulness of the different methods.

2.2 Joint Definition

Steel building frames consist of beam and column elements assembled together by means of joints. These joints may consist of beam-to-beam splices, beam-to-column joints or column-to-foundation bracing joints. However, in practice, and in much of the literature, the terms joint and connections are often used interchangeably when discussing the interactions between members. The two terms actually refer to different areas of interest. The definition employed by Eurocode 3: Annex J (1998) appears to be the most consolidated one and has been accepted by a number of researchers (Nethercot & Zandonini, 1990; Faella et al, 2000; Kirby et al, 1990). In this definition, the connection is defined as the set of physical components that comprise the joint as well as the actual location of the fastening between the structural elements. The joint is defined as the connection combined with the interaction zone of the elements under consideration. This is illustrated in Figure 2.1.

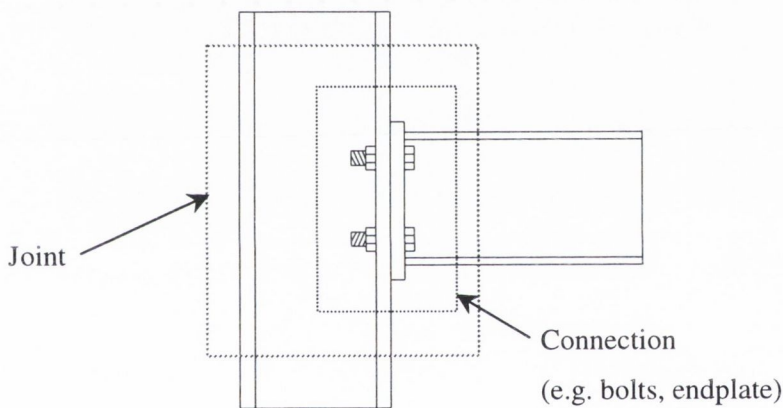


Figure 2.1: Illustrated definition of joint and connection

The actual components of the connection set vary depending on the type of joint that is being considered. For flush end-plate joints, as are investigated in this study, six main components that must be considered. These components are shown in Table 2.1, together with the principal forces affecting each of them. In a major axis beam-to-column joint, it is possible to identify three main sources of joint deformability. These are shown in Figure 2.2 and are as follows:

- The shear deformation of the column web which is assumed to be caused by the forces carried through the beam flanges. These forces can also be assumed to be statically equivalent to the beam moment;


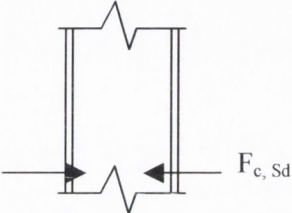
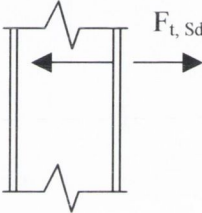
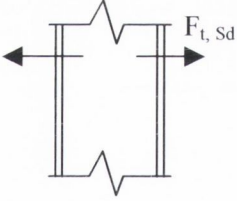
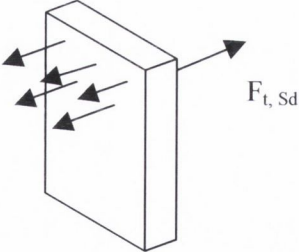

Component Description	Component Diagram	Component Diagram
1 Column Web panel in Shear		
2 Column Web in compression		
3 Column Flange in bending		
4 Column Web in tension		
5 End-Plate in bending		
6 Bolts in tension		

Table 2.1: List of components for flush end-plate connections

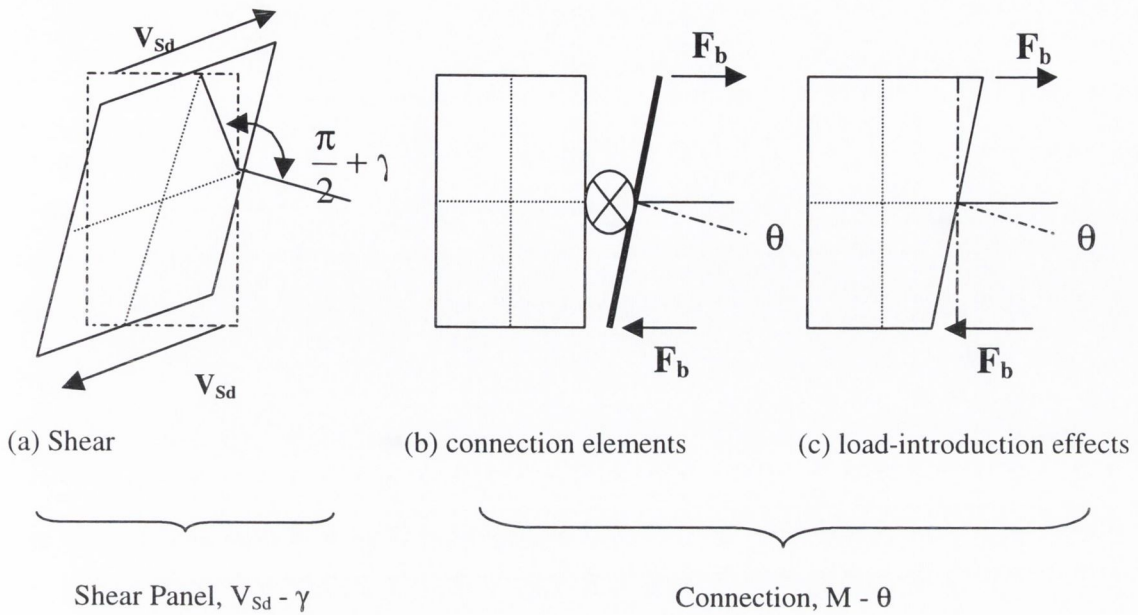


Figure 2.2: Sources of joint deformability

- The deformation of the connection which is defined as the rotational deformation of the connection elements, such as the end-plate, bolts and the column flange; and
- The deformation effects of load-introduction on the column web from the connecting elements.

To obtain the full moment-rotation characteristics for a joint it is necessary to combine the moment-rotation curve of the connecting elements, the moment-rotation curve of the load-introduction effects and the shear-deformation for the shear panel.

Eurocode 3 also defines four other important structural properties that are associated with the behaviour of a joint which are illustrated in Figure 2.3, and are defined as follows:

- The design moment resistance of a joint, M_{Rd} , which is equal to the peak value of the design moment-rotation characteristics;
- The design moment of a joint, M_{Sd} , is the moment imposed on the joint at a particular point in the loading life;
- The rotational capacity of a joint, θ_{Cd} , is taken as the rotation achieved in the joint at the maximum design moment resistance, M_{Rd} (likely to be conservative);
- The rotational stiffness of a joint, S_j , is taken as the secant stiffness of the moment-rotation characteristics for a particular joint. The initial rotational stiffness used in Eurocode 3, $S_{j,ini}$, is the stiffness associated with the elastic range of the design moment-rotation relationship

Once the structural properties of the joint have been determined, these can then be integrated into a global frame analysis.

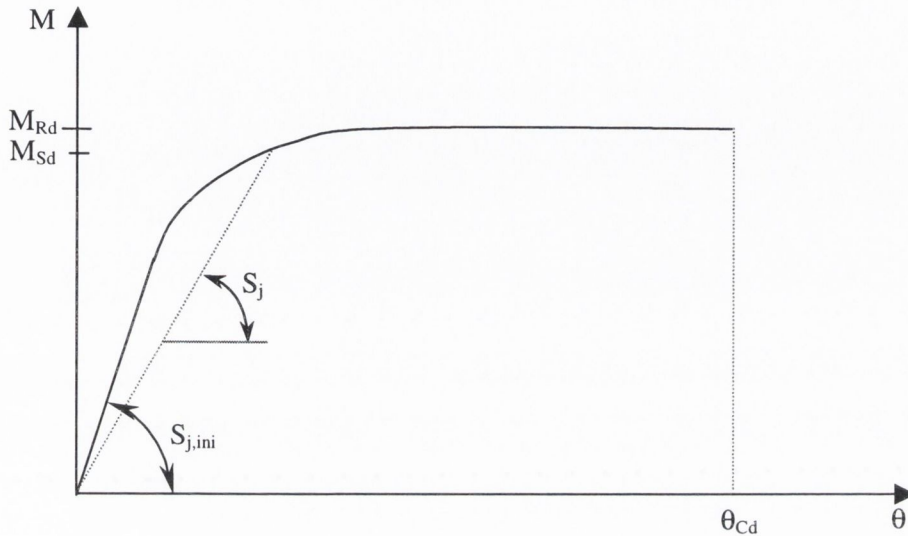


Figure 2.3: Structural properties of a joint

2.3 Classification of Steel Frames

Eurocode 3 classifies steel frames according to the structural system used to provide resistance to lateral displacements. The two classifications are braced and unbraced frames. A frame is considered to be braced if adequate resistance to lateral displacements is supplied by a bracing system. Eurocode 3: clause 5.2.5.3 states that this bracing system must contain sufficient stiffness to reduce the horizontal displacements by a minimum of 80% (CEN, 1992). This allows the designer to safely assume that all of the horizontal loads imposed upon the structure are resisted by the bracing system. If these conditions are not fulfilled, the frame is classified as unbraced.

A second classification may also be made based on the sensitivity of the frame to second order effects in the elastic range. A frame may be classified as non-sway if the in-plane lateral stiffness is sufficiently high to justify neglecting second order effects in internal forces and moments. Any other frame is classified as a sway frame and second-order effects must be considered. Eurocode 3 states that a frame may be classified as non-sway for any given load case if the elastic critical load ratio is less than or equal to 10, or stated numerically:

$$\frac{V_{Sd}}{V_{Cr}} \leq 10 \quad \text{Eqn. 2.1}$$

where V_{sd} is the design load value for a particular load case and V_{Cr} is the elastic critical load for failure in a sway mode.

In traditional design methodologies, engineers have usually assumed that the joints in a steel frame behave in one of two different manners: nominally pinned or rigid. In a nominally pinned joint, it is assumed that the joint is incapable of transferring any beam moment to the column. Therefore, the joints only have to transfer the shear force from the beam to the column. In comparison, a rigid joint has a very high rotational stiffness. Therefore, the beam end reaction and the end moment are transferred to the beam and continuity is preserved with no rotation of the beam relative to the column. Frames with these types of joints are modelled as *pinned*, in the first case, and *continuous* for the second case. In reality, most joints behave somewhere in between these two ideals, or in a semi-rigid manner. The joint usually possesses some rotational stiffness that allows the transfer of moment from the beam to the column. Modern design codes allow for this behaviour and have introduced the *semi-continuous* model, allowing the design of a steel frame to be based on the actual load versus deformation behaviour of the joint. Based on the joint classification (see section 2.4) and the type of global analysis required, the type of frame model required may be determined, as illustrated in Table 2.2

Method of Global Analysis		Classification of Joint	
Elastic	Pinned	Rigid	Semi-Rigid
Rigid-Plastic	Pinned	Full-Strength	Partial-Strength
Elastic-Plastic	Pinned	Rigid and Full Strength	Semi-Rigid and Partial Strength Semi-Rigid and Full Strength Rigid and Partial Strength
Type of Frame Model	Simple	Continuous	Semi-Continuous

Table 2.2: Eurocode 3 frame model type

A similar method of classification has been introduced by the American Institute of Steel Construction (AISC, 1986, 1989) for the design of steel frames. The Allowable Stress Design, or ASD, specifications (AISC, 1989) lists three frame types for use in the design of a multi-storey frame:

- **Type 1** frames are rigid frames in which the joint stiffness is assumed to be sufficiently high to prevent any rotation between the members. These joints are sometimes referred to

as moment connections as they are capable of transferring all of the moment between members with no deformation. Type 1 frames are similar to the continuous model in Eurocode 3.

- **Type 2** frames are analogous to the pinned model in Eurocode 3. The joints in these frames are incapable of transferring any moment and are referred to as shear connections. These joints are only capable of resisting gravity and other vertical loads.
- **Type 3** frames are designated as semi-rigid frames. These frames are based on intermediate values of moment capacity and rotational stiffness. They fall into a category between the Type 1 and Type 2 frames and are similar to the semi-continuous model in Eurocode 3.

The load and resistance design factor, or LRDF, specifications (AISC, 1986) allow for two types of frames based on the restraint type:

- **Type FR**, or fully-restrained, which corresponds to the ASD Type 1 frame.
- **Type PR**, or partially-restrained, which covers Type 2 and 3 from the ASD specifications. If type PR is to be used, the effects of joint rotation must be considered in the design of the structure.

However, all frame types may still be classified as braced or unbraced frames regardless of which type or model is chosen.

2.4 Classification of Structural Steel Joints

Eurocode 3 and BS5950 classify joints in two different ways: by stiffness and by strength, based on the properties of the frame for which the joints are intended. The classifications provided are pinned, semi-rigid and rigid for stiffness, and pinned, partial strength and full strength for strength. Based on the classification of the joint, a global analysis methodology may be determined for the steel frame.

Joint classifications by stiffness and strength are set out below as defined in Annex J of Eurocode 3 (1998). The concepts are discussed and the governing formulae are presented. It has also been proposed (Kuhlmann & Fürch, 1997) that in order to correctly classify joints, the ductility, or rotational capacity of the joint must also be considered, and this classification method is also discussed below.

2.4.1 Classification by Stiffness

The classification of joints using stiffness is based on the comparison of the design joint stiffness to two stiffness boundaries. This is illustrated in Figure 2.4, in which M_j is the moment in the joint, θ_j is the rotation of the joint and $S_{j,ini}$ is the initial stiffness of the joint as defined in section 2.2. For the sake of simplicity in design, the boundaries have been defined to allow a direct comparison with the *initial* design joint stiffness.

The classification of joints are dependant on the ratio $\frac{EI}{L}$, which is the flexural stiffness of the connected member, and $S_{j,ini}$ which is the initial stiffness of the joint..

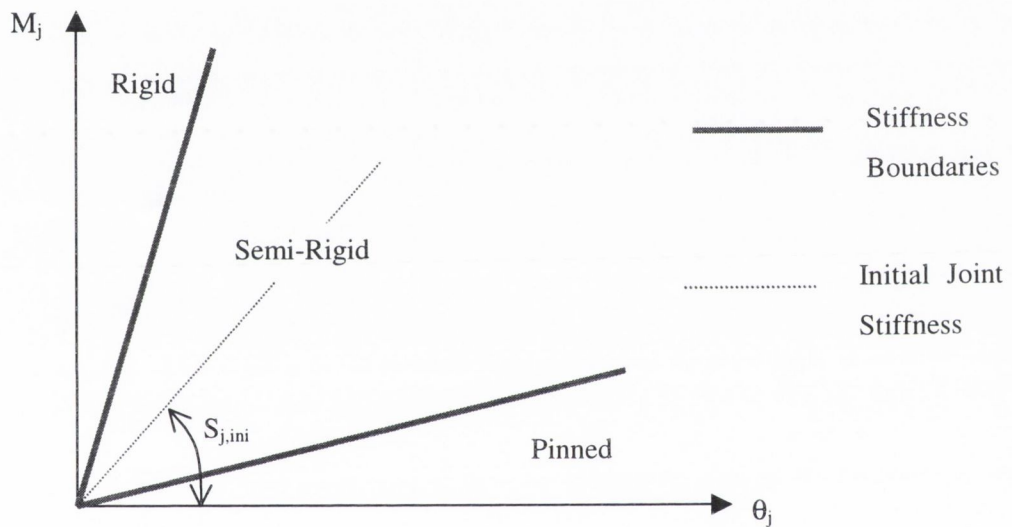


Figure 2.4: Stiffness Classification Boundaries

However, the boundaries depend on whether the type of frame to be analysed is braced or unbraced. This allows for the greater flexibility expected in unbraced frames or sway frames. The stiffness boundaries for the classification are given as follows:

- **Rigid Joint**

$$S_{j,ini} \geq \frac{25EI}{L} \quad (\text{Unbraced Frames}) \quad \text{Eqn. 2.2}$$

$$S_{j,ini} \geq \frac{8EI}{L} \quad (\text{Braced Frames}) \quad \text{Eqn. 2.3}$$

- **Semi-Rigid Joint**

$$\frac{EI}{2L} < S_{j,ini} < \frac{25EI}{L} \quad (\text{Unbraced Frames}) \quad \text{Eqn. 2.4}$$

$$\frac{EI}{2L} < S_{j,ini} < \frac{8EI}{L} \quad (\text{Braced Frames}) \quad \text{Eqn. 2.5}$$

- **Pinned Joint**

$$S_{j,ini} \leq \frac{EI}{2L} \quad (\text{All Frames}) \quad \text{Eqn. 2.6}$$

2.4.2 Classification by Strength

To classify joint behaviour by strength, the design moment resistance of the joint, $M_{j,Rd}$, is compared to the moment resistance of the weaker of the connected elements, either the beam or the column as shown in Figure 2.5. In the case of strength classification, the full-strength boundary is taken as the lower of the beam or column moment resistances. The pinned value is assumed to be one-fourth of the full-strength value. If the joint moment resistance is lower than this value, it is assumed that it is unable to transfer any moment to the column.

The classification boundaries based on the strength of the joint are as follows:

- **Full-Strength Joint**

$$M_{j,Rd} \geq M_{\text{Full-Strength}} \quad \text{Eqn. 2.7}$$

- **Partial Strength Joint**

$$\frac{M_{\text{Full-Strength}}}{4} < M_{j,Rd} < M_{\text{Full-Strength}} \quad \text{Eqn. 2.8}$$

- **Pinned Joint**

$$M_{j,Rd} \leq \frac{M_{\text{Full-Strength}}}{4} \quad \text{Eqn. 2.9}$$

where $M_{\text{Full-Strength}}$ is the design resistance of the weaker of the member elements.

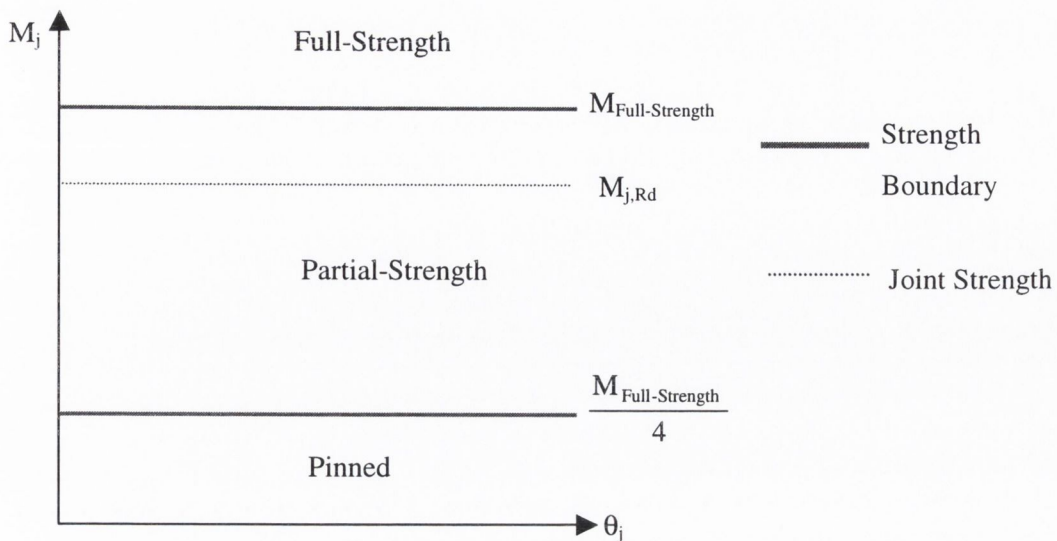


Figure 2.5: Strength Classification Boundaries

2.4.3 Classification by Rotation, or Ductility, Capacity

A classification system based on the rotational capacity of joints for use in plastic analysis has recently been proposed under the framework of the COST program in the University of Stuttgart (Kuhlmann & Fürch, 1997). The rotational capacity of a section, whether a member or joint, characterises the ability of a plastified section to rotate while maintaining the ultimate design moment resistance. However, due to strain-hardening effects, the actual resistance moment often exceeds the ideal plastic moment. Based on their web and flange slenderness, members can be divided up into four distinct classes as given in Eurocode 3 section 5.3.2. These classifications are widely accepted and thus a verification of rotation capacity is not required here. It is proposed that joints be classified according to the rotation capacities derived from their connection elements' deformation capacity. The deformation capacity of these components can be distinguished by their mode of failure which falls into one of the three categories defined below.

- **Components with High Ductility:** These components, such as the column web in shear, column flange in bending or the end-plate in bending, have a plateau type response as shown in Figure 2.6 (a). The deformation capacity of these components is very high or nearly unlimited.
- **Components with Limited Ductility:** After reaching a maximum load level, the resistance of these components decreases, normally due to buckling or instability. At a certain point, the resistance of the component falls below the ultimate resistance, F_{Rd} , as shown in Figure

2.6 (b). The deformation at this point, δ_c , is considered the failure point for the component. Components with limited ductility include column webs in compression or beam flanges and webs in compression.

- **Components with Little or No Ductility:** These components, such as bolts in tension, allow very little deformation as the load increases. They are liable to fail in a sudden or brittle manner, with little or no warning. It is possible that these components will be unable to reach the full resistance. This is shown in Figure 2.6 (c).

It has been proposed that joints should be classified in a system that is analogous to that defined in Eurocode 3 for members. To this end the following classes of joints have been defined:

- **Class 1** joints are those able to reach the ultimate design moment resistance, and with a sufficiently good rotation capacity to allow plastic design of the frame.
- **Class 2** joints are those able to reach the ultimate design moment resistance, but with a reduced plastic rotation capacity. A plastic verification of the sections is allowed.
- **Class 3** joints are those where brittle failure (or inherent instability) limits the moment resistance and does not allow full redistribution of the internal forces in the joint.

This classification system has yet to be finalised. A great deal of work has to be completed to verify the rotation capacity for various joint typologies. As the verification of all of the connection components and the interplay of the various effects described above is too complex to consider at present, simplified rules such as those used for member cross-sections are required.

2.5 Discussion of Joint Failure Modes

Some modern design codes allow for the modelling of certain joint typologies using an equivalent tee-stub method to represent joint components. These codes include Eurocode 3 (1998) and BS 5950 (1990). The typologies considered include top- and seat-angles, beam splices, fully-welded, extended and flush end-plate joints.

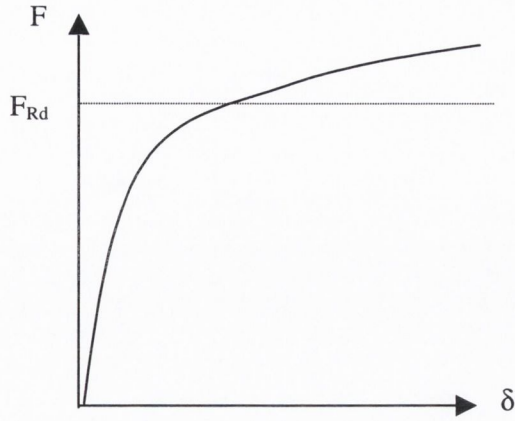


Figure 2.6 (a): Components with High Ductility

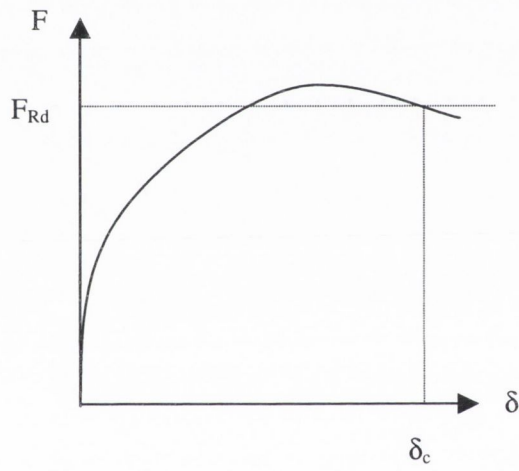


Figure 2.6 (b): Components with Limited Ductility

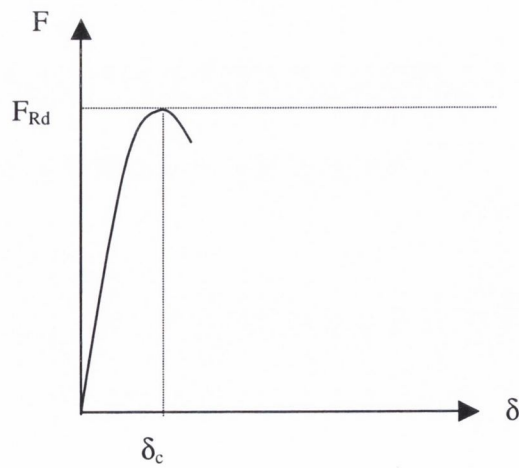


Figure 2.6 (c): Components with Brittle Failure

Figure 2.7 illustrates the equivalent tee-stub for a single bolt row in a flush end-plate joint. The effective length, l_{eff} , of the tee-stub is a notional length and does not necessarily correspond to the actual physical length of a joint component. The effective length of the tee-stub is calculated from the joint geometry, the assumed yield line pattern, the location of the bolt row and the number of bolt-rows being considered. The yield line patterns can be circular or non-circular as shown in Figure 2.8. In the case of the joints in this study, there are no inner bolts, so only the end-bolt row case applies as detailed in Eurocode 3: Annex J.

Using these equivalent tee-stubs it is possible to further classify joints according to their failure mode. Eurocode 3: Annex J and BS 5950 both define three failure modes for a tee-stub. These failure modes may be used to sub-classify a joint. For example it is possible that a semi-rigid partial strength joint could be Mode 1, Mode 2 or Mode 3. This sub-classification is used extensively throughout this study, and is illustrated in Figure 2.9. The Mode 1 failure mechanism is defined as yielding of the end-plate, or column flange, only. This results in plastic hinges forming at the bolt-line and at the beam web line. In this failure mode, the bolts are expected to remain perfectly elastic throughout the joint response. The second failure mechanism, Mode 2, results when the end-plate yields at the beam flange line, followed by yielding of the bolts. Mode 3 failures occur when the end-plate remains elastic while the bolts yield. In general, Mode 1 joints can be expected to possess the highest ductility, but also the lowest stiffness and moment resistance. In contrast, Mode 3 joints tend to have the highest levels of moment resistance but are subject to a brittle failure mechanism, with little or no prying forces. Mode 2 joints can resist intermediate moments, while remaining reasonably ductile.

The failure mode of a particular tee-stub is dependant upon the geometry of the joint (Figure 2.9(a)), the axial resistance of the bolt, B_{Rd} , and the flexural resistance of the end-plate, $M_{\text{f,Rd}}$, where

$$M_{\text{f,Rd}} = \frac{l_{\text{eff}} t_f^2}{4} f_y \quad \text{Eqn. 2.10}$$

The ratio of flexural design resistance to axial bolt resistance is defined as:

$$\beta_{\text{Rd}} = \frac{4M_{\text{f,Rd}}}{2B_{\text{Rd}}m} \quad \text{Eqn. 2.11}$$

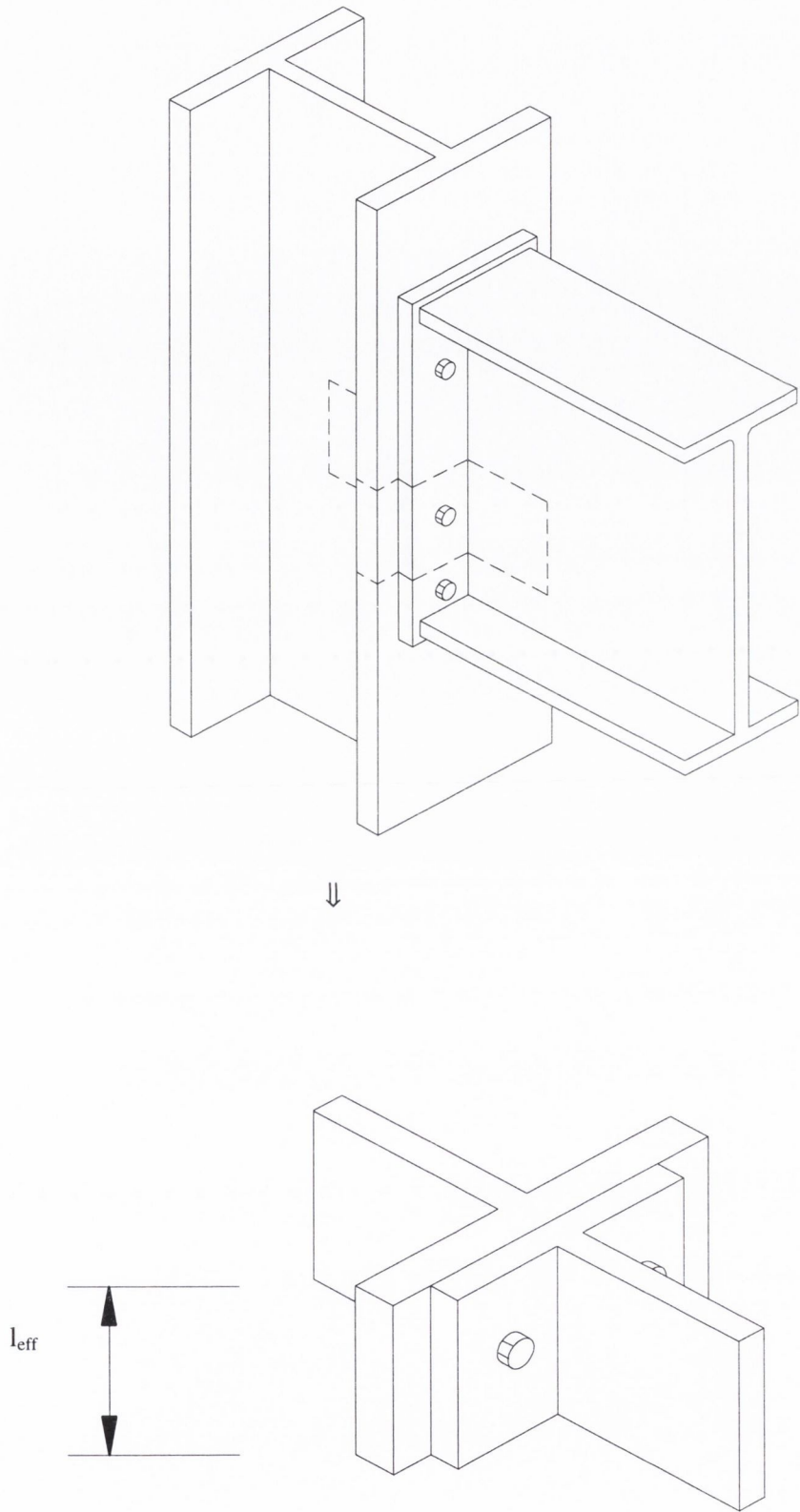


Figure 2.7: Equivalent Tee-Stub for a flush end-plate joint

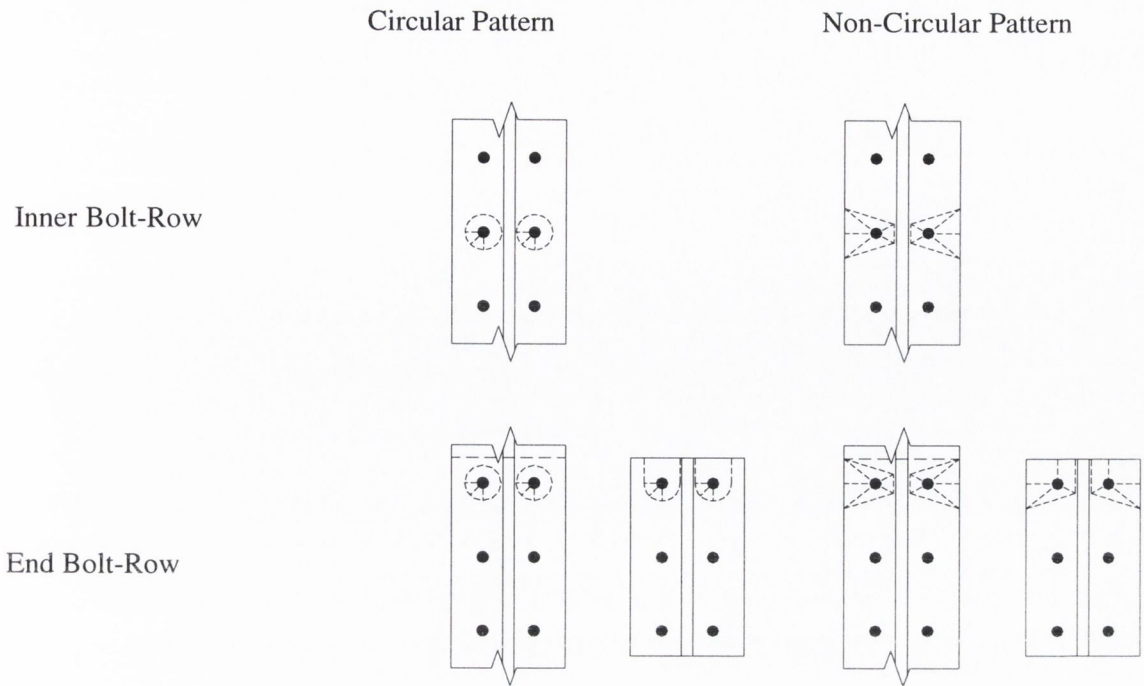


Figure 2.8: Yield line patterns for equivalent tee-stubs (Eurocode 3, 1998)

In Eurocode 3: Annex J, the following limit values for the design resistance, F_{Rd} , are defined to determine the failure mechanism for a particular tee-stub.

$$F_{Rd} = \min\{F_{1,Rd}, F_{2,Rd}, F_{3,Rd}\} \quad \text{Eqn. 2.12}$$

where

$$F_{1,Rd} = \frac{4M_{f,Rd}}{m} \quad \dots \text{ Mode 1} \quad \text{Eqn. 2.13}$$

$$F_{2,Rd} = \frac{2M_{f,Rd} + 2B_{Rd}n}{m+n} \quad \dots \text{ Mode 2} \quad \text{Eqn. 2.14}$$

$$F_{3,Rd} = 2B_{Rd} \quad \dots \text{ Mode 3} \quad \text{Eqn. 2.15}$$

where l_{eff} is the effective length of the tee-stub, t_f is the thickness of the plate and f_y is the yield strength of the material.

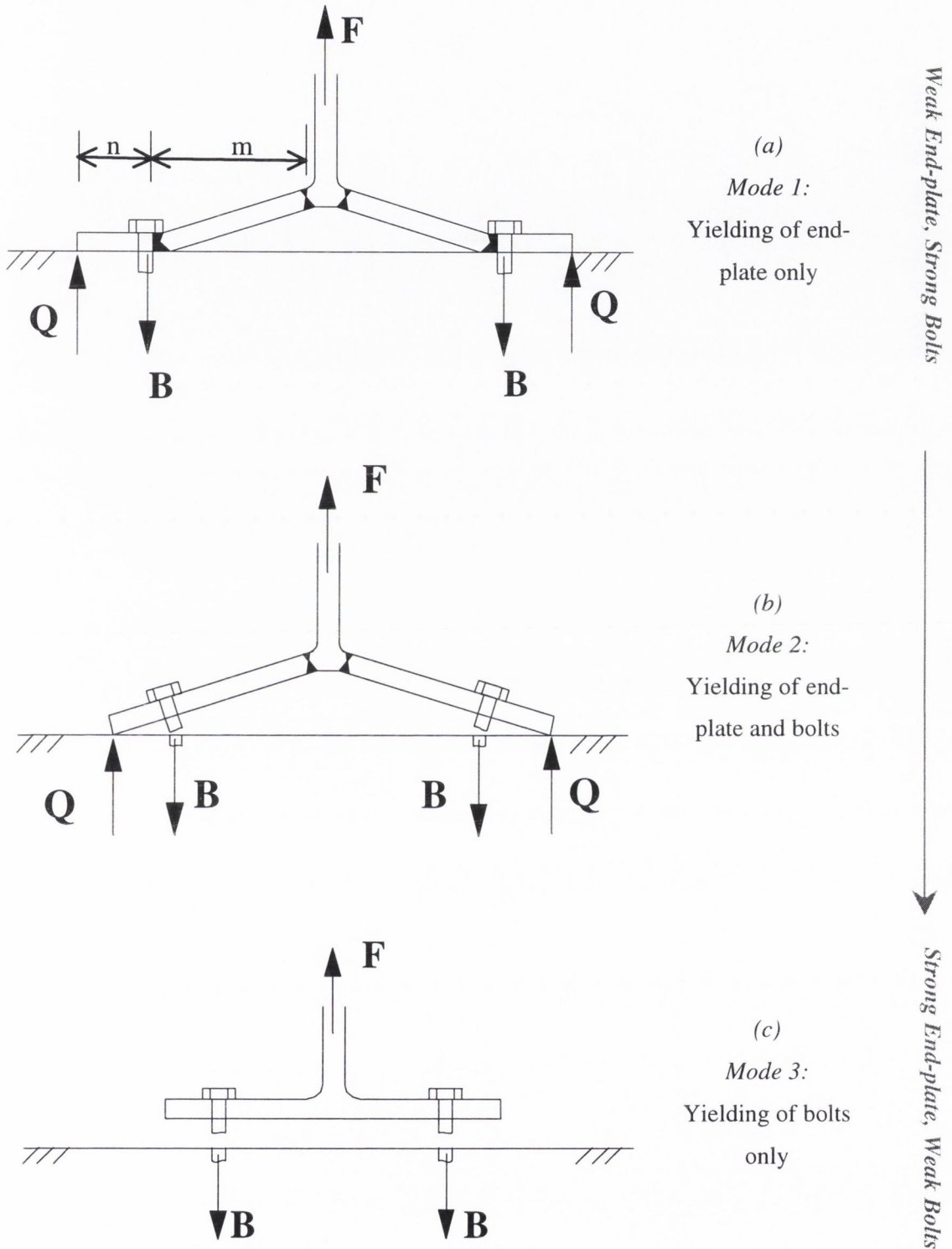


Figure 2.9: Failure Modes of equivalent Tee-stubs

It is recognised that the failure mechanism of a tee-stub is governed by β_{Rd} which is also the ratio of design resistances for Mode 1 and Mode 3 mechanisms. Defining a non-dimensional geometric

parameter $\lambda = n/m$, the following conditions may be derived:

- Mode 1 mechanism occurs when $\beta_{Rd} \leq \frac{2\lambda}{1+2\lambda}$;
- Mode 2 mechanism occurs when $\frac{2\lambda}{1+2\lambda} < \beta_{Rd} \leq 2$; and
- Mode 3 mechanism occurs when $\beta \geq 2$.

These conditions are represented graphically in a non-dimensional form in Figure 2.10.

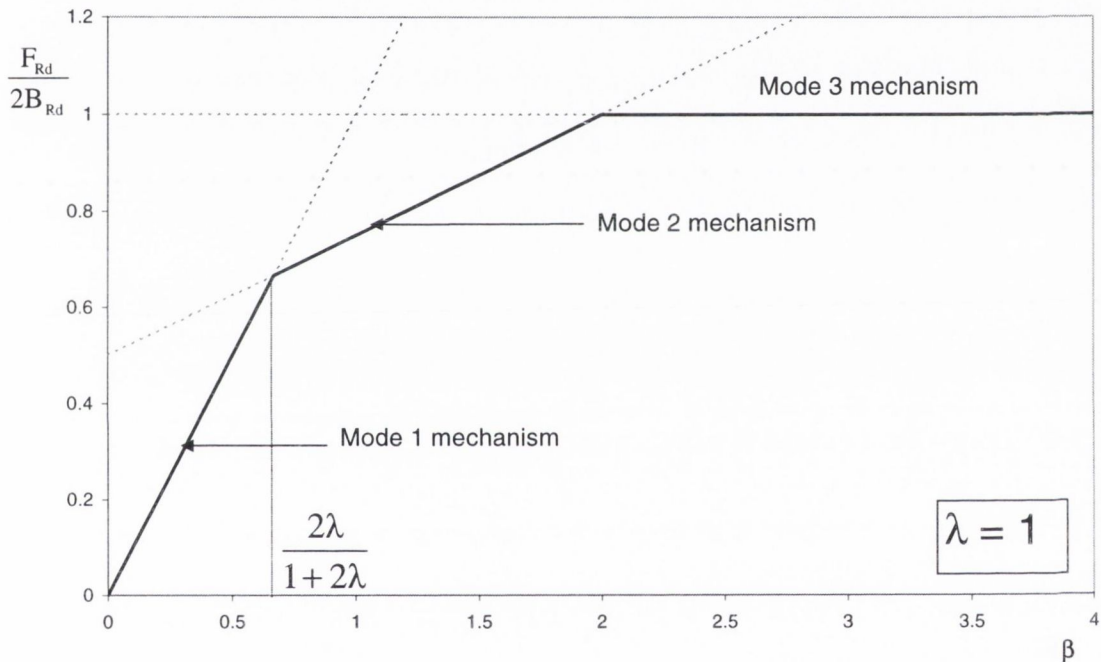


Figure 2.10: Graphical representation of failure mechanisms (Eurocode 3, 1998)

It should be noted that the above equations do not take into account moment-shear interaction in the tee-stub. Research done in this area, notably by Faella et al (2000) has shown that the moment-shear interaction influence is related to the ratio m/t_f . The following equation for the design resistance for a Mode 1 failure mechanism was developed using internal equilibrium equations:

$$F_{1,Rd} = \frac{2V_{f,Rd}}{\sqrt{3}} \frac{m}{t_f} \left\{ \left(1 + \frac{3}{\left(\frac{m}{t_f} \right)^2} \right)^{\frac{1}{2}} - 1 \right\} \quad \text{Eqn. 2.16}$$

The ratio, $\bar{F}_{1,Rd}$ between the design resistance of a Mode 1 mechanism including moment-shear interaction and the design resistance of the same mechanism neglecting moment-shear interaction is therefore:

$$\bar{F}_{1,Rd} = \frac{F_{1,Rd}^m}{4M_{f,Rd}} = \frac{2}{3} \left(\frac{m}{t_f} \right)^2 \left\{ \left[1 + \frac{3}{\left(\frac{m}{t_f} \right)^2} \right]^{\frac{1}{2}} - 1 \right\} \quad \text{Eqn. 2.17}$$

Using Eqn. 2.17, it may be shown that for $m/t_f \geq 2.5$, the reduction in the design resistance due to moment-shear interaction is less than 10% and may therefore be neglected. A similar equation has been developed for Mode 2 failure mechanisms, from which it is found that the reduction in design resistance is less than 4% for $m/t_f \geq 2.5$. Due to the geometric proportions required to obtain a Mode 2 failure mechanism, this ratio is nearly always exceeded, and therefore moment-shear interaction effects may be neglected. Mode 3 mechanisms are not affected by moment-shear interaction influences as the critical component are the bolts.

2.6 Strain-rate Effects on Steel Members and Joints

As the majority of testing is carried out in a quasi-static manner, concerns have been raised with regard to the rate of loading imposition on the specimens. As quasi-static loading is carried out at a relatively slow rate, strain-rate effects may be neglected as internal forces are able to equalise as the loading is imposed. In an earthquake load, or other type of pulse loading such as blast or impact, the loading is imposed at a much higher rate. This may lead to different material properties being displayed. This is especially relevant for near-source earthquakes where spectral velocities can be much higher than those assumed in design.

The first research work carried out on the effects of strain-rate on material behaviour was carried out by Manjoine (1944). Tests were carried out using strain-rates varying from $9.5 \times 10^{-7} \text{ sec}^{-1}$ to 0.3 sec^{-1} . The results, reproduced in Gioncu (2000) and shown in Figure 2.11, indicate an increase in yield stress with strain-rate. The increase in the ultimate tensile strength was less dramatic. Due to the change in the ultimate to yield stress ratio, a decrease in the material ductility occurs.

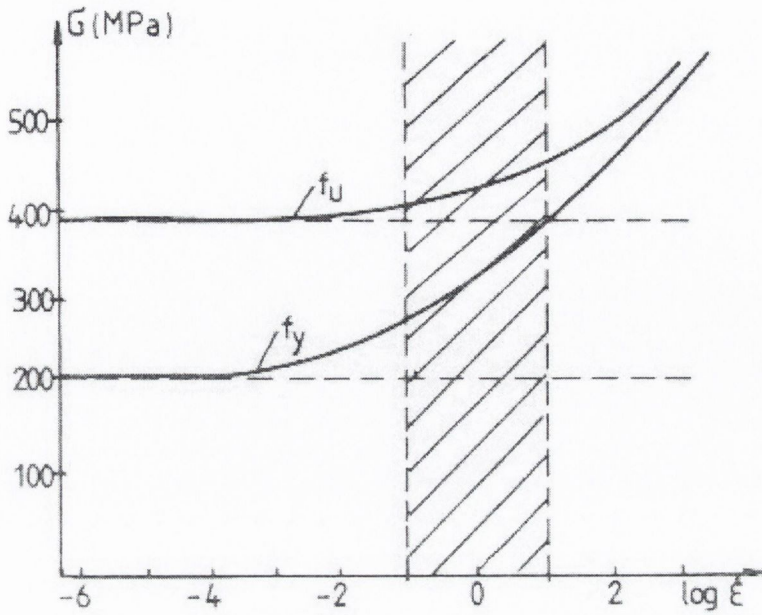


Figure 2.11: Influence of strain-rate effects on properties of steel (Gioncu, 2000)

In recent years, experimental results have confirmed previous studies and allowed material laws to model the influence of strain-rate (Wright & Hall, 1964, Soroushian & Choi, 1987, Kasser & Yu, 1992). Using these constitutive material laws, it is possible to relate the yield stress and the ultimate stress of a material to the strain-rate as shown.

Wright & Hall (1964): $10^6 < \dot{\epsilon} < 10^3$

$$\frac{f_{ys}}{f_y} = 1 + 2.77 \exp[0.162(\log \dot{\epsilon} - 3.74)] \quad \text{Eqn. 2.18}$$

Soroushian & Choi (1987): $10^{-4} < \dot{\epsilon} < 10^1$

$$\frac{f_{ys}}{f_y} = 1.46 - 4.51 \times 10^{-7} f_y + (0.0927 - 9.2 \times 10^{-7} f_y) \log \dot{\epsilon} \quad \text{Eqn. 2.19}$$

$$\frac{f_{us}}{f_u} = 1.15 - 7.7 \times 10^{-7} f_y + (0.0497 - 2.44 \times 10^{-7} f_y) \log \dot{\epsilon}$$

Wallace & Krawinkler (1989): $10^{-5} < \dot{\epsilon} < 10^1$

$$\frac{f_{ys}}{f_y} = 0.973 + 0.45(\dot{\epsilon})^{0.53} \quad \text{Eqn. 2.20}$$

Kasser & Yu (1992): $10^{-4} < \dot{\epsilon} < 10^1$

$$\frac{f_{ys}}{f_y} = 1.289 + 0.109 \log \epsilon + 0.009 (\log \dot{\epsilon})^2 \dots \dots f_y = 320 \text{ N/mm}^2$$

$$\frac{f_{ys}}{f_y} = 1.104 + 0.302 \log \epsilon + 0.002 (\log \dot{\epsilon})^2 \dots \dots f_y = 495 \text{ N/mm}^2$$

Eqn. 2.21

where f_{ys} and f_{us} are the yield and ultimate stresses due to strain-rate effects, $\dot{\epsilon}$ is the strain rate, and f_y and f_u are the nominal yield and ultimate stresses. Under earthquake conditions, the likely strain rate is approximately 10^{-3} . Based on the above relationships and assuming $f_y = 275 \text{ N/mm}^2$, this results in a f_{ys} of approximately 285 N/mm^2 . Therefore, it may be assumed that the yield stress of mild steel is not significantly affected by the increased strain rate encountered under earthquake loading.

In the last few years, the emphasis on strain-rate testing has moved from how material properties alter under different strain-rates towards how members and beam-to-column subassemblies respond under increased strain-rates. Uang & Bondad (1996) carried out a series of five tests on pre-Northridge bolted-web welded-flange joints to investigate the effects of increased strain-rates. Three of the tests were carried out in a quasi-static manner using the ATC-24 protocol, while the remaining two specimens were tested dynamically using a modified version of the protocol. The strain-rate effect on the following parameters was investigated: plastic deformation capacity, energy dissipation characteristics and the failure mode of the joints. A comparison of the static and dynamic test results showed that the deformation capacity and the energy dissipation characteristics were reduced by an increase in the strain-rate. It was found that the deformation capacity was reduced by approximately 50%, while the energy dissipation was at the lower bound of the static test results. It was also noted that the increased loading rate resulted in brittle cracking of the joints being propagated and the final fracture pattern being altered.

Beg et al (2000) carried out a large series of tests to investigate the effects of increased strain-rate on fillet and butt welds in joints. The experimental results displayed no significant change in the ultimate strain when the strain rate was increased. However, it was determined that welds that were intended to be used in joints subjected to high strain-rates should be designed to be as strong as the connection elements. Based on the results from the weld tests, a series of full-scale joints were tested under increased strain-rates. These joints consisted on both welded and bolted end-plate joints. It was seen that the increase in strain-rate resulted in an increase in the yield and ultimate resistance of the joint, in agreement with the previous work on material properties. In the bolted joints, ultimate failure was due to brittle fracture of the beam flange. This is similar to the

ultimate failure mode of these joints under quasi-static loading. It was also seen that the ductility of all of the joints was dramatically reduced, in some cases by up to 50%. It was concluded that although the failure mode of these joints were not affected by the strain-rate, the effects on the joint response were significant and could not be neglected.

Sanchez & Plumier (2000) carried out further tests based on the above work. These experiments consisted of three joint types, the extended end-plate, the dog-bone joint and a partial strength joint. The loading was imposed as sinusoidal waveforms with two distinct frequencies, 0.4 Hz and 0.025 Hz, to give different strain-rates. It was observed that the increased strain-rate increased both the yield and ultimate stresses in the joint. However, the yield stress, f_y , was increased more than the ultimate stress, f_u . This resulted in the creation of local concentrations of plastic strains in the joint and brittle failures, therefore reducing the available ductility. Such increased local strain demand has the knock-on effect of reducing the fatigue life of the specimens. It was also noted that the energy dissipation capability of the joints was reduced as the strain-rate was increased. However, in contrast with Uang and Bondad, there was no evidence reported to suggest that the ultimate failure mode was altered by the increased strain-rate.

Based on previous work with regard to strain-rate effects on the properties of steel and steel beam-to-column joints, the following points may be determined.

- An increase in the strain-rate will result in an increase in both the yield stress, f_y , and to a lesser degree, the ultimate tensile strength, f_u ;
- The resulting change in the yield to ultimate strength ratio generates higher local plastic strain demands. This has the effect of inducing brittle failures in the material. In turn, these brittle failures reduce the available ductility of the material, and consequently of the joints.
- Increased strain-rates also reduce the energy dissipation characteristics of the material, which in turn contributes to brittle failure, and reduces the plastic deformation capacity available.
- There is differing opinion on the influence of the strain-rate on the ultimate failure mode of the specimen.

2.7 Experimental Studies on Joint and Frame Behaviour

In the last two decades, a great deal of experimental research has been carried out into the behaviour of semi-rigid joints under static and monotonic loads. This research has varied from tests on beam-column sub-assemblages to experiments carried out on full scale frames. Most of this work has concentrated on testing angle joints and extended end-plates. Although there has been some experimental work on flush end-plate joints, this has not been to the same extent as with other joint typologies. The research reported in this section therefore examines the behaviour of numerous types of semi-rigid partial strength joints and not just flush end-plate joints. The section is divided into two parts. The first section reviews tests carried out on semi-rigid joints outside of the entire frame. While this type of experiment is the most common and is relatively easy to set-up, there are limitations in the application of the experimental data to full-scale frame response. The second section discusses experimental work on frames utilising semi-rigid joints and investigating how these joints influence overall frame behaviour. While these tests are usually much more comprehensive, but are also more difficult to set-up and execute, as well as more expensive.

2.7.1 Beam-to-Column Sub-assembly Tests

Testing of beam-to-column sub-assemblages has been carried out for many years with early experiments carried out on riveted joints by Baker and Rathbun in the early 1900s (Nethercot & Zandonini, 1990). However, only since the early 1970s has the usefulness of testing semi-rigid joints truly been realised.

Kennedy (1969) carried out large series of 24 tests on angle and end-plate shear joints with differing levels of moment-shear interaction. The results from these tests showed a number of points when the results between the angles and plates were compared. The end-plate joints behaved in a very similar overall manner to the angle joints, although detailed behaviour differed. All of the joints displayed the same moment-rotation behaviour regardless of the moment-shear interaction ratio. There was also a certain degree of stiffness hardening noted. This was attributed to the lower beam flange bearing against the column. As will be seen in chapter 4, this is also important when investigating the behaviour of flush end-plate joints.

In 1987, Davison et al carried out a series of static cruciform experiments on a variety of different joint typologies including cleats, extended and flush end-plate joints. These connections were attached to both the column flange and web for comparison. The goal of the test series was to comparatively assess the different joints in terms of rotational stiffness, ductility and moment resistance capacity. The web cleat joints showed very flexible behaviour until the beam flange

came into contact with the column, as had already been noted by Kennedy (1969). Flange cleat joints behaved in a bi-linear fashion with a constant stiffness up to approximately 15% of the beam moment capacity at which point the stiffness quickly degraded until the behaviour became nearly perfectly plastic. Similar behaviour was observed for the top- and seat angle joints. The flush end-plate joints displayed large differences in behaviour depending on whether the plate was connected to the column web or the unstiffened column flange. The flush end-plate joints were also tested without the beam flange welds and this did not appear to seriously affect joint performance. It was noted that the use of a lighter column section reduced the initial rotational stiffness while increasing the ductility of the joint.

Popov (1987) investigated the effects of the column panel zone and continuity plates (column web stiffeners) on joint flexibility. A series of full scale welded-flange bolted-web joint specimens were tested cyclically. In order to remove the panel zone contribution to the moment-rotation characteristics, a number of the specimens were rigidly attached to a testing frame. These joints were tested and compared with tests results from joints where the panel zone was allowed to contribute to the behaviour. The panel zone was found to make a large contribution to the joint ductility, so that a properly designed column may be used to prevent inelastic rotations of the connected beam. Further improvements in moment capacity and rotational capacity may be achieved by the use of column web stiffeners in these types of joints.

Ghobarah et al (1990, 1992) carried out two series of cyclic tests on extended end-plate joints. The first series of experiments consisted of five beam-to column joint sub-assemblages tested in the inelastic range to determine the effects of design parameters on the moment-rotation characteristics. These design parameters included end-plate thickness, column flange stiffeners and bolt pre-tension loading. In all cases it was found that the design forces predicted were conservative, with an average ratio of actual force to design force of 1.4. Based on these results it was concluded that if the following rules are adhered to, end-plate joints can provide adequate ductility for use in seismic zones:

- The use of unstiffened columns is not recommended. If the column is unstiffened, the end-plate should be designed to sustain 1.3 times the plastic moment capacity of the weaker connected member to allow for strain hardening.
- As significant drop-offs in the bolt pre-tension load was noted during the test, the bolts should be designed to a minimum force of 1.3 times the plastic moment capacity of the beam.

The second test series consisted of four beam-to-column sub-assemblages. The behaviour of

individual components of the joint, such as the beam, column, connection elements and panel zone, was examined, as was the overall behaviour. The performance of the joint and its components was assessed in terms of stiffness, strength, ductility and energy dissipation capacity. As in the first series, the experimental capacity of each joint exceeded the design capacity. It was found, as in the case of Popov (1987), that the column panel zone is a very ductile component when correctly designed and is capable of undergoing large numbers of strain reversals without displaying any significant distress. By comparing the energy dissipation characteristics of the column panel zone, beam and connection, it was observed that the joints that provide the best performance in terms of moment capacity and ductility levels are those where the panel zone and beam are allowed to yield together. By allowing these two components to provide higher load carrying capacity through strain hardening, and higher ductility through large inelastic deformations, the connecting elements (end-plate, bolts, and column flange) can remain elastic. This may be used to avoid severe damage to the joint. It was also seen that the end-plate of the joint effectively controlled the plastic deformation of the panel zone. This was done by comparing the experimental panel zone deformation with a model prediction. Finally the authors recommended more research into the contribution of the panel zone into the overall joint behaviour.

Tsai and Popov (1992) carried out a limited number of cyclic tests on extended end-plate joints to investigate the use of stiffeners and the contribution of the bolts to joint response. A standard joint was first tested as a control. This joint was then modified by the addition of flange stiffeners and the use of an increased bolt diameter. It was observed that the end-plate was much more rigid near the inner bolts than outside of the beam flanges. It was noted that the addition of flange stiffeners below the beam flange caused the forces in the bolts to equalise between the inner and outer bolts. The use of stiffeners together with an increased bolt diameter was seen to increase the rotational capacity of the joint by 45%; an increase in the end-plate thickness had a similar effect.

Static cruciform tests were carried out on a series of flush and extended end-plate joints by Bose and Hughes (1995) and Bose (1998). The purpose of these experiments was to investigate the moment-rotation response of joints with varying end-plate thicknesses and bolt sizes. In the case of all but one test, the observed moment capacities were between 60% and 120% greater than those predicted by Annex J of Eurocode 3. From these tests, three different types of joint failure were identified as column web buckling, bolt failure and end-plate fracture. It was also observed that there were two distinct types of bolt failure: a classical fracture mechanism and stripping of the bolt threads. Based on the experimental observations, it was recommended that joints with a rotational capacity of 30 mrad or greater should be considered to be ductile while those joints with a capacity of 20 mrad or less should be considered brittle. When the experimental results from these tests were compared with predictions made by the Eurocode and BS 5950, it was found that both codes

resulted in unconservative estimates of initial stiffness and moment capacity. Of greater importance, it was discovered that BS 5950 predicts unsafe buckling resistances for these joint types when compared to the experimental results and Eurocode 3.

Adey et al (1998, 2000) carried out a series of cyclic tests on extended end-plate joints in which the details of the joints were varied. The details varied included the beam size, bolt layout, end-plate thickness and the inclusion of stiffeners. It was found that an increase in beam size resulted in a reduction in the energy dissipation capacity of the joint, while increasing the thickness of the end-plate increased the energy dissipation capacity. However, the greatest increase in performance was achieved by the joints including extension stiffeners. These joints combined high moment capacity, high rates of energy dissipation per cycle and high total dissipated energy. The joints with a tight bolt configuration were observed to display rupture of the end-plate at the outer side of the beam flange and had comparatively low energy dissipation characteristics.

2.7.2 Full-scale Semi-Rigid Frame Experiments

There has been very little experimental work carried out on full-scale semi-rigid frames. Instead, a common practice has been to carry out tests on beam-to-column sub-assemblages and use the data obtained to analyse the frames. This is likely due to the large scope of the tests and the expense of full-scale tests compared to sub-assemblages. However, in the last decade, a number of full-scale tests have been carried out investigate the effects of semi-rigid joints on the global frame behaviour.

In 1992, Takanashi et al (Elnashai & Elghazouli (1994), Elghazouli (1996)) carried out experiments on five frames employing both rigid and semi-rigid joints. These frames were subjected to monotonic, cyclic and pseudo-dynamic testing regimes. The rigid joints consisted of fully-welded beam-columns, while the semi-rigid joints employed top- and seat-angles. In the frames employing semi-rigid joints, the rigid joints were simply replaced with the semi-rigid counterparts. It was found that the semi-rigid frames displayed much lower stiffness as well as lower yield and ultimate capacities. It was also noted that the response displacements of the semi-rigid frames were lower than the rigid frames indicating a higher period of vibration for the structure. It was also noted that the hysteresis curves of the frame displayed stable and ductile responses for the semi-rigid frames.

Elnashai et al (1998) carried out three cyclic tests on similar semi-rigid frames in addition to the five discussed above. Based on the results of these and the previous tests, it was determined that semi-rigid frames could be used for seismic design. It was observed that the hysteretic behaviour

of the frames was highly stable through out the loading process. It was also noted that the elastic stiffness of the joint had a significant effect on the global frame stiffness. For a reduction of 50 – 60% in the joint stiffness, a corresponding decrease of 20 – 30% was noted in the frame stiffness. It was also seen that a decrease in the joint capacity resulted in a decrease in the frame capacity. As would be expected, the interstorey drift of the frame was the limiting factor in all of the semi-rigid frames. Although very large rotations could be achieved in every test, it was observed that the interstorey drift limit of 3% was violated. At this level of interstorey drift, joint over-strength factors of 1.4 – 1.6 were observed. Finally, it was noted that current seismic design codes did not include provisions for this type of structure.

Yu et al (1998) carried out a tests on ten frames employing extended end-plate joints. The joint details were varied by changing the end-plate thickness and the bolt diameter. The frames were subjected to the combined actions of beam loads, column axial loads and horizontal loads. The series was designed to investigate the joints under hogging and sagging moments. It was determined that different behaviour of extended end-plate joints under these moments must be considered when carrying out an analysis of frames of this type. It was found that the joint stiffness is the critical component when providing resistance to sway and load carrying capacity, but the column base stiffness also plays a larger part than expected.

Kozlowski (1999) carried out field testing on a steel frame during construction. The frame employed flush end-plate joints similar to those being examined in this study. As the frame could not be tested to destruction, all loading and deformations were limited to two-thirds the nominal yield values. It was found that the column base was closer to the rigid joint boundary rather than the pinned case, as is usually assumed in practice. This influenced the frame behaviour against sway under horizontal loads. A secondary influence on the frame behaviour is the level of bolt pre-loading. The tests were carried out for increasing levels of bolt pre-load. It was observed that the stiffness of the frame was increased as the pre-load was increased.

Iványi & Varga (1999, 2000) tested six frames with flush end-plates under cyclic loads. The frames consisted of two story, one-bay frames with pinned column bases. The tests were set up to determine the level of influence supplementary web plates would have on the global frame behaviour. Preliminary results show that the use of web plates resulted in a significant increase in joint stiffness and hence in the frame stiffness. In one test, the plates were omitted in order observe the drop in joint capacity. However, there was little effect on the capacity of the joint or the frame.

2.8 Methods of Joint Modelling

This section examines a number of prediction models ranging from the early mathematical models to mechanical analogues and the newer sophisticated finite element packages. Each type of prediction model is discussed with regard to its advantages and disadvantages compared to the other available methods. Finally, conclusions are drawn as to which type of model is the most suitable for flush end-plate design and seismic loading conditions.

Much of the early work in the modelling of joint behaviour consisted of fitting mathematical expressions to experimentally obtained data. While this work expanded the understanding of semi-rigid joint behaviour, the accuracy of the experimental work and the amount of available data limited its applicability. One of the biggest problems in modelling the experimental behaviour of steel joints is the large range of joint types available. Therefore, no matter how many experiments are carried out on semi-rigid joints, other types not covered by the data will always remain. However, it is possible to select the types of joints being tested to ensure that the more common types are all accounted for. Over the last three decades modelling of steel beam-to-column joint behaviour has become more feasible with the development of computers and non-linear analysis techniques. One such method uses mechanical analogues that represent each part of the joint as a plate or a stiffened spring. Each part is assigned certain characteristics that are representative of the connection properties. A great deal of work has been carried out in this area in the last number of years, but as will be explained below, it is still limited in its application. Finite element analysis has also been used to examine the behaviour of joints under dynamic loads, and has been shown to give very accurate results. However, this accuracy is dependant upon the careful selection of appropriate elements and mesh.

2.8.1 Mathematical Models

There are two main approaches to $M-\theta$ curve prediction using mathematical models. The first of these fits curves to experimental data, while the second method uses simple analytical models. This second type relies on determining the major sources of flexibility in the joint by observing its experimental behaviour. Therefore, both of these types of models depend on accurate experimental data, are therefore limited in application.

2.8.1.1 Experimental Curve Fitting Models

Much of the early work in this field was limited due to the nature of analytical abilities when dealing with elastic-plastic behaviour, and consisted of a straight-line tangent to the initial $M-\theta$ curve. This early work is attributed to the efforts of Rathbun (1936) and Baker (1934) and led to

the definition of a semi-rigid joint factor, Z , defined as the rotation per unit moment (Nethercot & Zandonini, 1989).

$$Z = \frac{\theta}{M} \quad \text{Eqn. 2.22}$$

However, it wasn't until the late 1960's that proper curve fitting techniques were used. These consisted of using bi-linear curves to approximate M - θ curves. It was noted that most M - θ curves consisted of a linear section at the start, followed by a non-linear section, which in turn became linear again before failure was reached. A reasonable representation of such a M - θ curve could be approximated by using two straight lines at tangents to the two linear sections of the curves shown in Figure 2.12.

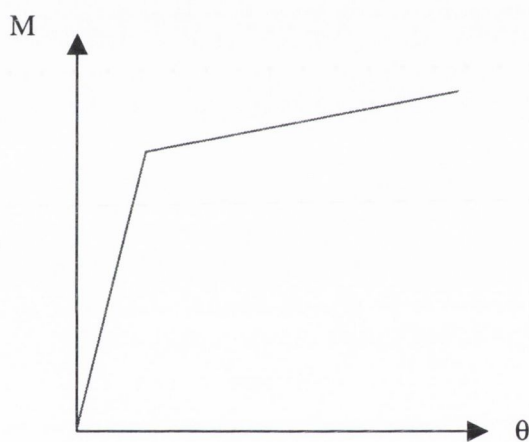


Figure 2.12: Bi-linear Curve Approximation

This type of representation recognised the change in stiffness as the rotation increases and used a linear analysis technique with a variable stiffness matrix (Lionberger & Weaver, 1969; Romstad and Subramanian, 1970). These techniques resulted in formulae which relate experimentally derived joint constants to the moment and rotation of angle joints as shown below.

$$M = \frac{0.87C^2(0.72\theta L)^{0.4}}{10^n(1-0.3\theta L)^{1.4}} \quad \text{Eqn. 2.23}$$

where M is the joint moment; L is the joint length; θ is the joint rotation; and C and n are experimentally derived joint constants (Romstad & Subramanian, 1970).

M - θ curves have also been idealised using a tri-linear relationship. This is done by connecting the initial slope of the curve to the strain hardening section using an intermediate line to improve the accuracy over the non-linear section of the M - θ curve (Moncarz & Gerstle, 1981). This model

comprises of initial, secondary and final stiffnesses, k_1 , k_2 and k_3 , together with the elastic yield moment, M_{el} and failure moment M_u illustrated in Figure 2.13. Other multi-linear analysis techniques have also been developed using a larger number of stiffness values (Poggi & Zandonini, 1985) shown in Figure 2.14. A number of non-linear models, shown in Figure 2.15, have also been developed, all of which depend upon mathematical curve fitting. These include polynomial models, Ramberg-Osgood type equations and multi-parameter models.

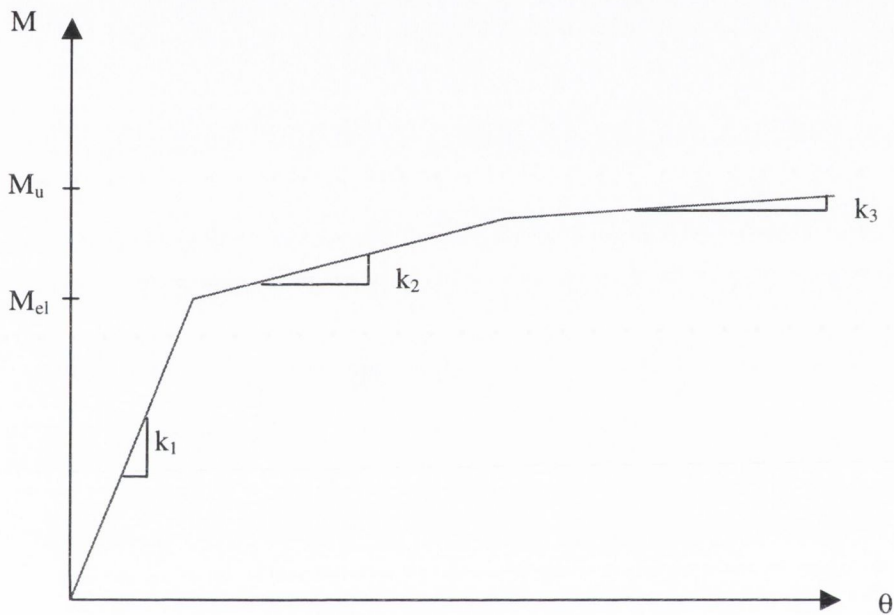


Figure 2.13: Tri-linear Curve Approximation

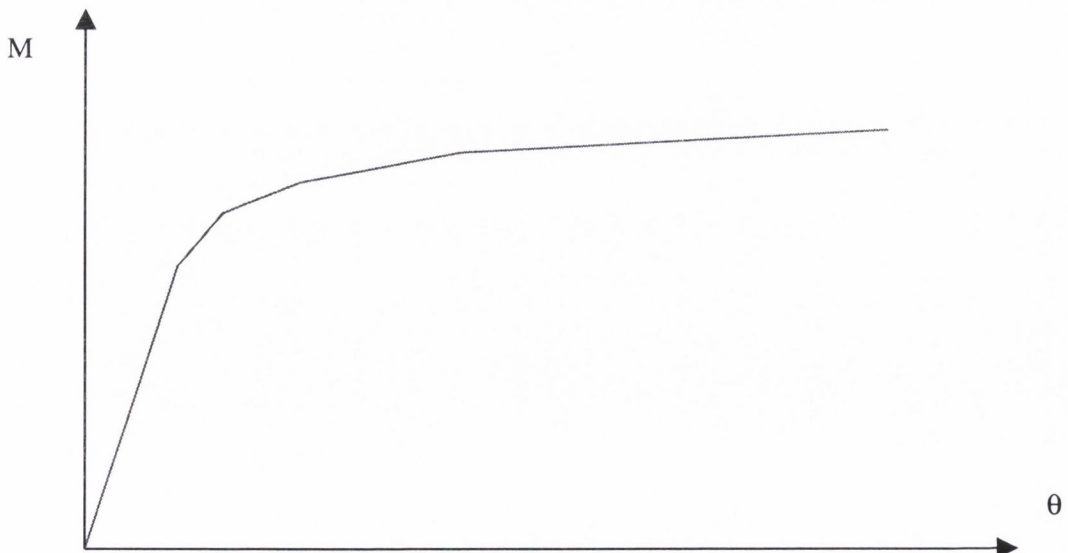


Figure 2.14: Multi-linear Curve Approximation

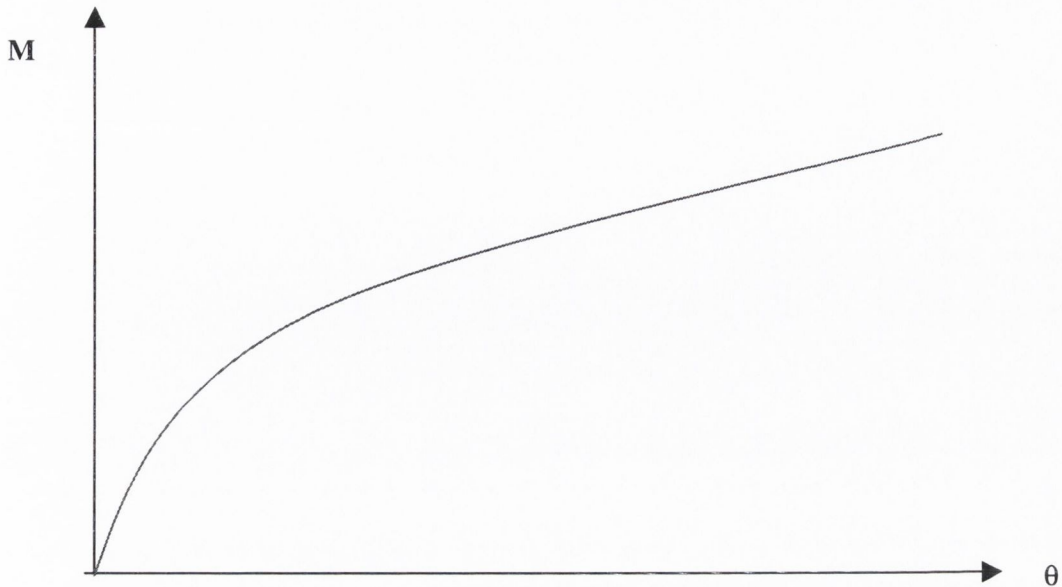


Figure 2.15: Non-linear Curve Approximation

Polynomial models (Frye & Morris, 1975; Kennedy, 1969) are similar to the tri-linear models in that they recognise a progressive change in stiffness as rotation increases. However, they also take into account the continuously varying nature of this relationship. One such method (Frye and Morris, 1975) uses a series of experimental M - θ curves and the least-squares method of curve fitting. The following formula was developed:

$$\theta = c_1 (kM)^1 + c_2 (kM)^3 + c_3 (kM)^5 \quad \text{Eqn. 2.24}$$

where θ is the rotational deformation of the joint, M is the moment applied to the joint, k is a dimensionless standardisation factor whose value depends on the parameters for the particular joint being considered and c_i is a curve fitting parameter (for $i = 1$ to 3).

However, it was found that in extreme cases, these polynomial solutions could give negative stiffnesses at the initial rotation of the joint. Further methods were therefore developed to eliminate this problem. An alternative to these types of polynomial equations is a Ramberg-Osgood type equation that will always provide a positive slope for the rotational stiffness (Ang & Morris, 1984):

$$\frac{\theta}{\theta_0} = \frac{k \times M}{[kM]_0} \left[1 + \left(\frac{k \times M}{[kM]_0} \right)^{n-1} \right] \quad \text{Eqn. 2.25}$$

where θ_0 and $[kM]_0$ are defined in Figure 2.16, k is defined above and n is a curve fitting parameter

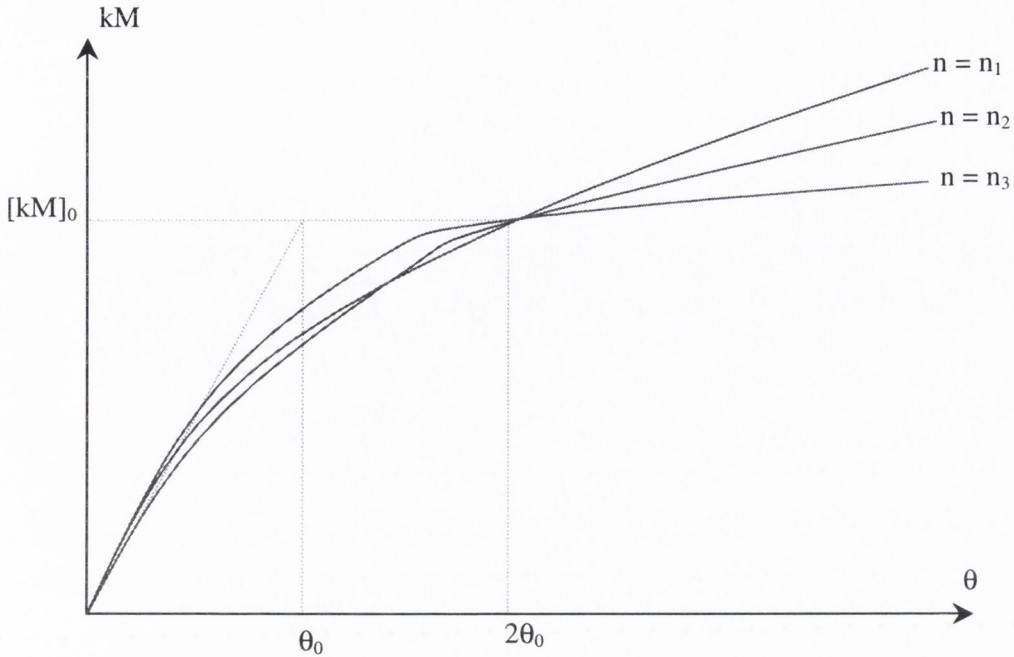


Figure 2.16: Standardised Moment-Rotation Function

Another method suggested to overcome the shortcomings of the polynomial method is B-spline curve fitting (Jones et al, 1981) in which a single polynomial function is fitted to an experimental curve. It was found that the cubic B-spline curve fitting method eliminated the possibility of a negative initial stiffness. This method divided the possible joint rotation into a finite number of points for the B-spline techniques. These techniques, combined with a least squares routine performed on the experimental data gives the following formula (Nethercot & Zandonini, 1989):

$$\theta = \sum_{j=0}^3 a_j M_j + \sum_{j=1}^m b_j \left(\langle M - M_j \rangle \right)^3 \quad \text{Eqn. 2.26}$$

where a_j and b_j are the experimental data coefficients obtained by a least squares method, m is the number of finite points chosen, and

$$\begin{aligned} \langle M - M_j \rangle &= M - M_j & \text{for } M - M_j \geq 0 \\ &= 0 & \text{for } M - M_j < 0 \end{aligned} \quad \text{Eqn. 2.27}$$

where M_j is the upper bound moment in the j th part of the curve. This method of curve fitting is limited to computer programming implementations as it involves large amounts of data.

Another non-linear method that has been developed is the exponential method (Lui & Chen, 1986).

This method uses a beam-column method of analysis combined with the finite element technique in conjunction with the principle of virtual work. This allows a numerical iteration of the Newton-Raphson type for the elemental stiffness matrices. The following formula was developed:

$$M = M_0 + \sum_{j=1}^n C_j \left[1 - \exp\left(-\frac{|\theta_r|}{2j\alpha}\right) \right] + R_{kf} |\theta_r| \quad \text{Eqn. 2.28}$$

where M = moment, $|\theta_r|$ = absolute value of the rotational deformation of the joint, M_0 = initial moment, R_{kf} = strain hardening rotational stiffness of the joint, α = scaling factor and C_j = joint model data parameters determined by curve fitting to a set of moment-rotation data. This equation also depends on whether the joint is being loaded or unloaded. If the joint is being loaded the tangent stiffness to the M - θ curve is used:

$$R_k = R_{kt} = \frac{dM}{d\theta_r |_{\theta_r}} = \sum_{j=1}^n \frac{C_j}{2j\alpha} \exp\left[-\frac{|\theta_r|}{2j\alpha}\right] + R_{kf} \quad \text{Eqn. 2.29}$$

or if the joint is being unloaded the initial stiffness is used:

$$R_k = R_{ki} = \frac{dM}{d\theta_r |_{\theta_r=0}} = \sum_{j=1}^n \frac{C_j}{2j\alpha} + R_{kf} \quad \text{Eqn. 2.30}$$

Another curve fitting equation that has been developed is known as the Richard Equation (Richard & Abbott, 1975; Richard et al, 1980), which allows the relationships between moment-rotation, and the stress-strain/force-deflection relationships, to be represented mathematically. The equation is a variation of the three-parameter Ramberg-Osgood polynomial and has been incorporated into finite element packages.

Of the above methods, very few have been designed or altered to accommodate cyclic response analysis and it is recognised that for the complete behaviour of joints to be understood, much research has still to be carried out in this area. Most of the methods discussed above should be adaptable to cyclic behaviour, and this has been done in some cases. Moncarz and Gerstle (1981) set-up a tri-linear method to analyse steel frames containing non-linear joints. This method utilises the matrix displacement method with a set of assumptions based on previous experimental work. It is similar to the tri-linear method discussed above (Moncarz & Gerstle, 1981), utilising the k_1 , k_2 and k_3 parameters. However, the model also makes the following assumption:

1. elastic unloading occurs with modulus, k_1 , which is identical to the elastic loading modulus;
2. the constancy of the elastic range is equal to twice the elastic moment; and

3. the hysteresis curve has equal positive and negative strength envelopes.

Using this method the following hysteresis curve, presented in Figure 2.17 was developed.

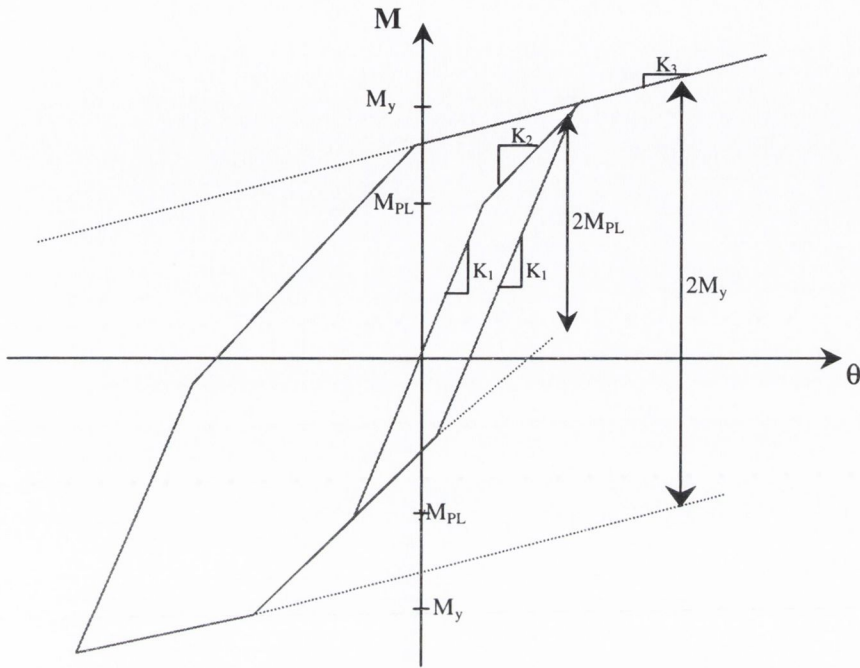


Figure 2.17: Tri-linearised Moment-Rotation Loops

Another method developed to model the cyclic behaviour of joints uses a Ramberg-Osgood function in combination with the previous cycle behaviour and a specialised slip function (Ballio et al, 1986; Mazzolani, 1988). The model, shown in Figure 2.18, represents the moment-rotation curve with the following formula:

$$\theta = \theta_1 + \theta_2 + \theta_3 \quad \text{Eqn. 2.31}$$

where θ_1 = the residual rotation of the previous cycle (= 0 for the first cycle), θ_2 = a Ramberg-Osgood type equation with numerical parameters obtained by curve fitting and θ_3 = the increment of rotation which is due to slip between M' and M'' which corresponds to a function of $\Delta\theta_s$.

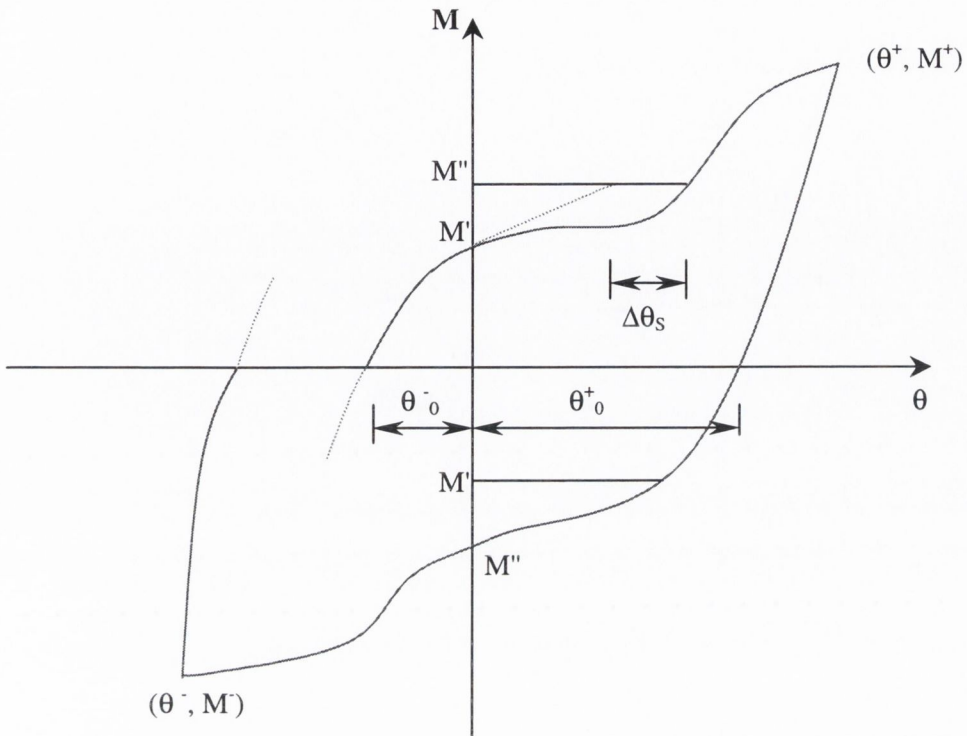


Figure 2.18: Cyclic Moment-Rotation Curve Model

2.8.1.2 Simplified Analytical Models

This type of analysis model is based on using experimental data to determine the most flexible part of a joint. It is then assumed that this section is the main source of flexibility in the joint. An elastic method is normally used to determine the stiffness of the section followed by a plastic analysis to determine the moment capacity. Using these two parameters, the final moment-rotation curve is found using mathematical fitting. These types of methods are usually only used in the analysis of the most flexible types of joints such as seat or web angle joints. Generally the flexibility of the shear panel, column flange and other beam-column components are ignored in favour of the actual joint elements.

Lothers (1951) published a method based on the semi-rigid joint constant, Z , for web angle joints. The concept of this joint constant, Z , was introduced above where it was defined as the rotational change per unit moment. The initial slope of the moment-rotation curve is the reciprocal of this constant, which is also the initial stiffness of the joint. Lothers proposed the following formula:

$$K_i = \frac{1}{Z} = \frac{Eht^3y^2}{6g^3} \times \frac{(4g + g_1)}{(g + g_1)} \quad \text{Eqn. 2.32}$$

where K_i = initial stiffness, E = young's modulus of steel, h = depth of the joint, t = angle thickness, g and g_1 = gage lengths of the angle legs and y relates the neutral axis to the depth of the joint. This formula neglects all other sources of flexibility except that due to the angles under bending. This resulted in any possible bolt slip, column flange strain or shear deflection of the angle being ignored.

In 1981, Johnson & Law introduced a prediction method for the initial stiffness of composite flush end-plate joints. The method superimposes the stiffnesses from the steel components and the concrete slab. By using a partial interaction approach for the concrete slab, it was found that the tensile resistance of the concrete could be neglected. This method could also be employed for flush end-plate joints. Assuming that the joint rotates about the bottom edge of the joint, illustrated in Figure 2.19, they were able to assume that the initial rotational stiffness of the joint is accounted for by the steel joint only. This gave the following formula for the elastic rotational stiffness of the joint:

$$K_s = \frac{d_b^2}{0.5 \left(\frac{1}{C_b} + \frac{1}{C_c} \right) \left(\frac{d_b}{h} \right)^2 + \frac{1}{C_p}} \quad \text{Eqn. 2.33}$$

where K_s is the initial stiffness of the joint, d_b is the depth of the beam, h is the lever arm distance, C_c , C_b , and C_e are rotational constant for the deformation due to the column flange, bolts and end-plate respectively. In Figure 2.19, M is the applied moment, T is the corresponding force equal to M divided by d_b , Δ_c is the deformation of the column flange, Δ_b is the deformation due to the bolts, and Δ_e is the deformation of the end-plate.

One of the most commonly used methods for the prediction of moment-rotation curves for bolted joints is the T-stub method employed in Annex J of Eurocode 3 (1993). This method divides the joint into a number of different T-stubs sections and looks at the tension and compression zones for each of these sections. Each component of the T-stub (end-plate, column flange, bolts, etc) is examined to determine which is most vulnerable to applied moments, and that section is used for the analysis. The rotational stiffness of the joint is then defined as:

$$S_j = \frac{Eh_1^2 t_{wc}}{\sum \frac{\mu_i}{k_i} \left[\frac{F_i}{F_{i,Rd}} \right]^2} \quad \text{Eqn. 2.34}$$

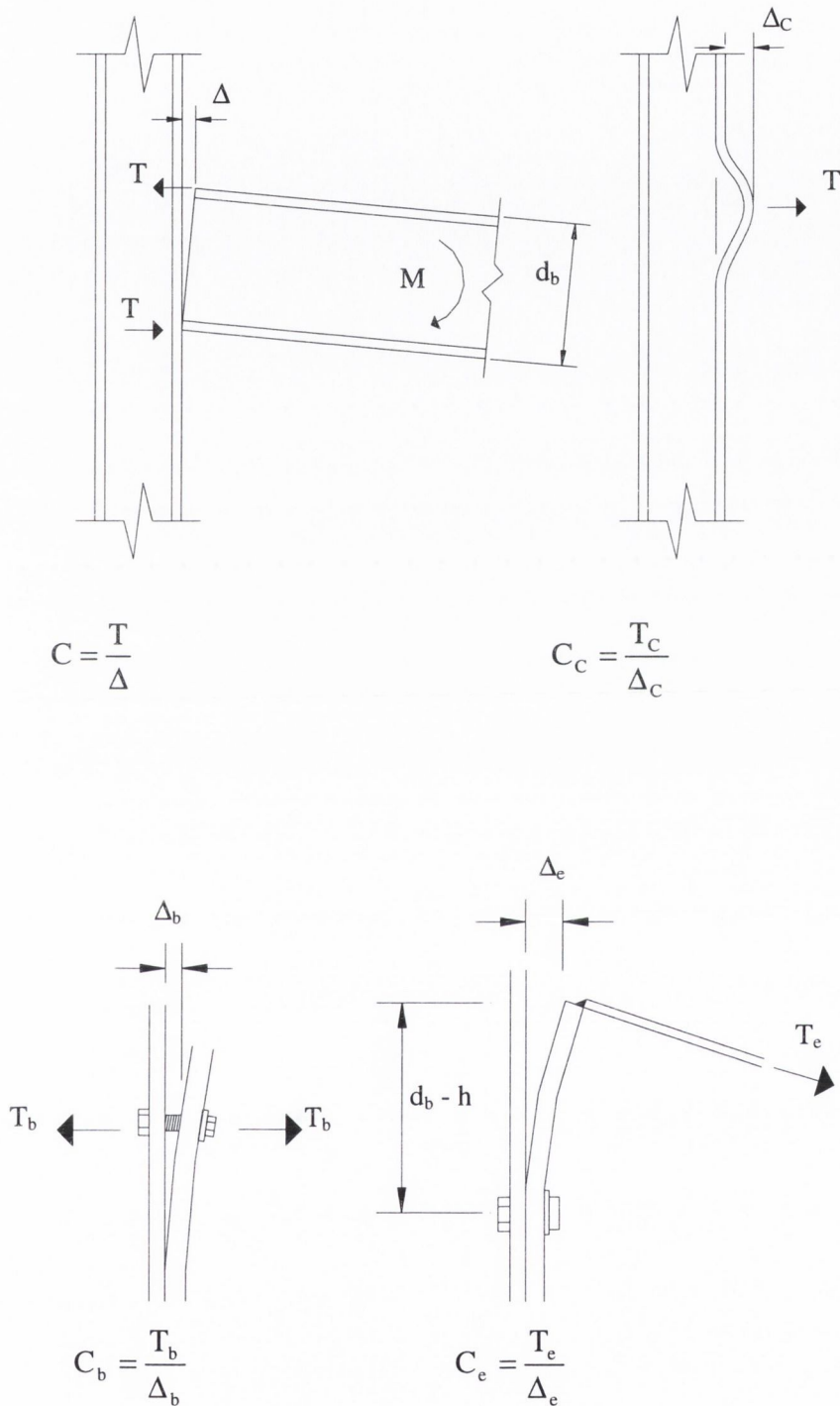


Figure 2.19: Deformation of Flush End-Plate Joint (Johnson & Law, 1981)

where S_j = secant stiffness with respect to a particular moment in the joint ($M \leq M_{Rd}$, M_{Rd} = design moment resistance of the joint), h_1 = distance from the first bolt-row below the tension flange of the beam to the centre of resistance of the compression zone, μ_i = modification factor as defined in

EC3, k_i = stiffness factor for component i , F_i = force in component i due to the moment M and $F_{i,Rd}$ = design resistance of component i . This method also provides formula for the calculation of stiffnesses and rotations of joints with stiffeners or welded joints.

A similar model to predict the non-linear behaviour of end-plate joints was developed in 1996 by Shi et al. This model assumes that the joint characteristics depend on the behaviour of each individual component in the tension zone, compression zone and the shear zone. The model considers the end-plate and the column flange as a series of T-stubs based around the methodology recommended in Eurocode 3. Using yield line theory and beam theory, an elastic-plastic force-deflection relationship for each T-stub is found using the following formula for the first plastic hinge.

$$\delta = \frac{l^3}{24E} \left(\frac{1}{I_f} + \frac{1}{I_e} \right) \left[F - B \left(\frac{3e}{l} - \frac{4e^3}{l^3} \right) \right] \quad \text{Eqn. 2.35}$$

where $l = 2(m + e)$; I_f and I_e = the second moments of area of the column flange and endplate T-stubs; F = tension force applied on T-stub; B = bolt tension force; and m and e are parameters defined in Annex J of Eurocode 3. After the formation of the initial plastic hinge, any subsequent deformation is determined, depending on the point of yield. For Mode 2 failure (the most common type, described in section 2.5), where the first plastic hinge form at the beam web line, the separation increment is given by

$$\Delta\delta = \Delta F \left[\frac{l_b}{E_b A_s} + \frac{l_m^3}{24E} \left(\frac{1}{I_f} + \frac{1}{I_e} \right) \right] \quad \text{Eqn. 2.36}$$

where E_b = elastic modulus of the bolts; l_b = elongation length of the bolts; $l_m = 2m$; and A_s = tensile area of the bolts. This model also allows the column web in compression, tension and shear to be incorporated in the joint behaviour. Part of this model has been adopted for use in the proposed T-stub model developed in this study and will be discussed in much greater depth in Chapter 6.

Kishi et al, 1988a (Kishi et al, 1988b) proposed a model for the prediction of model moment-rotation curves for double and single web angle joints with top or seat angles. This method used a Richard type power equation to fit analytically obtained values for the initial stiffness and ultimate moment capacity, resulting in the following relationship:

$$\theta = \frac{M}{R_{ki} \left\{ 1 - \left(\frac{M}{M_u} \right)^n \right\}^{\frac{1}{n}}} \quad \text{Eqn. 2.37}$$

where θ = joint rotation, M = moment at the joint, R_{ki} = initial joint stiffness, M_u = ultimate moment capacity of the joint and n is a curve fitting parameter. It is assumed that the connecting members remain rigid at all times, thus concentrating on the actual joint elements.

Yee and Melchers (1986) developed a four parameter exponential method. This formula was developed for both stiffened and unstiffened bolted end-plate eave joints. The formula states that

$$M = M_p \left\{ 1 - \exp \left[\frac{-(K_i - K_p + C\theta)\theta}{M_p} \right] \right\} + K_p \theta \quad \text{Eqn. 2.38}$$

where M = moment at joint, θ = rotation of the joint, M_p = maximum moment that can be transmitted by the joint without strain-hardening occurring, K_i = initial stiffness of the joint, K_p = the strain-hardening stiffness of the joint and C is determined from experiment test data. Formulas were then derived for M_p , K_i and K_p for both the stiffened and unstiffened joint types depending on the different failure modes.

Brown et al (2001) developed a formula to predict the initial stiffness of flush end-plate joints. This formula only considers the flexibility of the column flange and end-plate as these are the main sources of deformation in an end-plate joint. All other sources of deformation are accounted for by the use of a correction factor. The following formula was developed:

$$K_j = \frac{0.2L_a^2}{\left(\frac{m_{cf}^2}{t_{cf}^3} + \frac{m_{ep}^2}{t_{ep}^3} \right)} \text{ kNm/rad} \quad \text{Eqn. 2.39}$$

where K_j is the initial stiffness of the joint, L_a is the lever arm distance, m_{cf} and m_{ep} are the distances from the centre of the bolt to the beam web fillet weld for the column flange and end-plate respectively, and t_{cf} and t_{ep} are the thickness of the column flange and end-plate respectively.

2.8.2 Finite Element Based Models

The use of the finite element technique in the modelling of structural steel joints has the potential to become one of the most powerful prediction models in structural engineering. One of the greatest advantages that finite element modelling has over other analytical models is the ability to measure and define local effects that the other methods may neglect. However, in order to accurately predict the moment-rotation curves a number of special elements are needed to model the non-linear behaviour of the joint. This non-linear behaviour includes the slippage of the bolt due to bolthole clearance, local failure at bolts or welds and the effects of plastic hinges opening and closing. In order for these representations to be accurate enough for design purposes, new finite element formulations are required. In general, these formulations require modelling of the following properties:

- geometrical properties of the joint;
- 3-dimensional effects;
- non-linear material properties of the steel;
- bolt pre-loading and behaviour under complex loads;
- the interaction between the joint components, such as contact between the bolt shank and the hole surface;
- bolt slippage due to lack of fit
- the behaviour of any welds under highly complex loading conditions, and;
- the presence of any irregularities in the joint.

One of the first attempts to use the finite element method to predict the moment-rotation behaviour of joints was made by Bose et al (1972). This study investigated welded beam-to-column joints and concluded that the column web was the critical component due to buckling failure. Because the column web undergoes a very complex state of stress during loading (axial, shear and bending stresses), the main parameters of the study were the strength and stability of the column web. The resulting formula is based on energy concepts of finite element analysis and examines both the elastic and elastic-plastic states. The model incorporates material plasticity and strain hardening. The strain hardening is simplified using an isotropic rule.

Patel & Chen (1984) investigated the behaviour of fully or partially welded joints using a commercially available finite element package called NON-linear Structural Analysis Program (NONSAP). A 2-dimensional model was utilised and the joints were analysed as a plane stress problem. The force-deformation behaviour, the spread of the yielded zones and the stress distribution in the shear panels were all plotted and compared with experimental results. The model was found to have a good correlation with test results as shown in Figure 2.20.

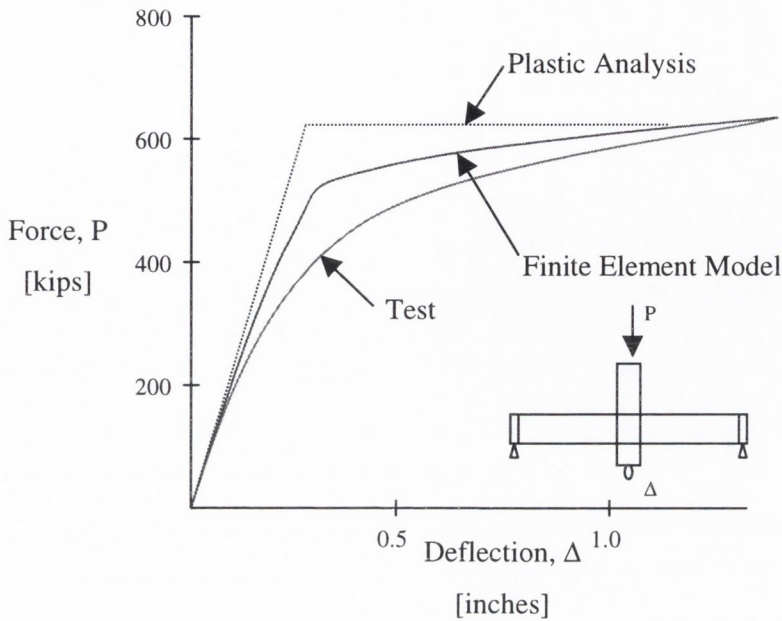


Figure 2.20: Load-Deflection Behaviour (Patel & Chen, 1984)

Another study carried out on single angle bolted-welded joints was by Lipson & Haque (1978). Although this study was not concerned directly with the moment-rotation behaviour of the joints, it determined the different stress states in the joints under both monotonic and cyclic loading. The joint is modelled as a rigidly supported elastic-plastic plate with forces to simulate the bolt interaction. These forces were calculated using a series of load-deformation tests carried out on single bolts connecting two plates.

In 1983, Richard et al carried out an investigation into the behaviour of double web angle joints. This investigation was based on the Richard Formula, which is described in section 2.8.1.1, and employed the non-linear finite element package INELAS. In order to model the double framing angles accurately shear tests were carried out on joints. The resulting orthotropic yield surface is shown in Figure 2.21. An element was then developed based on this surface and incorporated into the INELAS program. The resulting behaviour is calculated using a numerical iteration based on the Von Mises yield criteria. The results were compared with experimental results and a satisfactory correlation was found.

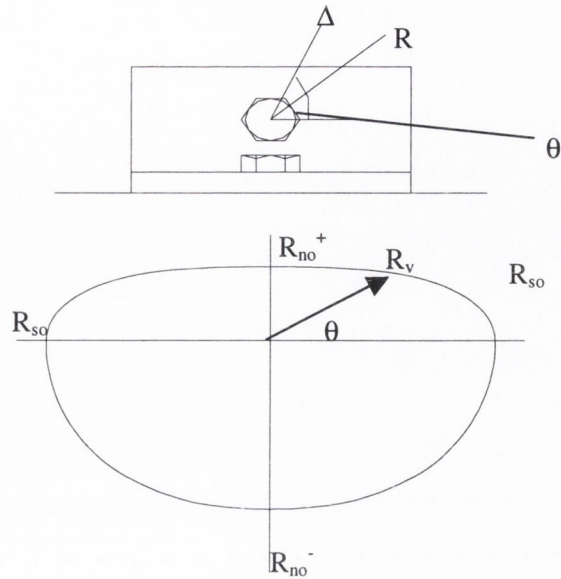


Figure 2.21: Orthotropic Surface Results for Double Angle Joints

Patel & Chen (1985) carried out an investigation of fully bolted web angle joints using the NONSAP program and a 2-dimensional model. Isoparametric, numerically integrated elements were shown to be the most efficient type available and were used to model the beam, column and joint plates. A special configuration of bar elements was used to model the bolts, as shown in Figure 2.22. Elements one and three simulate the axial force, such as the pre-tensioning force, that passes through the bolts, while element two simulates the shear forces in the bolts. In order to accurately model the bolts, the stress-strain relationship of the material was modelled using a tri-linear relationship. The model was validated against experimental results. However, the model neglects slip in the bolts and this introduces some discrepancy in the results.

Beaulieu & Picard (1988) used a similar method to predict the moment-rotation behaviour of web angle joints. However, an extra contact element was introduced in the bolt model to account for perfect slip and friction forces. This fourth bar element is coupled with the shear element. The characteristics for this element were calibrated against experimental data.

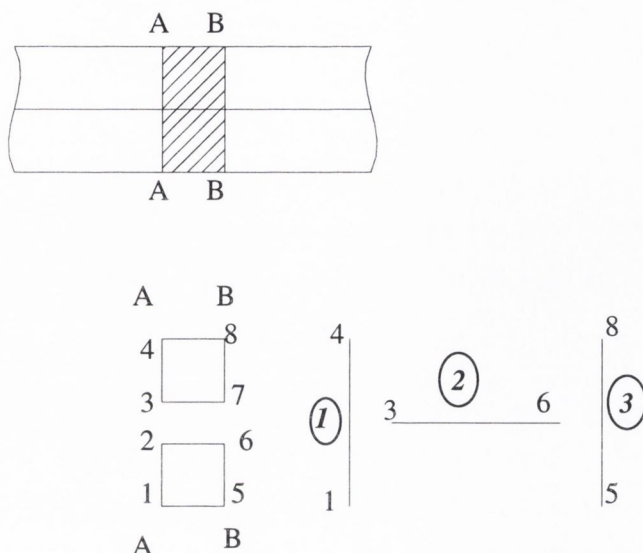


Figure 2.22: Modelling of Bolts with Bar Elements (Patel & Chen, 1985)

A 2-dimensional model was developed for the analysis of flush end-plate joints by Kukreti et al (1987). The analysis was carried out on a plane stress model taken parallel to the plane of the mid-thickness of the web. It was assumed that the stress-strain relationships for the end-plate, beam flange and beam web was perfectly elastic-plastic, while the bolt shank material was bi-linear. Because 3-dimensional models are more flexible than 2-dimensional ones, due to the added degrees of freedom, simulations were carried out using both types. A correlation factor was obtained by comparing the results from both types. It was found that the 2-dimensional model could be accurately used to model the 3-dimensional behaviour. A parametric study was then carried out using experimental work and the finite element modelling, and numerical expressions for the joint behaviour developed.

An analysis of extended end-plate joints was also carried out using the finite element method (Krishnamurthy et al, 1979; Krishnamurthy, 1980). The method used was similar to that used by Kukreti et al, where the bolts are idealised as plates set transversely across the section. The final 2-dimensional mesh is shown in Figure 2.23. A parametric study was also carried out for the end-plate joints and a set of prediction equations were developed. A comparison between the experimental results, finite element analysis and prediction equations was made, and correlation factors were calculated.

Another study carried out on extended end-plate joints was conducted by Bahaari & Sherbourne (1996). Using ANSYS v4.4, a finite element package, they considered the end-plate joints under

pure bending in a 3-dimensional model. Tri-linear stress-strain curves were adopted for the material properties to account for strain hardening. The simulations were run for bolts that were hand-tightened and pre-tensioned. The pre-tensioning force was accounted for by imposing an initial strain on the bolts before loading started. The interaction between the bolt pre-load and stiffness, prying actions and stress distribution were investigated, as was the effect of end-plate thickness on the above. One of the more interesting results was that the pre-load force on the bolt had no effect on the prying forces and action, while the size of the bolt was the critical factor.

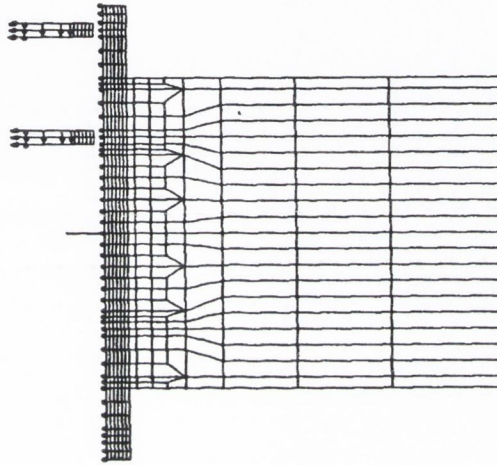


Figure 2.23: Typical 2D mesh for End-plate Joint Analysis (Krishnamurthy, 1980)

Another 3-dimensional model for stiffened and unstiffened extended end-plate joints was developed by Choi & Chung (1996). The method was developed to examine beam-to-beam joints and beam-to-column joints. The final beam-to-beam mesh configuration is shown in Figure 2.24. A new gap element was introduced to simulate the interaction between the end-plate and the column flange. This new element involved the programming of a new contact algorithm into the ADINA finite element package. Comparisons carried out with tests using the standard elements showed a large improvement in accuracy with the use of the new element types.

A finite element model for unstiffened flush end-plate joints was developed in 1997 by Bose et al. This method uses a variety of element types to accurately model the behaviour of the joints. 3D continuum elements are used for the column web, column flange, end-plate, beam web and beam flange, while bar elements are used to represent the bolts in tension and compression. At the locations where the prying forces will occur, special joint elements are used to tie continuum elements together. Comparisons are made with experimental results for the moment-rotation characteristics, bolt strains, prying forces and strains at select points in the joint. Some discrepancies were noted in the $M-\theta$ curves but these could be explained by bolt tightening and

lack of fit. Very good correlation factors were found in the bolt strains with any discrepancies being explained as being due to the pre-tensioning forces which were not include in the finite element analysis. However, the model does neglect deformations due to the welds, bolt heads and the column fillets.

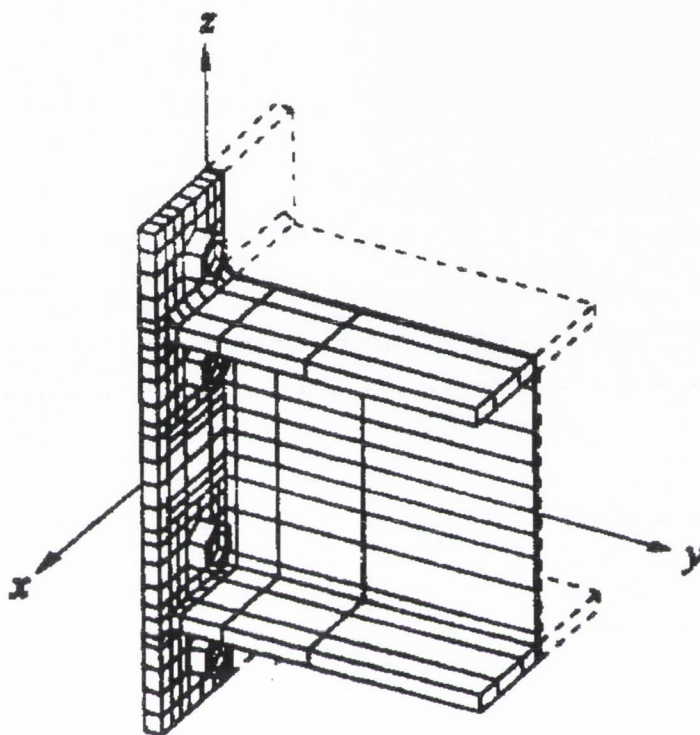


Figure 2.24: Finite Element Mesh for Beam-to-Beam Joint (Choi & Chung, 1996)

Modelling currently being undertaken (Fanning et al (2000), Tucker (2002)) involves the development of a finite element model to predict the cyclic behaviour of flush end-plate joints. Solid elements are employed for the beam, column, endplate, bolt heads, bolt nuts and bolt shafts in order to build up a 3-dimensional model as shown in Figure 2.25 and Figure 2.26. Symmetry is utilised to reduce the size of the model, thus saving on computational time and computer space. This is illustrated in Figure 2.25. A non-linear solution algorithm (Newton – Raphson) is used to account for material non-linearities, geometric non-linearities and contact non-linearities. A bilinear kinematic hardening rule is employed for the material properties, requiring the input of Young's modulus, yield stress and post-yield stiffness. Contact elements are used on adjoining surfaces to simulate the behaviour of interacting surfaces. These include surfaces that could go into contact or separate during an analysis. There are contact elements between the column flange/end-plate, bolt-heads/end-plate, bolt-nuts/column flange and bolt shafts/bolt-holes. Friction is also included in the model for the contact algorithm. As this study was run in conjunction with this

study, the experimental results discussed in Chapter 4 were used to calibrate the model and a good correlation was obtained.

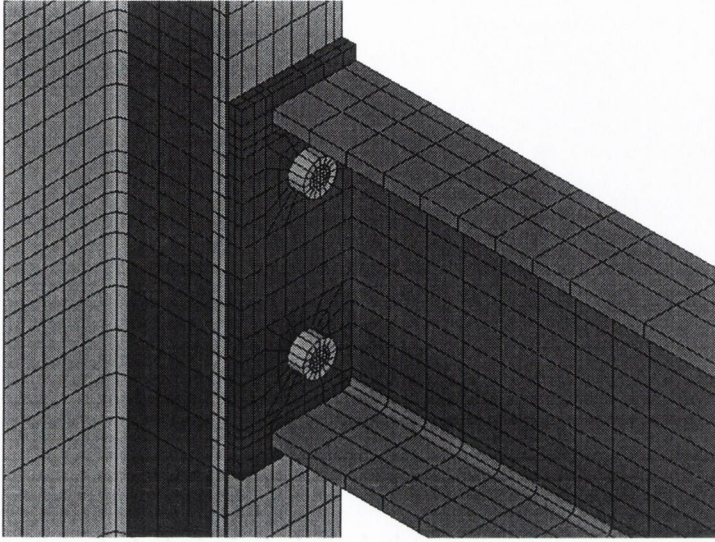


Figure 2.25: Finite element model of flush end-plate joint (Tucker (2002))

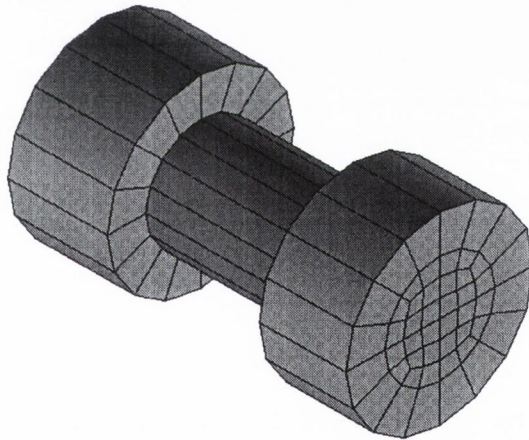


Figure 2.26: Modelling of bolts (Tucker (2002))

2.8.3 Mechanical Analogue Models

This type of model, also known as a component-based model, is capable of representing the entire range of joint behaviour without referring to experimental data. This is carried out by considering the joint as a series of components, rather than as a single entity. Therefore, the non-linear behaviour of the joint is derived from the analytical inelastic response of each of the separate components. These models appear to be advantageous as they allow the joint response to be predicted throughout the entire range of the elastic and plastic phases. Because these methods do not rely on experimental data, the actual shape of the moment-rotation curve can be obtained.

However, it should be noted that some of these models use the component method (Madas, 1993; Calado & Ferreira, 1995) as their basic approach and then turn to standard finite element packages to solve the actual deformations. These models are still considered to be mechanical models as the fundamental approach is component-based, while the finite element method is only used for the solution.

A model developed by Wales & Rossow (1983) for double angle joints uses a spring-basis to predict the behaviour of the joints. The model, which is presented in Figure 2.27, consists of two rigid bars connected by a homogeneous continuum of non-linear springs. It should be noted that the rigid foundation for the left bar is not to imply that the bar is fixed in space, but instead that it is fixed in the joint co-ordinate system. The model utilises the tri-linear relationship of the load-deformation function to determine the parameters of the joint in each of the six distinct deformation states: elastic-plastic-compression, elastic-compression, elastic-plastic, elastic, compression and plastic. This is done by analysis of numerical models of the angle for tension or compression. The model also considers coupling between the moment and axial force stress resultants when calculating the stiffness matrices at each deflection increment. However, the model neglects shear deformations, bolt slippage and strain hardening.

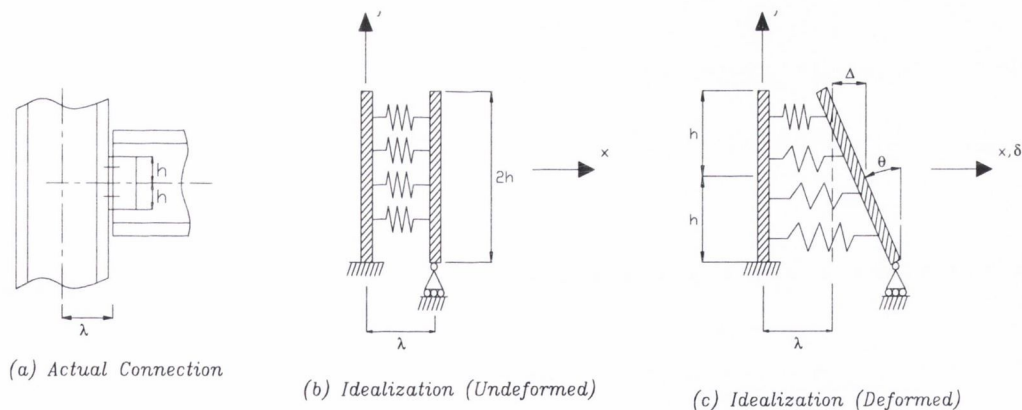


Figure 2.27: Mechanical Model of Double Angle Web Joints
(Wales & Rossow, 1983)

A similar approach was taken used by De Stefano et al (1993) who also investigated the response of double angle joints. However, this prediction model only requires the stress-strain laws of the steel and the geometrical properties of the joint. This model is one of the few that are capable of dealing with cyclic loading of the joint and achieves this by taking into account contact effects and kinematic hardening. This was done by coupling the load-deformation behaviour in pure tension

and in pure compression. Gap elements are also introduced to account for the non-linear behaviour of the column flange and angle. These elements are only activated when the deformation is less than zero. Comparisons with experimental work showed that the model gives very good initial stiffnesses, strength and ductility ratios. However, no allowance is made to the softening of the steel due to cyclic deterioration. This has the effect of reducing the material stiffness and strength. The model also neglects bolt slippage, which may be considered as another source of material degradation.

An investigation into the response of welded joints suggested a slightly different model to predict their behaviour (Tschemmerneegg, 1988). This model represents the joint as a series of springs, as shown in Figure 2.28. Springs A represent the load introduction from the beam to the column, where springs B represents the flexibility of the shear panel zone of the column web. The model was developed using a series of three different tests in which different loading types were examined. The first series examined the introduction of forces from the beam flange into the joint, while the second series extended the first set by looking at the additional effect of the beam web on the load introduction to the joint for symmetrical loading. The third series of tests examined the effects of non-symmetrical shear loading. Then using superposition, the force-deformation relationship could be determined. These tests were carried out for numerous sizes of welded joints using both cruciform types, as shown above, and cantilever types.

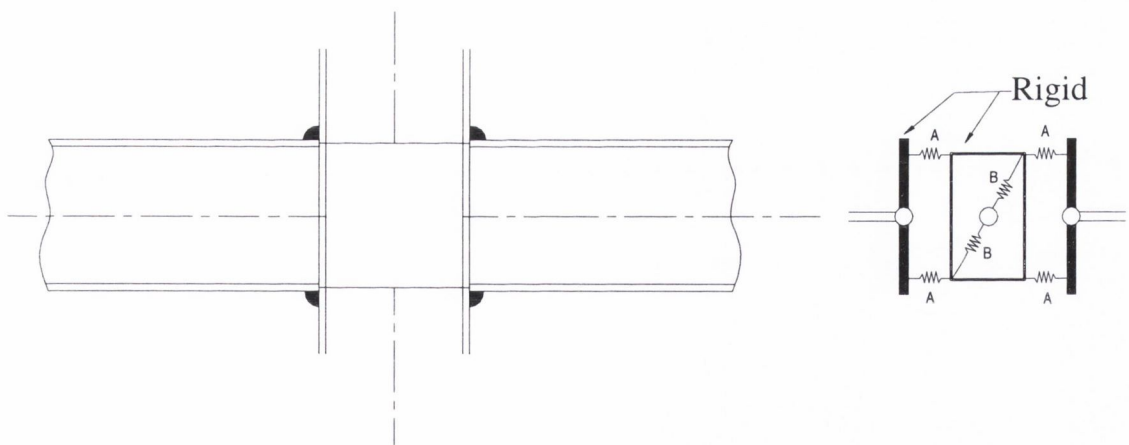


Figure 2.28: Mechanical Model of a Full Welded Joint (Tschemmerneegg, 1988)

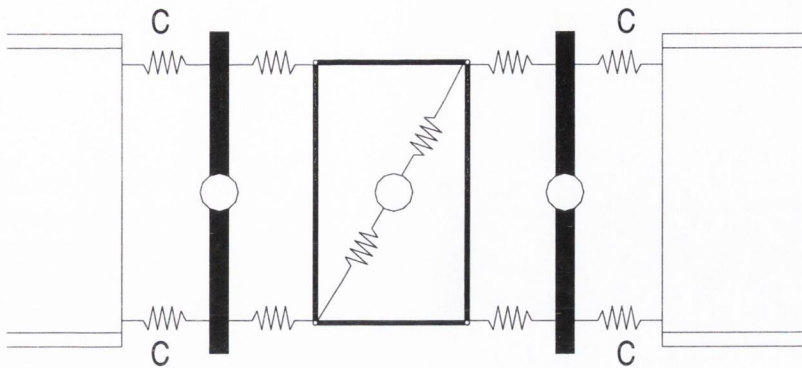


Figure 2.29: Mechanical Model of a Bolted Joint (Huber & Tschemmernegg, 1998)

Research into this type of model is still continuing (Huber & Tschemmernegg, 1998) and it has been developed further to include both bolted and composite joints, where springs C account for other sources of flexibility such as the deformation of bolts (Figure 2.29).

Madas (1993) used a similar method to investigate the monotonic and cyclic behaviour of steel and composite joints. This model is capable of predicting the moment-rotation behaviour of a multitude of different joint types including web angle, top- and seat-angle cleats, flush end-plate and composite joints. The model takes into account the coupled moment-axial force behaviour deformational response of the connecting elements, such as bolt elongation and slippage, the non-linear behaviour of the beam and column, interactions of the connecting elements and the connected elements. However, the effects of shear forces on the deformation of the connecting elements are neglected. The results from the model were compared with published results for monotonic and cyclic loading. Under these loading conditions the model exhibited a high degree of accuracy with regard to the moment-rotation behaviour and energy absorption ratios.

Driscoll (1987) used linear line elements to predict the monotonic elastic-plastic behaviour of top- and seat-angle joints. This method assumes that the beam and column remain elastic and concentrates on the inelastic behaviour of the flexible connecting elements. The method models the angle joints as a series of flexible line elements, as shown in Figure 2.30. Driscoll assumes that the only part of the angle section that contributes to the moment-rotation is the length between the heel and the bolt line. The method also assumes that each component is initially defined as a cantilever and modifies the stiffness matrices according to the location of the plastic hinges as the analysis proceeds. The function of the rigid dummy member is to transfer any centre line deformations and rotation from the beam and column to the joint elements.

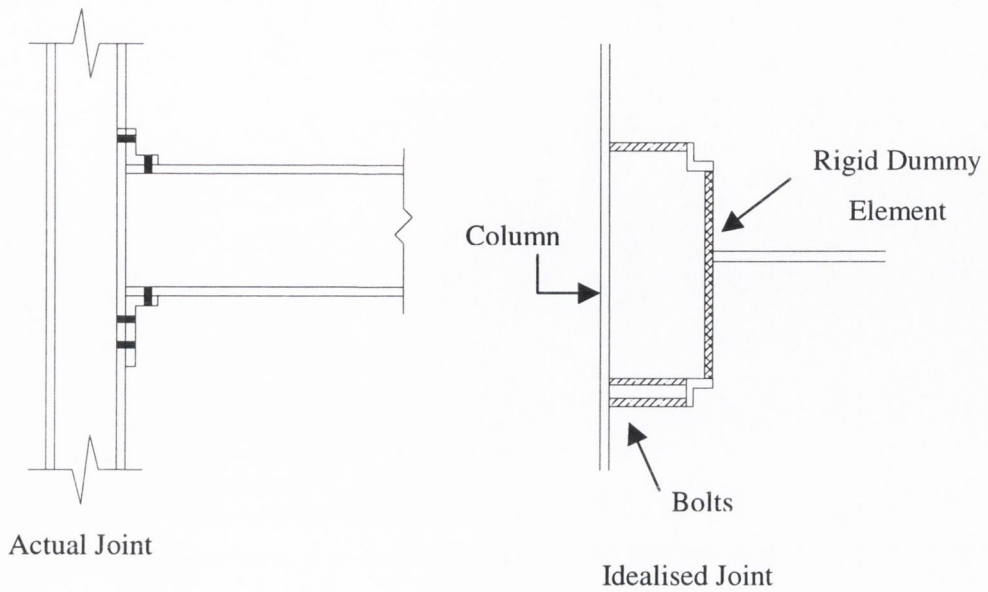


Figure 2.30: Joint modelled using Line Elements (Driscoll, 1987)

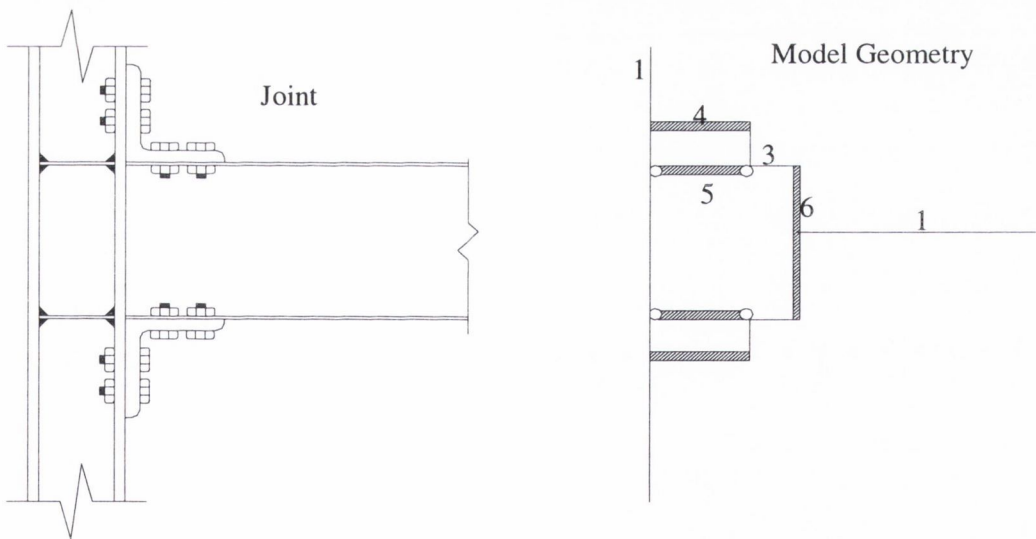


Figure 2.31: Type of Joint to be modelled and Model Geometry (Calado & Ferreira, 1995)

A similar method was used by Calado & Ferreira (1995) to predict the cyclic behaviour of top- and seat-angle joints. The model, shown in Figure 2.31, requires the mechanical characteristics of the material and the geometrical properties of the joint. Elements 1 and 2 represent the column and the beam, respectively, element 3 represents the angle sides between the heel and the first line of bolts, element 4 simulates the join of the vertical side of the angle to the centreline of the column. This

element must consider the column web as well as the deformation characteristics of the column flange and the bolt. Element 5 simulates the propping effect of the beam flange to the column flange with the stiffeners, and element 6 represents the section of the beam web between the bolts and the centreline of the beam. The difference between the mechanical method suggested by Driscoll and the above model is in a variation of the rigidity. This additional rigidity is to take account of the vertical leg of the angle joint contacting the column flange. The results from the model were compared with experimental results using four parameters. These were the absorbed energy ratios, full ductility ratios, resistance ratios and the force displacement curves. In each instance, a good comparison was found with the proposed model being found to agree with the experimental results to within 10%.

A model using similar T-Stubs to those used in Eurocode 3: Annex J was also developed for partial end-plate joints (Kennedy & Hafez, 1984). These T-stubs, as shown in Figure 2.32, are used to represent the tension and compression zones of the joint.

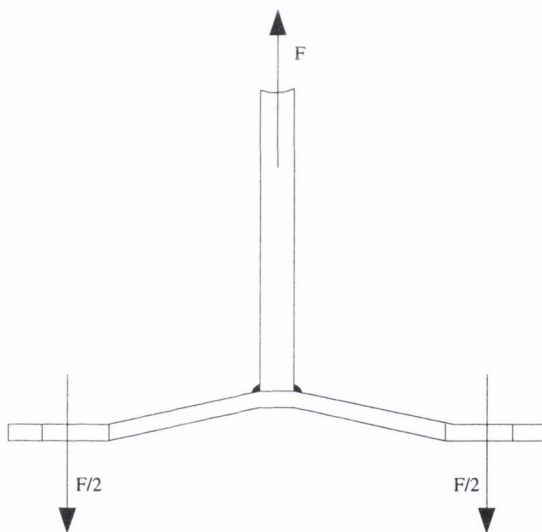


Figure 2.32: T-Stub Model (Kennedy & Hafez, 1984)

Numerical representations were developed for the T-stubs in tension and compression and validated against experimental data. The model uses these representations and an assumption of the location of the instantaneous neutral axis to calculate any point of the moment-rotation curve. The average ratio of predicted moment capacity to experimental moment capacity was determined to be 1.01 with a coefficient of 0.11, which is very accurate. However, the ratios of predicted corresponding rotations to the experimental values were much more varied, with an average of 1.11 and a coefficient of variation of 0.27. This deviation was suggested to be due to the fact that the joint stiffness is dependent on the location of the neutral axis being correct. These deviations may

also be due to the fact that the model neglects bolt elongation, deformations in the column web and any tensile deformation in the beam web. Modifications were suggested for when the model is used as a direct rotation check in joint design.

Faella et al (2000,2001a, b) presented a T-stub model for extended end-plate joints. This model was based on the moment-curvature relationship of a notional rectangular plate. This model has been adapted for use with flush end-plate joints as discussed in chapter 6, and is therefore not fully discussed here. The results from the model were compared with experimental studies carried out on T-stub sections and a good correlation between the experimental and theoretical results was obtained.

2.8.4 Conclusions on Modelling Techniques

It may be concluded from the review of joint modelling methods that there are still a number of inadequacies that must be overcome:

- Many of the available models only consider the flexibility of the connecting elements in the joints (bolts, end-plates, angles, etc), while neglecting the interaction between the joint and the connected elements (e.g. column shear panel, beam flanges and web).
- There are very few cyclic models available at the present time. Most of the mathematical models and finite element models have been developed only for monotonic loading conditions.
- Many of the models neglect important factors such as friction, slippage and lack of fit. Although these may prove to be insignificant to the joint response, when these models are incorporated into frame analysis programs the effects may prove more serious.

The mathematical models are probably the easiest type of prediction method to develop and use. They are usually equations fitted to previously attained experimental data. One of the greatest problems with this type is that they cannot be extended outside the range of the calibration data. It is also very difficult to incorporate different material or geometrical properties. However, most of the currently available models fall into this category.

The finite element analysis models are capable of giving very accurate results and are probably the most powerful analysis models available. They allow the moment-rotation characteristics of the curve and the stress-strain rates throughout the joint to be examined in great detail. However, when the models are incorporated into frame analysis programs, they become very costly and time-consuming even with modern computer processors. The joint models are also often difficult to set-up. Due to this, many finite element models are used to develop prediction equations to be placed

into the frame analysis programs, which results in the same calibration problems that the mathematical models experience.

The mechanical, or component-based, models are probably the most suitable for the prediction of joint behaviour. They are capable of giving very accurate moment-rotation characteristics, while allowing the material and geometrical properties of the joint to be changed. However, they do require a very detailed understanding of the response of each component in the joint, which must be modelled separately. It is, however, reasonably simple to incorporate these component-based models into frame analysis programs

2.9 Conclusions

This chapter reviewed some of the important concepts in the use of semi-rigid partial strength joints in moment-resisting frames. The differences between a joint and a connection were detailed, as this is a concept commonly misunderstood and misused in practice. The different components in a flush end-plate joint were discussed as were the important structural properties of a joint.

The classification methods used for steel frames were presented. The two classifications from Eurocode 3 were set out, namely braced/unbraced and sway/non-sway. Frames were classified as braced or unbraced based on the lateral stiffness available. The effects of second order effects determine whether a frame is a sway frame. Depending on the joint model assumed in the design different frame models are allowed. These include simple, continuous and semi-continuous frames as detailed in Eurocode 3. Similar methods are allowed in the ASD (1989) and AISC (1986) specifications.

Three different methods of classifying joints were then presented. Classification by stiffness and strength are accepted and detailed in BS 5950 and Eurocode 3: Annex J. Classification by stiffness leads to joints being labelled as rigid, semi-rigid or pinned in relation to the flexibility of the connected members. Classification by strength allows a joint to be labelled as full-strength, partial strength or pinned in relation to the strength of the weaker connected member. The third classification system, rotational capacity, has recently been proposed but has not yet been accepted for use in practice. This method allows a joint to be classified based on the rotational capacity of the connection elements.

The main types of joint failure were presented for any joint that may be modelled as a tee-stub. These are as follows:

- **Mode 1:** Yielding occurs at both the fillet line and the bolt line. This failure mode is characteristic of joints with strong bolts and weak end-plates,
- **Mode 2:** Yielding occurs at the fillet line and in the bolts. This is the most common type of failure.
- **Mode 3:** Yielding occurs only in the bolts, with the end-plate remaining elastic. This failure mode is characteristic of a strong end-plate with weak bolts.

Formulae for calculating the failure mode of a tee-stub were presented and shown graphically. The influence of shear on the failure modes was also discussed and shown to be negligible. It is possible to use these failure modes to further sub-classify joints. This sub-classification is not an official method and is used for convenience.

The next section presented the effects of strain rate on both material and joint properties. It has been observed in previous work that an increase in the strain rate causes a corresponding increase in the yield and ultimate strengths of the material. The increase in the ultimate strength, however, does not correspond directly to the increase in yield strength. A similar response was noted for the yield capacity of joints and members. However, the energy dissipation characteristics of the members was seen to be reduced by an increase in strain rate.

Some of the experiential work that has been carried out on joint sub-assemblages and frames was then presented. This represents only a small section of the huge volume of the available research and is not intended to be exhaustive. Based on the work carried out, it may be concluded that it is highly important for the joint stiffness to be included in any frame design or analysis as it seriously affects the overall frame behaviour.

The final section presented a review of techniques for modelling the response of a beam-to-column joint. A number of inadequacies that exist in modelling joint behaviour were noted, and the advantages and disadvantages of numerous techniques were discussed. These techniques range from simple analytical methods, such as curve fitting and mathematical modelling, mechanical models that utilise springs to capture the material behaviour, to highly complex finite element modelling using state-of-the art computer applications. The models are capable of determining the response for a wide range of different joint typologies including flush end-plate joints.

Chapter 3

Test Procedure and Software

3.1 Introduction

This chapter discusses the experimental programs and equipment developed as part of this study. The programs that are described in this chapter were developed for the testing of structural joint sub-assemblages. The system combines the following components:

- Structural control software;
- Input/output Data Acquisition System;
- Data measurement devices (LVDTs, strain gauges, load cells);
- Signal conditioning units;
- Actuator control system; and
- Servo-hydraulic actuator.

The second section details the methods employed to create the waveforms used in the cyclic tests. These procedures provide a unified method of testing structural steel elements throughout the world. Two testing methods are detailed, and the specialised definitions required for each are provided.

The next section looks at the three types of control programs that were developed as part of this study. The requirements for this new structural element testing program were that it must be able to control the servo-hydraulic actuator system to a sufficiently high level of accuracy. The control system had to be capable of performing a wide range of experiments ranging from simple monotonic tests to full cyclic tests. A number of different configurations of these programs were developed and these are discussed here.

The fourth section explains how the cyclic loading system was integrated. A brief description of the equipment used is given and the principles by which it controls the servo-hydraulic actuators are explained. The method in which the new computer software controls the system is set out.

In the final section of this chapter, the capabilities of the new loading control system are detailed. Results investigating the level of accuracy achieved by the system are presented which compare internal displacement transducer measurements, with an external transducer measurements and the required displacement. Finally, a number of cyclic tests carried out on concrete beam-column sub-assemblages are described briefly.

3.2 Recommended Testing Procedures

The testing procedure that was used throughout the experimental work was developed as an European reference standard (ECCS, 1986) for the cyclic testing of structural steel throughout the world. This testing procedure is very similar to the American standard known as ATC-24 (Applied Technology Council, 1992). This reference standard was developed because the actual response of a steel element to a cyclic load may be far removed from the elastic-plastic behaviour that is assumed in many of the national building codes (BS 5950, ASIC). This elastic-plastic stress relationship has also been adopted for use in Eurocode 3 that is due to replace the older national codes shortly.

Two separate testing procedures were set out in the ECCS document and both of these were utilised in the experimental study. The first method is known as the “Complete Testing Procedure” and involves both monotonic and cyclic testing of specimens to obtain a complete picture of the response of the element. The second method is known as the “Short Testing Procedure” and only uses cyclic testing of specimens. However, both of the testing methods are dependant on the definition that is taken for the yield force and the yield displacement of the specimen. A number of possible definitions are also set out in the following section.

3.2.1 Definition of Force and Displacement

In the following testing procedures, the force is taken to have a very general meaning. It refers to the normal working characteristic of the structural element that is undergoing testing. Hence it may be a tensile force load, a bending moment, a shear force, or any combination of loading actions. Similarly, the displacement is taken as the corresponding movement due to that force, i.e. a rotation θ for a bending moment, an elongation δ for a tensile force or an angle γ for shear.

There are also a number of possible definitions of the elastic force, F_y , of an element. For this experimental study, the following definition is taken. From a recorded force-displacement curve as shown in Figure 3.1, the elastic range limit, F_y , is calculated as follows:

- The tangent at the origin of the curve is evaluated to give the elastic, or initial, stiffness of the element, E_t ;
- The secondary stiffness with a slope of $E_s = \frac{E_t}{10}$ is calculated;
- The tangent to the curve with the secondary stiffness, E_s , is found;
- The intersection of the initial stiffness and the secondary stiffness defines the elastic limit, F_y ;
- e_y is the displacement corresponding to the intersection point.

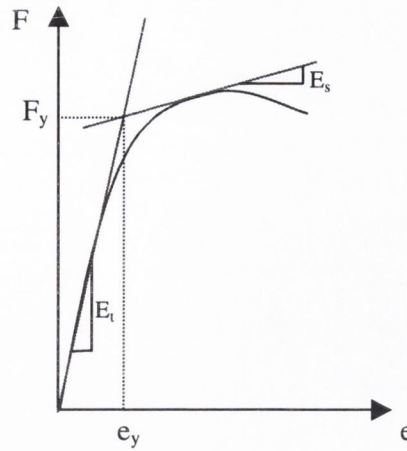


Figure 3.1: Force-Displacement Curve

3.2.2 Complete Testing Method

The complete testing method involves the testing of three separate identical specimens. The first test is a classical monotonic test. The displacement is increased in order to impose a load on the specimen, which is defined as positive. A force-displacement curve such as that shown in Figure 3.1, is recorded. From this curve, the following parameters are determined:

- The initial stiffness, E_t^+ ;
- The yield force, F_y^+ ; and
- The yield displacement, e_y^+ .

The superscript denotes the loading direction on the specimen, with the sign convention of tension being defined as a positive force and compression as a negative force. The second test is also a classical monotonic test with compression, or negative, loading of the specimen. From this test, the parameters E_t^- , F_y^- and e_y^- are determined.

The third test is a cyclic displacement test with increasing amplitude. The imposed displacement waveform has the following characteristics:

- One cycle in the $\frac{e_y^+}{4}, \frac{e_y^-}{4}$ range;
- One cycle in the $\frac{2e_y^+}{4}, \frac{2e_y^-}{4}$ range;
- One cycle in the $\frac{3e_y^+}{4}, \frac{3e_y^-}{4}$ range;

- One cycle in the e_y^+ , e_y^- range;
- Three cycles in the $2e_y^+$, $2e_y^-$ range;
- Three cycles in the $(2+2n)e_y^+$, $(2+2n)e_y^-$ range, where $n = 1, 2, 3, \dots$;

More cycles at each displacement interval may be added if necessary, as well as different intervals depending on the experimental requirements. This waveform is shown in Figure 3.2.

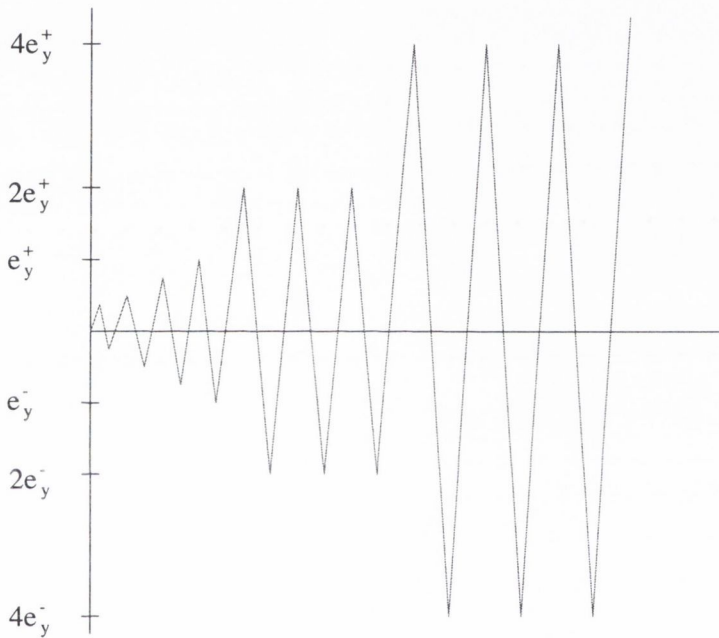


Figure 3.2: Cyclic displacement waveform for ECCS procedures

3.2.3 Short Testing Method

The short testing method is very similar to the complete testing method in that the same cyclic test is performed with the same characteristics. In the short testing method, the two monotonic tests are not performed. However, because the parameters, F_y^- , F_y^+ , e_y^- and e_y^+ , are unknown at the beginning of the test, the following procedure is used to evaluate them. A number of very small displacement increments are imposed upon the specimen. These displacement steps should be of small enough magnitude to ensure a minimum of 4 displacement levels between zero and e_y^- and e_y^+ . From the recorded force-displacement data, the initial stiffnesses, E_t^+ and E_t^- , are evaluated.

As defined in section 3.2.1, the yield force is identified as the intersection of two tangential lines. The first of these lines is the initial stiffness of the test specimen. The second line is a tangent to the curve envelope as shown in Figure 3.3. From these two lines, the parameters F_y^+ and e_y^+ are determined. Similarly, the parameters F_y^- and e_y^- can be found from E_1^- . Once the required parameters have been determined, a cyclic test is executed as described above for the complete testing method.

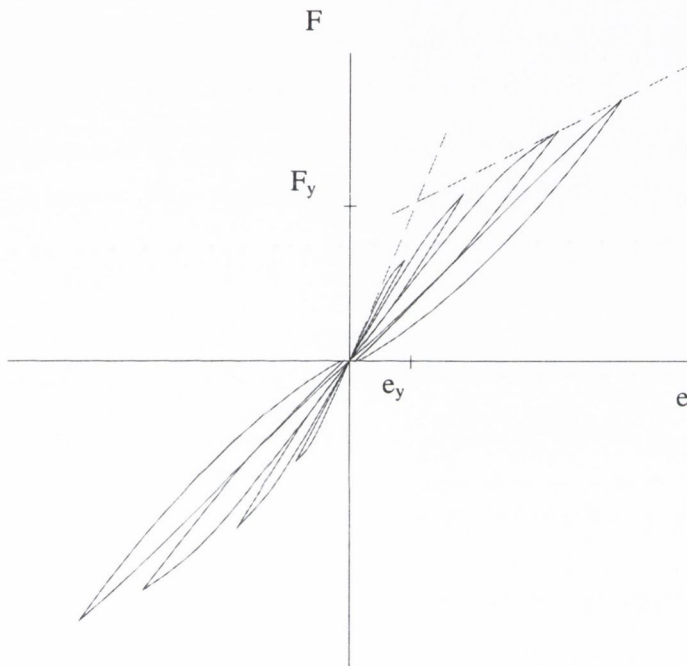


Figure 3.3: Method for determining cyclic parameters using the short testing procedure

3.3 Structural Testing Control Software

Three main loading programs were developed for use with equipment in the structures laboratories. Their primary role is to control the servo-hydraulic actuators discussed in section 3.4. All of these programs are written in the graphical programming language LabVIEW, which has been specially developed to meet the requirements of engineers and scientists employing data acquisition equipment.

The following section introduces the scanning program that forms the basis of all the control programs developed during the course of this research project. In all programs, the basic scanning code is capable of scanning the response of multiple strain gauges, load cells and LVDTs. Only the output section changes between the different program applications.

The third section introduces the shakedown test program. This program was designed to impose a series of very small displacements on a test specimen to ensure that all measurement devices are operating correctly without damaging the specimen.

The second program, the constant amplitude cyclic waveform program, developed is examined in the fourth section. This is designed to impose a large number of constant amplitude displacement cycles on a test specimen.

The fifth section looks at the structural element cyclic testing program developed as a fundamental part of this research study. This program has been designed to impose the cyclic displacement waveform described in section 3.2.

3.3.1 Basic Scanning Program

The input program code, shown in Figure 3.4, was adapted from a previous impact loading program (Prichard, 2000). The program initialises and creates a new binary data file with the default name of DATA.BIN. A binary file is used because binary numbers can be written to the computer hard disk at a much faster rate than decimal or text data.

At the same time the analog inputs are configured. This is done using the *AI CONFIG* sub-program shown in Figure 3.4. The input limits determines the type of measurements the program is able to read in. If these limits are set to 0, the default settings, the program automatically uses the hardware defaults as determined by the data acquisition card (DAQcard) configuration utility. This is the optimum setting for the card and it is not recommended they are changed. It allows the card to scan any devices that return a voltage in the range $\pm 10V$. The device number is a number that the computer assigned the DAQcard when it was originally installed. This is determined by the computers operating system. If this number is incorrect, the program will be unable to register the existence of the DAQcard and a general fault will occur. The interchannel delay is the time between channel scans. The default value in this case is -1.0 as this automatically allows the hardware to determine and scan at its optimum rate. The scan rate is measured in scans per second and is a user-defined attribute.

The buffer size determines the maximum number of scans that the computer will retain in memory. The default value for this is 500 scans. This allows the program to continue scanning if the computer running the system hangs up for any reason during the test so that experimental data is not lost.

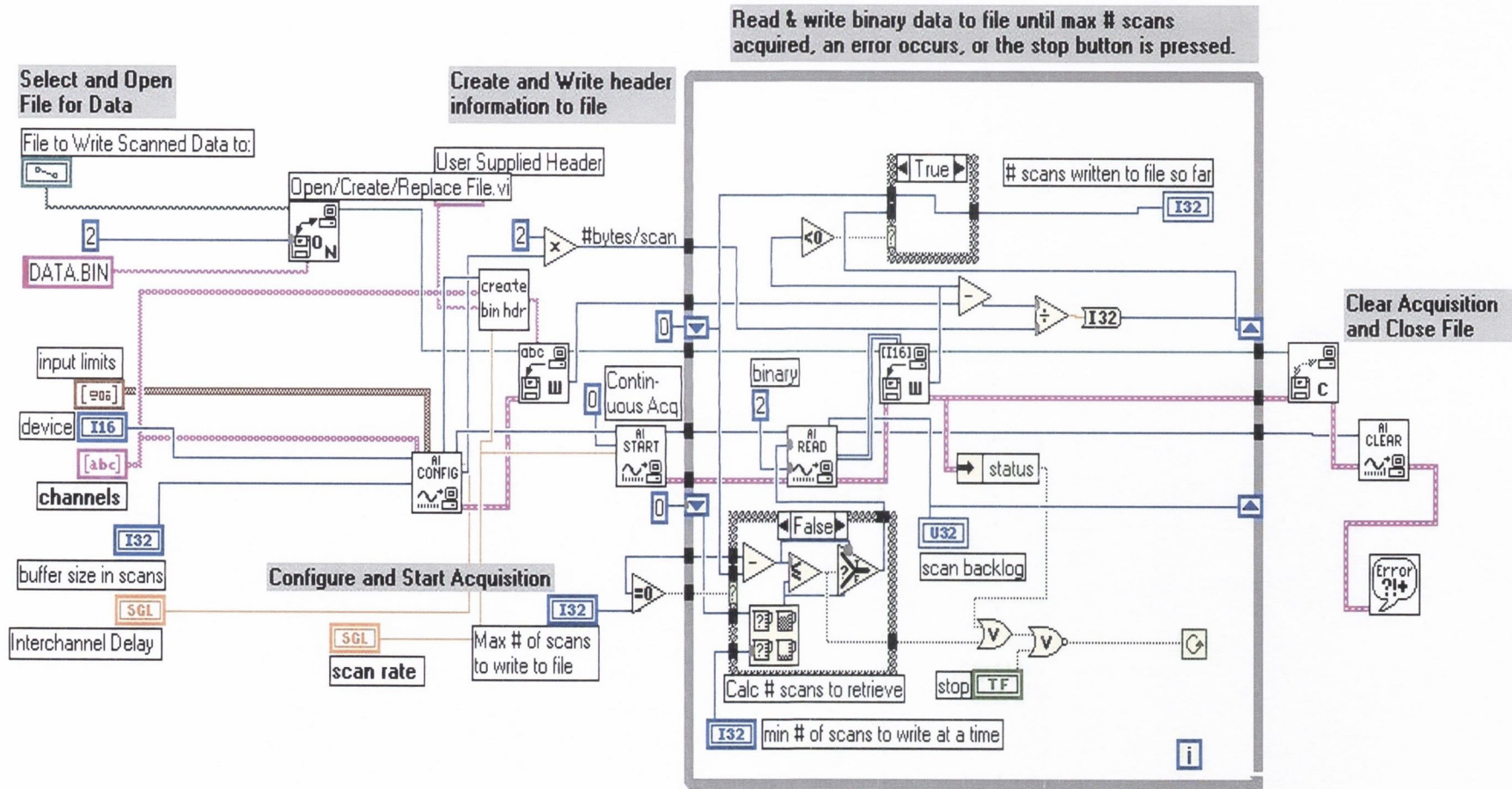


Figure 3.4: Program Code for All Loading Program Inputs

The final piece of information required to configure the inputs is the channels that are to be scanned from. It is this that determines whether the channels will be scanned singly or multiplexed as described above. For example, the code *ob0!sc1!md1!0:3* informs the configuration utility that channels 0 to 3 on module 1(md1!) from SCXI chassis 1(sc1!) are to be multiplexed on to the DAQcard channel 0 (ob0!). It is possible to add further strain gauge channels to this DAQcard channel by referring to a second module on the chassis by using the code *ob0!sc1!md2!0:3*, and so on. The User defined header, scan rate, input channels and buffer size is all inputted from the user interface and may vary slightly with each type of program or test being performed described below.

The program then begins to scan on the indicated channels using the sub-program *AI START*. The type of scanning is initialised during the first scan where it is set to continuous scan. The program treats the scanning as a conditional loop. The program continues to scan at the set rate until one of three possibilities occurs: the maximum number of scans is acquired, an error occurs or the stop button is pressed on the interface screen (shown below). This loop begins by checking that the maximum number of scans hasn't occurred using a true/false loop. If the program passes this check, it enquires whether the stop button has been pressed, or if an error has occurred. It then scans all of the required channels as binary values and writes them to the buffer. The program then calculates the number of scans that it has completed and reports this value on the user interface. If the minimum number to scans to write to file value has been reached in the buffer, it then writes the entire buffer to the output file. The program then passes the any values to the graph on the interface panel. Should the program exit this conditional loop, it stops scanning and writes any remaining scans in the buffer to the file and closes the output file. If an error was the cause of the program exiting, the error is reported on screen.

As stated above, the scanning section of the programs creates a binary file into which all of the scanned experimental data is written. However, this data must be converted from binary format to decimal format before it can be analysed. This operation is carried out using a separate program. The program reads the scanned data in as an array, converts the data into decimal format and then plots it. The user is then able to choose the range of data that they wish to analyse. The chosen data range is then saved as a text file that can be opened using any commonly available spreadsheet package.

3.3.2 Shakedown Testing Program

The shakedown test program has been designed to fulfil two important functions. The first is to ensure that all experimental equipment is working correctly. The second is to impose the small amplitude cyclic displacements as required for the short testing procedure described in section 3.2.3. The reasons for each use is discussed below.

The first use of the program is to allow the data acquisition equipment to be tested and calibrated. A shakedown test is suggested by Leon & Deierlein (1996) to allow the user to check and calibrate all of the measuring devices and data acquisition equipment. The shakedown test allows any slip in the joints or gauge malfunctions to be pre-determined, avoiding problems during the full test.

The second use of the shakedown testing program is in the short testing method. The imposed waveform uses the amplitudes of 0.5, 1.0, 1.5 and 2.0 mm when calculating the waveform, as shown in Figure 3.5. A maximum displacement of two millimetres is used as this should be below the yield displacement of the specimen. If it is felt, that this value is too large, or small, it may be easily changed in the program code. The program begins by holding the actuator at the zero point for 50 scans. A full cycle at each amplitude is then imposed in the above order. Once the 2.0 mm cycle has been imposed, the order is reversed and the displacements imposed again. Once the final cycle is complete, the program again holds the actuator at the zero point for 50 further scans before automatically shutting off. This data can then be used to calculate the elastic yield points of the test specimen. The user interface for the program is shown in Figure 3.6. As discussed above in section 3.3.1, the user is required to input the following list of input characteristics:

- the scan rate;
- channels to be read;
- maximum number of scans to be read;
- buffer size; and
- the number of scans to be written to the hard drive at any one time.

However, the user must also insert an update rate and the number of scans for four cycles (N_4). These characteristics determine the frequency of the waveform that is being imposed on the test specimen. It is recommended that the update is the same as the scan rate. The number of samples for four cycles is used to determine the length of each cycle. It is this parameter that is used in conjunction with the update rate to find the frequency. The program code required to implement the shakedown test program is shown in Figure 3.7.

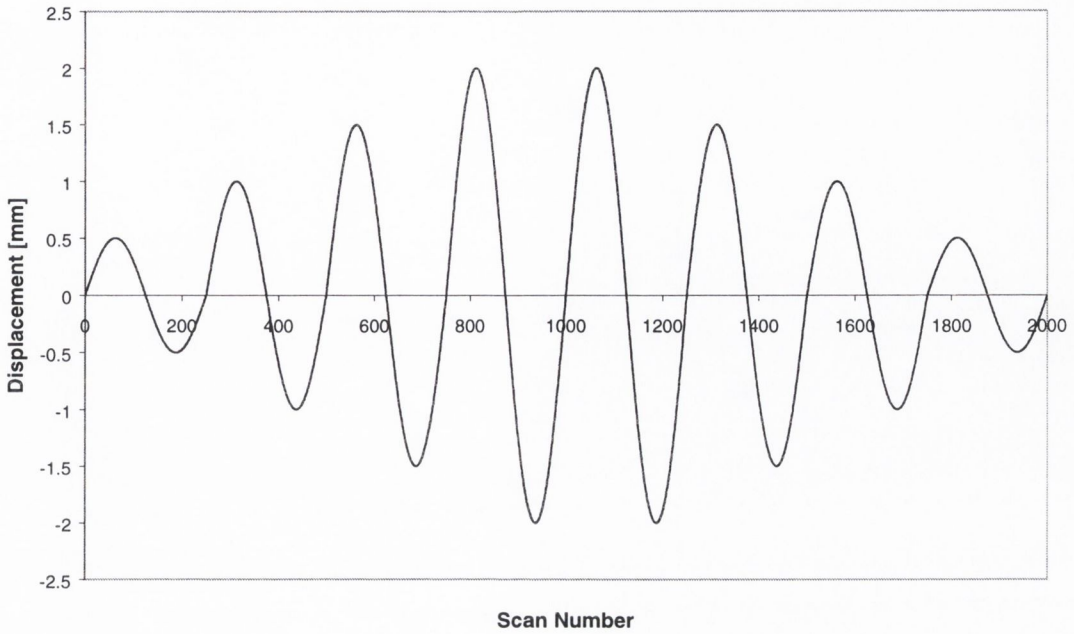


Figure 3.5: Imposed Waveform for Shakedown Test Program

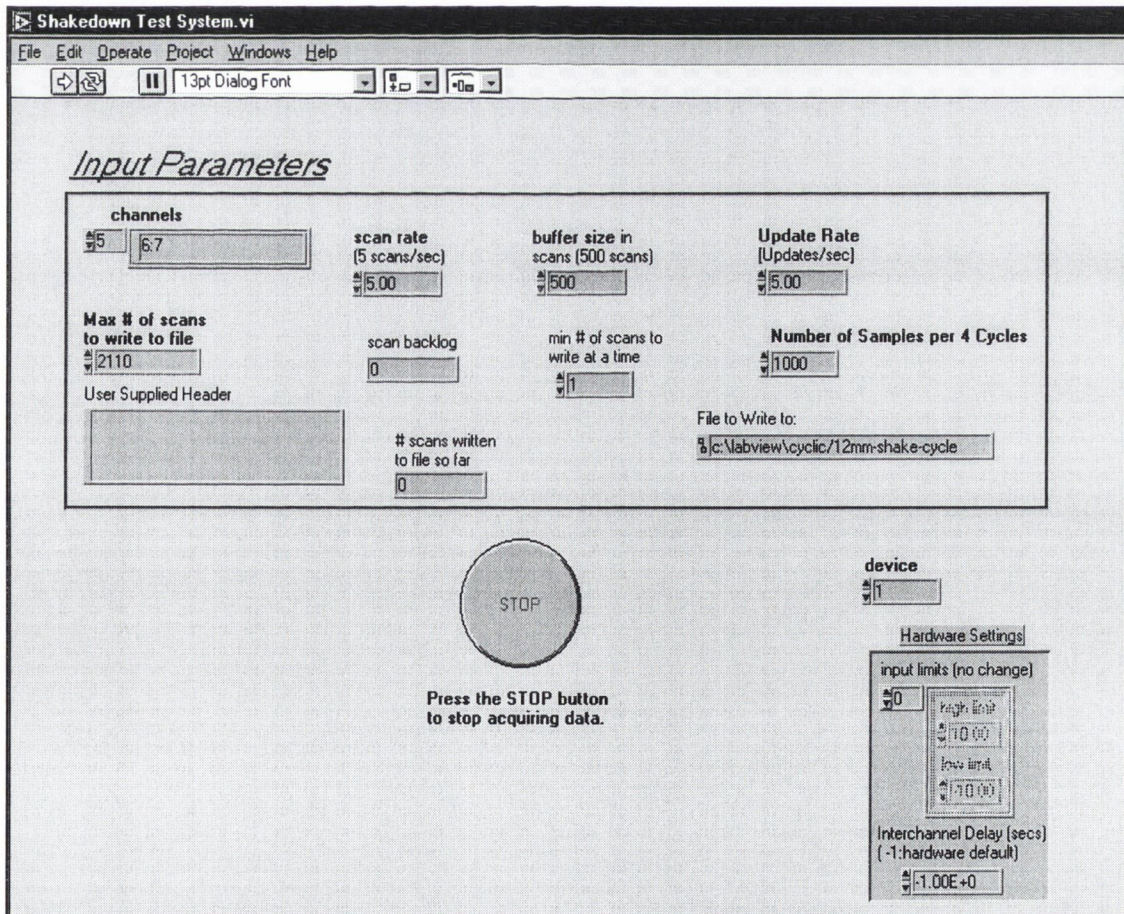


Figure 3.6: User Interface for Shakedown Testing Program

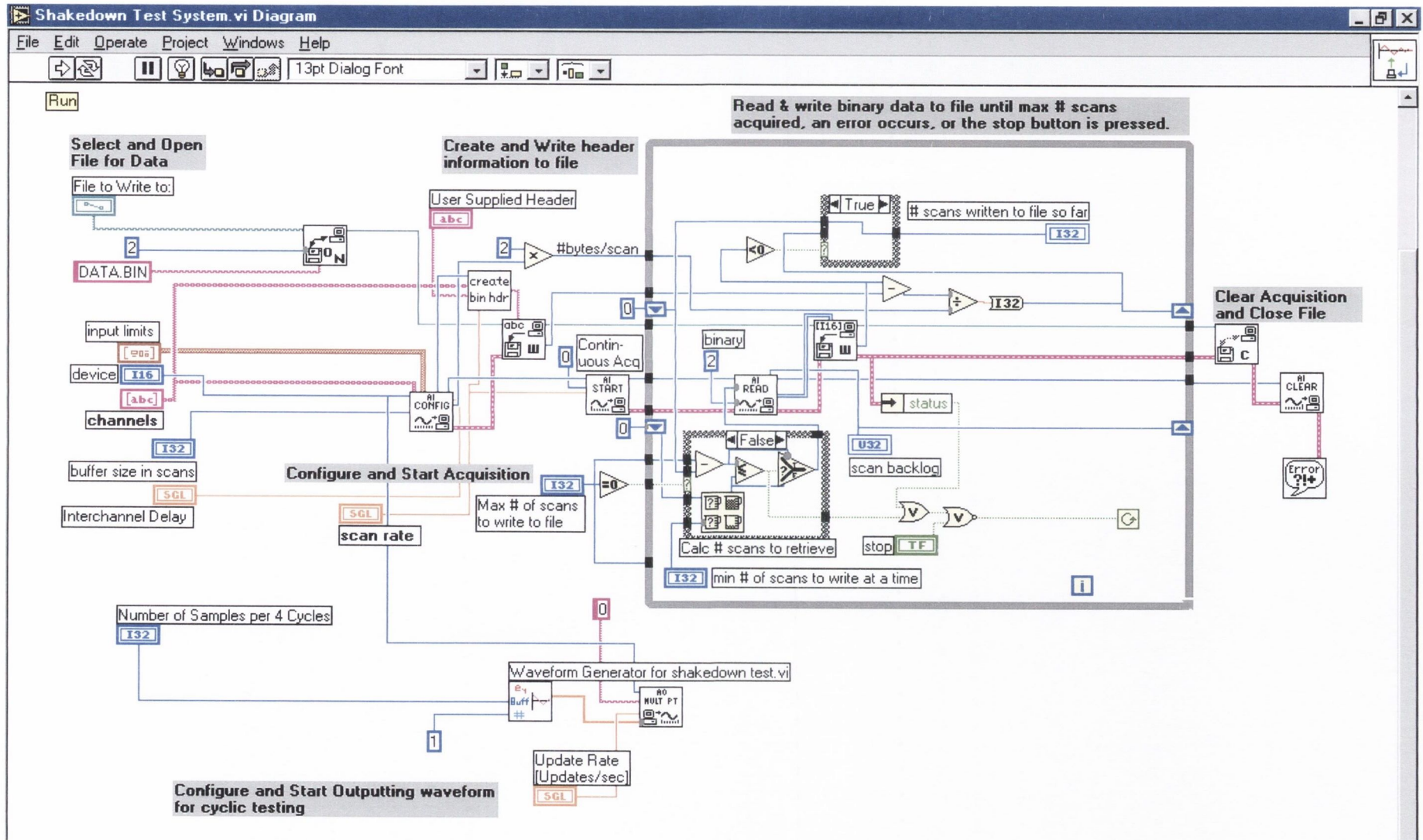


Figure 3.7: Program Code for Shakedown Test Program

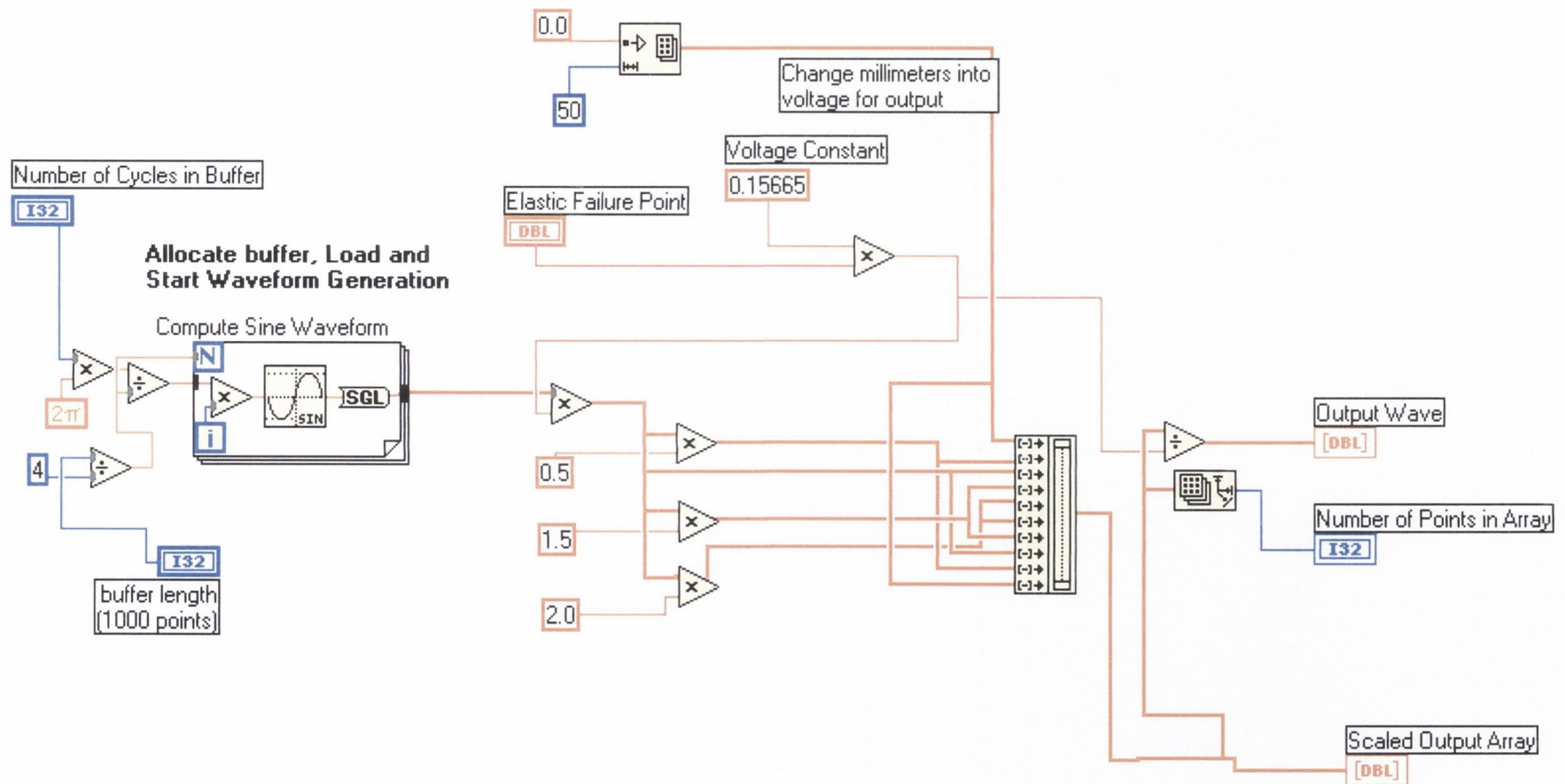


Figure 3.8: Program Code for *Waveform Generator for shakedown test.vi* sub-routine

The program begins by initialising the input characteristics given by the user as explained in section 3.3.2. At the same time, the program passes the variable N_4 into a sub-routine called *Waveform Generator for shakedown test.vi*. This sub-routine, shown in Figure 3.8, creates the waveform to be imposed upon the specimen. The sub-routine first creates a sine wave with a length of $N_4/4$. This sine wave takes the form of an array of numbers. This array is scaled by the actuator calibration constant, and then duplicated and scaled by 0.5, 1.5 and 2.0. The overall array is then created by combining the scaled arrays to give a total length of N_4 . This final array is then passed back to the main program. There is also a function to graph the waveform array to assist with debugging should any changes prove necessary at a later time.

Once the sub-routine has created the output waveform, it is passed into an output routine. This is a standard sub-routine within the programming language. It requires the DAQcard device number, the number of updates/second, and the array. This sub-routine commands the DAQcard to output the required voltages in the order they are placed in the array. The program continues to run until the required number of scans has been obtained, or until the output array has been completed.

3.3.3 Constant Amplitude Cyclic Waveform Program

This program was originally developed to impose monotonic loading conditions on the structural specimens. However, the program was expanded to impose a number of cycles of constant amplitude. This allows a greater diversity of test types to be run using the same equipment. This gives the program two important uses;

- (a) If a specimen is capable of surviving through a full cyclic test, the program may be used to impose a number of large amplitude cycles to determine if the demand of constant loading will induce a fatigue failure of the specimen; and
- (b) The program may also be used to obtain a monotonic force-displacement curve if a cyclic response is not required. This is because the first cycle in a series will result in a monotonic response.

The user interface for this program is shown in Figure 3.9. Although the basic functions are similar to that in the shakedown program, there are also a number of additional features. The two most important of these are the graphs shown in Figure 3.9. The top graph shows the full waveform to be imposed upon the test specimen. The lower graph plots the scanned data versus scan number as the test proceeds. This allows the user to detect unusual trends or sudden failures during the experiment. It should be noted that this scanned data is shown without calibration constants, and can therefore only be used as an indication of the specimen behaviour.

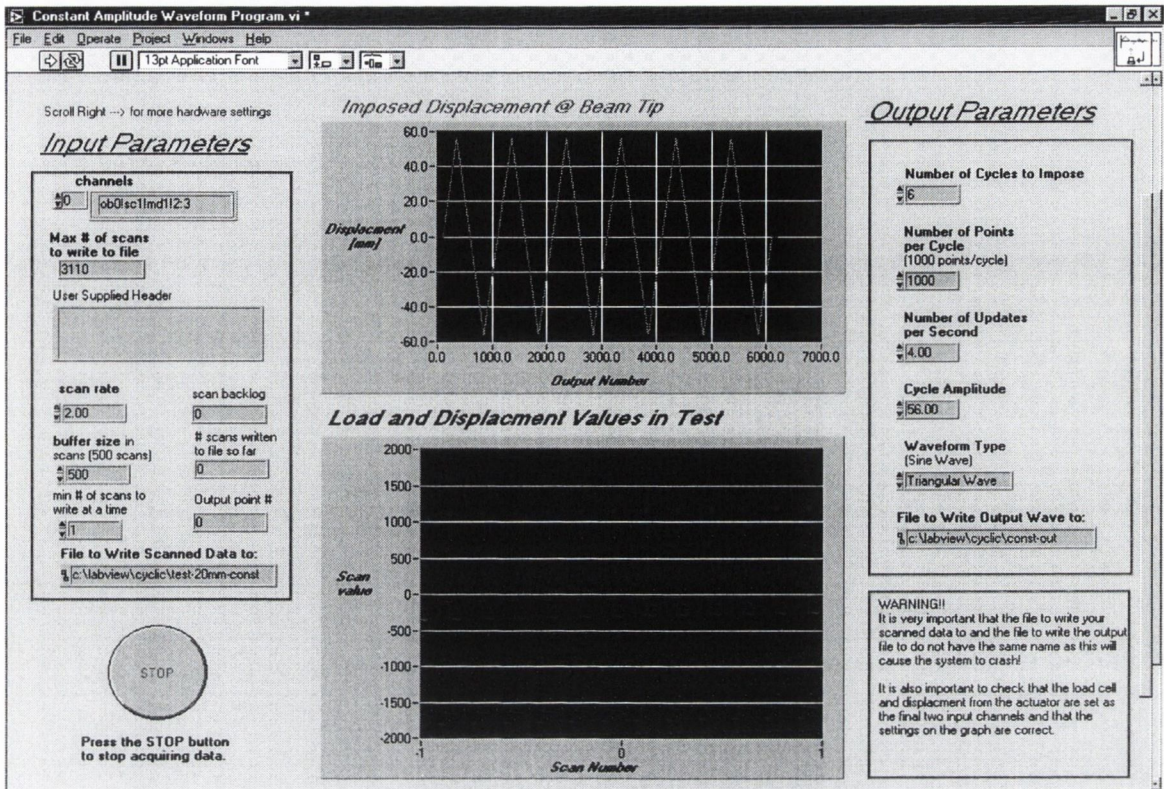


Figure 3.9: User Interface for Constant Amplitude Waveform Program

As in the shakedown test program, the user is required to enter a number of input parameters. These include the channels to be scanned, the scan rate, buffer size, the number of scans to write to file at a time and the name of the file to write the scanned data to. However, unlike in the shakedown test program, the user is not required to enter the maximum number of scans to write to file. This is calculated by a small sub-routine that reads the scan rate, the output rate and the size of the output array. Using these values, the number of scans necessary to complete the entire array is found.

The user is also required to select a number of output parameters. The first is the number of cycles to be imposed upon the test specimen. The program is capable of imposing anywhere between 1 and 999 cycles. However, very large cycle numbers impose a limit on the number of samples in each cycle depending on the computer capacity. The user is also required to input a number of characteristics for the output waveform, which are listed below:

- The number of updates per second. As in the shakedown test program, the default value for this is 5 updates per second;
- The amplitude of the cycle must also be input before the test begins. The default value for this is set at 50mm, which is the maximum allowable travel on the standard hydraulic actuator as discussed in section 3.4;

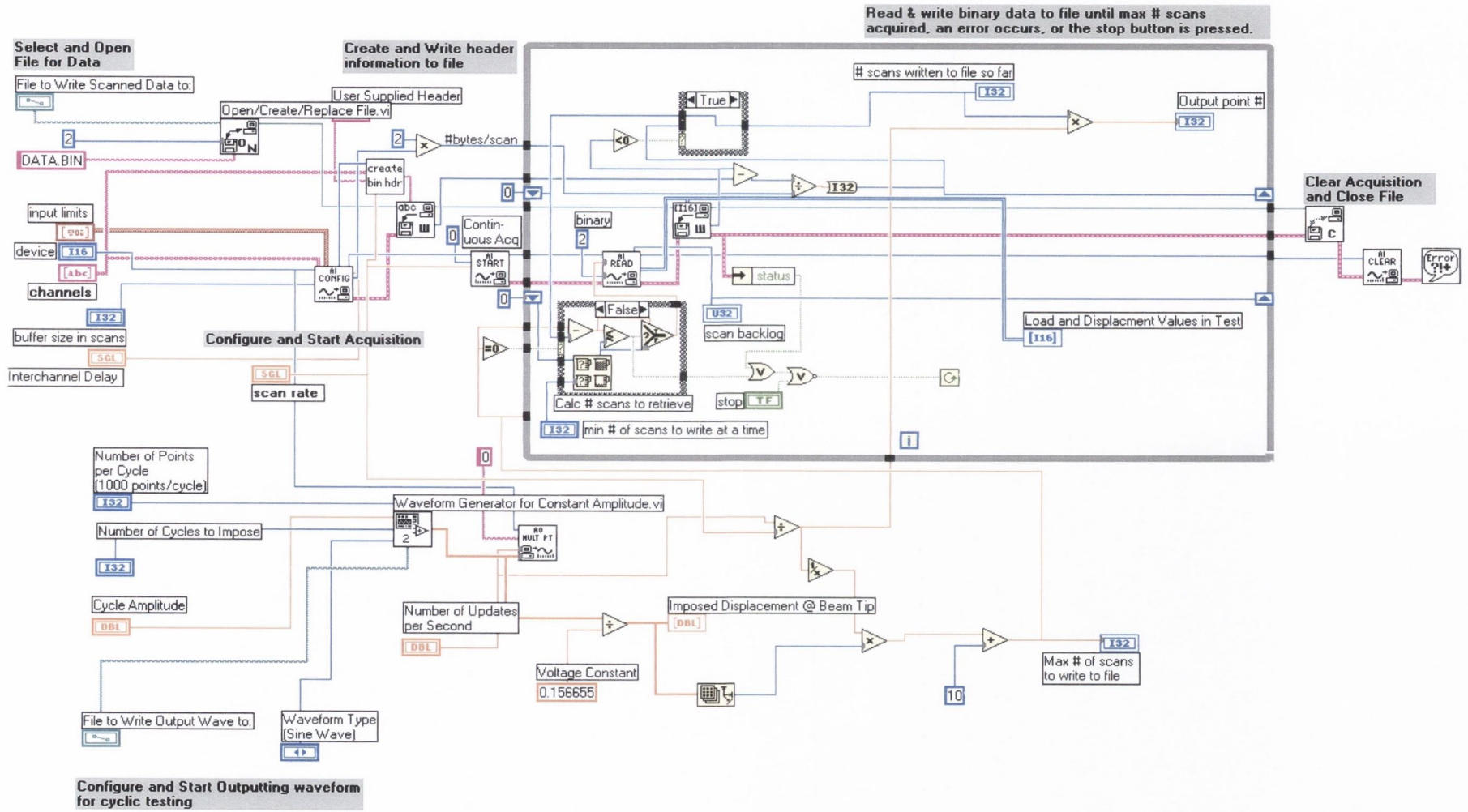


Figure 3.10: Code Diagram for Constant Amplitude Waveform Program

- The waveform type. At present, it is possible to select either a sine or a triangular wave, although the program has been designed to allow for the addition of further types such as a sawtooth or square waveform; and
- A file location and name to write the waveform data to. The output file has been provided to allow a comparison between the intended displacement at a particular time and the actual actuator displacement. It is important to note that the name and location of this file must be different to the name and location of the scanned data file or a fatal error will occur in the program.

As in the shakedown test program, the user inputted variables are passed from the main program to a sub-routine, *Waveform Generator for Constant Amplitude.vi*, where they are used to create the output waveform. The code for this sub-routine is shown in Figure 3.11. The program first determines the type of waveform that is to be produced from the user inputs. The program then employs the number of cycles and the number of samples per cycle to produce an array with the required pattern and a maximum amplitude. The user defined amplitude is converted into a voltage, which is used to scale the array. One hundred samples with a amplitude of zero are then added to the beginning and end of the array to ensure that there are an easily identifiable start and finish point for the scanning program to use. The scaled array is then passed through a data limiting block which ensures that none of the values are beyond the capabilities of the actuator, i.e. $\pm 50\text{mm}$. The array is written to the user defined output file before being passed back to the main program. However, because this program sub-routine was set up in anticipation of further changes being made, such as the addition of other waveform types, a front panel was incorporated. When the sub-routine is called as part of the main program, this front panel is not seen but allows the user to test changes to the sub-routine without running the full program. The panel includes all of the user inputs required as well as a graph to allow visual inspection of the final waveform.

When the array is passed back from the sub-routine to the main program, a number of operations are performed on it as follows:

- The waveform is graphed so the user can determine that it is correct.
- The total number of samples is also determined for the array. This number is then used to automatically calculate the correct maximum number of scans for the main program using the array size, number of scans per second and the number of updates per second using a simple mathematical equation.
- Once these calculations have been performed, the array is passed to the output sub-routine as in the shakedown test program.

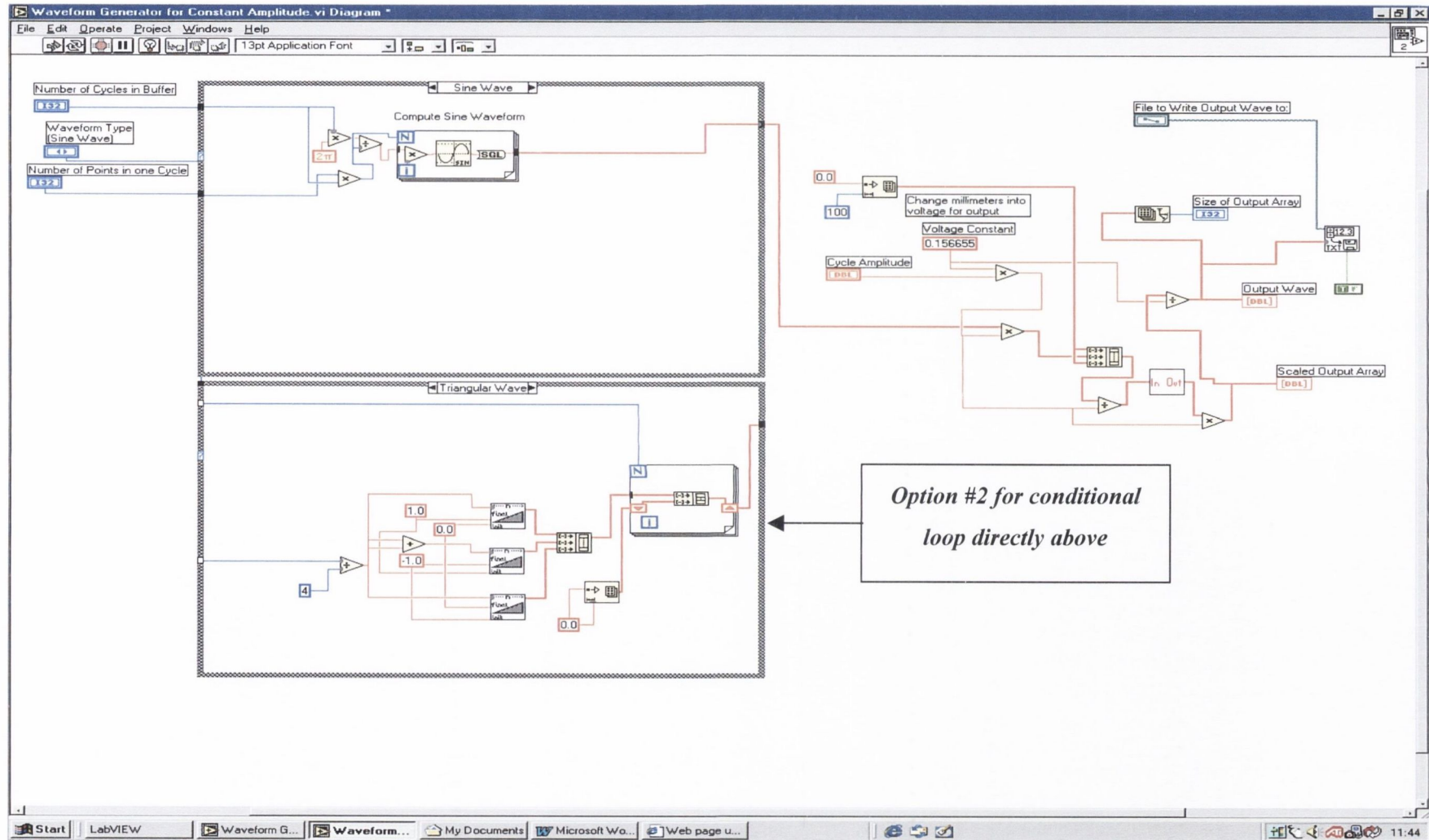


Figure 3.11: Program code for Waveform Generator for Constant Amplitude.vi sub-routine

- The program then runs until the full array has been outputted by the DAQcard, or the user halts the execution.

This program can also be used to impose a monotonic load on a specimen. This is done by setting the number of cycles to 0.5. That is, the actuator will impose the required displacement on the specimen and then return to the zero point. This allows the program to be used to perform the two monotonic tests required under the complete testing method described in section 3.2.2.

3.3.4 Structural Element Cyclic Loading Program

The structural element cyclic loading program was developed to test structural steel joints under cyclic displacement conditions. As can be seen from Figure 3.12 and 3.13, the program is very similar to the Constant Amplitude Cyclic program discussed above. All of the user inputs for the scanning parameters are identical to those discussed above as well as the updates per second, waveform type and output file name. However, there are a number of changes to the output characteristics to enable the system to create the waveform discussed in section 3.2.2.

The first additional feature on this program is that the user is required to input the elastic yield limit of the specimen. This is the value of e_y determined from either of the two testing methods described above. Because of the symmetry of the specimens to be tested and for ease of programming, it has been assumed that the tension and compression yield displacements are identical.

There is also an additional input called the waveform starting point. This allows the user to set the point around which the waveform will oscillate. For example, it is possible to set this value to –30mm, giving the actuator 80mm of travel in one direction but only 20mm travel in the opposite direction. The other additional feature of the program is called the waveform multiplier. In the ECCS procedures, the recommended waveform has four cycles less than or equal to the yield displacement, then three cycles at 2 times the yield displacement, three cycles at 4 times the yield displacement as stated above in section 3.2.2. However, using the waveform multiplier, it is possible to increase or decrease the difference between each group of three cycles. The user is also required to enter the variable N_4 and the number of samples for each of the remaining cycles. This is to allow the smaller, or elastic, cycles to be imposed on the specimen at a different frequency to the larger inelastic cycles.

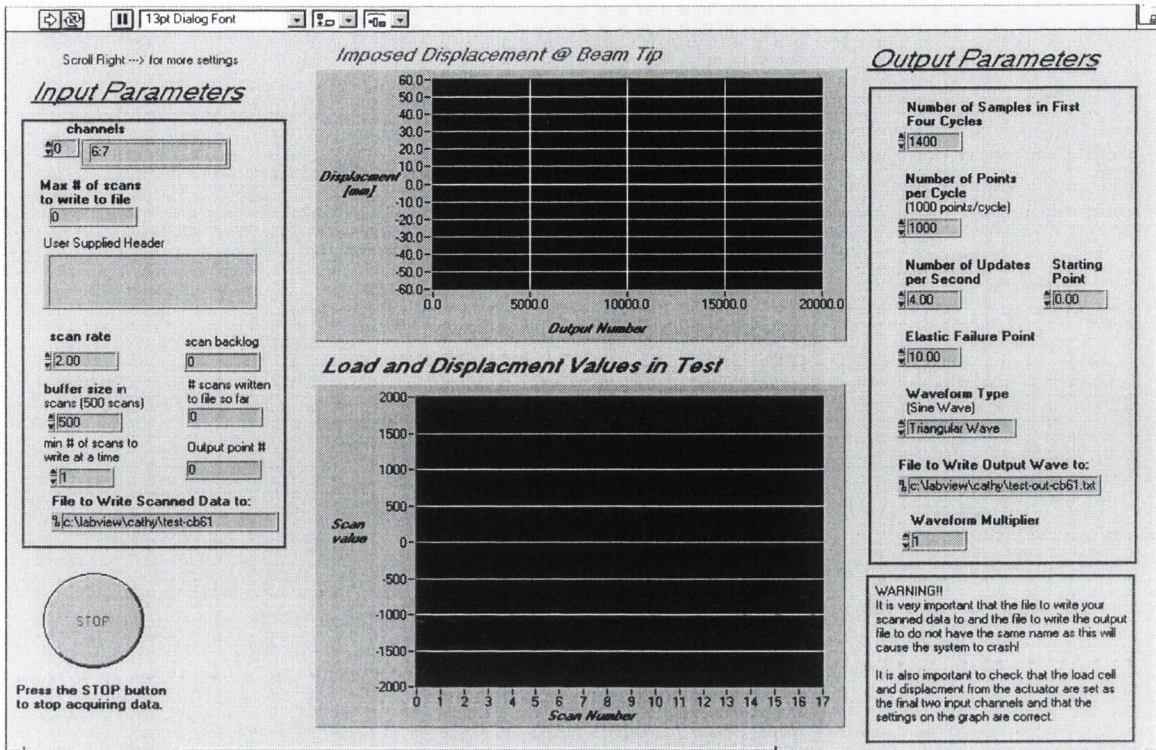


Figure 3.12: User interface for *Structural Element Cyclic Loading* program

As in the other programs, the output variables are passed into a sub-routine *Waveform Generator for Full Test.vi* to initialise the waveform. The program code is shown in Figure 3.14. The sub-routine begins by creating two separate arrays based on the user defined inputs. The first array is for one cycle of the first four cycles (the elastic cycles) while the second array is for one cycle of the post-elastic cycles. These arrays are then passed into a second sub-routine which is simply called *Construct Array.vi*. This sub-routine, shown in Figure 3.15, uses a sequential loop to create the final array for the first four cycles. This loop takes the sub-array created in the waveform generator and scales it to a quarter of elastic yield point inputted by the user. It is then combined four times to create the final array for this section of the waveform. At the same time, the second sub-array created is entered into a conditional loop. This conditional loop calculates the maximum allowable number of increments based on the waveform multiplier, the elastic yield point, the actuator starting point and the maximum travel of the actuator. The loop then constructs an array for all of the post-elastic cycles up to the point where the amplitude of the waveform is greater than the travel available on the actuator. The two arrays created by these loops are then combined to give the final waveform array, which is then passed back to the upper level sub-routine.

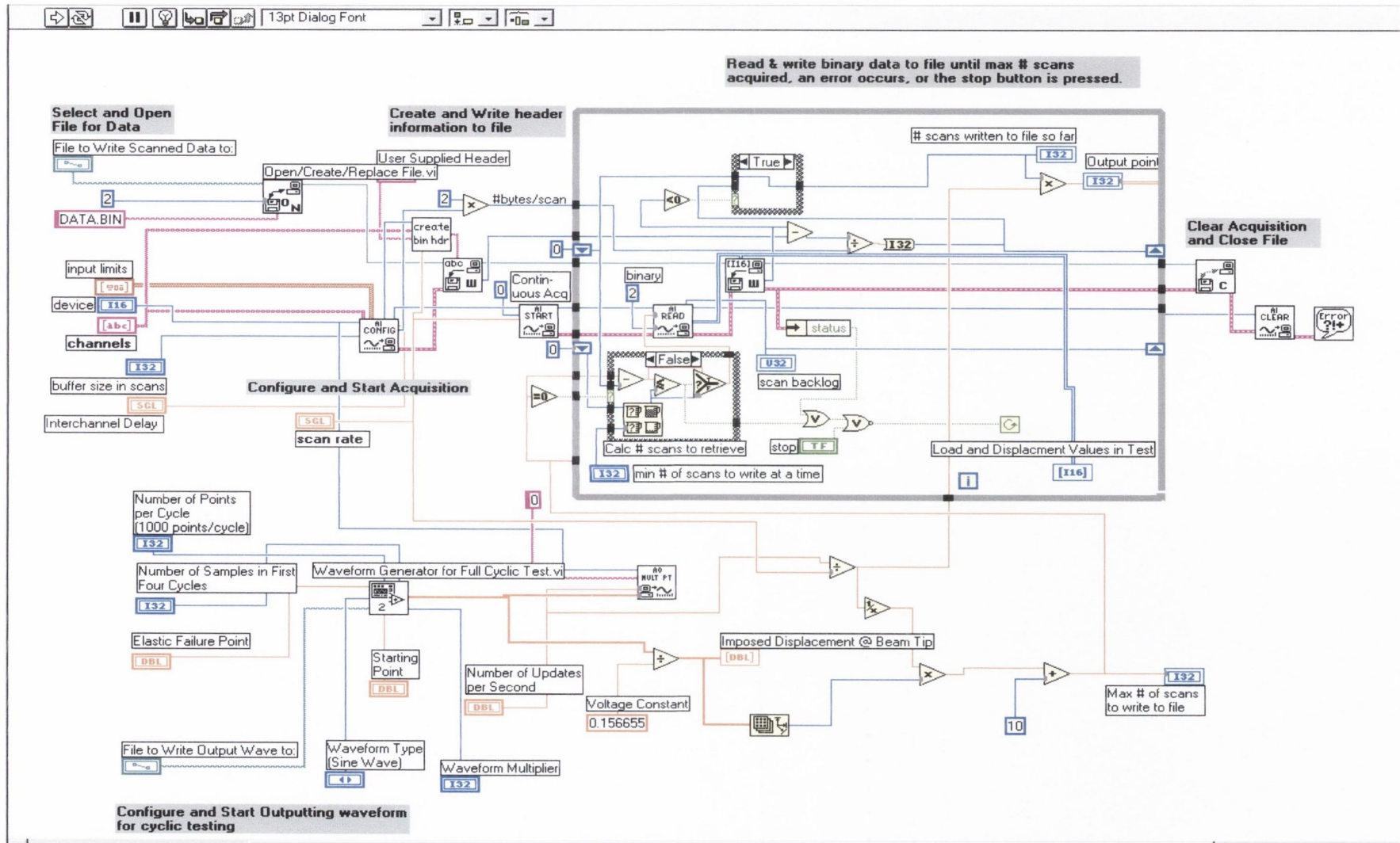


Figure 3.13: Code for Structural Element Cyclic Loading Program

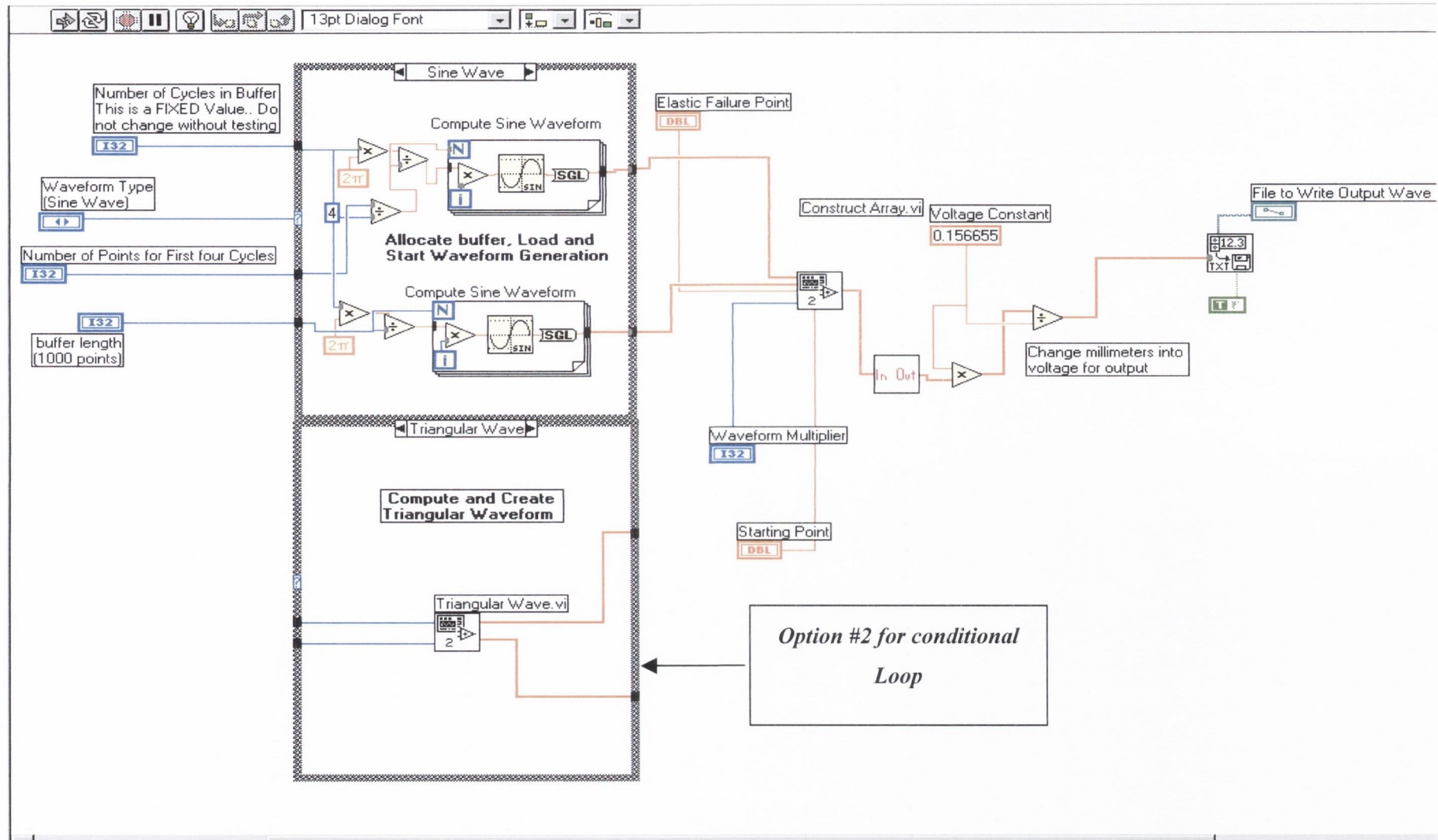


Figure 3.14: Program Code for *Waveform generator for Full Test.vi*

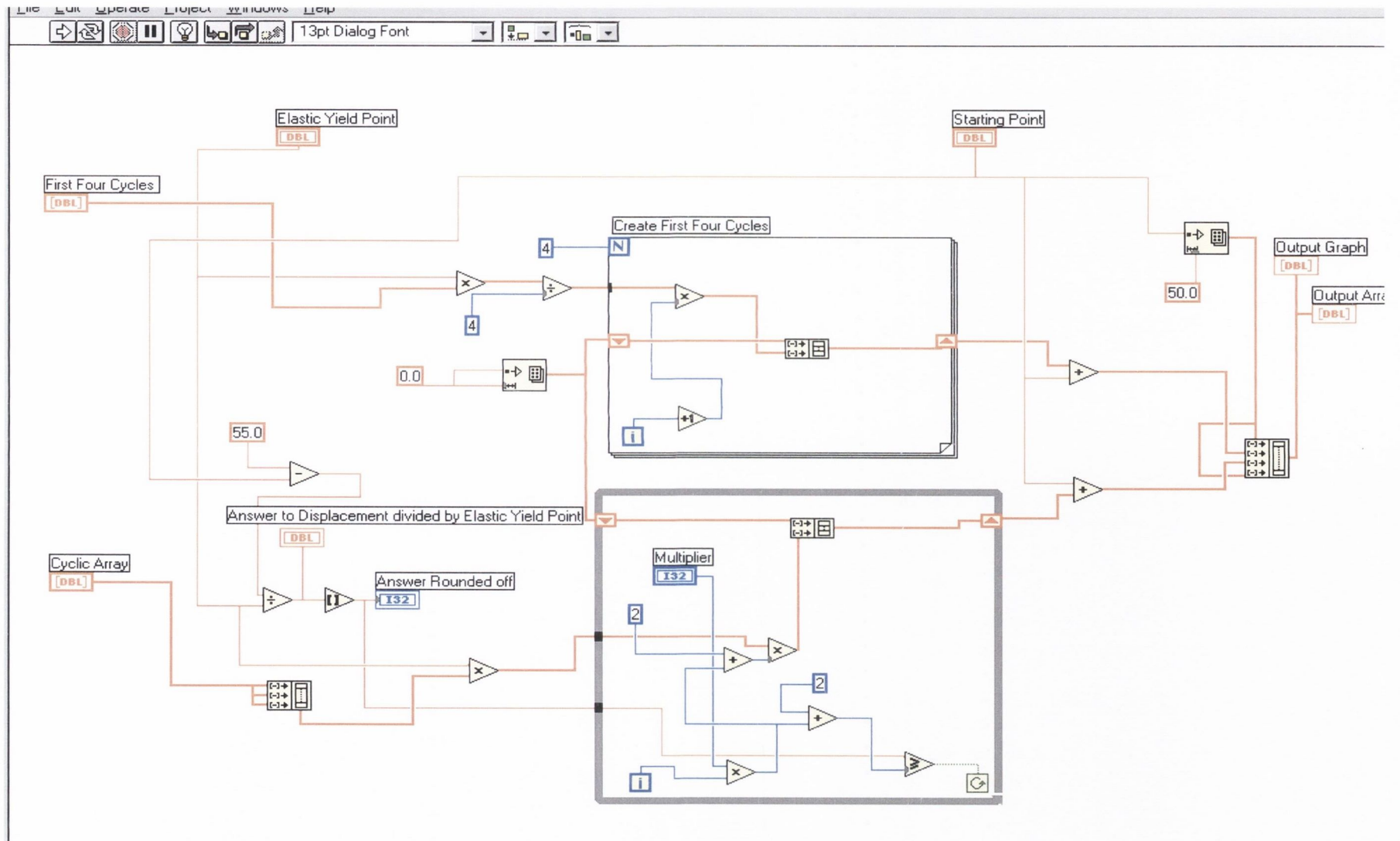


Figure 3.15: Program code for *Construct Array.vi* sub-routine

The maximum amplitude of the array is then checked and converted from a displacement to a voltage for output. The full array is passed back to the main program. As in the case of the *Constant Amplitude Cyclic Loading* program above, both of the sub-routines have had diagnostic panels incorporated into the code. Again, these panels are not called when the sub-routines are being used as part of the main program. Once the completed waveform array is passed back to the main program, it is output in the same manner as in the shakedown program and the constant amplitude programs described above.

3.4 Control System Integration

This section explains how the software described above was integrated into the actuator command process. The control mechanism of the servo-hydraulic actuator is first described followed by a brief description of the computer equipment required. The manner in which the computer system handles the required signals to control the actuator and measure the load and displacement is also explained. The components necessary for the system integration are as follows:

- Pentium computer (minimum recommended processor speed of 133Mhz) with Microsoft Windows 95 and LabVIEW software;
- Control software discussed in section 3.3;
- Suitable data acquisition computer card;
- Signal conditioning chassis and modules;
- Servo-hydraulic actuator command console;
- Servo-hydraulic actuator;
- Measurement devices; and
- Experimental specimen.

Figure 3.16 illustrates the method in which the above components interact with each other. V_{out} is the voltage signal moving the servo-value, V_{ret} is a return voltage from the actuator servo-value to the command console, and the updated signal V_{out} is a corrected output signal based on the original V_{out} and the return signal V_{ret} . This will be discussed in more detail in section 3.4.3. As may be seen below, signals are passed from software, based on the user inputs, through the signal conditioning unit to the servo-hydraulic command unit. The response is measured and returned to the software again via the signal conditioning unit to the software, where the data is transferred to the computer hard disk.

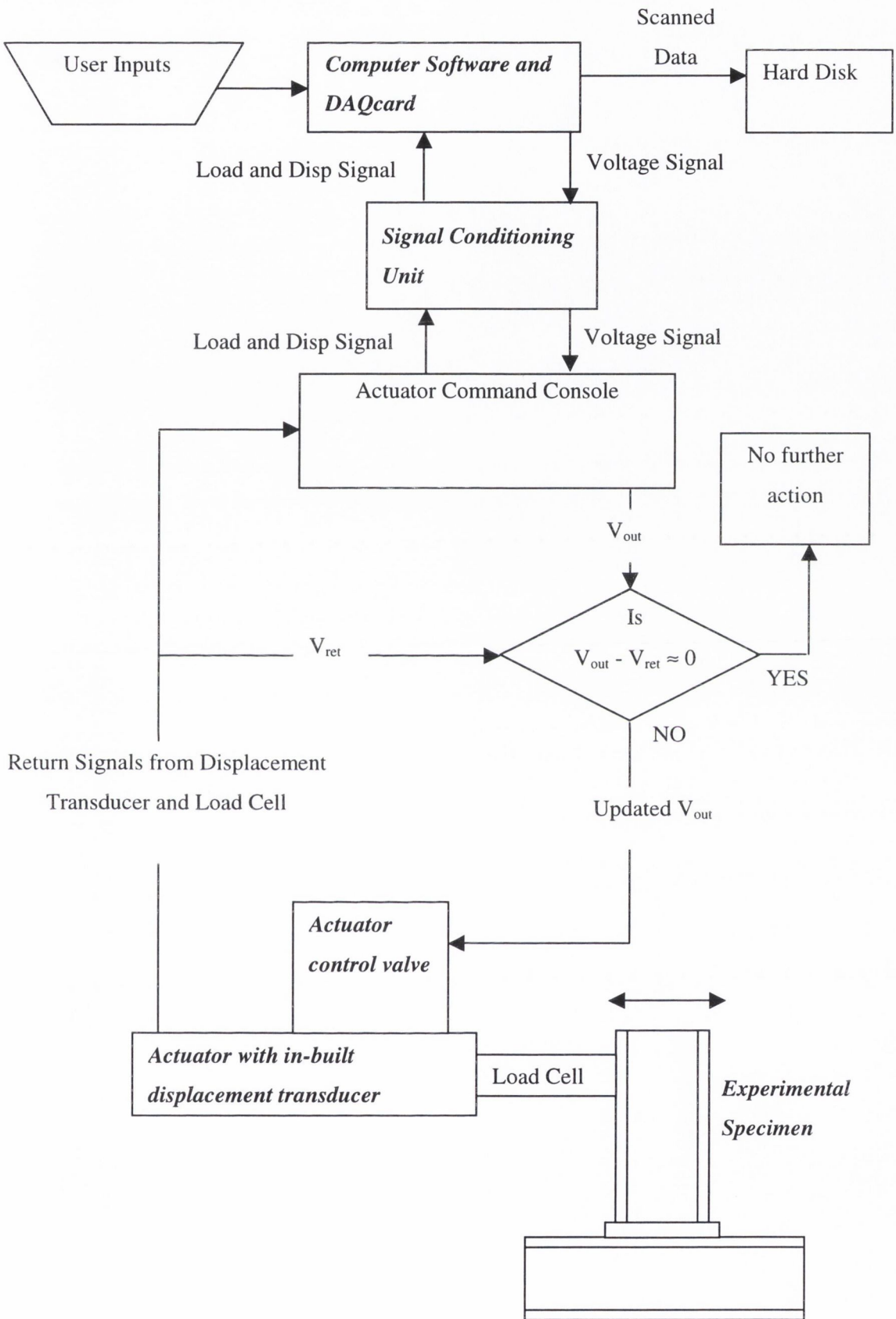


Figure 3.16: Flowchart detailing system integration

3.4.1 Servo-Hydraulic Actuator Command Process

The cyclic loading system was designed to be capable of controlling the displacements of any of the servo-hydraulic actuators present in the structural laboratories. These actuators consist of a hydraulic ram, together with an internal displacement transducer, load cell, servo-valve and control console.

The actuators are controlled using a command console, shown in Figure 3.17 and Figure 3.18. This console allows the actuator to be controlled in one of three ways:

- *BALANCE* mode allows the user to manually control the load or displacement of the actuator. Normally used to set the actuator to its centre, or zero position; also allows a pre-load or an initial displacement to be imposed.
- *DISP* mode allows the actuator to be controlled in displacement using the internal displacement transducer.
- *LOAD* mode allows the internal load cell to be the controlling device in the actuator.

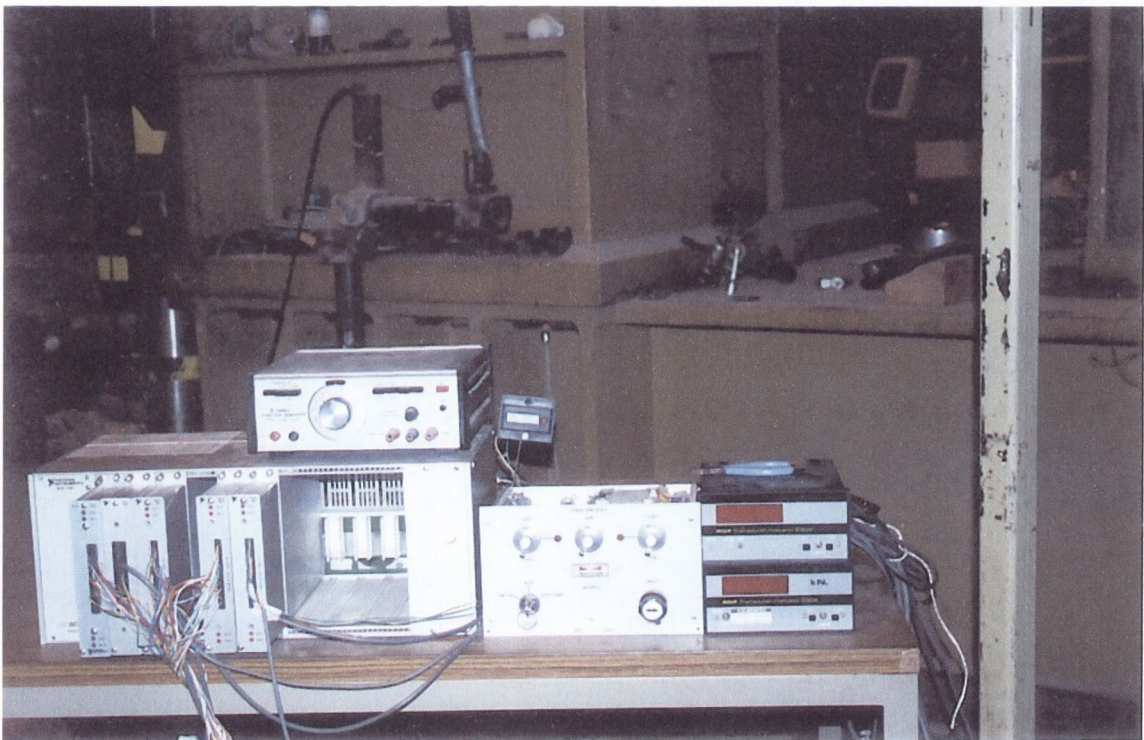


Figure 3.17: Separated actuator command console with signal conditioning unit

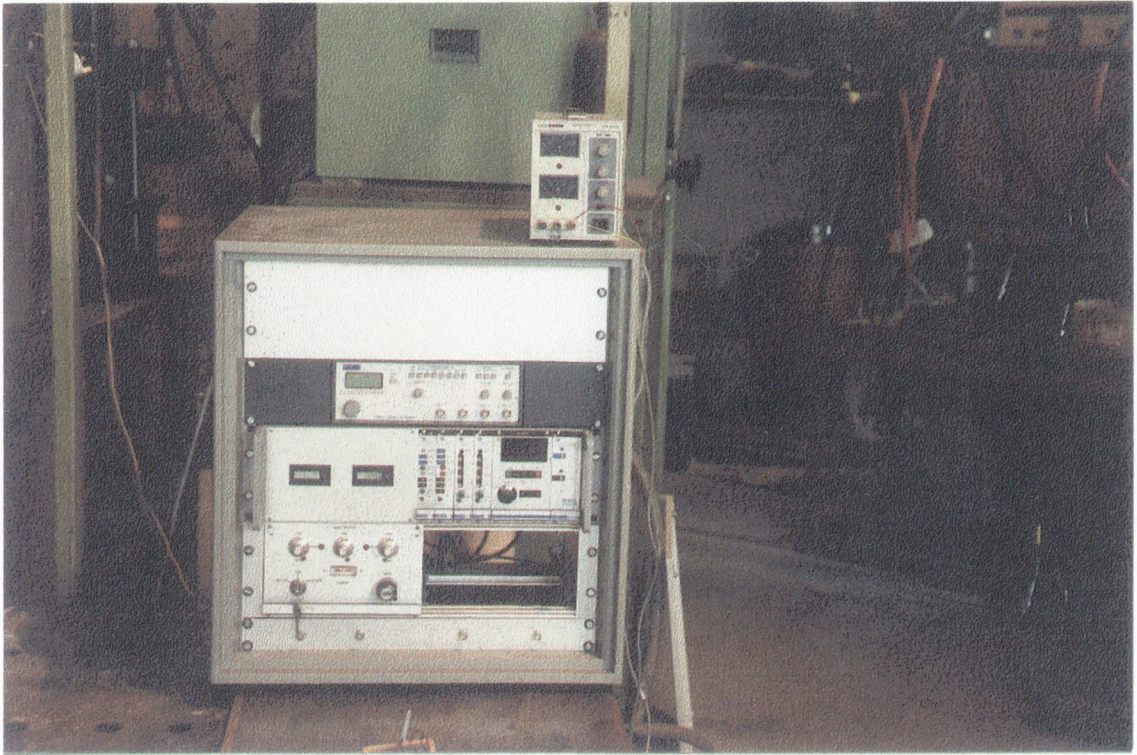


Figure 3.18: Integrated actuator command console

The console controls the actuator by means of a continually updated voltage signal in the range of $\pm 10\text{V}$. This voltage operates on a feedback principle from the controlling device in the actuator. The command console provides an initial voltage to the servo-valve of the actuator, which opens or closes as necessary to move the actuator to the required load or position. The displacement transducer and load cell return a voltage signal to the command console that corresponds to the actual position of the actuator. Depending on the control mode selected, the appropriate signal is compared to the initial signal and the difference calculated. A new signal is then sent to the servo-valve to open or close as necessary to move the actuator to the correct position. Again, the two devices send a return signal for comparison. This process continues until the actuator is in the required position. The original signal is usually provided by a in-built function generator but this may be bypassed by inputting an external voltage signal. This latter approach is employed in the case of the experimental system described below.

3.4.2 Signal Conditioning Principles

A National Instruments PCI-MIO-16E-1 data acquisition card, henceforth referred to as the DAQcard, was used for communication between the software and the actuator command console. This DAQcard is a multi-channel input-output device developed for engineering systems in a wide variety of situations. It has been especially designed to be employed with the LabVIEW programming environment, and consists of both digital and analogue input-output channels for use

in different situations. In the case of test control, only the analogue functions are used. The card itself consists of a series of digital-to-analogue converters and analogue-to-digital converters connecting an input/output connector to a standard PCI bus. Incorporated in the hardware are numerous timing and conditioning amplifiers to enable signals to be passed through as needed and to control the signal conditioning modules.

The analogue output capabilities of the DAQcard are used to control the actuator by sending a voltage to the command module of the actuator. This voltage tells the actuator what distance to move and in what direction. The DAQcard contains two output channels and has an internal reference voltage of 10V. The card may be set to uni- or bi-polar output resulting in an output of 0V to 10V, or a range of $\pm 10V$ respectively. The DAQcard was set to bi-polar to allow the actuator to move in two directions (positive and negative), the sign of the signal telling the actuator what direction to move.

The analog input capabilities of the DAQcard consist of 8 differential channels or 16 single ended channels, depending on the signal types being read. For the tests carried out in this research, the card was set to differential mode. This means that each of the signals fed into the DAQcard is compared with a second reference signal. This reduces the number of channels to eight to compensate for the extra reference signals.

Although this reduces the number of channels available to the user, the DAQcard contains two different sampling methods which can be used. The first is direct sampling of the data in which only one signal is set up on each channel allowing the board to sample at its fastest possible rate (1.25 million scans per second). The second method, which is used for the tests described below, is known as multiplexing. This method allows multiple signals to be feed into a single channel., but reduces the maximum speed at which the DAQcard is able to acquire data because the multiplexer switches between the multiple signals on each channel and scans each separately. A time skew is consequently generated between each sample, which is the time taken for the DAQcard to switch between signals. This method is appropriate for applications where the time relationship between the samples is not required (i.e. static load tests) or where scan rates are less than 1,000 scans/sec (Pritchard, 2000). This limit was found using calculations based on the Nyquist frequency, which is the maximum frequency which can be measured from a signal, and may be determined from the sampling rate. Based on a gain of 1000, and a sampling rate of 1000 scans/second, the time slew due to the multiplexing is approximately $2\mu s$. As the maximum scan, or sampling, rate is 50 scans/sec. in this study, and is usually only 5 scans/sec. or less, this does not have a significant effect on the data.

The signals passed to and from the DAQcard via a shielding cable are filtered through a signal conditioning unit that may be seen in Figure 3.17. This signal conditioning unit consists of a chassis and a number of module and terminal blocks. The two types of modules used in this study were SCXI-1121 and SCXI-1180, with terminal blocks SCXI-1321 and SCXI-1302 respectively. The terminal blocks allow the signals from the different measurement devices to be fed into the modules. The SCXI-1321 terminal block is used for the strain gauges and external LVDTs, and allows for null offset and shunt calibration of up to four devices, while the SCXI-1302 terminal block is used for the actuator load cell and LVDT. The SCXI-1302 terminal block is also used for the output voltage to the actuator command console.

The SCXI-1121 is a four channel isolated translator module. This allows for isolated amplification and signal conditioning on four separate device signals. Each module is capable of setting a different gain, filter, completion network, excitation mode and level for each device. The different levels are manually set in the module by a series of jumpers. In the case of the strain gauges, the following settings were employed:

- Gain level of 1000;
- 10kHz bandwidth filter to remove extraneous noise;
- Completion network disabled, as ‘dummy’ strain gauges were employed; and
- Voltage excitation enabled with 3.33V.

In the case of the displacement transducers, the following configuration was employed:

- Gain level of 1, or 5 in cases where very small displacements are expected;
- 4kHz bandwidth filter;
- Completion network enabled; and
- Voltage excitation enabled with 10V.

Signals from the module have a possible error of 0.15% of the maximum reading. Therefore in the case of the strain gauges, the maximum error is 0.004995V (maximum signal of 3.33V) and 0.015V for the LVDTs with a maximum signal of 10V. Using these settings, calibration constants were found for the strain gauges and LVDTs.

The SCXI-1180 module is a feedthrough module that does not impose any conditioning on the signals and simply passes them straight through to the DAQcard via the shielded cable. This module was used in the cases of the actuator load cell and displacement transducer as these signals

did not require any amplification or excitation. This module was also employed to pass the output signal from the DAQcard to the actuator command console with no conditioning.

3.4.3 Computer Integration and Control

The integration of the computer control into the servo-hydraulic actuator system is a very straightforward task. When used as a stand-alone unit, the actuator command console has a built-in signal generator that creates waveforms of differing frequency, amplitude and type. These waveforms are then sent to the actuator which is set to either *DISP* or *LOAD* control. To integrate the computer system into this set-up, the signal generator was removed and replaced by the output cable from the signal conditioning unit. The signal sent from the DAQcard through the conditioning unit causes the actuator command console to react in the same manner as if the signal generator was sending the voltage. The command console receives the voltage signal from the computer and passes it to the servo-valve control which opens, or closes, to move the actuator to the required position as seen in Figure 3.16. Both the load cell and the actuator displacement transducer send a return voltage, V_{ret} , to the command console. For the computer control system, the V_{ret} that is compared to the original V_{out} signal is taken from the displacement transducer. If the actuator has not reached the correct position, V_{out} is updated and sent to the servo-valve control.

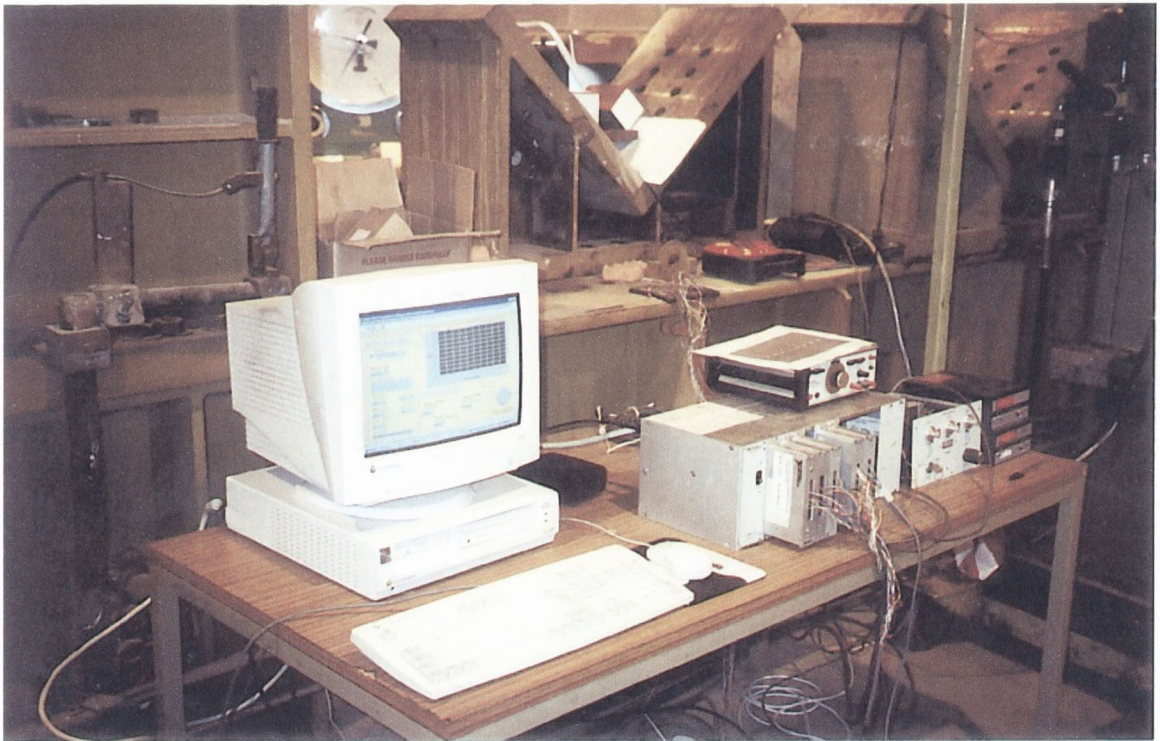


Figure 3.19: Actuator Control System with Computer Control and Signal Conditioning Unit

This is a continuous process in the actuator command console and may be assumed to happen virtually instantaneously. At the same time, the return signals from the actuator load cell and displacement transducer are passed into the signal conditioning unit and then to the DAQcard. This data is then written to the hard disk of the computer as dictated by the user preferences inputted into the programs described in section 3.3.

3.5 Control System Accuracy

This section demonstrates the accuracy of the developed control system for use in structural testing. The actual achieved displacement is compared with the intended displacement for both external displacement transducers and the internal actuator displacement transducer. This illustrates the high level of accuracy that may be achieved using the computer control system for cyclic testing of structural specimens.

In order to display the applicability of the system to other structural materials and configurations, other than steel joints and beam-column sub-assemblages, a number of results from a study into the response of wireball-reinforced concrete structural members are also presented. These results demonstrate the range of responses that the system is capable of accurately measuring.

3.5.1 Test System Accuracy

Measurements were taken on the accuracy of the control system during every test by attaching an external displacement transducer to the actuator body and the ram. Results from this transducer were then compared with measured results from the internal displacement transducer from the actuator and the intended waveform provided by the software. Although early results showed differences of up to 15%, these were soon eliminated by re-calibrating the output voltage to the actual actuator movement.

Figure 3.20 shows a comparison between the intended actuator displacement and the recorded displacement from the external displacement transducer for test 2.1, which was carried out under a constant amplitude waveform of 50mm displacement. As can be observed, the two are virtually identical, with a maximum difference of 0.16mm being recorded, giving a maximum possible error of 0.32%. However, it must be noted that this does not take into account the contribution due to optimisation errors in signal conditioning or extraneous noise from the digital signal. When the intended displacement is compared to the internal actuator displacement, the maximum difference increases to 0.27mm as shown in Figure 3.21, giving an error of 0.54%. It may also be seen that the difference between the intended displacement and the actual displacement is of a non-linear relationship. This is attributed to signal noise as well as the constantly shifting actuator ram.

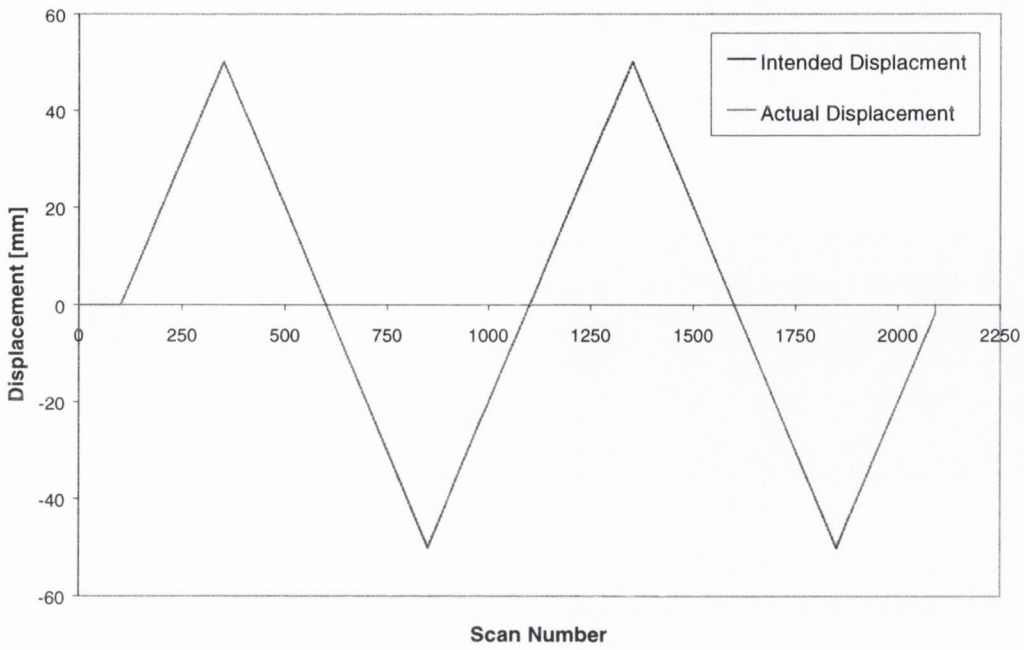


Figure 3.20: Comparison of intended displacement with external displacement transducer for Test 2.1

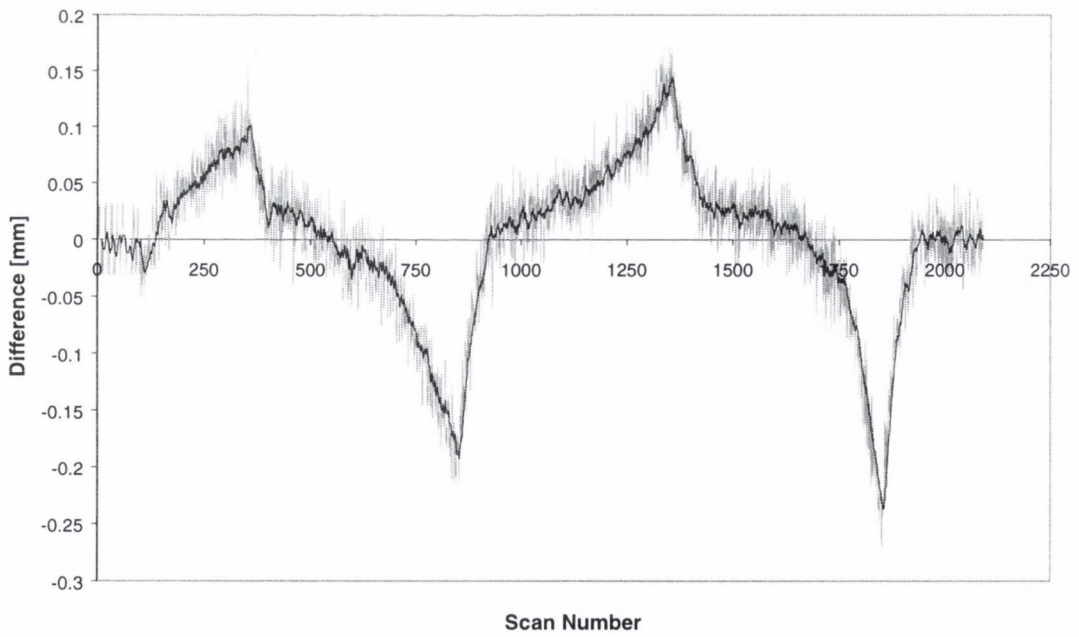


Figure 3.21: Difference between internal displacement transducer and intended displacement for Test 2.1 (Constant amplitude)

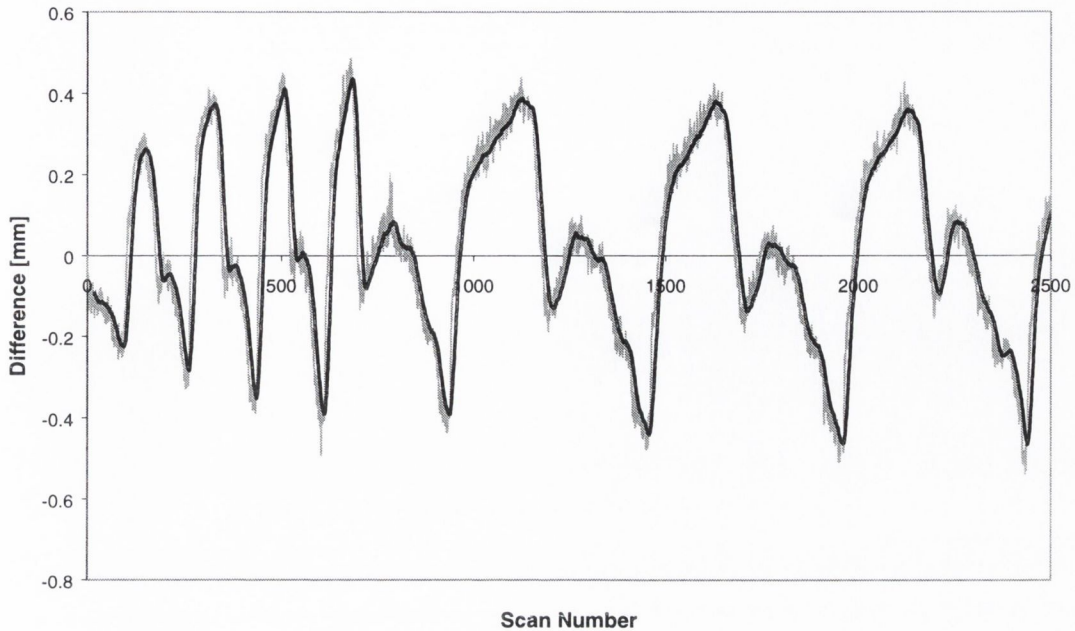


Figure 3.22: Difference between intended displacement and internal actuator displacement transducer measurement for Test 2.6 (Cyclic)

Under cyclic displacements of increasing amplitude, as is the case under the majority of specimens tested in this study, this error increases to a maximum of 2.51%, or 1.26mm in a 50mm cycle. This higher level of inaccuracy may be observed in Figure 3.22, which illustrates the displacement error over the first 20mm displacement cycles. Similar levels of accuracy were noted in all tests except for tests 1.1 through 1.3 where the displacement errors were 14.6%, 8.55% and 5.1%. However, as all experimental results are based on the measured displacement and not the intended displacement, this inaccuracy will not affect the presented results.

3.5.2 Wireball-Reinforced Concrete Beam-Column Members

Although the control programs and system described in sections 3.3 and 3.4 were developed specifically to test the response of structural steel joint sub-assemblages, it is easily adapted to the testing of other materials and specimen types. A research project recently completed into the seismic resistance of reinforced concrete also used the system described above (Ryan, 2001). This research investigated the confinement effects of a new type of reinforcement, namely wireball reinforcement, on beam-column members under axial and lateral cyclic loading conditions. In each specimen, axial load is expressed as a percentage of the compressive capacity. The objective of the experimental work in this project was to investigate whether the use of wireball reinforcement, combined with conventional reinforcement, would increase the rotational ductility capacity of the members. A number of test results from this study are presented in this section to illustrate the capabilities of the new control system.

Figure 3.23 shows the force-displacement response for specimen C.B.6.2 which consisted of a beam-column member with standard reinforcement with shear links at 105mm spacing and 30% axial load. This specimen was expected to give a stable and ductile response throughout the imposed loading. As may be seen, the hysteresis curve remains stable for the early cycles but then serious degradation occurs with ultimate failure occurring on the 40mm cycle. Figure 3.24 shows the force-displacement response for specimen C.B.6.2 which contained wireball reinforcement with links at 125mm and 30% axial load. The measured response for this specimen resulted in a highly stable hysteresis curve with no failure of the specimen observed during the experiment up to a maximum of 50mm displacement. Figure 3.25 gives the force-displacement of specimen C.B.6.3 which consisted of a beam-column member with wireball reinforcement, links at 145mm spacing and an axial load of 40%. As can be seen, the hysteresis curve remains very stable until the second 40mm displacement cycle. At this point failure occurs very rapidly with complete failure of the specimen having occurred by the end of the third 40mm cycle. This is attributed to the level of the axial load which is just below the level which would promote an over-reinforced failure.

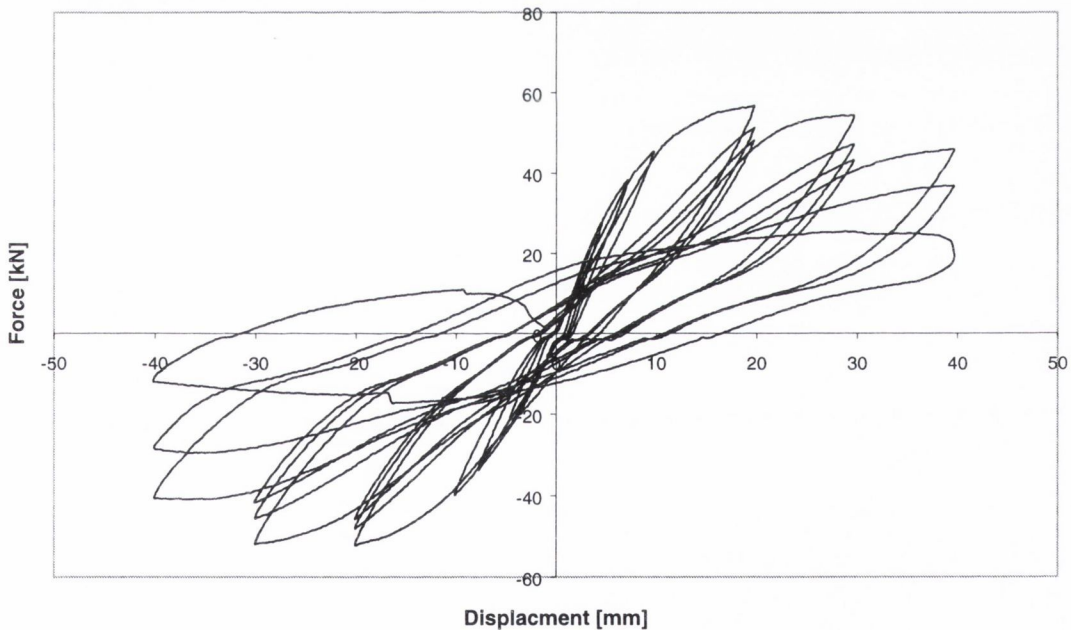


Figure 3.23: Force-Displacement response for specimen C.B.6.1 (Ryan, 2001)

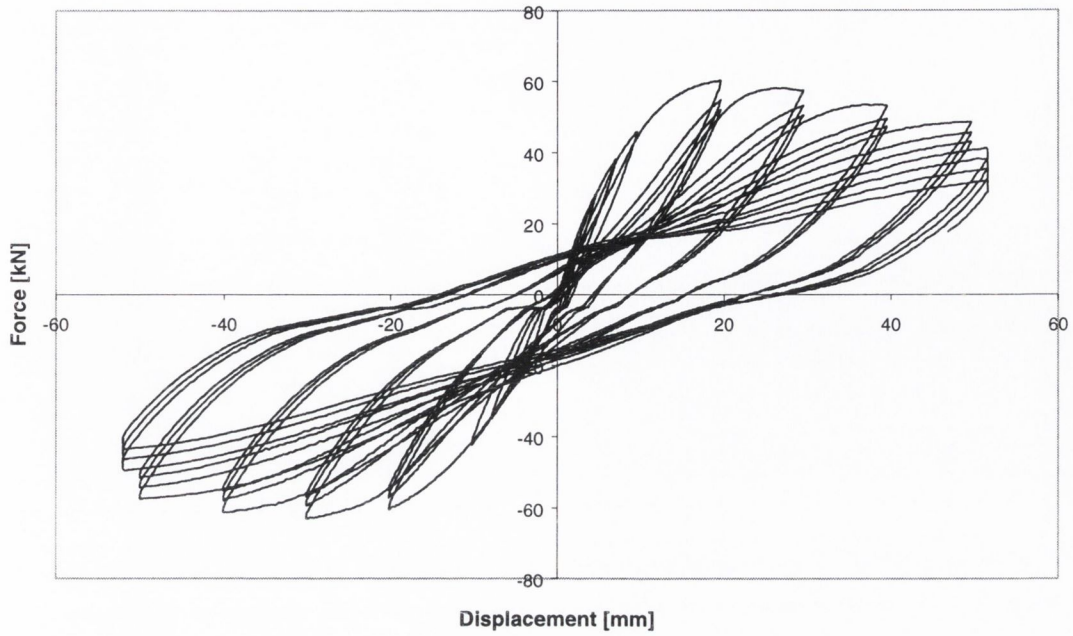


Figure 3.24: Force-displacement response for specimen C.B.6.2 (Ryan, 2001)

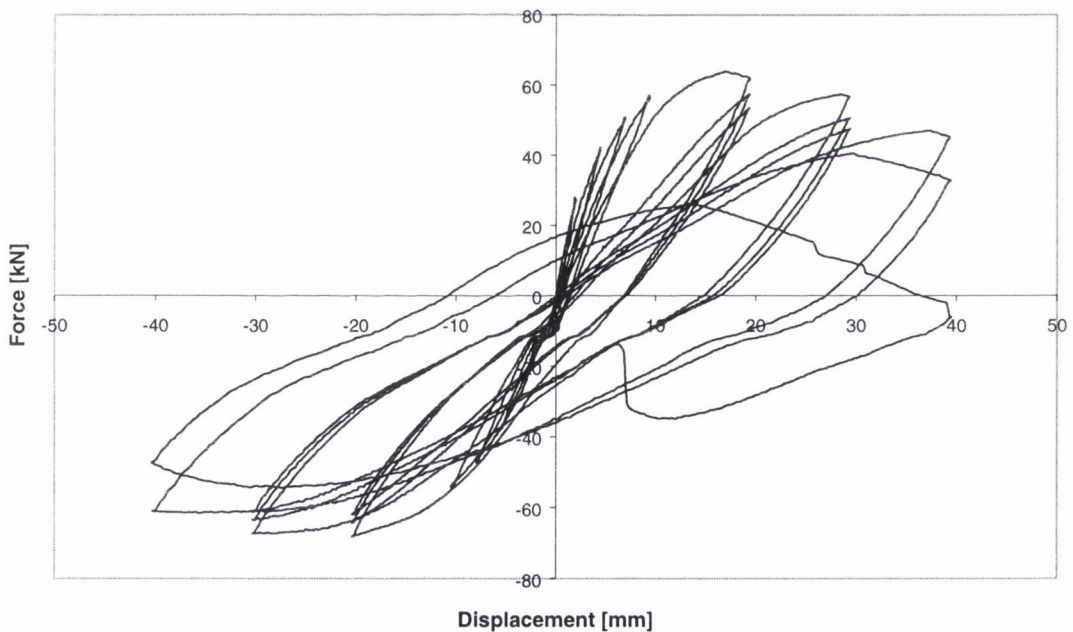


Figure 3.25: Force-displacement response for specimen C.B.6.3 (Ryan, 2001)

Although it is not directly relevant to this study, it is interesting to note that the test results show that wireballs do increase local confinement and therefore, enhance member ductility. A particularly interesting aspect of the results is the extent to which the improved confinement effects may be exploited to reduce the amount of transverse reinforcement required for a given ductility demand. This reduction is limited by the need to prevent buckling of the longitudinal reinforcement or shear failure. The results clearly show that specimens containing wireballs

outperform those specimens without wireballs, in terms of ductility and energy dissipation, even when the link spacing of the wireball reinforced specimens is larger than that of the standard reinforced specimen. Specimens with wireballs are also seen to display greater ductility, than specimens without wireballs, with higher axial load levels.

In order to carry out the experimental tests on the concrete beam-column members, it was necessary to change the scan rate, scanned channels, the variable N_4 and the output rate. These experiments demonstrate the applicability of the above test system to different materials and configurations.

3.6 Conclusions

This chapter presents the new cyclic testing system developed as part of this study. The test system is based around the ECCS (1986) procedures for the cyclic testing of structural steel elements. Two testing procedures are set out, namely the complete testing method and the short testing method and all relevant definitions are given.

Three separate control software programs are explained in detail. These programs were developed using the graphical programming language, LabVIEW, which was designed for scientific applications. The user interfaces of each program are illustrated and the program code discussed. In each program, a number of user-inputted variables are required and these are explained fully. The programs are as follows:

- *Shakedown test program:* this program imposes a series of small amplitude displacement cycles on the test specimen in order to ensure that the full system is working correctly. This works out any slip in the specimen and allows the operator to ensure all devices are measuring correctly.
- *Constant amplitude cyclic program:* this program imposes a series of constant amplitude displacement cycles on the specimen. This program also allows the user to determine the monotonic response of a specimen. It is also capable of determining the intended displacement and the measured data;
- *Structural element cyclic loading program:* This program was designed to impose an increasing amplitude waveform as described in the ECCS procedures. The program is capable of reading on multiple channels and graphing the measured data.

In the third section of the chapter, the principles behind the actuator command console are outlined. This is then followed by an explanation of the signal conditioning and data acquisition equipment

employed as part of the system. The method by which the computer tells the actuator command console the required displacement is then explained.

Graphs of intended displacement versus actual displacement of the actuator are then presented in order to determine the accuracy of the control system. It was seen that the constant amplitude program is accurate to 0.5%, while the cyclic displacement program is accurate to within 2.5%. These levels were sufficient for the purposes of this study. However, a method of increasing the accuracy of the cyclic displacement program is given.

Finally, a number of force-displacement responses from a study into the seismic resistance of beam-column members utilising a new form of reinforcement are presented. These hysteresis curves are intended to demonstrate the ability of the new control system to be applied to materials and structural members other than steel flush end-plate joints.

Chapter 4

Experimental Set-up and System Verification

4.1 Introduction

This chapter describes the experimental set-up and verification carried out using the control programs described in chapter 3. The first section describes the experimental set-up and the basic configuration of the test specimens.

The second section defines the parameters used to evaluate the moment-rotation relationship of each specimen. These parameters include the rigidity ratio, ductility ratio, resistance ratio and resistance drop ratio.

The third section describes the experimental specimens that were tested in this study. The specimens are described and any unusual aspects are fully described. The objectives of each test series are presented in this section as well. The Eurocode 3: Annex J design characteristics are presented and discussed. Locations of strain gauges and displacement transducers are also presented in this section.

The results from the first test series, which was used to verify the experimental programs discussed in chapter 3, are then presented. The six specimens were also used to solve any problems with the experimental set-up which were discovered. Due to this, not all of the specimens were successful. These six specimens are presented in this chapter separately from the other sixteen specimens for this reason.

4.2 Experimental Procedures and Specimens

The experimental set-up of the specimens is shown in Figure 4.1. In order to facilitate loading of the specimens, the universal column section was placed in a horizontal position while the beam was placed in a vertical position. The servo-hydraulic actuator is attached to the specimen by means of a hinge arrangement as shown in Figure 4.1. In order to eliminate moment induced damage to the actuator ram, a hinge mechanism is used to attach the actuator to the reaction frame. This ensures that the specimen is only loaded along the actuator axis. The specimen is held in place using a reaction block, a small hydraulic jack and a specialised tie system. This tie system consists of two sections with a steel bars attached to the top of each section. The column section is then placed on the bars and two similar sections are placed on the top column flange. These sections are then tightened together using four threaded bars, two on each side of the specimen effectively pinning the section preventing any lifting of the specimen during the test. This arrangement may be seen clearly in Figure 4.2.

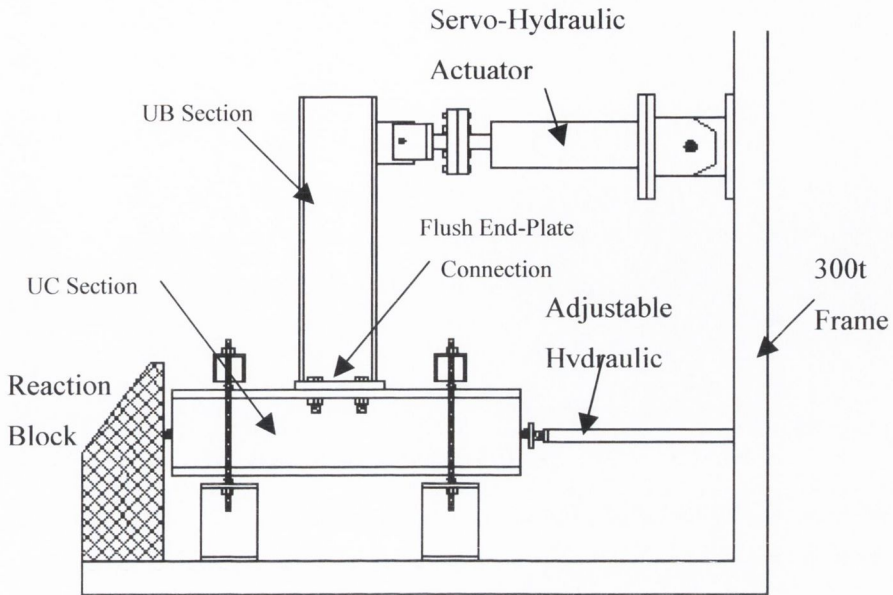


Figure 4.1: Schematic Diagram of Experimental Specimen Set-up

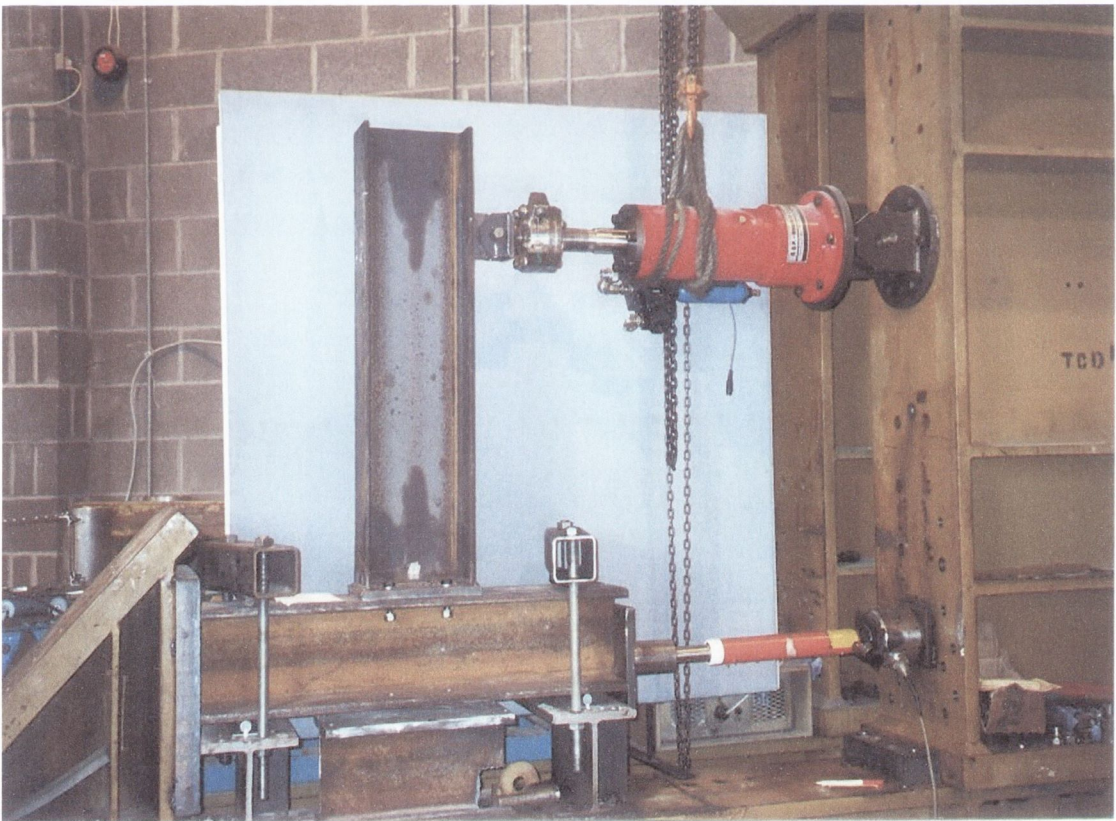


Figure 4.2: Experimental Set-up (specimen 2.5)

The small hydraulic jack is used to place a small axial load on the column section. This prevents the specimen from slipping during the experiment by continuously pushing the specimen against a reaction block, as can be seen in Figure 4.1 and Figure 4.2. In order to distribute this load, steel plates are inserted between the jack and the specimen. The load in the jack was monitored throughout each test to ensure that it remains constant. This value of the load was limited according to Section J.1.1 (6) of Eurocode 3, which states that the maximum axial load that may be applied for its design rules to be valid is 10% of the resistance of the member cross-section.

All of the sub-assemblages tested as part of this research consisted of flush end-plate joints. Each joint had two bolt rows with two bolts per row. The specimens consisted of a one metre length of universal column section attached to a one metre length of universal beam. The steel used for all of the experimental specimens was of Grade 43. The bolts used in the experimental work were either Grade 8.8 or Grade 10.9, both of which are industry standard. All welds were full strength continuous fillet welds designed to section 6.6 of Eurocode 3.

4.3 Experimental Evaluation Parameters

The ECCS (1986) recommends that the cyclic characteristics of structural steel elements be interpreted in terms of ductility, resistance ratios, resistance drop ratio and the rigidity ratio. This allows the critical characteristics from numerous tests carried out in different facilities to be compared in a logical and consistent manner. The procedures also allow these defining parameters to be compared for one cycle, a group of three cycles or the entire test. In order to determine the parameters correctly, the following information is required:

- The initial yield displacements, e_y^+ & e_y^- , and the corresponding forces, F_y^+ & F_y^- ;
- The extremes of displacement for each cycle, e_i^+ & e_i^- (Figure 4.3);
- The values of the forces, F_i^+ & F_i^- , corresponding to the extremes of displacement, e_i^+ & e_i^- (Figure 4.3);
- The extremes of displacement in the +ve and -ve force range for each cycle, Δe_i^+ & Δe_i^- (Figure 4.3);
- The tangent modulus at the change of loading direction, α_i^+ and α_i^- (Figure 4.3);
- The positive and negative areas, A_i^+ & A_i^- , of the cycle (Figure 4.4).

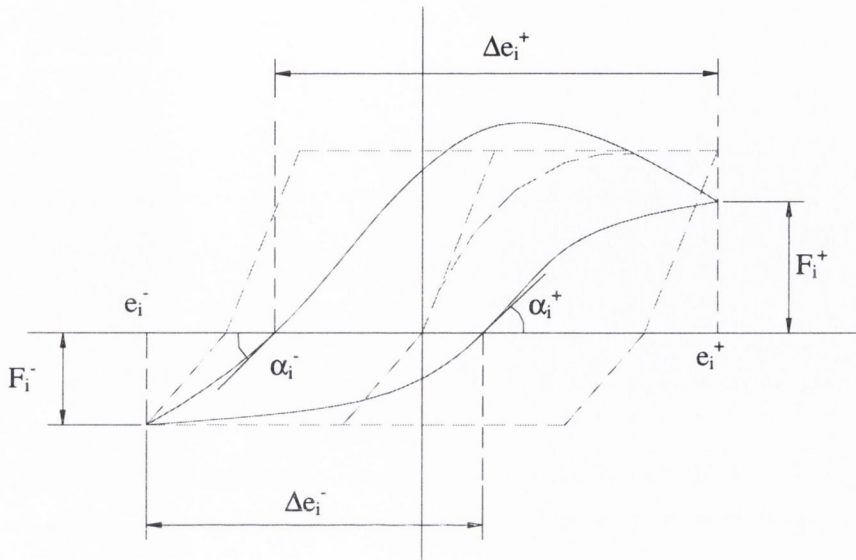


Figure 4.3: Cyclic Parameters for a single cycle

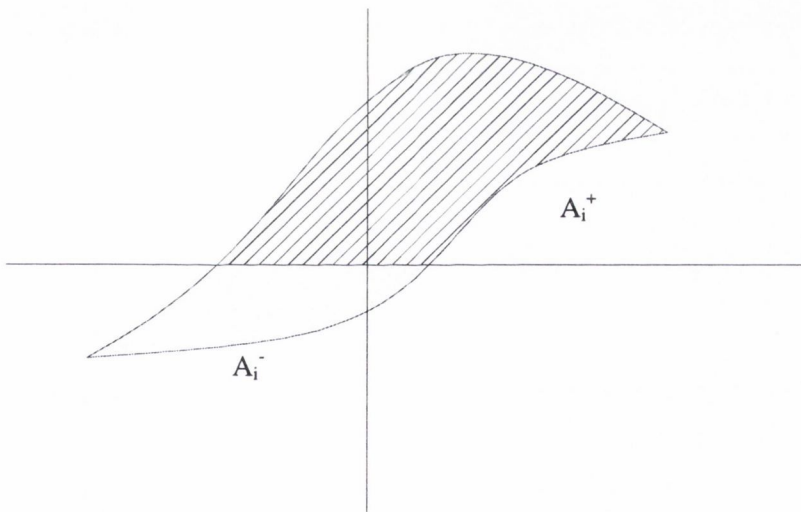


Figure 4.4: Cyclic Area Parameters for a single cycle

For convenience and ease of understanding when discussing the experimental results in this chapter and chapter five, the joint is referred to be on the tension side when the actuator load cell was reading a positive value, or was pulling on the specimen. The joint are said to be on the compression side of the hysteresis curve when the actuator load cell was returning a negative value, or was pushing against the specimen.

4.3.1 Ductility

The ductility capacity of a structural system may be defined as the maximum ratio of the imposed deformation to yield deformation that the system can withstand under a specified number of complete deformation cycles without experiencing significant loss of strength or stiffness. This deformation may be defined as bending rotation for moments, shear rotation for shear or displacement for force, as in Eqn. 4.1.

$$\mu_{oi}^+ = \frac{e_i^+}{e_y^+} \quad \text{and} \quad \mu_{oi}^- = \frac{e_i^-}{e_y^-} \quad \text{Eqn. 4.1}$$

where μ_{oi}^+ and μ_{oi}^- are the partial ductility factors for the i^{th} cycle in tension and compression. Two other ductility parameters are also defined in the ECCS recommendations which are the full ductility and full ductility ratio. These are defined in Eqn. 4.2 and Eqn. 4.3. Although these parameters may be calculated for the test results, it is the opinion of the author that in most cases they do not provide any extra understanding of the cyclic behaviour characteristics when used instead of partial ductility. Therefore, these two parameters are not used for all of the experimental results, but only in those tests where they provide further useful information:

$$\mu_i^+ = \frac{\Delta e_i^+}{e_y^+} \quad \text{and} \quad \mu_i^- = \frac{\Delta e_i^-}{e_y^-} \quad \text{Eqn. 4.2}$$

where μ_i^+ and μ_i^- are the full ductility factors for the i^{th} cycle in tension and compression; and

$$\psi_i^+ = \frac{\Delta e_i^+}{(e_i^+ + (e_i^- - e_y^-))} \quad \text{and} \quad \psi_i^- = \frac{\Delta e_i^-}{(e_i^- + (e_i^+ - e_y^+))} \quad \text{Eqn. 4.3}$$

where ψ_i^+ and ψ_i^- are the full ductility ratios for the i^{th} cycle for the components.

When determining the ductility parameters for a group of three cycles, the full ductility ratio is examined, using the partial ductility factor, μ_{oi} , as a variable, where the index i is taken as the last cycle in the group. When determining the full ductility ratio for a group of three cycles of equal displacement, the minimum of the three ratios is taken and defined as $\psi_i^+(\mu_{oi}^+)$ and $\psi_i^-(\mu_{oi}^-)$.

4.3.2 Resistance and Rigidity Ratios

The resistance ratio of the structural joint is a comparison between the force required for elastic yield to occur and the maximum force during that cycle. The resistance ratios for a single cycle in

tension and compression, ϵ_i^+ and ϵ_i^- , are defined as

$$\epsilon_i^+ = \frac{F_i^+}{F_y^+} \quad \text{and} \quad \epsilon_i^- = \frac{F_i^-}{F_y^-} \quad \text{Eqn. 4.4}$$

When determining the resistance ratio for a group of three cycles of equal displacement, the minimum of the three ratios is taken and defined as $\epsilon_i(\mu_i)$. This is the resistance ratio as a function of the partial ductility

However, over the course of three cycles it is possible that the resistance will drop so a new characteristic parameter is introduced known as the resistance drop ratio, $\epsilon^*(\mu_{oi})$ and is evaluated using

$$\epsilon^{+*}(\mu_{oi}^+) = \frac{F_i^+}{F_{i-2}^+} \quad \text{and} \quad \epsilon^{-*}(\mu_{oi}^-) = \frac{F_i^-}{F_{i-2}^-} \quad \text{Eqn. 4.5}$$

The rigidity ratio, ξ_i , is a comparison between the slope of the tangent modulus at the elastic yield point and the tangent modulus of the cyclic curve for the i^{th} cycle. It can also be described as the ratio of the stiffness of the i^{th} cycle to the initial stiffness. The rigidity ratio is defined as

$$\xi_i^+ = \frac{\text{tg}(\alpha_i^+)}{\text{tg}(\alpha_y^+)} \quad \text{and} \quad \xi_i^- = \frac{\text{tg}(\alpha_i^-)}{\text{tg}(\alpha_y^-)} \quad \text{Eqn. 4.6}$$

where $\text{tg}(\alpha)$ is the slope to the curve when F changes from negative to positive. When evaluating the rigidity ratio for a group of three cycles, it is assumed that the rigidity ratio is taken as the minimum of the three rigidity ratios in the group in terms of the partial ductility

4.4 Experimental Specimens and Design Calculations

A total of twenty-two beam-to-column joint sub-assemblages were tested in this study in three separate series. The first series consisted of six specimens which were primarily used to solve any problems discovered in the experimental programs and set-up. Due to these problems, only three of the specimens were considered to be successes although valuable information was gained from five of the tests. The second and third series consisted of eight specimens each. Seven of the eight specimens were successful in the second series. All eight of the specimens tested in the third series were successful.

Specimen Number	Description of Joint
1.1	8 mm plate thickness and Grade 8.8 M20 bolts- Cyclic test
1.2	8 mm plate thickness and Grade 8.8 M20 bolts – Cyclic test
1.3	12 mm plate thickness and Grade 8.8 M20 bolts – Cyclic test
1.4	12 mm plate thickness and Grade 8.8 M20 bolts – Cyclic test
1.5	20 mm plate thickness and Grade 8.8 M20 bolts – Cyclic test
1.6	20 mm plate thickness and Grade 8.8 M20 bolts – Cyclic test
2.1	12 mm plate thickness and Grade 8.8 M20 bolts – Large Amplitude test
2.2	12 mm plate thickness and Grade 8.8 M20 bolts – Cyclic test
2.3	12 mm plate thickness and Grade 10.9 M20 bolts – Cyclic test
2.4	12 mm plate thickness and Grade 8.8 M20 bolts and Grade 10.9 nuts – Cyclic test
2.5	20 mm plate thickness and Grade 8.8 M16 bolts – Large Amplitude test & no preload
2.6	20 mm plate thickness and Grade 8.8 M16 bolts – Cyclic test & no preload
2.7	20 mm plate thickness and Grade 8.8 M16 bolts – Cyclic test & preload of 200 Nm
2.8	20 mm plate thickness and Grade 8.8 M16 bolts – Cyclic test & preload of 100 Nm
3.1	10 mm plate thickness and Grade 8.8 M20 bolts – Large Amplitude test
3.2	10 mm plate thickness and Grade 8.8 M20 bolts – Cyclic test
3.3	15 mm plate thickness and Grade 8.8 M20 bolts – Large Amplitude test
3.4	15 mm plate thickness and Grade 8.8 M20 bolts – Cyclic test
3.5	12 mm plate thickness and Grade 8.8 M20 bolts with smaller column section – Large Amplitude test
3.6	12 mm plate thickness and Grade 8.8 M20 bolts with smaller column section – Cyclic test
3.7	12 mm plate thickness and Grade 10.9 M20 bolts – Large Amplitude test
3.8	12 mm plate thickness and Grade 10.9M20 bolts – Cyclic test

Table 4.1: Description of experimental specimens

Table 4.1 presents a list of the experimental specimens with a brief description of each. The description lists the end-plate thickness and the bolt grade and size. The type of test carried out is also listed. The specimens are denoted in the form x.y, where x is the test series number and y is the specimen number in that series.

In addition to the full-scale tests that are described below, a number of material tests were carried out on the steel from the beams, columns and end-plates to ensure that the material properties assumed in the mechanical model and Eurocode 3 were correct. These results are presented in Appendix A. The tensile samples taken from the beam and column sections were detailed as set out in BS 10002-1:1990. The samples taken from the end-plates were non-standard as the bolt holes prevented the correct length being obtained. It was observed that the yield stress and ultimate stress of the tensile specimens were consistently higher than the assumed notional values. The average yield stress was 294.14 N/mm^2 compared to the notional value of 275 N/mm^2 , with the ultimate values ranging from $470 - 560 \text{ N/mm}^2$ compared to a notional value of 460 N/mm^2 . A number of sample bolts were also tested to confirm their material properties. These bolts were randomly selected from the same batch that the bolts used in the full-scale tests. These tests consisted of both cyclic and monotonic experiments to determine the behaviour characteristics. The results from these tests are also presented in Appendix A. These results were observed to agree closely with the notional yield results. However, the ultimate failure of the bolt was observed in many cases to be premature due to the stripping of the threads.

4.4.1 Test Series One

The specimens in test series one were originally designed according to the procedure set out in the first draft of Eurocode 3: Annex J (1992) rather than the revised version (1998). However, all of the calculations were later verified using the Annex J (revised) calculations which are presented in this section. The first test series had two objectives:

- To test the newly developed experimental system described in Chapter 3.
- To investigate if the failure modes defined in Eurocode 3: Annex J, and discussed in section 2.5, were valid under cyclic loading as well static loading.

As a reference specimen, an industry standard joint was selected from the British Constructional Steel Association publication on moment joints (1995). The joint consisted of a 12 mm thick end-plate welded to the end of the beam section using 8 mm full-strength continuous fillet welds. Although the original design calculations set a minimum weld throat thickness as 8 mm, in the revised version of Annex J this requirement has been removed. Instead, a number of design requirements for fillet welds are set out that must be fulfilled. The weld sizes used in this test series have been checked against these newer requirements and were found to be adequate. The plate was bolted to the column flange using four Grade 8.8 M20 high tensile bolts. The column section used for the joints in this test series was a 1.0 m section of 203 x 203 x 86 kg/m UC, while

the beam was a 1.0 m length of 254 x 102 x 22 kg/m UB. The dimensions and geometrical properties of the joints are presented in Figure 4.5 and Table 4.2. Eurocode 3: Annex J calculations showed that this joint would be subject to a mode 2 failure mechanism. In order to evaluate the validity of all three possible failure modes, the thickness of the end-plate was changed while keeping all other details the same. To this end, the end-plate thickness was reduced to 8 mm in order to give a mode 1 failure mechanism, while a 20 mm end-plate was used to give a mode 3 failure.

As can be seen in Table 4.2, specimens 1.1 and 1.2 are identical, as are specimens 1.3 and 1.4, and specimens 1.5 and 1.6. This was intended to ensure that the results could be duplicated if necessary. Unfortunately, this test series was not a complete success, as problems arose with the experimental equipment that had not been anticipated. These problems were mostly due to a malfunctioning load cell, or slippage of the specimen. Due to this, only three of the six completed experiments can be considered fully: tests 1.2, 1.4 and 1.6. However, it was possible to salvage some data such as the initial stiffness, yield points and failure modes from the remaining three tests. The experimental results are presented below together with a discussion of the problems encountered in a particular test.

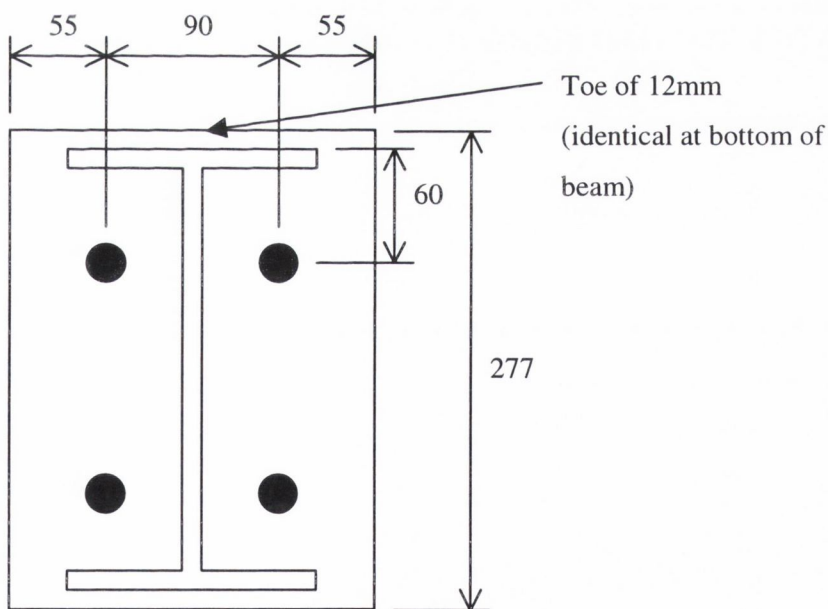


Figure 4.5: End-Plate Dimensions for Test Series One

Specimen Number	End-Plate Thickness [mm]	Bolt Size	Bolt Grade	Test Type
1.1	8	M20	8.8	Cyclic
1.2	8	M20	8.8	Cyclic
1.3	12	M20	8.8	Cyclic
1.4	12	M20	8.8	Cyclic
1.5	20	M20	8.8	Cyclic
1.6	20	M20	8.8	Cyclic

Table 4.2: Joint Properties for Test Series One

Table 4.3 and Figure 4.6 show the design parameters calculated from Eurocode 3: Annex J for the three separate joints in test series one. As discussed in Chapter 2, Eurocode 3 provides no method to determine the rotational capacity of a joint. Instead, criteria that must be met to determine whether a joint possesses sufficient rotation capacity for a plastic frame analysis to be carried out are listed. As can be observed in Table 4.3, the joints with the 8 mm and 12 mm thick end-plate do possess sufficient rotation capacity for a plastic global analysis to be carried out, whereas the joints with the 20 mm thick end-plate do not. This is due to the predicted brittle failure mechanism of the mode 3 joint.

Specimen Number	Initial Stiffness, $S_{j,ini}$ [kNm/mrad]	Yield Rotation [mrad]	Yield Moment [kNm]	Ultimate Moment [kNm]	Predicted Failure Mode	Sufficient Capacity for Plastic Global Analysis?
1.1 & 1.2	8.54	1.66	14.20	21.29	1	Yes
1.3 & 1.4	11.62	2.38	27.71	41.56	2	Yes
1.5 & 1.6	12.88	2.81	36.24	54.36	3	No

Table 4.3: Design Parameters for Test Series One

There are large differences in the ultimate moment resistances of the three joints presented, with the mode 3 joints having the largest resistance and the mode 1 joints having the lowest resistance levels. This is consistent with the theory presented in section 2.5. There is less difference in the design initial stiffness values for the three joints. One interesting point to note is that the joint which theoretically is the least ductile, i.e. the mode 3 joint, has the highest yield rotation while the most ductile joint, in theory, has the lowest.

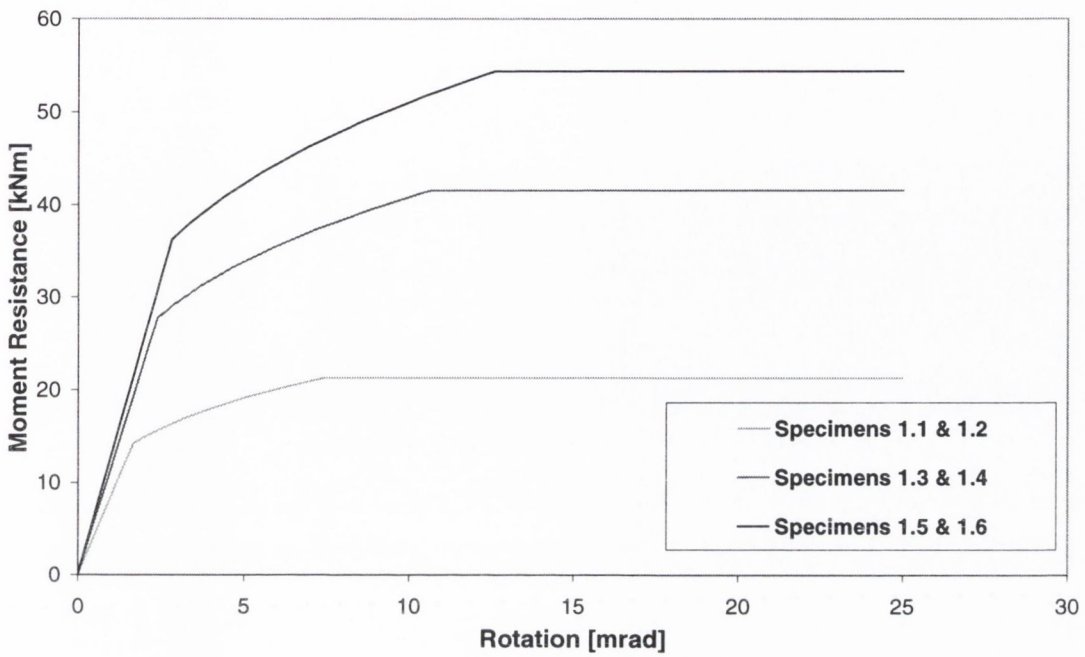


Figure 4.6: Eurocode 3: Annex J Design Moment-Rotation Characteristics

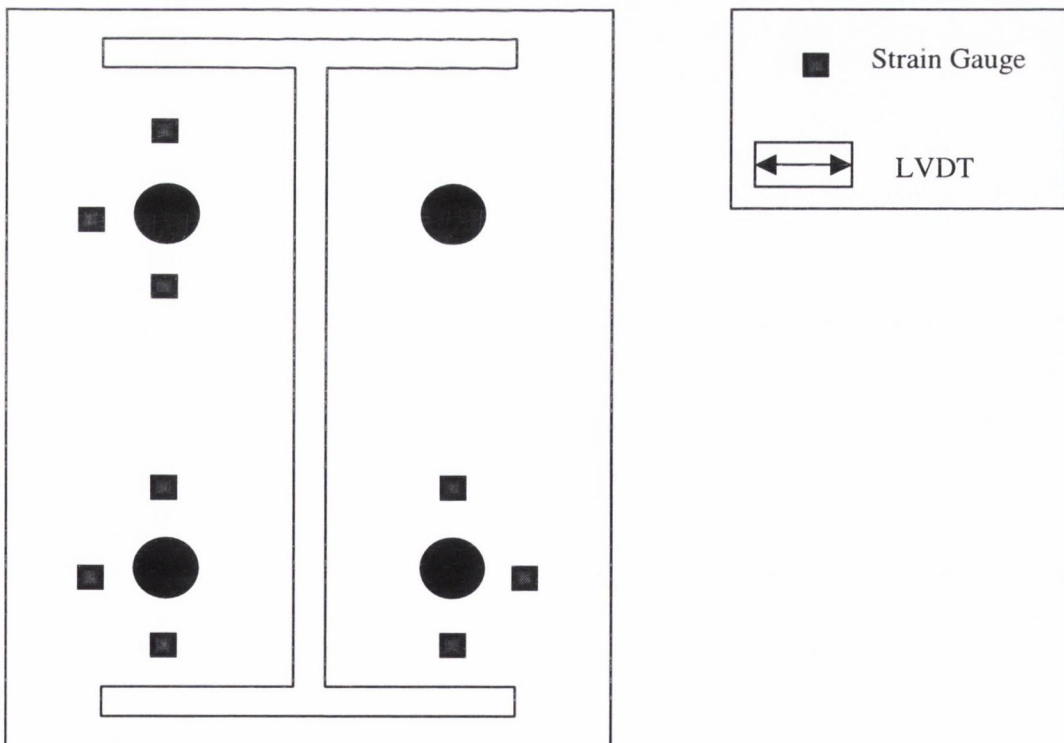


Figure 4.7 (a): Measurement device locations in test series one (plan view)

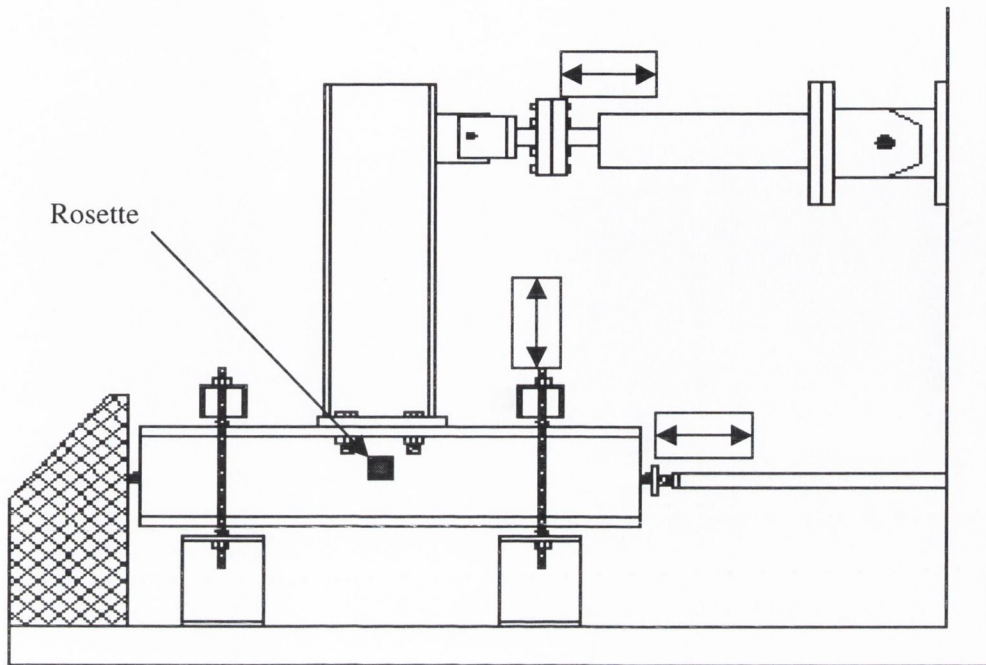


Figure 4.7 (b): Measurement device locations in test series one (elevation)

A total of 12 strain gauges and 3 linear variable displacement transducers (LVDTs) were used in each test in this series. The locations of these devices are shown in Figure 4.7. The strain gauges were placed in the locations thought to give the most detailed information on yielding of the end-plate, while 3 gauges were placed on the column shear panel to check that it remained elastic. The LVDT on the actuator was used to measure the accuracy of the control system, while the remaining two LVDTs were placed to measure any slippage and uplift of the column.

4.4.2 Test Series Two

The eight specimens in test series two were designed using the revised version of Eurocode 3: Annex J (1998). This test series was designed with a number of objectives following the analysis of test series one. These objectives are as follows:

- To further examine the Eurocode 3 failure modes to assess the validity under cyclic as well as monotonic loading conditions, especially for joints close to the mode 1/mode2 boundaries;
- To investigate methods of improving joint behaviour and ductility;
- To determine the effect of bolt pre-load on the initial rotational stiffness of the joint.

As in the case of test series one, a similar industry standard joint was chosen as the reference joint, again with a 12 mm thick end-plate. However, a larger beam size was employed to prevent the local buckling observed in specimen 1.5, hence the beam consisted of a 254 x 146 x 37 kg/m UB section, while the column section was identical to that employed in test series one. Specimens were tested under both monotonic and cyclic loading conditions. The dimensions and geometrical properties of the joints are shown in Figure 4.8 and Table 4.4.

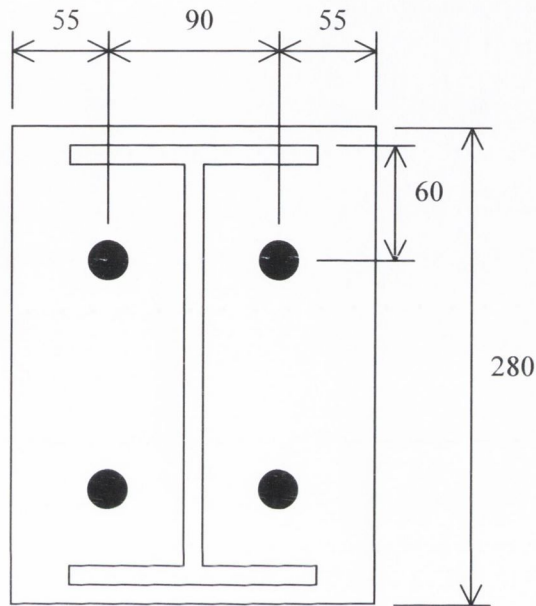


Figure 4.8: End-Plate Dimensions for Test Series Two

Specimen Number	End-Plate Thickness [mm]	Bolt Size	Bolt Grade	Test Type	Notes
2.1	12	M20	8.8	Monotonic	Reference joint
2.2	12	M20	8.8	Cyclic	Reference joint
2.3	12	M20	10.9	Cyclic	Higher grade bolts
2.4	12	M20	8.8	Cyclic	Grade 10.9 nuts
2.5	20	M16	8.8	Monotonic	No-preload
2.6	20	M16	8.8	Cyclic	No-preload
2.7	20	M16	8.8	Cyclic	Preload of 200 Nm
2.8	20	M16	8.8	Cyclic	Preload of 100 Nm

Table 4.4: Joint Properties for Test Series Two

Specimens 2.1 and 2.2 are identical in all material and geometrical properties as these were the reference joints for the series. These specimens were intended to respond with a mode 2 mechanism, with ultimate failure being due to failure of the bolts. In an attempt to improve the failure mode, and hence the ductility, of the joint without adversely affecting the moment capacity, the bolts were changed from grade 8.8 to grade 10.9 in specimen 2.3. All other properties of the joint were left unchanged. Based on results from the Eurocode 3 model, this change should have altered the failure mode of the joint from mode 2 to mode 1. Specimen 2.4 also employed a 12 mm thick end-plate and grade 8.8 M20 bolts. However, in order to prevent the stripping of the nut threads, as observed in test series one, the nuts were replaced with grade 10.9 nuts in a further attempt to improve the ductility of the joint.

Specimens 2.5 through to 2.8 were designed to investigate the effects of bolt pre-loading. In order to ensure that bolt behaviour controlled these experiments, a 20 mm thick end-plate was employed. As a small degree of end-plate bending had been observed with this size end-plate in test series one, the bolts were reduced to M16 from M20. Specimens 2.5 and 2.6 were used as reference joints for the investigation of the influence of bolt pre-loading. Specimen 2.5 was loaded monotonically while specimen 2.6 was subjected to a cyclic load of increasing amplitude. The bolts in both specimens were tightened by hand and this torque was determined to be approximately 50 Nm. In specimen 2.7 a torque of 200 Nm was employed, which is approximately 60% of the maximum recommended value for grade 8.8 M16 bolts. Based on the response for these specimens, a torque of 100 Nm was applied in specimen 2.8.

Specimen Number	Initial Stiffness, $S_{j,ini}$ [kNm/mrad]	Yield Rotation [mrad]	Yield Moment [kNm]	Ultimate Moment [kNm]	Predicted Failure Mode	Sufficient Capacity for Plastic Global Analysis?
2.1 & 2.2	11.48	2.37	27.40	41.11	2	Yes
2.3	11.48	2.75	31.61	47.40	1	Yes
2.5 - 2.8	10.92	2.10	22.98	34.46	3	No

Table 4.5: Predicted Design Parameters for Test Series Two

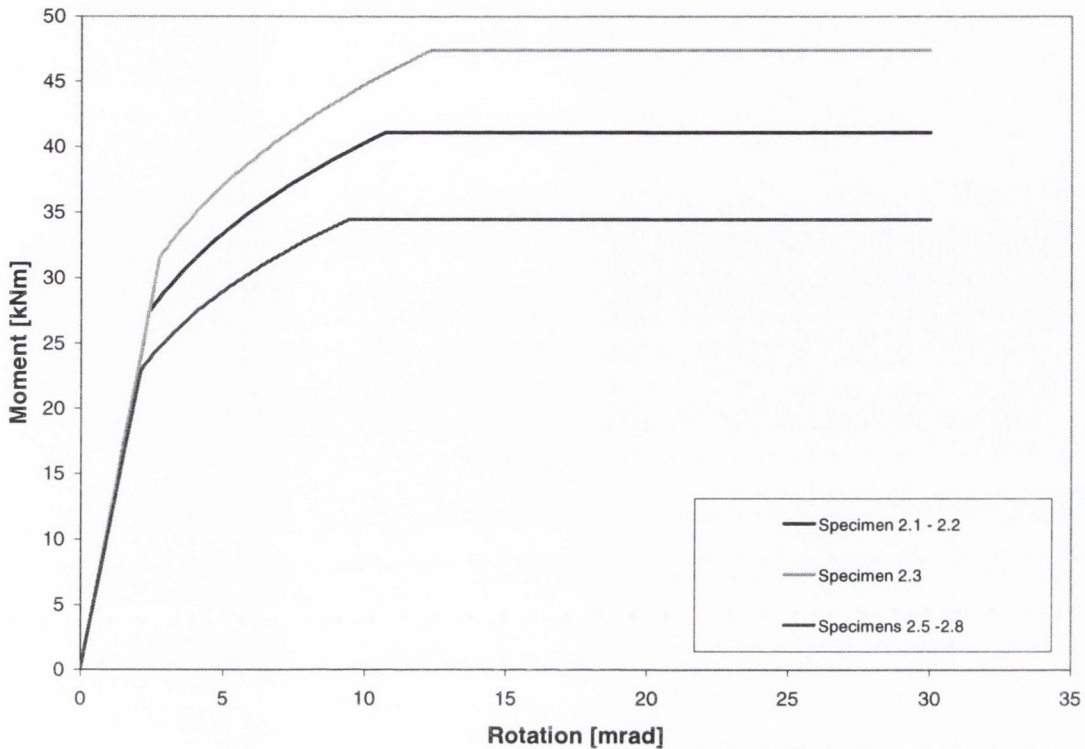


Figure 4.9: Predicted Moment-Rotation Relationship for Test Series Two

Table 4.5 presents the design response values for the joints in this test series. Eurocode 3: Annex J does not provide guidance on the moment-rotation relationship of joints with bolt pre-loads and therefore, the predictions given above assume non-loaded bolts. Eurocode 3: Annex J is also incapable of predicting the moment-rotation relationship of specimen 2.4 where a mixture of bolt grades are used for the bolts and nuts, and therefore, there is no prediction given for that specimen. The design moment-rotation characteristics are illustrated in Figure 4.9. As may be seen above, there is very little difference in either the initial rotational stiffnesses of the specimens, or their yield rotations.

As would be expected, the joints with the lowest predicted capacity are specimens 2.5 – 2.8 where the ultimate moment capacity is dominated by the tensile strength of the bolts. The Eurocode 3 model suggests that the change in bolt grade for specimen 2.3 will result in an increase in its moment capacity and yield rotation, because the bolts are no longer the critical component of the joint.

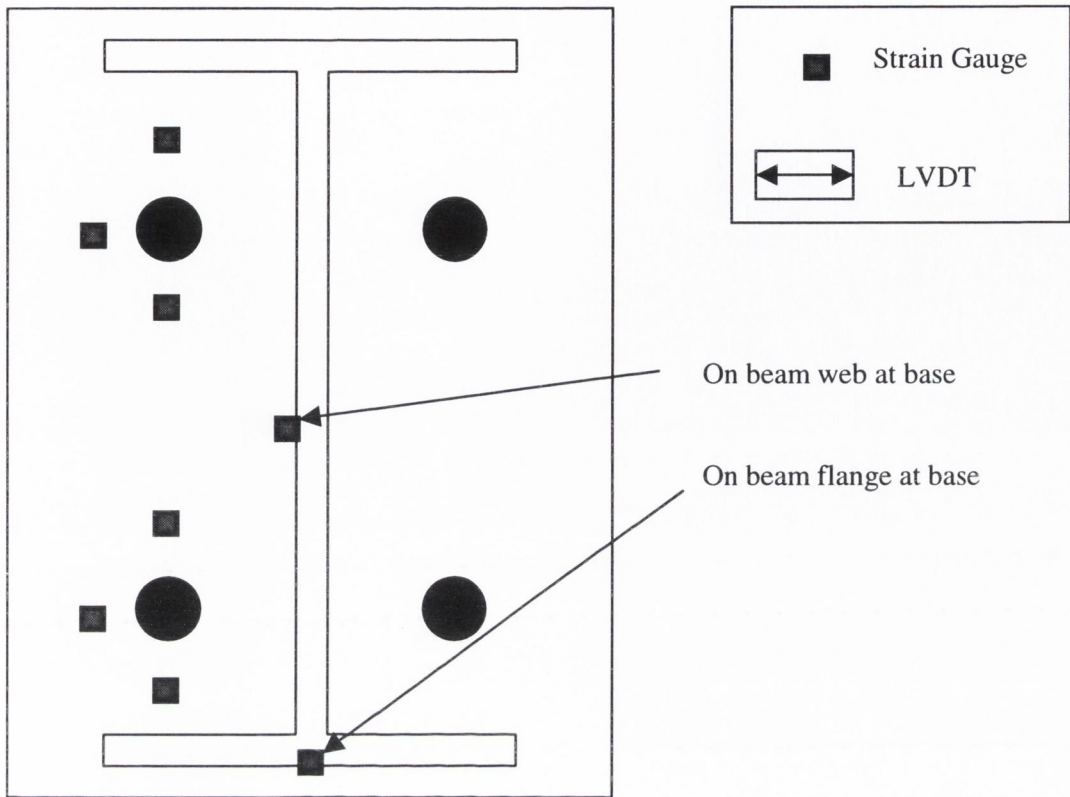


Figure 4.10 (a): Measurement device locations in test series two (plan view)

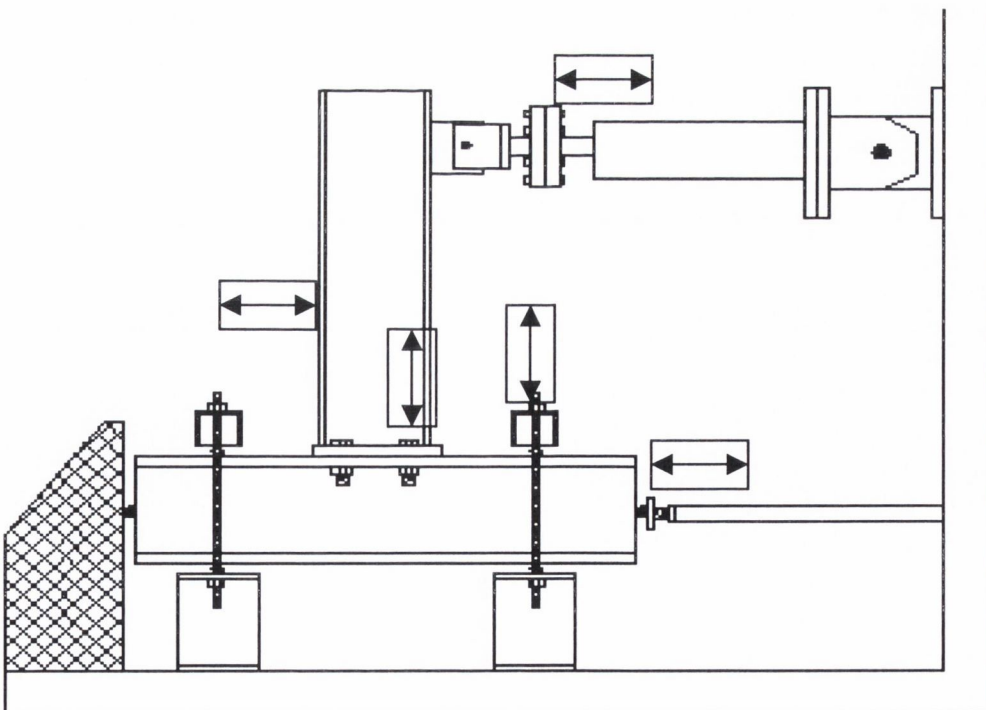


Figure 4.10 (b): Measurement device locations in test series two (elevation)

In this test series, eight strain gauges were employed along with five LVDTs, as shown in Figure 4.10. Two gauges were placed on the beam web and beam flange as close to the end-plate as possible to determine whether the beam experienced any local buckling or yielding in these regions. The remaining six strain gauges were placed around the bolts to determine how the end-plate yielded in this area. An additional two LVDTs were added to the three locations in test series one. The first was attached to the beam flange 400 mm up from the base of the end-plate. This was to allow a check on the beam rotation and end-plate rotation to be calculated. The second LVDT was attached to the end-plate where the beam flange was welded to the plate. This LVDT was used to measure the uplift displacement of the end-plate on each cycle.

4.4.3 Test Series Three

Eight full-scale specimens were tested in the third test series which consisted of four separate joint configurations. The objectives of in this series were as follows:

- To repeat tests with joint configurations identical to specimen 2.3;
- To obtain further experimental results on mode 1 and mode 2 joints to allow validation of the mechanical model;
- To confirm previous work carried out into strain rate effects on joints and to verify the performance of the experimental system at higher loading rates;
- To investigate the effects of utilising a column with a flange thickness approximately the same as the joint end-plate thickness.

The geometrical properties of the joint end-plates in this series are identical to those in test series two and shown in Figure 4.8, apart from the thicknesses of the end-plates which are given in Table 4.6. The beam size used throughout the series was 254 x 146 x 37 kg/m UB and all of the bolts were of size M20. In six of the eight specimens, a large column size, identical to that employed in the previous test series, was used in order to concentrate the joint deformations in the end-plate. In the remaining two specimens, a light column section was employed to allow deformation in both the end-plate and column flange.

Each joint configuration was tested twice. The first test was a constant amplitude cyclic test in which a waveform of ± 52 mm was imposed on the specimen. The first cycle in this test is similar to a monotonic test and allows the monotonic joint properties to be calculated. The second test carried out on each configuration is an increasing amplitude cyclic test as recommended in the ECCS procedures (see section 3.2). In the case of specimens 3.3 and 3.4, the constant amplitude test was replaced with a second increasing amplitude cyclic test, executed at a higher loading rate.

Specimen Number	End-Plate Thickness [mm]	Column Size [kg/m UC]	Bolt Grade	Test Type
3.1	10	203 x 203 x 86	8.8	Large Amplitude
3.2	10	203 x 203 x 86	8.8	Cyclic
3.3	15	203 x 203 x 86	8.8	Cyclic
3.4	15	203 x 203 x 86	8.8	Cyclic
3.5	12	203 x 203 x 52	8.8	Large Amplitude
3.6	12	203 x 203 x 52	8.8	Cyclic
3.7	12	203 x 203 x 86	10.9	Large Amplitude
3.8	12	203 x 203 x 86	10.9	Cyclic

Table 4.6: Specimen properties for test series three

Table 4.7 and Figure 4.11 show the design moment-rotation relationships as calculated by Eurocode 3: Annex J. It may be observed that the design values for specimen 3.3 and 3.7 are very similar to each other. Joint specimen 3.3 employs a 15 mm thick end-plate and the failure mode of the joint is mode 2. In contrast, specimen 3.7 employs a thinner end-plate, 12 mm thickness, but uses a higher bolt grade resulting in a mode 1 failure. This is attributed to the change in the β_{Rd} value versus capacity ratio as discussed in section 2.5. Eurocode 3 predicts a similar initial stiffness for specimen 3.1, but a much lower moment capacity. Eurocode 3 predicts the lowest stiffness for specimen 3.5 with a mid-range moment capacity. The failure mode for this specimen is mode 2. However, unlike the other three configurations in this test series, the column flange is predicted to yield first rather than the end-plate.

All of the joints in this test series possess sufficient rotation capacity for plastic global analysis, as laid down under Eurocode 3 requirements.

Specimen Number	Initial Stiffness, $S_{j,ini}$ [kNm/mrad]	Yield Rotation [mrad]	Yield Moment [kNm]	Ultimate Moment [kNm]	Predicted Failure Mode	Sufficient Capacity for Plastic Global Analysis?
3.1 & 3.2	10.28	2.13	21.95	32.925	1	Yes
3.3 & 3.4	12.17	2.6	31.62	47.433	2	Yes
3.5 & 3.6	7.37	3.57	26.28	39.415	2	Yes
3.7 & 3.8	11.37	2.78	31.61	47.41	1	Yes

Table 4.7: Predicted Design Parameters for Test Series Two

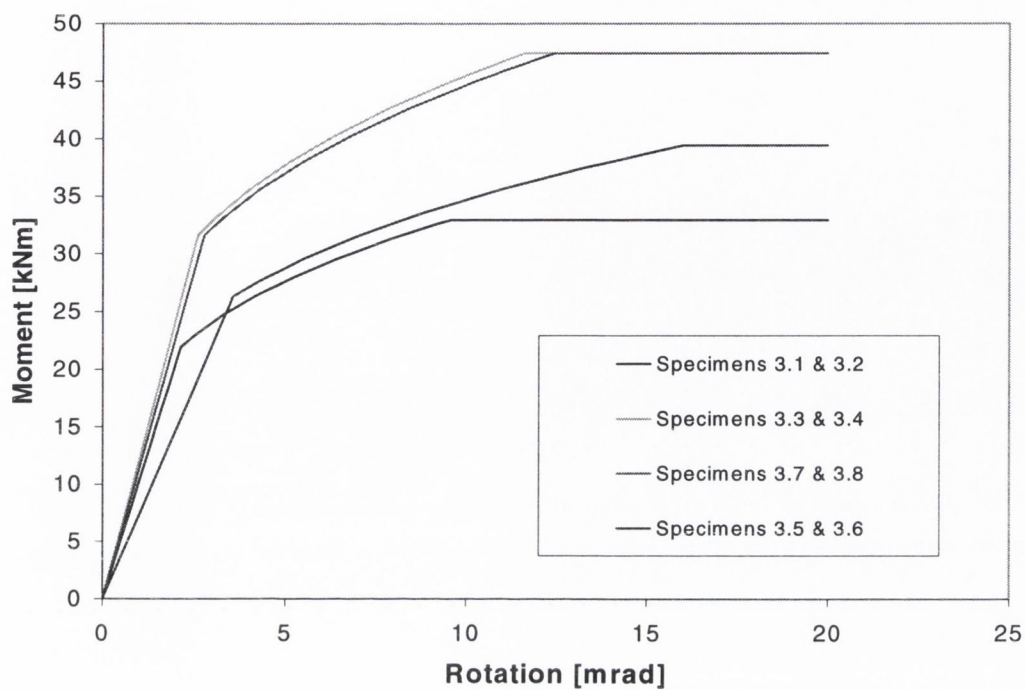


Figure 4.11: Eurocode 3: Annex J predictions for Test series 3

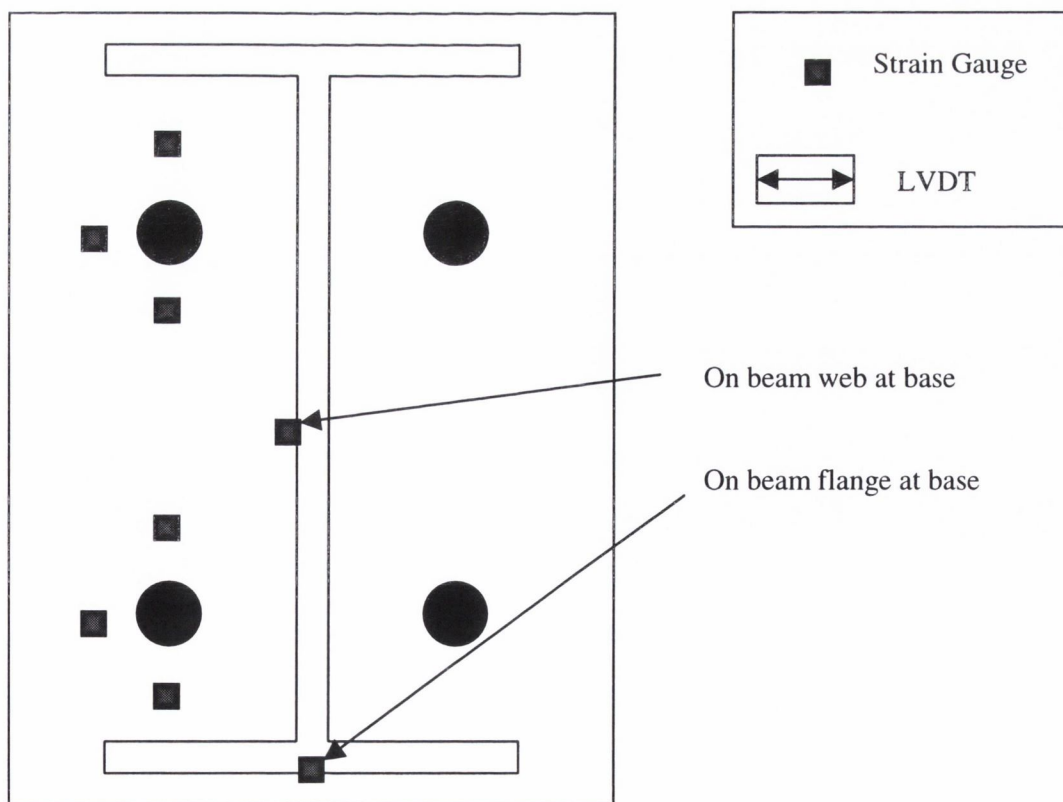


Figure 4.12 (a): Measurement device locations in test series three (plan view)

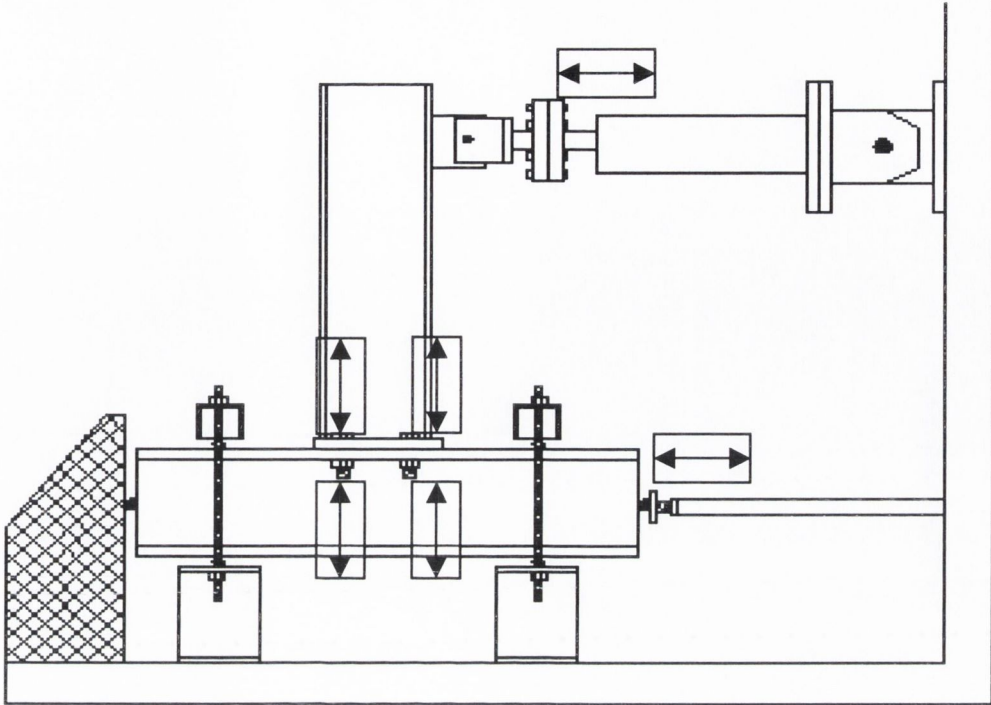


Figure 4.12 (b): Measurement device locations in test series three (elevation)

The same eight strain gauge locations were used for test series three, as shown in Figure 4.1012 (a). However, six LVDTs were employed in this test series, as shown in Figure 4.12 (b). As results from both of the first two series had shown no lifting of the column during the test, it was decided to dispense with the LVDT measuring this, and concentrate on the behaviour of the end-plate. As smaller column sections were to be used in two of the specimens, it was necessary to measure the displacement of both the column flange and the end-plate. This allowed the overall displacement to be measured at a point. The first pair of LVDTs were placed at the weld between the beam flange and the end-plate with the second LVDT directly below attached to the column flange. The second pair was attached to the head and nut of the bolt at the other end of the joint. This allowed the bolt elongation to be measured as the test proceeded as well as the contribution of bolt elongation to joint rotation.

4.5 Test Series One Experimental Results

As stated above, one of the objectives of this test series was to determine whether the failure modes defined in section 2.5 remain valid for joints tested under cyclic loads. Although some of the tests cannot be considered a complete success, it is possible to determine the joint failure mode from five of the six experiments. The only test where it is not possible to determine the failure mode is

in test specimen 1.5, where local buckling of the beam flange occurred.

Specimens 1.1 and 1.2 were observed to yield in the manner prescribed for a mode 1 failure. This was evident from examination of the end-plate at the end of the experiment, strain gauge results and from a post-experimental examination of the bolts. Yielding of the end-plate was observed along the beam web line as well as at the bolt-line. Examination of the four bolts in either joint showed no permanent elongation and hence no plastic yielding.

In the case of specimen 1.4, yielding of the end-plate was observed during the test followed by stripping of the bolt threads. Examination of the strain gauge results shows that yielding of the end-plate at the beam web line occurred first, with stripping of the bolts occurring at approximately the same time as initial yielding of the end-plate along the bolt-line. This is discussed in further detail later in this section. Therefore, it is possible that the joint would have had a mode 1 failure mechanism instead of the mode 2 predicted as only the premature stripping of the bolts prevented yielding of the end-plate along the bolt-line. This stripping of the bolt threads was also observed in both specimens 1.5 and 1.6 which were designed to fail in mode 3. Examination of the strain gauge results from both of these specimens identified no yielding of the end-plate along the bolt-line or the beam web line. Therefore, failure of these joints occurred in the bolts only, as prescribed for mode 3 mechanisms. The failure modes for each joint specimen are given in Table 4.8, along with other relevant properties. It should be noted that the properties reported in Table 4.8 for some of the specimens are inaccurate (shown in brackets) or are not reported due to experimental problems, as in the case of specimen 1.5.

Specimen	Initial Stiffness [kNm/mrad]	Yield Rotation [mrad]	Yield Moment [kNm]	Ultimate Rotation [mrad]	Ultimate Moment [kNm]	Actual Failure Mode
1.1	(4.07)	(5.54)	(22.15)	(69.13)	(39.10)	1
1.2	8.50	3.42	29.03	66.97	53.92	1
1.3	(3.56)	(5.11)	(18.21)	(77.10)	(62.44)	1 / 2
1.4	10.21	4.31	44.01	37.45	67.71	2
1.5	-	-	-	-	-	3/Beam
1.6	3.19	13.93	44.45	59.12	54.41	3

Table 4.8: Specimen Experimental Properties for Test Series One

4.5.1 Experimental Results & Observations: Specimen 1.1

This was the very first test to be run using the newly developed control programs described in Chapter 3. It can be seen in Figure 4.13 that the resistance of the joint is not the same on both sides. It is possible that this could be accounted for by irregularities in the material or geometrical properties, although these would be unlikely to cause such a large difference. A more likely explanation for this difference is that some slip occurred. As the actuator pulled back, the jack at the end was able to stop the column from sliding on its supports. However, when the actuator pushed the joint, a small gap between the column end and the reaction block allowed the column to slip slightly. Another problem identified when analysing the results was the presence of a small initial displacement and load (2.7 mm and 7.9 kN). This has resulted in the moment-rotation curve starting off centre, rendering the analysis a great deal more complicated.

Due to this slip, and initial load and displacement, it is only possible to determine general information from the joint, and not some of the more detailed data discussed in section 4.3. These problems also cast doubt on some of the above information such as the ultimate moment and yield values. Very early on in the test, significant bending was observed in the toe of the end-plate, which is the slight protrudence of the end-plate past the beam flange (Figure 4.5). Deformation of the end-plate was also observed in the form of circular patterns, as described in Eurocode 3: Annex J. Strain gauges located along the bolt-line and the fillet line confirmed that these locations had yielded before the end of the test, and that the specimen had therefore behaved in the manner described for a mode 1 failure mechanism.

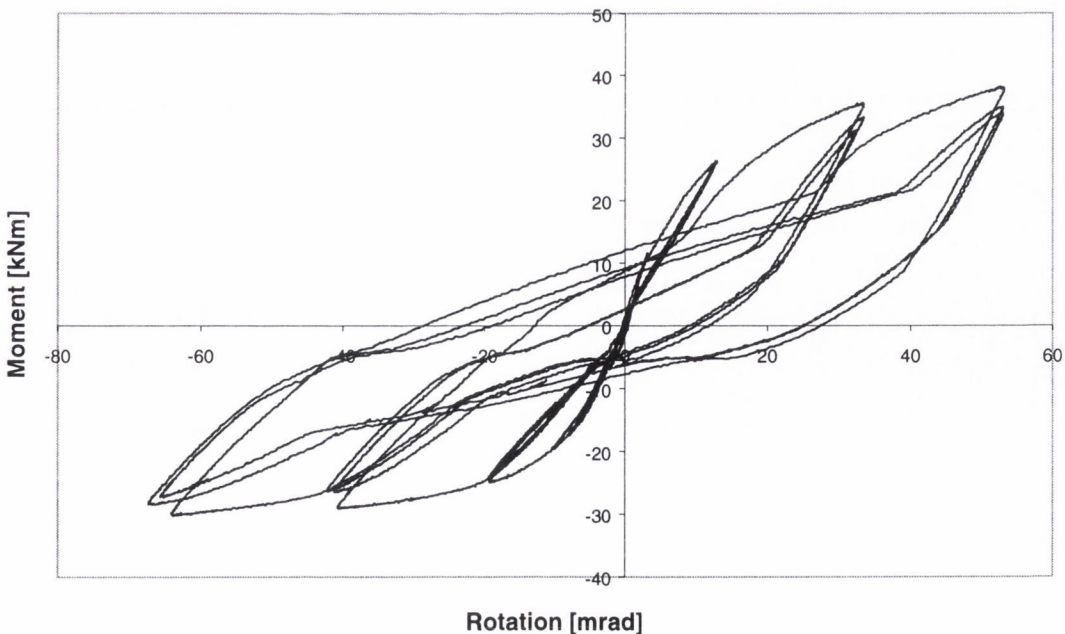


Figure 4.13: Moment-Rotation Relationship for Specimen 1.1

The initial stiffness of the specimen was measured at 4.07 kNm/mrad in the full cyclic test compared to 6.52 kNm/mrad in the shakedown test. This difference in the initial stiffness is accounted for by the magnitude and rate of loading between the test runs. However, the initial stiffness from the full cyclic test is more reliable as the shakedown test is designed to remove any unintended tightness in the test set-up prior to the full test. The yield rotation and moment resistance of the specimen have been calculated in relation to the initial points as it proved impossible to zero the specimen results without invalidating the analysis techniques. It was seen that the elastic yield point of the specimen occurred with an imposed rotation of 5.5 mrad and an imposed moment of 22.1 kNm. The ultimate rotation capacity of the specimen was not achieved during the imposed loading as the specimen did not fail during the test. However, post-experimental examination of the specimen showed that low cycle fatigue tearing of the underside of the end-plate had begun along the beam web line. This is consistent with the expected location of high stresses. It is expected that this would have resulted in the ultimate failure of the joint being due to the propagation of these tears throughout the depth of the end-plate. At this point, the moment resistance of the joint would have completely vanished. It may be seen from the moment-rotation relationship that this joint displays a very high level of ductility. Although the joint achieved the same displacement in both loading directions, due to slippage of the specimen, the partial ductility on the compression side of the joint is 10.23 while that on the tension side is 12.56.

One further interesting point observed in Figure 4.13, is the stiffness hardening that occurs close to the end of each of the inelastic cycles. This may be due to the elastic rebound properties of the toe combined with the prying forces. It is possible that this phenomena is also partly due to the strain hardening characteristics of the steel. In later tests, this was investigated further by placing strain gauges in different locations.

When the experimental results are compared to the predictions made by Eurocode 3: Annex J, it can be seen the Eurocode 3 predictions are very conservative. The experimental initial stiffness of the joint is approximately half that predicted, which is highly conservative for earthquake engineering purposes. The predicted response is also highly conservative in terms of yield rotation, as well as yield and ultimate moment resistances. The yield rotation is under-predicted by a factor 3.4. The yield moment capacity achieved by the joint is approximately equal to the ultimate capacity predicted by Eurocode 3. This was not entirely unexpected as Eurocode 3 assumes that the moment-rotation relationship follows a plastic behaviour once when the elastic yield strength of the material is reached. The ratio between the experimental ultimate moment resistance and the predicted ultimate moment resistance is 1.87. This large difference may lead to capacity design problems, as is discussed later.

4.5.2 Experimental Results & Observations: Specimen 1.2

As can be seen from Table 4.8, this specimen was identical in its geometrical properties to that of specimen 1.1. As this was the fifth of the six tests carried out in test series one, all of the problems with the experimental process had been encountered and solved. This allowed the collection of a full set of results for analysis. The moment-rotation relationship shown Figure 4.14 is highly stable throughout the entire loading.

From this it may be assumed that a similar hysteresis curve would have been obtained for specimen 1.1 if the experimental difficulties discussed above in section 4.5.1 had not arisen. Figure 4.14 shows that ultimate failure of the joint did not occur within the range of the maximum actuator displacement, while a post-experimental examination of the bolts after the test showed no elongation or stripping. The final deformed shape of the joint is illustrated in Figure 4.15. It may be seen that the deformation is concentrated in the end-plate component with the bolts continuing to hold the end-plate tight at their locations. Examination of the underside of the end-plate showed the same low-cycle tearing along the line of the beam web that was observed in specimen 1.1. However, in the case of specimen 1.2, tearing of the underside of the end-plate was also observed along the beam flange lines. The exact location of the tearing is shown in Figure 4.16. Unfortunately, photographs taken of the tearing did not show it clearly. It is expected that if the joint was subjected to further cycles at the maximum amplitude, this tearing would extend from the beam web towards the bolt holes. Evidence of this was observed as the tear has begun to spread towards three of the four holes.

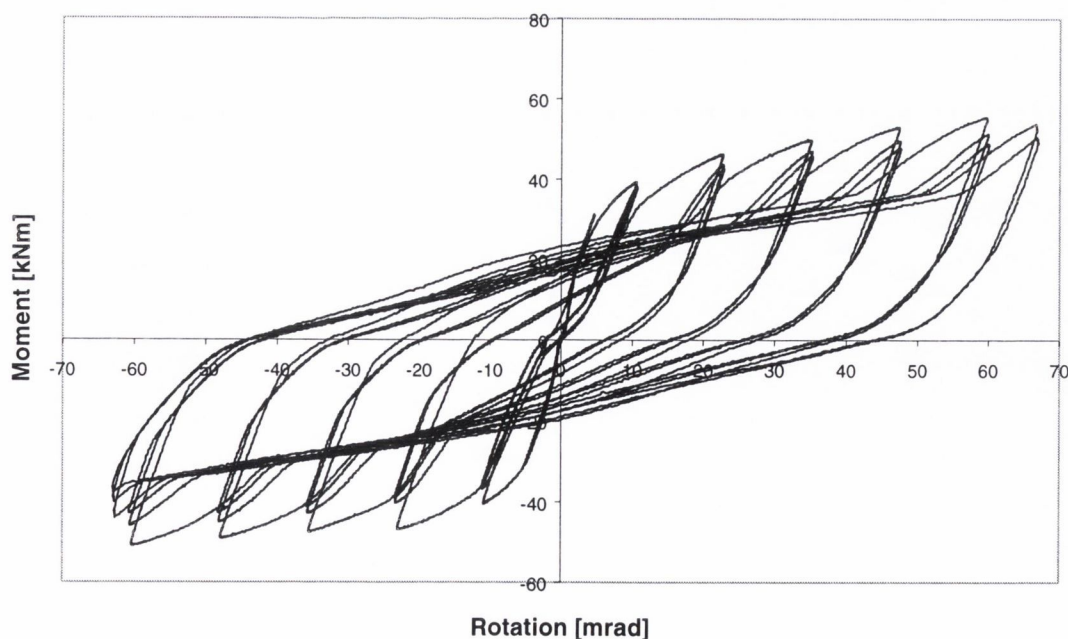


Figure 4.14: Moment-rotation hysteresis curve for Specimen 1.2

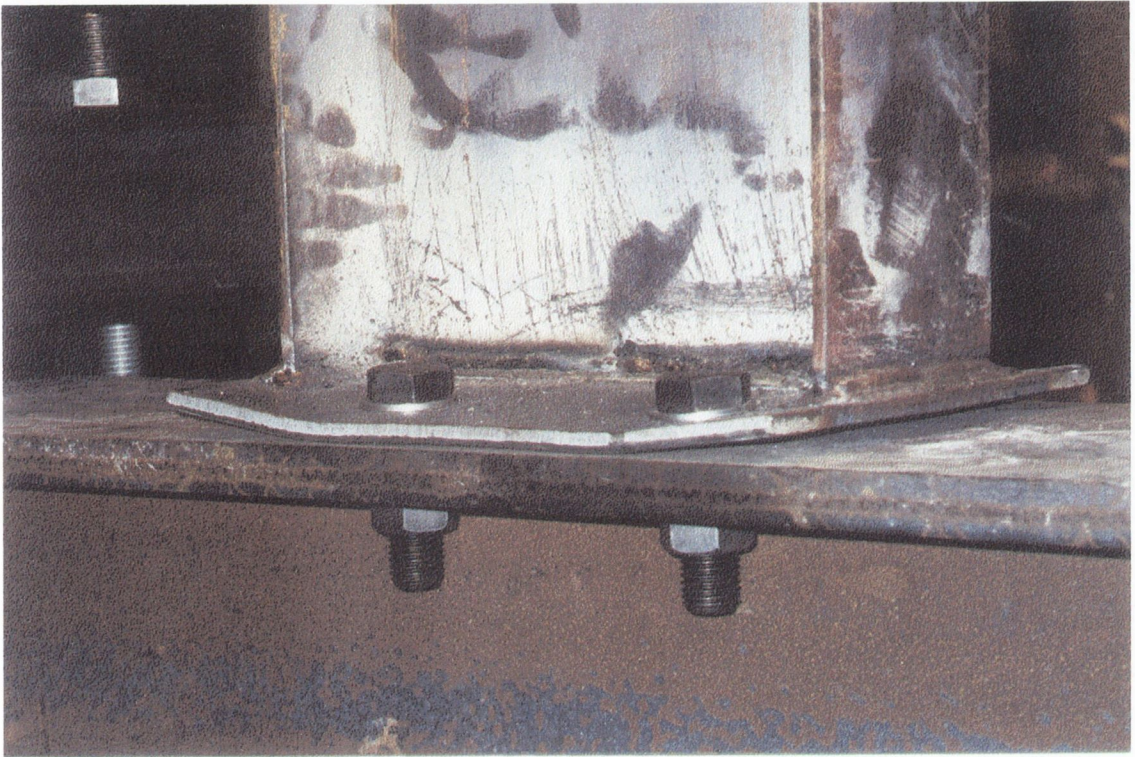


Figure 4.15: Final Deformed Joint for Specimen 1.2

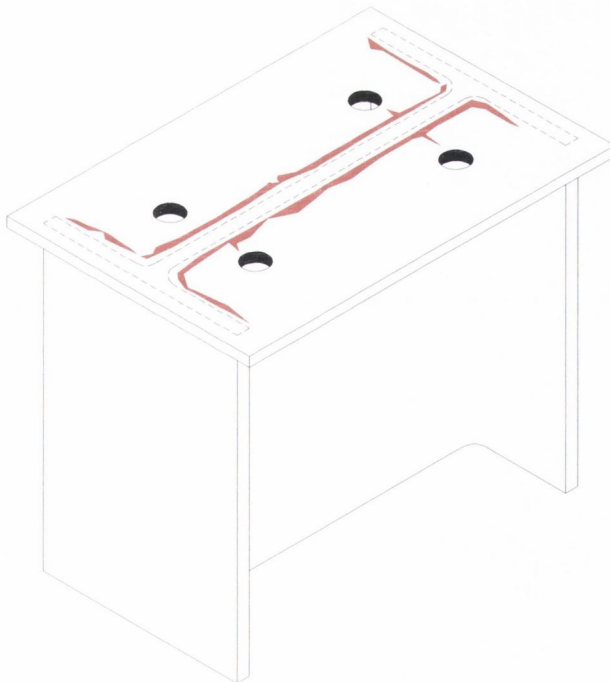


Figure 4.16: Low cycle fatigue tearing of specimen 1.2 end-plate

The experimental properties of the joint are presented in Table 4.8, and it may be observed that the initial stiffness for this joint is higher than that displayed by specimen 1.1. However, as there were no problems encountered during the execution of this test, the results obtained are considered to be more reliable. As can be seen from Figure 4.14, the joint exhibits a very high level of rotational ductility with a maximum partial ductility of 19.5 being obtained before the experiment was halted when the actuator displacement limit was reached. From the above moment-rotation relationship, it can be seen that little or no resistance degradation occurred. Figure 4.17 compares the variation in three cyclic evaluation parameters with partial ductility. The resistance ratio of the joint rises in a highly elastic manner to a value close to 1, when the force at that partial ductility level is approximately equal to the yield force of the joint. At this point, there is a slight drop in the resistance ratio as the steel yields before the ratio continues to rise. The resistance ratio for specimen 1.2 reaches a maximum at a level of approximately 1.6, indicating that the ultimate moment capacity of the joint is 160% greater than the yield capacity.

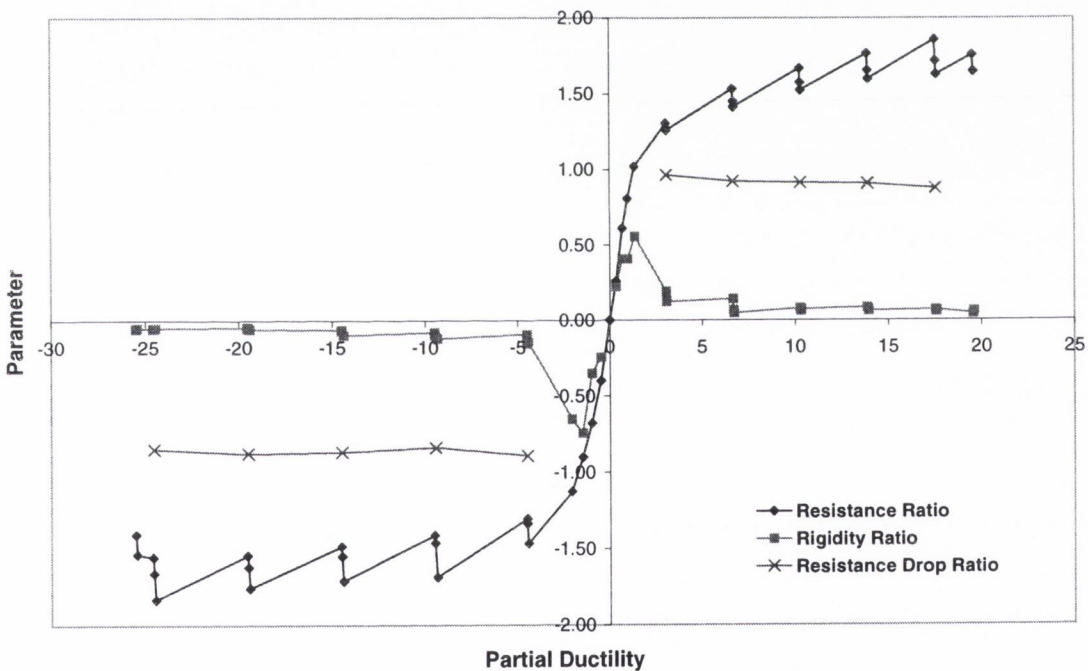


Figure 4.17: Cyclic evaluation parameters for specimen 1.2

The resistance drop ratio remains reasonably constant throughout the test, decreasing only slightly as the partial ductility of the joint increases. This confirms the stable nature of the moment-rotation relationship of the joint. Examining the rigidity ratio of the joint, it may be observed that once the joint has begun to yield, the ratio drops quickly from one to practically zero. This indicates that the joint experiences non-recoverable deformation in the toe of the end-plate very early in the imposed displacement. Once the rigidity ratio has reached a value of approximately

0.04, it remains reasonably constant for the remainder of the experiment.

4.5.3 Experimental Results & Observations: Specimen 1.3

This test was the second of the six experiments in this series. The specimen was designed to give a mode 2 failure and is also one of the two benchmark specimens, as its details were extracted directly from the BSCA moment connection book. However, the method that was used to eliminate the slippage of the specimen as noted above for specimen 1.1 failed to accomplish its goals and introduced a new problem which badly affected the moment-rotation curve. Another problem that occurred during the test, is that the actuator was not centred, despite all the efforts to do so, and hence an initial load and displacement were placed on the specimen further disrupting the results.

Although thorough analysis of the experimental results is not justified, the experimental observation recorded during the test did reveal a number of interesting points. This joint was expected to display a mode 2 failure, that is the end-plate was expected to yield near to the beam web line followed by yielding of the bolts. Instead, the joint did not actually reach its ultimate failure mode during the course of the test. There was some elongation noted in the bolts but it was not clear whether this was due to the bolts stretching or the threads stripping. There was also a large degree of bending in the end-plate itself, especially at the toes. From this it is anticipated that the joint would have resulted in a mode 2 failure although this cannot be stated definitively.

4.5.4 Experimental Results & Observations: Specimen 1.4

The geometrical properties of specimen 1.4 are identical to specimen 1.3, being one of the two reference joints tested within this series. The specimen was designed to fail in a mode 2 mechanism. The moment-rotation curve obtained is shown in Figure 4.18. The end-plate was seen to yield in bending, followed by failure of the bolts. However, the bolts in this test did not fail by snapping or a sudden fracture, but rather by stripping of the threads on the inside of the nut, and elongation of the threaded bolt length. The point of failure of the first bolt is indicated as point X in Figure 4.18. The second bolt in that row continued to provide resistance until the cyclic displacement was increased to the next amplitude increment (point Y). The point of failure is taken as that where the first bolt in the bolt row failed (point X). Although the joint retains a large proportion of its moment capacity after this bolt yields, there is still a significant drop in the moment resistance. The final condition of the joint is shown in Figure 4.19. It is clear that the end-plate has undergone significant plastic deformation while the threads of the bolts have stripped allowing the nut to be pushed down the bolt shank. As can be seen in Figure 4.19, the bolts on the compression side did not deform, or strip their threads, to the degree as those on the tension side.

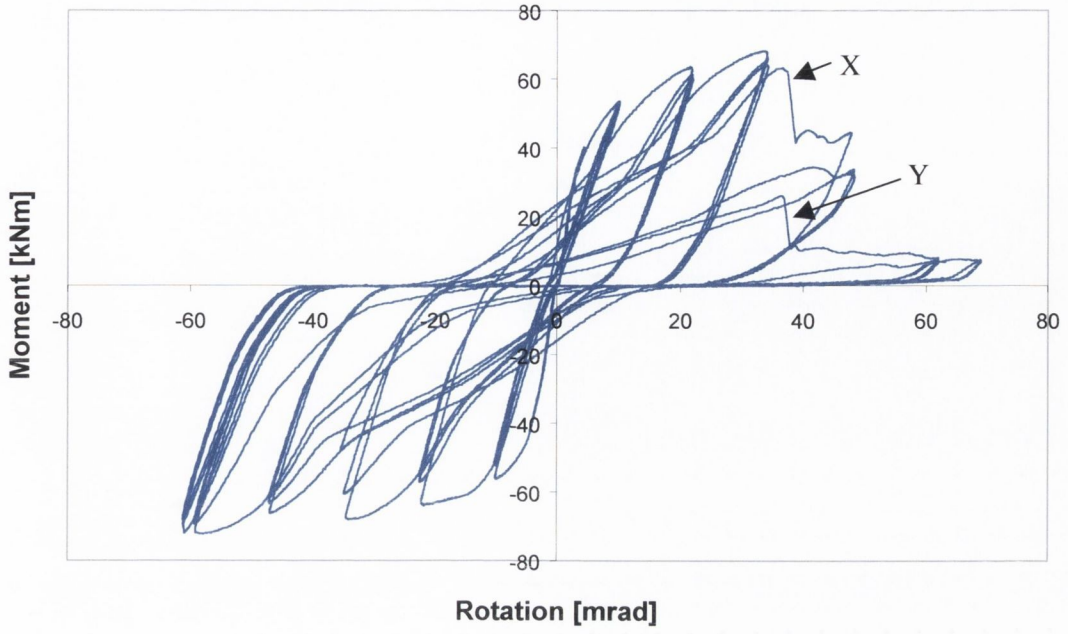


Figure 4.18: Moment-Rotation Curve for Specimen 1.4

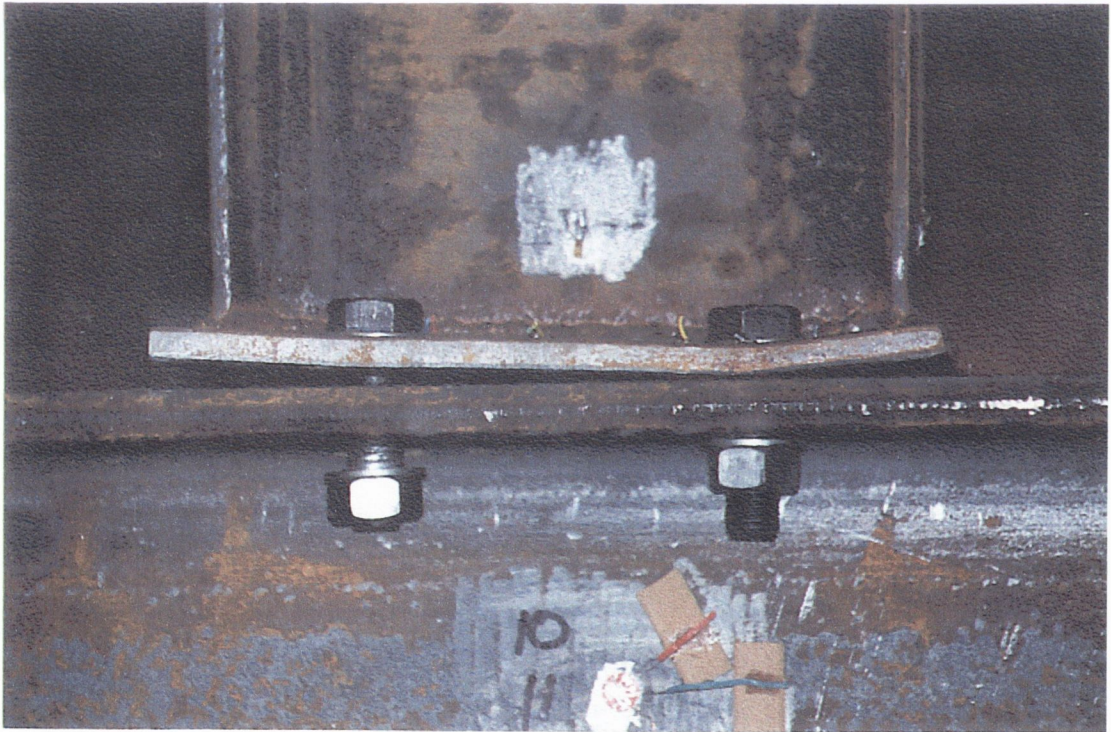


Figure 4.19: Final Deformed Shape of Specimen 1.4

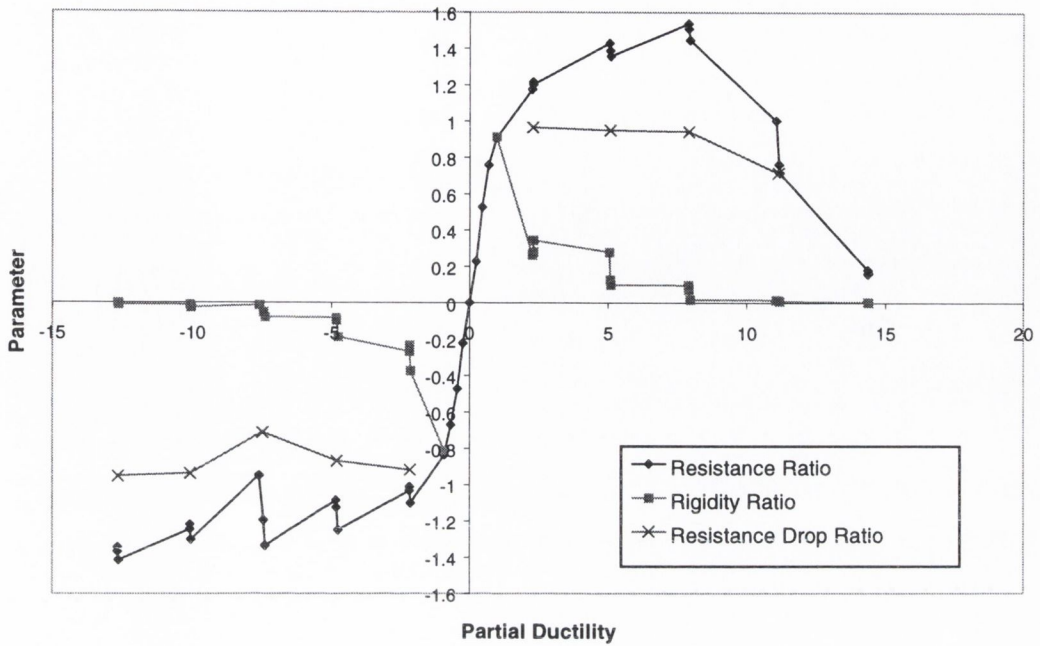


Figure 4.20: Cyclic Evaluation Parameters for Specimen 1.4

Figure 4.20 illustrates the cyclic evaluation parameters for this specimen. It should be noted that the evaluation parameters for a joint do not result in negative values as are shown in Figure 4.20, but are depicted in this manner to allow the different tension and compression values to be easily discerned. The ductility of this joint is dictated by the failure of the bolts, the degree of yielding in the end-plate and the assumption of the ultimate failure point. The partial ductility of the joint at failure was 8.7, which is significantly lower than that measured in the joints with mode 1 failure mechanisms. The resistance ratio of this joint behaves in a typical manner, with the ratio climbing to a maximum of 1.45 on the cycle before failure occurs. Once failure of the joint has occurred, the resistance ratio on the tension side of the joint drops rapidly until it stabilises at approximately 10%. The remaining resistance is due to the bolts on the compression side of the joint and the shear action of the two tension bolts that stripped. The resistance ratio on the compression side of the joint remains constant at approximately 1.35, except for a sudden reduction during the cycle in which the first bolt failed. On the tension side, the resistance drop ratio remains constant up to failure, with a value of approximately 0.95. At the point of failure this drops to 0.71 and then to a final value of 0.2 as the joint failed completely on the tension side. On the compression side of the joint, the resistance drop ratio is in the range 0.9-0.95 until it drops suddenly to a value of 0.76 during the failure cycle. It then returns to a value of 0.91 where it remains constant for the remainder of the test. The rigidity ratio behaves as would be expected for this type of joint: on the tension side of the joint a maximum value of just below 1.0 is obtained at the end of the four elastic cycles, by the end of the first group of three inelastic cycles, it has fallen to 0.25 of the initial

stiffness and then to 0.01 just before failure. A very similar behaviour is seen on the compression side. As the rigidity ratio has reached such low levels before the joint fails, it may be said that the rigidity ratio is not dependant on the failure of the joint.

Stiffness hardening is evident on the tension side of the moment-rotation curve before failure occurs. However, it can also be seen on the compression side of the joint where no failure took place. Examination shows that the stiffness hardening in this joint was not as pronounced as that seen for specimen 1.1 and 1.2. It was hoped that examination of the strain gauge results for this specimen would indicate that this hardening in the moment-rotation hysteresis curve was due to a combination of the elastic-plastic behaviour of the end-plate and the level of prying forces present in the joint. However, the two strain gauges located of the bolt-line on the end-plate, which would have been expected to give the most detailed information on this phenomenon, did not survive long into the experiment before becoming loose and reading zero strain.

4.5.5 Experimental Results & Observations: Specimen 1.5

This joint was the third in the test series and the first of the mode 3 specimens to be tested. In order to ensure a mode 3 failure mechanism, the end-plate thickness was increased from the industry standard value of 12 mm to a thickness of 20 mm. However, during the experiment the beam flange buckled, preventing the joint from obtaining its full moment capacity. The measured moment-rotation relationship for the specimen is shown in Figure 4.21. As can be seen, once the beam flange buckles the moment resistance of the joint is unable to be increased above 64.1 kNm on the compression side, while the maximum capacity of 79.6 kNm is realised on the tension side. However, it was also seen that the bolts in the joint stripped their threads and hence the final failure mode of the joint was in fact mode 3. This stripping of the bolt threads was not completely unexpected as it has been reported in work carried out by other researchers as detailed in section 2.7.1.

As can be seen in Figure 4.21, the moment-rotation relationship does not begin at zero moment and zero rotation. When the test started, the moment present in the joint immediately shifted to -27 kNm (compression), with no corresponding shift in the imposed rotation. The reason for this sudden load has not been determined, but it is suspected that it is related to the problems encountered with the second test in the series, specimen 1.3, where the load cell was accidentally jammed against the actuator ram. This sudden jump did not reoccur in any subsequent test. This problem appeared to cause a large drop in the measured resistance of the specimen when it was at the maximum actuator limits. Reasons for this error were not discovered. It was also not observed in any subsequent experiments in this study.

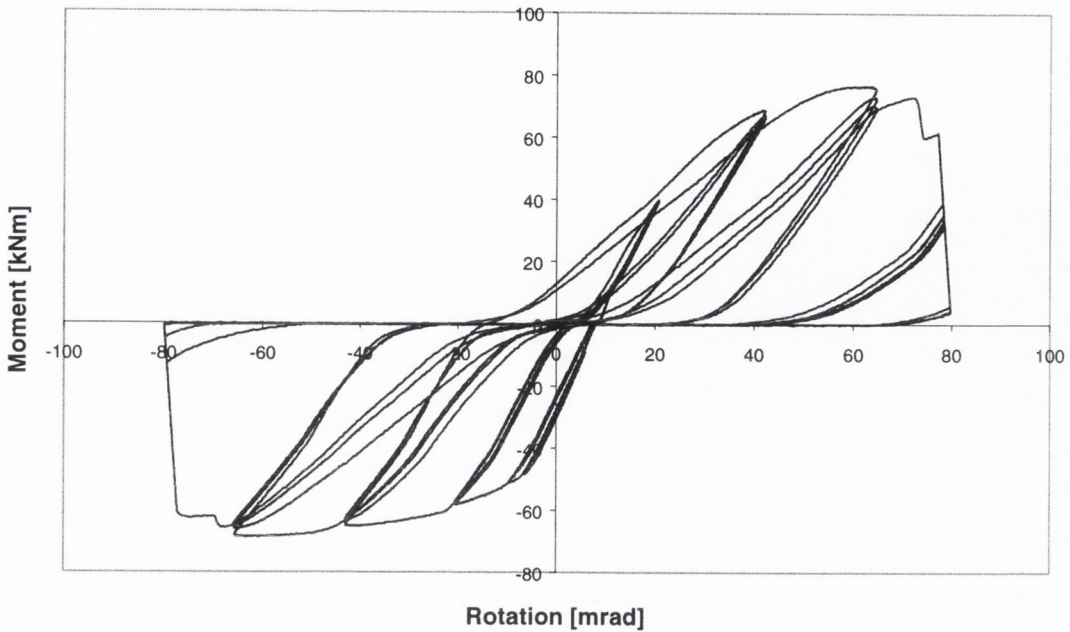


Figure 4.21: Moment-Rotation Curve for Specimen 1.5

Based on the results obtained for the test, it was possible to determine some of the cyclic evaluation parameters set out in section 4.3, but not all. The partial ductility of the joint varies from 22.8 on the compression side to 2.95 on the tension side. These results for ductility and similarly, the resistance ratio, cannot be relied upon to accurately explain the joint behaviour. The resistance drop ratio, if considered separately for each group of three cycles rather than for the test as a whole, exhibits a consistent value of 0.95 throughout the test. It may also be seen that little or no stiffness hardening is displayed, as was observed in both the mode 1 and mode 2 type joints. This would appear to confirm that this hardening is related to the prying forces in the end-plate and plastic deformation of the end-plate toe.

4.5.6 Experimental Results & Observations: Specimen 1.6

This joint was the fourth in the series to be tested and as it had identical geometrical properties to specimen 1.5, it was also expected to fail in mode 3. A mode 3 failure was observed with very little end-plate bending but substantial bolt deformation. The moment-rotation relationship is presented in Figure 4.22. On the compression side of the joint, the ultimate moment resistance is much lower than that developed on the tension side of the joint. This may be explained by the behaviour of the bolts during the test. The exact description of the failure mode is as follows: the bolts on the negative side necked and then stripped as the displacement was increased, at which point the joint is considered to have failed. However, the bolts on the positive side of the joint did

not strip their threads in either the bolt or the nut. There was however, some elongation observable when the bolts were examined after the experiment had been completed. This allowed the moment resistance of the tension side of the joint to continue to rise until the test had been completed.

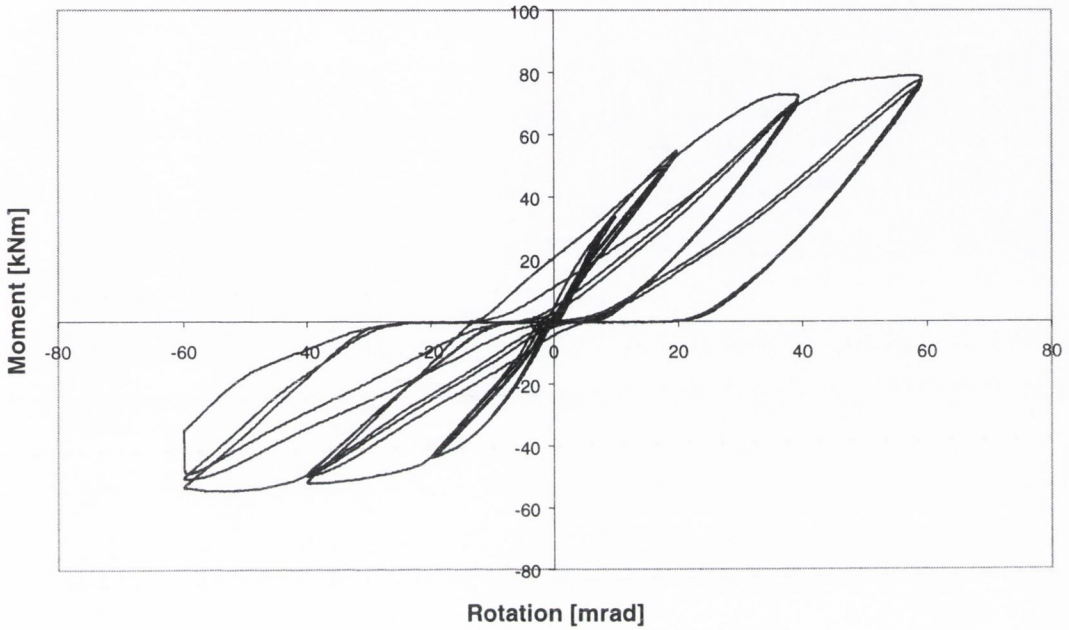


Figure 4.22: Moment-Rotation Curve for Specimen 1.6

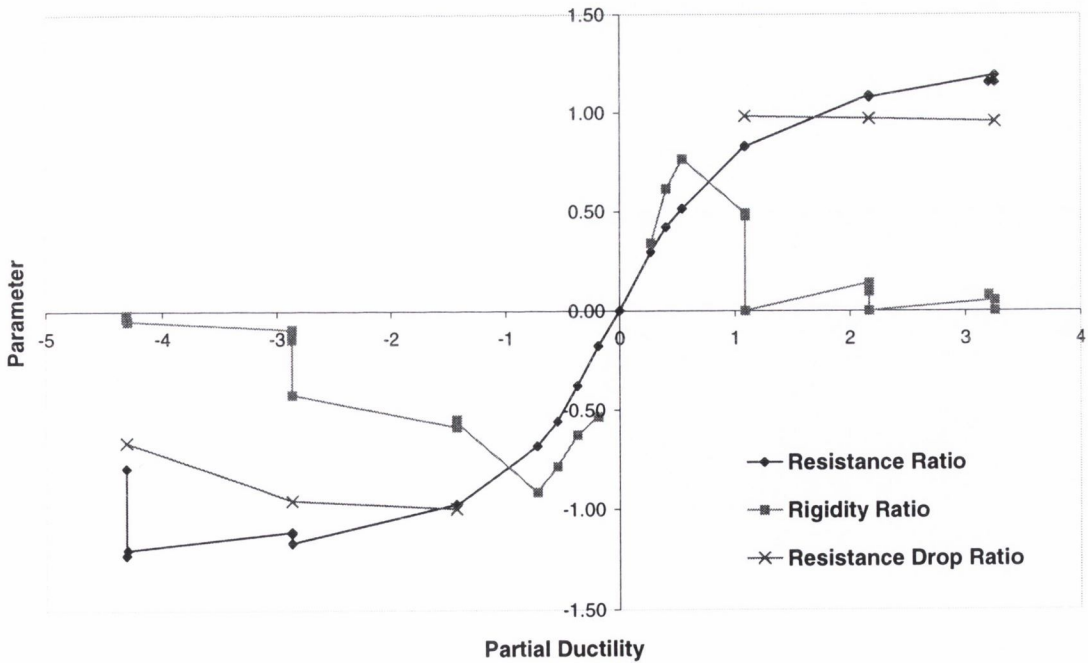


Figure 4.23: Cyclic Evaluation Parameters for Specimen 1.6

As expected, the ductility level for specimen 1.6 is much lower than that found for either the mode 1 or mode 2 joints, with a maximum partial ductility ratio of 4.3 obtained at the point of bolt failure. The resistance drop of the joint behaves in a typical manner. On the tension side of the moment-rotation curve, the ratio peaks at a value of 1.15 and holds there for the remainder of the test and failure does not occur on this side. On the compression side, the resistance ratio peaks at 1.21 of the yield resistance and holds there until failure of the bolts occurs. The rigidity ratio of the joint follows the pattern observed in other tests. The ratio starts at approximately 1.0 and then drops rapidly away. At the end of the first group of three cycles it has fallen to 0.5, and by the end of the second group of cycles it is less than 0.01. The resistance drop ratio for this joint remains very high for the entire loading sequence, with values between 0.94 and 0.98, up to the point where the bolt fails. At this point the values fall to 0.65 and then immediately fall to nearly zero.

As was noted in specimen 1.5, very little stiffness hardening is evident in the hysteresis curve. This confirms that the stiffness hardening behaviour is linked to the plastic response of the end-plate.

4.5.7 Test Series One Conclusions

As stated above, this test series was designed to meet two objectives. The first was to ensure that the test programs discussed in chapter 3 were all operating correctly and to develop a reliable test set-up, while the second was to investigate the effects of cyclic loading conditions on the static failure modes defined in Eurocode 3 and elsewhere. It was found that the test control programs did operate correctly in all cases, but there were unanticipated problems with the experimental set-up that seriously affected three of the six tests in the series. These problems involved slippage of the specimen at its restraints, centring problems with the actuator and load cell difficulties. The slippage of the specimen during the test was solved by monitoring during the test to maintain a constant axial load on the column. The load cell and centring problems were solved by trial and error until the best method for the experimental set-up was found.

Even with only three complete tests, it was still possible to evaluate the failure mode of the joints under cyclic loading. In all cases, the joint behaved in the manner predicted by Eurocode 3: Annex J (revised). Specimens 1.1 and 1.2 were predicted to display mode 1 failures, and this was observed with both specimens. Post-experimental examination of these joints showed no plastic elongation of the bolts, and extensive circular deformation patterns in the end-plate, both of which are consistent with a mode 1 failure mechanism. In both cases, low cycle fatigue tearing of the end-plate was observed and it is expected that this would lead to the ultimate failure of the joint.

A mode 2 failure mechanism was predicted for specimens 1.3 and 1.4. However, as specimen 1.3

did not reach its ultimate failure rotation during the experiment, it is not possible to confirm that it experienced a mode 2 failure. Specimen 1.4, however, did obtain its ultimate rotation, and displayed a mode 2 failure. During this test, significant deformation of the end-plate was noted, but ultimate failure was due to the stripping of the bolts. However, the specimen only failed when the actuator was in tension, and not in compression.

Specimen 1.5 and 1.6 were intended to display to a mode 3 failure mechanisms. Specimen 1.5 failed in two distinct ways. The first was buckling of the beam flange at the joint, while the second was stripping of the bolts in tension. The buckling of the beam flange prevented the joint from obtaining its full moment capacity on the compression side, but the stripping and hence failure of the bolt indicates a mode 3 failure. Post-experimental evaluation of the joint identified no deformation in the end-plate. Specimen 1.6 also responded in mode 3, with failure of the bolts being observed.

From these observations, it may be said that the failure modes predicted by Eurocode 3: Annex J for joints under static loading conditions remain valid under cyclic loading conditions. Further work may be necessary to determine if the modes also remain valid during seismic response in which a joint undergoes sudden large load reversals. An interesting feature of the test series is that rather than a classical fracture failure mechanism, many of the bolt failures observed were due to stripping of the threads on the bolt length or in the nuts.

Specimen	$S_{i,exp} / S_{i,EC3}$	$\theta_{y,exp} / \theta_{y,EC3}$	$M_{y,exp} / M_{y,EC3}$	$M_{ult,exp} / M_{ult,EC3}$
1.2	0.99	2.06	2.05	2.53
1.4	0.88	1.81	1.59	1.63
1.6	0.25	7.1	1.23	1.01

Table 4.9: Comparison between Experimental Results and Eurocode 3 Predictions

Table 4.9 compares the experimental results with design predictions using the methods given in Eurocode 3: Annex J, in which

- $S_{i,exp}$ = initial stiffness measured in experiment;
- $S_{i,EC3}$ = initial design stiffness from Eurocode 3: Annex J;
- $\theta_{y,exp}$ = design yield rotation measured in experiment;
- $\theta_{y,EC3}$ = design yield rotation predicted by Eurocode 3: Annex J;
- $M_{y,exp}$ = yield moment measured in experiment;
- $M_{y,EC3}$ = design yield moment predicted by Eurocode 3: Annex J;

- $M_{ult,exp}$ = yield moment measured in experiment; and
- $M_{ult,EC3}$ = design yield moment predicted by Eurocode 3: Annex J.

As can be seen, Eurocode 3 over-predicts the initial stiffness of the joint in all cases, although two of the specimens give quite good comparisons. However, the degree of error between the experimental and predicted stiffness values is very large. The yield rotation and moment are significantly under-predicted by Eurocode 3. The ultimate moment is also under-predicted, except in the case of specimen 1.6 where the experimental and predicted values differ by only 1%. Specimen 1.6 also displays the lowest difference between predicted and observed yield moment, which can be attributed to the fact that the bolts were the critical component of this joint, thus simplifying the mechanical model.

The mode 1 joint, specimen 1.2, has the greatest maximum resistance ratio with a value of 1.6. In comparison, the mode 2 and mode 3 joints have maximum resistance ratios of 1.45 and 1.17 respectively. This is probably due to the fact that the ultimate moment capacities of these joints were controlled by the capacity of the bolt which is the critical component in each, while the bolt capacity is not a factor in specimen 1.2. Specimen 1.6, which displayed a mode 3 failure, had a resistance ratio of 1.17. This is similar to the ratio of bolt ultimate strength to yield strength of 1.25. In contrast to the resistance ratio, the resistance drop ratio of the mode 3 joint was 0.98, that of the mode 1 joint was approximately 0.85, while the mode 2 joint displayed a ratio of 0.93. The rigidity ratio displays very similar behaviour for all of the joint types. In each case, the rigidity ratio starts at a value near one, which corresponds to the initial stiffness of the joint. Once the specimen has begun to yield the rigidity ratio drops quickly to approximately 0.25 – 0.5 at the end of the first group of three cycles and then continues to drop to approximately 0.04, where it remains constant for the remainder of the test.

One of the most interesting points that this test series has raised is with regard to the stiffness hardening evident in the moment-rotation hysteresis curves. It is believed that this hardening is due to a combination of the elastic rebound of the end-plate as well as the prying forces present in the joint. The elastic rebound occurs in the toe of the end-plate, that is the small section of the plate that extends beyond the beam flange. This toe undergoes elastic and plastic deformation on each cycle. When the joint is loaded in the opposite direction, the end-plate is able to recover the elastic deformation. However, on the next cycle the end-plate is deformed again. On this cycle, some plastic deformation is already present in the toe. This model is corroborated by an examination of the hysteresis curves for the three types of failure modes. Mode 1 joints exhibit the highest level of stiffness hardening, while mode 3 joints exhibit no stiffness hardening. Stiffness hardening is also noted in the mode 2 specimen although to an intermediate degree. In theory, mode 1 joints are

subjected to the highest level of prying forces while the mode 3 joints have little or no prying forces.

4.6 Conclusions

This chapter began by discussing the experimental set-up that was employed in this study. It was seen that the column sections were placed in a horizontal position, while the beam sections were located upright for ease of loading. The system used to hold the specimens in place was explained and the basic configuration of the sub-assemblages detailed.

The different parameters used to evaluate the cyclic properties of steel elements were then defined. These include the ductility ratio, resistance ratio, resistance drop ratio and the rigidity ratio. Formulae for calculating the different parameters were presented.

The experimental specimens tested in this study were then discussed. The beam-to-column sub-assemblages were detailed and dimensions of the different specimens given. The specimens tested possessed different details such as the end-plate thickness, bolt grade and size, beam size and column size. The Eurocode 3 design parameters of each specimen were presented. It was observed that the design stiffness of the specimens is very similar throughout, with the yield and ultimate capacities changing as the joint details are altered. Locations of strain gauges and displacement transducers for each series of tests were also detailed.

The results for test series one were presented. Problems with some of the specimens resulted in only three of the six sub-assemblages being of use. These problems were mostly in relation to the setting up of a new testing system. The specimens were examined to determine if the design failure modes from Eurocode 3 were valid under cyclic loading as well as static loads. It was observed that the specimens behaved as expected in this regard. However, when the experimental results were compared to the design calculations, it was observed that Eurocode 3 seriously over-predicts the initial stiffness of the joint. This would lead to under-estimations of the lateral displacements in a frame. It was also observed that the yield and ultimate moment capacity were under-predicted by up to 205%. The other two test series will investigate these observations further. The evaluation parameters for the three specimens were also examined. It was seen that the ductility of the joint was greatest for the mode 1 joints while at its lowest for the mode 3 specimens, as expected. It was determined that the rigidity ratio was not of great use in discussing the behaviour of flush end-plate joints due to the severity of the rocking present in the joints as the bolts elongate and the end-plate deforms. The resistance ratio was observed to follow a stable pattern up to failure, where it dropped quickly away. The resistance drop ratio was seen to remain steady as the imposed

displacement was increased.

It was determined that further tests were necessary to determine the usefulness of the resistance ratio and the resistance drop ratio. Two series of tests were carried out and the results of these tests are presented in the following chapter.

Chapter 5

Experimental Observations and Results

5.1 Introduction

This chapter presents the results and observations from the second and third test series. These series consisted of a total of sixteen tests of which fifteen were successful. The experimental set-up that was perfected in the first test series was used for both of these series. The second test series consisted of eight beam-to-column sub-assemblages which were detailed in section 4.4.2. Seven of the eight specimens were successfully tested. The eighth specimen was successfully tested, but the data acquisition system did not accurately record the results. The specimens in this series were designed to provide further information on the joint failure modes discussed in section 2.5, and to investigate the effects of bolt torque on the joint moment-rotation response. The third test series also consisted of eight specimens tested under large amplitudes and increasing amplitude cyclic waveforms. The specimens in this series are described in section 4.4.3. The specimens are intended to further investigate mode 1 and mode 2 joints, including the effects of yielding in the column flange. Finally, joints with identical details to specimen 2.3 are tested as this test did not work properly in the second series.

For the two series, general observations on joint behaviour are first presented. This includes failure mode, any problems with the tests and a summary of experimental results. Following this, each specimen is compared to the other specimens and Eurocode 3 design calculations.

Finally, conclusions are drawn with regard to the use of these joint configurations. Comparisons with the Eurocode 3 design calculations are made. Recommendations are made with regard to over-design factors for column capacity design. The usefulness and behaviour of the cyclic evaluation parameters are discussed. Improvements in joint behaviour are also noted and further recommendations in this area are made.

5.2 Test Series Two Experimental Results

Table 5.1 presents the experimental results and observed failure mode from this test series. Overall, it was observed that the Eurocode 3 model gave accurate failure mode predictions except for specimens 2.1 and 2.2. These specimens were designed to lie close to the boundary between the Modes 1 and Modes 2, as shown in Figure 5.1. The variables used in this figure are defined in section 2.5. For specimens 2.1 and 2.2, λ is equal to 1.8 and β_{Rd} is equal to 0.845, resulting in a ratio of plate force to bolt force of 0.795. The critical ratio between mode 1 and mode 2 mechanisms is 0.783, and a small change in the plate and bolts strengths could easily affect the failure mode.

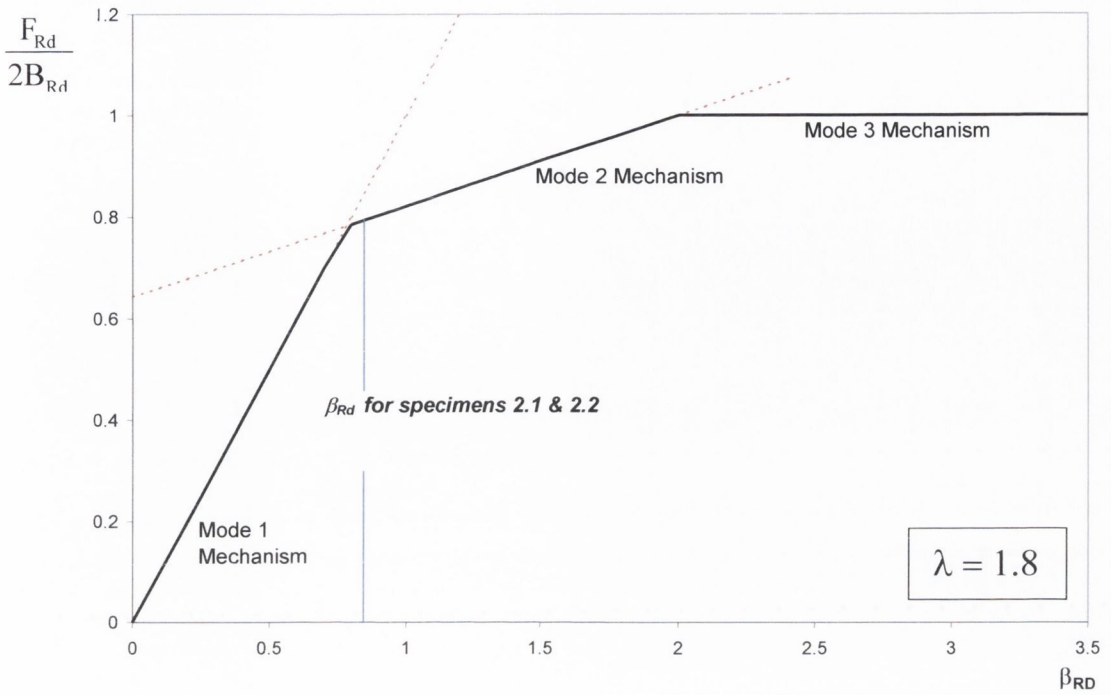


Figure 5.1: Failure mode interaction diagram for specimens 2.1 and 2.2

Specimen 2.3 was intended to improve on the ductility of specimen 2.2 while retaining the moment capacity. However, the measured moment capacity of this specimen was much less expected. This was related to a poor connection in the DAQ system, casting doubt on the force measured. Specimen 2.4 was designed to lessen the possibility of the threads of the bolts or nuts stripping, and this was achieved.

Specimen	Initial Stiffness [kNm/mrad]	Yield Rotation [mrad]	Yield Moment [kNm]	Ultimate Rotation [mrad]	Ultimate Moment [kNm]	Actual Failure Mode
2.1	7.34	6.35	39.21	62.77	55.81	1
2.2	3.55	10.37	36.81	65.18	51.86	2
2.3	5.53	4.43	24.48	60.02	41.24	1
2.4	3.98	7.53	29.67	67.7	40.26	2
2.5	3.83	11.22	42.98	28.26	47.25	3
2.6	3.20	11.03	35.33	23.78	39.90	3
2.7	4.49	7.62	34.24	23.98	38.81	3
2.8	2.75	13.18	36.21	21.61	37.76	3

Table 5.1: Specimen Experimental Properties for Test Series Two

Specimens 2.5 through to 2.8 were intended to investigate the effects of bolt pre-torque. The observed moment-rotation characteristics were very similar for all four specimens. However, in specimen 2.7, a higher initial rotational stiffness was observed, leading to decrease in yield rotation. No other properties were affected as bolt torque does not influence material properties in the inelastic range.

5.2.1 Experimental Results & Observations: Specimen 2.1

This specimen was tested under a large amplitude cyclic waveform. The stable moment-rotation plot shown in Figure 5.2 was achieved, and failure of the specimen did not occur. The joint was expected to have a mode 2 failure, that is yielding of the end-plate followed by yielding of the bolts. However, upon examination of the strain gauge results, yielding of the end-plate at both the bolt-line and the beam web line could be observed, as would be expected in a mode 1 mechanism. However, examination of the bolts on completion of the test showed that stripping of the nut threads had begun, although only very slightly. Based on these observations, it is unclear whether the joint would ultimately fail due to the plastic hinges forming in the end-plate or stripping of the bolts. However, based on the presence of the initial formation of plastic hinges at the bolt-line, the failure mode has been classified as a mode 1 mechanism. As seen in Figure 5.1, the β_{Rd} value for this specimen is very close to the boundary between mode 1 and mode 2. Similar bolts to those used in this joint were tested uniaxially [see Appendix A], and it was found that the actual yield stress of the bolts was generally higher than its nominal value. Tensile tests carried out on steel end-plate in used in this specimen gave a yield stress of 280 N/mm^2 compared to the notional yield value of 275 N/mm^2 .

After the first monotonic loading, the specimen unloads with the same stiffness as initially displayed. The stiffness then reduces when the applied load reaches zero. However, upon further loading this stiffness increases slightly (point A). Strain gauge results from a number of different tests indicate that this stiffness increase is due to 2 factors:

- residual plastic deformation in the toe of the end-plate; and
- degree of prying forces present in the joint tee-stub.

Similar increases were noted on further cycles, at points B & C on the graph. Closer examination reveals that while this stiffness increase slowly vanishes as the number of cycles is increased on the compression side (pt. B) of the curve, it remains on the tension side (pt. C). It should also be noted that after the first full cycle there is a certain amount of ‘rocking’ present in the joint, that is a displacement change where the moment is equal to zero.

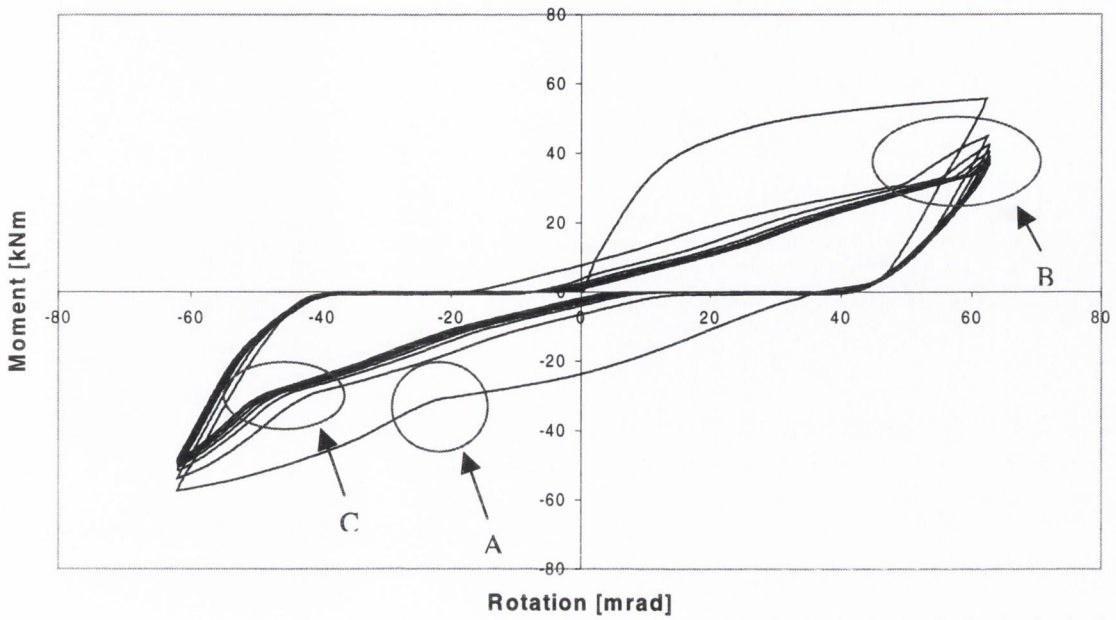


Figure 5.2: Moment-Rotation response for Specimen 2.1

Figure 5.3 compares the resistance ratio versus number of imposed cycles relationships on the tension and compression side of the moment-rotation relationship. The ratio reaches a maximum of 1.46 on the tension side and 1.42 on the compression side. After the first inelastic incursion, it may be observed that the resistance ratio of the specimen decreases due to the repeated inelastic loading and associated damage.

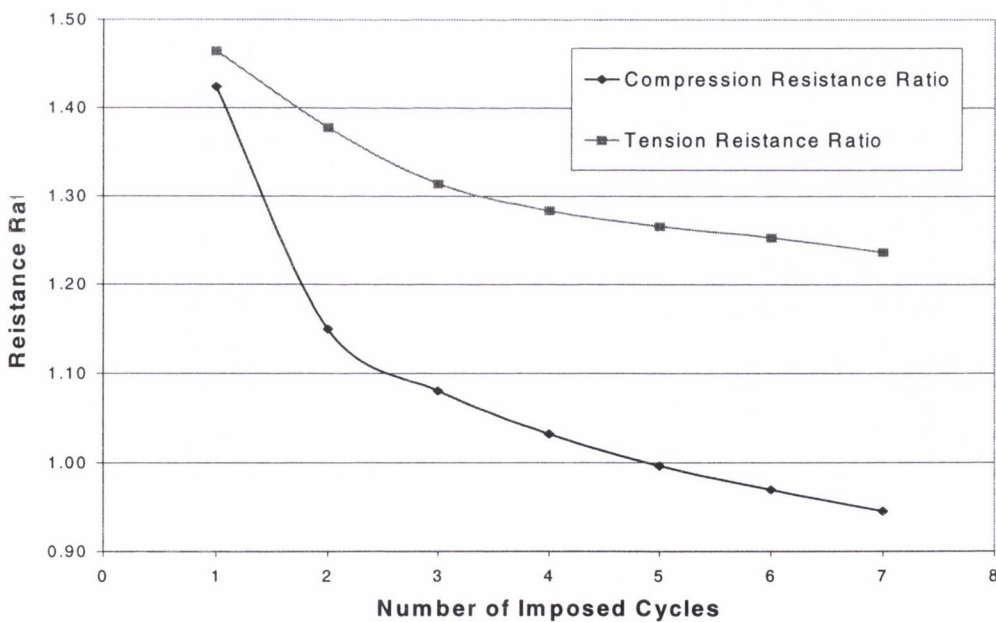


Figure 5.3: Resistance Ratio for Specimen 2.1

5.2.2 Experimental Results & Observations: Specimen 2.2

Figure 5.4 shows the cyclic moment-rotation characteristics for specimen 2.2. A comparison between the experimental properties of specimen 2.1 and 2.2 shows a significant difference in initial rotational stiffness, as shown in Table 5.1. As the yield moment capacity in the monotonic and cyclic tests are very similar, this difference in the stiffness leads to a increase in the yield rotation of the joint from 6.35 mrad in the case of specimen 2.1, to 10.37 mrad for specimen 2.2. The specimen was able to withstand the full displacement of the actuator without failure. Its ultimate capacity is 7% lower than that of the monotonically loaded case. The joint was designed to fail in a mode 2 manner. Unlike in specimen 2.1, post-experimental examination revealed that the threads of the bolts had begun to strip while strain gauge results determined that no yielding had occurred at the bolt-line, but was present at the beam web line. Therefore, it is expected that the ultimate failure mode of the joint would be consistent with a mode 2 mechanism. Due to the fact that the ultimate failure of the specimen did not occur, the ultimate ductility could not be determined. The maximum partial ductility obtained was between 6.35 and 7.1 on the tension and compression side of the joint respectively, as shown in Figure 5.5.

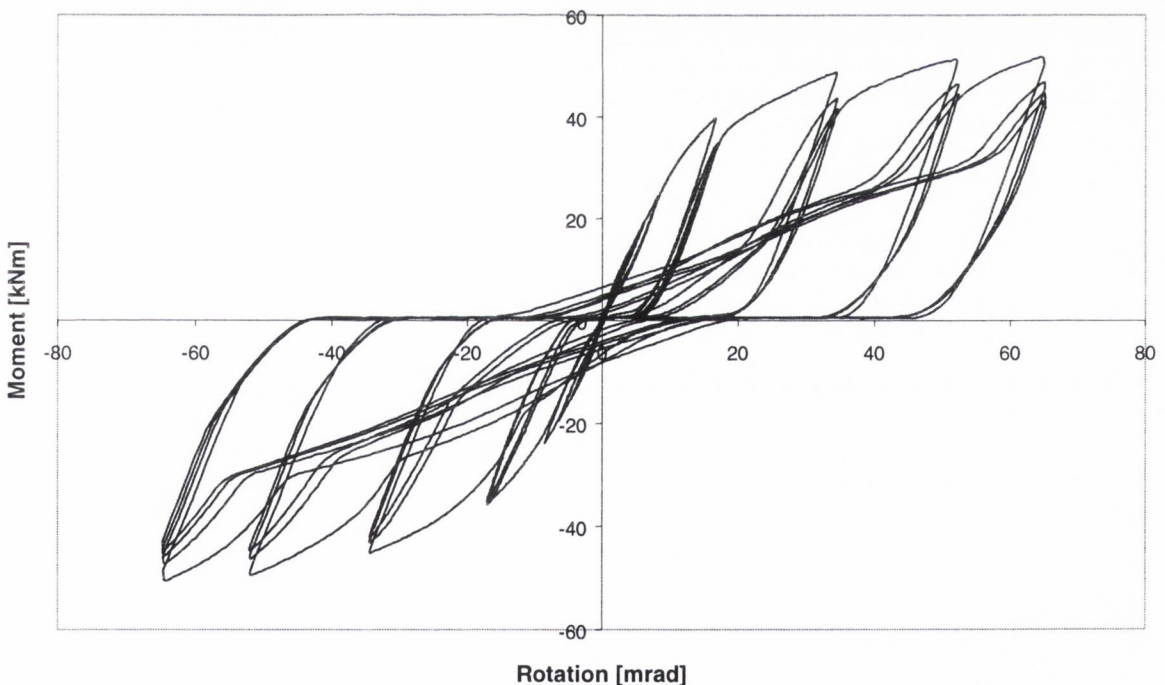


Figure 5.4: Moment-Rotation Relationship for Specimen 2.2

The rigidity of the joint follows expected patterns in that as soon as yield occurs in the joint, the ratio drops from approximately 1.0 to approximately 0.25 of the initial stiffness. The same rocking motion observed in test 2.1 can be seen in the moment-rotation curve. As can be seen from the moment-rotation curve, there is no loss of moment resistance in the joint when the rotation

amplitude is increased. This is consistent with other tests observed such as tests 1.4 and 1.5, where the failure mechanism is a sudden failure of the bolts and nuts. The resistance ratio of the joint remains at approximately 1.2.

It can be seen in Figure 5.4 that there is considerable stiffness hardening of the joint similar to that found in test 2.1 and in test series 1. When the joint unloads, the resistance quickly drops off to approximately zero, where it remains while the imposed displacement is reversed. Once the rotation has been reduced to a certain level, the resistance of the joint begins to increase again. The stiffness remains linear until a sudden stiffness hardening occurs. For the first in a group of three cycles, this hardening occurs close to the maximum rotation of the previous cycle. The new stiffness is actually very similar to the elastic stiffness. A similar pattern is noted on the opposite side of the joint on the first cycle in a group. On the second cycle in the group, slightly different behaviour is displayed. The moment-rotation relationship follows the same unload line as before. However, hardening does not occur until later in the displacement cycle. In fact, it appears to occur approximately halfway between the maximum of the previous cycle and the maximum of the cycle that is currently being imposed. On the third cycle in the group, the pattern is the same but the hardening happens slightly later into the imposed wave.

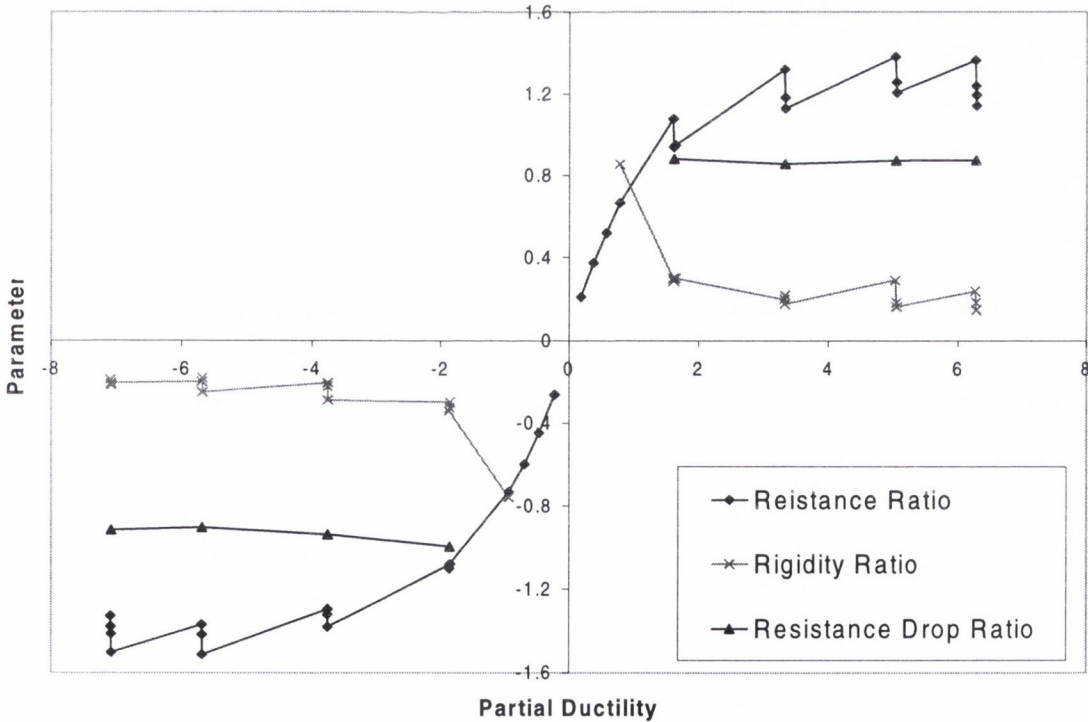


Figure 5.5: Experimental evaluation parameters for specimen 2.2

5.2.3 Experimental Results & Observations: Specimen 2.3

Due to experimental errors in the data acquisition equipment, this test may not be considered a complete success. When the results from specimen 2.3 were factored and plotted originally, a problem was discovered with the recorded data. A large amount of signal noise was present in the data, which had not been present in any of the previous tests and originally went unexplained. It was later found that a cable carrying the load data from the actuator command console to the SCXI terminal box had become loose. A number of filters were investigated to see if this noise could be removed. However, these all proved to be either too complicated or incapable of maintaining the integrity of the data. It was decided to employ a rolling average to smooth the data curves. The recorded data from one of the test cycles is shown in Figure 5.7, together with the smoothed data line.

A post-experimental examination of the test specimen identified yielding of the end-plate in a beam-type pattern. Strain gauge results also showed early yielding of the end-plate along the bolt-line and the beam flange web line. Examination of the bolts also showed that none of the bolts had elongated by more than one millimetre. Therefore, it may be concluded that the failure mechanism of the joint is consistent with a mode 1 mechanism. Comparing the experimental values with the Eurocode 3 model design calculations, large differences are observed. The measured initial rotational stiffness for the joint is 5.53 kNm/mrad compared to a predicted value of 11.48 kNm/mrad.

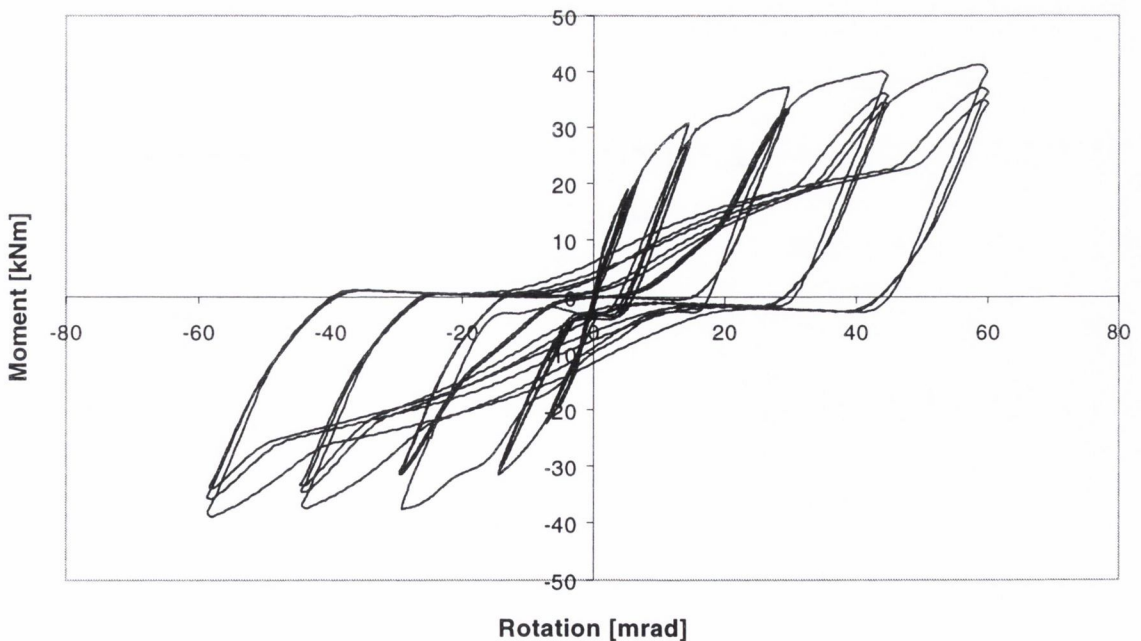


Figure 5.6: Moment-Rotation characteristics for specimen 2.3

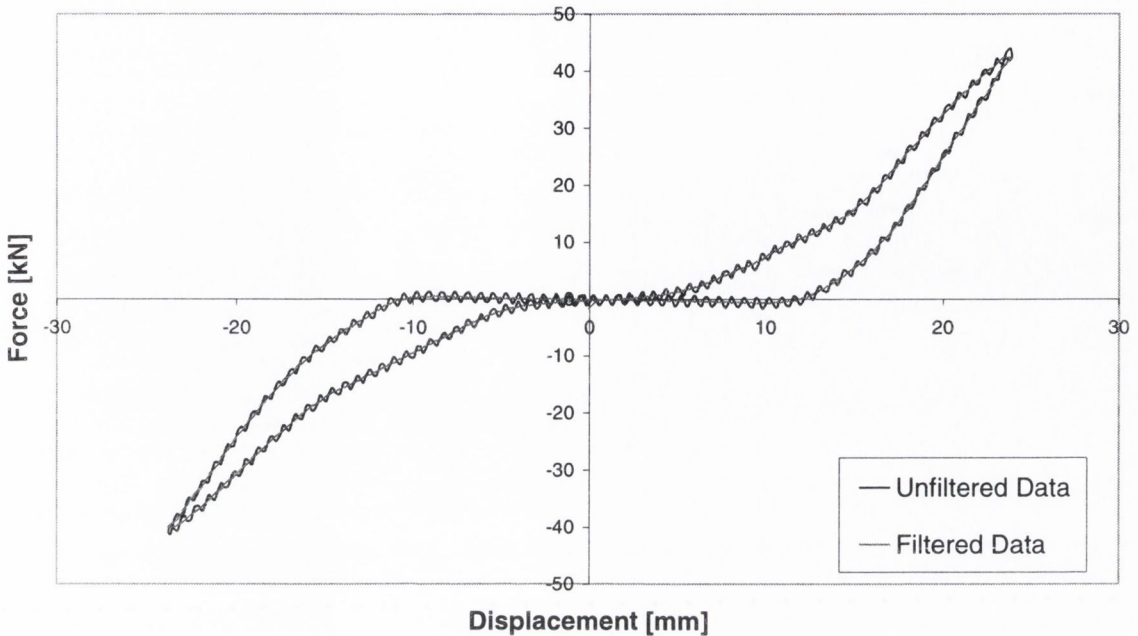


Figure 5.7: Example of applied filter for specimen 2.3

The ratio of experimental to predicted yield moment capacity is 0.77 with the ultimate experimental to predicted moment ratio equal to 0.87. This is the only joint in this study in which Eurocode 3 over-predicts both the yield and ultimate moment capacities. Based on these comparisons and the wiring problem with the SCXI system, it seems likely that the experimental results are inaccurate. This conclusion is also reached after considering the moment-rotation characteristics for the joint. As may be seen in Figure 5.6, a large degree of ‘rocking’ is present on the unload arm of each cycle when compared with other test results. Therefore, it was decided that a specimen with these joint details would be tested again in the third series.

5.2.4 Experimental Results & Observations: Specimen 2.4

Figure 5.8 presents the cyclic moment-rotation relationship for specimen 2.4. Post-experimental examination of the bolts and nuts showed that the upgrading of the nuts to grade 10.9 achieved the goal of preventing the nut threads from stripping. However, in a mode 1 failure, the bolt should not exhibit any elongation. The bolts in this experiment, however, did display significant elongation of up to 3.5mm.

From this it appears that the joint would ultimately fail in the manner prescribed by mode 2. Again, the ultimate failure point on the joint was not reached before the maximum travel of the actuator was obtained. As may be seen in Figure 5.9, a number of constant amplitude cycles were

carried out at the maximum actuator displacement amplitude to investigate if the fatigue loading would have any significant effect on the moment-rotation characteristics. These cycles were imposed after the standard cyclic test had been completed. As may be observed, a constant drop is observed in the moment resistance of the specimen as the number of inelastic incursions is increased. Figure 5.10 shows the resistance ratio of the joint for the first nine constant amplitude cycles imposed with a rotation of 67 mrad. It is observed that the resistance ratio of the joint slowly drops as the number of cycles is increased.

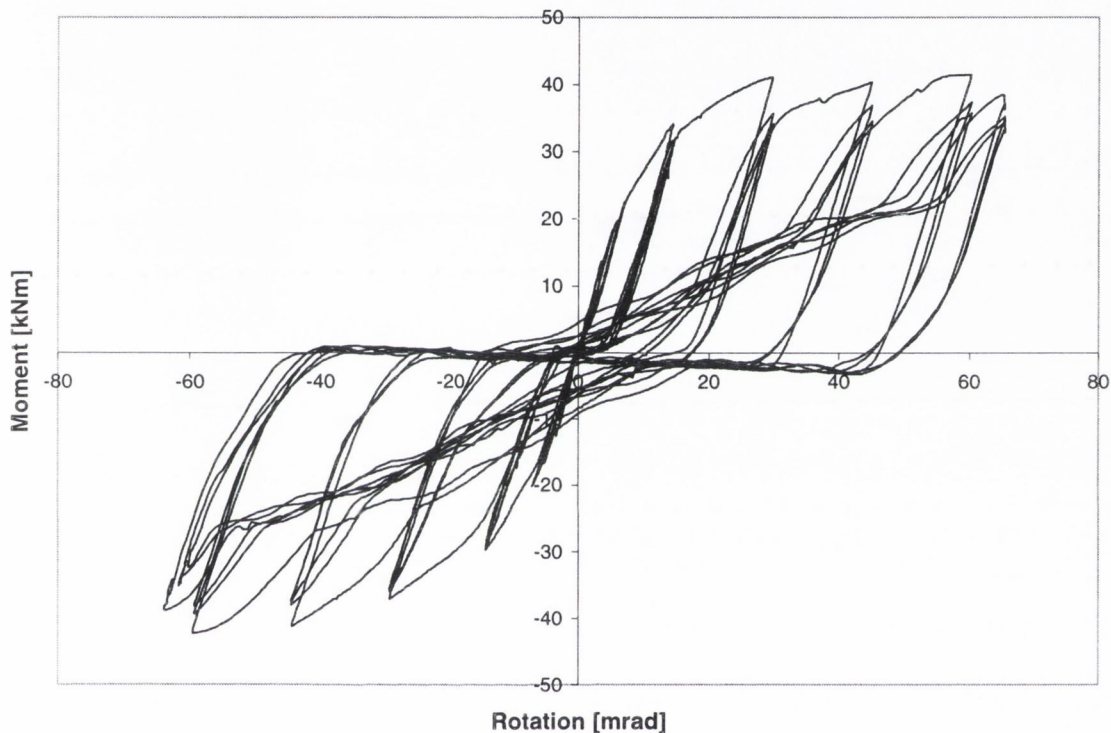


Figure 5.8: Moment-Rotation characteristics for specimen 2.4

Analysis of the joint results has raised a number of interesting points with regard to the ductility of this modified joint over the standard BSCA joint. The partial and full ductility factors gained from the test show an increase in the ductility over that exhibited by the standard mode 2 joint. However, this increase does not bring it up to the level of the mode 1 joints previously tested, although this is largely a product of an increased yield rotation. Larger ductility levels would have been observed if the actuator limit was greater.

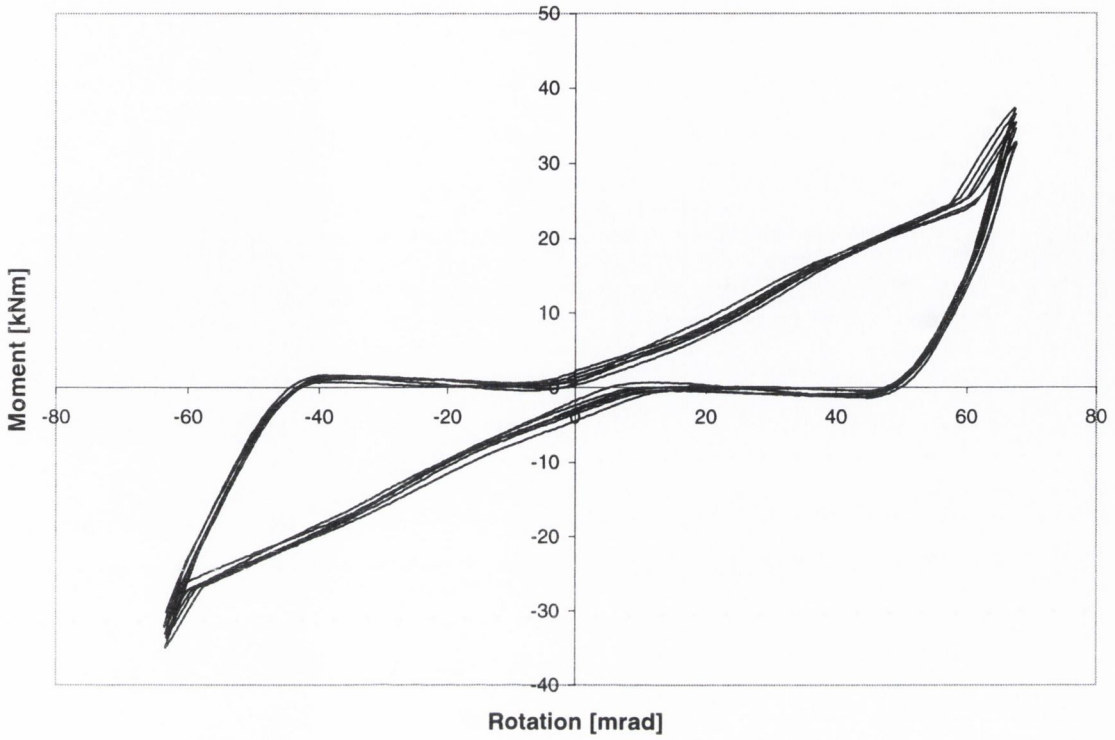


Figure 5.9: Constant Amplitude Moment-Rotation characteristics for specimen 2.4

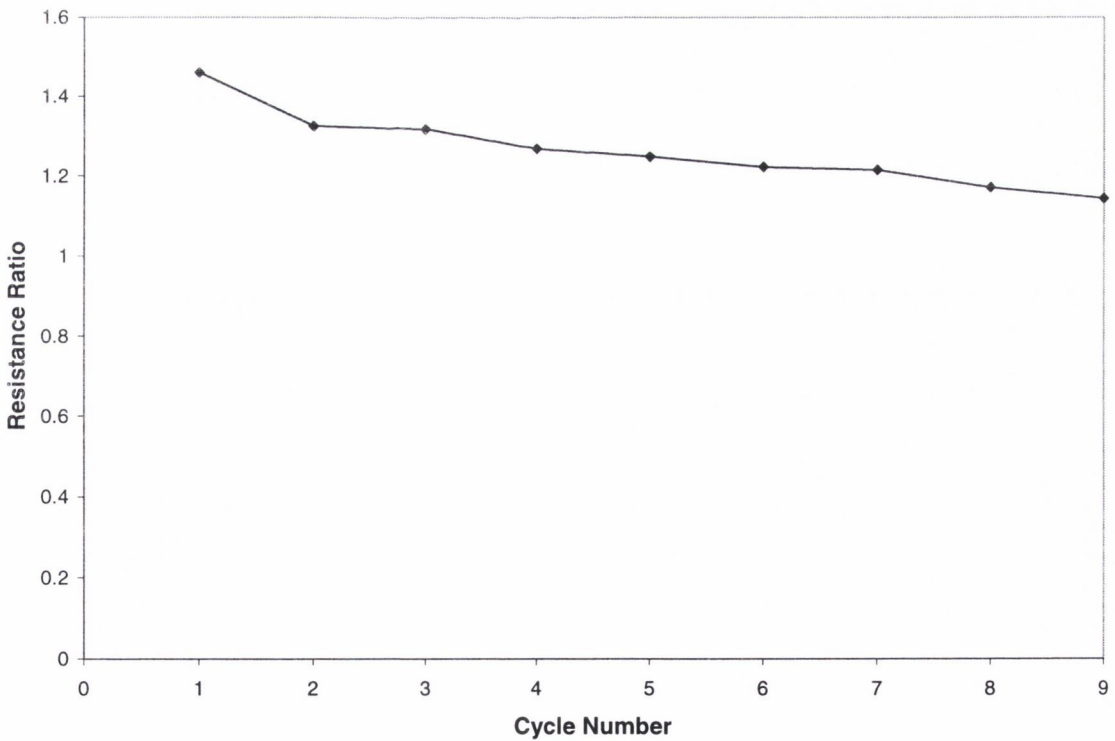


Figure 5.10: Resistance ratio for constant amplitude cycles for specimen 2.4

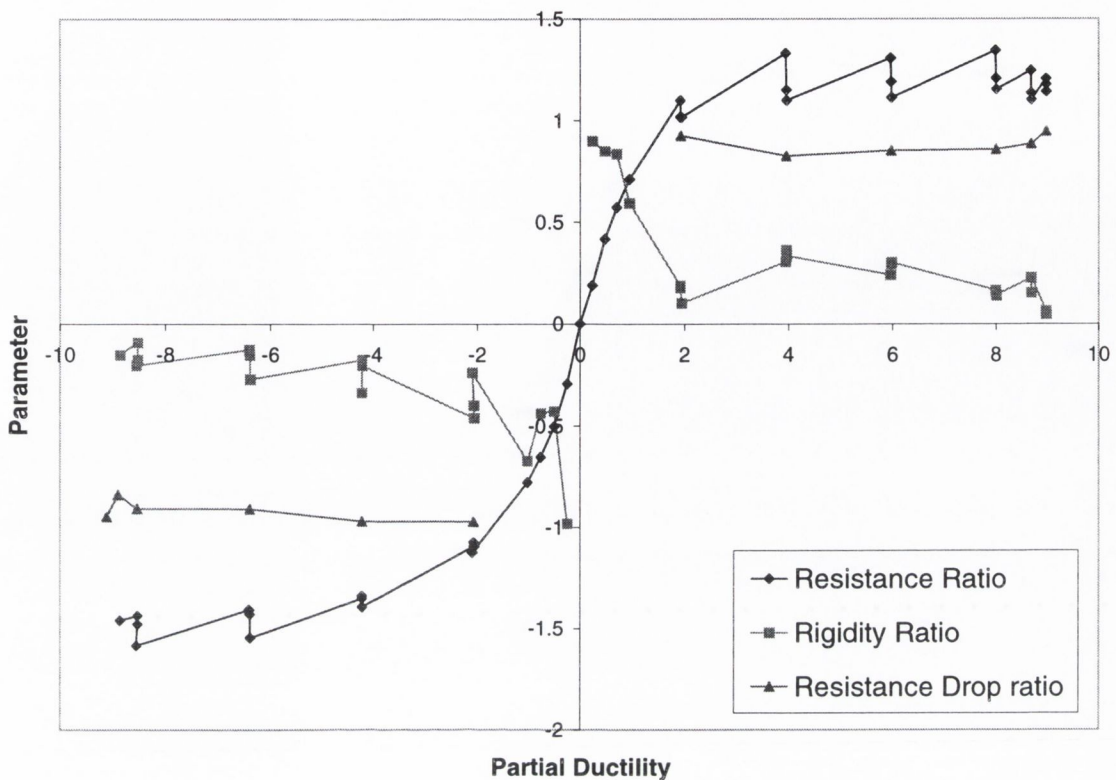


Figure 5.11: Cyclic evaluation parameters for specimen 2.4

Figure 5.11 shows the cyclic evaluation parameters for specimen 2.4. As may be observed, the resistance ratio of the joint behaves in a similar manner to that observed in the other tests. It may be seen that the resistance ratio on the tension side of the joint is higher than that recorded on the compression side. Similarly, the rigidity ratio of the joint behaves in a typical manner, quickly dropping as rocking of the joint sets in. This rocking results in the joint having a large section of virtually no stiffness. Slight increases in the rigidity ratio occur in the first cycle in each displacement group. In the second and third cycle in each group, it may be seen that the rigidity ratio again drops off as the joint sustains further damage. As expected, the resistance drop ratio remains reasonably steady throughout the entire test, with a value of approximately 0.85 – 0.9.

Figure 5.12 shows the final deformed shape of specimen 2.4. One interesting point in the picture is the stress lines that are evident on the beam web where the mill-scale has spalled. As may be observed, they appear to radiate out from the apparent bend in the end-plate. This will be discussed in further detail when test series three is described in section 5.3. On the reverse face of the joint, similar stress lines may be seen. This phenomenon was unique to this specimen in this series, although it was noted in a number of the specimens in test series 3. Also evident in the photograph is a small degree of buckling of the left-hand beam flange. The beam was designed to remain elastic under the maximum possible applied moment of 80 kNm. As the maximum moment in this

joint was only 40.26 kNm, this local buckling was unexpected.

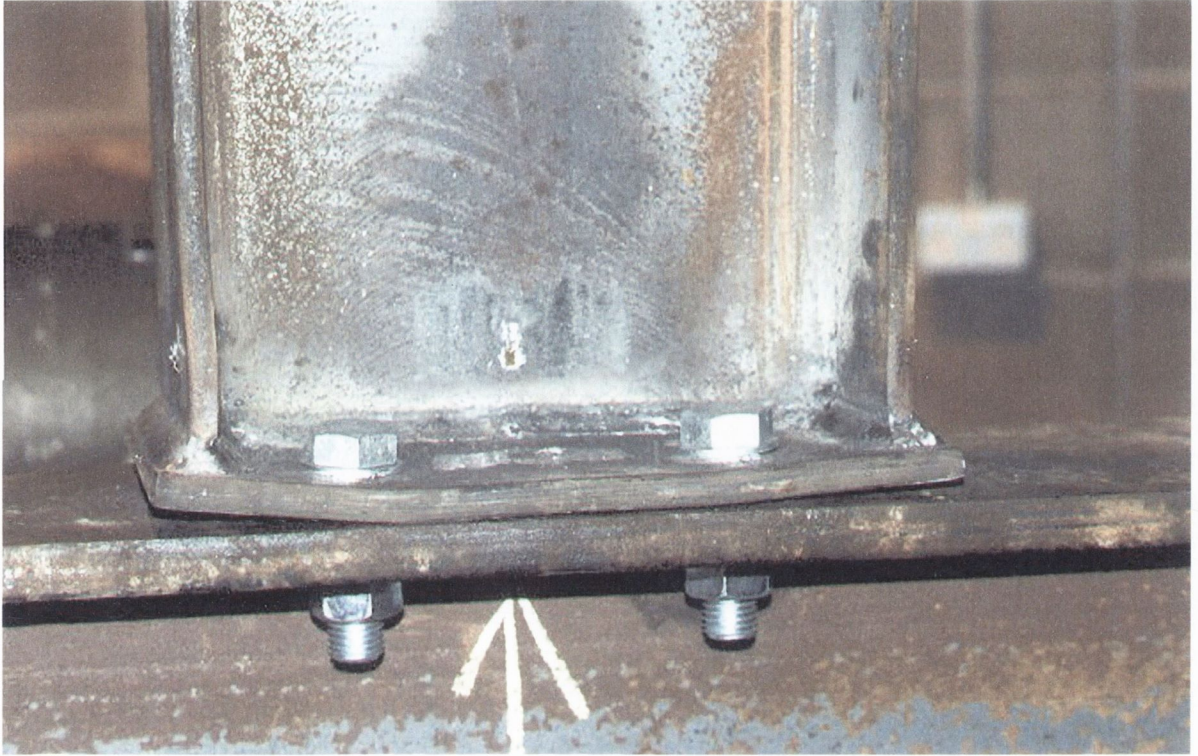


Figure 5.12: Final deformed shape of specimen 2.4

5.2.5 Experimental Results & Observations: Specimen 2.5

Specimen 2.5 was a modified joint designed to give a mode 3 failure mechanism. It was intended to be used as a baseline joint for a set of tests investigating the influence of bolt pre-loading on the cyclic moment-rotation characteristics of a joint. The moment-rotation response for this joint is shown in Figure 5.13. One of the bolts on the tension side of the joint fractured suddenly resulting in a large drop in moment resistance (point X). The second bolt in the bolt row, however, retained its capacity and allowed the rotation to be further increased, with a gradual reduction in resistance. This second bolt's threads stripped suddenly at point Y when the joint lost nearly all of its remaining moment capacity. The ductility capacity of this joint, evaluated at point X, is very low at only 2.5.

Comparing the experimental results with the Eurocode 3 model predictions, large differences in initial stiffness and hence yield rotation are observed. The predicted initial rotational stiffness is 10.92 kNm/mrad against an experimental value of 3.83 kNm/mrad, giving an over-estimation of 285%. Due to this difference, the observed yield rotation of the joint was much larger than the predicted value, with a ratio of experimental to predicted rotation of 4.1. Eurocode 3 also under-

estimates the ultimate moment capacity of the joint with a experimental to design capacity ratio of 1.37.

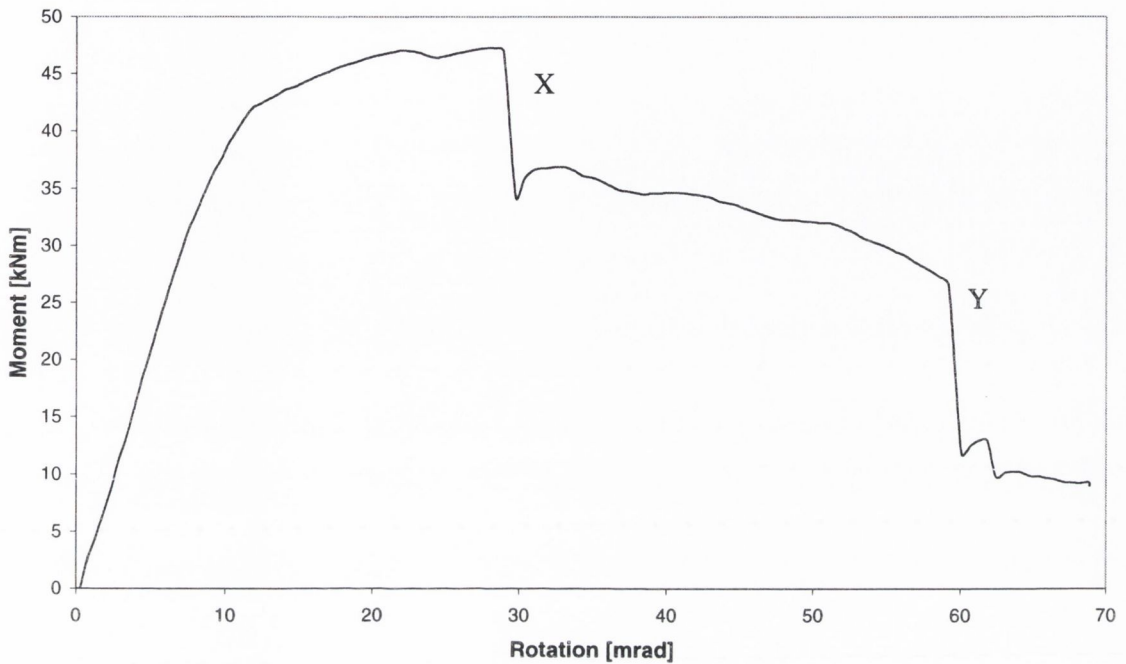


Figure 5.13: Moment-rotation response for specimen 2.5

5.2.6 Experimental Results & Observations: Specimen 2.6

In this test, a specimen identical to specimen 2.5 was tested under cyclic loading conditions. Again, the bolts were not subjected to any preloading beyond that induced by hand-tightening. This was found to be 48 Nm in this case, when checked using a torque wrench. The moment-rotation curve is shown in Figure 5.14. As may be observed, ultimate failure of the joint was obtained during the experimental test. It was expected that this joint would fail in a mode 3 manner. The nuts on the tension side of the joint began to strip on cycle number 8. The point where this occurs is taken as the failure point for the joint. On the compression side of the same cycle, the bolts on the other side also showed signs of stripping. Once this has occurred, the joint never manages to regain the same resistance. On the next amplitude increase on the compression side one of the bolts fractures (point A). At the same time, the other bolt in the bolt row stripped its remaining threads. In comparison, on the tension side of the hysteresis curve neither of the bolts snapped, although they did strip their threads.

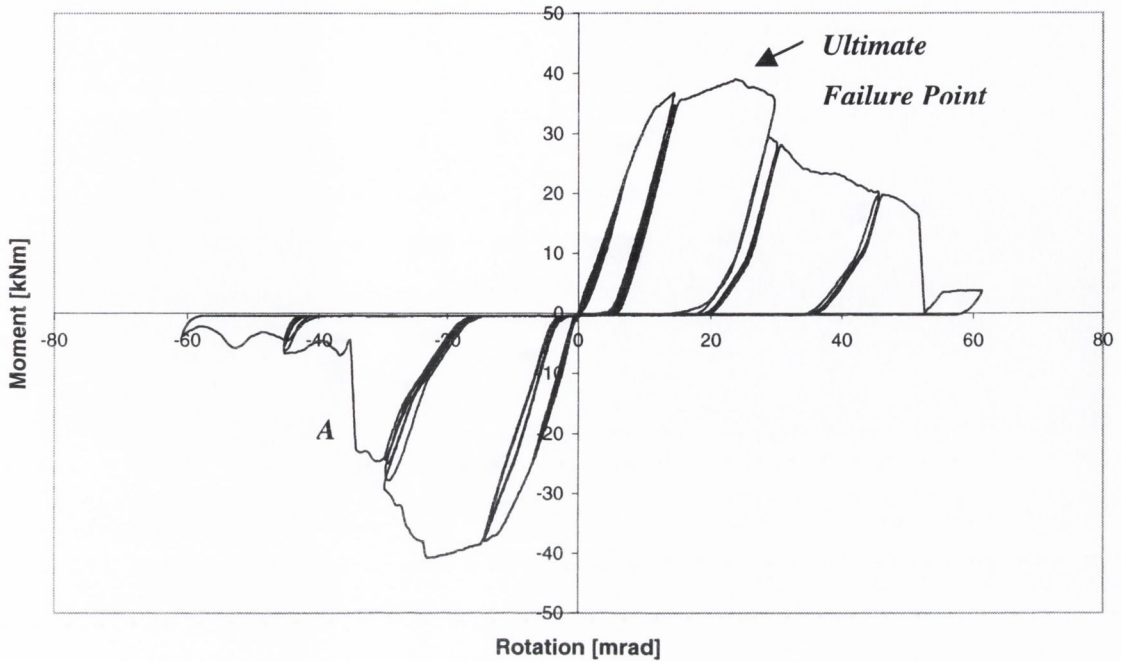


Figure 5.14: Moment-Rotation response for specimen 2.6

The ductility ratios displayed by this joint are very low. The partial ductility at the assumed failure point is less than 2.5 on both sides on the joint. Even the full ductility ratios are extremely low, with a maximum value at failure of 4.12. The yield rotation of the joint, and hence to its ductility, increases over the mode 1 and mode 2 joint failure modes. Although the stiffness does not to be altering very much as the failure mode changes (as Eurocode 3 predicts), the yield rotation is changing as the failure mode of the joint changes.

Eurocode 3 overpredicts the initial rotational stiffness by 243% with a predicted stiffness of 10.92 kNm/mrad for all the mode 3 specimens (specimens 2.5 – 2.8). This over-prediction also results in a large difference in the yield rotation of the joint, with the experimental value of 7.62 mrad compared to the 2.1 mrad predicted by Eurocode 3. The ultimate moment capacity values are more similar, with a ratio of design to experimental results of 0.89.

Figure 5.15 illustrates the resistance and rigidity ratios for specimen 2.6. As can be seen, the resistance ratio of the joint reaches a peak value of 1.04 before dropping away as the joint fails. This reflects a very small difference between joint yield capacity and the ultimate capacity, as would be expected in a brittle failure mechanism. The rigidity ratio of the joint may be seen to quickly fall from its peak value, close to one, towards zero. This is due to the thickness of the end-plate compared to the size of the bolts, where the end-plate remains elastic throughout the test. As

all of the rotation must be accommodated in the bolts, a degree of rocking is quickly present in the joint. This is evident from the moment-rotation response shown above, where in the second and third cycle of the displacement group the moment-capacity remains close to zero until late in the cycle. The resistance drop ratio is not shown for this specimen as the joint was only able to withstand one group of inelastic cycles before failure occurred. For this group of three cycles, the resistance drop ratio was 0.97 for the tension loading and 0.95 for the compression loading.

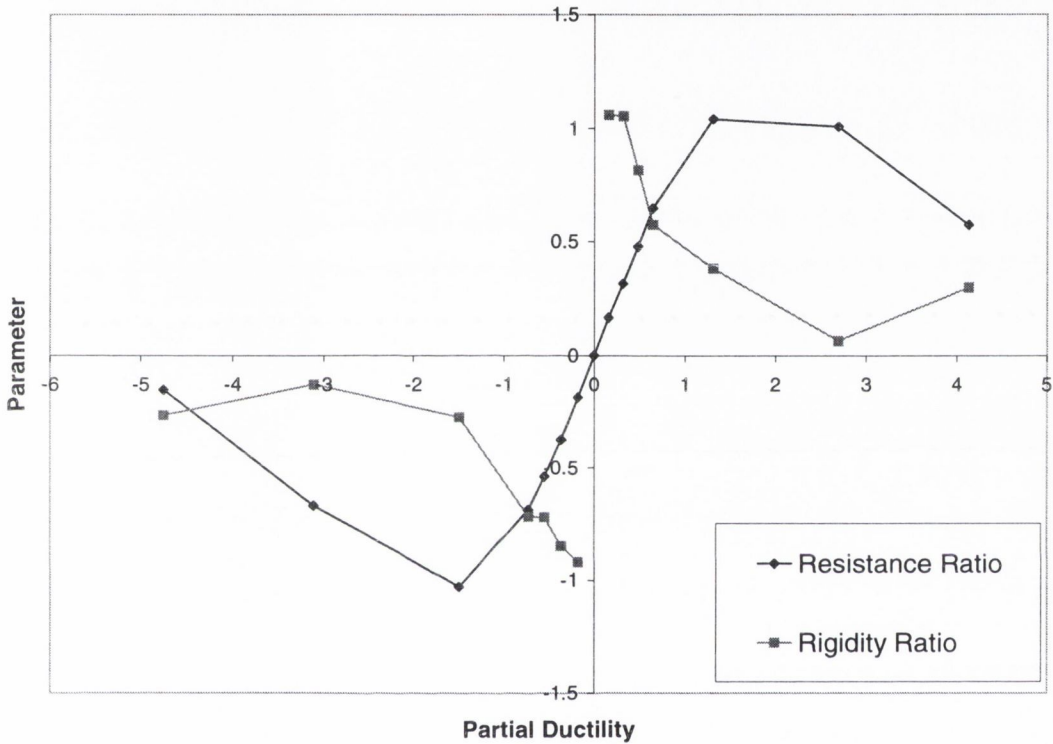


Figure 5.15: Cyclic evaluation parameters for Specimen 2.6

5.2.7 Experimental Results & Observations: Specimen 2.7

Failure in this specimen occurred due to the sudden stripping of one row of bolts, on the tension side of the joint. This was followed by stripping of the bolt threads on the other bolt row. Once the bolts have stripped, a small moment capacity remains as the plate is tries to lift and slide from one side to the other. As the bolts did not actually fracture or shear, they are still able to resist this motion, and the joint behaves as a simple hinge.

Comparing the experimental results with those from specimens 2.5 and 2.6, it may be noted that the application of the pre-load has not had any adverse effect on the moment capacity of the joint. This was expected as the pre-load did not actually change the material properites of the bolts or end-

plate. However, the initial rotational stiffness of the joint has been slightly increased by approximately 25%. This resulted in a decrease in the yield rotation. These results differ greatly from the design values of Eurocode 3. The ductility of the joint at the failure point was 3.15, which is an improvement on the joint with no bolt pre-loading. However, this is due to the decrease in the yield rotation of the joint, rather than any increase in the ultimate failure rotation.

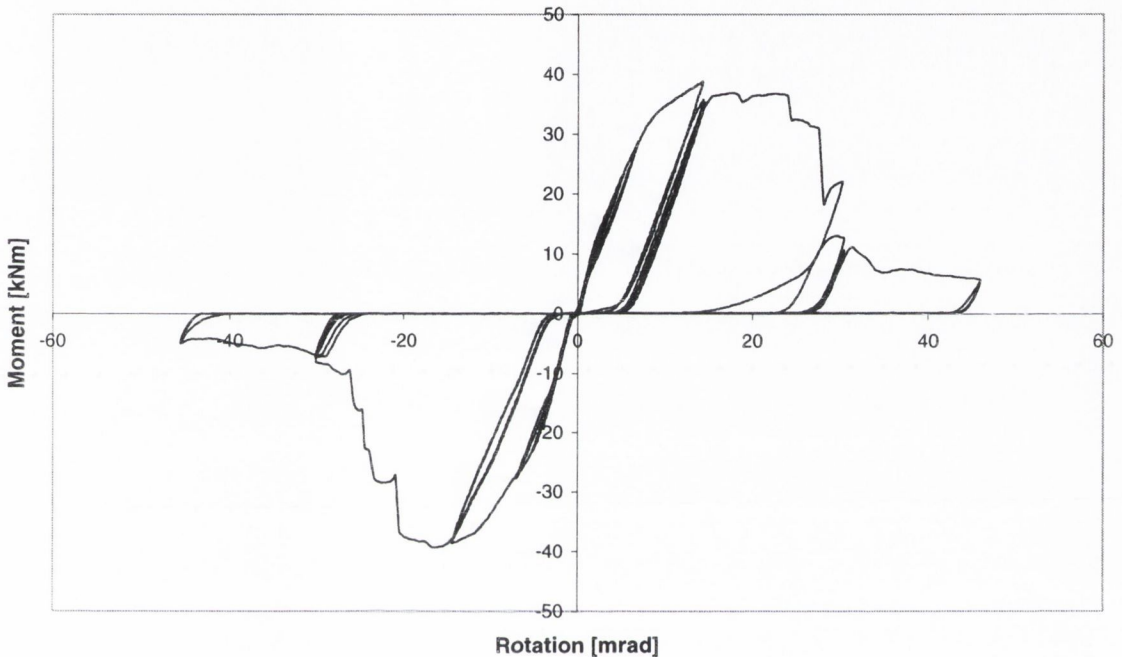


Figure 5.16: Moment-Rotation characteristics for specimen 2.7

Due to the rapid onset of rocking in the joint, the rigidity ratio displays a rapid reduction once the elastic yield point has been reached. Because of the degree of the rocking, it is very difficult to calculate the exact point where the moment-rotation curve reaches the zero force line, as can be observed in Figure 5.16. Before ultimate failure of the joint occurs, the resistance drop of the joint remains close to unity, and exceeds unity in one group of three cycles (#5-7) reaching maximums of 1.17 and 1.08 on the tension and compression sides, respectively. The difference in these values is not remarkable because the moment-rotation curve is in tension first. Once failure occurs, the resistance drop reduces to approximately 13 – 16%. Before failure, the joint displays very little resistance drop, with ratios between 0.93 and 0.97. However, once failure has occurred the resistance drop ratio of the joint decreases to 0.35.

5.2.8 Experimental Results & Observations: Specimen 2.8

Figure 5.17 presents the moment-rotation relationship for specimen 2.8. As expected, this joint failed in mode 3. The end-plate and beam remained elastic (according to strain gauges), and all of

the yielding occurs in the bolts. However, in this test there was no sudden snapping or stripping of the bolts. The failure of the joint was much more gradual than in the other tests, and the identification of the ultimate rotation point was more difficult. This was taken at the moment peak on cycle #8, after which the moment resistance begins to drop rapidly.

Comparing the experimental results with those taken from specimens 2.6 and 2.7, the increase in initial rotational stiffness experienced by specimen 2.7 is not present. In fact, the initial stiffness observed is the lowest of any of the mode 3 specimens in this test series and leads to the largest yield rotation of 13.18 mrad. However, there are no significant differences in yield or ultimate moment resistance values, or in ultimate rotational capacity.

The increased yield rotation results in a reduced partial ductility of 1.65. The resistance ratio of the joint behaves in a very typical manner. As the rotation, and hence the moment resistance, of the joint increase towards the failure point, the resistance ratio of the joint increases until it is just greater than one. At this point, it begins to gradually drop away until it stabilises at 0.17-0.22. The drop off in the resistance ratio is much more gradual than had been seen in some of the previous tests. The resistance drop of the joint also behaves in the manner typical of a mode 3 joint. Before failure of the joint occurs, the resistance drop ratio of the joint lies between 96% and 98%. However, when failure occurs it falls to 72%.

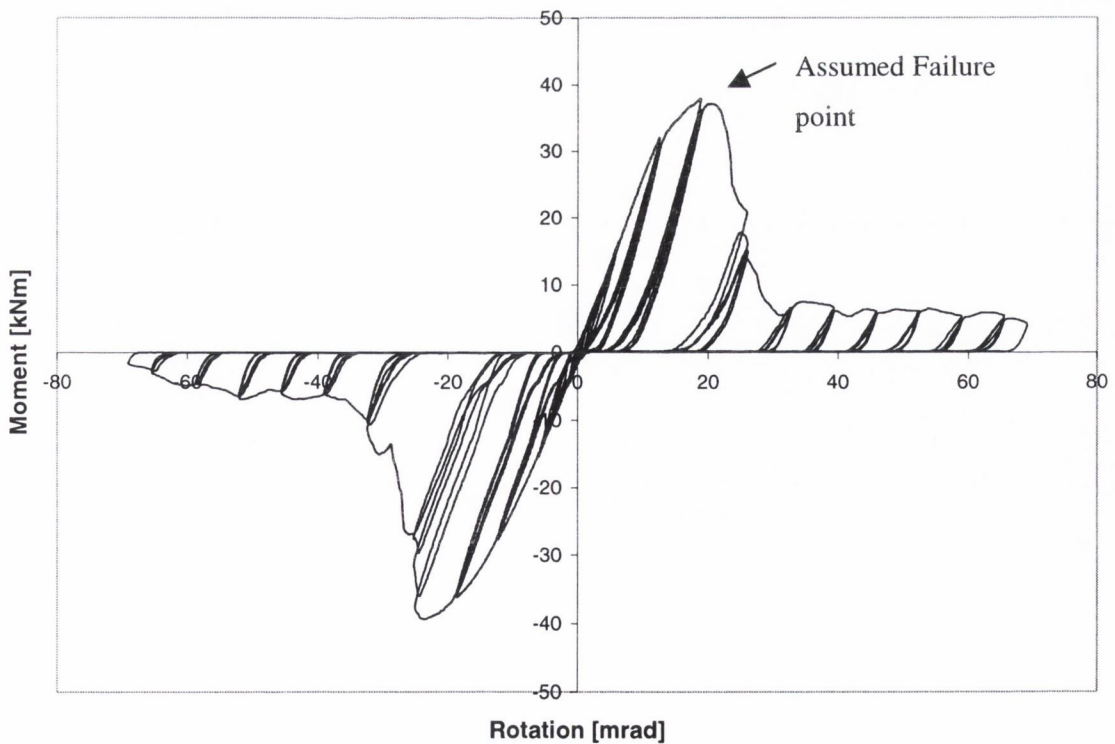


Figure 5.17: Moment-Rotation response for specimen 2.8

5.2.9 Test Series Two Conclusions

As stated above, the second test series had three main objectives, which were investigated in eight experiments. These were as follows:

- To further examine the Eurocode 3 prediction model and failure modes to determine its validity under cyclic as well as monotonic loading conditions.
- To investigate methods of improving joint failure mode and ductility while simultaneously preventing an adverse effect on the moment resistance capacity;
- To determine the influence of bolt pre-load on the moment-rotation response of the joint.

5.2.9.1 Eurocode 3 Design Model

Table 5.2 compares the experimental and Eurocode 3 design results for all specimens except 2.4. This specimen may not be analysed using the methods in Eurocode 3 as these make no provisions for different grade nuts and bolts. However, it is expected that the predicted results would be close to those predicted for specimens 2.1 and 2.2. Eurocode 3 consistently overpredicts initial stiffness by between 50 and 70%. The only exception is specimen 2.1 for which the Eurocode 3 value is only 35% greater than the experimental result. Examination of the yield rotations and the yield and ultimate moment capacities show that in all cases bar one, the model underpredicts the values. The exception is specimen 2.3 where the yield and ultimate moment capacity ratios are 0.77 and 0.87 respectively. However, this anomaly is attributable to the experimental problems discussed above.

Specimen	$S_{i,exp} / S_{i,EC3}$	$\theta_{y,exp} / \theta_{y,EC3}$	$M_{y,exp} / M_{y,EC3}$	$M_{ult,exp} / M_{ult,EC3}$
2.1	0.64	2.68	1.43	1.36
2.2	0.31	4.38	1.34	1.26
2.3	0.48	1.61	0.77	0.87
2.5	0.35	5.34	1.87	1.37
2.6	0.29	5.25	1.54	1.15
2.7	0.41	3.63	1.49	1.13
2.8	0.25	6.28	1.58	1.10

Table 5.2: Comparison between Experimental Results and Eurocode 3 Prediction Model

Comparing the observed and predicted failure modes reveals a number of discrepancies. As part of this test series, it was decided to investigate joints that were close to the boundary between the mode 1 and mode 2 mechanisms. To this end, one monotonic and one cyclic test were carried out on specimens 2.1 and 2.2. Eurocode 3 predicted that these joints would be subjected to a mode 2

failure as shown in Figure 5.1. However, this predicted failure mode was not displayed by one of the specimens, specimen 2.1. This was caused by small differences between the actual and the notional yield stress of the bolts and end-plate used. However, in the case of specimen 2.2 which was geometrically identical to specimen 2.1, the observed behaviour was indicative of a mode 2 failure mechanism with yielding of the bolts occurring. Material tests carried out on this specimen did not display the small increase in yield stress of the material observed in the previous test. From this it may be concluded that the failure mode of joints is highly dependant on the differences between the actual and notional material properties when the joint is close to the mode 1/mode 2 boundary. However, based on the material tests carried out as part of this study [see Appendix A], the notional yield values are all lower than the measured values. Comparing the predicted failure modes from the two sets of values, it is noted that the actual values always predict a more ductile joint. Specimen 2.3 was predicted to have a mode 1 failure mechanism. Although it was not possible to confirm it, the experimental evidence appears to indicate that this was the case. There was no stripping or elongation of the bolts present in the post-experimental examination, and the strain gauge results appear to indicate that the yielding was confined to the end-plate. Specimen 2.4 yielded in a mode 2 manner. It was not strictly possible to predict a failure mode for this joint as it mixed grade 8.8 bolts with grade 10.9 nuts. However, it is likely that the joint can be modelled using grade 8.8 bolts and nuts, as this is the weaker material. In this case, the predicted mode agrees with the experimental response which showed significant elongation of the bolts. The four remaining specimens were all designed to fail as mode 3 joints, and to this end employed strong plates and weak bolts. Mode 3 failures were observed in all cases, with the majority of the bolts failing by stripping, or shearing, of the threads.

5.2.9.2 Improved Joint Behaviour

As part of this test series, two joints were tested with modified details: specimen 2.3 in which the standard grade 8.8 bolts were replaced with grade 10.9 bolts, and specimen 2.4 in which only the nuts were replaced with the higher grade. As stated above, specimen 2.3 was not a complete success due to experimental problems. However, the replacement of the bolts with those of higher grade did appear to change the failure mode of the joint from mode 2 to mode 1, thus improving the ductility. For specimen 2.4, it was observed from the experimental results and in a post-experimental examination that the replacement of the bolts did have the intended effect of preventing the stripping of the threads. This resulted in the elongation of the bolts with a maximum elongation of 3.5 mm being recorded. The failure mode of the joint, however, was not improved as hoped. Strain gauge results indicated that the end-plate yielded along the beam web line but not along the bolt-line. This yielding in conjunction with the plastic elongation of the bolts, is indicative of a mode 2 failure mechanism. The modifications did not result in any significant

change in initial stiffness or yield rotation. However, both the yield and ultimate moment resistance capacity of the joint were reduced by 20% and 22%, respectively, compared with those measured in specimen 2.2.

5.2.9.3 Bolt Pre-loading

The final objective of this test series was to investigate the influence of pre-loading the bolts. Four mode 3 specimens were employed in this part of the investigation. A monotonic and cyclic test were carried out to use as reference experiments. These joints had identical geometrical details with grade 8.8 M16 bolts. The bolts in these tests were tightened by hand and this was found to correspond to a pre-load of approximately 50Nm. It was noted that the moment capacity of the cyclic test, specimen 2.6, was 15% lower than that measured during the monotonic test of specimen 2.5. Specimen 2.7 also had identical details to these specimens, but the bolts were given a pre-load of 200Nm, or 60% of the recommended load for this bolt type. It was noted that this pre-load had the result of increasing the initial rotational stiffness of the joint by 40%, hence reducing the yield rotation of the joint by approximately 30%. It was also noted that the yield moment of the joint was not adversely affected by the application of the pre-load, nor was the ultimate moment or rotational capacity. Based on the results from specimen 2.7, a fourth specimen with identical properties was also tested. The bolts in specimen 2.8 were subjected to a 100Nm preload, or 30% of the recommended value. This level of pre-load did not have a similar effect on initial stiffness or the yield rotation. In fact, the measured stiffness of the joint was slightly lower than that of the previous specimens. Again, neither the yield moment capacity nor the ultimate values were affected by the bolt pre-load. From these results, it was determined that low levels of bolt pre-load do not appear to effect the moment-rotation characteristics of mode 3 joints. However, as the pre-load is increased past a particular level, as yet undetermined, the initial rotational stiffness and hence the yield rotational capacity of the joint are affected. It must be stressed that these tests were only carried out on mode 3 joints and the results from mode 1 and mode 2 joints may differ.

As observed in test series one, the resistance ratio of the specimens in this series appeared to be related to the experimental failure mode. The highest resistance ratios was observed in joints with mode 1 failure mechanisms, especially specimens 2.1 and 2.3, which had ratios in the range 1.4 – 1.5. The three cyclic mode 3 specimens, that is specimens 2.6 – 2.8, all had resistance ratios in the region of 1.15, while the mode 2 specimens displayed ratios of approximately 1.3 – 1.4. The reasons for this were discussed in section 2.5 The rigidity ratio for the joints in this series is seen in all cases to quickly drop from one towards an average of 0.1. However, due to the degree of rocking that is present in the joints, the use of this ratio is questionable when characterising the joint behaviour.

5.3 Test Series Three Experimental Results

Table 5.3 presents the measured experimental moment-rotation characteristics of the eight specimens tested in this series. It may be observed that all four joint configurations resulted in higher capacity values than predicted by the design calculations in section 4.4.2. As in the previous test series, it was observed that Eurocode 3: Annex J was able to accurately predict the failure mode of each joint, apart from specimen 2.1.

Specimens 3.1 and 3.2 were designed for a mode 1 failure mechanism. This was observed in both cases with no plastic bolt elongation found in the post-experimental examination. Specimen 3.1 displayed a very low initial stiffness compared with specimen 3.2. However, the strain gauge results from this test indicated local buckling in the beam flange. This will be discussed in further detail in the following section.

Specimen	Initial Stiffness [kNm/mrad]	Yield Rotation [mrad]	Yield Moment [kNm]	Ultimate Rotation [mrad]	Ultimate Moment [kNm]	Actual Failure Mode
3.1	2.21	17.33	38.33	71.08	49.78	1
3.2	3.48	8.468	29.44	65.95	44.02	1
3.3	3.13	15.02	47.02	38.69	59.06	2
3.4	3.55	13.94	49.49	36.66	59.36	2
3.5	3.51	9.92	34.81	65.07	50.13	2
3.6	3.16	10.36	32.73	65.87	45.76	2
3.7	4.72	8.83	41.67	65.66	59.11	1
3.8	4.23	8.43	35.69	66.32	51.91	1

Table 5.3: Specimen Experimental Properties for Test Series Three

Specimens 3.3 and 3.4 were designed to fail in a mode 2 mechanism and were designed with thicker end-plates to ensure this mode. Both specimens were tested under cyclic loading conditions with specimen 3.3 being loaded at a rate of 0.025 Hz, while specimen 3.4 was loaded at the standard rate of 0.01 Hz. In the case of both specimens, failure was due to yielding of the end-plate followed by sudden stripping of the bolt threads. The test results that the loading rate did not affect the failure mode of the joint, or the moment-rotation characteristics recorded.

In contrast to all of the other specimens tested as part of this study, specimens 3.5 and 3.6 were designed to induce failure in the column flange rather than the end-plate. To this end, a column with a flange thickness of 12.5 mm was employed instead of the standard column with a thickness

of 20.5 mm. Eurocode 3: Annex J calculated that this would cause initial yielding to occur in the column flange tee-stub, followed by yielding of the bolts, resulting in a mode 2 failure. Both tests, the column flanges was observed to deform significantly more than the end-plate. Post-experimental examination of the joint revealed elongation of the bolts combined with a small degree of stripping of the threads, confirming that the joints both failed in a mode 2 manner.

Specimens 3.7 and 3.8 repeated test 2.3. Specimen 3.7 was subjected to a constant large amplitude cyclic test while specimen 3.8 was subjected to an increasing amplitude cyclic test. These specimens displayed the highest initial stiffness values for the entire test series. Post-experimental examination of the specimens found no bolt elongation, although the bolt washers were significantly deformed by crushing underneath the bolt heads. These specimens both experienced mode 1 failures, as predicted by Eurocode 3. As in test series two, increasing the bolt grade caused the failure mode to be changed to a more ductile response.

5.3.1 Experimental Results & Observations: Specimen 3.1

Test 3.1 consisted of a large amplitude cyclic test as may be seen in Figure 5.18, from which the monotonic moment-rotation relationship may be determined from the first imposition of displacement. The moment-rotation characteristics measured for this test result in a highly stable hysteresis curve. The initial stiffness of this specimen is 2.21 kNm/mrad, approximately 33% lower than the value obtained for specimen 3.2, an identical specimen. This low initial stiffness results in a higher yield rotation for the specimen which is approximately twice that of specimen 3.2.

The specimen was designed to have a mode 1 failure mechanism, and this did occur. This was confirmed by a post-experimental examination of the specimen. This specimen was observed to yield in the circular pattern described in Eurocode 3 and section 2.5 with some yielding occurring along the beam web line, as may be seen in Figure 5.19.

When the experimental results are compared to the design calculations of Eurocode 3, it may be seen that the ultimate moment in the experiment is 50% higher than the design value, and the yield moment is 74% greater. In contrast, both the experimental yield rotation and the initial stiffness of the joint are significantly lower.

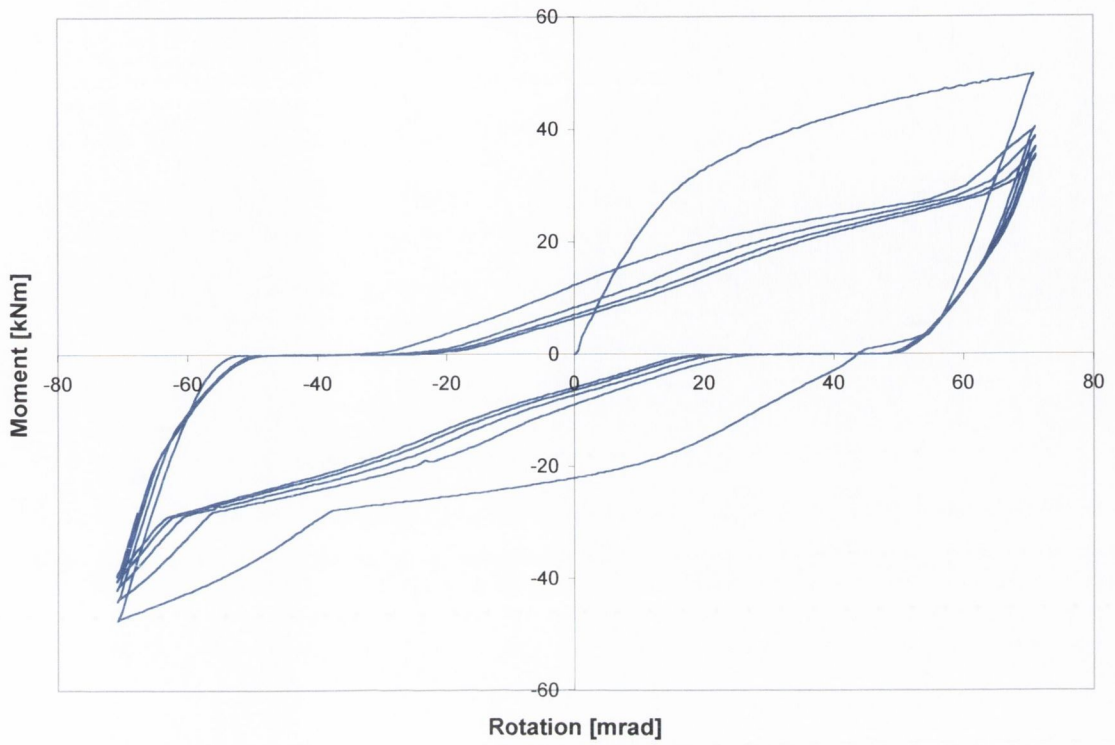


Figure 5.18: Moment-Rotation relationship for Specimen 3.1

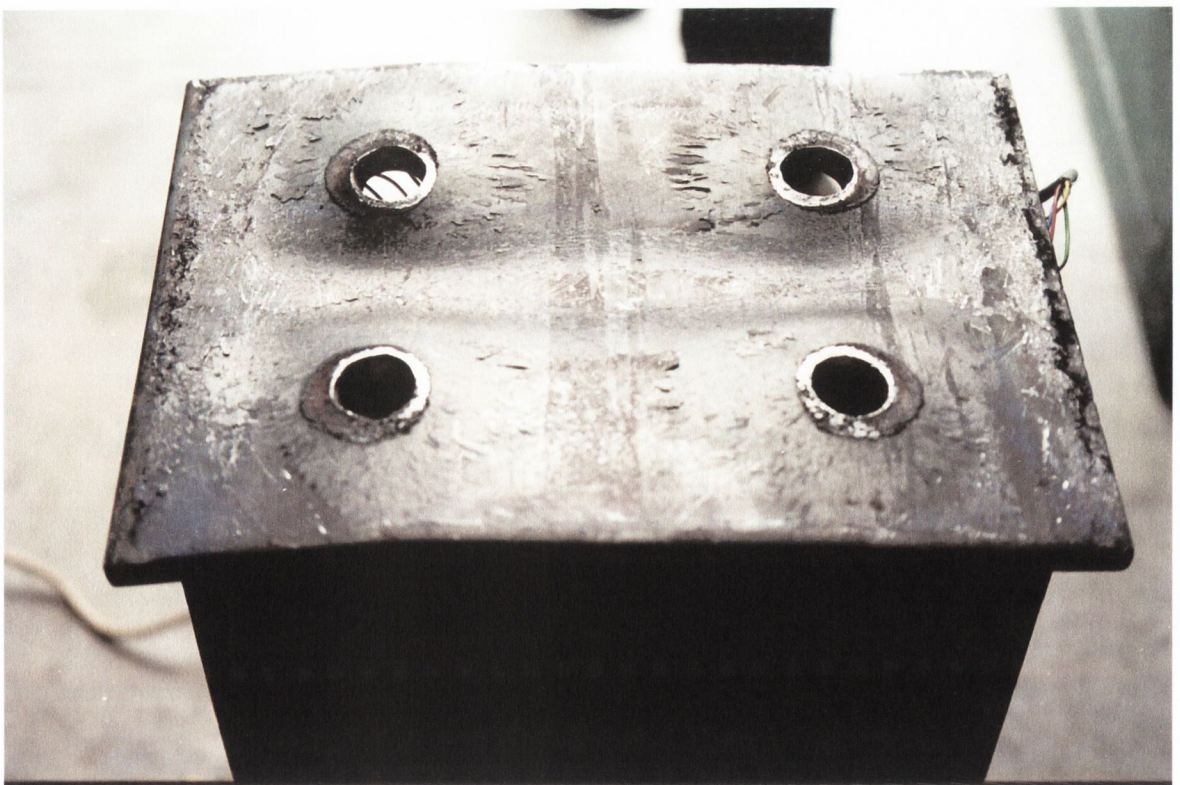


Figure 5.19: Underside of specimen 3.1 (post-test)

As may be observed from the moment-rotation relationship, there is a large degree of resistance drop between the first and second cycles of the test. This drop is approximately 20% on the tension side and 10% on the compression side. As the joint is pulled to the tension side first and is undamaged at the beginning of the cycle, this accounts for the larger drop. Over the next four cycles in the test, both sides continue to show some drop in moment resistance, with a further drop of 10% on both sides of the hysteresis curve.

Examination of the strain results from this test showed that the plate behaved in mode 1, with all of the end-plate strain gauges going off-scale [see Appendix B], or detaching from the steel on the first cycle. However, the strain gauges on the beam web and flange (# 3, 7 and 8), indicated permanent inelastic strain present. This is especially true for strain gauge #8, where compression strains of between 1000 and 4500 $\mu\epsilon$ were measured. Strain Gauge #3, on the beam web, also exhibited a certain degree of inelastic compression strain, in the range of 500 to 600 $\mu\epsilon$.

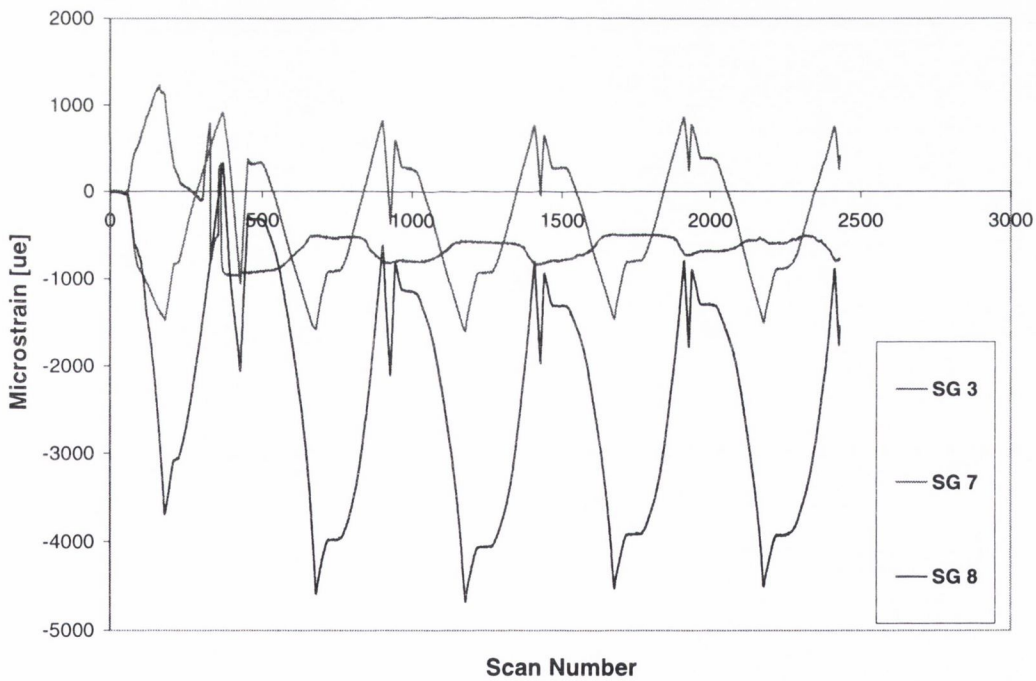


Figure 5.20: Beam strain gauge results (specimen 3.1)

As noted in both of the previous two test series, the moment-rotation characteristics exhibited some stiffness hardening close to the maximum amplitude of each cycle. It was confirmed in this test that this is due to the closing of the gap between the deformed end-plate and the column flange. This may be observed in Figure 5.21 where the LVDT reading (LVDT # 2) returns to

approximately zero at the same time that the compression load increases sharply. This confirms that this stiffness hardening is due to the permanent plastic deformation of the end-plate. Figure 5.22 presents the deformed shape of the end-plate with the actuator at the maximum amplitude on the compression side. The stiffness hardening is caused when the actuator pulls the specimen onto the tension side and the gap that may be seen between the deformed end-plate and the column flange is closed.

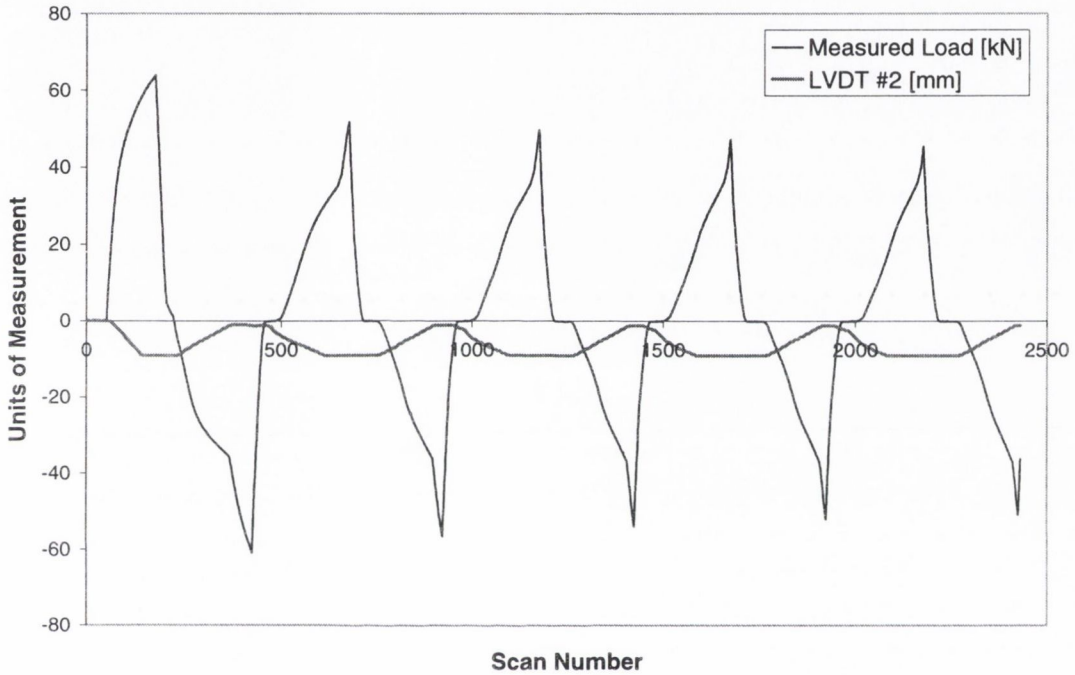


Figure 5.21: Comparison of measured load and displacement (specimen 3.1)

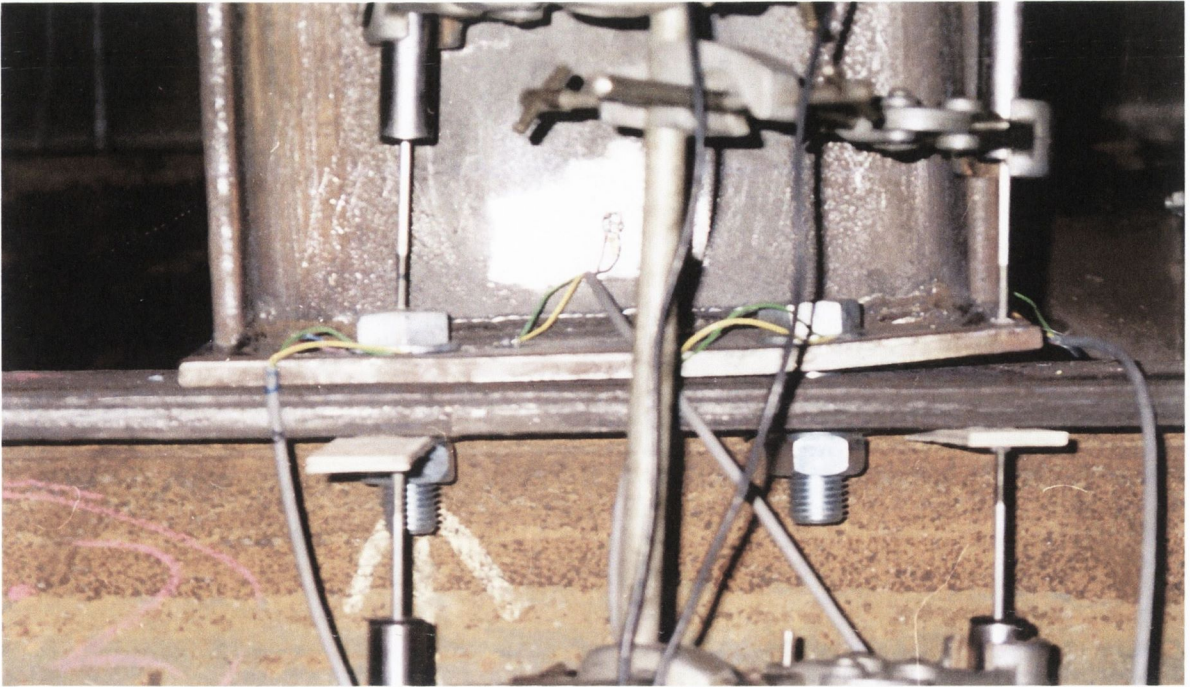


Figure 5.22: Deformed shape of specimen 3.1

5.3.2 Experimental Results & Observations: Specimen 3.2

Figure 5.23 presents the moment-rotation characteristics for specimen 3.2, which was tested under an increasing amplitude cyclic waveform. The hysteresis curve is highly stable, but with a large degree of rocking present after each unloading section of the curve. As may be seen in Table 5.3, the initial stiffness of this specimen is higher than that noted for specimen 3.1 with a value of 3.48 kNm/mrad. This results in a yield rotation of 8.47 mrad compared to the 17.33 mrad seen for the previous specimen. Comparing the ultimate moment resistance of the joint with the monotonic value, the cyclic resistance is 13% lower. When this value is compared to the Eurocode 3: Annex J design values, the experimental value is 33% greater. However, the measured initial stiffness is approximately three times lower than the design value.

This specimen was designed for a mode 1 failure which occurred. Post-experimental examination of joint showed the same circular yield patterns around the bolt holes as was observed for specimen 3.1. It was also seen that one of the four bolts had begun to elongate slightly with an increase in length of 1.8 mm. However, the remaining three bolts did not experience any measurable elongation. Based on the strain gauge results in Appendix B, which located plastic hinges at the beam web line and the bolt line, the joint was determined to fail in a mode 1 manner, regardless of the bolt elongation.

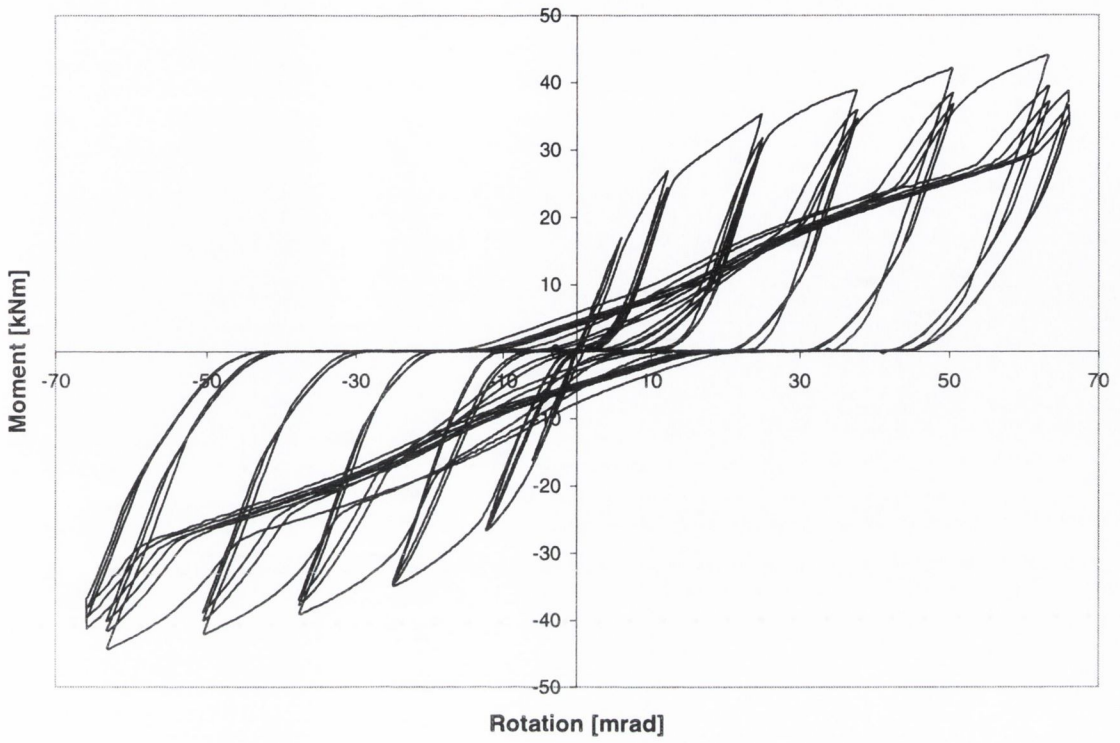


Figure 5.23: Moment-rotation relationship for specimen 3.2

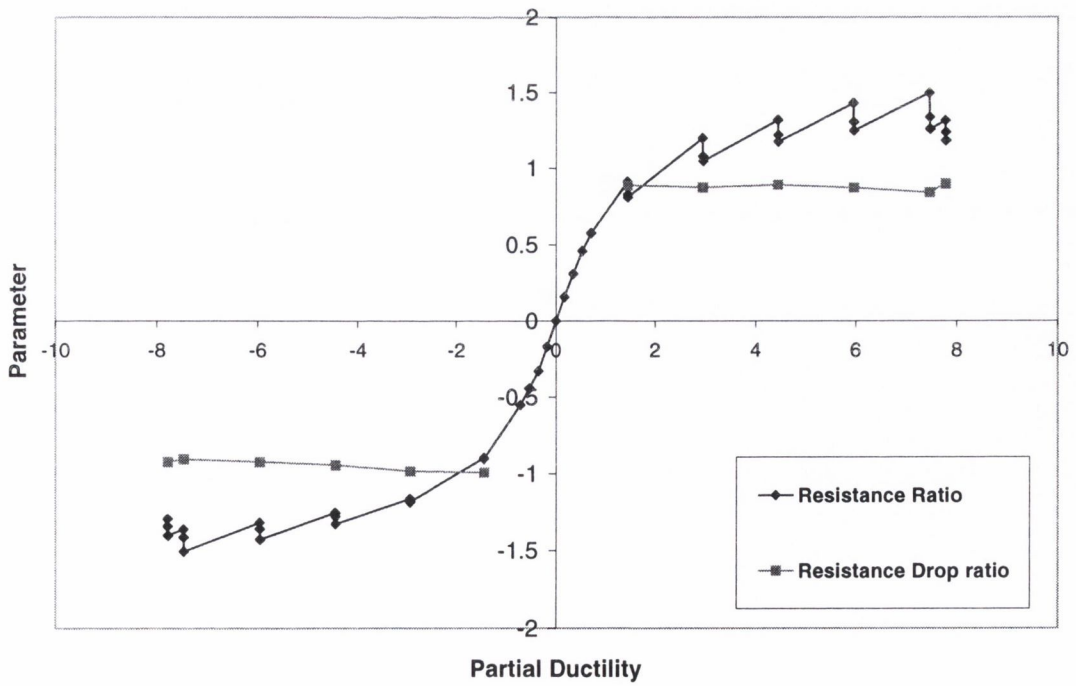


Figure 5.24: Cyclic evaluation parameters for specimen 3.2

Figure 5.24 presents the cyclic evaluation parameters for this specimen. As the specimen did not reach its ultimate displacement within the actuator limitations, the maximum partial ductility is evaluated at 7.79, at the point of maximum displacement. It is expected that the specimen would be able to withstand a greater displacement and hence the ultimate partial ductility of the specimen would also be greater. It may be seen that the resistance ratio of the specimen reaches a peak at 1.5 on both the tension and compression sides of the curve. The resistance drop ratio is the range of 0.85 to 0.87 on the compression side, while the tension side shows a ratio of 0.9 – 0.92.

This specimen also exhibited the stiffness hardening discussed in specimen 3.1. Examination of the displacement transducer results again showed that this was due to the closing of the deformed end-plate with the column flange [Appendix B].

5.3.3 Experimental Results & Observations: Specimen 3.3

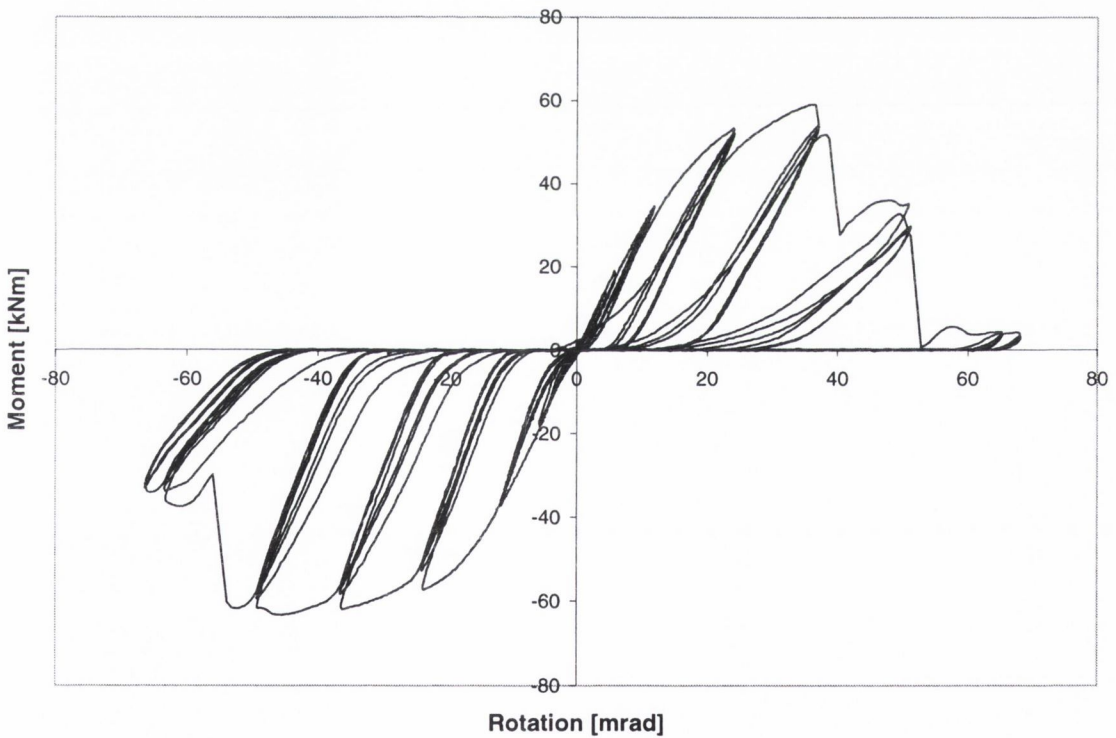


Figure 5.25: Moment-Rotation relationship for specimen 3.3

Figure 5.25 presents the experimental moment-rotation relationship of specimen 3.3. This specimen was tested at an increased loading rate of 0.025 Hz or 25 updates per second, compared to the standard 0.01 Hz. The effects of this loading rate are examined in section 5.3.4. As may be observed, the failure point in this specimen is clearly defined as the point where the moment

resistance suddenly drops. The specimen was designed for a mode 2 failure, and this was observed. The exact details of failure are very similar to that observed for specimen 1.4 in that one bolt in the bolt row failed on one cyclic displacement group while the second bolt did not fail until the next displacement increment. It was also observed during the test that the failure of this specimen was highly brittle, with sudden stripping of the bolt threads occurring. Figure 5.26 shows the yielding pattern for specimen 3.3. As may be observed, circular yield patterns are visible around the bolt bolts. In addition, yield patterns may be seen extending along each side of the beam web line confirming the mode 2 failure. Post-experimental examination of the specimen revealed significant elongation of the bolts had occurred. In one case, the bolt had lengthened by 5.1 mm, or by 6.25 %. The other three bolts showed elongations in the range of 3.7 – 4.2 mm during the test. Due to this elongation, there was a great deal of ‘rocking’ present in the moment-rotation curve. There is also very little stiffness hardening to be seen in the moment-rotation relationship for the reasons discussed in section 5.2.



Figure 5.26: Underside of specimen 3.3 showing yield pattern

Comparing the experimental results to the Eurocode 3 design values, it may be seen that the specimen displays a much lower initial stiffness. The ratio between the design and experimental values is 3.89. In contrast to this, the ratio of experimental to design ultimate moment resistance is 1.25. Similar ratios were observed for other specimens in this study.

The partial ductility at failure is 2.4. This is much lower than observed for some specimens in this study, and appears more in line with that measured for specimens 2.5 – 2.8. Figure 5.27 presents the resistance ratio and the resistance drop ratio for this specimen. As may be observed, the resistance ratio climbs steadily and peaks at a value of approximately 1.18 on both sides of the curve. This is consistent with previous mode 2 specimens. The resistance drop ratio is observed to remain very high, in the range of 0.92 – 0.95, until the stripping of the bolts occurs and which point it quickly drop towards zero.

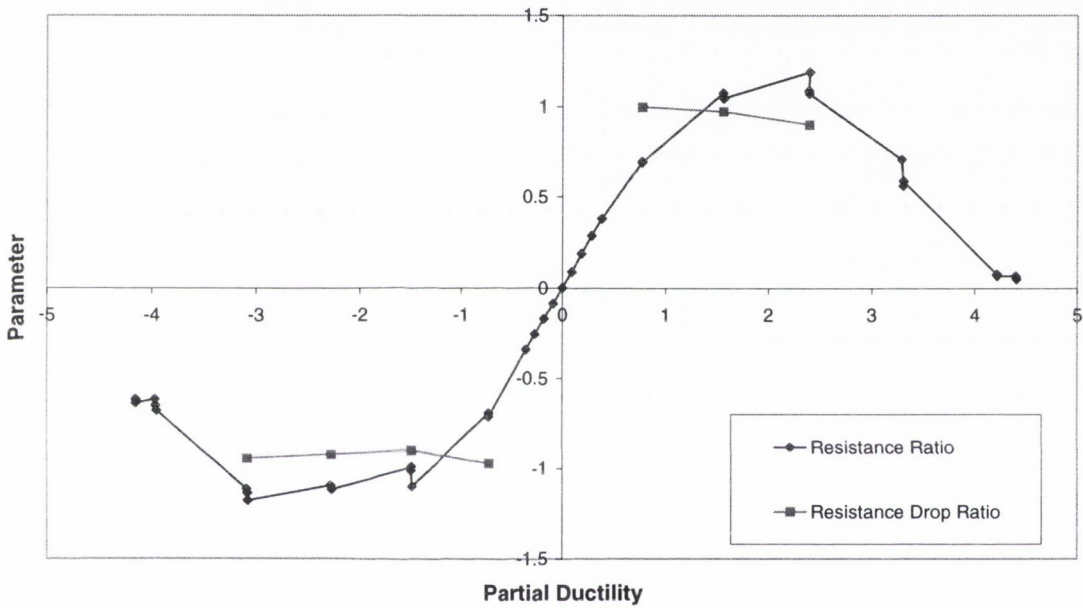


Figure 5.27: Cyclic evaluation parameters for specimen 3.3

5.3.4 Experimental Results & Observations: Specimen 3.4

Specimen 3.4 was designed to be identical to specimen 3.3 in all geometrical properties. Figure 5.28 presents the moment-rotation relationship of this specimen. As may be observed, the relationship is very similar to the previous specimen. However, the bolts in the row in this specimen both failed on the same displacement cycle, unlike the previous test. This specimen failed in the mode 2 manner it was designed for. Again, there was large degree of rocking present in the joint as the bolts elongated. This prevented any significant stiffness hardening from occurring as may be observed.

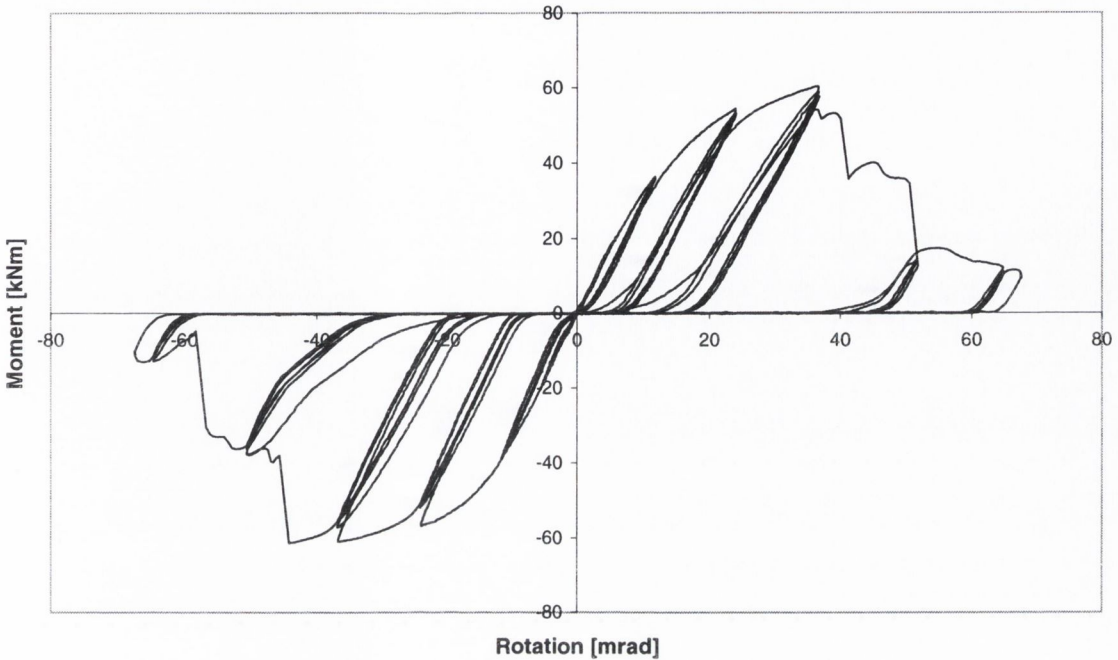


Figure 5.28: Moment-Rotation relationship for specimen 3.4

As stated above, specimen 3.3 and 3.4 were both tested under an increasing displacement amplitude cyclic waveform. However, specimen 3.3 was tested at a higher loading rate, of 25 updates per second, while specimen 3.4 was tested at a rate of 10 updates per second. This resulted in a waveform frequency of 0.025 Hz and 0.01 Hz for specimens 3.3 and 3.4, respectively. This allowed the effects due to the higher loading rate to be investigated.

It may be observed that the failure mode was not affected by the increased rate. Both specimens failed in mode 2. The increase in the loading rate slightly decreases the measured initial stiffness from 3.55 kNm/mrad in the case of specimen 3.4, to 3.13 kNm/mrad for specimen 3.3. It may be seen from Table 5.3 that the yield and ultimate moment-rotation characteristics are very similar for both specimens. The rotation values are slightly higher by 6 – 7% for specimen 3.3, while the moment resistance characteristics are greater in specimen 3.4. Based on the discussion in section 2.6, these results were not expected to differ much from each other.

The cyclic evaluation parameters for this specimen are shown in Figure 5.29. The partial ductility at failure is 2.6 on the tension side of the curve and 3.35 on the compression side, similar to the values seen in section 5.3.3 for specimen 3.3. The resistance ratio peaks at a value of 1.22 on the tension side and 1.14 on the compression side. The resistance drop ratio remains high on both sides with little drop, in the range of 0.92 – 0.95, until stripping of the bolt threads occurs. At this

point, the ratio decreases to 0.41 on the tension side and 0.59 on the compression side.

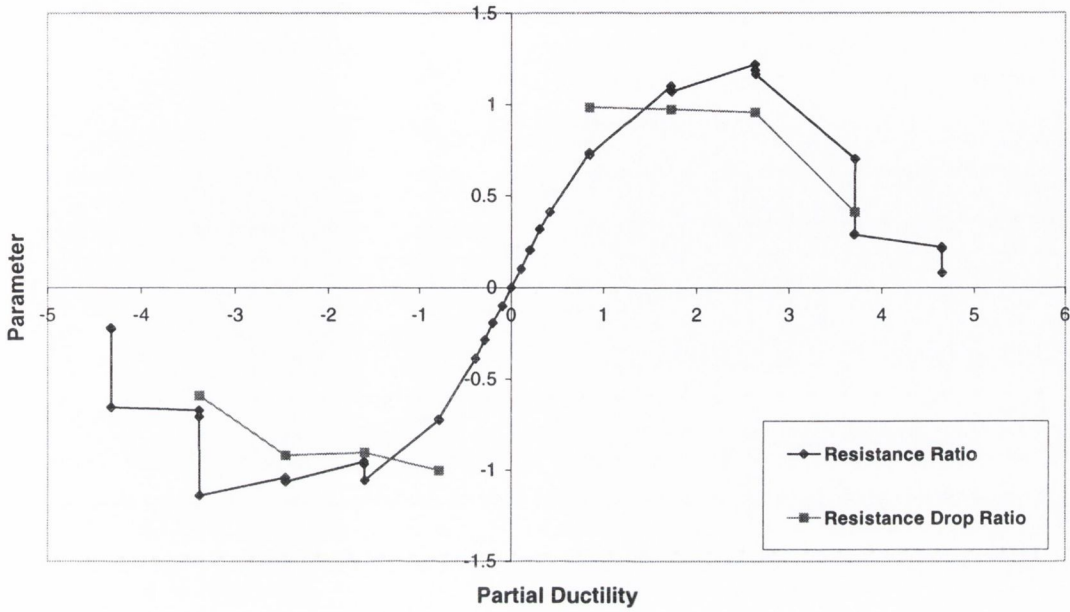


Figure 5.29: Cyclic evaluation parameters for specimen 3.4

5.3.5 Experimental Results & Observations: Specimen 3.5

Figure 5.30 presents the moment-rotation relationship for specimen 3.5. This specimen was designed to have a column flange with approximately the same thickness as the end-plate. To this end, a column size of 203 x 203 x 52 kg/m UC was employed with an end-plate thickness of 12 mm. This specimen was subjected to a large amplitude test cycle and the measured response was highly stable throughout the test.

Specimen 3.5 was designed to fail in a mode 2 manner. However, unlike the other specimen configurations in this study, the column flange was expected to yield instead of the end-plate. It was observed during the test that the end-plate of the specimen appeared to remain nearly elastic with very little visual evidence of bending occurring. This may be seen in Figure 5.31. It is interesting to note that the slightly thicker column flange, with a thickness of 12.5 mm actually yielded before the end-plate which had a thickness of 12 mm as shown by strain gauge results. This is due to the stiffening action caused by the beam flanges and the welds. Post-experimental examination of the bolts did not show significant amounts of yielding which contrasts with the mode 2 failure.

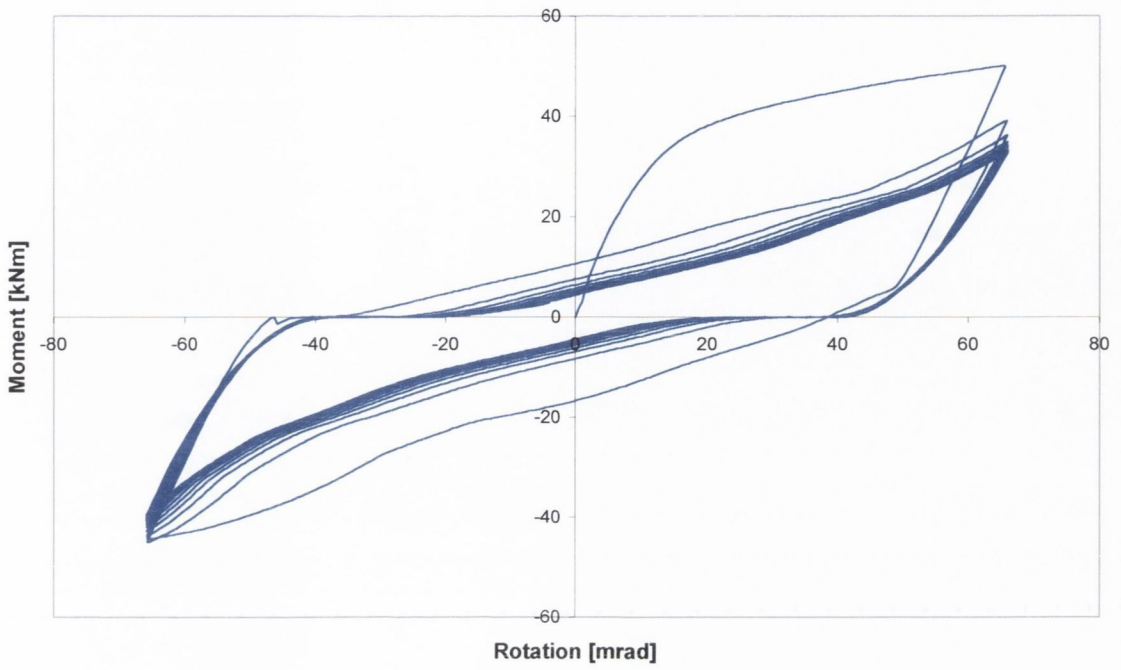


Figure 5.30: Moment-rotation relationship for specimen 3.5



Figure 5.31: Final deformed shape of specimen 3.5

As may be seen in Table 5.3, the initial stiffness of the joint was 3.51 kNm/mrad with a yield capacity of 34.8 kNm. This corresponds to a yield rotation of 9.92 mrad. The joint did not reach its ultimate failure point during the test amplitude. However, the ultimate obtained moment capacity of the joint is 49.92 kNm. Comparing these results to the design calculation of Eurocode 3, it may be seen that, as in previous test, the code proves to be highly conservative with the initial stiffness being over-designed by 210% with the design capacity being under-designed by 75%.

The stiffness hardening that has been noted and discussed in previous tests was also observed in this specimen's moment rotation relationship. However, as may be seen in Figure 5.30, it is much less pronounced in this experiment. Examination of the displacement transducers [Appendix B] reveal that this hardening is due to the same reason as seen in other tests in this series; that is the closing of the gap between the column flange and the end-plate.

Figure 5.32 presents the resistance and resistance drop ratio for specimen 3.5 versus the number of imposed cycles. As may be observed the resistance ratio peaks just below 1.5 on both the tension and compression sides. On the tension side, the resistance ratio quickly drops away to unity, where it holds steady. The drop on the compression side is not as pronounced. This is due to the damage done to the joint on the the first cycle in the tension range before it is reversed to the compression range. As in previous tests, the ratio drops away from the maximum value before levelling off and stabilising.

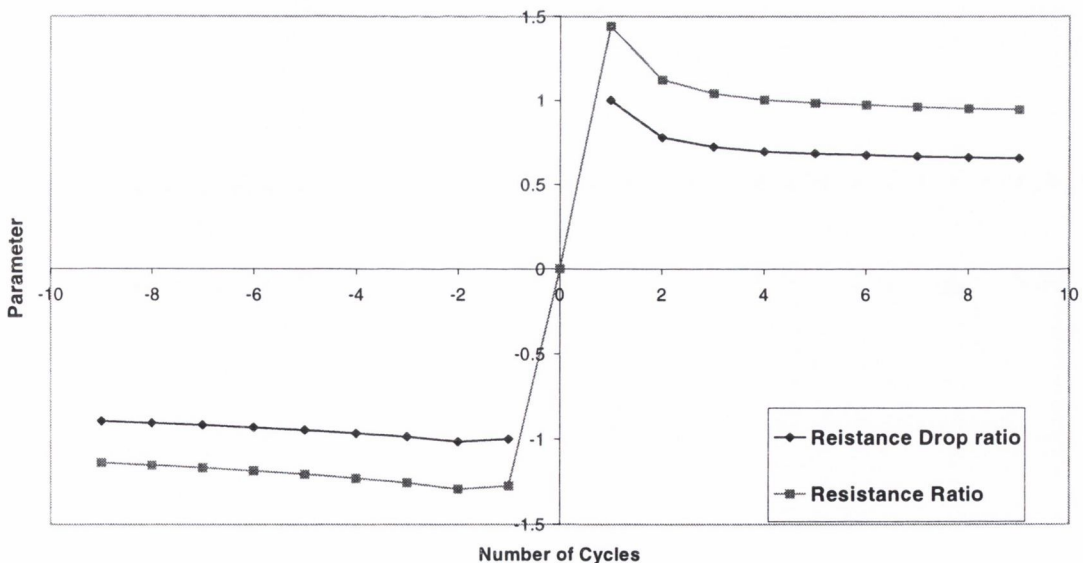


Figure 5.32: Cyclic evaluation parameters for specimen 3.5

5.3.6 Experimental Results & Observations: Specimen 3.6

The experimental moment-rotation relationship of specimen 3.6 is presented in Figure 5.33. This specimen was geometrically identical to specimen 3.5. Again, it may be observed that the specimen response was highly stable for the entire loading history. This specimen was subjected to a full cyclic test employing an increasing amplitude waveform.

As for specimen 3.5, this specimen was intended to fail in a mode 2 manner with the column flange being the critical component. The joint did not reach its ultimate failure point during the experiment. The actual behaviour of the joint was very similar to specimen 3.5 with the end-plate appearing to remain rigid for the entire test, while bending was confined to the column flange. Examination of the strain gauge results revealed that while the end-plate did experience some inelastic strains, the levels were not as high as experienced in other specimens and similar to those measured in specimen 3.5, with maximum strains of approximately $4000\mu\epsilon$. Being obtained. However, unlike in specimen 3.5, post-experimental examination of the bolts showed that there was significant elongation and stripping of the bolts.

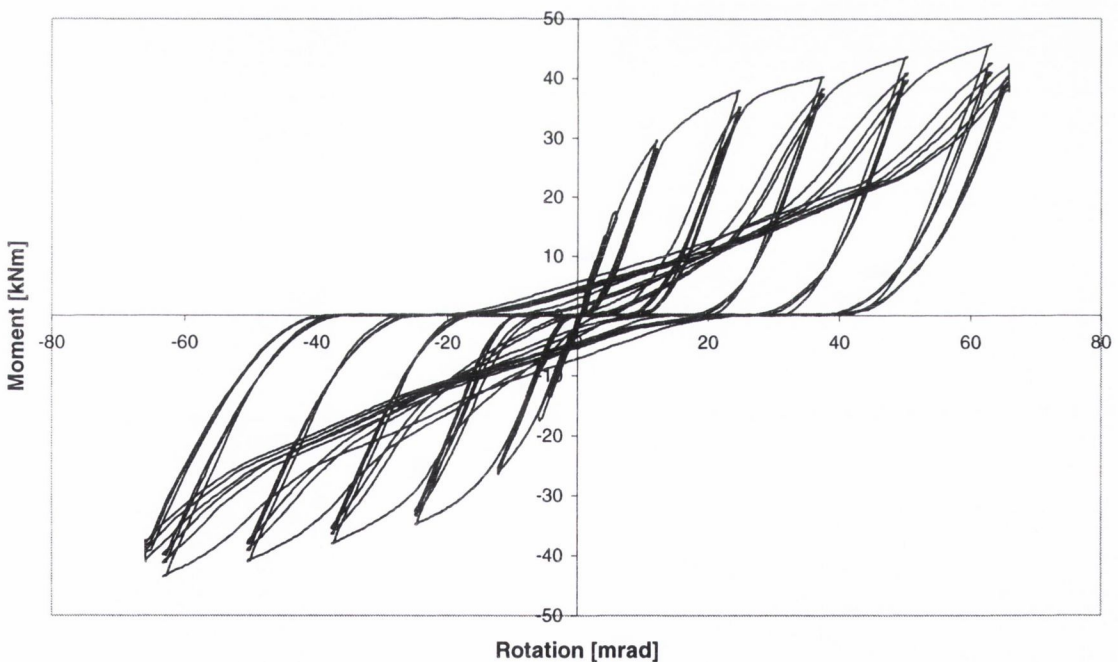


Figure 5.33: Moment-rotation relationship for specimen 3.6

Comparing the results from this test to those obtained for specimen 3.5, it may be seen that the ratio of initial stiffnesses was 0.9, with a value of 3.16 kNm/mrad , resulting in a slightly higher yield rotation of 10.36 mrad . Both the yield and ultimate moment capacity of the joint were

approximately 8% lower than seen in specimen 3.5. Comparing the results to the design calculations from Eurocode 3, it may be observed that the specimen behaved in a similar manner to that discussed in section 5.3.5.

One interesting point to note about the moment-rotation relationship is the stiffness hardening that is present. As may be observed in Figure 5.33, this hardening starts much earlier in the cycle than noted on specimens with heavier column sections and at a much lower capacity level. The change in the stiffness is also not as large as has been observed in previous specimens. This is attributed to the yielding of the column flange rather than the end-plate in the other specimens.

Figure 5.34 presents the cyclic evaluation parameters for specimen 3.6. The resistance ratio continues to rise as the partial ductility rises. This indicates that the ultimate capacity of the joint would actually be higher than the 45.76 kNm measured during the test. It may also be seen that the resistance drop ratio of the specimen is very constant throughout the test, only dropping slightly.

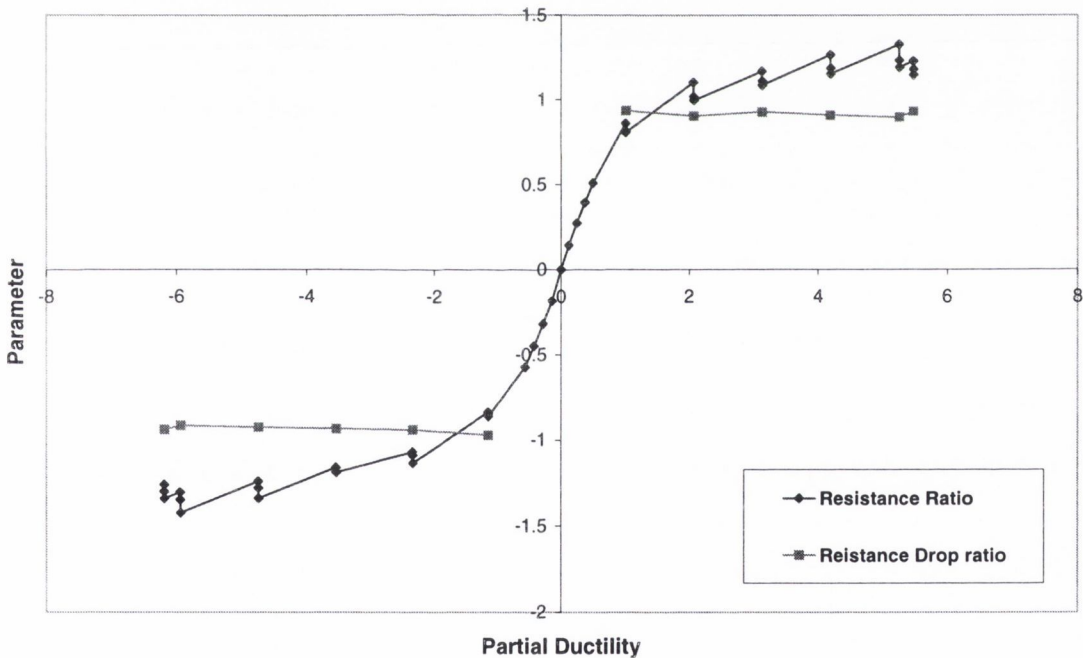


Figure 5.34: Cyclic evaluation parameters for specimen 3.6

5.3.7 Experimental Results & Observations: Specimen 3.7

Figure 5.35 presents the moment-rotation relationship for specimen 3.7. The specimen was tested using the large amplitude program and the resulting moment-rotation hysteresis curve is highly stable. The initial stiffness of this joint was 4.72 kNm/mrad, the highest measured value in the test

series. This compares with the design stiffness of 11.37 kNm/mrad, which is 241% greater than the experimental value. The yield capacity of the joint was measured at 41.67 kNm, resulting in a yield rotation of 8.83 mrad. Eurocode 3 calculates the yield moment as 31.61 kNm and the yield rotation as 2.78 kNm. The experimental ultimate capacity of the specimen was measured at 59.11 kNm, compared to a design value of 47.41 kNm, a difference of 25%.

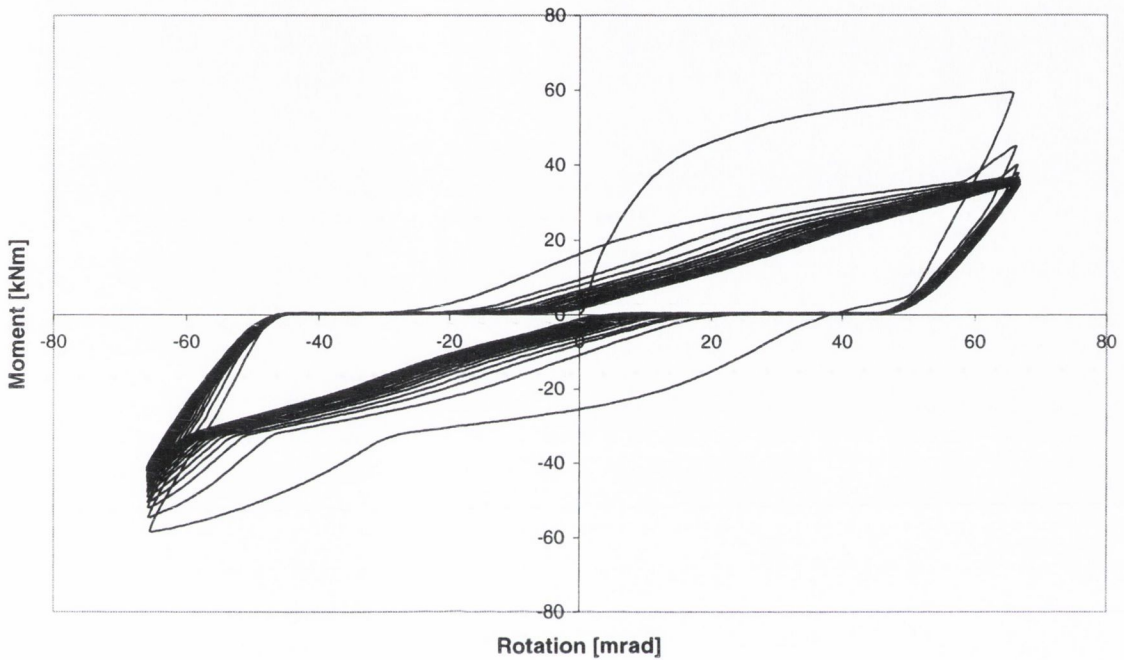


Figure 5.35: Moment-rotation relationship for specimen 3.7

The joint was designed to fail in a mode 1 manner. This was achieved by increasing the bolt grade from 8.8 to grade 10.9. Unfortunately, an unknown error with the strain gauges rendered them useless, as the results fluctuated widely. It may be observed in Figure 5.35 that the joint did not reach its ultimate rotation during the imposed loading. However, based on observations made during the test, and a post-experimental examination of the joint, it was determined that the joint did behave in the manner it was designed for. The washers used in the specimen were crushed under the bolt head, reducing their thickness by approximately 1mm, resulting in approximately 5 mrad of additional rotation. Measurements before and after the experiment showed that no bolt elongation occurred. It may also be observed from Figure 5.35 that the stiffness hardening observed in the majority of the other tests is also present in this specimen. For reasons unknown, it is more pronounced on the compression side of the joint compared to the tension side. Displacement transducers showed that the end-plate deformed by approximately the same distance on each side and the closure happened as expected.

Figure 5.36 presents the resistance ratio and resistance drop ratio for specimen 3.7; their behaviour is similar to that observed in specimen 3.5. The resistance ratio peaks at 1.42 and -1.4 (negative in Figure 5.36) on the tension and compression sides, respectively. The ratio then quickly drops away until it steadies at approximately 0.9 – 1.0 on each side. The resistance drop ratio behaves in a similar manner to that seen in previous tests reaching values of 0.6 and -0.7 on the tension and compressions sides with respect to the maximum measured capacity.

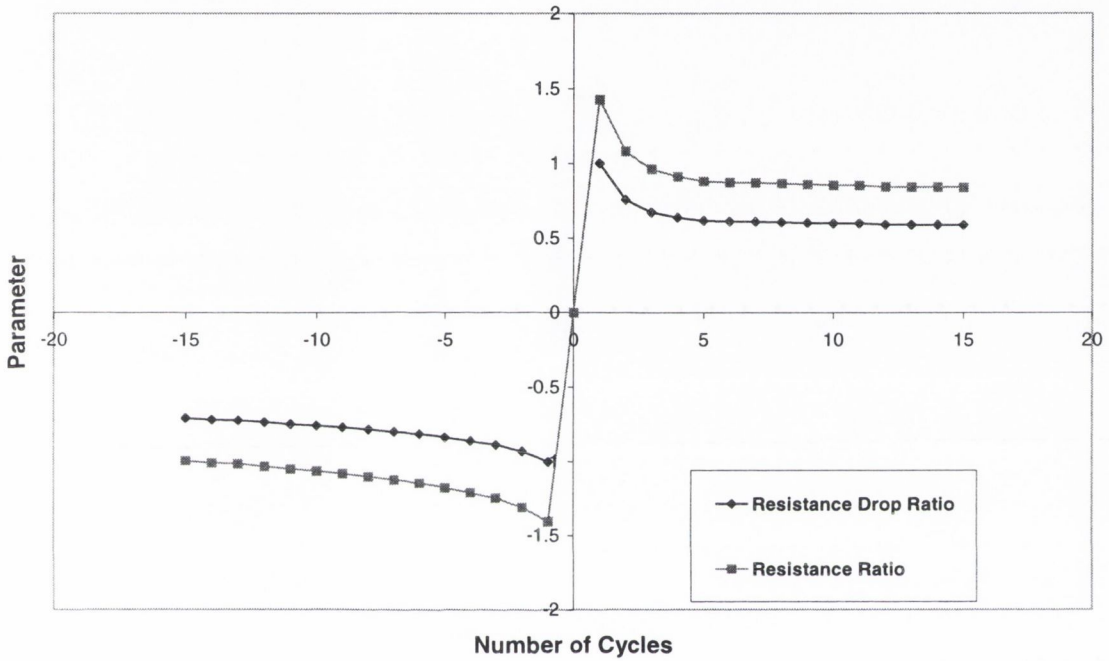


Figure 5.36: Cyclic evaluation parameters for specimen 3.7

5.3.8 Experimental Results & Observations: Specimen 3.8

The moment-rotation relationship for specimen 3.8 is presented in Figure 5.37. This specimen was geometrically identical to specimens 2.3 and 3.7. It was tested under an increasing amplitude cyclic waveform. As may be observed, the resulting hysteresis curve is highly stable throughout the loading process. The initial stiffness of the joint was 4.23 kNm/mrad, which is slightly lower than that measured for specimen 3.7, but within experimental allowances. The yield values were 8.43 mrad and 35.69 kNm. These values are both slightly lower than those from specimen 3.7, while the ultimate measured capacity of the joint was 51.91 kNm. The fact that these values are slightly lower is consistent with nearly all of the tests carried out in pairs. This is due to the fatigue loading of the specimen as it is subjected to constant load reversals.

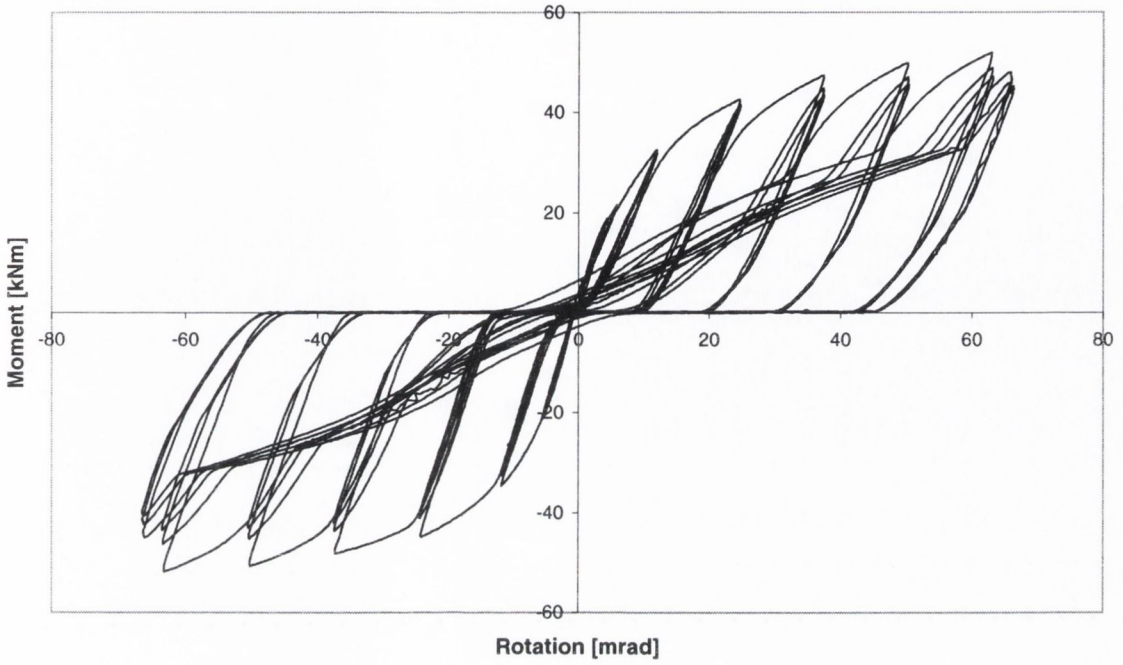


Figure 5.37: Moment-rotation relationship for specimen 3.8

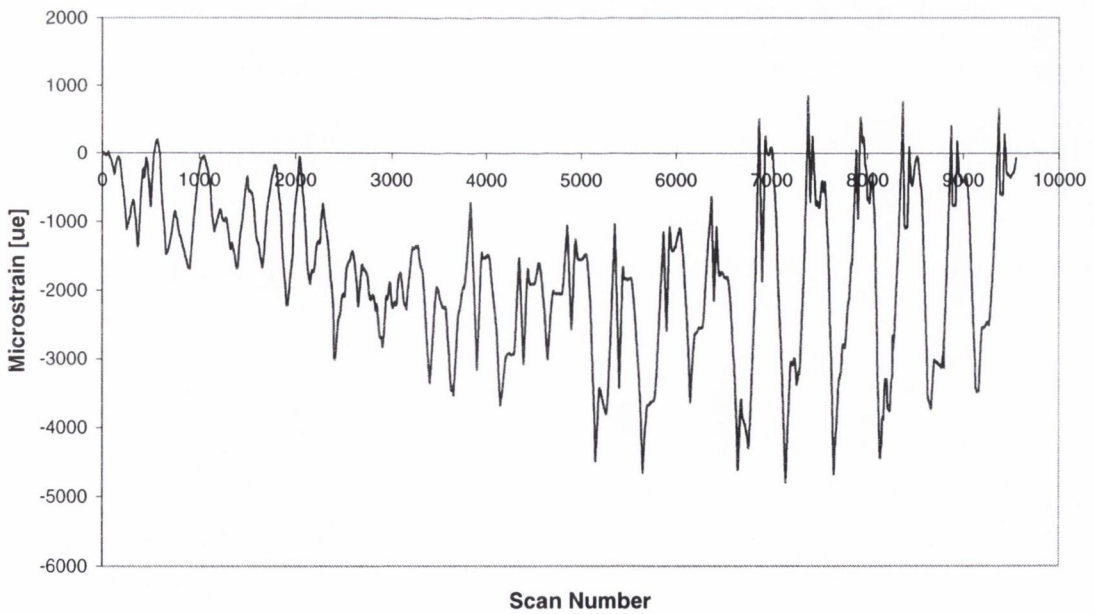


Figure 5.38: Strain gauge #2 result from specimen 3.8

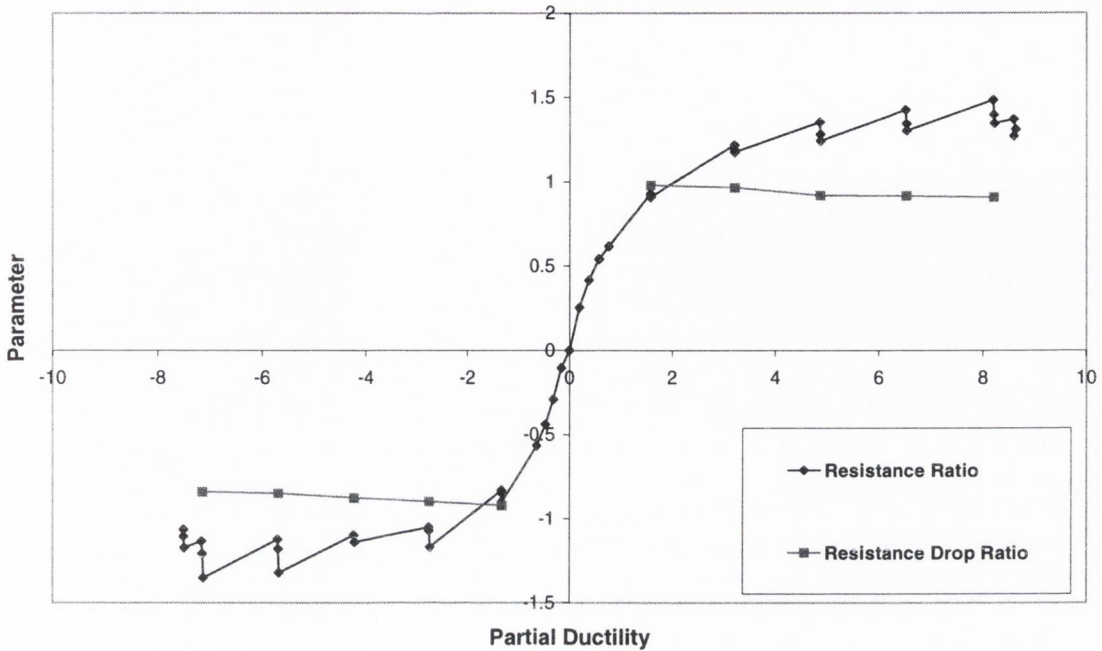


Figure 5.39: Cyclic evaluation parameters from specimen 3.8

This specimen also yielded in a mode 1 manner, with no bolt stripping or elongation present. Strain gauge results for the specimen showed that the yielding of the end-plate was mostly confined to the area of the plate between the bolt line and the beam web line. However, strain gauge #2 showed yielding of the end-plate close to the edge as illustrated in Figure 5.38. This was unexpected based on previous results from this location.

Figure 5.39 presents the cyclic evaluation parameters for this specimen. As may be observed, the behaviour of the resistance ratio is very constant and behaves in a very similar pattern to that discussed before. Similar behaviour is noted for the resistance drop ratio.

5.3.9 Test Series Three Conclusions

As stated above, the objectives of this test series were as follows:

- To obtain further experimental results on mode 1 and mode 2 joints;
- To confirm previous work carried out into strain rate effects on joints;
- To investigate the effects of utilising a column with a flange thickness approximately the same as the joint end-plate thickness;
- To repeat tests with joint configurations identical to specimen 2.3.

Eight tests were performed with four separate joint configurations employing different details with regard to the end-plate thickness and bolt grade. A monotonic and a cyclic test were performed on three of the four configurations, while two cyclic test were performed on the fourth. Two of the joint were designed to have mode 1 responses while the other two configurations were designed to have mode 2 responses.

All of the tests in this series were carried out with few experimental problems. In one test, specimen 3.7, the strain gauges were observed to fluctuate widely and it was determined that the results were of no practical use. Those gauges that were not either unreadable or fluctuating widely that are not presented in this chapter are presented in Appendix B for the reader's information.

Specimens 3.1 and 3.2 were designed with a 10mm thick end-plate to ensure that all of the yielding was confined to the end-plate. These specimens behaved as designed. However, it was noted that specimen 3.1 had a much lower stiffness value than with specimen 3.2, resulting in a higher yield rotation and moment. This is attributed to material irregularities and experimental differences. In contrast, specimens 3.3 and 3.4 were designed with a 15 mm thick end-plate. These specimens were designed for a mode 2 failure mode which was observed. In both specimens, yielding of the end-plate was followed by sudden stripping of the bolts. Specimens 3.5 and 3.6 were designed to induce yielding of the column flange followed by yielding of the bolts. This was observed in the tests, with post-experimental examinations showing that yield of the bolts did occur. Specimens 3.7 and 3.8 were repeats of specimen 2.3. Both specimens were designed for mode 1 failures which were observed. Yielding of the end-plate was observed, with post-experimental examination revealing no elongation or stripping of the bolts.

5.3.9.1 Eurocode 3 Design Comparison & Failure Modes

Table 5.4 presents a comparison between the experimental results and the Eurocode 3 design calculations, where $S_{i,exp}$ = initial stiffness measured in experiment, $S_{i,EC3}$ = initial design stiffness from Eurocode 3: Annex J, $\theta_{y,exp}$ = design yield rotation measured in experiment, $\theta_{y,EC3}$ = design yield rotation predicted by Eurocode 3: Annex J, $M_{y,exp}$ = yield moment measured in experiment, $M_{y,EC3}$ = design yield moment predicted by Eurocode 3: Annex J, $M_{ult,exp}$ = yield moment measured in experiment, $M_{ult,EC3}$ = design yield moment predicted by Eurocode 3: Annex J. As may be observed, the ratio of experimental stiffness to design stiffness varies from a low of 0.22 (specimen 3.1) to a maximum of 0.48 (specimen 3.5). This illustrates that the design stiffness is much higher than the actual stiffness of the joints. This difference is of critical importance when determining the lateral displacement of a frame. This error in the stiffness value would in turn lead to underestimations of the natural frequency and, hence overestimations of the period of vibration.

Specimen	$S_{i,exp} / S_{i,EC3}$	$\theta_{y,exp} / \theta_{y, EC3}$	$M_{y,exp} / M_{y, EC3}$	$M_{ult,exp} / M_{ult, EC3}$
3.1	0.22	8.14	1.75	1.51
3.2	0.34	3.98	1.34	1.34
3.3	0.26	5.78	1.49	1.25
3.4	0.29	5.36	1.57	1.25
3.5	0.48	2.79	1.33	1.27
3.6	0.43	2.90	1.25	1.16
3.7	0.42	3.18	1.32	1.25
3.8	0.37	3.03	1.13	1.10

Table 5.4: Comparison between experimental results and Eurocode 3 design calculations

Comparing the yield capacities of the joint, it may be seen that the experimental values are higher in every case. The joint capacity is under-designed by a minimum of 1.13 and a maximum of 1.75. This has serious implications for the capacity design of columns in frames. This will be discussed in detail in section 5.4. Similar capacity ratios may be observed for the ultimate moment in each specimen.

5.3.9.2 Loading Rate Effects

Specimens 3.3 and 3.4 were tested at two different loading rates. This allowed the strain rate effects on the joint response to be investigated. As previous work has been carried out in this area, discussed above in section 2.6, only two tests were carried out to confirm this research. Specimen 3.3 was loaded at a rate of 0.025 Hz while specimen 3.4 was loaded at the standard rate of 0.01 Hz. These two tests also allowed the control system capabilities to be tested at different loading rates.

As shown in Table 5.3, the experimental responses of these two specimens are very similar. The ratio of initial stiffness between specimens 3.3 and 3.4 is 0.88. In comparison, the ratio of yield rotation is 1.08. The ratios of the yield and ultimate moment capacities are 0.95 and 0.995, respectively. As may be observed, the increased loading ratio has increased the yield rotation of the joint, while slightly decreasing the initial stiffness and the yield moment. The ultimate capacity of the joint has not really been affected.

It may also be observed that the failure mode of the joint was not affected by the increase in loading rate, in contrast to some previous research discussed in section 2.6. Both joints failed with a mode 2 response. Bolts in both specimens failed by sudden stripping of the threads at approximately the same level of imposed rotation, 38.69 mrad and 36.66 mrad for specimens 3.3

and 3.4 respectively.

Based on the experimental results, this increase of 250% on the standard loading rate does not significantly affect the response of the joints. It is expected that if the loading rate was further increased, the joint characteristics would be affected with the ductility of the specimens being reduced as the damage due to fatigue increased. However, this is outside the scope of the current research project.

5.3.9.3 Improved Joint Behaviour

As stated above, specimen 3.7 and 3.8 were repeats of specimen 2.3. It was intended to improve the joint response characteristics without changing any of the geometrical details. To this end, the joints were tested with grade 10.9 bolts instead of 8.8. Comparing the results to those obtained for specimens 2.1 and 2.2, it may be observed that the initial stiffness is increased, while the yield and ultimate moment capacity remains approximately the same. However, the most important improvement is in the failure mode and hence the ductility of the joint. Eurocode 3: Annex J calculates the failure mode of specimens 2.1 and 2.2 as mode 2 with the ultimate cause of failure being due to the bolts. However, specimens 3.7 and 3.8 were designed to give a mode 1 failure where all of the yielding and ultimately failure is confined to the end-plate of the joint. This was confirmed in the tests where no elongation of the bolts was observed.

A further two specimens were tested to determine the effects of plastic hinges forming in the column flange. As may be observed from Table 5.3, the response characteristics are very similar to those measured for the specimens with the higher bolt grade. However, where specimens 3.7 and 3.8 displayed no plastic elongation of the bolts, the bolts in both specimens 3.5 and 3.6 displayed considerable plastic deformation. This would result in a mode 2 failure mechanism and hence a lower ductility level. It was observed that the end-plate remained almost perfectly elastic during the test while the plastic deformation was concentrated in the column flange. This is because the beam web and flanges act as stiffeners to the end-plate.

5.4 Experimental Conclusions & Recommendations

5.4.1 Eurocode 3: Annex J Design Implications

A comparison of the experimental results with the Eurocode 3 design calculations has revealed a number of major differences. Table 5.2 and Table 5.4 presented these differences for the two test series. As may be observed in both series, the initial design stiffnesses of the joints are over-predicted by at least 36% (specimen 2.1) with an average over-prediction of 66%. Previous research, discussed in section 2.7.2, has shown that the initial stiffness of the joints can have a significant affect on frame stiffness. A comparison of the yield capacities of the joints also shows large differences between the design value and the experimental values. With the exception of one test, specimen 2.3, the ratio of experimental to design yield capacity ranged from 1.13 – 1.75 with an average value of 1.36. Similar values were noted for the ultimate capacity of the joints. These values have serious implications for the capacity design of columns in moment-resisting frames.

Capacity design relies on determining the location of the yield points in a frame. This is usually done so to cause the formation of plastic hinges in the joints or in the beams near the joints. To this end, columns are designed to possess a greater moment capacity than the joints and beams. However, if the joints are capable of withstanding 36% more moment, it is easily possible that the columns would have been designed to take less than this value. Even allowing for the 20% over-design factor in Eurocode 8, there is still a large difference in the design and actual capacities. This would lead to the formation of column hinges and the frame would be likely to collapse under increased loads.

The implications of the differences between the design calculations and the experimental results also extends to seismic design of frames which is a type of capacity design. Seismic design represents the process of providing adequate lateral stiffness to control drift and adequate lateral strength to limit inelastic deformation, while ensuring ductility supply. Based on the design values, it appears clear that any lateral drift checks will be highly inaccurate. Unfortunately, Eurocode 3 does not provide any method of estimating the ductility of a joint.

5.4.2 Bolt pre-load

Eurocode 3: Annex J does not make any provision for the pre-loading of the bolts in a joint. However, it is common practice to place a pre-determined level of torque on the bolts. Due to this, a number of joints were tested to investigate the effects of the pre-load. Joints were tested with 100 Nm and 200 Nm. The joints used for the testing were all mode 3 joints. This allowed the bolt behaviour to be assessed directly with the end-plate remaining elastic throughout. It was observed

that the joint with 200 Nm torque had an increase in the initial stiffness. However, this increase still did not bring the stiffness to the levels predicted by Eurocode 3. This increase in stiffness resulted in a lower yield rotation for the joint but did not affect the moment capacity values or the ultimate rotation of the joint. This is because the torque does not change the material properties of the joint. A similar increase in the stiffness was not observed for the joint with a torque of 100 Nm. It was determined that for the bolt pre-load to have a significant affect on the initial stiffness of a joint, a certain level of torque is required. As the 100 Nm and the 200 Nm torque levels applied corresponded to 30 and 60% of the recommended maximum values for Grade 8.8 M16 bolts, this level is felt to lie somewhere between these values.

5.4.3 Cyclic Evaluation Parameters

Three parameters are used to evaluate the cyclic behaviour of the joints in this study. These are the partial ductility, resistance ratio and the resistance drop ratio. The partial ductility is a measurement of the displacement of the specimen at any particular point in relation to the yield displacement. It was observed from the test results that the joints with a mode 3 failure mechanism had the lowest ductility, while those joints that mode 1 failures were observed for had the highest. The mode 3 joints generally displayed partial ductility levels up to a maximum of 3 before failure occurred. Mode 2 joints exhibited partial ductility levels of 3 or greater with a maximum of 6 being observed. Mode 1 joints exhibited much higher levels in the range of 9 or greater. It must be noted that the partial ductility levels for some of the mode 1 and mode 2 specimens are not fully reported. This is because the specimens did not always reach their ultimate rotation due to the hydraulic actuator limits.

The resistance ratio also showed a difference depending on the failure mode of the joint. mode 1 joints displayed higher values than mode 2 and mode 3 joints. The mode 1 joints, typically, exhibited a resistance ratio in the range 1.4 – 1.5 with the mode 3 joints in the range of 1.1 – 1.25. The mode 2 joints exhibited ratios of 1.2 – 1.35. This is consistent with the type of failure expected for each of these failure modes. Mode 1 joints are expected to exhibit a very ductile response with a long plastic slope. In contrast, mode 3 joints have a very brittle failure mode and are prone to low ductility levels. Mode 2 joints are usually in between these extremes.

The resistance drop ratio displays the lowest loss in the mode 3 specimens where the ratio is in the range of 0.95 – 0.99. This is due to the absence of yielding in the end-plate with all of the force concentrated in the bolts. The mode 2 specimens typically showed resistance drop ratios in the range of 0.85 – 0.93 while the mode 1 specimens showed the lowest values in the range of 0.75 – 0.85.

These values agree with the theory on tee-stub failure modes presented in chapter 2. The mode 1 joints are the most ductile, with all of the yielding being concentrated in the end-plate and the bolts remaining elastic throughout the test. The mode 3 specimens are the most brittle, with all of the yielding being concentrated in the bolts and the end-plate remaining elastic. The mode 2 specimens display both end-plate and bolt yielding.

5.4.4 Stiffness Hardening

Stiffness hardening of the moment-rotation curve was observed in all of the mode 1 and mode 2 specimens tested in this study. This hardening occurred during groups of inelastic cycles on the second and third cycle of each group. It was most pronounced in the case of the mode 1 specimens with little or no hardening being observed in the mode 3 specimens. Mode 2 specimens displayed an intermediate level of hardening.

Examination of the experimental results showed that this hardening is related to the plastic deformation of the end-plate and column flange at the join between the beam flange and the end-plate. By examining displacement transducer results, it was observed that a gap opened between the end-plate and the column flange as a rotation was imposed on the specimen. On the first cycle in a group of inelastic cycles, the end-plate is subjected to plastic deformation greater than that experienced in the previous cycles. On the second and third cycles, the gap closes slightly due to the elastic rebound properties of the end-plate. The stiffness hardening occurs when this gap is closed and the end-plate and column flange come into contact with each other again. Obviously, a thin end-plate, typical of a mode 1 joint, is subjected to larger deformations and hence the stiffness hardening is more pronounced. In a mode 3 joint, the end-plate is designed to remain elastic with little or no deformation and hence, there is very little stiffness hardening. The mode 2 joints are subject to deformation greater than the mode 3 joints, but not as much as the mode 1 joints, therefore, displaying an intermediate level of hardening. In the case of specimens 3.5 and 3.6, it is column flange that is deforming and closing with the end-plate as smaller column sections are employed.

5.4.5 Improved Joint Behaviour

In addition to the joints tested with different failure modes, two additional configurations were tested. One of the major problems observed in the joint failure modes was the manner in which the bolts often stripped suddenly, resulting in a premature and brittle ultimate failure. This was especially true for the mode 2 joints where the yielding of the end-plate is followed by yielding and

failure of the bolts.

The first modified joint was specimen 2.4 where the standard grade 8.8 nuts were replaced with grade 10.9 nuts. It was intended that the improved nut grade would help to prevent the threads on the bolt and nut from stripping as had been observed in some of the other tests. It was also hoped that the failure mode of the joint would be changed from mode 2 to mode 1. The first objective of preventing stripping was achieved during the imposed displacement. However, significant elongation of the bolts was observed in the range of 6 – 7%. The failure mode of the joint, therefore, remained as mode 2.

The second joint configuration to be tested was a variation on specimen 2.1 and 2.2. Instead of employing grade 8.8 bolts, grade 10.9 were used instead. It had been noted that the mode 1 joints resulted in higher levels of ductility but at the cost of reduced moment capacity due to the use of a thinner end-plate. This joint was designed to retain the higher moment capacity of a mode 2 joint, while improving the ductility, which was achieved. Comparing the moment capacity of the improved joint with that of the standard joint, the moment capacity was increased slightly as was the initial stiffness. Also noted was the absence of bolt elongation in the new configuration, as well as the lack of stripping of the threads. However, the bolts in the standard joints, specimens 2.1 and 2.2, were found to have stripped slightly on completion of their tests. Therefore, the change in the bolt grade from 8.8 to 10.9 was successful in improving the standard joint behaviour.

5.4.6 Failure Modes

A large part of this study was to investigate the validity under cyclic loads of the joint failure modes presented in BS5950 and Eurocode 3. The failure mode of all of the tested specimens was determined. This was carried out under both large amplitude (monotonic) and increasing amplitude cyclic displacements. In all but two of the tests, the design failure mode was observed. Specimen 1.5 failed due to local buckling of the beam and specimen 2.1 failed in a mode 1 manner rather than the mode 2 for which it was designed. It should be noted that the failure mode was not always readily evident, as a number of the specimens did not reach their ultimate displacement within the actuator limits. In the case of these specimens, the failure mode was determined by examining strain gauge results and post-experimental examinations of the end-plate and the bolts.

Specimen 2.1 was designed to lie close to the boundary between the mode 1 and mode 2 failure mechanisms. From this, it was observed that a small difference between the notional material properties and the actual properties can cause a change in the failure mode.

5.4.7 Ductility

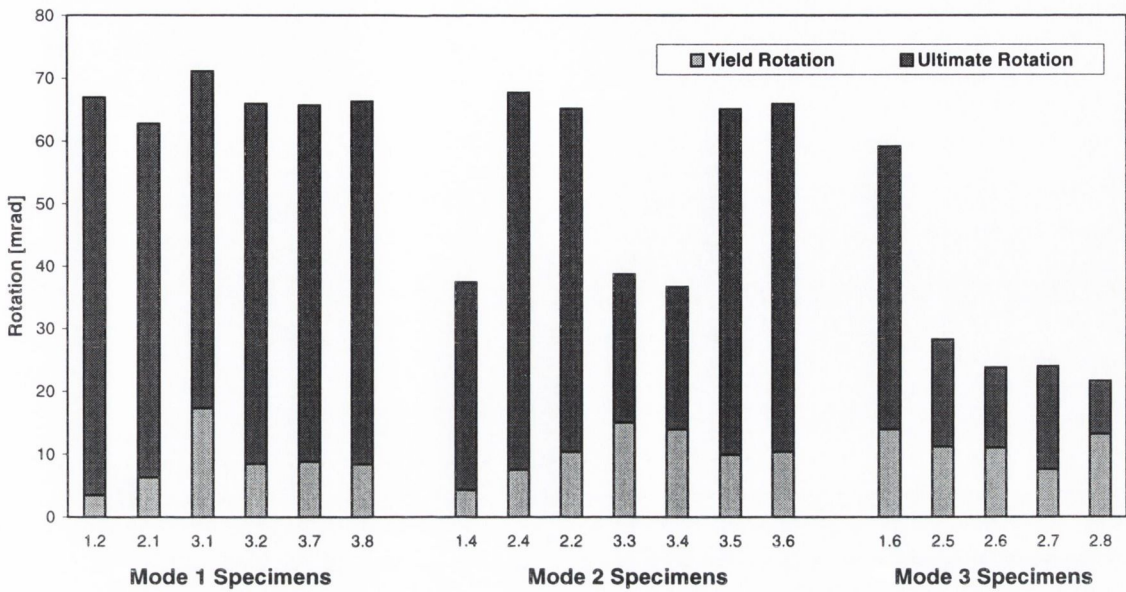


Figure 5.40: Comparison of yield and ultimate rotation values

Figure 5.40 compares the yield and ultimate rotations of the different specimens, grouped by failure mode. For those specimens that did not fail during the load application, the maximum obtained rotation is presented. The mode 1 specimens all displayed high ultimate rotations, with the lowest value of 62.77 being reported for specimen 2.1. None of these specimens failed during testing, and only specimen 1.2 showed tearing of the end-plate or any other indication of imminent failure. With the exception of specimen 3.1, the mode 1 joints displayed comparatively low yield rotations. The mode 3 joints all reached their ultimate rotation. The majority of these occurred at rotations of 30 – 40 mrad, with specimen 1.6 being the exception. The yield rotations were generally higher than those displayed by the mode 1 specimens, being between 11 and 13 mrad. The mode 2 joints displayed two distinct behaviours, with some behaving similar to mode 1 joints, and others behaving similar to mode 3 joints. Four of the seven specimens did not fail under the imposed loading. The failure modes for these specimens is based on post-experimental examinations which revealed bolt plasticity or some other indication of mode 2 failure. For those specimens that did fail, their ultimate rotations are higher than those displayed by the mode 3 specimens, but much lower than the mode 1 joints. The yield rotation for these specimens is generally higher than those of the mode 1 specimens, ranging from 7 mrad to 15 mrad.

Similar patterns are displayed by the partial ductility capacities, presented in Figure 5.41. The mode 1 joints exhibit ductility levels with an average value of approximately 7.5 and a maximum of 19.6. The mode 3 joints display the lowest ductility ratios ranging from 1.6 – 3.1. Again, the

mode 2 joints display values that vary between the mode 1 and mode 3 values.

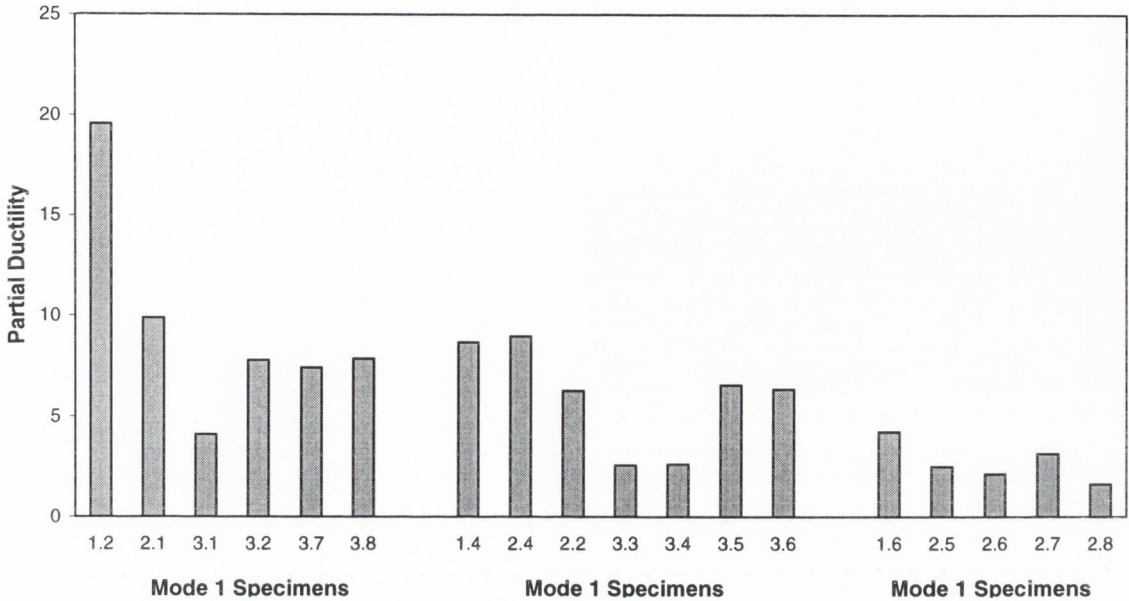


Figure 5.41: Comparison of partial ductility capacities

5.4.8 Recommendations

Based on these comparison between the experimental and design calculations, two recommendations are made on the use of the Eurocode 3 design model. These recommendations are only valid for flush end-plate joints similar to those tested in this study. When performing checks for lateral movements, the initial stiffness should be assumed to be one-third of the design value. This will ensure that the lateral displacements will not be underestimated due to the over-prediction of the initial stiffness. For the capacity design of columns where the moment capacity of the joint is of critical importance, an over-design factor of 40% for the joint capacity is recommended.

It has also been concluded that mode 3 joints are not desirable for use in moment-resisting frames where inelastic behaviour is expected. They are suitable for structures which are designed to remain elastic at all times. This is due to the low ductility levels that are exhibited and the brittle failure mechanisms displayed. Although mode 1 joints do exhibit the highest levels of ductility, this is often at the expense of moment capacity. In comparison, mode 2 joints displayed high levels of moment capacity with a corresponding reduction in ductility. One problem noted in joints with mode 2 failures is the likelihood of stripping of the bolt threads, and hence a premature loss of moment capacity. Therefore, designers must decide whether the ductility levels or the resistance

capacity of the joints are of critical importance for a particular building.

Two solutions to this problem were presented. The first is to replace the nuts used with a higher grade. Although this did prevent the stripping of the threads, it failed to significantly improve the ductility. The second method was to replace the bolts and nuts with a higher grade material. This improved joint resulted in a higher stiffness and moment capacity as well as improving the failure mode and hence the ductility of the joint. Therefore, it is recommended that in cases where both high moment capacity and high ductility are requirements of the design, such as seismic design, this simple improvement be actively considered.

5.5 Conclusions

This chapter presents the experimental results for the second two series of joints to be tested. General observations for each series are presented followed by a detailed discussion of each specimen. Conclusions were then drawn on the behaviour of the specimens in each test series. These conclusions are broken down in a number of different sections. Comparisons are shown between the Eurocode 3 design calculations and the experimental results. It was noted that there were large differences present between the two. The effects of increased loading rates are examined. The cyclic evaluation parameters defined in section 4.3 are then discussed with regard to the full spectrum of test results. The effects of bolt pre-load are also examined. This is not accounted for in Eurocode 3: Annex J and was found to increase the initial stiffness of the joints but not effect the capacities or failure mode. The characteristics of two suggested improved joint configurations are then discussed in comparison to the standard joint tested. This is followed by a discussion of the validity of the static failure modes to cyclic and dynamic tests. It was observed that the failure modes were valid in all cases bar two.

Finally a number of recommendations are mad with regard to use of flush end-plate joints in frame design. The use of over-design factors for the initial stiffness and moment capacity are recommended when performing design checks using characteristics developed from the Eurocode 3 model. These factors are considered of critical importance when concerning lateral displacements and capacity design calculations of columns.

The use of joints subject to mode 3 failure mechanism is also discouraged due to their brittle nature. The advantages and disadvantages of mode 1 and mode 2 joints is presented. It is recommended that the simple improvement of increasing the bolt grade be considered for situations where both capacity and ductility are of importance.

Chapter 6

Prediction Modelling of Joint Response

6.1 Introduction

In order to ensure satisfactorily behaviour from moment joints, three main areas must be considered: strength, stiffness, and ductility. Therefore, an understanding of the joint's moment-rotation ($M-\theta$) curve is vital if the most efficient and economical design is to be achieved.

This chapter presents a proposed joint model for the prediction of the moment-rotation relationship for flush end-plate joints. The model consists of the combination of two existing models. The first model is a T-stub model developed to predict the force-displacement curve of two equal T-stubs. The second model is used to determine the joint moment-rotation relationship by allowing for the column web in tension, compression and shear.

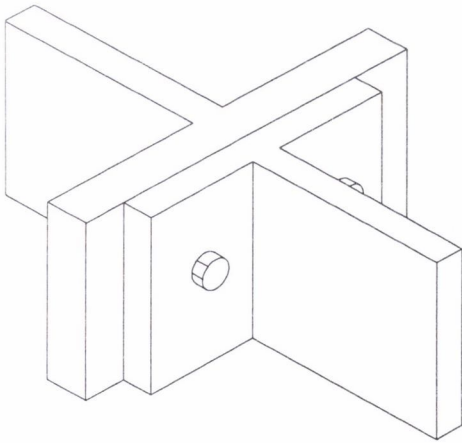
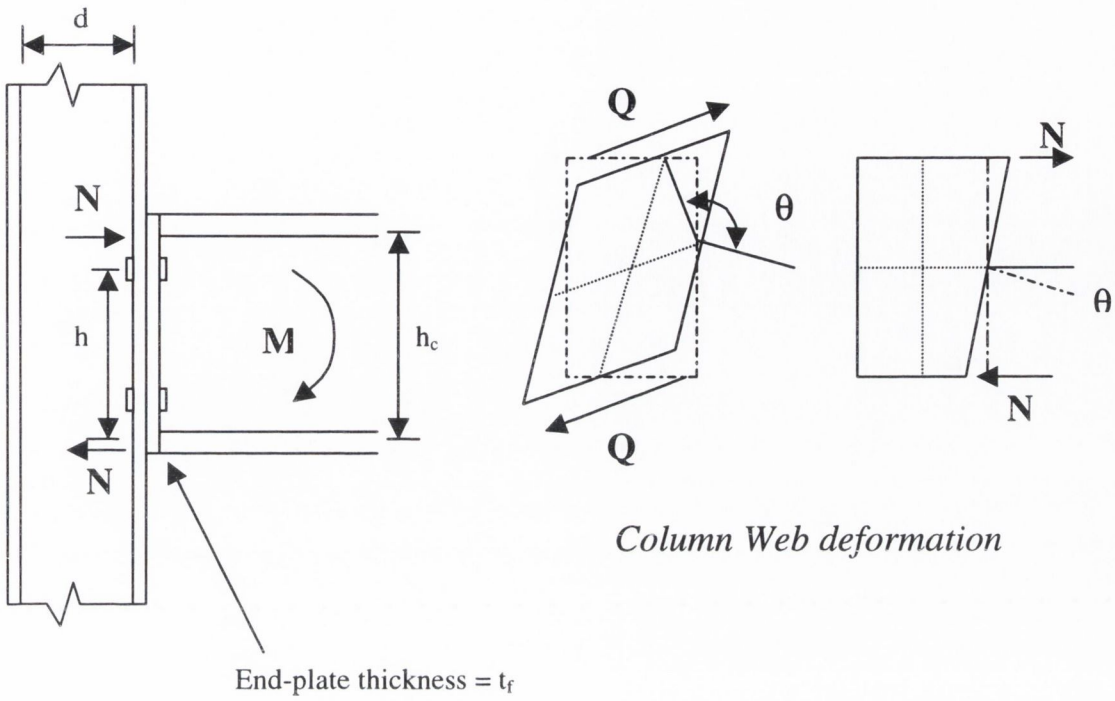
The next section gives details of the model that was adopted for the response predictions. Formulae are laid out and fully explained. The changes made to the adopted models are fully detailed. The following section compares the results from the prediction model with the experimental results presented in chapters 4 and 5. The initial stiffness, yield values and ultimate values are compared and any discrepancies commented upon.

6.2 Proposed Joint Model

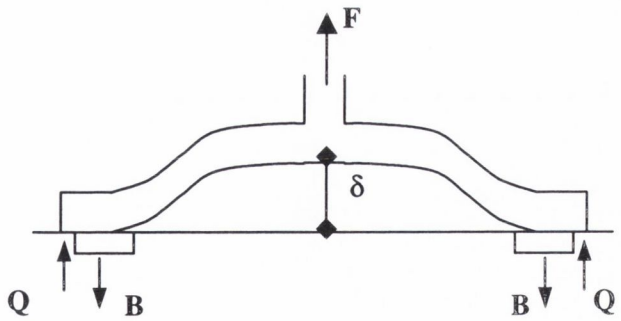
The model proposed for use with flush end-plate joints was adapted from two other methods discussed in chapter 2. The first method is a T-stub model based on the three failure modes defined in section 2.5 and Eurocode 3: Annex J. A force-displacement relationship is determined for a notional T-stub, and this is then used to determine the moment-rotation characteristics of the joint using the second method. The basis for the proposed model is presented graphically in Figure 6.1.

The T-stub model is based on a model proposed by Faella et al (2000, 2001a, b). This model was originally developed to predict the ultimate plastic displacement of a T-stub within an extended end-plate joint. The model is presented in the following section together with the proposed changes that allow it to be used for flush end-plate joints similar to those tested in this study.

The second model was a T-stub model for flush and extended end-plate joints, that incorporated the column web behaviour (Shi et al, 1996). However, it was determined that this model was not sufficiently accurate for the purposes of this study. The proposed model employs the column web behaviour section of Shi et al's model together with its method of translating the force-displacement relationship into moment-rotation characteristics.



Notional T-Stub
(see Fig. 2.7)



Rectangular T-Stub
deformation

Figure 6.1: Graphical representation of model concepts

6.2.1 T-Stub Modelling Technique

6.2.1.1 Basis of Approach

The theoretical approach is based on the three failure modes for a T-stub. These failure modes depend on the ratio of flexural resistance of the end-plate and column flanges to the axial resistance of the bolts, as fully explained in section 2.5. The resistance of each failure mode may be derived from simple equilibrium equations and hence the bending moment along the flange may be determined. From this, the corresponding curvature diagram may also be found. By integrating the curvature diagram, the ultimate plastic deformation may be determined.

The prediction of the deformation capacity of a bolted T-stub is an extremely complex operation. Both geometrical and material non-linearities arise, as do contact problems and three-dimensional effects. In order to allow the plastic capacity of a T-stub to be determined, a simplified model must be accepted and hence a number of assumptions and approximations must be made. The model is based on the following approximations:

- 3-dimensional effects are neglected;
- geometrical non-linearities are neglected;
- failure of the material occurs at the attainment of the ultimate strain in T-stub flanges;
- the influence of shear action on the plastic behaviour of the flange is neglected; and
- prying forces are taken into account using an approximate method.

6.2.1.2 Material Model

The problem is reduced to the evaluation of the plastic rotation supply of a notional rectangular plate representing the notional T-stub. As this rotation supply may be seriously affected by the inelastic properties of the material, accurate modelling of the stress-strain relationship is important. However, material properties measured using standard coupon tests are only nominal values, as the stress is related to the original area of the section and the strain is related to a reference length. This relationship is characterised by a softening branch that develops as necking of the specimen occurs. In contrast, the true stress and natural strain relationship is always hardening.

If Poisson's ratio is assumed to be equal to 0.5 in the range of large deformations, the volume of the specimen remains unchanged under deformation. It may be demonstrated that the following relationship holds true:

$$\varepsilon = \ln(1 + \varepsilon_n) \quad \text{Eqn. 6.1}$$

where ϵ is the natural strain and ϵ_n is the nominal strain. The ultimate natural strain may be evaluated by the following relationship (RILEM, 1990):

$$\epsilon_u = \ln \frac{A_0}{A_f} \quad \text{Eqn. 6.2}$$

where ϵ_u is the ultimate natural strain, A_0 is the original area of the test specimen and A_f is the final area of the test specimen at fracture.

The true stress-natural strain relationship may be modelled using a multi-linear curve as shown in Figure 6.2. Suggested values (Faella et al, 2000) for the material parameters are given in Table 6.1 for grade 43 steel, as used in this study. It may also be assumed that $E_u = f_u$ for the final branch of the stress-strain relationship.

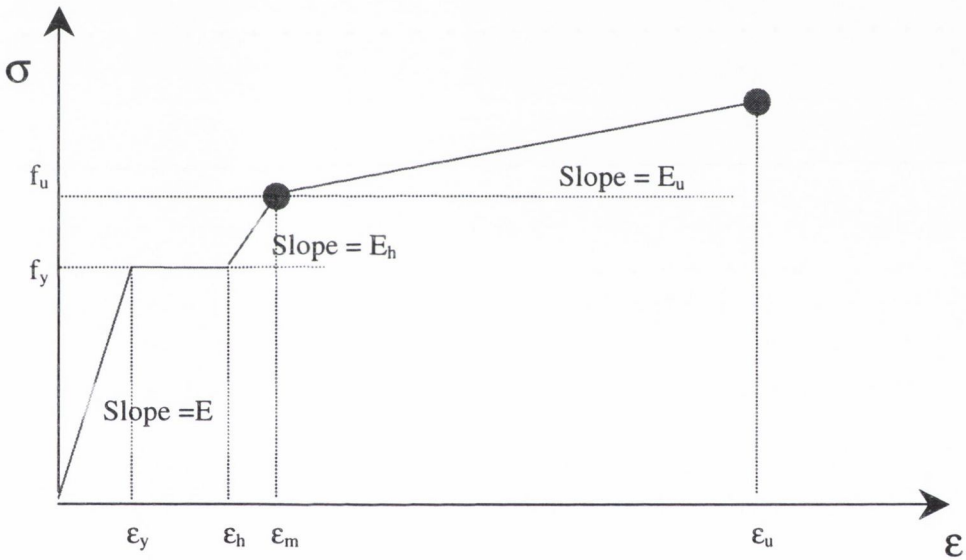


Figure 6.2: σ - ϵ relationship

f_y [N/mm ²]	f_u [N/mm ²]	$\frac{\epsilon_h}{\epsilon_y}$	$\frac{\epsilon_u}{\epsilon_y}$	ϵ_u [%]	$\frac{E}{E_h}$	$\frac{E}{E_u}$
275	430	11.0	425	55	52.8	486.1

Table 6.1: Suggested material properties for Grade 43 steel (Faella et al, 2000)

6.2.1.3 Moment-Curvature Relationship

As stated in the previous section, the problem may be considered as a rectangular section with a width of b , and a thickness of t_f , as shown in Figure 6.1. Based on the material constitutive law

defined above, yield moment and corresponding curvature may be derived in the non-dimensional form $M/M_y - \chi/\chi_y$ where:

$$M_y = \frac{b \cdot t_f^2}{6} f_y \quad \text{and} \quad \chi_y = \frac{2\varepsilon_y}{t_f} \quad \text{Eqn. 6.3}$$

Using equilibrium equations between internal stress and external bending, the following equations are defined for the non-dimensional moment-curvature relationship:

$$\text{for } \frac{\chi}{\chi_y} \leq 1$$

$$\frac{M}{M_y} = \frac{\chi}{\chi_y} \quad \text{Eqn. 6.4}$$

$$\text{for } 1 < \frac{\chi}{\chi_y} \leq \frac{\chi_h}{\chi_y}$$

$$\frac{M}{M_y} = \frac{1}{2} \left[3 - \left(\frac{\chi_y}{\chi} \right)^2 \right] \quad \text{Eqn. 6.5}$$

$$\text{where } \chi_h = \frac{2\varepsilon_h}{t_f}$$

$$\text{for } \frac{\chi_h}{\chi_y} < \frac{\chi}{\chi_y} \leq \frac{\chi_m}{\chi_y}$$

$$\frac{M}{M_y} = \frac{1}{2} \left[3 - \left(\frac{\chi_y}{\chi} \right)^2 \right] + \frac{1}{2} \frac{E_h}{E} \left(\frac{\chi - \chi_h}{\chi_y} \right) \left(1 - \frac{\chi_h}{\chi} \right) \left(2 + \frac{\chi_h}{\chi} \right) \quad \text{Eqn. 6.6}$$

$$\text{where } \chi_m = \frac{2\varepsilon_m}{t_f}$$

$$\text{for } \frac{\chi_m}{\chi_y} < \frac{\chi}{\chi_y} \leq \frac{\chi_u}{\chi_y}$$

$$\begin{aligned} \frac{M}{M_y} = & \frac{1}{2} \left[3 - \left(\frac{\chi_y}{\chi} \right)^2 \right] + \frac{1}{2} \frac{E_h}{E} \left(\frac{\chi - \chi_h}{\chi_y} \right) \left(1 - \frac{\chi_h}{\chi} \right) \left(2 + \frac{\chi_h}{\chi} \right) \\ & - \frac{1}{2} \frac{E_h - E_u}{E} \left(\frac{\chi - \chi_m}{\chi_y} \right) \left(1 - \frac{\chi_m}{\chi} \right) \left(2 + \frac{\chi_m}{\chi} \right) \end{aligned} \quad \text{Eqn. 6.7}$$

$$\text{where } \chi_u = \frac{2\varepsilon_u}{t_f}$$

As M_u is determined by substituting χ with χ_u in Eqn 6.7, it may be noted that M_u/M_y is a parameter solely based on the mechanical properties of the material and may be written as follows:

$$\frac{M_u}{M_y} = \frac{1}{2} \left[3 - \left(\frac{1}{\bar{\epsilon}_u^2} \right) \right] + \frac{1}{2} \frac{E_h}{E} (\bar{\epsilon}_u - \bar{\epsilon}_h) \left(1 - \frac{\bar{\epsilon}_h}{\bar{\epsilon}_u} \right) \left(2 + \frac{\bar{\epsilon}_h}{\bar{\epsilon}_u} \right) - \frac{1}{2} \frac{E_h - E_u}{E} (\bar{\epsilon}_u - \bar{\epsilon}_m) \left(1 - \frac{\bar{\epsilon}_m}{\bar{\epsilon}_u} \right) \left(2 + \frac{\bar{\epsilon}_m}{\bar{\epsilon}_u} \right)$$

Eqn. 6.8

where $\bar{\epsilon}_h = \frac{\epsilon_h}{\epsilon_y}$ $\bar{\epsilon}_m = \frac{\epsilon_m}{\epsilon_y}$ $\bar{\epsilon}_u = \frac{\epsilon_u}{\epsilon_y}$

Eqn. 6.9

6.2.1.4 Failure Modes

As already discussed in section 2.5, there are three main failure modes for a T-stub. The failure mode for a particular T-stub is governed by a parameter relating the flexural resistance of the flange to the axial resistance of the bolts as defined in Eqn. 2.11. If this parameter is related to the ultimate moment capacity, rather than the design capacity, it may be rewritten as:

$$\beta_u = \frac{4 \frac{b.t_f^2}{6} f_y \frac{M_u}{M_y}}{2B_u m} = \frac{4M_u}{2B_u m}$$

Eqn. 6.10

where B_u is the ultimate axial resistance of the bolts.

Therefore, Eqns. 2.13 – 2.15 may also be rewritten as follows to obtain the ultimate resistance for the T-stub.

$$F_{u,1} = \frac{4M_u}{m} \text{ or } F_{u,1} = \frac{(32n - 2d_w)M_u}{8mn - (m+n)d_w}$$

Eqn. 6.11

which occurs for $\beta_u \leq \frac{2\lambda}{(1+2\lambda)}$ where $\lambda = \frac{n}{m}$

$$F_{u,2} = \frac{2M_u + 2B_u n}{m+n}$$

Eqn. 6.12

which occurs for $\frac{2\lambda}{(1+2\lambda)} < \beta_u \leq 2$

$$F_{u,3} = 2B_u$$

Eqn. 6.13

which occurs for $\beta_u \geq 2$

where $F_{u,1}$ is the ultimate force corresponding to a mode 1 failure, $F_{u,2}$ is the ultimate force corresponding to a mode 2 failure and $F_{u,3}$ is the ultimate force corresponding to a mode 3 failure.

The second equation for $F_{u,1}$ takes account of the washer diameter, nut diameter and bolt head diameter as set out in Eurocode 3. Depending on the failure mode for a particular T-stub, different formulae are used to determine the ultimate plastic displacement of the section as detailed, in the following three sections.

6.2.1.5 Ultimate plastic displacement: Mode 1 failure mechanism

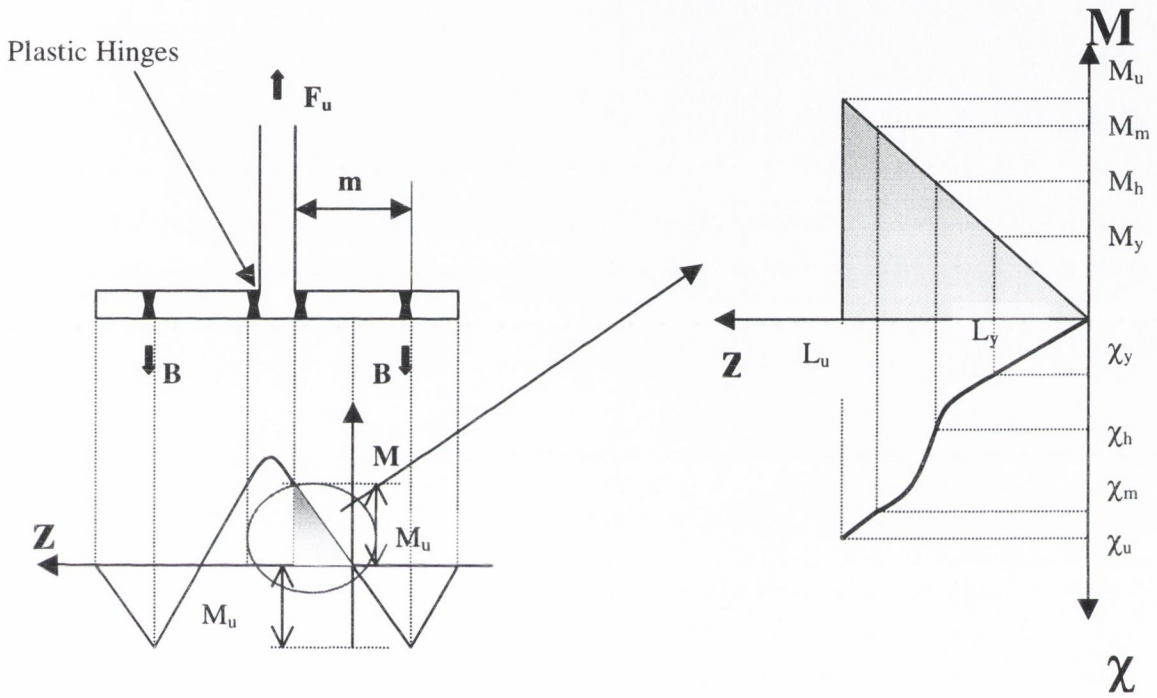


Figure 6.3: Moment-curvature diagrams for a mode 1 failure mechanism

From Figure 6.3, it may be seen that a T-stub with a mode 1 failure mechanism is subjected to double curvature between the two plastic hinges. If the distance between the point of zero moment and the plastic hinges is defined as L_u which is equal to $m/2$, the problem can be reduced to that of two equal cantilevers. The plastic displacement of the T-stub may therefore be expressed as:

$$\delta_p = 2L_u \theta_p = \theta_p m \quad \text{Eqn. 6.14}$$

where θ_p is the ultimate plastic rotation of each cantilever and is given by:

$$\theta_p = \theta_u - \theta_y = \theta_u - \frac{\chi_y L_u}{m} \quad \text{Eqn. 6.15}$$

where θ_u may be calculated as:

$$\theta_u = \int_0^{L_y} \chi(z) dz = \chi_u L_u - \int_0^{L_y} z(\chi) d\chi \quad \text{Eqn. 6.16}$$

If the elastic length of each cantilever is given by:

$$L_y = \frac{L_u}{\frac{M_u}{M_y}} \quad \text{Eqn. 6.17}$$

the following formulae may be derived:

$$\int_0^{\chi_u} z(\chi) d\chi = L_y \int_0^{\chi_y} \frac{M(\chi)}{M_y} d\chi = \frac{\chi_y L_y}{2} (1 + C_1 + C_2 + C_3) \quad \text{Eqn. 6.18}$$

$$C_1 = \frac{\int_{\chi_y}^{\chi_h} z(\chi) d\chi}{\chi_y \left(\frac{L_y}{2} \right)} = \frac{1}{\chi_y} \int_{\chi_y}^{\chi_h} \left[3 - \left(\frac{\chi_y}{\chi} \right)^2 \right] d\chi \quad \text{Eqn. 6.19}$$

$$C_2 = \frac{\int_{\chi}^{\chi_m} z(\chi) d\chi}{\chi_y \left(\frac{L_y}{2} \right)} = \frac{1}{\chi_y} \int_{\chi_h}^{\chi_m} \left[3 - \left(\frac{\chi_y}{\chi} \right)^2 \right] d\chi + \frac{1}{\chi_y} \frac{E_h}{E} \int_{\chi_h}^{\chi_m} \frac{\chi - \chi_h}{\chi_y} \left(1 - \frac{\chi_h}{\chi} \right) \left(2 + \frac{\chi_h}{\chi} \right) d\chi \quad \text{Eqn. 6.20}$$

$$C_3 = \frac{\int_{\chi_m}^{\chi_u} z(\chi) d\chi}{\chi_y \left(\frac{L_y}{2} \right)} = \frac{1}{\chi_y} \int_{\chi_m}^{\chi_u} \left[3 - \left(\frac{\chi_y}{\chi} \right)^2 \right] d\chi + \frac{1}{\chi_y} \frac{E_h}{E} \int_{\chi_m}^{\chi_u} \frac{\chi - \chi_h}{\chi_y} \left(1 - \frac{\chi_h}{\chi} \right) \left(2 + \frac{\chi_h}{\chi} \right) d\chi \\ - \frac{1}{\chi_y} \frac{E_h - E_u}{E} \int_{\chi_m}^{\chi_u} \frac{\chi - \chi_m}{\chi_y} \left(1 - \frac{\chi_m}{\chi} \right) \left(2 + \frac{\chi_m}{\chi} \right) d\chi \quad \text{Eqn. 6.21}$$

These expressions for C_{1-3} may be simplified to:

$$C_1 = 3 \frac{\chi_h}{\chi_y} + \frac{\chi_y}{\chi_h} - 4 \quad \text{Eqn. 6.22}$$

$$C_2 = \frac{\chi_h (3\chi_m^2 + \chi_y^2) - \chi_m \chi_y^2 - 3\chi_h^2 \chi_m}{\chi_y \chi_h \chi_m} + \frac{E_h}{E} \frac{(\chi_m - \chi_h)^3}{\chi_y^2 \chi_m} \quad \text{Eqn. 6.23}$$

$$C_3 = \frac{\chi_h(3\chi_m^2 + \chi_y^2) - \chi_m\chi_y^2 - 3\chi_h^2\chi_m}{\chi_y\chi_h\chi_m} + \frac{E_h}{E} \frac{(\chi_m - \chi_h)^3}{\chi_y^2\chi_m} + \frac{E_h}{E} \frac{\chi_h^2(\chi_u - \chi_m) - 3\chi_h\chi_m\chi_u(\chi_u - \chi_m) + \chi_m\chi_u(\chi_u^2 - \chi_m^2)}{\chi_m\chi_u\chi_y^2} \quad \text{Eqn. 6.24}$$

Substituting back into Eqn 6.18:

$$\int_0^{\chi_u} z(\chi) d\chi = \frac{L_y\chi_y}{2} \left(3\frac{\chi_h}{\chi_y} + \frac{\chi_y}{\chi_h} - 3 \right) + \frac{L_y\chi_y}{2} \frac{E_u}{E} \left(\frac{\chi_u^2}{\chi_y^2} + 3\frac{\chi_m^2}{\chi_y^2} - 3\frac{\chi_m\chi_u}{\chi_y^2} - \frac{\chi_u^3}{\chi_u\chi_y^2} \right) + \frac{L_y\chi_y}{2} \frac{E_h}{E} \left(\frac{\chi_m^3}{\chi_u\chi_y^2} + 3\frac{\chi_m\chi_u}{\chi_y^2} - 3\frac{\chi_m^2}{\chi_y^2} + 3\frac{\chi_h^2}{\chi_y^2} - \frac{\chi_h\chi_u}{\chi_y^2} - \frac{\chi_h^3}{\chi_u\chi_y^2} \right) \quad \text{Eqn. 6.25}$$

By incorporating Eqn 6.15. & Eqn. 6.25, the ultimate plastic rotation of the cantilever may be calculated as:

$$\theta_p = \theta_u - \theta_y = \chi_u L_u - \int_0^{\chi_u} z(\chi) d\chi - \frac{L_u\chi_y}{2} = \frac{L_u}{t_f} C \quad \text{Eqn. 6.26}$$

where:

$$C = 2 \left\{ \bar{\epsilon}_u - \frac{1}{2 \left(\frac{M_u}{M_y} \right)} \left(3\bar{\epsilon}_u + \frac{1}{\bar{\epsilon}_u} - 3 + \frac{E_h}{E} C_h + \frac{E_u}{E} C_u \right) - \frac{1}{2} \right\} \epsilon_y \quad \text{Eqn. 6.27}$$

with:

$$C_h = \frac{\bar{\epsilon}_m^3}{\bar{\epsilon}_u} + 3\bar{\epsilon}_m\bar{\epsilon}_u - 3\bar{\epsilon}_m^2 + 3\bar{\epsilon}_h^2 - 3\bar{\epsilon}_h\bar{\epsilon}_u - \frac{\bar{\epsilon}_h^3}{\bar{\epsilon}_u} \quad \text{Eqn. 6.28}$$

$$C_u = \bar{\epsilon}_u^2 - 3\bar{\epsilon}_m\bar{\epsilon}_u + \bar{\epsilon}_m^2 - \frac{\bar{\epsilon}_m^3}{\bar{\epsilon}_u} \quad \text{Eqn. 6.29}$$

Finally, by substituting back into Eqn. 6.14, the ultimate plastic displacement for a T-stub with a mode 1 failure mechanism is given by:

$$\delta_p = \theta_p m = \frac{mL_u}{t_f} C = \frac{m^2}{t_f} C \quad \text{Eqn. 6.30}$$

As may be noted, C is a parameter dependant only on the material properties.

6.2.1.6 Ultimate plastic displacement for a mode 2 failure mechanism

In the case of a mode 2 failure mechanism, the bending moment diagram between the bolt axis and the web is still in double curvature. However, the point of zero moment is not located in the centre of the section as in the mode 1 diagram. By considering the corresponding shear force for a force equal to $F_{u,2}$, the bending moment of the section at the bolt axis may be expressed as:

$$M = \xi M_u = \frac{F_{u,2}}{2} m - M_u \quad \text{Eqn. 6.31}$$

where

$$\xi = \frac{(2 - \beta_u)\lambda}{\beta_u(1 + \lambda)} \quad \text{Eqn. 6.32}$$

Referring to Figure 6.4, it may be observed that the ultimate plastic displacement of a mode 2 T-stub may be obtained using the following relationship:

$$\delta_p = \theta_{p1} m + (\theta_{p1} - \theta_{p2}) h = \theta_{p1} (1 + \lambda) m - \theta_{p2} \lambda m \quad \text{Eqn. 6.33}$$

This is true as long as two conditions are met, $\theta_{p1} - \theta_{p2} \geq 0$ and $\theta_{p2} \neq 0$, otherwise the flange does not lift at the bolt axis. In this case, $\delta_p = \theta_{p1} m$.

From this it may be recognised that θ_{p1} is given by:

$$\theta_{p1} = \frac{L_u}{t_f} C = \frac{m}{t_f(1 + \xi)} C \quad \text{Eqn. 6.34}$$

Where L_u is the distance from the point of zero moment to the location where the ultimate conditions occur.

The rotation, θ_{p2} , depends on the magnitude of ξM_u . Four cases may be identified as follows:

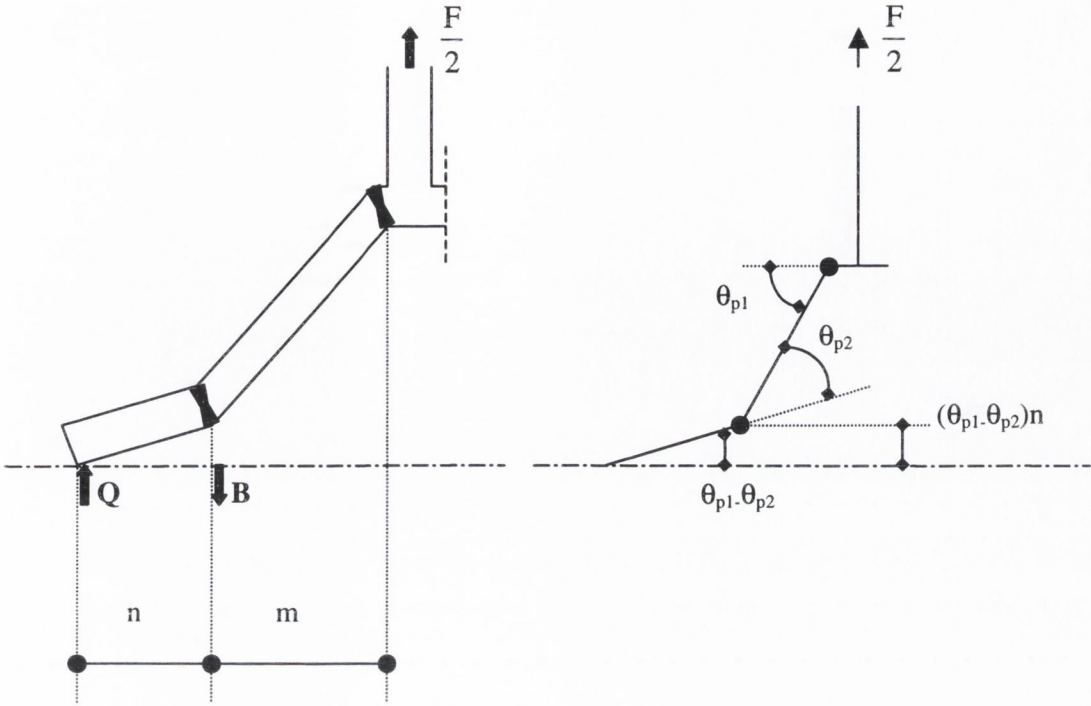


Figure 6.4: Plastic rotation for a mode 2 failure mechanism

$$\text{Case 1: } \xi \leq \xi_1 = \frac{M_y}{M_u}$$

$$\theta_{p2} = 0$$

Eqn. 6.35

This is because the section of flange close to the bolt axis remains elastic.

$$\text{Case 2: } \xi_1 < \xi \leq \xi_2$$

where:

$$\xi_2 = \frac{M_h}{M_u} = \frac{1}{2} \left[3 - \left(\frac{\chi_y}{\chi_h} \right)^2 \right] \frac{M_y}{M_u}$$

Eqn. 6.36

In this case, θ_{p2} is given by:

$$\theta_{p2} = \theta'_{p2} + \theta''_{p2}$$

Eqn. 6.37

where θ'_{p2} is the contribution to the plastic rotation due yielding of the flange between the bolt axis and the point of zero moment, and θ''_{p2} is the contribution due to the section of the T-stub between the bolt axis and the location of the prying force.

These are defined as follows:

$$\theta'_{p2} = \theta - \theta_y = \theta - \frac{\chi_y L'}{2} \quad \text{Eqn. 6.38}$$

$$\theta''_{p2} = \theta - \theta_y = \theta - \frac{\chi_y n}{2} \quad \text{Eqn. 6.39}$$

Where L' represents the distance between the point of zero moment and the bolt axis, and θ is the rotation due to the section of the flange between the bolt axis and the T-stub web, and corresponds to the attainment of F_{u2} . From Figure 6.5, it may be observed that L_y is related to L' by the following expression:

$$L_y = \frac{M_y}{\xi M_u} L' \quad \text{Eqn. 6.40}$$

For Eqn 6.38, the rotation corresponding to F_{u2} may be evaluated using the following formulae:

$$\theta = \int_0^{L'} \chi(z) dz = \chi_\xi L' - \int_0^{\chi_\xi} z(\chi) d\chi \quad \text{Eqn. 6.41}$$

$$\int_0^{\chi_\xi} z(\chi) d\chi = L_y \int_0^{\chi_\xi} \frac{M(\chi)}{M_y} d\chi = \frac{\chi_y L_y}{2} (1 + C_{1,\xi}) \quad \text{Eqn. 6.42}$$

$$C_{1,\xi} = \frac{\int_0^{\chi_\xi} z(\chi) d\chi}{\chi_y L_y / 2} = \frac{1}{\chi_y} \int_0^{\chi_\xi} \left[3 - \left(\frac{\chi_y}{\chi} \right)^2 \right] d\chi = 3 \frac{\chi_\xi}{\chi_y} + \frac{\chi_y}{\chi_\xi} - 4 \quad \text{Eqn. 6.43}$$

where χ_ξ is the curvature corresponding the bending moment ξM_u .

By substituting Eqns. 6.40 – 6.43 into Eqn 6.38, the contribution θ'_{p2} may be computed as:

$$\theta'_{p2} = \theta - \theta_y = \frac{\chi_y L'}{2} \left[2 \frac{\chi_\xi}{\chi_y} - \frac{1}{\xi} \frac{M_y}{M_u} \left(3 \frac{\chi_\xi}{\chi_y} + \frac{\chi_y}{\chi_\xi} - 3 \right) - 1 \right] = \frac{L'}{t_f} D(\xi) \quad \text{Eqn. 6.44}$$

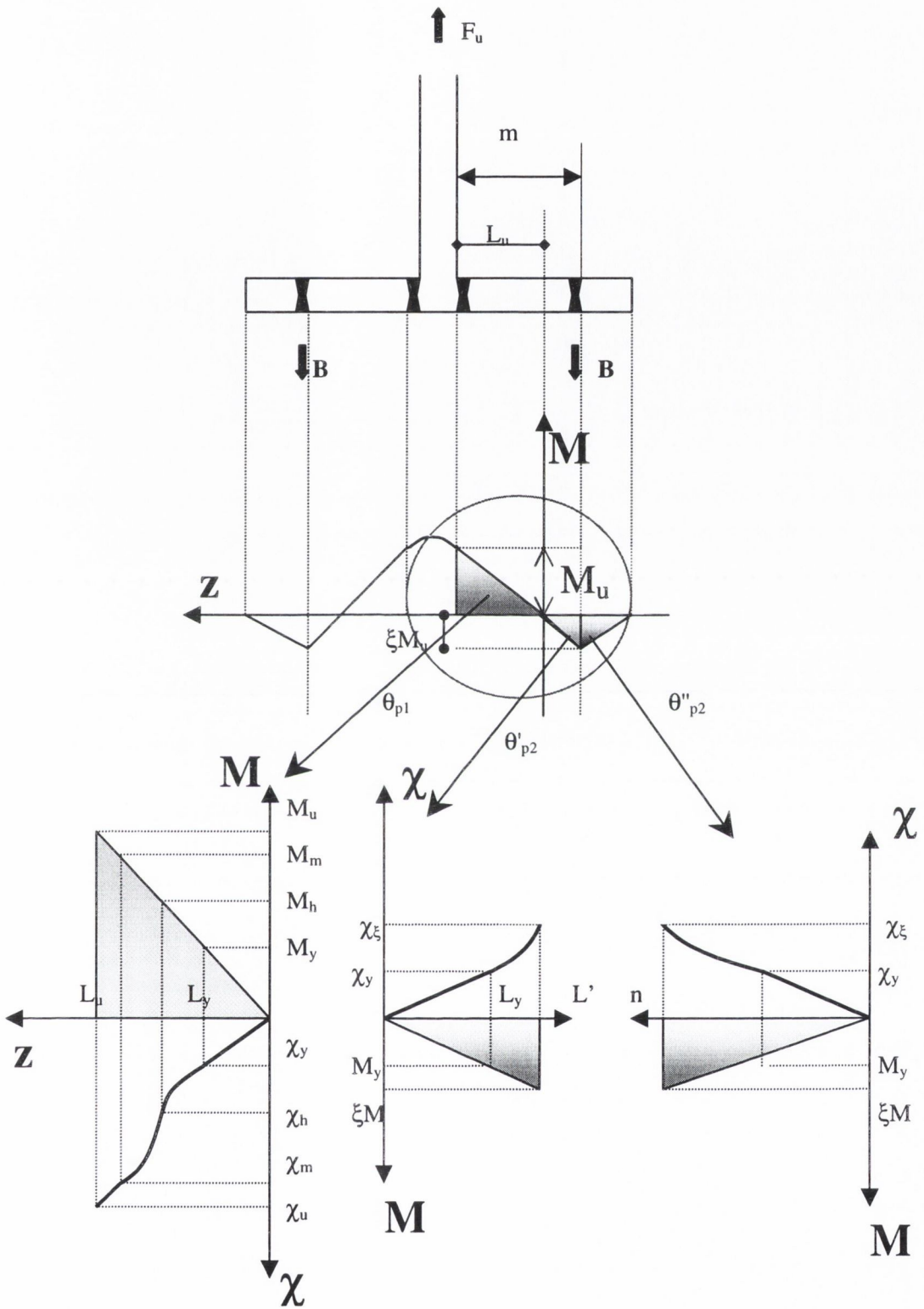


Figure 6.5: Moment-curvature diagrams for a mode 2: case 2 failure mechanism

where

$$D(\xi) = \varepsilon_y \left[2 \frac{\chi_\xi}{\chi_y} - \frac{1}{\xi} \frac{M_y}{M_u} \left(3 \frac{\chi_\xi}{\chi_y} + \frac{\chi_y}{\chi_\xi} - 3 \right) - 1 \right] \quad \text{Eqn. 6.45}$$

and χ_ξ is a function of ξ . A similar contribution to the plastic rotation is made by θ''_{p2} using the same formulae, provided that $L' = n$ is assumed. Therefore, from Eqn. 6.37, the plastic rotation at the bolt axis is determined by:

$$\theta_{p2} = \frac{L' + n}{t_f} D(\xi) \quad \text{Eqn. 6.46}$$

If $L' = \xi m / (1 + \xi)$ and $n = \lambda m$, this may be rewritten as:

$$\theta_{p2} = \frac{m}{t_f} \left(\frac{\xi}{1 + \xi} + \lambda \right) D(\xi) \quad \text{Eqn. 6.47}$$

Case 3: $\xi_2 < \xi \leq \xi_3$

where:

$$\xi_3 = \frac{M_m}{M_u} = \frac{1}{2} \frac{M_y}{M_u} \left[3 - \left(\frac{\chi_y}{\chi_m} \right)^2 \right] + \frac{E_h}{E} \left(\frac{\chi_m - \chi_h}{\chi_y} \right) \left(1 - \frac{\chi_h}{\chi_m} \right) \left(2 + \frac{\chi_h}{\chi_m} \right) \quad \text{Eqn. 6.48}$$

The plastic rotation is still calculated using Eqn. 6.37 assuming that θ'_{p2} and θ''_{p2} are correctly defined as shown in Figure 6.5.

θ'_{p2} may still be evaluated from Eqn 6.38 where the rotation corresponding to $F_{u,2}$ and:

$$\int_0^{\chi_\xi} z(\chi) d\chi = L_y \int_0^{\chi_\xi} \frac{M(\chi)}{M_y} d\chi = \frac{\chi_y L_y}{2} (1 + C_1 + C_{2,\xi}) \quad \text{Eqn. 6.49}$$

$$\begin{aligned} C_{2,\xi} &= \frac{\int_0^{\chi_\xi} z(\chi) d\chi}{\chi_y L_y / 2} = \left\{ \frac{1}{\chi_y} \int_{\chi_h}^{\chi_\xi} \left[3 - \left(\frac{\chi_y}{\chi} \right)^2 \right] d\chi + \frac{E_h}{E} \int_{\chi_h}^{\chi_\xi} \left(\frac{\chi - \chi_h}{\chi_y} \right) \left(1 - \frac{\chi_h}{\chi} \right) \left(2 + \frac{\chi_h}{\chi} \right) d\chi \right\} \\ &= \frac{\chi_h (3\chi_\xi^2 + \chi_y^2) - \chi_\xi \chi_y^2 - 3\chi_h^2 \chi_\xi}{\chi_y \chi_h \chi_\xi} + \frac{E_h (\chi_\xi - \chi_h)^3}{E \chi_\xi \chi_y^2} \end{aligned} \quad \text{Eqn. 6.50}$$

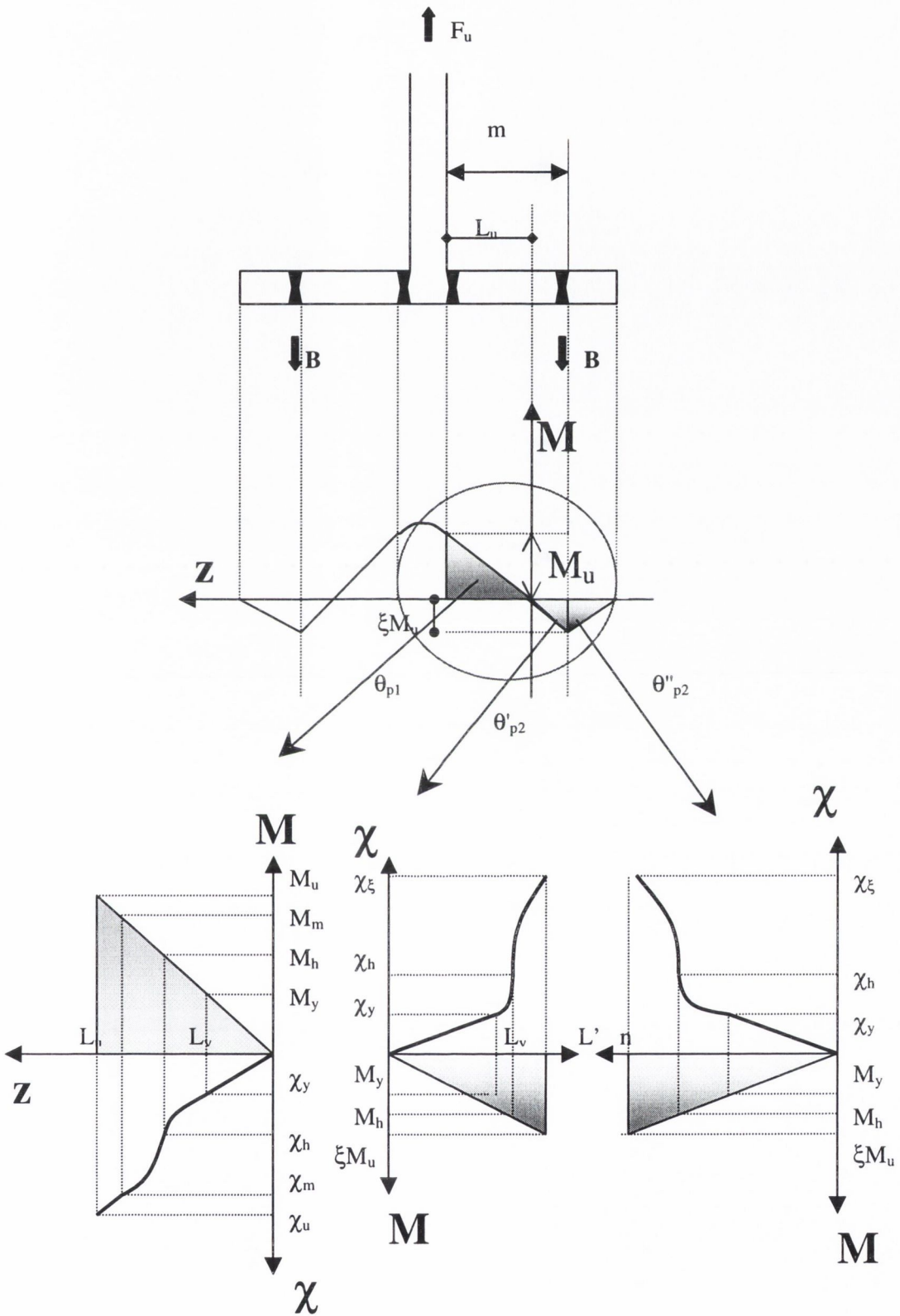


Figure 6.6: Moment-curvature diagrams for a mode 2: case 3 failure mechanism

By substituting back into Eqn.6.38, the rotation θ'_{p1} may be computed as:

$$\begin{aligned}\theta'_{p2} = \theta - \theta_y &= \frac{\chi_y L'}{2} \left[2 \frac{\chi_\xi}{\chi_y} - \frac{1}{\xi} \frac{M_y}{M_u} \left(3 \frac{\chi_\xi}{\chi_y} + \frac{\chi_y}{\chi_\xi} - 3 + \frac{E_h}{E} \frac{(\chi_\xi - \chi_h)^3}{\chi_\xi \chi_y^2} \right) - 1 \right] \\ &= \frac{L'}{t_f} F(\xi)\end{aligned}\quad \text{Eqn. 6.51}$$

where:

$$F(\xi) = \varepsilon_y \left\{ 2 \frac{\chi_\xi}{\chi_y} - \frac{1}{\xi} \frac{M_y}{M_u} \left(3 \frac{\chi_\xi}{\chi_y} + \frac{\chi_y}{\chi_\xi} - 3 + \frac{E_h}{E} \frac{(\chi_\xi - \chi_h)^3}{\chi_\xi \chi_y^2} \right) - 1 \right\} \quad \text{Eqn. 6.52}$$

As in case 3, the contribution θ''_{p2} may be calculated in a similar manner by taking $L' = n$. There θ_{p2} is given by:

$$\theta_{p2} = \frac{L' + n}{t_f} F(\xi) \quad \text{Eqn. 6.53}$$

Or, taking into account $L' = \xi m / (1 + \xi)$ and $n = \lambda m$:

$$\theta_{p2} = \frac{m}{t_f} \left(\frac{\xi}{1 + \xi} + \lambda \right) F(\xi) \quad \text{Eqn. 6.54}$$

Case 4: $\xi_3 < \xi \leq 1$

Figure 6.7 presents the moment-curvature diagrams for case 4. As before, the plastic rotation contribution may be calculated from Eqn 6.38 and Eqn 6.41 where:

$$\int_0^{\chi_\xi} z(\chi) d\chi = L_y \int_0^{\chi_\xi} \frac{M(\chi)}{M_y} d\chi = \frac{\chi_y L_y}{2} (1 + C_1 + C_2 + C_{3,\xi}) \quad \text{Eqn. 6.55}$$

and

$$\begin{aligned}C_{2,\xi} &= \frac{\int_0^{\chi_\xi} z(\chi) d\chi}{\chi_y L_y / 2} = \frac{1}{\chi_y} \int_{\chi_m}^{\chi_\xi} \left[3 - \left(\frac{\chi_y}{\chi} \right)^2 \right] d\chi + \frac{E_h}{E} \int_{\chi_m}^{\chi_\xi} \left(\frac{\chi - \chi_h}{\chi_y} \right) \left(1 - \frac{\chi_h}{\chi} \right) \left(2 + \frac{\chi_h}{\chi} \right) d\chi \\ &\quad - \frac{1}{\chi_y} \frac{E_h - E_u}{E} \int_{\chi_m}^{\chi_\xi} \left(\frac{\chi - \chi_m}{\chi_y} \right) \left(1 - \frac{\chi_m}{\chi} \right) \left(2 + \frac{\chi_m}{\chi} \right) d\chi\end{aligned}\quad \text{Eqn. 6.56}$$

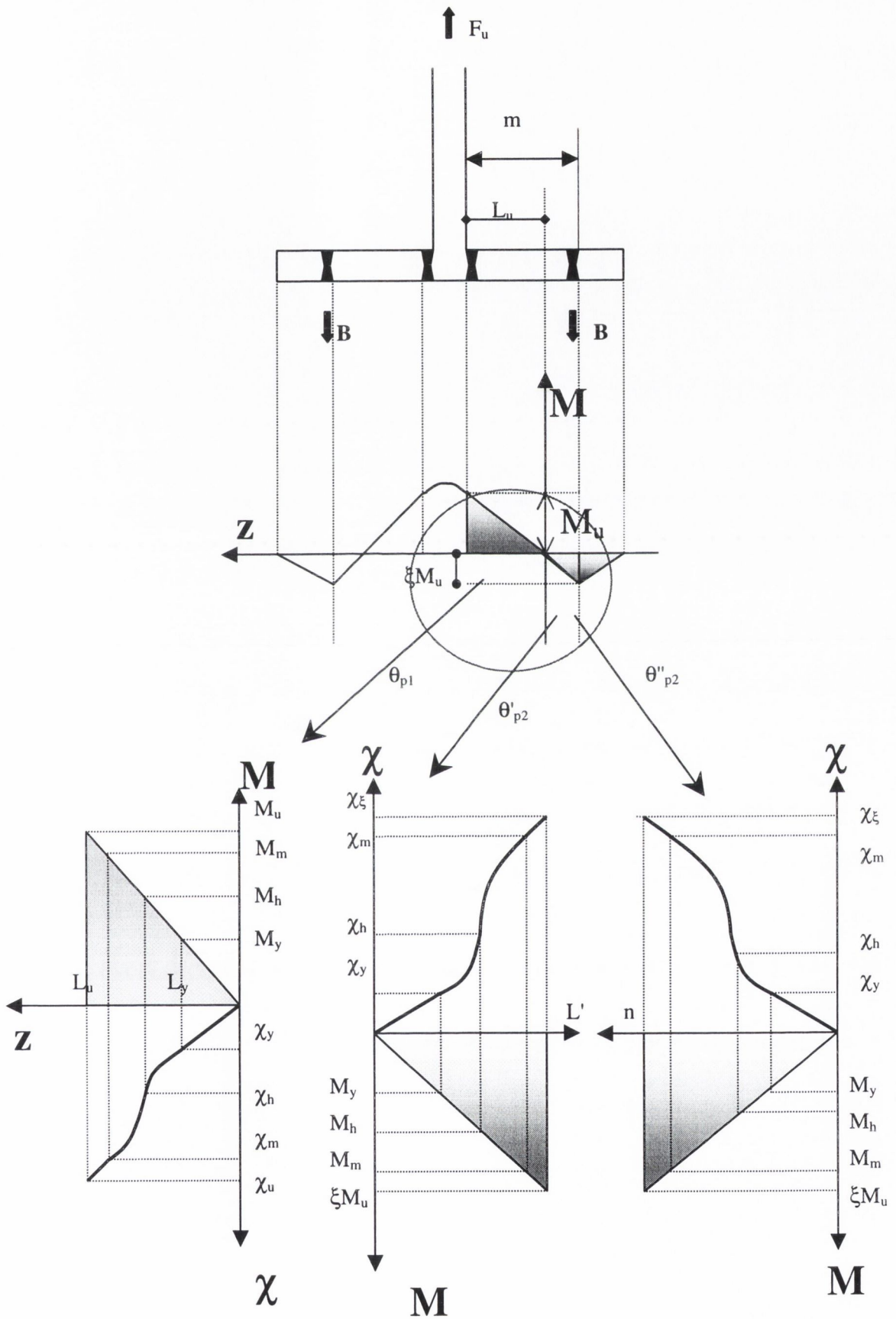


Figure 6.7: Moment-curvature diagrams for mode 2: case 4 failure mechanism

By solving the integrals, Eqn 6.56 may be expressed as

$$C_{3,\xi} = \frac{\chi_m(3\chi_\xi^2 + \chi_y^2) - \chi_\xi\chi_y^2 - 3\chi_m^2\chi_\xi}{\chi_y\chi_m\chi_\xi} + \frac{E_h - E_u}{E} \frac{(\chi_\xi - \chi_m)^3}{\chi_\xi\chi_y^2} + \frac{E_h}{E} \frac{\chi_h^2(\chi_\xi - \chi_m) - 3\chi_h\chi_m\chi_\xi(\chi_\xi - \chi_m) + \chi_m\chi_\xi(\chi_\xi^2 - \chi_m^2)}{\chi_m\chi_\xi\chi_y^2} \quad \text{Eqn. 6.57}$$

Substituting back into Eqn 6.38:

$$\theta'_{p2} = \frac{\chi_y L'}{2} \left[2 \frac{\chi_\xi}{\chi_y} - \frac{1}{\xi} \frac{M_y}{M_u} \left(3 \frac{\chi_\xi}{\chi_y} + \frac{\chi_y}{\chi_\xi} - 3 + \frac{E_h}{E} G_h + \frac{E_u}{E} G_u \right) - 1 \right] = \frac{L'}{t_f} G(\xi) \quad \text{Eqn. 6.58}$$

where:

$$G(\xi) = \varepsilon_y \left\{ 2 \frac{\chi_\xi}{\chi_y} - \frac{1}{\xi} \frac{M_y}{M_u} \left(3 \frac{\chi_\xi}{\chi_y} + \frac{\chi_y}{\chi_\xi} - 3 + \frac{E_h}{E} G_h + \frac{E_u}{E} G_u \right) - 1 \right\} \quad \text{Eqn. 6.59}$$

and

$$G_h = \frac{\chi_m^3}{\chi_\xi\chi_y^2} + 3 \frac{\chi_m\chi_\xi}{\chi_y^2} - 3 \frac{\chi_m^2}{\chi_y^2} + 3 \frac{\chi_h^2}{\chi_y^2} - \frac{\chi_h\chi_\xi}{\chi_y^2} - \frac{\chi_h^3}{\chi_\xi\chi_y^2} \quad \text{Eqn. 6.60}$$

$$G_u = \frac{\chi_\xi^2}{\chi_y^2} + 3 \frac{\chi_m^2}{\chi_y^2} - 3 \frac{\chi_m\chi_\xi}{\chi_y^2} - \frac{\chi_u^3}{\chi_\xi\chi_y^2} \quad \text{Eqn. 6.61}$$

Again a similar expression may be developed for θ'_{p2} provided that $L' = n$.

$$\theta_{p2} = \frac{L' + n}{t_f} G(\xi) \quad \text{Eqn. 6.62}$$

Hence,

$$\theta_{p2} = \frac{m}{t_f} \left(\frac{\xi}{1 + \xi} + \lambda \right) G(\xi) \quad \text{Eqn. 6.63}$$

6.2.1.7 Ultimate plastic displacement for a mode 3 failure mechanism

The ultimate plastic displacement for a T-stub with a mode 3 failure mechanism may be calculated with the following formula.

$$\delta_p = \theta_p m \quad \text{Eqn. 6.64}$$

θ_p may be determined using the same formulae given above for θ'_{p2} . However, it should be observed that the distance $L' = m$ as the point of zero moment occurs at the bolt axis and the coefficient ξ may be determined from the simplified expression:

$$\xi = \frac{M}{M_u} = \frac{B_u m}{M_u} = \frac{2}{\beta_u} \quad \text{Eqn. 6.65}$$

From, these equations it may be observed that the plastic rotation, and hence the plastic displacement are equal to zero if $\xi \leq \xi_1$.

6.2.1.8 Prediction of the force-displacement curve

In the previous sections, formulae are presented to calculate the ultimate plastic displacement of a bolted T-stub section. However, it is possible to use these expressions to determine the force-displacement curve over the loading life of the section. A quadrilinear curve, shown in Figure 6.8, may be modelled by identifying four characteristic points corresponding to the four points identified in the material law (Figure 6.2).

The first point (F_y, δ_y) corresponds to yielding of the material. The second point (F_h, δ_h) corresponds to the beginning of strain hardening while the third point (F_m, δ_m) corresponds to the achievement of the stress, f_u . The final point (F_u, δ_u) corresponds to the attainment of the ultimate conditions of the material. It should be noted that the original model as proposed by Faella et al (2000) was developed to compute the force-displacement curve of two equal T-stubs rather than the general case of two unequal sections encountered in this study. To calculate the overall force-displacement curve, a curve is first calculated for each T-stub separately, and these are combined at a later stage.

For a **Mode 1** failure mechanism, the force levels corresponding to the four points mentioned above may be computed by means of the following relationship:

$$F = \frac{(32n - 2d_w)M}{8mn - (m + n)d_w} \quad \text{Eqn. 6.66}$$

for, where $M_y - M_u$ are defined in section 6.2.1.3.:

- $F = F_y$ for $M = M_y$;
- $F = F_h$ for $M = M_h$;
- $F = F_m$ for $M = M_m$; and
- $F = F_u$ for $M = M_u$;

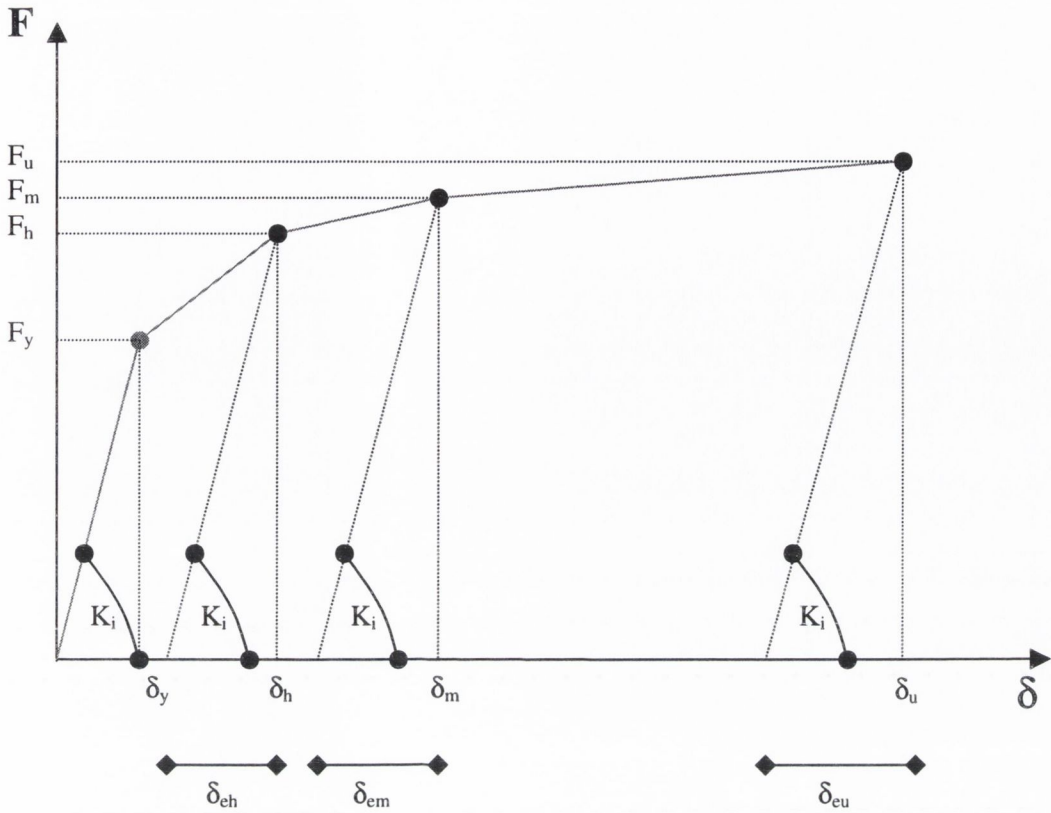


Figure 6.8: Quadrilinear modelling of the force-displacement curve

The displacement corresponding to the first yield point may be computed as F_y/K where K is the stiffness of the T-stub element and is given by:

$$K = 0.5E \frac{b_{\text{eff}} t_f^3}{m^3} \quad \text{Eqn. 6.67}$$

where b_{eff} is the effective *stiffness* width of the rectangular section and E is Young's modulus for steel. The yield displacement of a bolted T-stub section can then be computed as the displacement due to the plate section and the displacement due to the bolts and may be expressed as:

$$\delta_y = \frac{F_y}{K} + \delta_{b,y} \quad \text{Eqn. 6.68}$$

Where $\delta_{b,y}$ is the bolt elongation due to the force F_y :

$$\delta_{b,y} = \frac{B}{\left(\frac{EA_b}{L_b} \right)} = \frac{\frac{F_y}{2} + \frac{M_y}{n}}{\left(\frac{EA_b}{L_b} \right)} \quad \text{Eqn. 6.69}$$

Therefore the initial stiffness of the bolted T-stub section may be computed as:

$$K_i = \frac{F_y}{\delta_y} \quad \text{Eqn. 6.70}$$

The displacement corresponding to the beginning of the strain hardening curve, i.e. δ_h , is given by:

$$\delta_h = \delta_{eh} + \delta_{ph} \quad \text{Eqn. 6.71}$$

where $\delta_{eh} = F_h/K_i$ and is the elastic section of the curve and δ_{ph} is the plastic section of the curve.

This may be calculated using Eqn. 6.46 remembering that $L' = m/2$, giving:

$$\delta_{ph} = \theta'_{p2h} m = \frac{m^2}{2t_f} D(\xi_2) \quad \text{Eqn. 6.72}$$

where $D(\xi_2)$ is $D(\xi)$ evaluated for $\xi = \xi_2$ and $\chi_\xi = \chi_h$. It is useful to note that $D(\xi_2)$ is a constant related to the material properties and is presented in Table 6.2 along with other similar material dependent properties, determined using the properties presented in Table 6.1.

M_h/M_y	M_h/M_y	M_h/M_y	C	ξ_1	ξ_2	ξ_3	$D(\xi_2)$	$F(\xi_3)$
1.496	1.974	3.105	0.184	0.322	0.482	0.627	0.0012	0.0155

Table 6.2: Parameters depending on material properties

Similarly, it may be observed that the displacement corresponding to the stress f_u is given by:

$$\delta_m = \delta_{em} + \delta_{pm} \quad \text{Eqn. 6.73}$$

where $\delta_{em} = F_m/K_i$ and δ_{pm} is the plastic displacement at this stress level. Again, recalling that $L' = m/2$, δ_{pm} may be computed using Eqn. 6.52 giving

$$\delta_{pm} = \theta'_{p2m} m = \frac{m^2}{2t_f} F(\xi_3) \quad \text{Eqn. 6.74}$$

where $F(\xi_3)$ is the value of the function $F(\xi)$ evaluated at the point when the material attains a stress of f_u , so that $\chi_\xi = \chi_m$ and $\xi = \xi_3$. Finally the ultimate displacement of the of the T-stub may be computed from the following expression:

$$\delta_u = \delta_{eu} + \delta_{pu} \quad \text{Eqn. 6.75}$$

where $\delta_{eu} = F_u/K_i$ and δ_{pu} is the ultimate plastic displacement calculated using the expressions in section 6.3.1.4.

For a specimen subject to a **mode 2** failure mechanism, it may be observed that the ultimate force may be determined from Eqn 6.12, which in turn may be rewritten to give the force at a particular moment level:

$$F_{u,2} = \frac{2M_u}{m}(1 + \xi) \Rightarrow F = \frac{2M}{m}(1 + \xi) \quad \text{Eqn. 6.76}$$

The displacement at the yielding point may still be determined from Eqn. 6.67 and 6.68, but in this case, the elongation of the bolts is given by:

$$\delta_{b,y} = \frac{B}{\left(\frac{EA_b}{L_b}\right)} = \frac{\frac{F_y}{2} + \frac{\xi M_y}{n}}{\left(\frac{EA_b}{L_b}\right)} \quad \text{Eqn. 6.77}$$

For a mode 2 specimen, the location of the plastic hinge in the section is at a distance $L' = m/(1+\xi)$. From Eqn. 6.44 and 6.45, the plastic displacement may be determined from the following equations, again taking into account that $\xi = \xi_2$:

$$\theta_{p1h} = \frac{m}{t_f} \left(\frac{\xi}{1+\xi} + \lambda \right) D(\xi_2) \quad \text{Eqn. 6.78}$$

When the bending moment reaches the M_h value, the corresponding moment at the bolt axis is equal to δM_u and may be expressed as:

$$\xi_2^* = \frac{\xi M_h}{M_u} = \xi \frac{M_h}{M_y} \frac{1}{M_u/M_y} \quad \text{Eqn. 6.79}$$

It may be concluded that $\theta_{p2h} =$ is equal to zero when $\xi_2^* \leq \xi_1$, while for $\xi_2^* > \xi_1$, Eqn. 6.45 provides:

$$\theta_{p2h} = \frac{m}{t_f} \left(\frac{\xi}{1+\xi} + \lambda \right) D(\xi_2^*) \quad \text{Eqn. 6.80}$$

Where $D(\xi_2^*)$ is the value of the function $D(\xi)$ for $\xi = \xi_2^*$, and χ_ξ is the curvature corresponding to $\xi_2^* M_u$. Referring to Eqn. 6.33, the plastic distance of the T-stub corresponding to strain hardening is given by:

$$\delta_{ph} = \theta_{p1h} (1 + \lambda)m - \theta_{p1h} \lambda m \quad \text{Eqn. 6.81}$$

provided that $\theta_{p1h} > \theta_{p2h}$, else:

$$\delta_{ph} = \theta_{p1h} m \quad \text{Eqn. 6.82}$$

A similar method may be used to determine the plastic displacement at the stress level, f_u , or the bending moment M_m , to obtain the following expression:

$$\theta_{p1m} = \frac{m}{t_f} \left(\frac{\xi}{1 + \xi} + \lambda \right) F(\xi_3) \quad \text{Eqn. 6.83}$$

When the T-stub achieves the moment M_m , the moment at the bolt axis is equal to ξM_u which may be expressed as:

$$\xi_3^* = \frac{\xi M_m}{M_u} = \xi \frac{M_m}{M_y} \frac{1}{M_u / M_y} \quad \text{Eqn. 6.84}$$

Therefore, the plastic rotation of the hinge located at the bolt axis may be determined from the following expressions:

$$\theta_{p2m} = 0 \quad \text{for} \quad \xi_3^* < \xi_1 \quad \text{Eqn. 6.85}$$

$$\theta_{p2m} = \frac{m}{t_f} \left(\frac{\xi}{1 + \xi} + \lambda \right) D(\xi_3^*) \quad \text{for} \quad \xi_1 < \xi_3^* \leq \xi_2 \quad \text{Eqn. 6.86}$$

$$\theta_{p2m} = \frac{m}{t_f} \left(\frac{\xi}{1 + \xi} + \lambda \right) F(\xi_3^*) \quad \text{for} \quad \xi_2 < \xi_3^* \leq \xi_3 \quad \text{Eqn. 6.87}$$

where $F(\xi_3^*)$ is the value of the function $F(\xi)$ for $\xi = \xi_3^*$ and χ_ξ is the curvature corresponding to the moment $\xi_3^* M_u$. again referring to the geometry and Eqn 6.33, the plastic displacement of the T-stub may be computed as:

$$\delta_{pm} = \theta_{p1m} (1 + \lambda)m - \theta_{p1m} \lambda m \quad \text{Eqn. 6.88}$$

for $\theta_{p1m} > \theta_{p2m}$, else:

$$\delta_{pm} = \theta_{p1m} m \quad \text{Eqn. 6.89}$$

The ultimate displacement of the T-stub may be calculated using Eqn. 6.75 where δ_{pu} is the ultimate plastic displacement calculated from the expressions in section 6.3.1.5.

Regarding the **mode 3** failure mechanism, four cases may be identified which depends on the ratio of bolt axial stiffness to T-stub flexural stiffness. The first case is for $\xi \leq \xi_1$. In this case, the T-stubs do not undergo any plastic deformation so that $\delta_p = 0$ and the force-displacement curve develops linearly up to the force B_{um} .

The second case occurs for $\xi_1 < \xi \leq \xi_2$ and the force-displacement curve flows a bilinear relationship. The force for yielding of the T-stub is:

$$F_y = \frac{2M_y}{m} \quad \text{Eqn. 6.90}$$

As prying forces do not develop the displacement is calculated using:

$$\delta_y = \frac{F_y}{K} \quad \text{Eqn. 6.91}$$

where K is determined using Eqn. 6.67. The ultimate plastic displacement may be calculated from Eqn 6.75 where the plastic rotation is given by:

$$\theta_{pu} = \frac{m}{t_f} D(\xi) \quad \text{Eqn. 6.92}$$

which is found by recalling that for a mode 3 failure $L' = m$. As the ultimate force for the T-stub must be equal to $F_u = 2B_u$, the ultimate total displacement is expressed as:

$$\delta_u = \frac{F_u}{K} + \frac{m^2}{t_f} D(\xi) \quad \text{Eqn. 6.93}$$

The third case is for $\xi_2 < \xi \leq \xi_3$ and hence the force-displacement curve follows a tri-linear pattern. Eqn. 6.92 and 6.93 give the first point on the curve corresponding to yielding of the T-stub. The point corresponding to the occurrence of strain hardening (F_h, δ_h) may be found directly from Eqn. 6.93:

$$F_h = \frac{2M_h}{m} \quad \text{Eqn. 6.94}$$

$$\delta_h = \frac{F_h}{K} + \frac{m^2}{t_f} D(\xi_2) \quad \text{Eqn. 6.95}$$

In addition, it may be observed that the ultimate displacement for a force of $F_u = 2B_u$ may be given as:

$$\delta_u = \frac{F_u}{K} + \frac{m^2}{t_f} F(\xi) \quad \text{Eqn. 6.96}$$

Where the second part is obtained from Eqn. 6.51, noting that $L' = m$. The final case is for $\xi > \xi_3$ in which case, the force-displacement curve is quadrilinear. Similarly, to Eqns. 6.94 and 6.95, the point corresponding to the attainment of the moment level, M_m may be computed to give:

$$F_m = \frac{2M_m}{m} \quad \text{Eqn. 6.97}$$

$$\delta_m = \frac{F_m}{K} + \frac{m^2}{t_f} F(\xi_3) \quad \text{Eqn. 6.98}$$

As before, the ultimate displacement for a force $2B_u$ may be determined from the following formula:

$$\delta_u = \frac{F_u}{K} + \frac{m^2}{t_f} G(\xi) \quad \text{Eqn. 6.99}$$

Where the second part is found immediately from Eqn. 6.58 for $L' = m$.

Using these methods, the entire force-displacement curve displayed by a T-stub section may be determined and used in the overall joint model as described in section 6.2.3.

6.2.1.9 Proposed Change to the T-stub model

As the above T-stub model was developed for use with extended end-plate joints and not the flush end-plate joints investigated in this study, it was necessary to adapt the model slightly. It was found that the predicted moment resistance gave a good correlation to the experimental values. However, the initial stiffness of the joints was much higher than that observed. This was not unexpected as it is well accepted that flush end-plate joints often have a lower initial stiffness than extended end-plate joints, as well as lower resistance values. This is illustrated in Figure 6.9. Based on this observation, Eqn. 6.67 was amended to more accurately predict the initial stiffness of a flush end-plate joint.

The original model assumes that b_{eff} , the effective stiffness width for the rectangular section, is given by the following formula:

$$b_{\text{eff}} = 2m + d_h \leq b \quad \text{Eqn. 6.100}$$

where m is a geometrical parameter equal to the distance from the centre of the bolt hole to the beam flange (Figure 6.4) and d_h is the diameter of the bolt head. This value was varied, and its effect on joint stiffness observed. It was seen that assuming that b_{eff} equalled m gave a much improved comparison between the predicted initial stiffness and the experimental stiffnesses of the test specimens.

Brown et al (2001) employed similar assumptions in their initial stiffness model which was discussed in section 2.8.1.2. In this model, it is assumed that the end-plate and the column flange are the only significant contributors to the initial stiffness. The authors observed that the idealised yield line pattern in the vicinity of the bolts was a circular pattern. Taking this as the area which will be deformed by the applied load, they projected that it is reasonable to assume that the stiffness of the T-stub also acts over this length, m . This is illustrated in Figure 6.10.

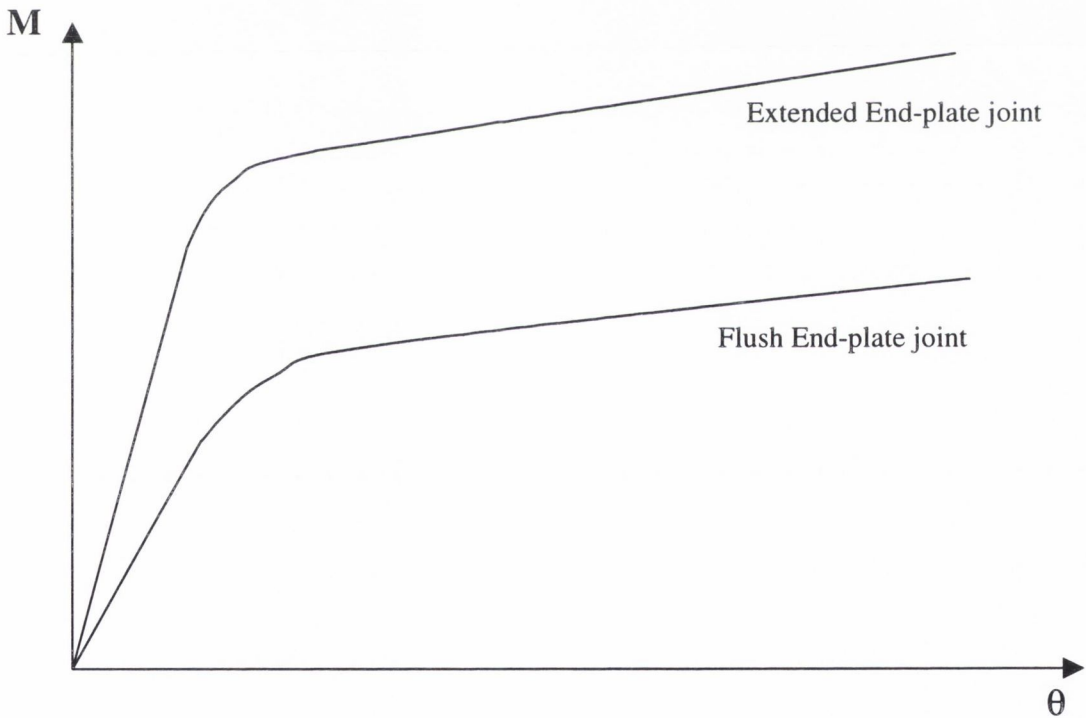


Figure 6.9: Typical moment-rotation for extended and flush end-plate joints

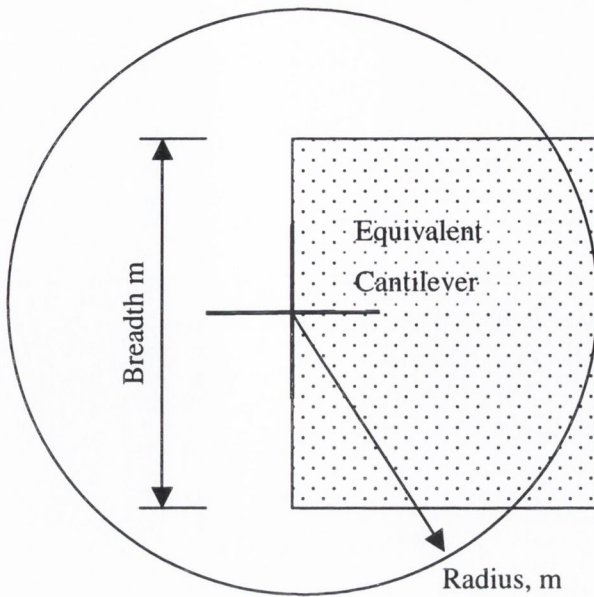
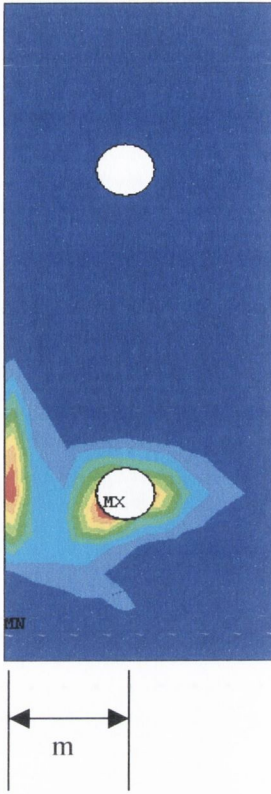


Figure 6.10: Equivalent length and breadth for cantilever approximation (Brown et al, 2001)

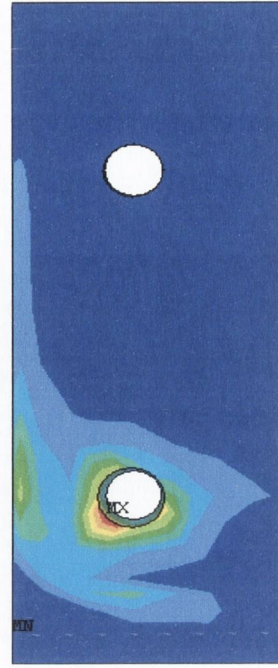
Therefore, Eqn. 6.67 may be rewritten as:

$$K = 0.5E \frac{b_{\text{eff}} t_f^3}{m^3} = 0.5E \frac{t_f^3}{m^2} \quad (b_{\text{eff}} = m) \quad \text{Eqn. 6.101}$$

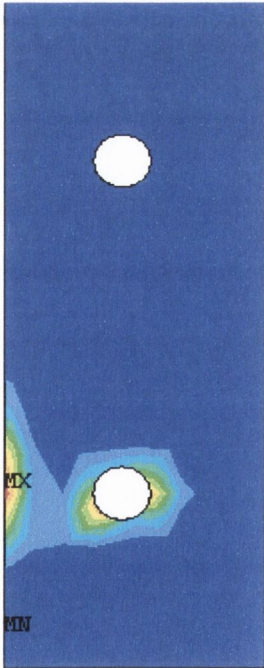
Results from the finite element modelling of flush end-plate joints carried out by Tucker (2002) were examined to investigate the extent of the deformed area over which the end-plate stiffness depends. The joints modelled by Tucker are identical to those tested as part of this study. Plots of the distribution of the equivalent strains in the end-plate were produced at a number of different displacement levels for different joints. Examples of these are shown in Figure 6.11. As these are equivalent strain plots, the contours do not give strain directly, but rather an indication of the magnitude. The blue is very low strain with the red being the highest strain levels. The ratio of high to low strain in each case is approximately 100. It may be observed that the strains are concentrated around the bolt holes in semi-circular patterns. The diameter of these patterns is approximately equal to the distance m . From this, it was determined that by allowing b_{eff} to be equal to m for flush end-plates with one bolt-row in tension, an accurate prediction of the initial stiffness of the T-stub may be obtained.



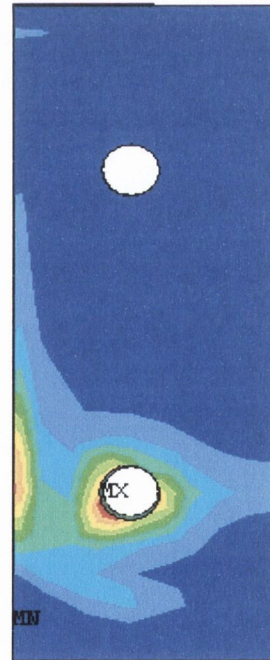
(a) Specimen 3.1 End-Plate
(Disp. = 3mm)



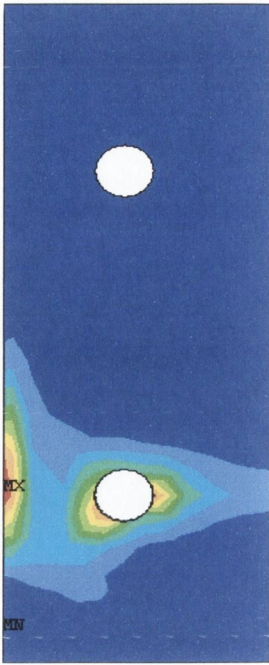
(b) Specimen 3.1 End-Plate
(Disp. = 5mm)



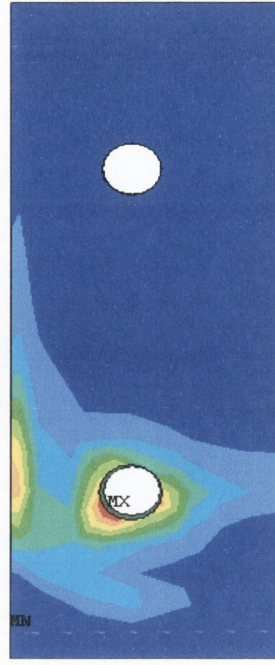
(c) Specimen 3.5 End-Plate
(Disp. = 5mm)



(d) Specimen 3.5 Column Flange
(Disp. = 14mm)



(e) Specimen 3.7 End-Plate
(Disp. = 4mm)



(f) Specimen 3.7 End-Plate
(Disp. = 10mm)

Figure 6.11: Equivalent plastic strains of end-plate (Tucker, 2002)

6.2.2 Column Web Modelling

The stress-strain relationship for the column web is taken as an elastic-perfectly plastic so that when the applied moment reaches the plastic moment, the component acts as a plastic hinge. This is shown in Figure 6.1.

6.2.2.1 Column Web in Shear

The rotation attributed to the shear deformation, θ_s , is given by:

$$\theta_s = \frac{Q}{GA_v} \quad \text{Eqn. 6.102}$$

where Q is the shear force on the column taken as being equal to the T-stub force, G is the elastic shear modulus and A_v is the shear area of the column. These are defined as follows:

$$G = \frac{E}{2(1+\nu)} \quad \text{Eqn. 6.103}$$

$$A_v = A - 2bt_f + (t_w + 2r)t_f \quad \text{Eqn. 6.104}$$

Where E , ν , A , b , t_f , t_w and r are Young's modulus of steel, Poisson's Ratio, section area, flange width, flange thickness, web thickness and fillet radius of the column respectively. If the shear force exceeds the yield strength of the steel (i.e. $Q \geq f_y A_v / \sqrt{3}$) it is assumed that the web can no longer support further increases in moment.

6.2.2.2 Column Web in Tension

The column web rotation under tension, θ_{wt} , is given as:

$$\theta_{wt} = \left(\frac{N}{EA_t} \right) \left(\frac{d}{h_t} \right) \quad \text{Eqn. 6.105}$$

where N is the resultant tensile force taken as being equal to the T-stub force, A_t is the effective area of the web in tension = $t_w b_{eff,t}$, $b_{eff,t}$ is the effective width of the column web in tension as calculated by Eurocode 3, h_t is the distance from the tensile force to the centre of compression taken as being equal to the lever arm, and d is the depth between the column fillets. This is illustrated in Figure 6.12.

When the tensile force exceeds the yield strength ($N_t = f_y A_t$), it is assumed that the moment may not be further increased.

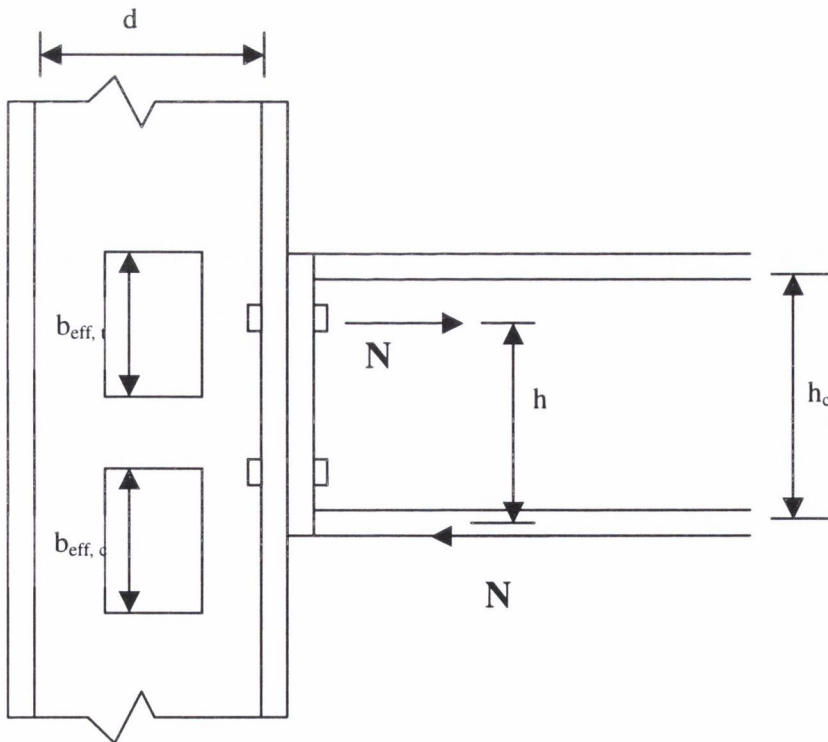


Figure 6.12: Column web effective widths

6.2.2.3 Column Web in Compression

As in the case of the column web under tension, the rotation due to the compression forces, θ_{wc} , is given by the following expression:

$$\theta_{wc} = \left(\frac{N}{EA_c} \right) \left(\frac{d}{h_c} \right) \quad \text{Eqn. 6.106}$$

where N is the resultant compressive force taken as being equal to the T-stub force, A_c is the effective area of the web in compression = $t_w b_{eff,c}$, $b_{eff,c}$ is the effective width of the column web in compression as calculated by Eurocode 3, h_c is equal to the beam depth minus the beam flange thickness, and d is the depth between the column fillets, as shown in Figure 6.10. When the compression force exceeds the yield strength ($N_c = f_y A_c$), it is assumed that the moment may not be further increased. At this point it is assumed that the deformation is infinitely large and the compression zone may buckle or yield.

6.2.3 Non-linear Moment-Rotation Modelling of Full Joint

From the deformation expressions detailed above, the non-linear moment-rotation characteristics for a joint may be determined. The relationship is controlled by a displacement control method where a rotational deformation θ is applied, and the corresponding moment calculated. Separate force-displacement plots are determined for the two T-stubs present in the joint, i.e. . one T-stub comprising of the end-plate and beam web, and a second T-stub comprising of the column flange and web. These two curves are then combined by ensuring that the same force acts on both T-stubs. From this a single force-displacement curve is obtained, as shown in Figure 6.13. The following steps provide the full moment-rotation relationship.

- A rotational deformation, θ_t , is imposed on the T-stub. The corresponding T-stub deformation is given by:

$$\delta = \theta_t h \quad \text{Eqn. 6.107}$$

where h is the length of the lever arm (Figure 6.1), taken as the distance from the centre of the beam flange in compression (rotation centre) to the bolt row in tension.

- The force due to this T-stub deformation, and hence the imposed rotation, may be determined from the T-stub force displacement curve previously calculated. The bending moment due to this force is given by

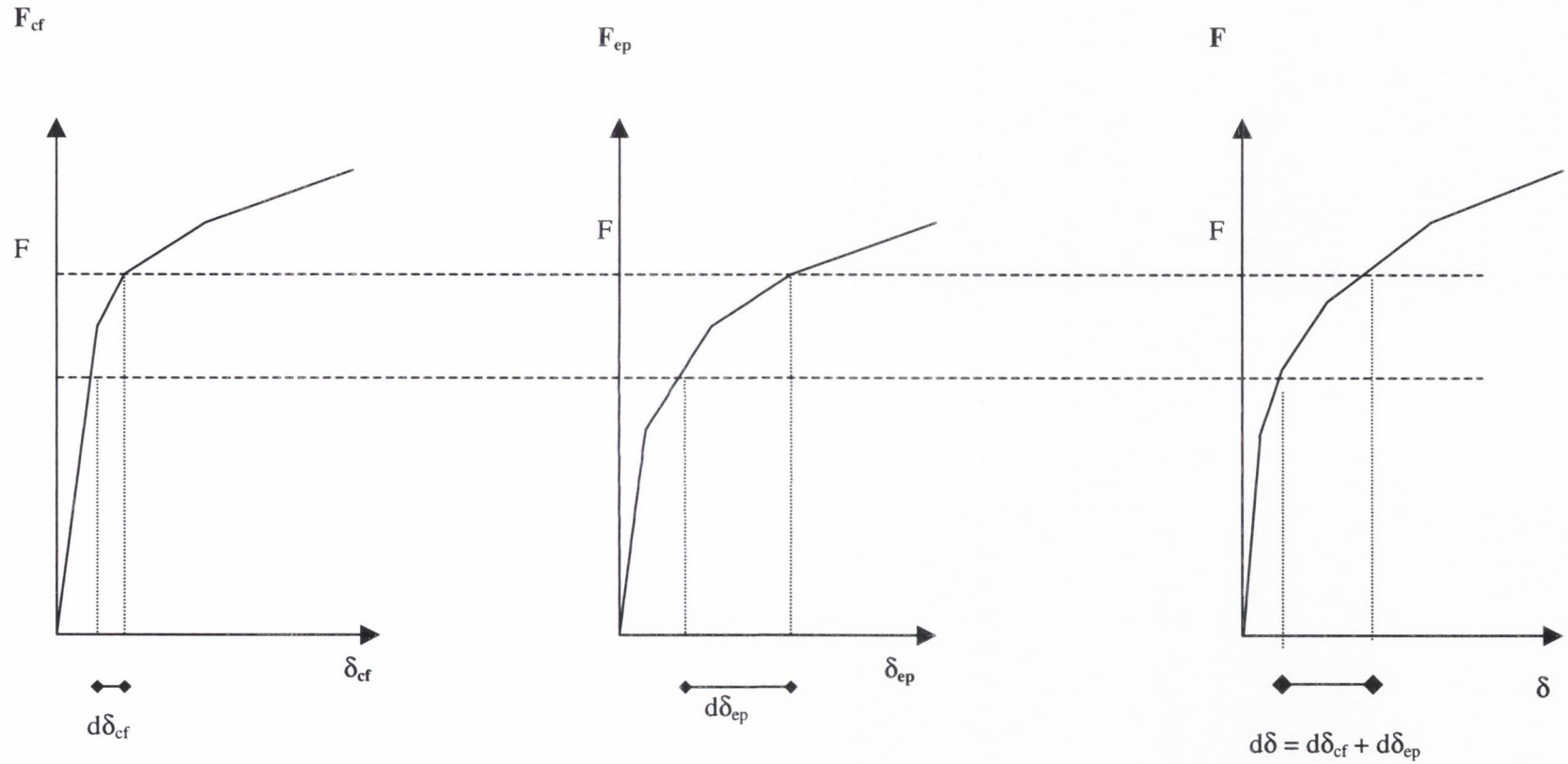
$$M = F \times h \quad \text{Eqn. 6.108}$$

- This bending moment produces additional deformations due to compression, tension and shear of the column web. These may be determined from the equations in section 6.3.2. These forces are calculated and checked to ensure that the column web has not yielded under the above conditions.
- The total joint rotation caused by the bending moment M computed above is given by:

$$\theta = \theta_t + \theta_s + \theta_{wc} + \theta_{wt} \quad \text{Eqn. 6.109}$$

By varying θ_t , a set of moment-rotation values are obtained.

- The above steps are then repeated until the maximum moment is obtained or one of the components fails. A full set of calculations is provided in Appendix C.



(a) Column Flange T-stub force-displacement curve

(b) End-plate T-stub force-displacement curve

(c) Combined T-stub force-displacement curve

Figure 6.13: Coupling between T-stub force-displacement curves

6.3 Model Validation

Table 6.3 compares the proposed model and experimental moment-rotation characteristics for Test Series Two and Three. As the model predicts a monotonic force-displacement curve and the majority of the tests carried out in this study were cyclic, the prediction characteristics are compared to the cyclic response skeleton curve where necessary. As many of the specimens have identical geometrical properties, it was only necessary to model six joint configurations. These were the four configurations for Test Series 3 and two for Test Series 2. In Test Series 2, specimens 2.1 and 2.2 have identical geometrical properties and, therefore identical model properties. The model is incapable of predicting the behaviour of specimen 2.4 as it cannot take the mixture of nut and bolt grades into account. However, this specimen has been included with specimens 2.1 and 2.2 as all other joint properties are the same. Specimens 2.5 – 2.8 are also identical and therefore also have the same model properties. Specimen 2.3 is not modelled as the experimental results are not considered reliable. In each case, the ultimate moment of the joint model was taken as that at a rotation of approximately 65 mrad.

Specimen	$\frac{S_{i,Model}}{S_{i,exp}}$	$\frac{\theta_{y,Model}}{\theta_{y,exp}}$	$\frac{M_{y,Model}}{M_{y,exp}}$	$\frac{M_{ult,Model}}{M_{ult,exp}}$
2.1	0.55	1.40	0.79	0.83
2.2	1.15	0.85	0.84	0.89
2.4	1.03	1.18	1.05	1.15
2.5	2.56	0.45	1.15	N/A
2.6	3.07	0.46	1.39	N/A
2.7	2.18	0.66	1.44	N/A
2.8	3.57	0.38	1.36	N/A
3.1	1.21	0.99	0.96	1.03
3.2	0.77	2.05	1.25	1.16
3.3	1.98	0.50	0.77	0.90
3.4	1.74	0.54	0.73	0.89
3.5	0.77	1.40	0.89	0.85
3.6	0.86	1.34	0.95	0.94
3.7	0.86	1.17	0.87	0.97
3.8	0.76	1.23	1.03	1.10

Table 6.3: Comparison between model and experimental results

S_i is the initial stiffness of the joint, θ_y is the yield rotation of the joint, M_y is the yield moment capacity of the joint and M_{ult} is the ultimate moment capacity of the joint.

The only exceptions to this are for specimens 2.5 – 2.8 where the ultimate moment of the model occurred at lower rotations, and specimens 3.3 and 3.4 where the ultimate moment is taken at the failure rotation of the experimental specimens.

As may be observed in Table 6.3, the model displays good agreement with experimental results in most of the cases. Specimens 2.5 – 2.8 and specimens 3.3 and 3.4 show significant differences between the predicted initial stiffness and the experimental values for specimens 2.5 - 2.8. The ratio of predicted to experimental ultimate moment capacity is not given as the model predicts no plastic bending in the end-plate of these specimens.

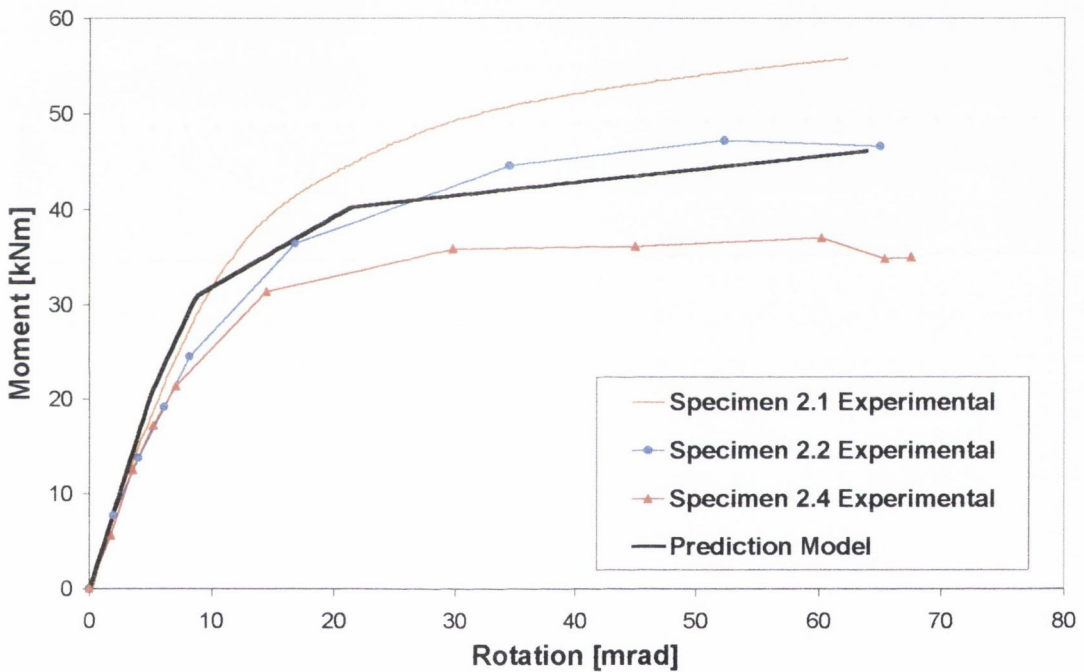


Figure 6.14: Prediction and experimental curves for specimens 2.1, 2.2 and 2.4

Figure 6.14 compares the model prediction moment-rotation curve and the experimental curves for specimens 2.1, 2.2 and 2.4. As may be observed, the model appears to give a good correlation to the experimental results, especially for specimen 2.2. The initial stiffness of the model was 4.08 kNm/mrad. This is lower than that measured in specimen 2.1, which was tested monotonically. However, it must be noted that the experimental stiffness of this specimen was the highest observed in either test series. The initial stiffnesses of specimens 2.2 and 2.4, however, are much more accurate, with differences of only 15% and 3% between the predicted and experimental results. In contrast, a difference of 222% was observed between the experimental stiffness and the Eurocode 3

design stiffness. Similar improvements over the Eurocode 3 model are achieved for the yield rotation and moment characteristics for these specimens.

Figure 6.15 presents the predicted and experimental moment-rotation curves for specimen 2.5. The same curve is generated for specimens 2.6 – 2.8 but the experimental results for those specimens are not shown here. The predicted stiffness is much higher than the experimental value. As may be observed, the model predicts a linear elastic curve up to failure. This is because the model does not take into account the rotation due to the bolts when determining the plastic rotation of a joint.

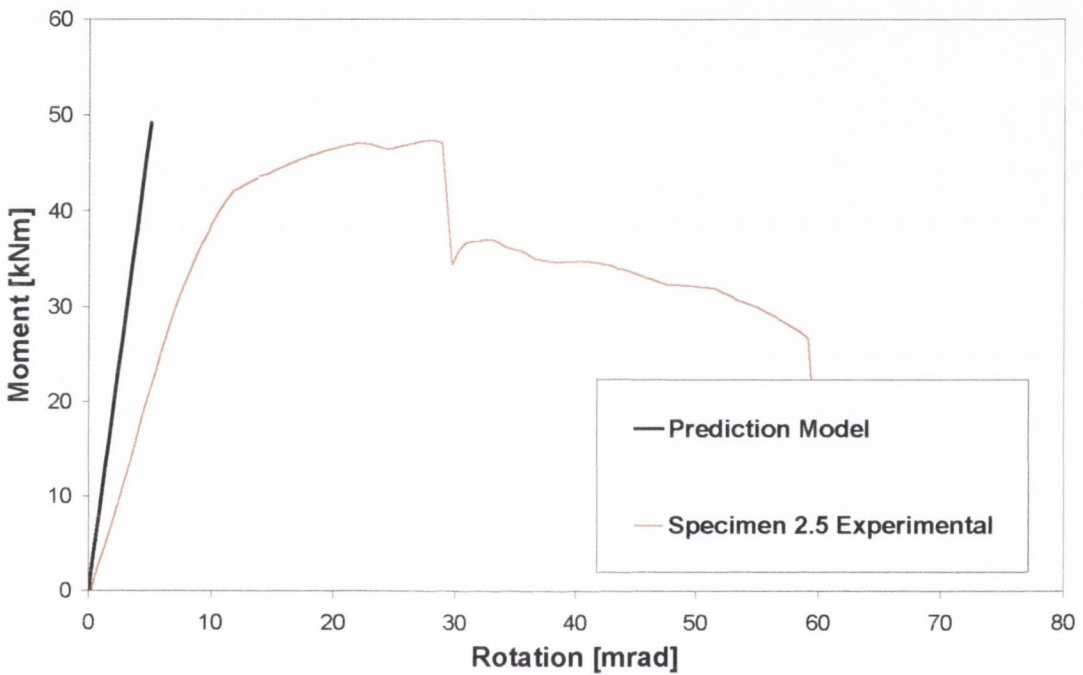


Figure 6.15: Prediction and experimental curves for specimens 2.5

Figure 6.16 displays the predicted and experimental moment-rotation curves for specimens 3.1 and 3.2. As may be observed, the two curves give a good agreement. The initial stiffness is higher than the experimental value for specimen 3.1, but slightly lower than that of specimen 3.2. The predicted and experimental yield rotations are within 1% for specimen 3.1. In contrast, there is a difference of 105% for specimen 3.2. This is attributable to the higher initial stiffness displayed by the specimen compared to the predicted results. The yield and ultimate moment resistance comparisons show good correlations between the predicted and the experimental results.

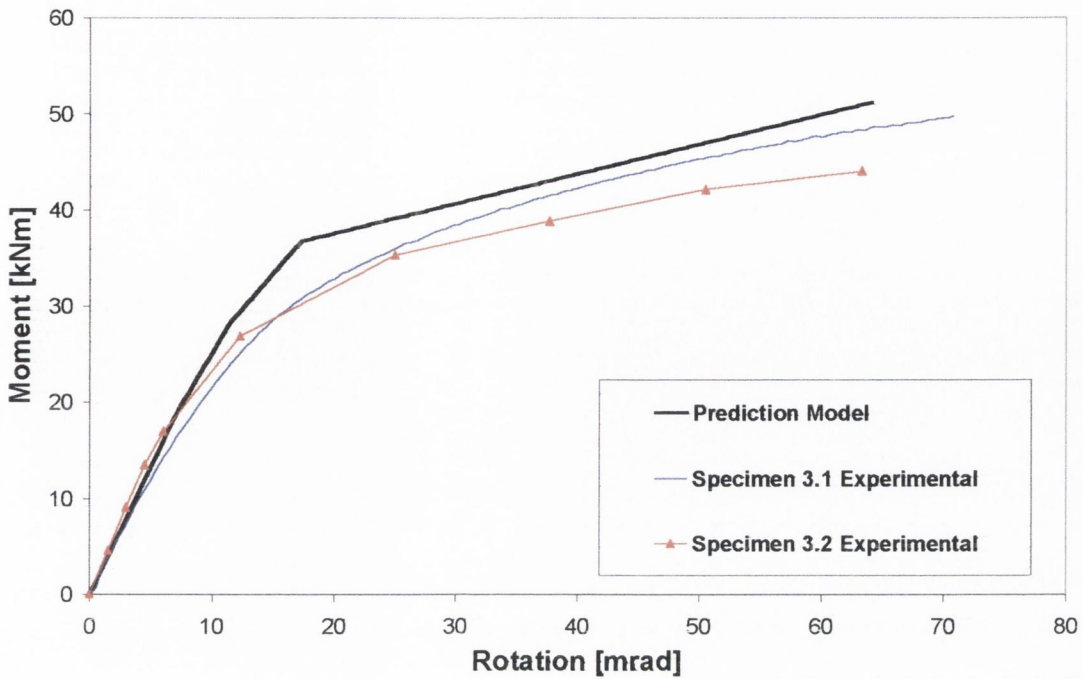


Figure 6.16: Prediction and experimental curves for specimens 3.1 and 3.2

The predicted and experimental curves for specimens 3.3 and 3.4 are presented in Figure 6.17. The predicted initial stiffness of this specimen configuration is 6.19 kNm/mrad which is nearly twice the experimental values. The ratios of predicted to experimental yield rotations are 0.5 and 0.54 for specimens 3.3 and 3.4, respectively. The ultimate experimental failure point of these specimens was taken at the point where the bolts fractured, giving ratios of predicted to experimental ultimate resistances of 0.9 and 0.89 for the two specimens.

Figure 6.18 presents the moment-rotation curves of specimens 3.5 and 3.6. As may be observed, the model gives a very good approximation to the experimental results. These specimens employed a lighter column section which was designed to yield to check whether the model can accurately determine this behaviour. The ratio of predicted to experimental initial stiffness for the two specimens is 0.77 and 0.86 respectively, with a predicted stiffness of 2.71 kNm/mrad. The predicted yield rotations are higher than the experimental values. However, the moment resistance values predicted by the proposed model are very similar to the experimental values. The ratios for the predicted to experimental yield moment are 0.89 and 0.95, while the ratios for the ultimate moment are 0.94 and 0.97.

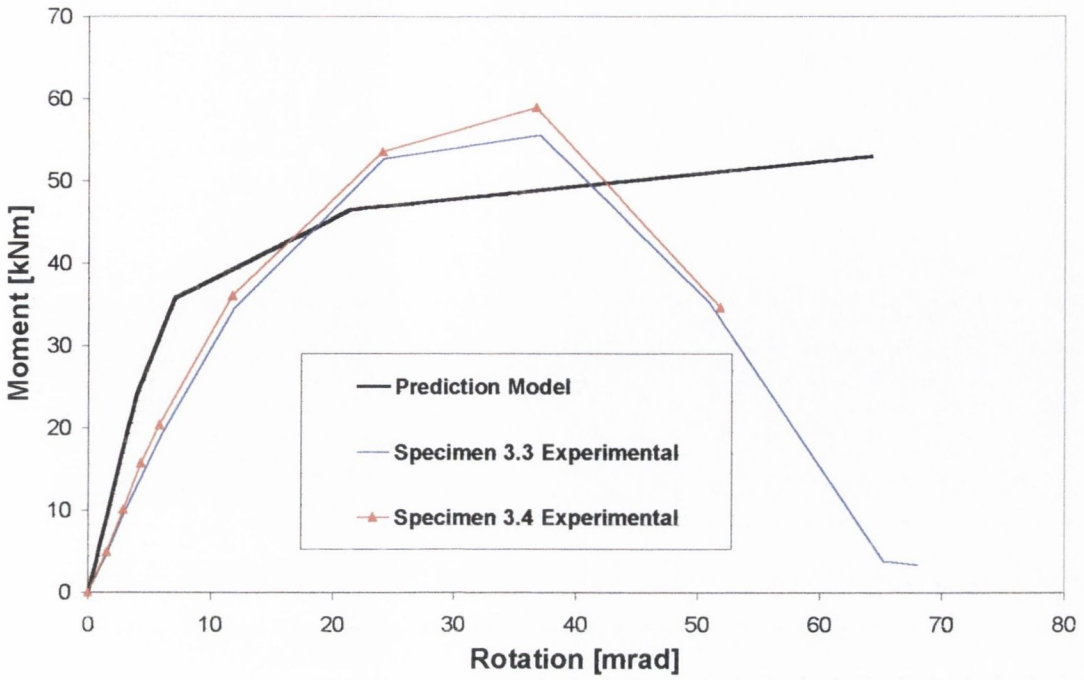


Figure 6.17: Prediction and experimental curves for specimens 3.3 and 3.4

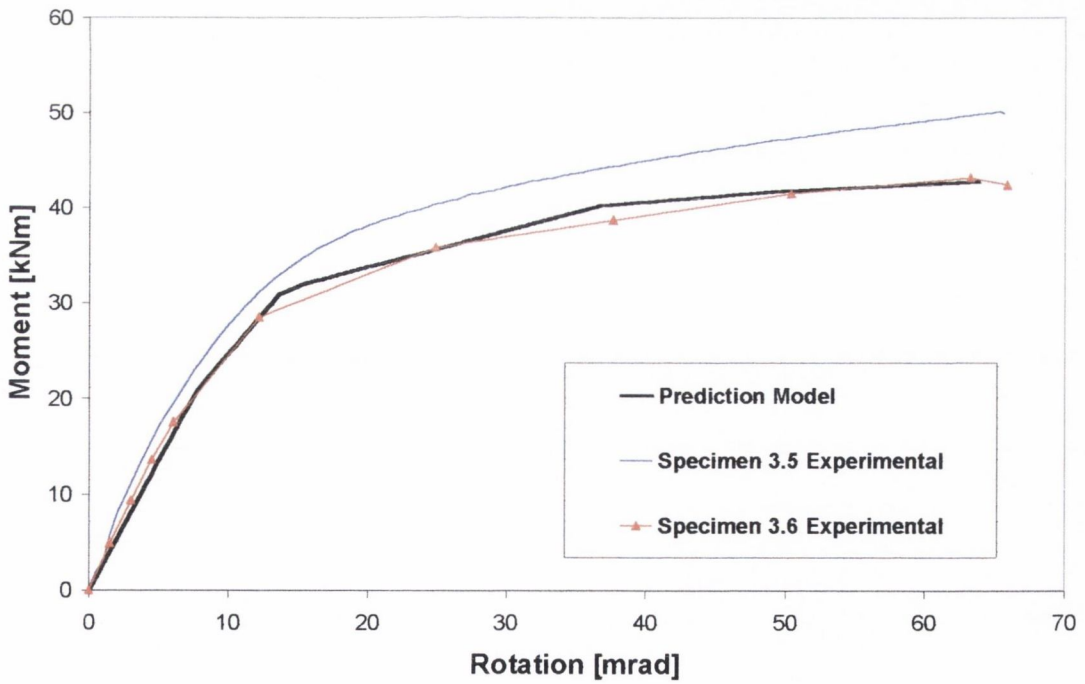


Figure 6.18: Prediction and experimental curves for specimens 3.5 and 3.6

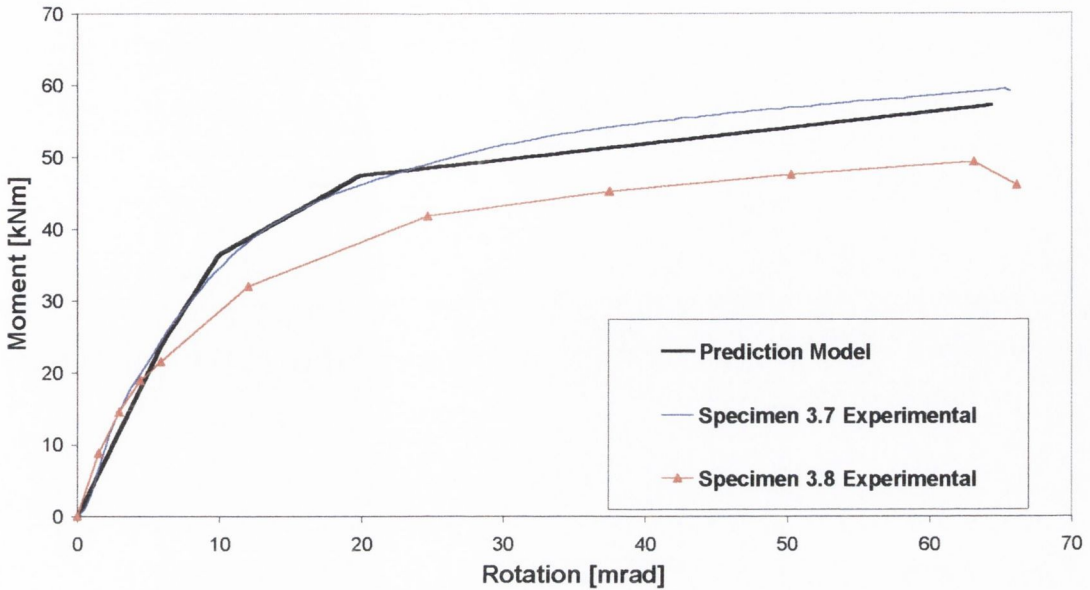


Figure 6.19: Prediction and experimental curves for specimens 3.7 and 3.8

The moment-rotation curves for specimens 3.7 and 3.8 are presented in Figure 6.19. These specimens were an improved joint employing grade 10.9 bolts and butts. The predicted stiffness of the joint is 4.05 kNm/mrad, giving a predicted to experimental stiffness ratio of 0.86 for specimen 3.7 and 0.76 for specimen 3.8. As in the case of specimens 3.5 and 3.6, the predicted yield rotation is higher than the experimental values in both cases. However, the predicted yield and ultimate moment resistance values are very close to the experimental values. In the case of specimen 3.7, a ratio of 0.87 is obtained for the predicted to experimental yield capacity and 0.97 for the ultimate capacity. For specimen 3.8, ratios of 1.03 and 1.10 are obtained for the yield and ultimate moment capacity, respectively.

As may be observed, the proposed model gives a good correlation with the experimental results for some of the test specimens. For specimens with 12 mm or thinner end-plates, the model is seen to be reasonably accurate. The initial stiffness is predicted to within 25% of the experimental values. The predicted stiffness is normally lower than the experimental stiffness, which will result in larger rotations in a frame, and larger storey drifts. The predicted yield moment capacity for these specimens is within 20% of the experimental values, with the ultimate capacity of the joints within 15%.

The model accuracy is significantly reduced if the end-plate thickness is increased to 15 mm or 20 mm. For 15 mm plates, the predicted initial stiffnesses are approximately twice the experimental values, while for 20 mm plates, the predicted stiffness is on average of 184% greater. These differences occur because the model considers the end-plate to be the major source of rotational

deformation. In joints with thicker end-plates, other sources of deformation become relatively more important. These include the bolt in bending and tension and column flexure. The large over-estimation of initial stiffness leads to the predicted yield rotations being much lower than the measured experimental values, ranging from 40 – 55% of the experimental values.

When the results from the proposed prediction model are compared to the design characteristics determined from Eurocode 3, a marked improvement may be observed. This may be seen for specimen 3.2 in Figure 6.20, and for specimen 3.7 in Figure 6.21. Similar improvements were noted for all specimens, including those with thicker end-plates, especially in terms of the initial stiffness. Eurocode 3 was observed to overpredict initial stiffness by as much as 250%, thus also underpredicting the yield rotation. The proposed model performs much better. Experimental yield capacities are also much closer to the model's predicted values than the EC design values. This is also the case with ultimate capacity, largely due to the values used to characterise material behaviour. Eurocode 3 assumes linear elastic-perfectly plastic behaviour for the steel, while the proposed model employs a multi-linear relationship, incorporating both the yield and ultimate stress of the material. By using this type of material law, both elastic and inelastic moment-rotation characteristics may be determined.

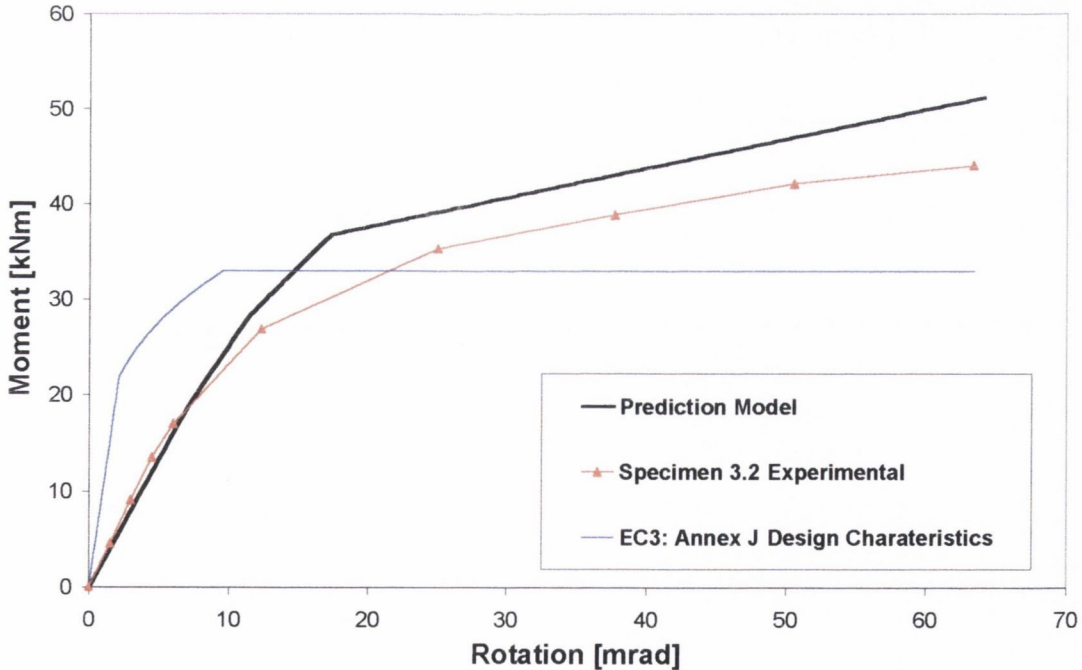


Figure 6.20: EC3: Annex J, predicted curve and experimental data for specimen 3.2

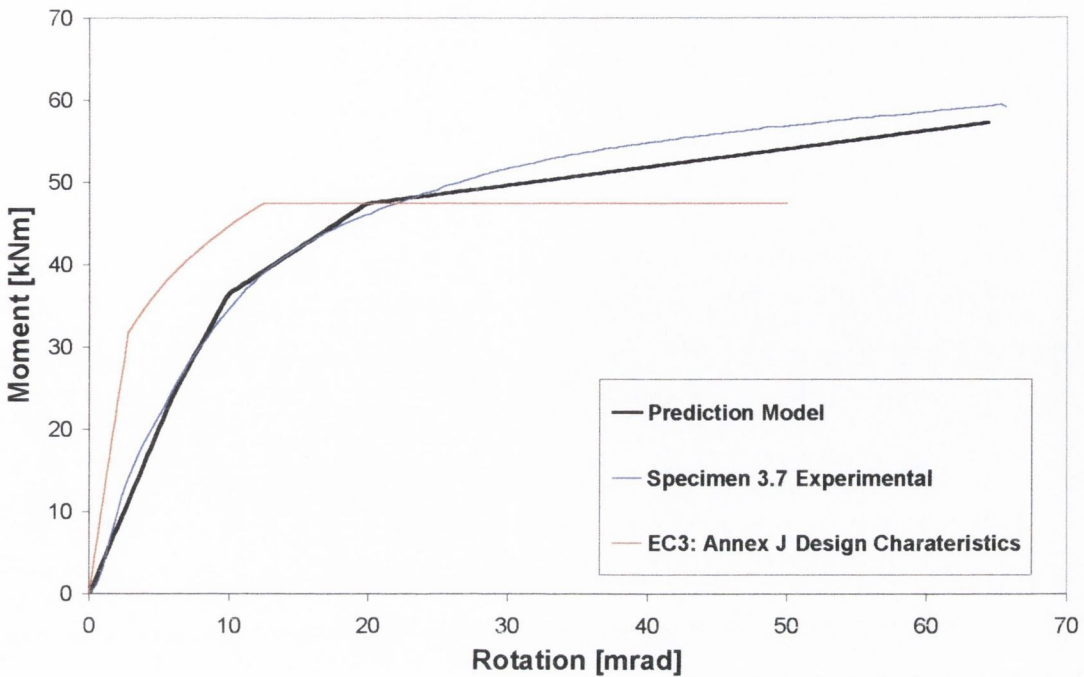


Figure 6.21: EC3: Annex J, predicted curve and experimental data for specimen 3.7

6.4 Conclusions

A proposed response model for flush end-plate joints has been presented. This model has been adapted from two existing models. The first part of the model is a T-stub force-displacement model. This model was originally developed for use with extended end-plate joints but has been successfully adapted for use with flush end-plates. The T-stub element is represented as a rectangular plate, for which the complete moment-curvature relationship is determined. Using this relationship, the ultimate plastic displacement of the section is determined. Similar equations are developed to predict the full force-displacement curve for the rectangular section. In order to accurately predict this behaviour of flush end-plate joints, the equation used to determine initial stiffness was amended. This change was verified on three bases:

- Previous work by Brown et al (2001) on the prediction of the initial stiffness of end-plate joints. This work suggested that the effective length, b_{eff} , that affected the initial stiffness had a longitudinal length equal to the distance from the bolt-hole to the beam flange, m ;
- Finite element modelling of flush end-plate joints carried out by Tucker (2002). The joints modelled were identical to those tested as part of this study. It was observed that the strained area in the end-plate corresponded approximately to the length of the parameter, m . Upon initial loads, this area quickly spread to cover this length, and then remained constant as higher loads were imposed; and

- A small parametric study was carried out using the length b_{eff} as the variable. From this, it was seen that the prediction model gave sufficiently accurate results when the effective stiffness length taken as m .

The second section of the model addresses the rotation deformation due to the response of the column web in tension, compression and shear. Linear elastic-perfectly plastic relationships were assumed for these components. Finally, the method of combining the force-displacement curve from the T-stub with the column web rotation was described.

The predicted results for the joints in Test Series Two and Three were compared to the experimental results. It was seen that the model accurately predicts the moment-rotation curve for the joints with thin end-plates. However, the model accuracy is significantly decreased for joints with end-plates of 15 mm or thicker. This is because the model assumes that the end-plates is the major contributor to the rotational deformation of the joint. As the end-plate thickness increases, the importance of the end-plate is reduced while the contributions of other components such as the column length and the bolts are increased. However, when the prediction results are compared to the design calculations from Eurocode 3: Annex J, it is seen that the proposed model gives a much better prediction of the initial stiffness of the joint, even for those specimens with thick end-plates. The yield and ultimate capacity predictions are also improved through the use of the multi-linear material law incorporated in the model. Based on the comparisons between the Eurocode 3 design characteristics, the experimental results and the predicted results, it is observed that the use of the proposed joint model within a frame analysis will lead to a much more accurate response than that obtained using the design characteristics.

Chapter 7

Seismic Design Case Studies

7.1 Introduction

With the availability of an accurate moment-rotation model for flush end-plate joint response, the applicability of these joints to seismic-resistant design may be evaluated through a number of design case studies. Four case studies are presented in this chapter of moment-resisting frames with various joint details. The approach taken is to evaluate the seismic design ground acceleration of frames designed to the wind-moment method, which has been well-established as a reliable design method.

The first section presents the basis of the wind-moment method briefly. The method employs the rotational stiffness of the joints to resist wind, or horizontal loads, while assuming the joints act as perfect hinges under gravity loads. Frames designed using such joints have been shown to be practical and economical when the method is used within recommended limits. These limits are presented in this section along with the disadvantages of the method.

This is followed by a discussion of the seismic design of structures and the definition of the design ground acceleration. The elastic response spectrum defined in Eurocode 8 (CEN, 2000) is presented, as is the method used to determine the design ground acceleration for a frame.

Four cases studies are presented in the third section. These four frames were designed using the wind-moment method and the ground acceleration required to exceed one of a number of limit states is determined using the procedures of Eurocode 3 and Eurocode 8. The effects of employing different joint details is examined for each frame by comparing the peak ground acceleration for standard flush end-plate joints with alternative configurations with different failure modes. The response of the frames is compared for joints modelled using both the Eurocode 3: Annex J method and the proposed model described in Chapter 6.

The final section presents some conclusions from these case studies on the use of flush end-plate joints in earthquake resistant design. The effects of the joint characteristics are discussed in terms of the frame responses calculated using the different joint models.

7.2 Basis of the Wind-Moment Design Method

The wind-moment method is an established method of designing unbraced frames that utilises the rotational stiffness of the joints to resist wind loading, while neglecting this stiffness under gravity loads, where the joints are assumed to act as pins. Under wind loads, the joints are assumed to be rigid with points of contra-flexure at mid-span and mid-height. The method is consistent with the

simple design approach in BS 5950 and type 2 construction in the AISC codes of practice. The method was originally justified by its satisfactory use in the design of buildings over many years. However, recently, it has been considered as a type of semi-rigid design and has been studied intensively for this purpose.

A frame is initially proportioned to withstand gravity loads. Combinations of wind and gravity loads are then applied in different loadcases. The initial section sizes are then altered to withstand these combined affects. As the frame is statically determinate, there is no need to repeat the analysis if the section sizes are changed. This is because the internal moments are not related to the relative stiffness of the members. However, the method does have a number of disadvantages that must be considered.

Beams are often over-designed due to the large sagging moments which arise at mid-span because these members are assumed to be simply supported under gravity loads. However, the semi-rigid nature of the joints will actually introduce hogging moments at the ends of the beams, thus reducing this sagging moment. In contrast, column members are normally under designed because the hogging moment at the joints is ignored. However, as columns are also designed to resist axial loads, this under design is not as critical. The joints in the frame will also normally be under-designed. As the beams are designed for the sagging moment at mid-span, and the joints are sized on the end-moments, the joints will be partial strength with respect to the beams.

In 1991, the Steel Construction Institute (Anderson et al, 1991) published the results of a study carried out on the wind-moment method. Using this method, a large number of single and multi-storey buildings were designed whose behaviour was then determined using computer analysis techniques. Based on these frames, a number of limitations were recommended for buildings designed using this method. This limitations are given in Table 7.1. The SCI publication also recommends that 10% fixity should be assumed at the beam ends to allow for the semi-rigid nature of the joints, and that only flush and extended end-plate joints should be considered for use in frames designed using this method. Three loadcases are recommended for use in the design. These are as follows:

1. 1.4 (Dead Loads) + 1.6 (Imposed Loads) + Notional horizontal loads;
2. 1.2 (Dead Loads + Imposed Loads + Wind Loads); and
3. 1.4 (Dead Loads + Wind Loads).

Where the notional horizontal loads should be taken as 0.5% of the factored dead and imposed loads. In addition, pattern loading should be considered where appropriate. Loadcase 1 usually

governs the design of the beams, while loadcase 2 or 3 will normally govern the column and joint design.

	Minimum	Maximum
Number of storeys	2	8
Number of bays	1	4
Bay width	4.5 m	9.0 m
Storey height (bottom storey)	4.0 m	6.0 m
Storey height (elsewhere)	3.0 m	5.0 m
Floor Dead Load	3.50 kN/m ²	5.00 kN/m ²
Floor Imposed Load	4.00 kN/m ²	7.50 kN/m ²
Roof Dead Load	3.75 kN/m ²	5.00 kN/m ²
Roof Imposed Load	1.50 kN/m ²	3.00 kN/m ²
Wind Speed	37 m/s	52 m/s
Bay width: Storey height (bottom storey)	0.75	2.00
Bay width: Storey height (elsewhere)	0.90	2.50
Greatest bay width: smallest bay width	1.00	2.00

Table 7.1: Recommendations for design using the Wind-Moment Method

As this method is widely accepted and used in practice, it has not been fully explained here. Further information is given in the Wind Moment Design Method book (Anderson et al, 1991).

7.3 Seismic Design

7.3.1 Seismic Design Spectrum

It is accepted in seismic design that the effects of earthquake ground motion on a building may be approximated by horizontal forces imposed at the floor levels. The sum of these horizontal forces is equal to the total base shear imposed on the structure. Using this approach, it is possible to determine the greatest ground acceleration that an individual structure can withstand.

Eurocode 8 (CEN, 2000) allows for five soil classifications to account for the influence of the local ground conditions. These are based on the stratigraphic profile of the soil and other geotechnical

parameters. These classifications range from class A, which consists of rock or other rock-like formation, to E, which consists of loose alluvium material. The frames in this study have all been designed assuming that soil class B applies. This relates to deposits of dense sand, gravel or very stiff clay.

In EC8, the ground motion at a particular point on the surface is usually defined in terms of an elastic acceleration response spectrum. Two spectra are defined based on the location and the expected magnitude of the earthquakes: Type 1 and Type 2. The type 1 spectrum is normally adopted for zones in which earthquakes are expected to generate a surface wave with a magnitude of greater than 5.5. Otherwise, it is recommended that the type 2 spectrum be used. As this study considers structures in zones of low to medium seismic activity, the type 2 spectrum has been adopted. A form of the spectrum is illustrated in Figure 7.1, where $S_e(T)$ is the ordinate of the elastic acceleration response spectrum, T is the vibration period of a linear single degree of freedom system, T_B and T_C are the period limits of the constant spectral acceleration and T_D is the period defining the beginning of the constant displacement range of the spectrum. The values of S , T_B , T_C and T_D are dependant upon the soil classification and are presented in Table 7.2.

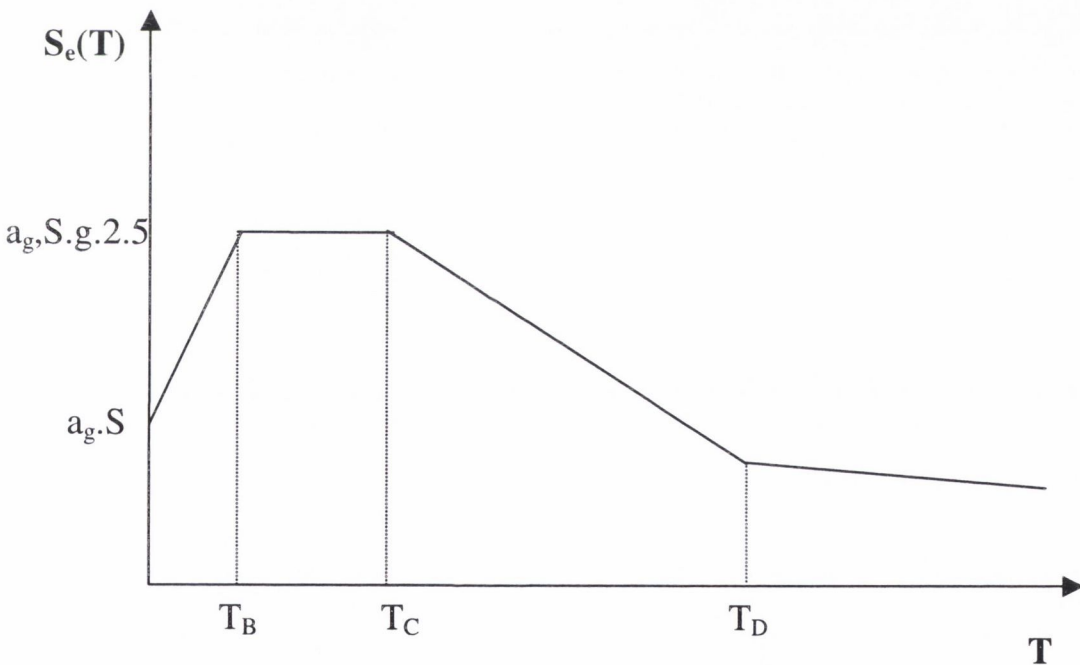


Figure 7.1: Elastic Response Spectrum (CEN, 2000)

Soil Classification	S	T _B	T _C	T _D
A	1.0	0.05	0.25	1.2
B	1.1	0.05	0.25	1.2
C	1.5	0.10	0.25	1.2
D	1.8	0.10	0.30	1.2
E	1.5	0.05	0.25	1.2

Table 7.2: Parameters for Type 2 response spectrum (CEN, 2000)

Using these parameters, a design spectrum for elastic analysis may be determined using the following formula:

- for $0 \leq T \leq T_B$

$$S_d(T) = \alpha \cdot S \cdot \left[1 + \frac{T}{T_B} \left(\frac{2.5}{q} - 1 \right) \right] \quad \text{Eqn. 7.1}$$

- for $T_B \leq T \leq T_C$

$$S_d(T) = \alpha \cdot S \cdot \frac{2.5}{q} \quad \text{Eqn. 7.2}$$

- for $T_C \leq T \leq T_D$

$$S_d(T) = \begin{cases} \alpha \cdot S \cdot \frac{2.5}{q} \left[\frac{T_C}{T} \right] \\ \geq [0.20] \alpha \end{cases} \quad \text{Eqn. 7.3}$$

- for $T_D \leq T$

$$S_d(T) = \begin{cases} \alpha \cdot S \cdot \frac{2.5}{q} \left[\frac{T_C T_D}{T^2} \right] \\ \geq [0.20] \alpha \end{cases} \quad \text{Eqn. 7.4}$$

where $S_d(T)$ is the ordinate of the design spectrum, α is the ratio of design ground acceleration, a_g , to the acceleration of gravity, g , and q is the behaviour factor. In seismic design, a fourth loadcase must be considered, in addition to the three defined for the wind-moment method above. This takes the form of:

- 1.0 (Dead Loads) + 0.3 (Imposed Loads) + Seismic Design Loads

The maximum value of the design ground acceleration is directly proportional to the behaviour factor, q , that is employed. This behaviour factor is defined in Eurocode 8 as “an approximation of

the ratio of the seismic forces that the structure would experience if its response was completely elastic with 5% damping, to the minimum seismic force that may be used in design". However, values of q are not actually given for structures that employ partial strength joints, even though Eurocode 3 and Eurocode 8 both allow the use of such joints. Instead, Eurocode 8 suggests behaviour factors based on the ductility class of the structure. Three ductility classes are defined in Eurocode 8 for steel structures based on the dissipative qualities of the structure. These are presented in Table 7.3, where ductility class I corresponds to a target global drift equal to 25 mrad and ductility class S corresponds to a target global drift of 35 mrad. For steel frames with fully rigid frames, Eurocode 8 recommends a behaviour factor of 6. In order to accurately determine the design ground acceleration of the structure, suitable behaviour factors were chosen for the joint failure modes that reflected the different rotational capacities and energy dissipation characteristics observed. Given that the ultimate rotations determined in this study ranged from 20 mrad up to 70 mrad, behaviour factors of 3 for mode 2 joints and 5 for mode 1 joints were determined to be reasonable.

Dissipative Quality	Recommended Behaviour Factor, q	Ductility Class of the Structure
Non-dissipative structure	$q = 1.5$	Ordinary, O
Dissipative Structure	$1.5 < q < 4$	Intermediate, I
Dissipative Structure	$q \geq 4$	Special, S

Table 7.3: Behaviour Factors and Structure ductility classes

Due to the highly brittle failure mechanisms and low rotational ductility of the joints subject to mode 3 failures, a non-dissipative design appears appropriate, for which a behaviour factor of 1.5 should be employed. These behaviour factors are summarised in Table 7.4.

Joint Failure Mode	Behaviour Factor, q
Rigid Joint	6
Mode 1	5
Mode 2	3
Mode 3	1.5

Table 7.4: Joint Failure Mode and Behaviour factors

7.3.2 Determination of Design Ground Acceleration

A set of horizontal forces are imposed on the specimen at the floor levels. These forces are scaled to the mass of the structure using the procedure in EC8 in combination with the dead and imposed loads as detailed above. This is illustrated in Figure 7.2, where F_b is the base shear, F_i is the corresponding seismic force at storey i , and λ is the load factor. The period of the structure is determined from an eigenvalue analysis of the frame using the LUSAS finite element software. A linear pushover analysis is performed on the structure to determine the minimum load factor that exceeds the failure conditions. It is accepted that

$$F_b = \lambda_{\min} \sum_{i=0}^n F_i = S_d(T_1) \cdot W \quad \text{Eqn. 7.5}$$

where W is the weight of the structure. As $\alpha = a_g/g$, using Eqns. 7.1 – 7.4, the design ground acceleration a_g may be determined.

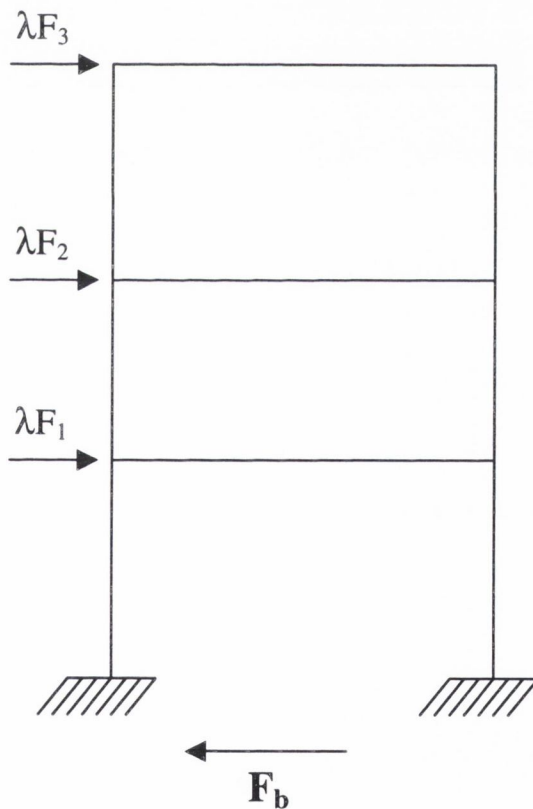


Figure 7.2: Equivalent Seismic Forces

7.4 Design Case Studies

Four moment-resisting unbraced frames employing flush end-plate joints were investigated. The frames consisted of the following configurations:

- Two storey, one bay frame;
- Four storey, one bay frame;
- Four storey, four bay frame; and
- Seven storey, two bay frame.

The members and joints were sized to resist the three standard loadcases, detailed above in section 7.2. The loading specifications for these design cases are presented in Appendix D. The joints were standard flush end-plate joints with one bolt row in tension employing either 12 mm or 15mm thick end-plates, and either M20 or M24 bolts. These joints were chosen directly from the BSCA moment-connection guide (BSCA, 1995) based on the beam size and the required moment resistance, determined from the wind-moment method. It was found that the standard joints would all display mode 2 failure mechanisms. Alternative joints were also examined for each frame. These alternative joints were adaptations of the standard wind-moment joints, achieved by altering the end-plate thickness or by increasing the bolt grade. These alterations were intended to produce mode 1 and mode 3 joints so that the behaviour of frames with a range of joints could be assessed. Once designed the seismic design resistance of the frame was evaluated using the loadcases discussed above, and summarised in Table 7.5, where λ is a load factor based on the design ground acceleration.

Loadcase	Dead Load	Imposed Load	Wind Load	Equivalent Seismic Load
1	1.4	1.6	0.0	0.0
2	1.2	1.2	12	0.0
3	1.4	0.0	1.4	0.0
4	1.0	0.3	0	λ

Table 7.5: Summary of design loadcases

Analyses were carried out using the structural analysis package LUSAS. Joint behaviour was modelled through the use of zero length rotational spring elements, JPH3, while the beams and columns were modelled using thick beam elements, BEAM. The joint elements were subjected to three degrees of freedom: translation along the x-axis, translation along the y-axis and rotation about the z-axis. The stiffness in the x- and y-direction was set as 1×10^{15} N/mm to prevent

movement in these directions, which was still low enough to prevent instability in the stiffness matrix. The input parameters for each joint were evaluated using three prediction methods:

1. rotational stiffness and moment resistance determined using the design equations detailed in Annex J of Eurocode 3 (EC3);
2. rotational stiffness determined using the prediction equation developed by Brown et al (2001), and moment resistance determined from Eurocode 3: Annex J (B/EC3); and
3. rotation stiffness and moment capacity determined using the proposed model described in the Chapter 6 and based on two existing models by Faella et al/Shi et al (F/S).

The following limit states were evaluated for different values of design ground acceleration:

- The ultimate column moments (M_{col});
- The interstorey drifts (Δ_i) which were taken as 1.5% of the storey height (Eurocode 8), where i is the i -th storey in the structure; and
- The joint yield moment (M_j).

The partial strength nature of the joints implies that the beam moment will never be critical. It must be noted that all of the design ground acceleration results shown in this section depend on the behaviour factors chosen. However, as the relationship between the ground acceleration and the behaviour factor is a linear one, it is a simple process to scale the results for different behaviour factors.

7.4.1 Case Study 1: Two-Storey, One-Bay frame

Figure 7.3 shows a two-storey, one-bay frame designed using the wind-moment method. The beam and column sizes are given along with the joint dimensions. The standard joints consisted of 12mm thick end-plates and M20 grade 8.8 bolts. This joint may be classified as a partial-strength semi-rigid joint with a mode 2 failure mechanism. Two alternative joints were investigated, one with a mode 1 failure and another with a mode 3 failure. The frame with the mode 1 joints is designated Frame M1-1, while the frames with the mode 2 and mode 3 joints are designated as M2-1 and M3-1, respectively.

Table 7.6 presents the value of design ground acceleration which caused each of the above limit states to be exceeded. The critical ground acceleration is highlighted in bold for each frame model.

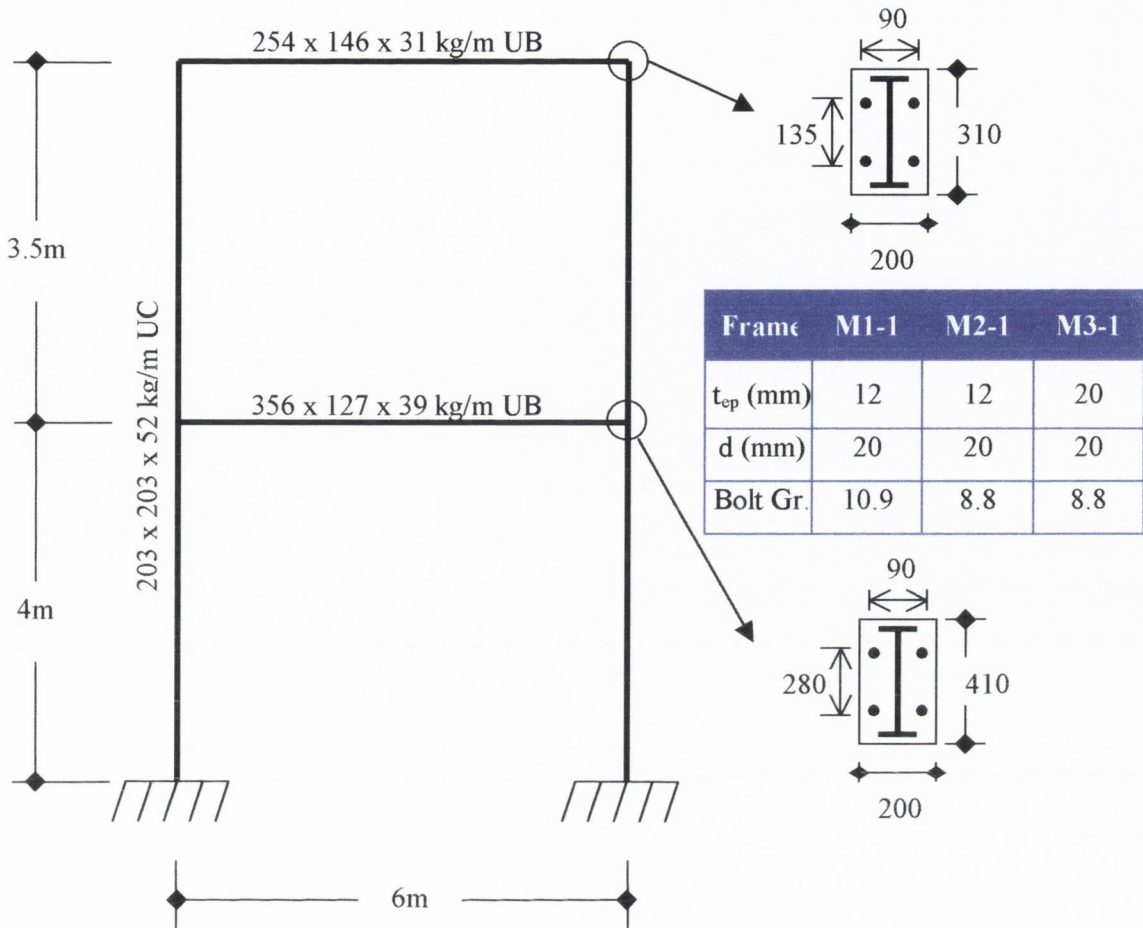


Figure 7.3: Case study 1 – 2-Storey, 1-bay frame

Limit State	Frame and Joint Model									
	Rigid Frame	Frame M1-1			Frame 2-1			Frame 3-1		
		EC3	BEC3	F/S	EC3	BEC3	F/S	EC3	BEC3	F/S
Δ_2	1.63g	0.96g	1.06g	0.58g	0.59g	0.54g	0.35g	0.30g	0.31g	0.21g
Δ_1	1.58g	1.11g	1.27g	0.85g	0.68g	0.66g	0.50g	0.35g	0.35g	0.28g
M_{Col}	1.28g	0.99g	1.05g	0.87g	0.61g	0.59g	0.51g	0.30g	0.31g	0.27g
$M_{j,2}$	N/A	0.27g	0.37g	0.51g	0.10g	0.13g	0.27g	0.11g	0.11g	0.13g
$M_{j,1}$	N/A	0.30g	0.24g	0.49g	0.18g	0.14g	0.24g	0.12g	0.11g	0.15g
T (s)	0.134	0.149	0.153	0.177	0.152	0.150	0.175	0.148	0.152	0.167

Table 7.6: Design Ground Acceleration (g) for Case study 1

The fundamental period of the structure always falls in the plateau section of the elastic response spectrum. The rigid frame model is observed to have the lowest period and the highest critical ground acceleration. In this case, the joints do not yield and failure can only be due to the column moment, or interstorey drift. The beam moments were also checked for this frame, but it was found that the mid-span moment was not critical due to the over-strength design of the wind-moment method. The conservatism of the wind-moment design approach leads to very high critical ground accelerations.

Comparing the Brown et al/Eurocode 3 model to the pure Eurocode 3 model for all three frames, it may be observed that the slightly lower joint stiffness given by Brown et al does not have a significant effect on the critical ground acceleration for the structure. Higher ground accelerations are noted for each limit state, except for the floor joint moment where the critical ground acceleration is lower. In contrast, the model proposed in Chapter 6 has a significant effect on both the fundamental period of the structure and the critical ground acceleration. For all three semi-rigid frames, it may be seen that the critical limit state is the joint moment capacity, although where this occurs varies between the roof joint and the floor joint.

The Eurocode 3 and the Brown et al/Eurocode 3 model lead to much higher critical ground accelerations for the column and interstorey drifts than for the joint moment capacity. The proposed Faella et al/ Shi et al model indicates a much more balanced design. This is because the proposed model predicts higher moment capacities and lower stiffnesses. These lower stiffness values lead to higher interstorey drifts under seismic loading and longer fundamental periods. The lower stiffness values also lead to lower joint moments due to gravity loads, leaving more capacity to resist the earthquake induced moments. It may be seen from Table 7.6 that the critical ground accelerations for the Frame M1-1 range from 0.24g to 0.49g, depending on the model employed. Frame M2-1 displays critical accelerations from 0.10g – 0.24g, while frame M3-1 displays critical accelerations from 0.11g – 0.13g. For all three frames, the Eurocode 3 and Brown et al/Eurocode 3 models displayed very similar values, while the use of the proposed model resulted in higher critical ground accelerations.

Frame M1-1, with mode 1 joints, displays the highest critical ground accelerations, representing the highest earthquake resistance, followed by frame M2-1 which employed mode 2 joints. This observation is true regardless of the model used to predict the joint moment-rotation relationship. Frame M3-1, employing mode 3 joints, displays the lowest critical ground acceleration due to the brittle nature of the joints, and the corresponding low q-factor employed

7.4.2 Case Study 2: Four-Storey, One-Bay Frame

Figure 7.4 presents the structural frame designed for the second case study, with the member details. Joint details are presented in Table 7.7 for the three different frame models. Frame M1-2 is the frame employing mode 1 joints, frame M2-2 employs mode 2 joints, and frame M3-2 employs mode 3 joints. It should be noted that, as in case study one, frame M2-2 employs standard wind-moment joints while the alternative joints employed in frames M1-2 and M3-2 are similar to those tested in this study.

Floor Level	Mode 1 Joints			Mode 2 Joints			Mode 3 Joints		
	Bolt Grade	Bolt Dia.	t_{ep}	Bolt Grade	Bolt Dia.	t_{ep}	Bolt Grade	Bolt Dia.	t_{ep}
1	10.9	20	12	8.8	20	15	8.8	20	20
2	10.9	20	12	8.8	20	15	8.8	20	20
3	10.9	20	12	8.8	20	15	8.8	20	20
4 (Roof)	10.9	20	12	8.8	20	12	8.8	20	20

Table 7.7: Joint details for Case Study 2

Limit State	Frame and Joint Model									
	Rigid Frame	Frame M1-2			Frame 2-2			Frame 3-2		
		EC3	B/EC3	F/S	EC3	B/EC3	F/S	EC3	B/EC3	F/S
Δ_4	1.74g	0.90g	0.83g	0.55g	0.55g	0.55g	0.33g	0.25g	0.33g	0.21g
Δ_3	1.20g	0.65g	0.60g	0.46g	0.40g	0.40g	0.27g	0.18g	0.23g	0.17g
Δ_2	0.92g	0.53g	0.49g	0.41g	0.32g	0.33g	0.24g	0.15g	0.18g	0.14g
Δ_1	0.87g	0.61g	0.60g	0.57g	0.37g	0.37g	0.34g	0.17g	0.20g	0.18g
M_{Col}	0.69g	0.57g	0.57g	0.60g	0.34g	0.34g	0.35g	0.15g	0.18g	0.17g
$M_{j,4}$	N/A	0.36g	0.36g	0.68g	0.15g	0.16g	0.40g	0.08g	0.07g	0.15g
$M_{j,3}$	N/A	0.17g	0.20g	0.44g	0.10g	0.10g	0.25g	0.06g	0.06g	0.12g
$M_{j,2}$	N/A	0.13g	0.15g	0.37g	0.08g	0.08g	0.20g	0.04g	0.04g	0.09g
$M_{j,1}$	N/A	0.12g	0.14g	0.36g	0.07g	0.07g	0.20g	0.04g	0.04g	0.09g
T (s)	0.227	0.273	0.288	0.334	0.271	0.270	0.332	0.270	0.257	0.292

Table 7.8: Design Ground Acceleration (g) for Case Study 2

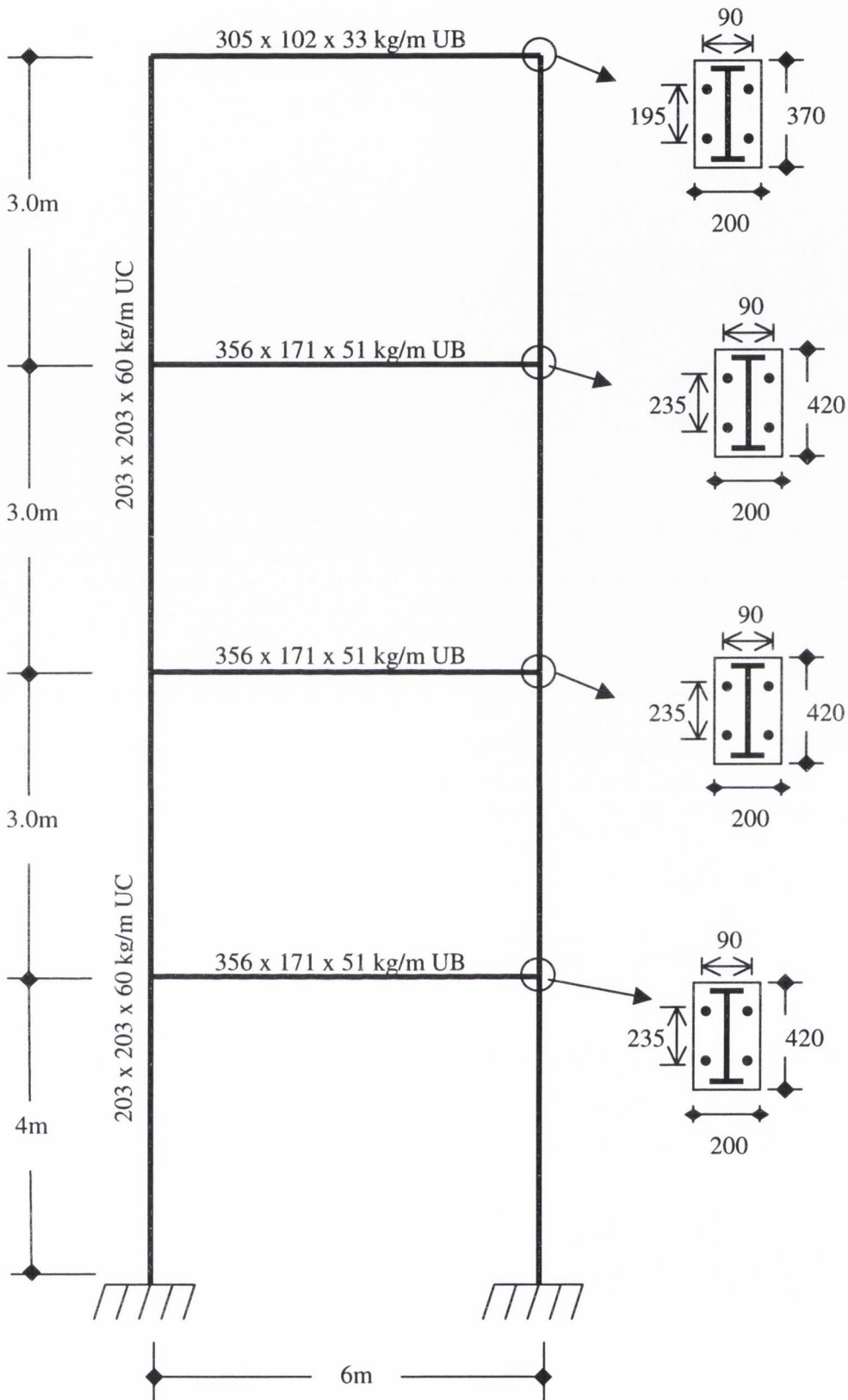


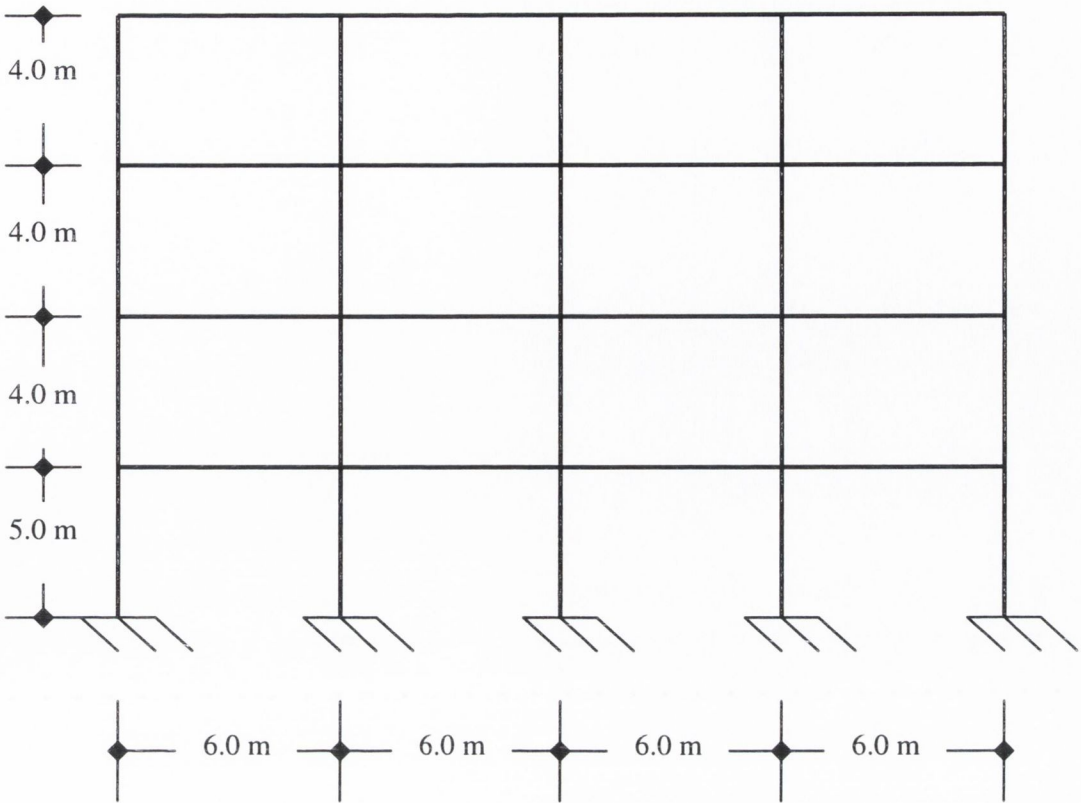
Figure 7.4: Case Study 2 – 4-Storey, 1-bay frame

Table 7.8 presents the critical ground accelerations for each frame model. In all of the semi-rigid partial-strength frames, the joint moment capacity is the critical component. As the period in all of the semi-rigid frames is greater than 0.25s, the frame is no longer on the elastic response spectrum plateau. However, the rigid frame period is 0.227s and therefore still falls on that section of the spectrum. The calculated period are very similar for the EC3 and B/EC3 models, but is 22% higher for the F/S model. This increase in period gives rise to lower earthquake design forces for a given level of ground acceleration.

As in the first case study, the results for the EC3 and B/EC3 models are very similar. This is reflected in very close critical ground accelerations for each limit state. Due to these similarities, it was felt that the B/EC3 model was not a significant improvement over the standard EC3 model and is therefore, not employed in the third and fourth case studies. As in Case Study 1, the F/S model is seen to lead to higher critical ground accelerations for all three frames. The ratio between the F/S model and the EC3 model results is approximately 2.5 in all cases. It may be observed that Frame M1-2 is capable of resisting moderate seismic forces, while frame M2-2 is capable of resisting only low seismic forces. Frame M3-2 does not possess any significant seismic resistance according to the EC3 and B/EC3 models, and only very low resistance according to the proposed model. It may be seen for Frame M3-2 that the joints in floors 1 and 2 have the same critical ground acceleration for all three models. This was unexpected as the moment in the lower floor is different.

7.4.3 Case Study 3: Four-Storey, Four-Bay frame

Figure 7.5 and Table 7.9 present the frame and joint details used for the third case study. This frame was taken directly from a study published on the wind-moment method (SCI, 1991). The same naming convention is used where frame M1-3 employs mode 1 joints, frame M2-3 employs mode 2 joints and frame M3-3 employs mode 3 joints. It should be noted that using the Eurocode 3 design method, it was not possible to provide mode 3 joints for the third floor and roof that would be capable of resisting the specified moments from the wind-moment method without a full re-design of those members. However, employing the proposed F/S model, the mode 3 joint was found to be adequate. This is due to the higher moment capacity predicted by the proposed F/S model. Based on the results from the first two case studies, it was determined that the use of the B/EC3 model, with the predicted reduced stiffness, did not show a significant improvement or alternation of the seismic design resistance of the overall frames compared to the Eurocode 3 model. Therefore, the model was not employed in this case study or in case study four.



Roof Beam:	305 x 165 x 54 kg/m UB
Floor Beams:	406 x 178 x 74 kg/m UB
Internal Columns:	(Ground-to-2 nd Floor): 254 x 254 x 89 kg/m UC
	(2 nd Floor-to-Roof): 203 x 203 x 52 kg/m UC
External Columns:	(Ground-to-2 nd Floor): 203 x 203 x 71 kg/m UC
	(2 nd Floor-to-Roof): 203 x 203 x 52 kg/m UC



Figure 7.5: Case Study 3 – 4-Storey, 4-bay frame

Floor Level	Mode 1 Joints			Mode 2 Joints			Mode 3 Joints		
	Bolt Grade	Bolt Dia.	t_{ep}	Bolt Grade	Bolt Dia.	t_{ep}	Bolt Grade	Bolt Dia.	t_{ep}
1	10.9	20	12	8.8	20	12	8.8	20	20
2	10.9	20	12	8.8	20	12	8.8	20	20
3	10.9	20	12	8.8	20	12	8.8	20	20
4 (Roof)	10.9	20	12	8.8	20	12	8.8	20	20

Table 7.9: Joint details for Case Study 3

Limit State	Frame and Joint Model						
	Rigid Frame	Frame M1-3		Frame M2-3		Frame M3-3	
		<i>EC3</i>	<i>F/S</i>	<i>EC3</i>	<i>F/S</i>	<i>EC3</i>	<i>F/S</i>
Δ_4	0.86g	0.50g	0.36g	0.31g	0.23g	-	0.13g
Δ_3	0.53g	0.34g	0.28g	0.21g	0.16g	-	0.11g
Δ_2	0.68g	0.38g	0.30g	0.24g	0.17g	-	0.10g
Δ_1	0.57g	0.43g	0.40g	0.27g	0.23g	-	0.13g
Internal M_{Col}	0.44g	0.39g	0.41g	0.24g	0.25g	-	0.12g
External M_{Col}	0.51g	0.46g	0.49g	0.28g	0.29g	-	0.14g
Internal $M_{j,4}$	N/A	0.07g	0.36g	0.04g	0.15g	-	0.05g
Internal $M_{j,3}$	N/A	0.08g	0.21g	0.05g	0.12g	-	0.04g
Internal $M_{j,2}$	N/A	0.05g	0.12g	0.03g	0.08g	-	0.06g
Internal $M_{j,1}$	N/A	0.04g	0.12g	0.02g	0.08g	-	0.05g
External $M_{j,4}$	N/A	0.16g	0.36g	0.09g	0.16g	-	0.06g
External $M_{j,3}$	N/A	0.09g	0.19g	0.05g	0.11g	-	0.04g
External $M_{j,2}$	N/A	0.08g	0.13g	0.04g	0.08g	-	0.06g
External $M_{j,1}$	N/A	0.08g	0.13g	0.04g	0.08g	-	0.06g
T (s)	0.298	0.369	0.440	0.369	0.455	-	0.386

Table 7.10: Design Ground Acceleration (g) for Case Study 3

Table 7.10 presents the critical ground accelerations for the different limit states. Due to the number of joints in the frame, only the lowest critical acceleration for any internal joint at each floor level is shown, along with the lower external joint value. This also applies to the ultimate column moment, where the lowest critical internal ground acceleration is presented, along with the critical external column ground acceleration.

As may be observed from Table 7.10, the joint moment capacity is the critical component of all the semi-rigid frames. In all of these frames, the internal joints are subjected to higher moments than the external joints and hence, reach their limit state first. However, in frame M2-3 and M3-3 using the F/S model, the external joints and internal joints reach the limit state at the same critical ground acceleration. For frame M2-3, the joints on the first and second floor level yield at the same ground acceleration, while in frame M3-3, the internal and external joint on floor level three yield at the same ground acceleration.

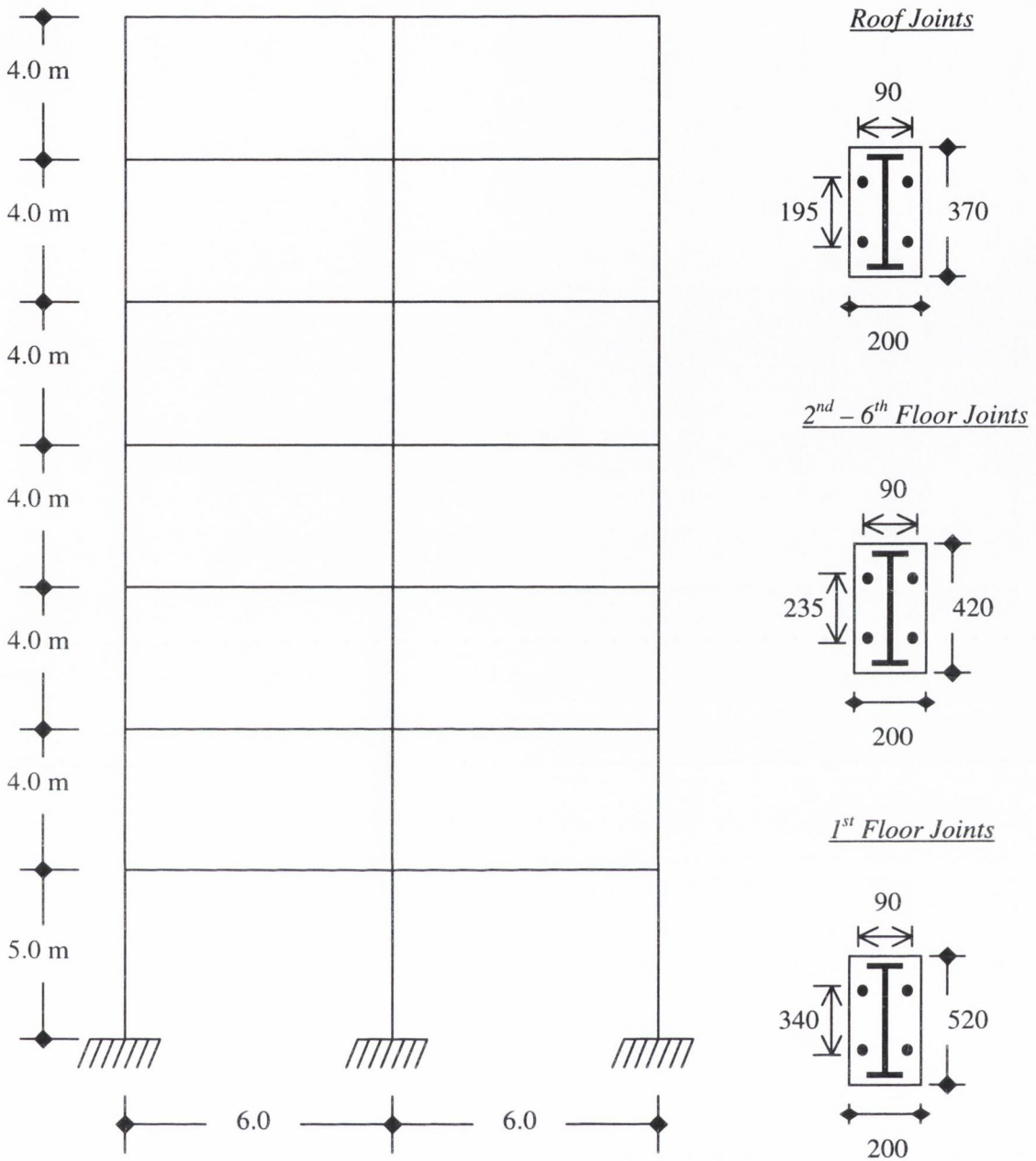
As observed in the previous two case studies, the proposed F/S model again predicts a higher critical ground acceleration than the EC3 design model. However, the overall design ground accelerations for this frame are lower than those determined in Case Study 2. This was not expected as the four bays of the frame were expected to provide additional redundancy but can be attributed to two main contributing factors:

- The frame in Case Study 3 carried higher dead and imposed loads on all floor levels than in case study 2, from the initial design. This increases the initial moment at the joints when the horizontal load factor is zero, leaving less capacity for seismic resistance;
- Different members sizes are used in the frames, and this affects the overall frame stiffness and hence the seismic resistance.

This reduction in seismic capacity is also observed in the rigid frame, where , joint moments are not an ultimate limit state. The observed critical ground accelerations for all three frame models are very low, with a maximum of 0.12g being obtained for frame M1-3 when the proposed F/S mode is used. Frame M3-3 exhibits the lowest critical ground acceleration for the proposed F/S model of 0.04g, with frame M2-3 exhibiting a critical ground acceleration of 0.08g. The Eurocode 3 model exhibits very low seismic resistance for both frames M1-3 and M2-3 with critical ground accelerations of 0.04g and 0.02g respectively.

7.4.4 Case Study 4: Seven-Storey, Two-Bay frame

The fourth case study carried out was on a seven storey, two bay frame. Originally a seven storey, one bay frame was examined, but it was found that flush end-plate joints could not support the necessary joint moments. The structural configuration and joint details are given in Figure 7.6 and Table 7.11. It should be noted at this point that this frame would not normally be designed using flush end-plate joints. The 1st floor beam has been increased in size to allow a flush end-plate joint to be employed. In practice, an extended end-plate joint would be used at that level in conjunction with a smaller beam section.



1 st Floor Beam:		457 x 191 x 82 kg/m UB
2 nd – 6 th Floor Beam:		356 x 171 x 51 kg/m UB
Roof Beam:		305 x 102 x 33 kg/m UB
External Column:	(Ground-to-4 th Floor):	203 x 203 x 86 kg/m UC
	(4 th Floor-to-Roof):	203 x 203 x 52 kg/m UC
Internal Column:	(Ground-to-4 th Floor):	254 x 254 x 107 kg/m UC
	(4 th Floor-to-Roof):	203 x 203 x 52 kg/m UC

Figure 7.6: Case Study 4 – 7-Storey, 2-bay frame

Floor Level	Frame M2-4			Frame M3-4		
	Bolt Grade	Bolt Dia.	t_{ep}	Bolt Grade	Bolt Dia.	t_{ep}
1	8.8	24	15	8.8	24	20
2	8.8	24	15	8.8	24	20
3	8.8	20	15	8.8	20	20
4	8.8	20	15	8.8	20	20
5	8.8	20	12	8.8	20	20
6	8.8	20	12	8.8	20	20
7 (Roof)	8.8	20	12	8.8	20	20

Table 7.11: Joint details for Case Study 4

The increased beam size employed was the smallest section size that could accommodate a standard flush end-plate joint that capable of resisting the moment of 119 kNm required by the wind-moment method. It was found that it was not feasible to alter the joints in the frames to provide either mode 1 or purely mode 3 failure mechanisms. All of the standard joints in frame M2-4 were predicted to fail in a mode 2 manner. However, the joints in frame M3-4 consist of a combination of mode 2 and mode 3 failures when designed to the Eurocode 3 method. Those joints that are predicted to fail in a mode 2 manner lie very close to the boundary between mode 2 and mode 3. As was noted in the experimental work described in Chapter 5, the definition of the modes of these joints is easily affected by variations in material properties. Therefore, the use of a non-dissipative behaviour factor of 1.5 was felt to be justified. When the moment-rotation characteristics of the joints were calculated using the proposed F/S model, all of the joints in this frame were predicted to fail in a mode 3 manner. However, based on the member sizes and the required moment capacities of the wind-moment design, joints with mode 1 mechanisms were again infeasible.

Table 7.12 presents the critical design ground accelerations for this case study. The rigid frame reaches its critical limit state based on the interstorey drift of the fifth floor at a ground acceleration of 0.66g. The period of this structure is 0.475s, which falls in the third section of the elastic response spectrum. However, it may be seen that all of the interstorey drift acceleration values for this frame are similar, with the exception of the 7th floor, or roof level. These are also close to the limiting acceleration of the columns in the structure, which have reach their limit state at accelerations of 0.71g and 0.85g for the internal and external columns respectively.

Limit State	Frame and Joint Model				
	Rigid Frame	Frame M2-4		Frame 3-4	
		EC3	F/S	EC3	F/S
Δ_7	1.43g	0.50g	0.31g	0.25g	0.25g
Δ_6	0.90g	0.32g	0.23g	0.16g	0.16g
Δ_5	0.66g	0.26g	0.22g	0.13g	0.12g
Δ_4	0.80g	0.31g	0.30g	0.15g	0.13g
Δ_3	0.73g	0.29g	0.28g	0.14g	0.13g
Δ_2	0.83g	0.33g	0.30g	0.16g	0.15g
Δ_1	0.94g	0.44g	0.42g	0.22g	0.22g
Internal M_{Col}	0.71g	0.39g	0.40g	0.20g	0.20g
External M_{Col}	0.85g	0.46g	0.48g	0.24g	0.24g
Internal $M_{j, 7}$	N/A	0.19g	0.20g	0.09g	0.31g
Internal $M_{j, 6}$	N/A	0.09g	0.15g	0.04g	0.19g
Internal $M_{j, 5}$	N/A	0.06g	0.12g	0.03g	0.13g
Internal $M_{j, 4}$	N/A	0.04g	0.09g	0.03g	0.09g
Internal $M_{j, 3}$	N/A	0.03g	0.09g	0.03g	0.08g
Internal $M_{j, 2}$	N/A	0.06g	0.12g	0.05g	0.11g
Internal $M_{j, 1}$	N/A	0.11g	0.15g	0.07g	0.13g
External $M_{j, 7}$	N/A	0.23g	0.20g	0.11g	0.30g
External $M_{j, 6}$	N/A	0.09g	0.13g	0.04g	0.16g
External $M_{j, 5}$	N/A	0.07g	0.11g	0.03g	0.11g
External $M_{j, 4}$	N/A	0.07g	0.09g	0.04g	0.08g
External $M_{j, 3}$	N/A	0.06g	0.09g	0.03g	0.08g
External $M_{j, 2}$	N/A	0.09g	0.14g	0.05g	0.12g
External $M_{j, 1}$	N/A	0.13g	0.16g	0.08g	0.14g
T (s)	0.475	0.580	0.640	0.591	0.626

Table 7.12: Design Ground Acceleration (g) for Case Study 4

Both semi-rigid frames exhibit low seismic resistance. As has been noted in the previous case studies, the proposed F/S model leads to longer periods and a higher critical design ground accelerations than the Eurocode 3 model. This is a direct result of the much reduced stiffness and increased moment capacity of the joints. Frame M2-4 is predicted to have a minimum critical design acceleration of 0.03g using the EC3 model, and 0.09g using the F/S model. Frame M3-4 has minimum design accelerations of 0.03g and 0.08g for the two models respectively. It may also

be noted that both internal and external joints reach their limit state at the same ground acceleration for three of the four semi-rigid frames modelled. It may also be noted that in the semi-rigid frames, the joints all obtain their limit state at a significantly lower acceleration than the interstorey drift or column moments.

7.5 Conclusions

This chapter presents four cases studies carried out on moment-resisting frames, which have been designed using the wind-moment method. The first section in the chapter provides a brief discussion on the design method. This method is a proven design tool and has been adopted by different international building codes. The recommended limitations of the method are presented along with the main disadvantages. The three different loadcases that must be considered when using the method are also presented.

The second section investigates seismic design of structures using an elastic response spectrum. This spectrum is defined and the necessary parameters are explained. Formula for the determination of the critical ground acceleration of a structure are presented. A fourth loadcase required for seismic design of structures is presented. Four loadcases required for the wind-moment method and seismic design are identified. This is followed by a short discussion of the method employed to calculate the design ground acceleration of a moment-resisting frame.

The third section presents the results from the four case studies. These frames were all designed using the wind-moment method and then evaluated to determine the critical design ground acceleration. The four frames varied in the number of storeys and the number of bays. In each frame, different joint details were employed to investigate the influence of joint failure mode on frame response. As the standard flush end-plate joints were all found to display mode 2 failures, these joints were altered to provide mode 1 and mode 3 failure mechanisms, where possible. It did not prove feasible to redesign the joints for these failure modes in all four frames, and other details are noted where they were employed. The joint moment-rotation characteristics were modelled using three methods: (1) the Eurocode 3 design method for stiffness and moment resistance; (2) a modified stiffness model in conjunction with the Eurocode 3 design moment resistance; and (3) the proposed model based on Faella et al and Shi et al. The frames were also modelled as fully rigid frames.

It was noted that for the frames with semi-rigid joints, the joint moment capacity was always the critical component which controlled the design ground acceleration. This was not unexpected as the joints employed in the frames were all partial strength in relation to the frame members. It was

observed that the frames employing mode 1 joints always had the highest critical design ground accelerations, whereas the mode 3 frames had the lowest. The frames employing the mode 2 joints, which are the standard industry joints, fall in the middle.

It was also observed that the different joint response models resulted in large differences in calculated critical ground accelerations. The Eurocode 3 model predicted the lowest acceleration values. This is due to the high initial design stiffness and low moment capacity which it predicts. The Brown et al/Eurocode 3 model did not result in a major difference to the critical ground acceleration for the frames. As the joint moment capacity is limiting factor in all of the designs this was not unexpected. This model employs the same resistance capacity equations as the Eurocode 3 model. The reduction in stiffness did affect the period of the structures slightly, but this was never sufficient to produce different critical accelerations. The proposed Faella et al/Shi et al, detailed in chapter 6, indicated higher critical ground accelerations for all of the frames modelled. The S_e value, were as much as three times greater than those determined with the Eurocode 3 model. As this model has been shown to predict improved values of stiffness and moment capacity for flush end-plate joints, the ground acceleration predicted is likely to be the more accurate. The results are summarised in Table 7.13.

Frame	Minimum Ground Acceleration, a_g	
	EC3 model	Proposed F/S model
M1-1	0.27	0.49
M2-1	0.10	0.24
M3-1	0.11	0.13
M1-2	0.12	0.36
M2-2	0.07	0.20
M2-3	0.04	0.09
M1-3	0.04	0.12
M2-3	0.02	0.08
M3-3	-	0.04
M2-4	0.03	0.09
M3-4	0.03	0.08

Table 7.13: Summary of critical design ground accelerations

It is important to note that all of the results shown depend on the acceptability of the design behaviour factors assumed above. The results suggest, however, that low-to-medium rise frames designed to the wind moment method with flush end-plate joints can possess appreciable

earthquake resistance. While eventual failure will be attributable to low joint resistance capacity, the relatively large member sizes dictated by the gravity and wind load design situations ensure that failure will not occur within the range of earthquake loading encountered in most areas of low or moderate seismicity. However, it is recommended that flush end-plates joints only be employed in low-rise buildings of four storeys or less. This is not likely to impose significant limitations on designers, as higher frames will require higher joint capacities than can be provided with flush end-plates.

Chapter 8

Conclusions

8.1 Summary of Research Study

The purpose of this thesis was to investigate the possibility of employing flush end-plate joints in frames in low-to-moderate seismic zones. Although a great deal of research has been carried out in the last decade on the use of semi-rigid joints in frames, this has concentrated on the monotonic, rather than cyclic and dynamic loading of the joints. In addition, the majority of research into joints has examined the behaviour of angles and extended end-plates. Flush end-plate joints are advocated for use in the wind-moment design method in the United Kingdom and considerable design guidance is available. In order to ensure a ductile response, careful selection of the design details, such as the end-plate thickness, bolt size and spacing among others, is necessary. Although the available guidance already considers these criteria as part of the ductility requirements, it is uncertain whether sufficient rotation capacity for seismic engineering applications is always provided. A further aim of the study was to investigate the validity of the Eurocode 3 design model for these joints. This design methodology is soon to be adopted throughout Europe and previous work has indicated that the design characteristics obtained may not be sufficiently accurate.

A new computer-based test control system was developed to allow the experimental work in this study to be carried out to a sufficiently high level of accuracy. Three control programs were developed to operate the servo-hydraulic actuators available. These control programs were designed to carry out a pre-test check of the experimental set-up, to impose a constant displacement amplitude cyclic waveform, and to perform a full cyclic test with an increasing amplitude displacement waveform. The new system is capable of controlling hydraulic actuators, while simultaneously recording the data from multiple measurement devices.

A total of twenty-two beam-to-column sub-assemblages consisting of flush end-plate joints were tested under monotonic and cyclic loading conditions. The cyclic tests were carried out according to the ECCS recommended test procedures. These were conducted using a servo-hydraulic actuator with a maximum displacement of ± 56 mm, and a maximum load of 100 kN. The experiments were executed using the control system developed as part of this study. The joints were designed to fail in one of three mechanisms defined in BS 5950 and Eurocode 3: Annex J. These failure modes are based on the ratio of flexure resistance of the end-plate, or column flange, to the axial resistance of the bolts. In order for this to occur, a range of end-plate thicknesses, beam and column members sizes, bolt diameters and bolt grades were employed in the specimens. Mode 1 joints were designed with either strong bolts, or thin end-plates, or some combination of the two. Mode 3 joints were designed with weak bolts and strong end-plates to ensure the required response, while Mode 2 joints were designed with intermediate end-plate thicknesses and standard bolts. In each experiment, up to eight strain gauges were used along with a maximum of six displacement

transducers. In addition, the load and displacement of the actuator were measured. Using this data, the moment-rotation behaviour of each joint configuration was determined. This behaviour was analysed in terms of initial stiffness, yield rotation, and moment capacity. The results from the experimental studies are compared to the design moment-rotation characteristics from Eurocode 3. In addition, a number of recommended cyclic evaluation parameters were examined. These were the partial ductility, the resistance ratio and the resistance drop ratio.

A prediction model was proposed for determining the moment-rotation relationship of flush end-plates similar to those tested in this study. It was based on the concept that flush end-plates, amongst others, may be represented as a series of notional T-stubs. This model was developed from two existing T-stub models. The first of these models was originally developed for the modelling of extended end-plate joints, while the second was developed to model both flush and extended end-plate joints. It was determined that the T-stub section of the second model was not sufficiently accurate for use in this study, hence this was replaced with a modified version of the first model. This model employs the moment-curvature response of a rectangular section to determine the force-displacement relationship of the notional T-stub. This model was adapted by amending the formulae used to determine the initial stiffness of the joint. This amendment was based on the concept that extended end-plate joints often exhibit higher stiffnesses than flush end-plate joints. The proposed model also contains formulae for the prediction of the rotational deformation of the column web in tension, compression and shear. The results from the model were compared to the experimental results obtained in this study, as well as the design characteristics from Eurocode 3.

To evaluate the usefulness of flush end-plate joints under low-to-moderate seismic loads, four case studies were examined. Four frames were designed using the wind-moment method, which is a widely accepted form of semi-rigid design. The four frames were designed using different storey numbers, heights and numbers of bays. The frames were designed with flush end-plates displaying each of the three failure modes. The joint characteristics were modelled using three different methods: the Eurocode 3 design method, a modified stiffness/Eurocode 3 design method, and the proposed prediction model. The frames were modelled using a structural finite element package, LUSAS and joint behaviour was included as rotational spring elements with bi-linear force-deformation characteristics. To determine the fundamental period of the structures an eigenvalue analysis was performed on each frame and joint configuration. The frames were analysed to ensure that the wind-moment method of design was adequate, and were then evaluated to determine their maximum safe design ground accelerations. This was done by imposing an incremental pushover load on the structure and determining the limit states for the different components. The limit states checked included the ultimate column moment, the interstorey drift and the joint moment capacity.

8.2 Principal Conclusions

The experimental and theoretical studies described above led to the following conclusions.

8.2.1 *Experimental Control Systems*

The test control system developed in this study was examined for accuracy and utility. The software is capable of recording up to 48 measurement devices and the actuator load cell and displacement transducer at the same time. It was observed that the constant amplitude program is accurate to 0.5%, while the cyclic displacement program is accurate to within 2.5%. These levels of accuracy were sufficient for the purposes of this study. The system is designed to have variable output rates, scanning rates and waveform types. It was also designed so that it could be easily adapted to other uses if necessary. In addition to the experimental work carried out in this study on steel flush end-plate joints, a total of 15 beam-column wireball reinforced concrete specimens have been tested using the new control system. In order to carry out these experiments, it was necessary to change the scan rate, scanned channels, the variable N_4 and the output rate. These experiments demonstrate the applicability of the above test system to different materials and configurations.

8.2.2 *Cyclic Behaviour of Flush End-plate Joints*

The validity of the three failure modes defined in Eurocode 3: Annex J were investigated under cyclic loading conditions. These failure modes have been accepted for joints tested under monotonic loads, but had not been examined under cyclic conditions. It was seen that these failure modes remained valid for most of the specimens tested in this study. However, it was noted that for joints designed as mode 2, but which lay close to mode 1 boundary, the joint would exhibit a mode 1 failure mechanism with no bolt yielding. In addition, mode 2 joints designed close the mode 3 boundary could display behaviour similar to that expected for mode 3 joints. This was due to premature failure of the bolts, caused by stripping of the bolt and nut threads. Therefore, it is concluded that the failure modes predicted by Eurocode 3 are valid under cyclic loading conditions, but the possibility of early bolt failure is acknowledged.

The rotational capacity, or ductility of the different joint failure modes was examined. It was observed that the joints subject to mode 1 failure mechanisms displayed the highest ductility, ranging from 9 to 25. The ultimate ductility was never determined for the mode 1 joints in this study as none of these joints actually reached their ultimate failure rotation within the available actuator stroke. Mode 2 joints exhibited varying levels of ductility from approximately 2.5 up to 8, whereas the mode 3 joint displayed the least ductility with partial ductility ratios varying from 2 to 4. The initial stiffnesses of most of the joints were very similar. This was unexpected, as the joints

details varied considerably (although the difference between bolt rows was more or less constant). The observed stiffnesses were reasonably low, with values in the range of 2.5 – 4.5 kNm/mrad. There were few exceptions to this, but these were attributed to the experimental set-up, as the difference was too great to be accounted for by inconsistencies in the material properties. With regard to the moment capacity, varying values of resistance ratios were noted depending on the failure mode of the joint. Mode 1 joints were noted have high resistance ratios as well as high resistance drop ratios. This is attributed to the higher levels of plastic deformation that these joints can withstand. In contrast, the mode 3 joints exhibited the lowest resistance ratios and the lowest resistance drop ratios. This is because these joint end-plates are not able to deform significantly and therefore the yield and ultimate capacities are very similar. The resistance ratio for these joints was usually 1.25, which is similar to the ratio of bolt yield and ultimate stresses. The mode 2 joints were observed to have intermediate levels of moment capacity and hence intermediate ratios. Therefore, it was concluded that the mode 1 joints exhibited the highest rotational capacity of the three types, but unless correctly designed, often also displayed the lowest moment capacity. In contrast, mode 3 joints displayed high moment capacity levels, but were subject to brittle failures due to stripping of the bolts. Joints designed with mode 2 failure mechanisms displayed intermediate qualities of both moment and rotational capacity.

It was noted that all of the joints exhibited highly stable hysteresis curves up to the point of failure. This points to high energy dissipation levels for the joints, especially for the mode 1 and mode 2 joints where failure did not occur rapidly. This is a desirable quality in joints that are expected to be subjected to inelastic rotations and deformations, as under earthquake loading. However, flush end-plate joints that have only two bolt-rows appear to be subject to high levels of rocking motion due to the elongation of the bolts, or crushing of the washers (as was noted for mode 1 joints). During this part of the moment-rotation relationship, the joints carries no load, but is still deformed.

8.2.3 Improvement of Joint Behaviour

It had been noted that the mode 1 joints resulted in higher levels of ductility but at the cost of reduced moment capacity due to the use of a thinner end-plates. Attempts were made to retain the mode 2 capacity while retaining the mode 1 ductility levels. This was achieved by increasing the bolt grade from the standard grade 8.8 to the higher strength grade 10.9. It was noted that this resulted in a mode 1 joint with an improved moment capacity, which would be highly desirable under large inelastic deformations. An attempt was also made to remove the stripping of the bolt threads that had been noted in the mode 2 and mode 3 tests. This was done by increasing the grade of the nuts, while retaining the standard bolt grade. This was only partially successful, because while it did prolong the life of the bolts, and therefore increase the ductility, thread stripping was

still ultimately responsible for the failure of the joint.

8.2.4 Eurocode 3: Annex J Design Characteristics

The experimental results were compared to the design characteristics determined using the method set out in Eurocode 3: Annex J. It was observed that the initial design stiffness of the joints was much higher than the experimental values. In some cases, the difference was up to 300%. This over prediction has serious implications for the design of sway frames. By over-estimating the stiffness of the joint, and hence the frame, the lateral displacements will be underestimated. Therefore, the interstorey drifts calculated for a frame may be much lower than the actual drifts. In contrast, the design moment capacity of the joint is highly conservative when compared to the experimental results. This is due to the material properties assumed in the method. The maximum allowed stress in the steel is the yield stress. Therefore the moment capacity is not determined using the full range of resistance but only the elastic section of the relationship. This has implications for the capacity design of columns in frames. If the joints are capable of resisting higher moments than predicted, it is important that the columns are also designed for these higher moments, otherwise yielding of the column may occur and stability issues arise. The over-estimation of initial stiffness and the underestimation of the moment capacity is attributed to the fact that the design method attempts to cover a wide range of joint types. These include any joints that may be represented by the use of notional T-stubs, such as top-and seat-angles, web cleats, extended end-plates and flush end-plates. The wide range of details that must be included appears to defeat the purpose of providing an accurate design model.

Another deficiency of the Eurocode 3: Annex J design model is the absence of a ductility prediction. Currently, the code provides a series of criteria that must be checked. It is assumed that if the joint meets these criteria, it possesses sufficient ductility to be used in a global plastic analysis, otherwise the joint may only be used in an elastic analysis. There is no method provided to quantify this ductility level, which leaves the concept very open and vague. A more accurate method of determining the level of ductility in a particular joint is needed to allow accurate modelling of frame response.

8.2.5 Joint Response Modelling

A new prediction model was developed in this study. This model was a combination of two existing T-stub models. It was found that the models proposed by Faella et al (1999) and Shi et al (1996) could be successfully combined to accurately model the response of flush end-plate joints. However, as the Faella et al model was originally developed for use with extended end-plate joints,

it was necessary to alter the formula for initial stiffness. This was done by allowing the effective stiffness width of the notional T-stub to be equal to a geometrical parameter m , which is equal to the length between the centre of the bolt-hole and the beam web weld. This amendment was originally noted in the literature and confirmed using finite element modelling and a comparison study. The model also includes predictions for the rotational deformation due to the column web in tension, compression and shear.

The proposed model was observed to provide reasonable predictions of initial stiffness and good predictions of moment capacity when compared to the experimental results. The predictions of moment capacity are particularly accurate. This is due to the material law adopted in the model, which employs the true stress-natural strain rather than nominal stress and engineering strain. The predictions of initial stiffness were noted to be within 25% of the experimental values for the joints with end-plates that were 12mm or thinner. When the end-plate thickness is increased, the accuracy was observed to decrease significantly. This is attributed to the fact that the model assumes that the end-plate and column flange are the primary contributors to the rotational deformation of the joint. As the thickness of the end-plate is increased, the relative importance of these other components is also increased.

When the model was compared with the design calculations of Eurocode 3, it was observed that the proposed model gave significantly improved predictions. This was true even for the joints with thicker end-plates. However, it was noted that the model was incapable of predicting the premature failure of the bolt threads which was the primary cause of ultimate failure in the mode 2 and mode 3 joints.

Inaccuracies noted in the model were investigated and their primary causes determined. The model does not accurately model bolt behaviour as the prying forces are determined using an approximate method. This leads to inaccuracies in the forces transmitted to the bolts. The bolt elongation is therefore only employed in the calculation of the initial stiffness of the joint. In addition, inaccuracies may be introduced by the elastic-perfectly plastic relationship assumed for the deformation of the column web. However, this was not relevant for the specimens investigated in this study.

8.2.6 Seismic Design of Frames

Based on the experimental observations made in this study, seismic design behaviour factors were suggested for moment-resisting frames employing flush end-plate joints. It was determined that mode 1 and mode 2 joints allowed a dissipative design approach, while mode 3 joints should be

considered only in non-dissipative design, due to their brittle failure mechanism. Using the suggested behaviour factors, critical design ground accelerations were identified for case studies of frames employing joints with different failure modes. It was observed that due to the semi-rigid nature of the wind-moment method, the joints were always partial strength with respect to the beams. Hence, the joint moment capacity was the critical component in each of the frames analysed. It was observed that frames employing mode 1 joints possessed the highest levels of seismic resistance while those employing mode 3 joints possessed little or no seismic resistance. The frames employing mode 2 joints, or industry standard joints, possessed intermediate seismic resistance.

The frames were modelled using three different methods: the Eurocode 3 design method, a modified Eurocode 3 method and the proposed model. It was observed that the Eurocode 3 design model and the modified Eurocode 3 model predicted very similar frame responses despite the different joint stiffnesses employed. In contrast, the proposed model indicated much higher critical ground accelerations than the other two models. This was attributed to the decrease in joint stiffness and the corresponding increase in the fundamental period of the frame, combined with a higher moment capacity. Based on the superior accuracy of the proposed model over the Eurocode 3 design model, it is concluded that the design ground accelerations calculated using the proposed model are more reliable.

Based on the results of the frame analysis, it is concluded that semi-rigid frames designed using the wind-moment method, and employing flush end-plate joints, do possess sufficient seismic resistance for use in areas of low-to-moderate seismic risk. However, it is recommended that these joints are only employed in low-to-medium rise structures. A limit of four storeys is suggested. In frames taller than this, it becomes difficult to design joints with sufficient moment resistance. This is not expected to limit the existing application of flush end-plate joints on the design of such structures already normally employ extended end-plates.

8.3 Suggestions for Further Study

Based on the above conclusions, and observations made during the course of this study, the following are suggestions for further research in this area.

8.3.1 Experimental Work

It is recommended that further experimental work be carried out on flush end-plate joints with various configurations. This further work could include specimens employing larger beams and columns to determine if the observations made during this study to remain valid as joint size is

increased. Joints with thicker end-plates could also be tested to gain a better understanding of the interaction between the different components. The joints in this study all consisted of end-plate joints with one-bolt row in tension; this could be increased to two or three rows in tension.

8.3.2 Improvements in the Prediction of Joint Response

Although the prediction model proposed in this study compared well to the experimental results and was a significant improvement over the Eurocode 3 method, there are still areas in which model accuracy could be increased. The comparisons of initial stiffness need to be improved for joints with thicker end-plate joints. Currently, the model overpredicts this stiffness in joints with 15 mm or thicker end-plates. This over-prediction could be reduced by improved modelling of the bolt behaviour in the joints. As previously stated, further experimental work to determine the interaction of the bolts and end-plate could be required to accomplish this. The ductility capacity predictions given by the model could also be improved significantly. Currently, the ductility of mode 3 joints is underpredicted, while the ductility capacity of the mode 1 and mode 2 joints is over-predicted. Again, this could be improved by more accurate modelling of the bolt behaviour and its influence on the rotation deformation of the joint.

8.3.3 Seismic Frame Design

A small series of frame design cases was carried out in this study. These could be extended to model a wider range of moment-resisting frames. These frames could include more bays and storeys, as well as altering the frame dimensions. The frames modelled in this study were all regular frames. Irregular frames and layouts should be modelled to determine the effects this would have on the design ground acceleration.

Although the behaviour factors chosen in this study were based on the experimental results, these could be improved. Non-linear pushover analyses and non-linear dynamic modelling employing earthquake accelerograms would allow the ratio between the formation of the first and final plastic hinge formation to be accurately determined. This would require accurate modelling of the joint moment-rotation characteristics up to failure, and an accurate cyclic model for dynamic analysis. From this, improved behaviour factors could be recommended for the use of flush end-plate joints with various failure modes.

References

- Adey, B.T., Grondin, G.Y. & Cheng, J.J.R. (1998) 'Extended End-Plate Moment Connections under Cyclic Loading', *Journal of Constructional Steel Research*, Vol. 46, No. 1 – 3, paper no. 133.
- Adey, B.T., Grondin, G.Y. & Cheng, J.J.R. (2000) 'Cyclic loading of end-plate moment connections', *Canadian Journal of Civil Engineering*, Vol. 27, pp. 683 – 701.
- American Institute of Steel Construction (AISC) (1986) *Load and Resistance Factor Design Specification for Structural Steel Buildings*.
- American Institute of Steel Construction (AISC) (1989) *Allowable Stress Design (ASD) Specification for Structural Steel Buildings*.
- Anderson, D., Reading, S.J. & Kavianpour, K. (1991) 'Wind-Moment Design for Unbraced Frames', Steel Construction Institute.
- Applied Technology Council. ATC-24. (1992) 'Guidelines for Cyclic Testing of Components of Steel Structures', Redwood City, USA.
- Azizinamini, A., Bradburn, J.H. & Radziminski, J.B., (1987) 'Initial Stiffness of Semi-Rigid Steel Beam-to-Column Connections', *Journal of Constructional Steel Research*, Vol. 8, pp. 71 – 90.
- Bahaari, M.R. & Sherbourne, A.N. (1996) 'Structural Behaviour of End-Plate Bolted Connections to Stiffened Columns' *ASCE, Journal of Structural Engineering*, Vol. 122 (8), pp. 926 – 935.
- Ballio, G., Calado, L., De Martino, A., Faella, C. & Mazzolani, F.M. (1986) 'Steel Beam-to-Column Joints under Cyclic Loads: Experimental and Numerical Approach' *Proceedings of the 8th European Conference on Earthquake Engineering*, Vol. 4(2), pp. 9-16.
- Beaulieu, D. & Picard, A. (1998) 'Finite Element Modelling of Connections' *Connections in Steel Structures: Behaviour, Strength and Design*, ed. Bjorhovde et al, pp. 96 – 103.
- Beg, D., Plumier, A., Remec, C. & Sanchez, L. (2000) 'Influence of Strain Rate' *Moment Resistant Connections of Steel Frames in Seismic Areas*, ed. F.M. Mazzolani, pp. 167 – 216.

- Bose, S.K., McNeice, G.M. & Sherbourne, A.N. (1972) 'Column Webs in Steel Beam-to-Column Connections: Part 1 - Formulation & Verification' *Computers & Structures* (1972), Vol. 2, pp. 253 – 279.
- Bose, B. & Hughes, A.F. (1995). 'Verifying the performance of standard connections for semi-continuous steel frames' *Proceedings of the Institute of Civil Engineers, Structures and Buildings*, Vol. 110, pp. 441 – 457.
- Bose, B., Wang, Z.M. & Sarkar, S. (1997). 'Finite-Element Analysis of Unstiffened Flush End-Plate Bolted Joints' *ASCE, Journal of Structural Engineering*, Vol. 123(12), pp. 1614 – 1621.
- Bose, B. (1998) 'Design Resistance of Unstiffened Column Web Subject to Transverse Compression in Beam-to-Column Joints' *Journal of Constructional Steel Research*, Vol. 45, No. 1, pp. 1 – 15.
- British Constructional Steel Association (1995). *Joints in Steel Construction: Moment Connections*. Steel Construction Institute (1995).
- British Standards Institute (BSI) (1990) *BS 5950: Structural use of steelwork in building: Part 1* British Standards Institution, London.
- British Standards Institution (1990) '*BS EN10002-1: 1990, Tensile testing of metallic materials, Part 1: Method of test at ambient temperature*', British Standards Institution, London.
- Broderick, B.M. & Thomson, A.W. (2000) 'Cyclic testing of flush end-plate semi-rigid steel connections' *Proceedings of STESSA 2000: Behaviour of steel structures in seismic areas*, pp. 135 – 140.
- Broderick, B.M. & Thomson, A.W. 'The Response of Flush End-plate Joints under Earthquake Loading', *Journal of Constructional Steel Research*, (accepted for publication.).
- Brown, N.D., Hughes, A.F. & Anderson, D. (2001) 'Prediction of the initial stiffness of ductile end-plate steel connections', *Proceedings of the Institution of Civil Engineers: Structures and Buildings* (2001), Vol. 146, pp. 17 – 29.

- Calado, L. & Ferreira, J.A Numerical Model for Predicting the Cyclic Behaviour of Steel Beam-to-Column Joints 10th European Conference on Earthquake Engineering (1995), Vol. 3, pp. 1721 – 1725.
- Choi, C.K. & Chung, G.T.(1996) 'Refined Three-Dimensional Finite Element Model for End-Plate Connections', *ASCE, Journal of Structural Engineering* , Vol. 122 (11), pp. 1307 – 1316.
- Davison, J.B., Kirby, P.A. & Nethercot, D.A.(1987). 'Rotational Stiffness Characteristics of Steel Beam-to-Column Connections', *Journal of Constructional Steel Research*, Vol. 8, pp. 17 – 54.
- De Stefano, M., De Luca, A. & Astaneh-Asl, A. (1993) 'Modelling of Cyclic Moment-Rotation Response of Double-Angle Connections', *ASCE, Journal of the Structural Division*, Vol. 120 (No. 1), pp. 212 – 229.
- Driscoll, G.C. (1987) 'Elastic-Plastic Analysis of Top- and Seat-Angle Connections' *Journal of Constructional Steel Research*, Vol. 8, pp. 119 – 135.
- ECCS Technical Committee 1 - Structural Safety and Loadings (1986). 'Recommended Testing Procedure for Assessing the Behaviour of Structural Steel Elements under Cyclic Loads', *European Convention for Constructional Steelwork*, 1st Edition.
- Elghazouli, A.Y. (1996) 'Ductility of Frames with Semi-Rigid Connections', *11th World Conference on Earthquake Engineering*, Paper No. 1126.
- Elnashai, A.S. & Elghazouli, A.Y. (1994). 'Seismic Behaviour of Semi-rigid Steel Frames', *Journal of Constructional Steel Research*, Vol. 29, pp. 149 – 174.
- Elnashai, A.S., Elghazouli, A.Y. & Denesh-Ashtiani, F.A. (1998). 'Response of Semi-rigid Steel Frames to Cyclic and Earthquake Loads', *ASCE, Journal of Structural Engineering*, Vol. 124, No. 8, pp. 857 – 867.
- European Committee for Standardisation (CEN) (1993), 'Eurocode 3 - Design of Steel Structures, Part 1-1: General Rules and Rules for Buildings', ENV 1993-1-1: 1992.
- European Committee for Standardisation (CEN) (1998), 'Eurocode 3 - Design of Steel Structures, Part 1-1: General Rules and Rules for Buildings, Annex J', ENV 1993-1-1: 1992/A2.

- European Committee for Standardisation (CEN) (2000), 'Eurocode 8: Design of structures for earthquake resistance, Part 1. General Rules, seismic actions and rules for buildings', Draft No. 1, prEN 1998-1.
- Faella C, Piluso V & Rizzano G. Structural Steel Semi-Rigid Connections: Theory, Design and Software. CRC Press. ISBN 0-8493-7433-2: 2000.
- Fanning, P., Tucker, M. & Broderick, B.M. (2000), 'Non-linear finite element analysis of semi-rigid bolted end-plate connections', *Proceedings of 5th International Conference on Computational Structures Technology*, pp. 397 – 403.
- Frye, M.J. & Morris, G.A. (1975), 'Analysis of Flexibly Connected Steel Frames', *Canadian Journal of Civil Engineering*, Vol. 2, pp. 280-291.
- Ghobarah, A., Osman, A. & Korol. R.M. (1990). 'Behaviour of extended end-plates connections under cyclic loading', *Engineering Structures*, Vol. 12, pp. 15 – 27.
- Ghobarah, A., Korol. R.M, & Osman, A. (1992). 'Cyclic Behaviour of Extended End-plate joints', *ASCE, Journal of Structural Engineering*, Vol. 118, No. 5, pp. 1333 – 1353.
- Gioncu, V. (2000). 'Influence of strain-rate on the behaviour of steel members', *Proceedings of STESSA 2000, Behaviour of steel structures in seismic areas*, pp. 19 – 26.
- Huber, G. & Tschemmerneegg, F. (1988). 'Modelling of Beam-to-Column Joints', *Journal of Constructional Steel Research*, Vol. 45, No. 2, pp. 199 – 216.
- Iványi, M. & Varga, G. (1999). 'Full-scale tests of steel frames under quasi-static cyclic loading', *Proceedings of Eurosteel '99, 2nd European Conference on Steel Structures*.
- Iványi, M. & Varga, G. (2000). 'Large scale tests of steel frames with semi-rigid connections under quasi-static loading', *Proceedings of STESSA 2000, Behaviour of steel structures in seismic areas*, pp. 503 – 511.
- Iványi, M. (2000). 'Full-Scale tests of steel frames with semi-rigid connections', *Engineering Structures*, Vol. 22, pp. 168 – 179.

- Johnson, R.P. & Law, C.L. (1981). 'Semi-Rigid Joints for Composite Frames' *Joints in Structural Steelwork*, ed. Howlett et al, pp. 3.3-3.19.
- Jones, S.W., Kirby, P.A. & Nethercot, D.A. (1981). 'Modelling of Semi-Rigid Connection Behaviour and its Influence on Steel Column Behaviour', *Joints in Structural Steelwork*, ed. Howlett et al, pp. 5.73-5.87.
- Kasser, M. & Yu, W.W. (1992). 'Effect of strain-rate on material properties of sheet steels', *ASCE, Journal of Structural Engineering*, Vol. 118, No. 11, pp. 3136 – 3150.
- Kennedy, D.J.L. (1969). 'Moment-rotation Characteristics of Shear Connections', *AISC, Engineering Journal*, October, pp. 105 – 115.
- Kennedy, D.J.L. & Hafez, M.A. (1984). 'A Study of End-Plate Connections for Steel Beams', *Canadian Journal of Civil Engineering*, Vol. 11 (pt. 2), pp. 139 – 149.
- Kirby, P.A., Zandonini, R. & Davison, J.B. (1990). 'On the Determination of Moment-Rotation Characteristics of Beam-to-Column Joints', *RILEM workshop: Needs in Testing Metals*, Naples.
- Kishi, N., Chen, W.F., Matsuoka, K.G. & Nomachi, S.G. (1988a). 'Moment-Rotation Relation of Top- and Seat- Angle with Double Web-Angle Connections', *Connections in Steel Structures: Behaviour, Strength and Design*, ed. Bjorhovde et al, pp. 121-134.
- Kishi, N., Chen, W.F., Matsuoka, K.G. & Nomachi, S.G. (1988b). 'Moment-Rotation Relation of Single/Double Web-Angle Connections', *Connections in Steel Structures: Behaviour, Strength and Design*, ed. Bjorhovde et al, pp. 135-149.
- Kozlowski, A. (1999). 'Experimental tests on steel and composite frame with semi-rigid joints', *Proceedings of Eurosteel '99, 2nd European Conference on Steel Structures*..
- Krishnamurthy, N., Huang, H.T., Jeffery, P.K. & Avery, L.K. (1976). 'Analytical M- θ curves for End-Plate Connections', *ASCE, Journal of the Structural Division*, Vol. 105 (ST1), pp. 133 – 145.
- Krishnamurthy, N. (1980). 'Modelling and Prediction of Steel Bolted Connection Behaviour', *Computers & Structures*, Vol. 11, pp. 75 – 82.

- Kuhlmann, U. & Fürch, A. (1997) 'Rotation Capacity of Steel Joints (2nd draft)', *COST project C1 "Semi-Rigid Behaviour"*, Report C1/WD2\97-07.
- Kukreti, A.R., Murray, T.M. & Abolmaali, A. (1987). 'End-Plate Connection Moment-Rotation Relationship', *Journal of Constructional Steel Research*, Vol. 8, pp. 137 – 157.
- Leon, R.T. & Deierlein, G.G. (1996). 'Considerations for the Use of Quasi-Static Testing', *Earthquake Spectra*, vol. 12, Number 1, pp. 87 – 110.
- Lewitt, C.W., Chesson, E. & Munse, W. (1969). 'Restraint Characteristics of Flexible Riveted and Bolted Beam-to-Column Connections', *Bulletin No. 500*, Engineering Experiment Station, University of Illinois, Chicago.
- Lionberger, S.R. & Weaver, W. (1969). 'Dynamic Response of Frames with Non-Rigid Connections', *ASCE, Journal of the Engineering Mechanics Division*, Vol. 95 (EM1), pp. 95-114.
- Lipson, S.L. & Haque, M.I. (1978). 'Elasto-Plastic Analysis of Single-Angle Bolted-Welded Connections using the Finite Element Method', *Computers and Structures*, Vol. 9, pp. 533 – 545.
- Lothers, J.E. (1951). 'Elastic Restraint Equations for Semi-Rigid Connections', *ASCE, Transactions*, Volume 1/6, pp. 480-502.
- Lui, E.M. & Chen, W.F. (1986). 'Analysis and Behaviour of Flexibly-Jointed Frames', *AISC, Engineering Journal*, Vol. 8, pp. 107-118.
- Macken, C. (1997). 'Testing of Steel Moment Connections', *M.Sc. Thesis*, Trinity College Dublin.
- Madas, P.J. (1996). 'Advanced Modelling of Composite Frames Subjected to Earthquake Loading', *Ph.D. Thesis*, University of London.
- Manjoine, M.J. (1944). 'Influence of strain-rate and temperature of yield stress of mild steel', *ASCE, Journal of Applied Mechanics*, Vol. 66, No. 11, pp. 211 – 218.
- Maranian, P. (1997). 'Vulnerability of existing steel framed buildings following the 1994 Northridge (California, USA) earthquake: considerations for their repair and strengthening', *The Structural Engineer*, Vol. 75, No. 10, pp. 165 – 172.

- Mazzolani, F.M. (1988). 'Mathematical Model for Semi-Rigid Joints under Cyclic Loads', *Connections in Steel Structures: Behaviour, Strength and Design*, ed. Bjorhovde et al, pp. 112-120.
- Moncarz, P.D. & Gerstle, K.H. (1981), 'Steel Frames with Non-linear Connections', *ASCE, Journal of the Structural Division*, Vol. 107 (ST8), pp. 1427-1441.
- Nethercot, D.A. & Zandonini, R. (1990). 'Methods of Prediction of Joint Behaviour', *Structural Connections: Stability and Strength*, ed. R. Narayanan, pp.23-62.
- Patel, K.V. & Chen, W.F. (1984). 'Non-linear Analysis of Steel Moment Connections', *ASCE, Journal of Structural Engineering*, Vol. 111 (ST8), 99. 1861 – 1875.
- Phillips, J. & Packer, J.A. (1981) The Effect of Plate Thickness on Flush End-plate Connections, In *Joints in Structural Steelwork*, ed. Howlett et al, pp. 6.77 - 6.92.
- Piluso V, Faella C, & Rizzano G. (2001a). 'Ultimate Behaviour of Bolted T-Stubs: 1 Theoretical Model', *ASCE, Journal of Structural Engineering.*, Vol. 127 (5): pp. 686 – 693.
- Piluso, V., Faella, C. & Rizzano, G., (2001b). 'Ultimate Behaviour of Bolted T-Stubs: 2 Model Validation', *ASCE, Journal of Structural Engineering.*, Vol. 127 (5): pp. 686 – 693, pp. 694 – 704.
- Poggi, C. & Zandonini, R. (1985). 'Behaviour and Strength of Steel Frames with Semi-Rigid Connections', *Connection Flexibly and Steel Frame Behaviour*, *ASCE*, ed. W.F. Chen.
- Popov, E.P. (1987). 'Panel Zone Flexibility in Seismic Moment Joints', *Journal of Constructional Steel Research*, Vol. 8, pp. 91 – 118.
- Prichard, S.J. (2000). 'Sleeved Concrete Cylinders subject to Hard Impact', *PhD Thesis*, University of Dublin.
- Ren, P. & Crisnel, M. (1995). 'Prediction Method for Moment-Rotation Behaviour of Composite Beam to Steel-Column Connection', *Proceedings of the 4th Pacific Structural Steel Conference*, Volume 2: Structural Connections, pp.33-46.
- Richard, R.M. & Abbott, B.J (1975). 'Versatile Elastic-Plastic Stress-Strain Formula', *ASCE, Journal of the Engineering Mechanics Division*, Vol. 101 (EM4), pp.511-515.

- Richard, R.M., Gillett, P.E., Kriegh, J.D. & Lewis, B.A. (1980). 'The Analysis and Design of Single Plate Framing Connections', *AISC, Engineering Journal*, Vol. 17 (2), pp. 38-52.
- Richard, R.M., Rabern, D.A., Hormby, D.E. & Williams, G.C.(1983). 'Analytical Models for Steel Connections', *Proceeding of Behaviour of Metal Structures*, Vol. 1, pp. 128 – 155.
- RILEM (1990). 'RILEM Draft Recommendation – Tension Testing of Metallic Structural Materials for Determining Stress-Strain Relations under Monotonic and Uniaxial Tensile Loading', *Materials and Structures*, Vol. 23, pp. 35 –46.
- Romstad, K.M. & Subramanian, C.V. (1970). 'Analysis of Frames with Partial Connection Rigidity', *ASCE, Journal of the Structural Division*, Vol. 96 (ST11), pp. 2283-2300.
- Ryan, C.A. (2001). 'Confinement in Wireball Reinforced Concrete Members', *PhD Thesis*, University of Dublin.
- Sanchez, L. & Plumier, A. (2000). 'Tests on the strain-rate effects on beam-to-column steel connection', *Proceedings of STESSA 2000, Behaviour of steel structures in seismic areas*, pp. 247 – 254.
- Shi, Y.J., Chan, S.L. & Wong, Y.L. (1996). 'Modelling for Moment-Rotation Characteristics for End-Plate Connections', *ASCE, Journal of the Structural Division*, Vol. 122 (No. 6), pp. 1300 – 1306.
- Soroushian, P. & Choi, K.B. (1987). 'Steel mechanical properties at different strain-rates', *ASCE, Journal of Structural Engineering*, Vol. 113, No. 4, pp. 863 – 872.
- Takanashi, K., Elnashai, A.S., Elghazouli, A.Y. & Ohi, K. (1992). 'Behaviour of Steel Frames with Semi-rigid connections under Earthquake Loading', *1st World Conference on Constructional Steel Design*, ed. P.J. Dowling.
- Thomson, A.W. & Broderick, B.M. (2000). 'Cyclic Testing and Analysis of Steel End-Plate Connections', *Abnormal Loading on Structures: Experimental and Numerical Modelling* , pp. 247 – 256.
- Thomson, A.W. & Broderick, B.M. (2000). 'Seismic Resistance of Flush End-Plate Connections', *The Structural Engineer*, Vol. 78, No. 17, pp. 28 – 33.

- Thomson, A.W. & Broderick, B.M., 'Cyclic Testing and analysis of semi-rigid flush end-plate joints' *Proceedings of 12th European Conference on Earthquake Engineering*, Paper Reference 101 (under review).
- Thomson, A.W. & Broderick, B.M. 'Earthquake Resistance of Flush End-Plate Steel Joints for Moment Frames', *Proceeding of the Institution of Civil Engineers, Buildings and Structures* (under review).
- Tsai, K.C. & Popov, E.P. (1992). 'Cyclic Behaviour of End-Plate Moment Connections', *Journal of Structural Engineering, ASCE*, Vol. 116, No. 11, pp. 2917 – 2930.
- Tschemmerneegg, F. (1988). 'On the Non-linear Behaviour of Joints in Steel Frames', *Connections in Steel Structures: Behaviour, Strength and Design*, ed. Bjorhovde et al, pp. 158 – 165.
- Tucker, M. (2002). 'Finite Element Modelling of Semi-Rigid Flush End-Plate Joints (Working Title)', *PhD. Thesis*, University College Dublin (to be submitted).
- Uang, C.M. & Bondad, D.M. (1996). 'Dynamic testing of full-scale steel moment connections', *Proceedings of the 11th World Conference on Earthquake Engineering*, Mexico, Paper 407, CD-ROM.
- Wales, M.W. & Rossow, E.C. (1983). 'Coupled Moment-Axial Force Behaviour in Bolted Connections', *ASCE, Journal of the Structural Division*, Vol. 109 (No. 5), pp. 1250 – 1266.
- Wallace, B.J. & Krawinkler, H. (1989). 'Small-scale model tests of structural steel assemblies', *ASCE, Journal of Structural Engineering*, Vol. 115, No. 8, pp. 1999 – 2015.
- Weynand, K., Jaspert, J.P. & Steenhuis M. (1995). 'The Stiffness Model of revised Annex J of Eurocode 3'. *Connections in Steel Structures III: Behaviour, Strength and Design.*, ed. R. Bjorhovde, 441–452.
- Wright, R.N. & Hall, W.J. (1964). 'Loading rate effects in structural steel design', *ASCE, Journal of the Structural Division*, Vol. 90, No. 55, pp. 11 – 37.
- Yee Y.L. & Melchers, R.E. (1986). 'Moment-Rotation Curves for Bolted Connections', *ASCE, Journal of Structural Engineering*, Vol. 112 (3) pp. 615-635.

Yu, C.H., Richard Liew, J.Y., Shanmugam, N.E. & Ng, Y.H. (1998). 'Collapse Behaviour of Sway Frames with End-plate Connections', *Journal of Constructional Steel Research*, Vol. 48, pp. 169 – 188.

Appendix A

Material Properties

A.1 Steel Tensile Test Results

Samples were taken from specimens in test series two and three. These samples were tested to failure in accordance with BS 10002-1:1990. The majority of the samples were standard specimens according to the code. However, samples taken from the end-plates were not standard samples due to the joint dimensions.

The samples tested from test series two were tested internally within the Department of Civil, Structural and Environmental Engineering in Trinity College Dublin. Strains were measured as the applied load. However, upon examination of the results it was discovered that the strains did not conform to any expected stress-strain relationship. Young's modulus was calculated for these specimens and was found to vary between 35,000 N/mm² and 161,000 N/mm². Therefore, it was felt that the strains gauge results could not be relied on for these tests. Plots of scan number versus imposed load were used to determine the yield and ultimate stress of the samples. These results are presented in Table A.1.

The samples taken from the beam flanges were taken at a distance of 500 mm from the end-plate. This corresponds to approximately two-thirds of the distance between the end-plate and the actuator connection piece. One sample was taken from each flange and were parallel to the flange direction. The sample taken from the beam web was also cut 500 mm from the end-plate. This sample was perpendicular to the beam flanges. The samples taken from the end-plate were removed parallel to the longer dimension in order to avoid the area of the weld. These samples were non-standard specimens due to the thickness of the end-plate and the spacing of the bolt holes.

Table A.2 presents the samples taken from the third test series. Due to the problems with the first set of samples, these were sent to Material Ireland in University College Dublin for testing. The results are presented in Table A.2, followed by the stress-strain curves for the eighteen samples. The samples were taken from the same location as described above. All of the specimens conformed to BS EN 10002-1: 1990.

It should be noted that a number of the end-plate samples do not show standard steel properties, especially those taken from joints that were subject to a mode I failure. This is due to the fact that the steel will already have undergone significant plastic yielding during testing of the joint.

<i>Sample Designation</i>	<i>Location from which sample taken</i>	<i>Yield Stress</i> [N/mm ²]	<i>Ultimate Stress</i> [N/mm ²]
A1	Specimen 2.1 beam flange	272.11	404.61
A2	Specimen 2.1 beam flange	263.93	411.91
A3	Specimen 2.1 beam web	275.41	413.92
A4	Specimen 2.1 end-plate (non-standard sample)	317.39	446.11
A5	Specimen 2.1 end-plate (non-standard sample)	325.84	432.76
A6	Specimen 2.2 beam flange	292.07	424.48
A7	Specimen 2.2 beam flange	272.05	413.91
A8	Specimen 2.2 beam web	302.39	415.79
A9	Specimen 2.2 end-plate (non-standard sample)	323.11	449.79
A10	Specimen 2.2 end-plate (non-standard sample)	327.72	465.7
A11	Specimen 2.5 beam flange	290.65	424.34
A12	Specimen 2.5 beam flange	281.97	413.54
A13	Specimen 2.55 beam web	303.76	405.99
A14	Specimen 2.5 end-plate (non-standard sample)	304.04	480.44
A15	Specimen 2.5 end-plate (non-standard sample)	339.82	436.58
A16	Specimen 2.1 Column Flange	286.51	468.84
A17	Specimen 2.1 Column Flange	289.06	459.87
A18	Specimen 2.1 Column Web	273.87	475.67

Table A.1: Material properties for samples taken from test series two

<i>Sample</i>	<i>Location</i>	<i>Young's Modulus [N/mm²]</i>	<i>Yield Stress [N/mm²]</i>	<i>Yield Strain</i>	<i>Ultimate Stress [N/mm²]</i>	<i>Ultimate Strain</i>
B1	Specimen 3.1 Column Web	210869.3	265.39	0.00175	470.74	0.2081
B2	Specimen 3.1 Column Flange	166656.1	270.37	0.00148	461.11	0.1145
B3	Specimen 3.1 Beam Web	201698.5	241.10	0.00129	348.52	0.1524
B4	Specimen 3.1 Beam Flange	364043.0	330.56	0.00126	429.25	0.1667
B5	Specimen 3.1 End-plate	194473.9	317.16	0.0021	487.18	0.2224
B6	Specimen 3.1 End-plate	196650.4	310.78	0.00152	477.80	0.0801
B7	Specimen 3.3 End-plate	209215.9	304.87	0.00146	525.66	0.2250
B8	Specimen 3.3 End-plate	186593.3	272.88	0.00149	485.21	0.2971
B9	Specimen 3.5 Column Web	207821.9	315.06	0.00152	478.41	0.2315
B10	Specimen 3.5 Column Web	181407.3	314.66	0.00193	477.31	0.2206
B11	Specimen 3.5 Column Flange	199174.5	340.28	0.00171	508.55	0.1027
B12	Specimen 3.5 Column Flange	202745.0	311.71	0.00154	389.08	0.0391
B13	Specimen 3.5 Beam Web	150122.2	235.62	0.00157	410.41	0.1988
B14	Specimen 3.5 Beam Flange	193940.4	306.83	0.00155	450.01	0.2270
B15	Specimen 3.5 End-plate	200136.4	287.34	0.00144	397.15	0.2419
B16	Specimen 3.7 Column Web	228039.1	254.25	0.00124	469.13	0.2199
B17	Specimen 3.7 Column Flange	180155.0	271.12	0.00163	457.67	0.2056
B18	Specimen 3.7 End-plate	119342.3	224.25	0.00412	350.12	0.1215

Table A.2: Material properties for samples taken from test series three

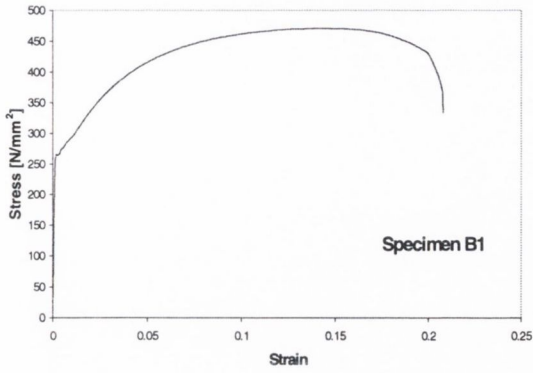


Figure A.1: Specimen B1

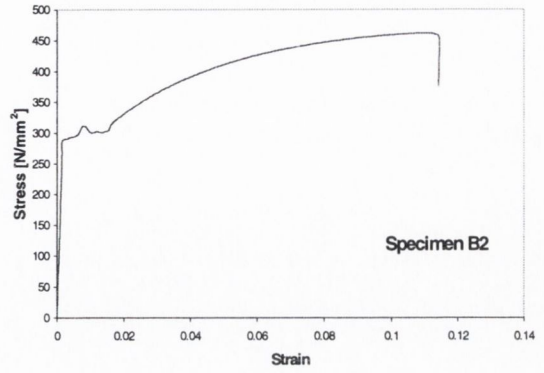


Figure A.2: Specimen B2

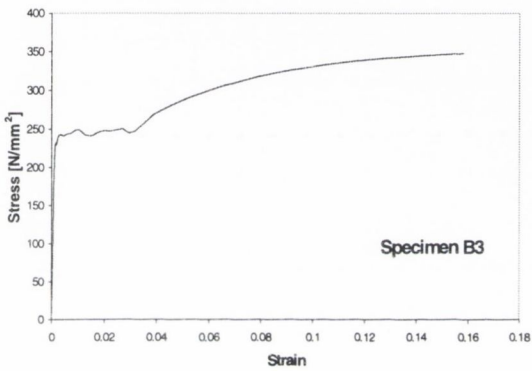


Figure A.3: Specimen B3

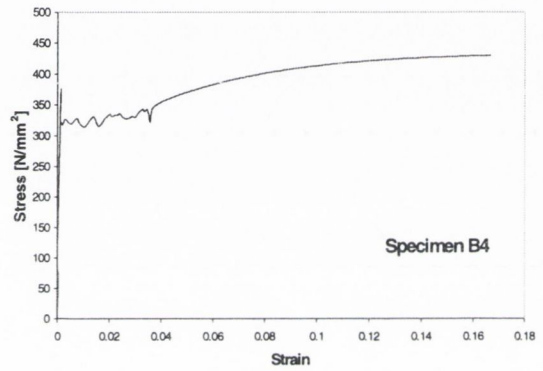


Figure A.4: Specimen B4

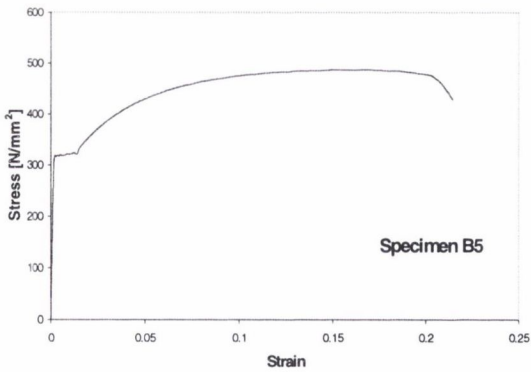


Figure A.5: Specimen B5

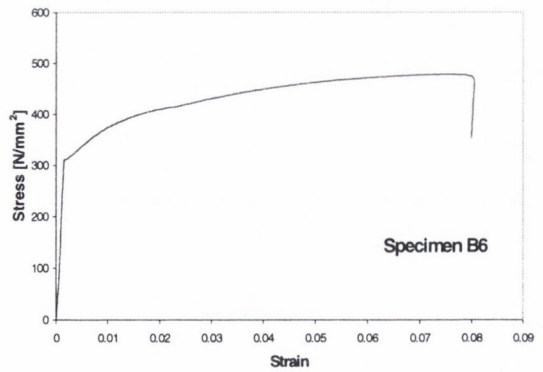


Figure A.6: Specimen B6

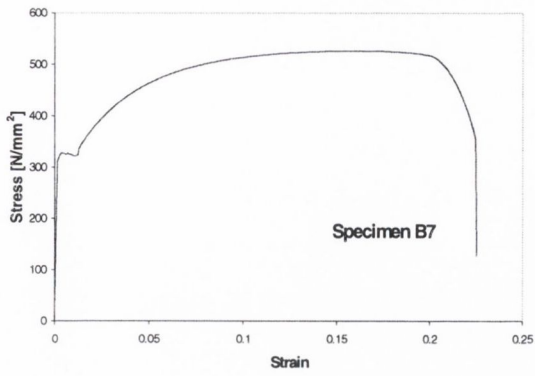


Figure A.7: Specimen B7

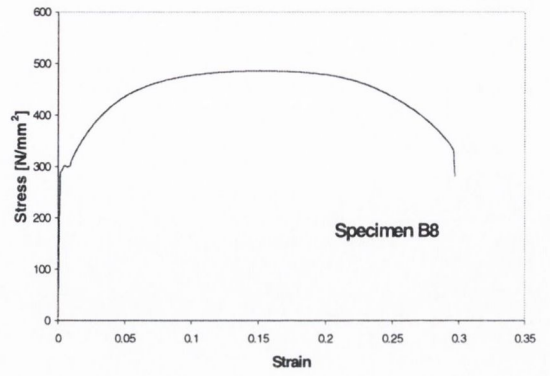


Figure A.8: Specimen B8

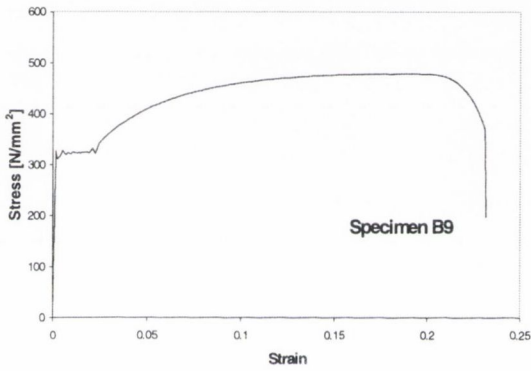


Figure A.9: Specimen B9

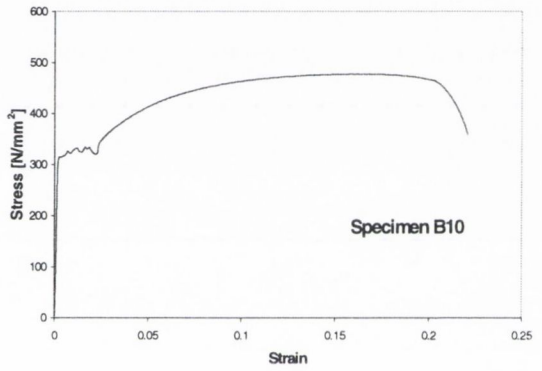


Figure A.10: Specimen B10

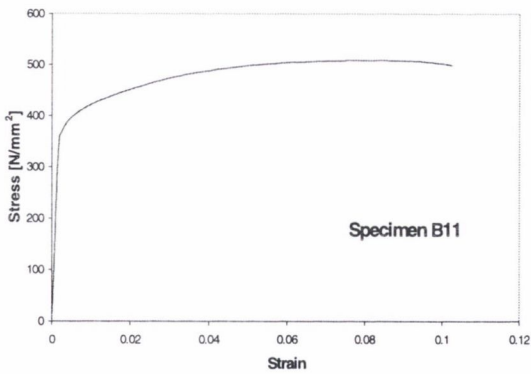


Figure A.11: Specimen B11

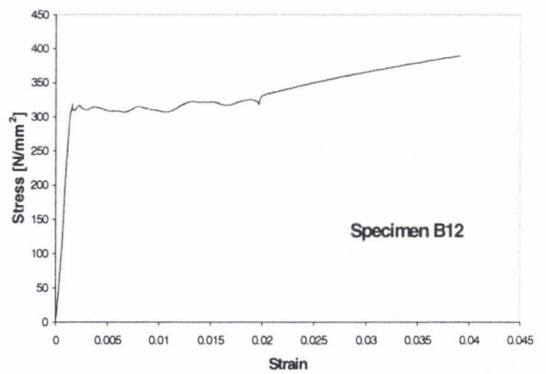


Figure A.12: Specimen B12

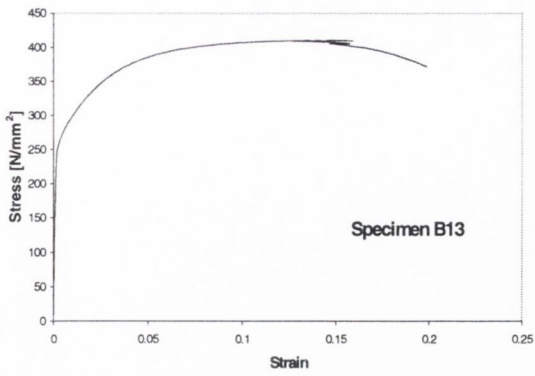


Figure A.13: Specimen B13

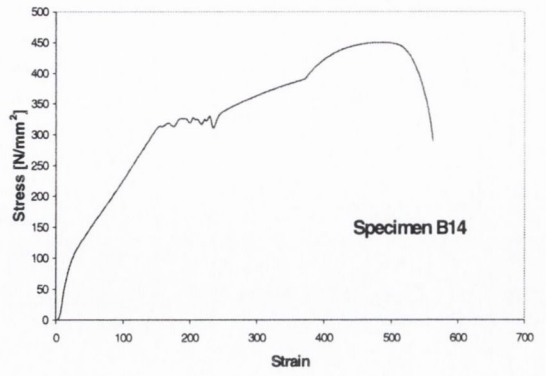


Figure A.14: Specimen B14

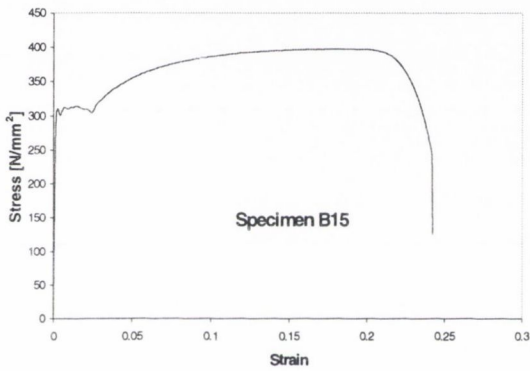


Figure A.15: Specimen B15

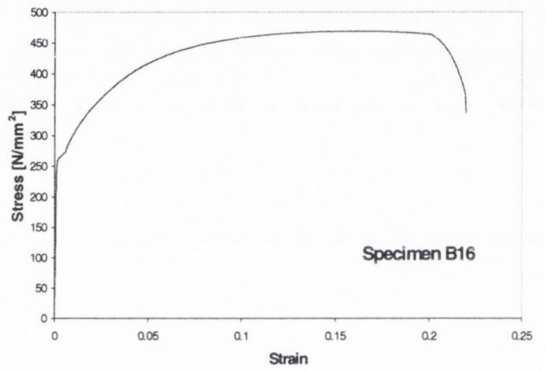


Figure A.16: Specimen B16

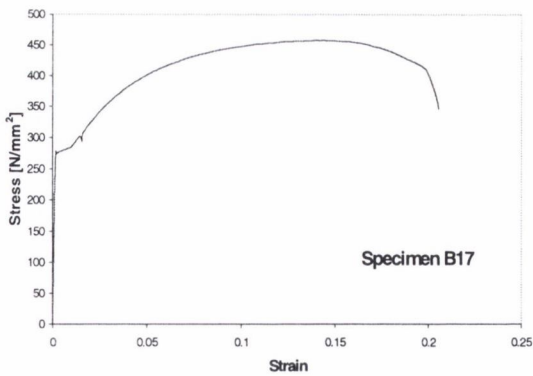


Figure A.17: Specimen B1

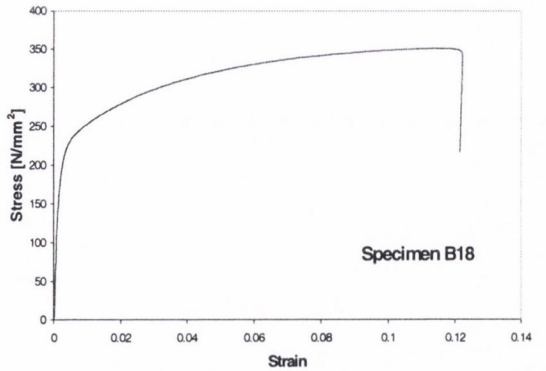


Figure A.18: Specimen B1

A.2 Bolt Tensile Test Results

<i>Test</i>	<i>Bolt Grade and Size</i>	<i>Yield Stress</i> [N/mm ²]	<i>Ultimate Stress</i> [N/mm ²]
1	Grade 8.8 M16	755.19	850.32
2	Grade 8.8 M16	636.82	878.44
3	Grade 8.8 M16	700.55	839.61
4	Grade 8.8 M16	637.61	820.89
5	Grade 8.8 M16	742.54	861.53
6	Grade 8.8 M16	693.25	840.76
7	Grade 8.8 M20	571.43	749.1
8	Grade 8.8 M20	622.74	651.23
9	Grade 8.8 M20	603.2	677.88
10	Grade 8.8 M20	631.63	645.89
11	Grade 8.8 M20	583.92	651.18
12	Grade 8.8 M20	612.25	645.87
13	Grade 10.9 M20	901.79	1095.53
14	Grade 10.9 M20	961.67	1012.99
15	Grade 10.9 M20	947.58	1010.75
16	Grade 10.9 M20	859.52	1040.93

Table A.3: Bolt properties

In addition to the material tests described above, tensile tests were carried out on a number of bolts identical to those used in the full-scale tests discussed in chapters 4 and 5. The purpose of these test was to determine yield and ultimate stresses for the different sizes and grades. The results from these tests are presented in Table A.3. These tests were carried out using a 50 tonne hydraulic actuator. It was not possible to determine the strains in the bolt shaft as the attachment of strain gauges would have resulted in adverse effects on the bolt properties. Therefore, the yield and ultimate stress values are determined from load versus displacement and load versus scan number relationships, examples of which are shown below. It was observed that all of the M16 size bolts failed in a classical fracture manner and therefore were able to develop the full stress range for the bolts. In contrast, all of the Grade 8.8 M20 bolts failed by sudden stripping of the bolt and nut threads as was observed during the joint experiments. None of these bolts reached their nominal ultimate stress of 800 N/mm². It was also seen that the yield stress values obtained for these bolts were also lower than expected, ranging from 571.43 to 631.63 N/mm². The grade 10.9 M20 bolts also failed by stripping of the bolts. However, the yield and ultimate stresses were very close to the nominal value for these bolts.

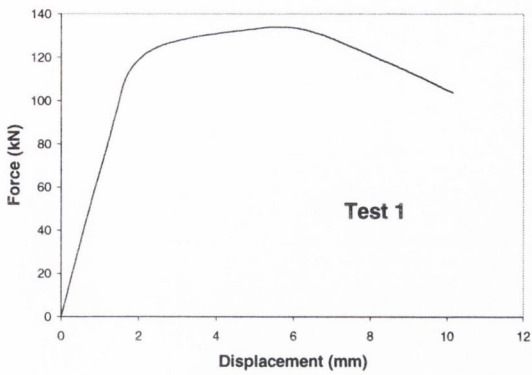


Figure A.19: Bolt Test 1

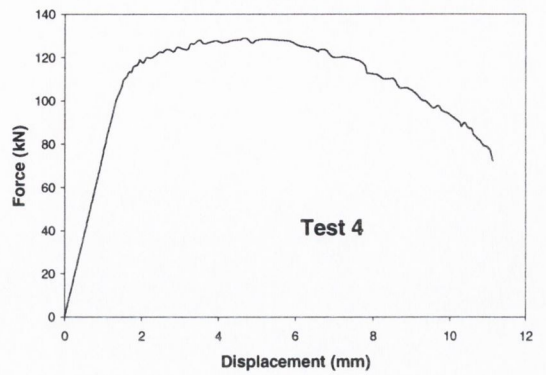


Figure A.20: Bolt Test 4

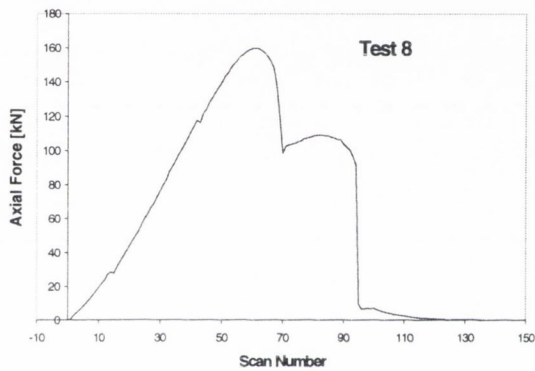


Figure A.21: Bolt Test 8

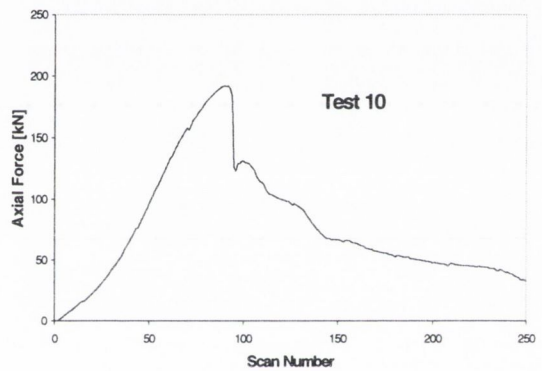


Figure A.22: Bolt Test 10

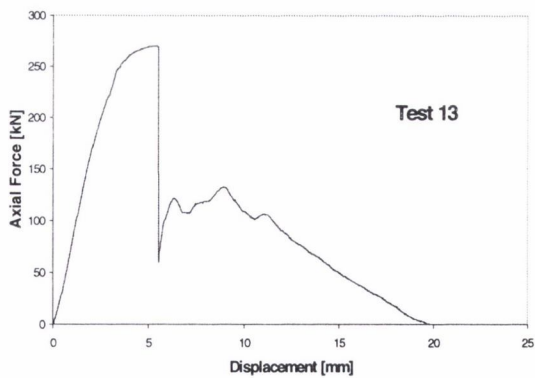


Figure A.23: Bolt Test 13

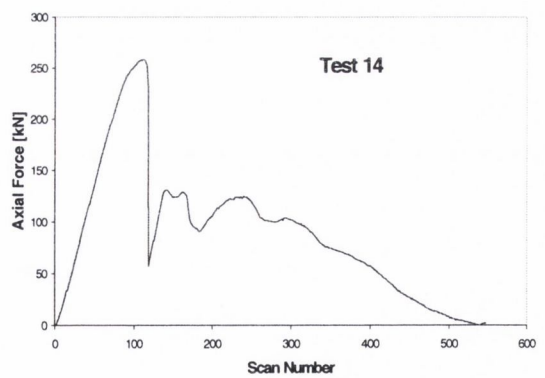


Figure A.24: Bolt Test 14

Appendix B

Strain Gauge Results

B.1 Test Series Two

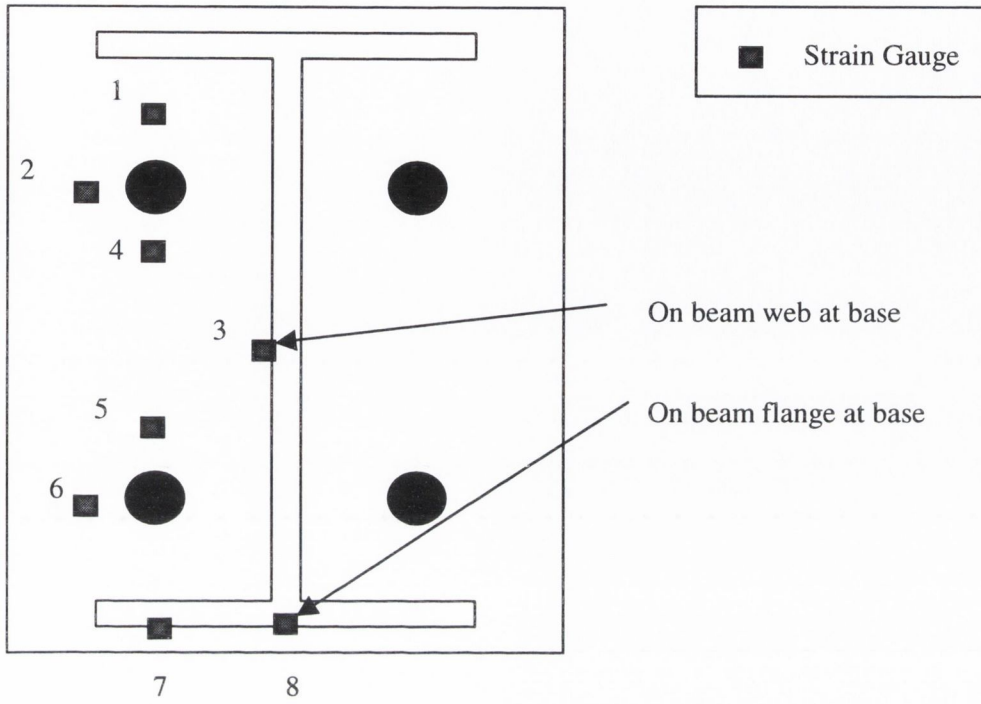


Figure B.1: Measurement device locations in test series two (plan view)

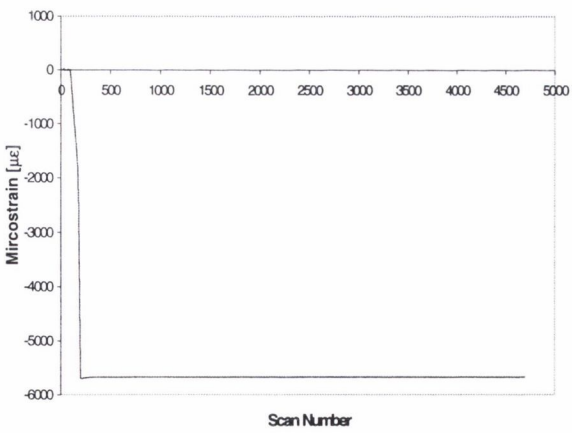


Figure B.2: Specimen 2.1, strain gauge 1

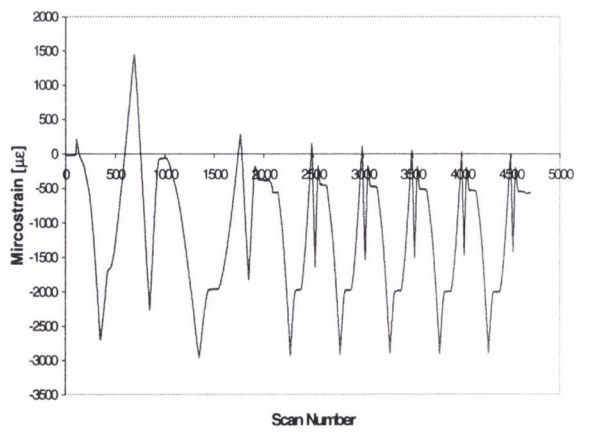


Figure B.3: Specimen 2.1, strain gauge 3

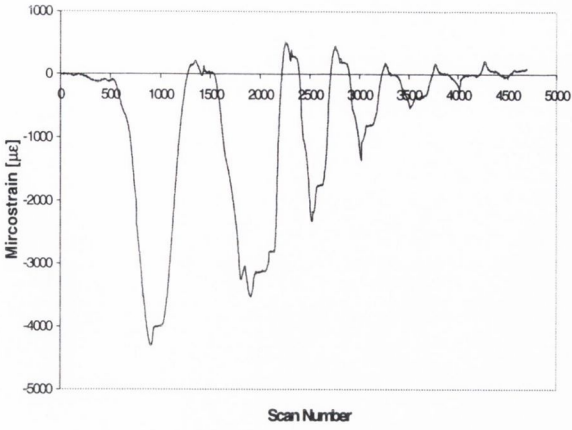


Figure B.4: Specimen 2.1, strain gauge 4

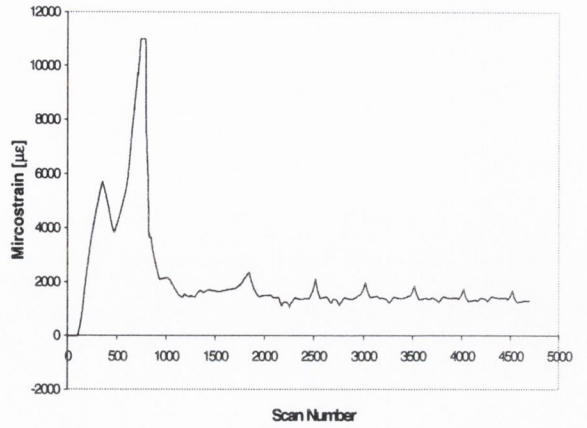


Figure B.5: Specimen 2.1, strain gauge 6

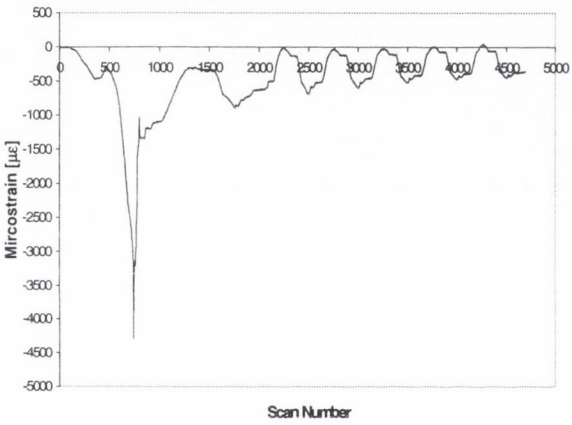


Figure B.6: Specimen 2.1, strain gauge 7

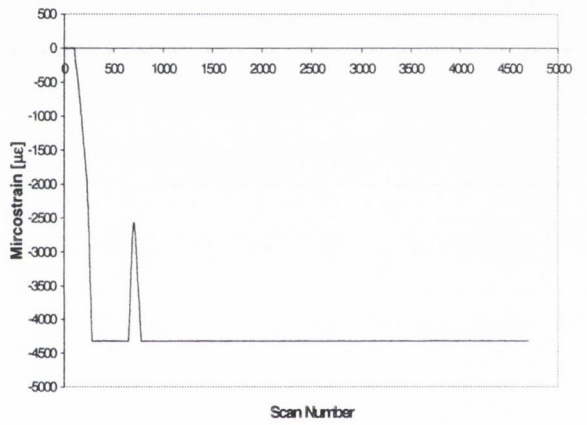


Figure B.7: Specimen 2.1, strain gauge 8

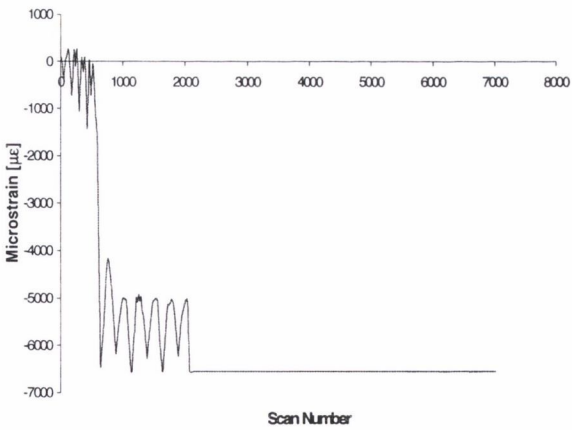


Figure B.8: Specimen 2.2, strain gauge 1

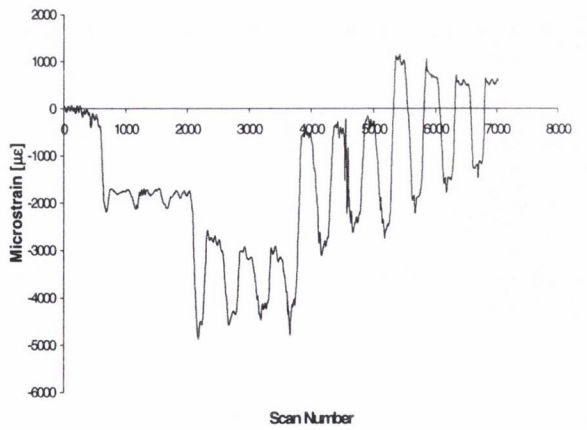


Figure B.9: Specimen 2.2, strain gauge 2

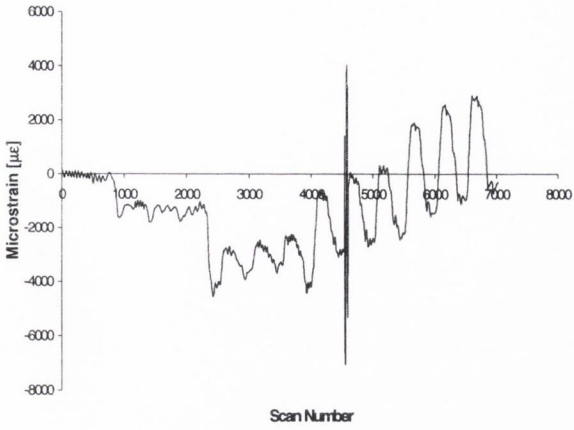


Figure B.10: Specimen 2.2, strain gauge 3

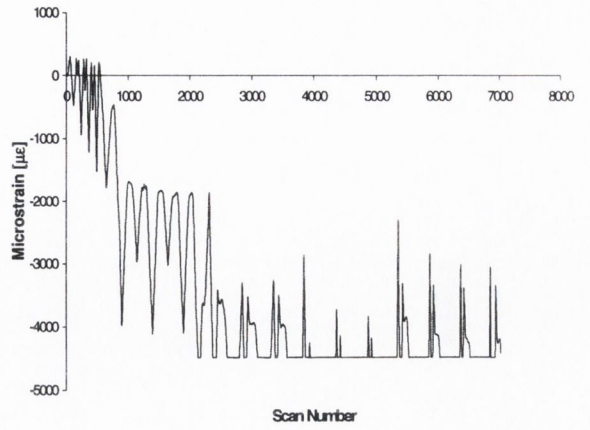


Figure B.11: Specimen 2.2, strain gauge 4

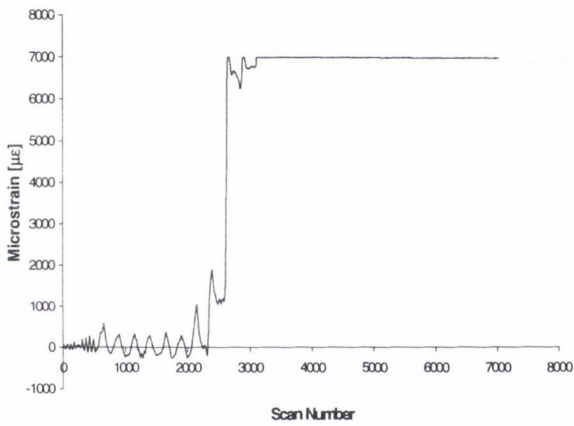


Figure B.12: Specimen 2.2, strain gauge 6

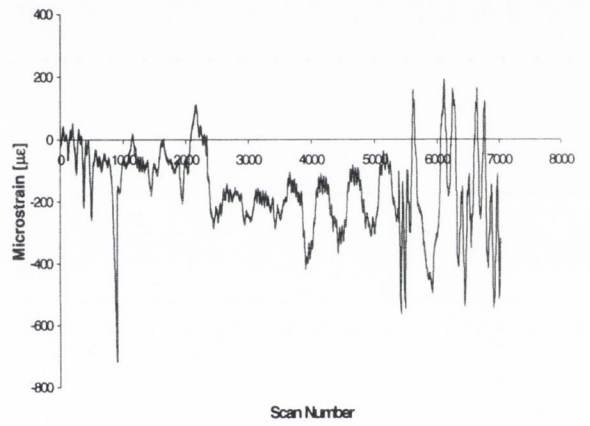


Figure B.13: Specimen 2.2, strain gauge 7

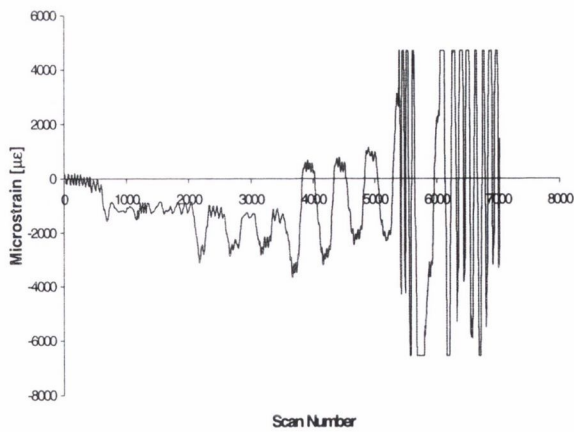


Figure B.14: Specimen 2.2, strain gauge 8

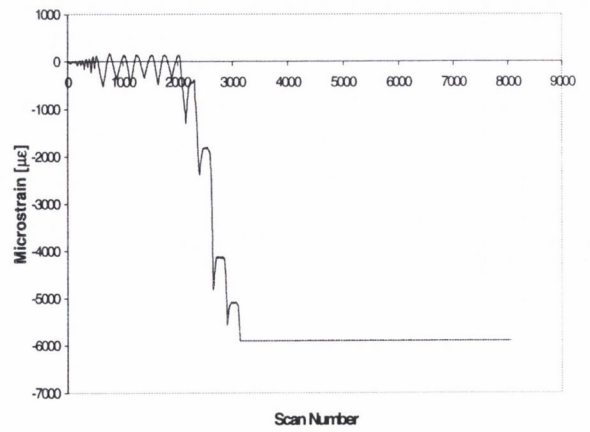


Figure B.15: Specimen 2.4, strain gauge 1

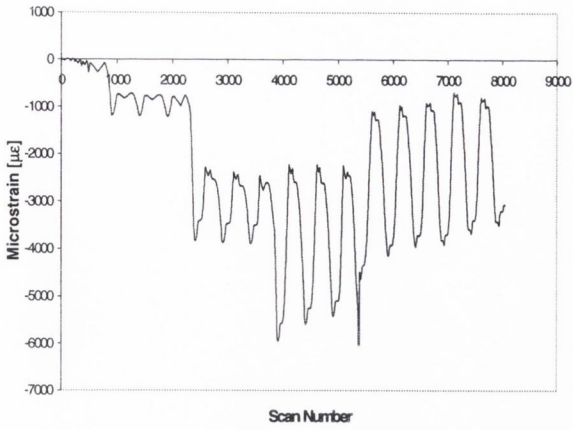


Figure B.16: Specimen 2.4, strain gauge 2

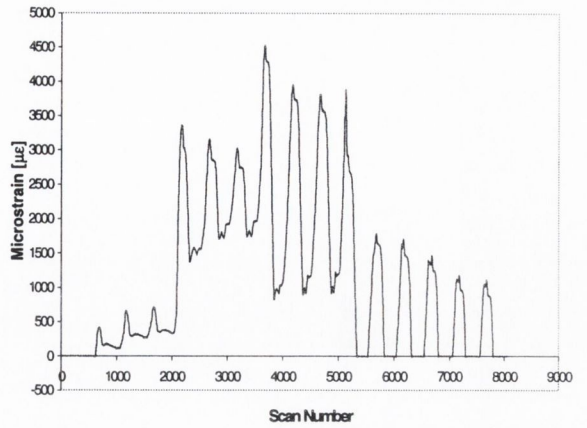


Figure B.17: Specimen 2.4, strain gauge 3

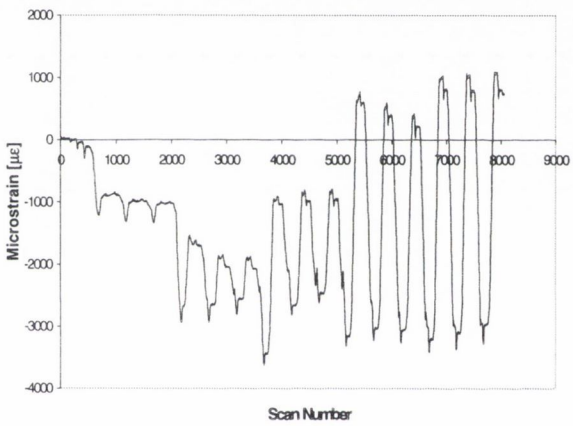


Figure B.18: Specimen 2.4, strain gauge 4

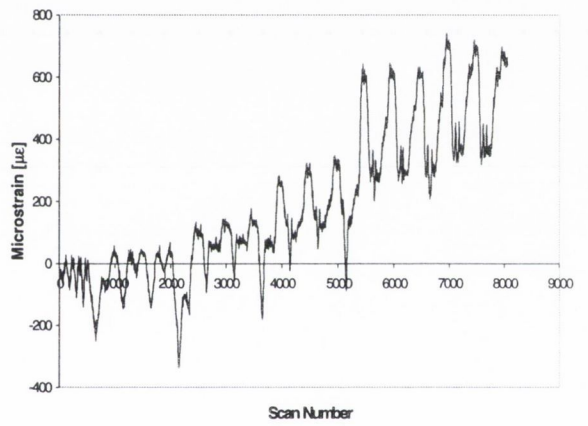


Figure B.19: Specimen 2.4, strain gauge 5

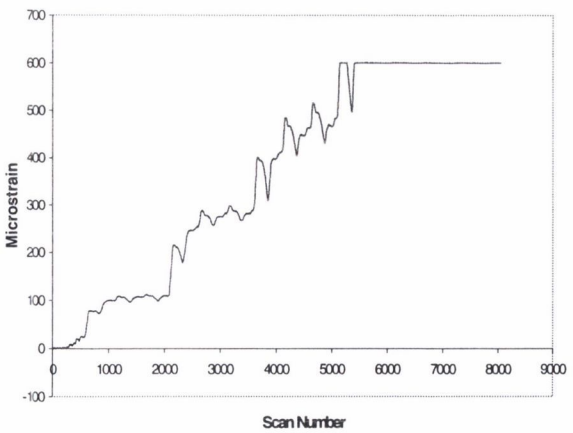


Figure B.20: Specimen 2.4, strain gauge 7

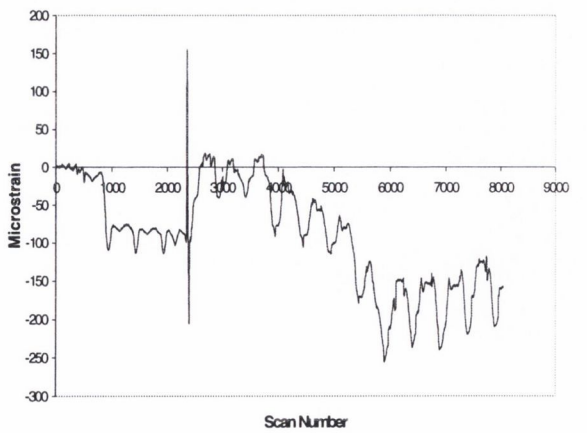


Figure B.21: Specimen 2.4, strain gauge 8

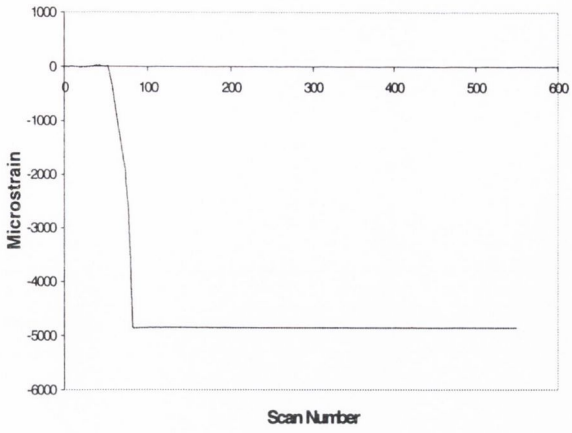


Figure B.22: Specimen 2.5, strain gauge 1

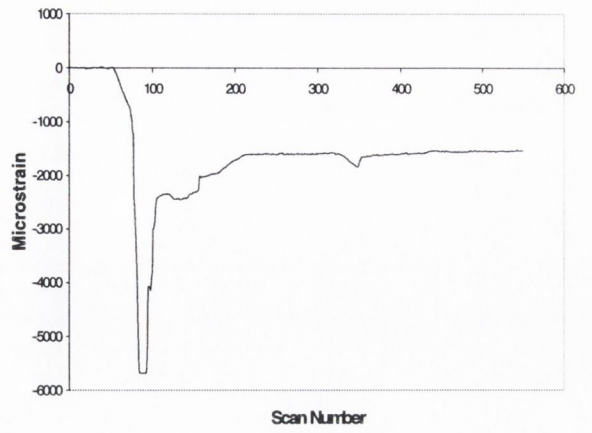


Figure B.23: Specimen 2.5, strain gauge 2

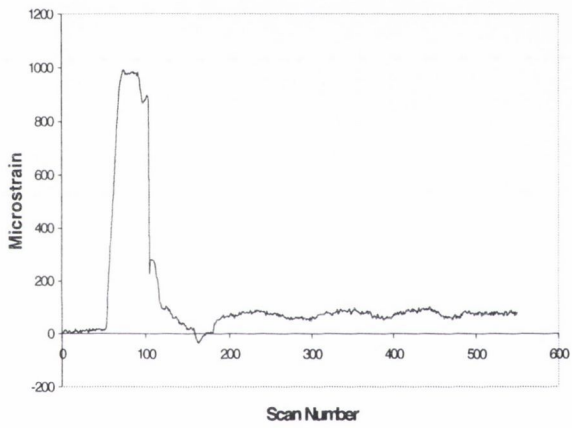


Figure B.24: Specimen 2.5, strain gauge 4

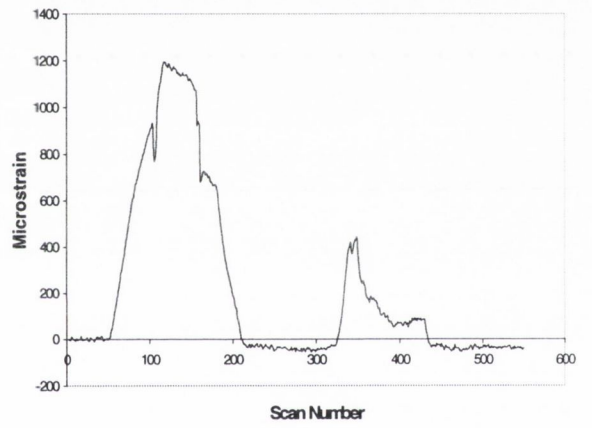


Figure B.25: Specimen 2.5, strain gauge 5

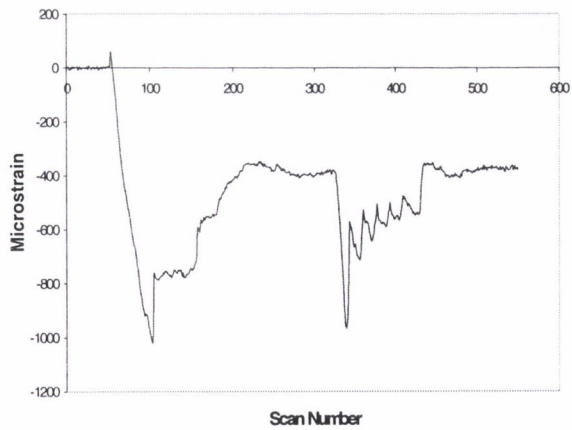


Figure B.26: Specimen 2.5, strain gauge 8

B.2 Test Series Three

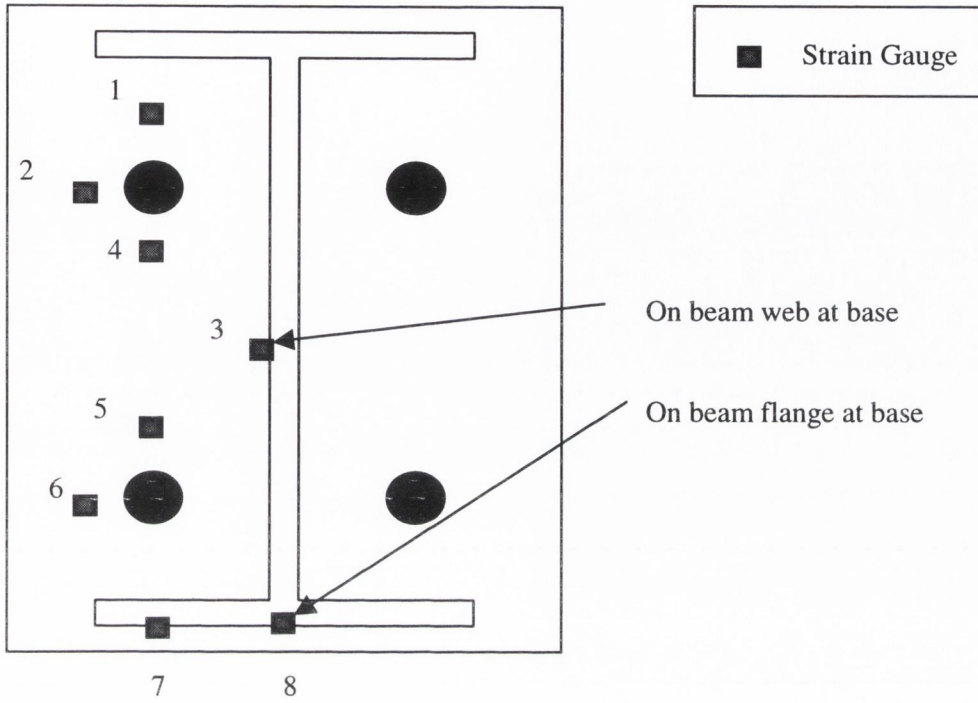


Figure B.27: Measurement device locations in test series two (plan view)

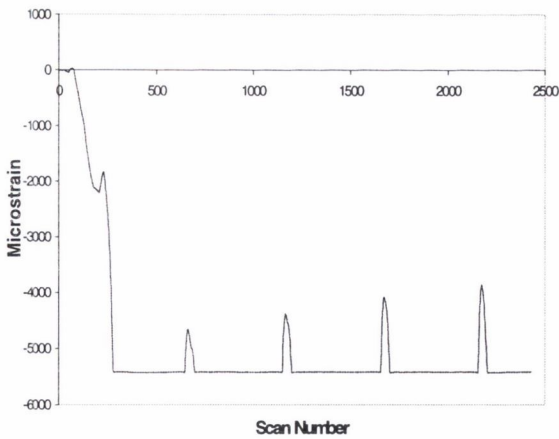


Figure B.28: Specimen 3.1, strain gauge 1

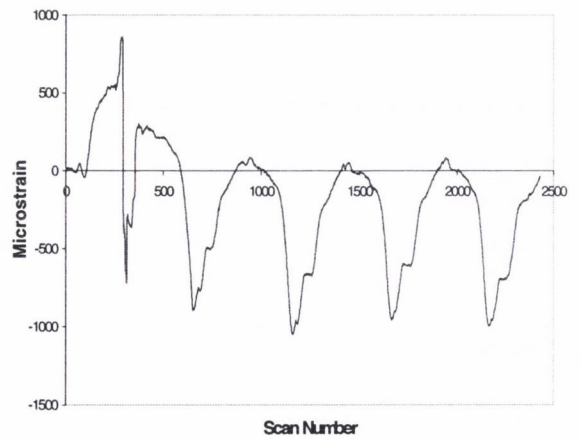


Figure B.29: Specimen 3.1, strain gauge 2

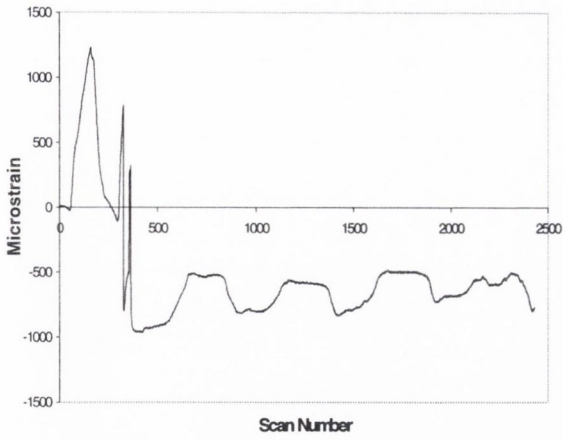


Figure B.30: Specimen 3.1, strain gauge 3

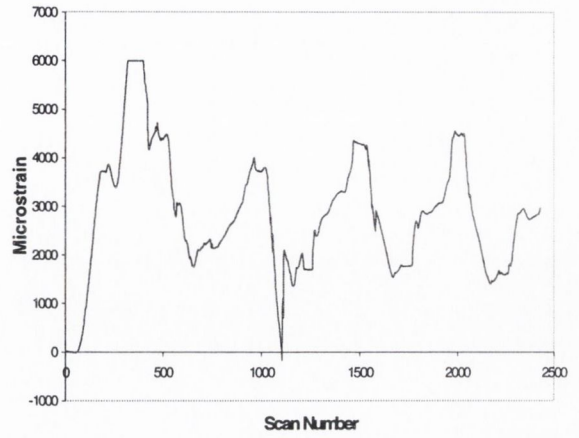


Figure B.31: Specimen 3.1, strain gauge 4

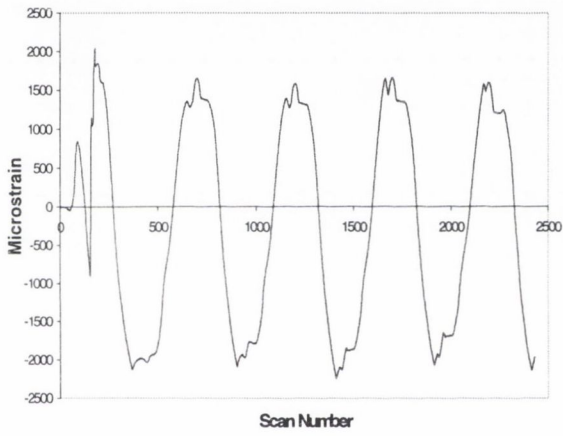


Figure B.32: Specimen 3.1, strain gauge 5

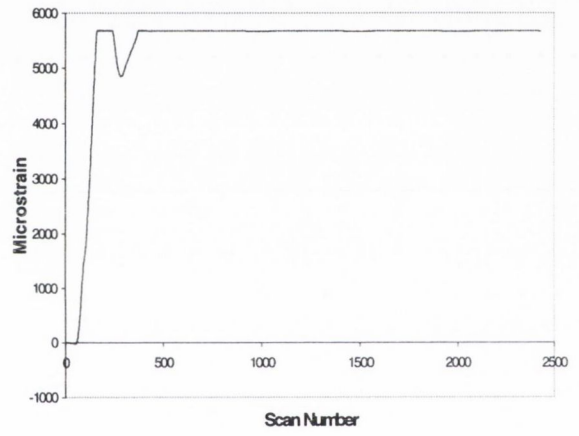


Figure B.33: Specimen 3.1, strain gauge 6

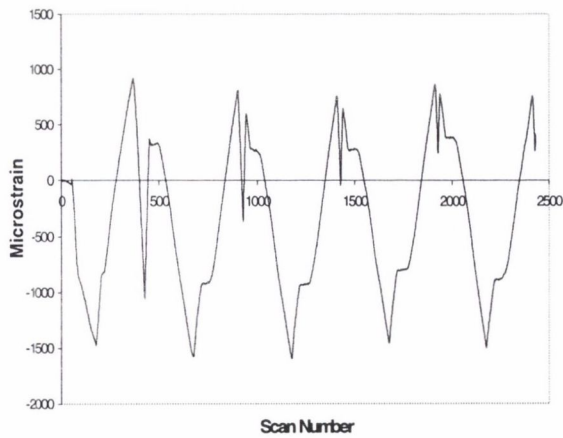


Figure B.34: Specimen 3.1, strain gauge 7

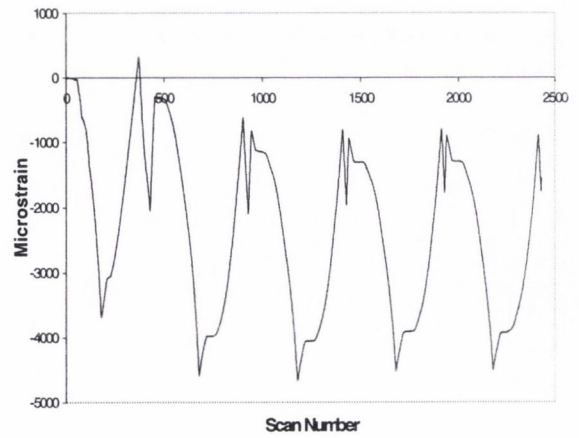


Figure B.35: Specimen 3.1, strain gauge 8

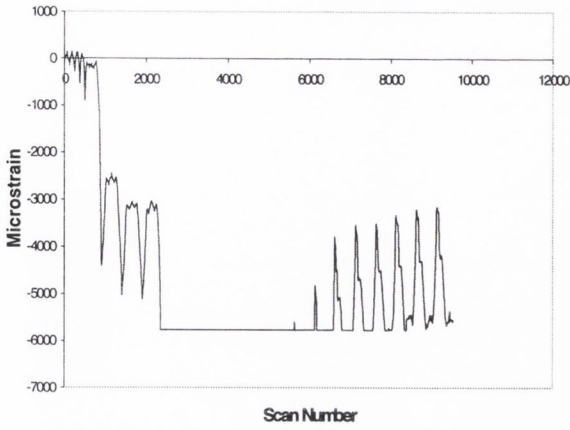


Figure B.36: Specimen 3.2, strain gauge 1

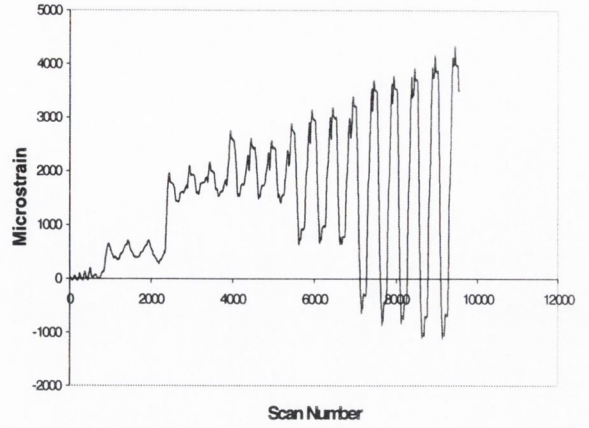


Figure B.37: Specimen 3.2, strain gauge 2

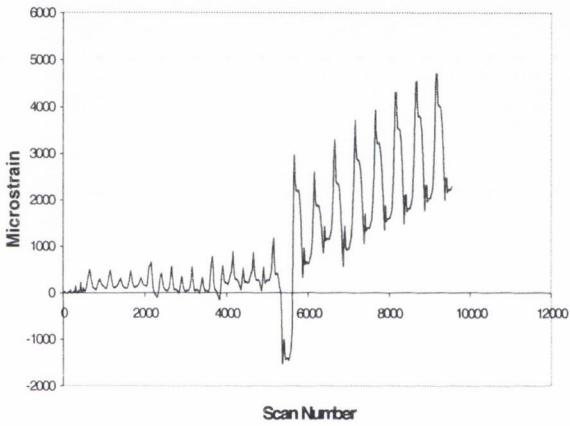


Figure B.38: Specimen 3.2, strain gauge 3

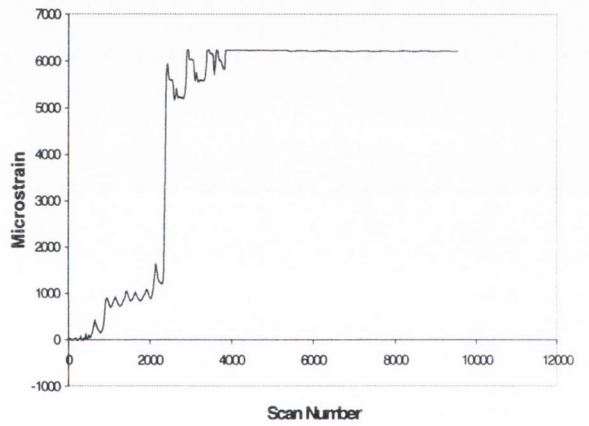


Figure B.39: Specimen 3.2, strain gauge 4

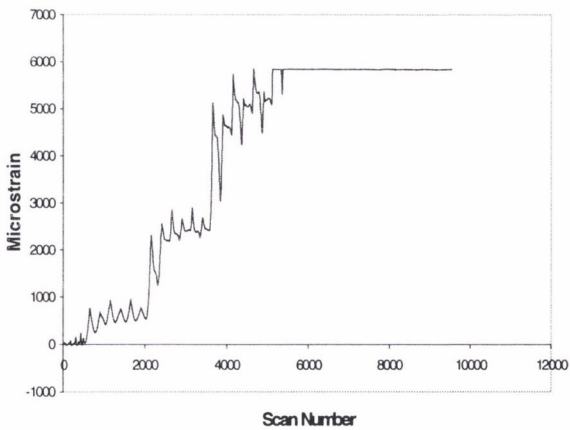


Figure B.40: Specimen 3.2, strain gauge 5

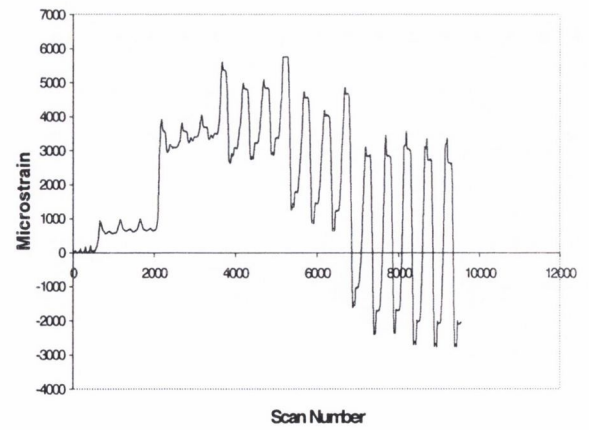


Figure B.41: Specimen 3.2, strain gauge 6

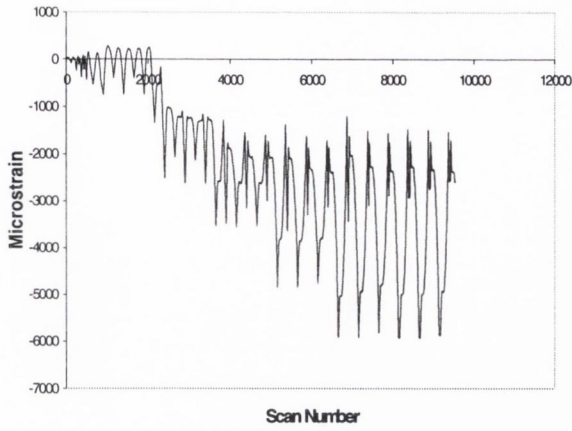


Figure B.42: Specimen 3.2, strain gauge 7

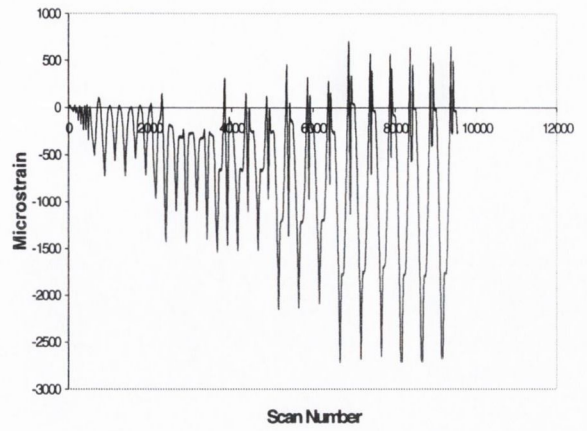


Figure B.43: Specimen 3.2, strain gauge 8

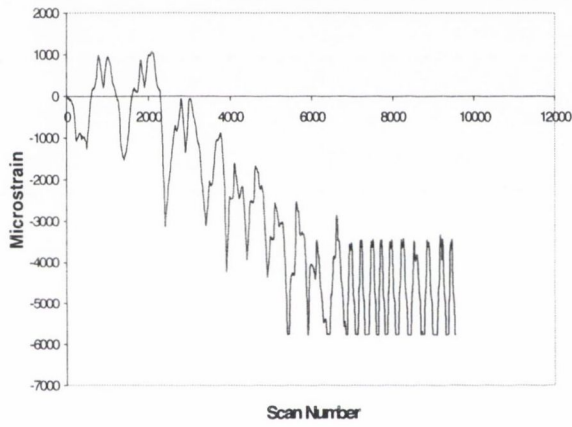


Figure B.44: Specimen 3.3, strain gauge 1

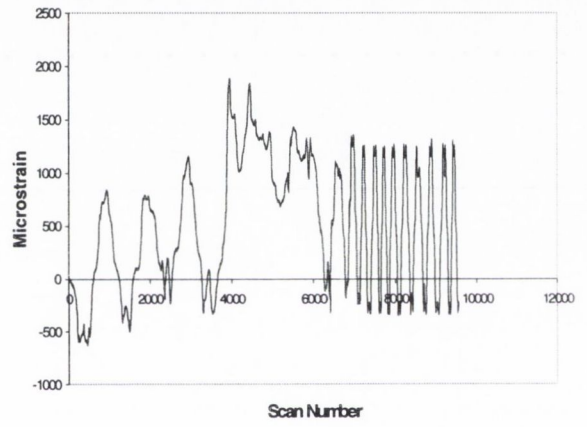


Figure B.45: Specimen 3.3, strain gauge 2

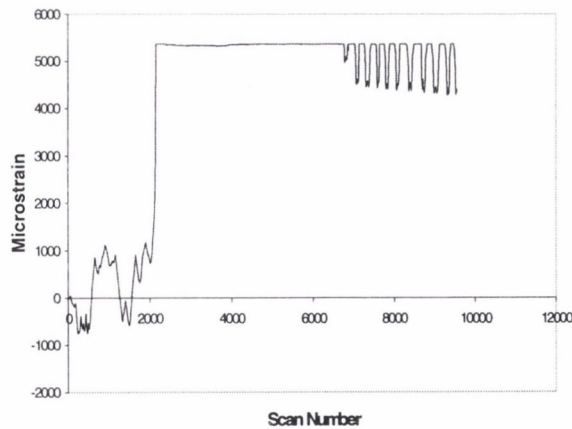


Figure B.46: Specimen 3.3, strain gauge 3

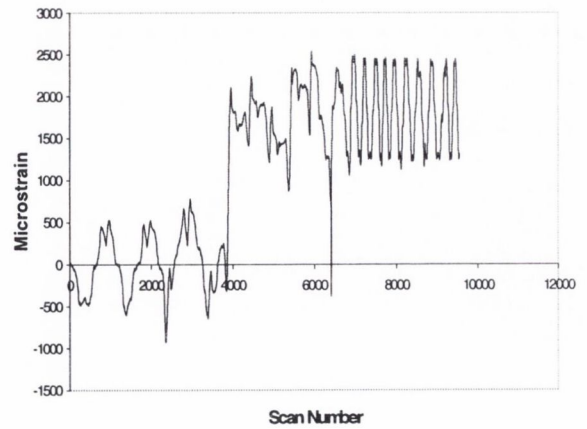


Figure B.47: Specimen 3.3, strain gauge 4

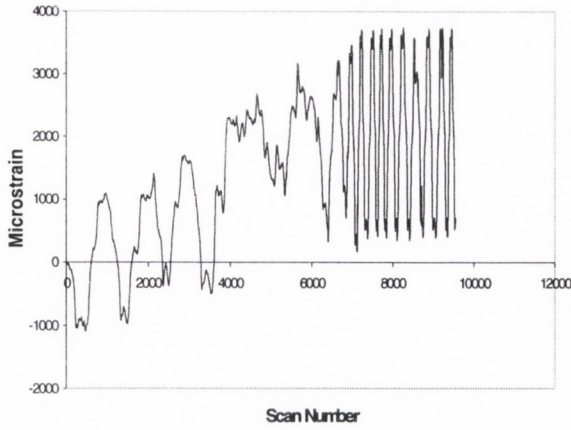


Figure B.48: Specimen 3.3, strain gauge 5

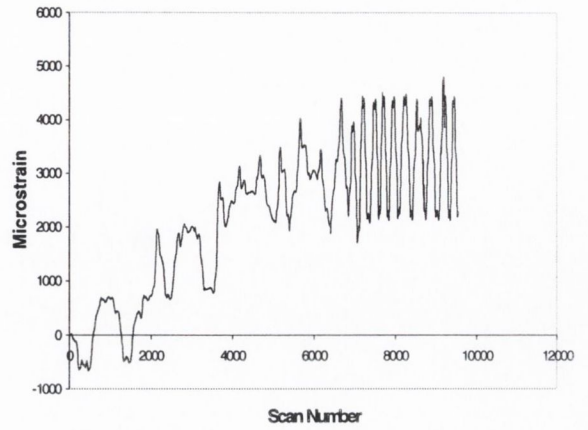


Figure B.49: Specimen 3.3, strain gauge 6

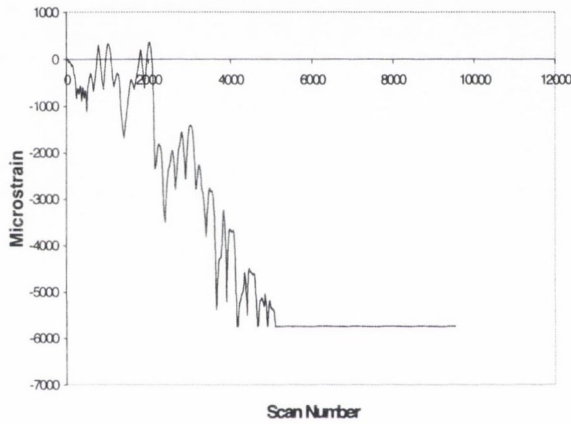


Figure B.50: Specimen 3.3, strain gauge 7

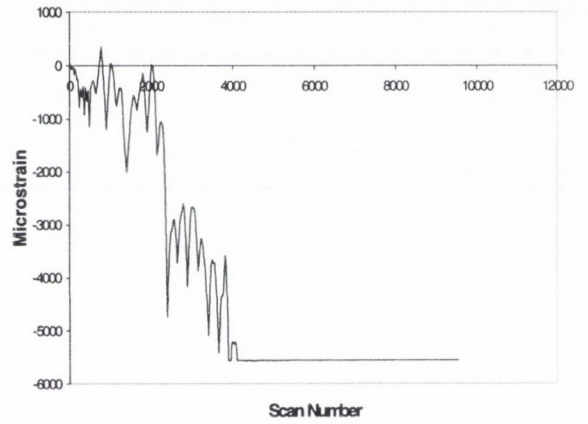


Figure B.51: Specimen 3.3, strain gauge 8



Figure B.52: Specimen 3.5, strain gauge 1

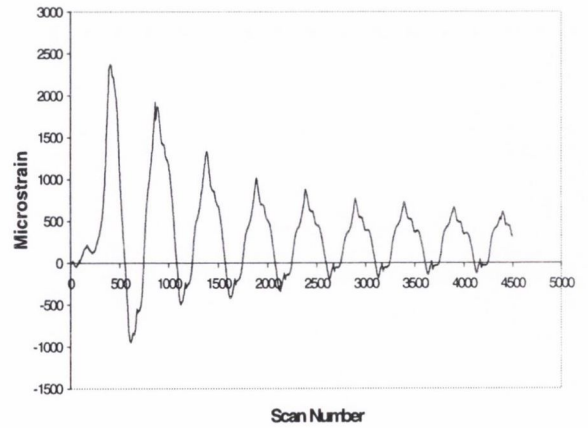


Figure B.53: Specimen 3.5, strain gauge 2

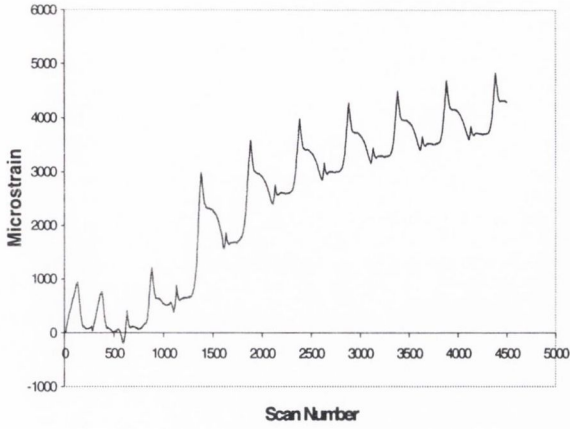


Figure B.54: Specimen 3.5, strain gauge 3

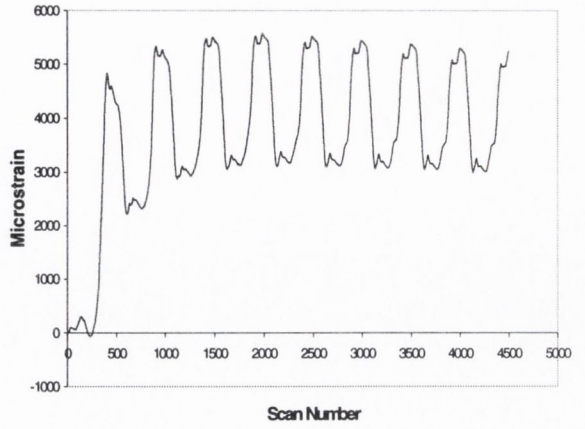


Figure B.55: Specimen 3.5, strain gauge 4

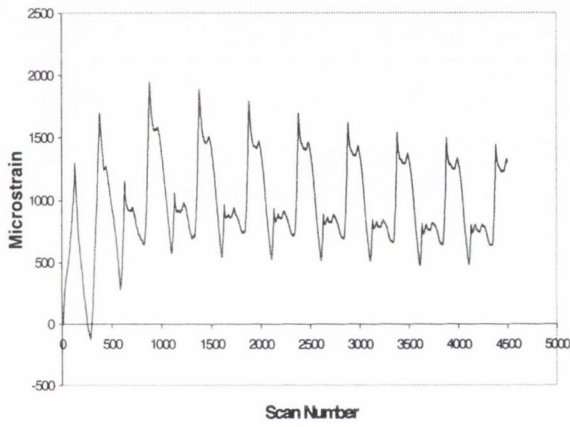


Figure B.56: Specimen 3.5, strain gauge 5

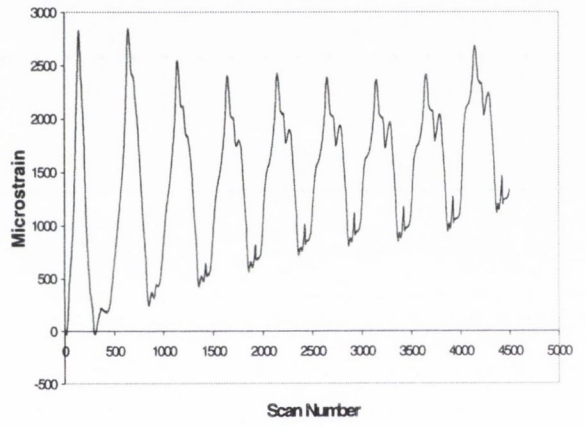


Figure B.57: Specimen 3.5, strain gauge 6

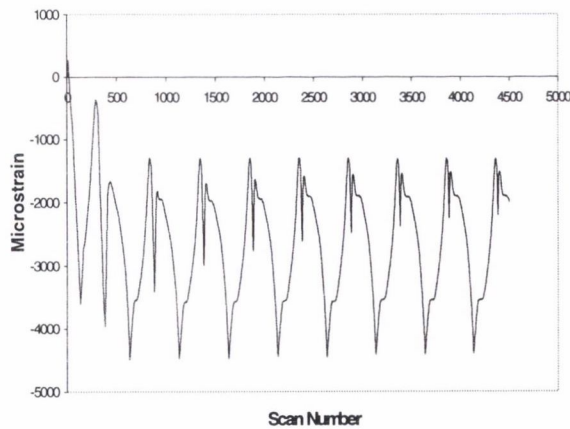


Figure B.58: Specimen 3.5, strain gauge 7

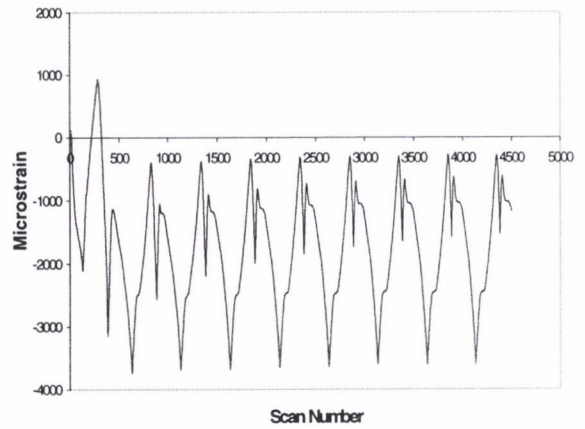


Figure B.59: Specimen 3.5, strain gauge 8

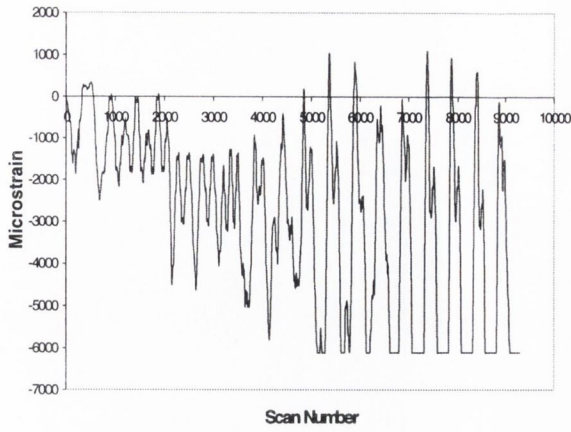


Figure B.60: Specimen 3.6, strain gauge 1

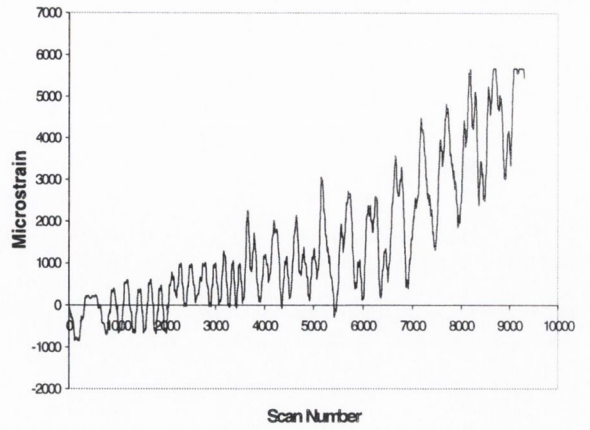


Figure B.61: Specimen 3.6, strain gauge 2

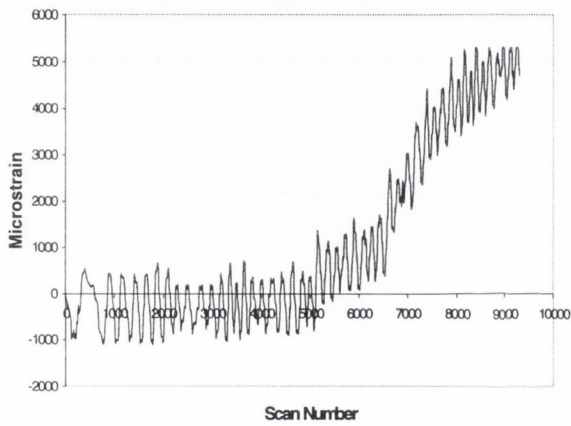


Figure B.62: Specimen 3.6, strain gauge 3

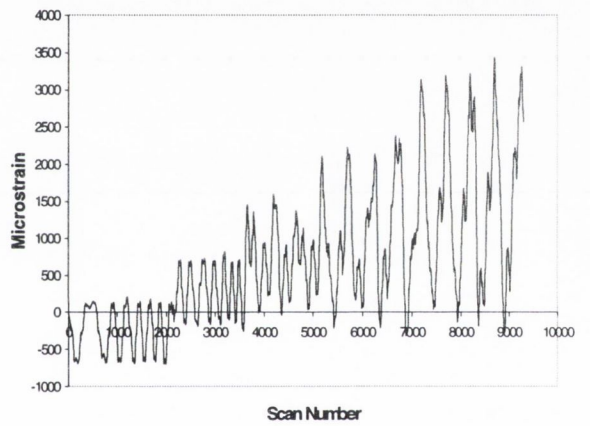


Figure B.63: Specimen 3.6, strain gauge 4

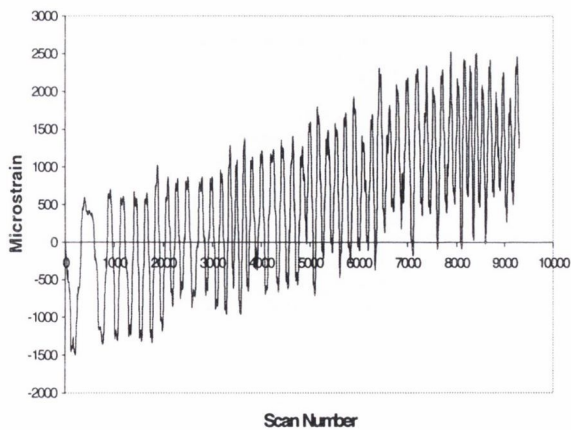


Figure B.64: Specimen 3.6, strain gauge 5

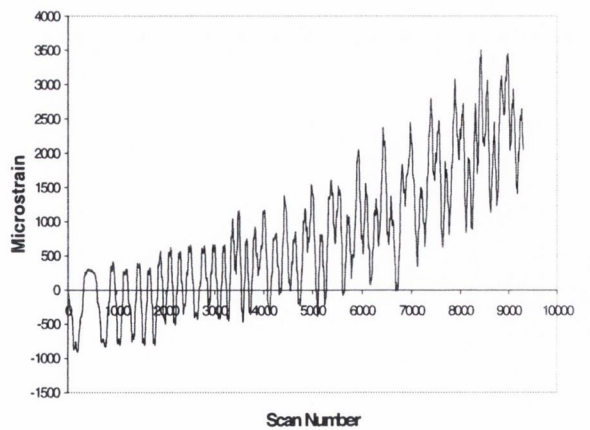


Figure B.65: Specimen 3.6, strain gauge 6

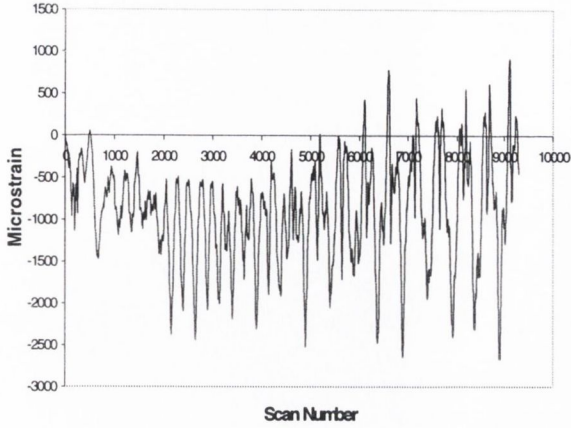


Figure B.66: Specimen 3.6, strain gauge 8

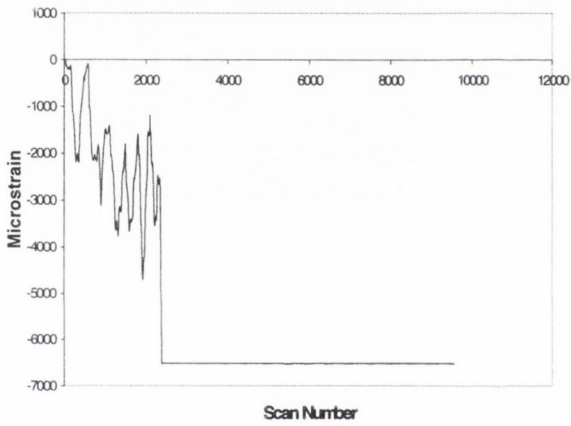


Figure B.67: Specimen 3.8, strain gauge 1

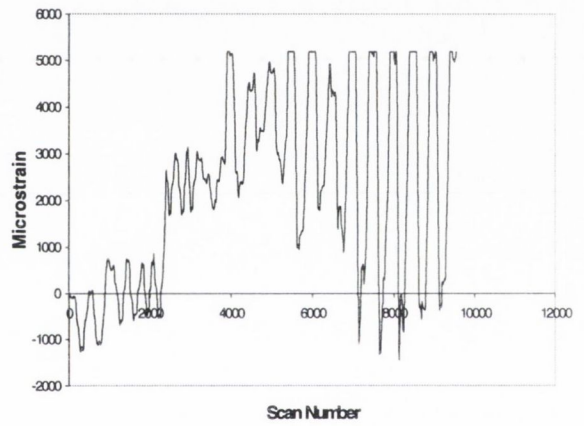


Figure B.68: Specimen 3.8, strain gauge 2

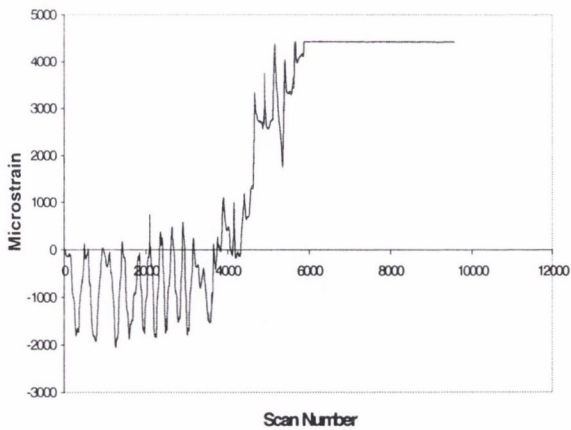


Figure B.69: Specimen 3.8, strain gauge 3

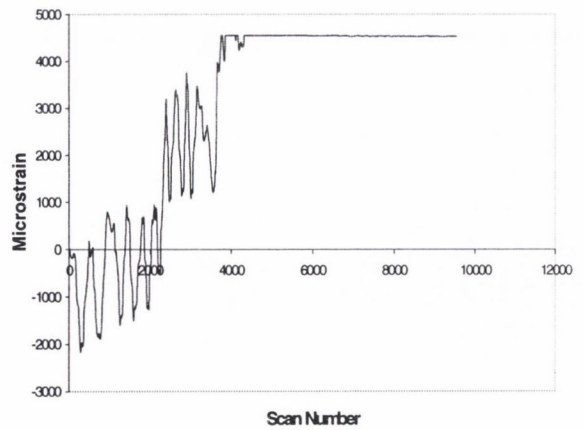


Figure B.70: Specimen 3.8, strain gauge 5

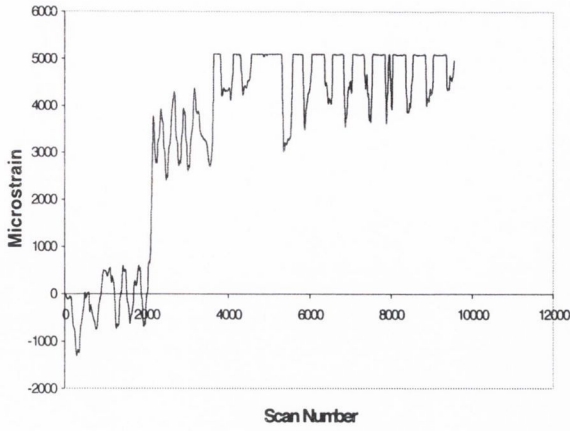


Figure B.71: Specimen 3.8, strain gauge 6

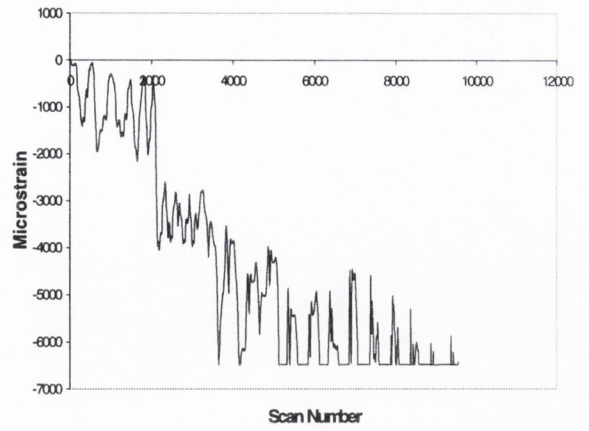


Figure B.72: Specimen 3.8, strain gauge 7

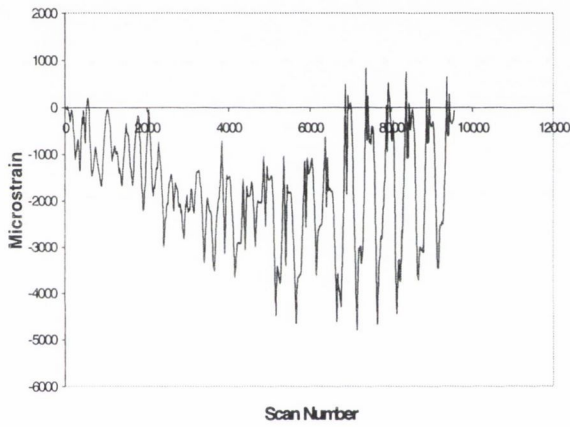


Figure B.73: Specimen 3.8, strain gauge 8

Appendix C

Sample Calculations for Proposed Joint Response Model

C.1 Worked Sample Calculations for Specimen 3.1

END-PLATE T-STUB:

Material Properties:

Steel Grade 43;

$$f_y = 275 \text{ N/mm}^2;$$

$$f_u = 430 \text{ N/mm}^2;$$

$$E = 210,000 \text{ N/mm}^2;$$

$$E_b = 210,000 \text{ N/mm}^2;$$

$$E_u = 430 \text{ N/mm}^2;$$

$$f_{ub} = 800 \text{ N/mm}^2;$$

$$\frac{\epsilon_h}{\epsilon_y} = 11.0; \quad \frac{\epsilon_u}{\epsilon_y} = 425.0; \quad \frac{E}{E_h} = 52.8 \Rightarrow E_h = 4906.54 \text{ N/mm}^2;$$

Geometrical Properties:

Bolt diameter, $d_b = 20\text{mm}$

Bolt effective area = 245 mm^2

Washer diameter = 37mm

$m = 33.93\text{mm}$

$n = 55\text{mm}$

$t_f = 10\text{mm}$

Moment-Curvature Calculations:

$$\epsilon_y = \frac{f_y}{E} = 1.3095 \times 10^{-3}$$

$$\epsilon_h = 11.0 \epsilon_y = 0.01441$$

$$\epsilon_m = \epsilon_h + \frac{(f_u - f_y)}{E_h} = 0.01441 + \frac{(430 - 275)}{4906.54} = 0.04600$$

$$\epsilon_u = 425.0 \times \epsilon_y = 0.5565$$

Curvature corresponding to the four strain levels:

$$\chi_y = \frac{2\varepsilon_y}{t_f} = 0.2619 \times 10^{-3}$$

$$\chi_h = \frac{2\varepsilon_h}{t_f} = 2.881 \times 10^{-3}$$

$$\chi_m = \frac{2\varepsilon_m}{t_f} = 9.199 \times 10^{-3}$$

$$\chi_u = \frac{2\varepsilon_u}{t_f} = 0.1113$$

Non-dimensional moments of T-stub:

$$\frac{M_h}{M_y} = \frac{1}{2} \left[3 - \left(\frac{\chi_y}{\chi} \right)^2 \right] = 1.4959$$

$$\frac{M_m}{M_y} = \frac{1}{2} \left[3 - \left(\frac{\chi_y}{\chi} \right)^2 \right] + \frac{1}{2} \frac{E_h}{E} \left(\frac{\chi - \chi_h}{\chi_y} \right) \left(1 - \frac{\chi_h}{\chi} \right) \left(2 + \frac{\chi_h}{\chi} \right) = 1.9473$$

$$\begin{aligned} \frac{M_u}{M_y} = \frac{1}{2} \left[3 - \left(\frac{\chi_y}{\chi} \right)^2 \right] + \frac{1}{2} \frac{E_h}{E} \left(\frac{\chi - \chi_h}{\chi_y} \right) \left(1 - \frac{\chi_h}{\chi} \right) \left(2 + \frac{\chi_h}{\chi} \right) \\ - \frac{1}{2} \frac{E_h - E_u}{E} \left(\frac{\chi - \chi_m}{\chi_y} \right) \left(1 - \frac{\chi_m}{\chi} \right) \left(2 + \frac{\chi_m}{\chi} \right) = 3.1053 \end{aligned}$$

Effective width of the T-stub:

$$b = \min(2\pi m, 4m + 1.25n) = 209.47 \text{ mm}$$

$$M_y = \frac{b \cdot t_f^2}{6} f_y = \frac{209.47 \times 10^2}{6} \times 275 = 937,154.167 \text{ Nmm}$$

hence:

$$M_h = 1,401,858.71 \text{ Nmm};$$

$$M_m = 1,824,871.457 \text{ Nmm};$$

$$M_u = 2,910,143.08 \text{ Nmm};$$

Determine Failure Mode:

$$\beta_u = \frac{4M_u}{2B_u m} = \frac{4 \times 2,910,142.08}{2 \times (245 \times 800) \times 33.93} = 0.8752$$

$$\lambda = \frac{n}{m} = 1.621$$

$$\frac{2\lambda}{1+2\lambda} = 0.764$$

$$\frac{2\lambda}{1+2\lambda} \leq \beta_u < 2 \quad \dots \quad \text{Mode 2 failure mechanism}$$

Determine Ultimate Plastic Displacement for Mode 2 failure mechanism:

$$\delta_p = \theta_{p1}(1+\lambda)m - \theta_{p2}\lambda m$$

Calculate θ_{p1}

$$\xi = \frac{(2-\beta_u)\lambda}{\beta_u(1+\lambda)} = 0.7949$$

$$C_h = \frac{\bar{\epsilon}_m^3}{\bar{\epsilon}_u} + 3\bar{\epsilon}_m\bar{\epsilon}_u - 3\bar{\epsilon}_m^2 + 3\bar{\epsilon}_h^2 - 3\bar{\epsilon}_h\bar{\epsilon}_u - \frac{\bar{\epsilon}_h^3}{\bar{\epsilon}_u} = 27,518.45$$

$$C_u = \bar{\epsilon}_u^2 - 3\bar{\epsilon}_m\bar{\epsilon}_u + \bar{\epsilon}_m^2 - \frac{\bar{\epsilon}_m^3}{\bar{\epsilon}_u} = 139,441.42$$

$$C = 2 \left\{ \bar{\epsilon}_u - \frac{1}{2 \left(\frac{M_u}{M_y} \right)} \left(3\bar{\epsilon}_u + \frac{1}{\bar{\epsilon}_u} - 3 + \frac{E_h}{E} C_h + \frac{E_u}{E} C_u \right) - \frac{1}{2} \right\} \epsilon_y = 0.1838$$

$$\theta_{p1} = \frac{m}{t_f(1+\xi)} C = \frac{33.93}{10(1+0.7949)} \times 0.1838 = 0.3475$$

Calculate θ_{p2}

$$\xi_1 = \frac{M_y}{M_u} = 0.3220$$

$$\xi_2 = \frac{M_h}{M_u} = 0.4817$$

$$\xi_3 = \frac{M_m}{M_u} = 0.6271$$

Therefore, case 4 applies as $\xi_3 < \xi \leq 1.0$

χ_ξ is the curvature that corresponds to $\xi M_u = 2,313,272.734$ Nmm

$$\chi_\xi = 0.0331$$

$$G_h = \frac{\chi_m^3}{\chi_\xi \chi_y^2} + 3 \frac{\chi_m \chi_\xi}{\chi_y^2} - 3 \frac{\chi_m^2}{\chi_y^2} + 3 \frac{\chi_h^2}{\chi_y^2} - \frac{\chi_h \chi_\xi}{\chi_y^2} - \frac{\chi_h^3}{\chi_\xi \chi_y^2} = 6136.372$$

$$G_u = \frac{\chi_\xi^2}{\chi_y^2} + 3 \frac{\chi_m^2}{\chi_y^2} - 3 \frac{\chi_m \chi_\xi}{\chi_y^2} - \frac{\chi_u^3}{\chi_\xi \chi_y^2} = 6004.273$$

$$G(\xi) = \varepsilon_y \left\{ 2 \frac{\chi_\xi}{\chi_y} - \frac{1}{\xi} \frac{M_y}{M_u} \left(3 \frac{\chi_\xi}{\chi_y} + \frac{\chi_y}{\chi_\xi} - 3 + \frac{E_h}{E} G_h + \frac{E_u}{E} G_u \right) - 1 \right\} = 0.04747$$

$$\theta_{p2} = \theta_{p2} = \frac{m}{t_f} \left(\frac{\zeta}{1+\zeta} + \lambda \right) G(\xi) = \frac{33.93}{10} \left(\frac{0.7949}{1+0.7949} + 1.621 \right) \times 0.04747 = 0.3324$$

Calculate δ_p :

$$\delta_{pu} = \theta_{p1}(1+\lambda)m - \theta_{p2}\lambda m = 12.621 \text{ mm}$$

Determine the Force-Displacement Curve:

$$As F = \frac{2M}{m} (1 + \xi);$$

$$F_y = 99,148.56 \text{ N}$$

$$F_h = 148,313.13 \text{ N}$$

$$F_m = 193,066.81 \text{ N}$$

$$F_u = 307,885.82 \text{ N}$$

1st Force Point

$$K = 0.5E \frac{b_{\text{eff}} t_f^3}{m^3} = 0.5 \times 210,000 \times \frac{33.93 \times 10^3}{33.93^3} = 91,205.62 \text{ N/mm}$$

$$\delta_{b,y} = \frac{\frac{F_y}{2} + \frac{\xi M_y}{n}}{\left(\frac{E_b A_b}{L_b} \right)} = \frac{\left(\frac{99,148.56}{2} \right) + \left(\frac{0.7949 \times 937,154.17}{55} \right)}{\left(\frac{210,000 \times 245}{(10 + 7.5 + 3)} \right)} = 0.0262 \text{ mm}$$

$$\delta_y = \frac{F_y}{K} + \delta_{b,y} = \frac{99,148.56}{91,205.62} + 0.0262 = 1.11 \text{ mm}$$

$$\text{Hence, } K_i = \frac{F_y}{\delta_y} = 89,058.87 \text{ N/mm}$$

2nd Force Point

$$F_h = 148,313.13 \text{ N}$$

$$\delta_h = \delta_{eh} + \delta_{ph}$$

$$\zeta_2^* = \frac{\zeta M_h}{M_u} = 0.3829$$

$$\text{Therefore, } \delta_{ph} = \theta_{p1h}(1 + \lambda)m - \theta_{p2h}\lambda m$$

$$\theta_{p1h} = \frac{m}{t_f(1 + \zeta)} D(\zeta_2) = \frac{33.93}{10(1 + 0.7949)} \times 0.0012 = 2.268 \times 10^{-3}$$

$$\theta_{p2h} = \frac{m}{t_f(1 + \zeta)} D(\zeta_2^*) = 0.486 \times 10^{-3}$$

where $D(\zeta_2^*)$ is the result of the function $D(\zeta)$ for $\zeta = \zeta_2^*$ and χ_{ζ} is the curvature corresponding to $\zeta_2^* M_u$

$$\text{Therefore, } \delta_{ph} = 0.1946 - 0.0267 = 0.1679$$

$$\text{And, } \delta_h = \delta_{eh} + \delta_{ph} = \frac{F_h}{K_i} + \delta_{ph} = 1.665 + 0.1679 = 1.833 \text{ mm}$$

3rd Force Point

$$F_m = 193,066.81 \text{ N}$$

$$\delta_{pm} = \theta_{p1m}(1 + \lambda)m - \theta_{p2m}\lambda m$$

$$\theta_{p1m} = \frac{m}{t_f(1 + \zeta)} F(\zeta_3) = \frac{33.93}{10 \times (1 + 0.7949)} \times 0.0155 = 0.02937$$

$$\zeta_3^* = \frac{\zeta M_m}{M_u} = \frac{0.7949 \times 1,824,871.457}{2,910,143.08} = 0.4985$$

$$\text{Therefore, } \theta_{p2m} = \frac{m}{t_f} \left(\frac{\zeta}{1 + \zeta} + \lambda \right) F(\zeta_3^*) = \frac{33.93}{10} \times \left(\frac{0.7949}{1 + 0.7949} + 1.621 \right) \times 0.002315 = 0.0162$$

where $F(\zeta_3^*)$ is the result of the function $F(\zeta)$ for $\zeta = \zeta_3^*$ and χ_{ζ} is the curvature corresponding to $\zeta_3^* M_u$

$$\delta_{pm} = (0.02937 \times (1 + 1.621) \times 33.93) - (0.0162 \times 1.621 \times 33.93) = 1.720 \text{ mm}$$

$$\text{And } \delta_m = \delta_{em} + \delta_{pm} = \frac{F_m}{K_i} + \delta_{pm} = 3.888 \text{ mm}$$

4th Force Point

$$F_u = 307,885.82 \text{ N}$$

$$\delta_{pu} = 12.621 \text{ mm}$$

$$\delta_u = \delta_{eu} + \delta_{pu} = \frac{F_u}{K_i} + \delta_{pu} = 3.457 + 12.621 = 16.078 \text{ mm}$$

From the above equations, the force-displacement curve shown in Figure C.1 may be illustrated.

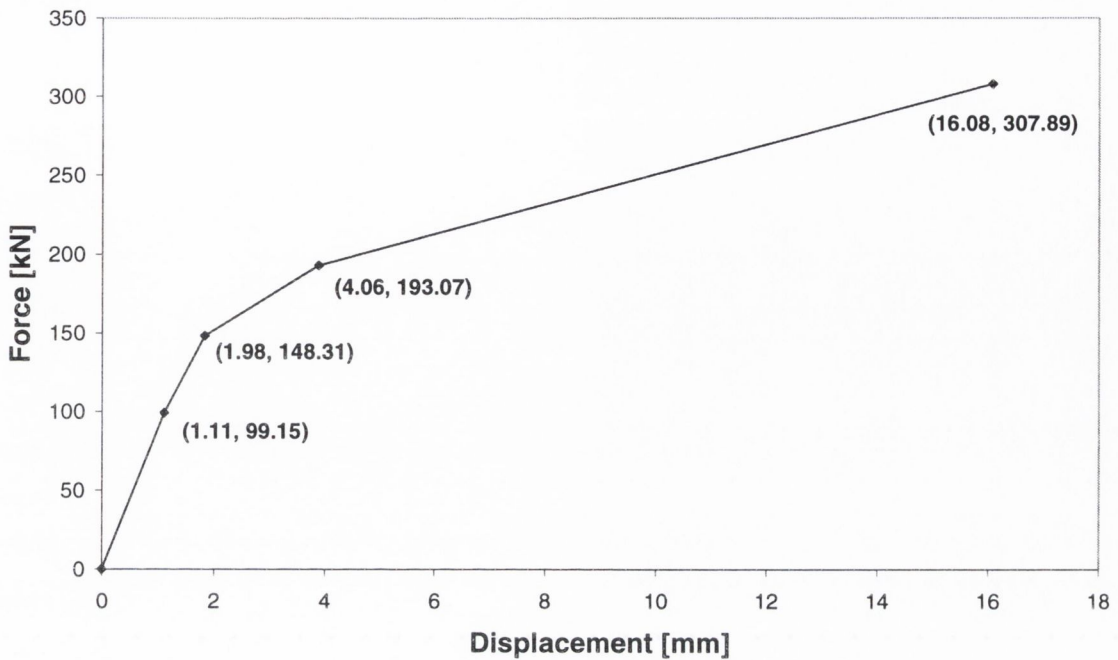


Figure C.1: Force-displacement curve for end-plate T-stub

Using the methods set out in chapter 6, a force-displacement curve may be calculated for the column flange T-stub. Due to the thickness of the column flange, this is a linear relationship.

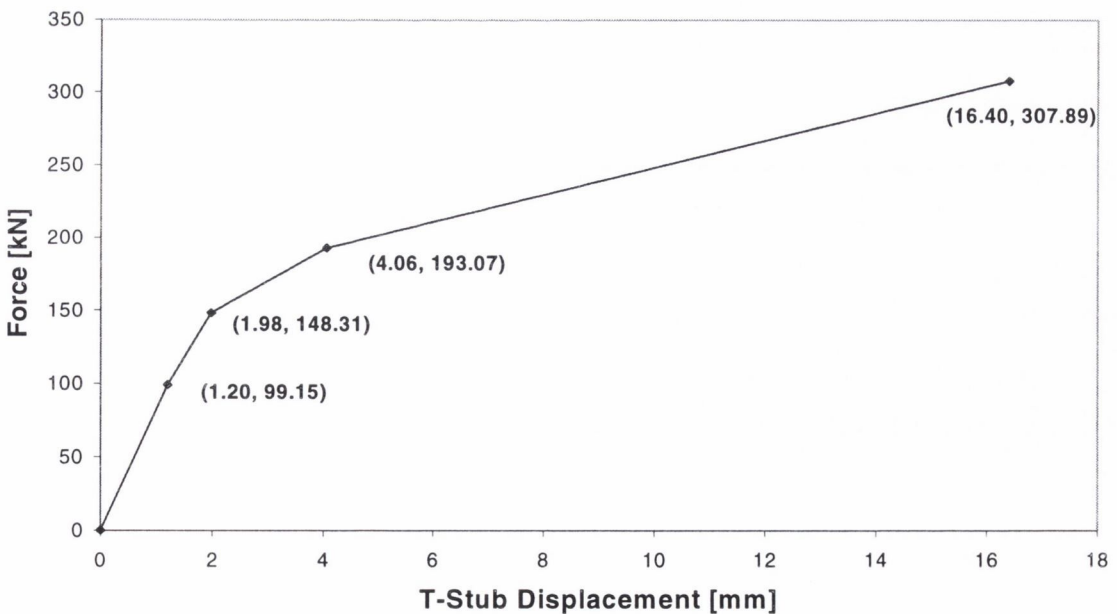


Figure C.2: Combined T-stub force-displacement relationship

Using superposition, the two force-displacement curves may be combined into an overall force-displacement relationship for the combined T-stubs. This relationship is shown in Figure C.2.

FULL JOINT MODELLING

Beam Size:	254 x 146 x 37 kg/m UB
Column Size:	203 x 203 x 86 kg/m UC
Young's Modulus, E:	210,000 N/mm ²
$b_{\text{eff,t}}$:	187.03 mm (determined from Eurocode 3)
$b_{\text{eff,c}}$:	211.03 mm (determined from Eurocode 3)
lever arm, h:	190.55 mm
Depth between Column Fillets, d:	160.8 mm
Column web thickness, t_w :	12.7 mm
Beam Depth:	256 mm
Beam Flange Thickness:	10.9 mm
Poisson's Ratio, ν :	0.3
Column Section Area:	11,000 mm ²
Column Flange Width:	209.1 mm
Column Fillet Radius, r:	10.2 mm
Column Flange thickness, t_f :	20.5 mm
Yield Strength of Steel, f_y :	275 N/mm ²
Maximum Tensile Force:	653,193.25 N
Maximum Compression Force:	737,013.25 N
Maximum Shear Force	493,056.41 N

Using these properties and the force-displacement relationship, the moment-rotation curve for a joint may be determined. Three points along the moment-rotation curve are calculated to illustrate the method explained in chapter 6.

Point 1:

Applied Rotation, $\theta_t = 3$ mrad

T-stub displacement, $\delta = \theta_t \times h = 0.003 \times 190.55 = 0.5717$ mm

Corresponding T-stub force, $F = 47,241.36$ N (OK in tension, compression and shear)

Therefore, applied moment, $M = F \times h = 47,241.36 \times 190.55 = 9,001,841.69$ Nmm

Calculate rotation due to column web in tension:

$$A_t = b_{\text{eff},t} \times t_w = 2375.25 \text{ mm}^2$$

$$\theta_{\text{wt}} = \left(\frac{N}{EA_t} \right) \left(\frac{d}{h_t} \right) = \left(\frac{47,241.36}{210,000 \times 2375.25} \right) \times \left(\frac{160.8}{190.55} \right) = 0.0799 \text{ mrad}$$

Calculate rotation due to column web in compression:

$$A_c = b_{\text{eff},c} \times t_w = 2680.05 \text{ mm}^2$$

$$h_c = \text{beam depth min us beam flange thickness} = 256 - 10.9 = 245.1 \text{ mm}$$

$$\theta_{\text{wt}} = \left(\frac{N}{EA_t} \right) \left(\frac{d}{h_t} \right) = \left(\frac{47,241.36}{210,000 \times 2680.05} \right) \times \left(\frac{160.8}{245.1} \right) = 0.055 \text{ mrad}$$

Calculate rotation due to column web in shear:

$$A_v = A - 2bt_f + (t_w + 2r)t_f = 11,00 - (2 \times 209.1 \times 20.5) + ((12.7 + (2 \times 10.2)) \times 20.5) = 3105.45 \text{ mm}^2$$

$$G = \frac{E}{2(1+\nu)} = \frac{210,000}{2 \times (1+0.3)} = 80,769.23 \text{ N/mm}^2$$

$$\theta_s = \frac{Q}{GA_v} = \frac{47,241.36}{(80,769.23 \times 3105.45)} = 0.188 \text{ mrad}$$

Determine Total Rotation:

$$\theta = \theta_t + \theta_s + \theta_{\text{wc}} + \theta_{\text{wt}} = 3 + 0.188 + 0.055 + 0.0799 = 3.323 \text{ mrad}$$

Point 2:

Applied Rotation, $\theta_t = 9 \text{ mrad}$

T-stub displacement, $\delta = \theta_t \times h = 0.009 \times 190.55 = 1.715 \text{ mm}$

Corresponding T-stub force, $F = 131,706.55 \text{ N}$ (OK in tension, compression and shear)

Therefore, applied moment, $M = F \times h = 131,706.55 \times 190.55 = 25,096,682.7 \text{ Nmm}$

Calculate rotation due to column web in tension:

$$\theta_{\text{wt}} = \left(\frac{N}{EA_t} \right) \left(\frac{d}{h_t} \right) = \left(\frac{131,706.55}{210,000 \times 2375.25} \right) \times \left(\frac{160.8}{190.55} \right) = 0.223 \text{ mrad}$$

Calculate rotation due to column web in compression:

$$\theta_{\text{wt}} = \left(\frac{N}{EA_t} \right) \left(\frac{d}{h_t} \right) = \left(\frac{131,706.55}{210,000 \times 2680.05} \right) \times \left(\frac{160.8}{245.1} \right) = 0.154 \text{ mrad}$$

Calculate rotation due to column web in shear:

$$\theta_s = \frac{Q}{GA_v} = \frac{131,706.55}{(80,769.23 \times 3105.45)} = 0.525 \text{ mrad}$$

Determine Total Rotation:

$$\theta = \theta_t + \theta_s + \theta_{wc} + \theta_{wt} = 9 + 0.525 + 0.154 + 0.223 = 9.901 \text{ mrad}$$

Point 3:

Applied Rotation, $\theta_t = 45.25 \text{ mrad}$

T-stub displacement, $\delta = \theta_t \times h = 0.04525 \times 190.55 = 8.622 \text{ mm}$

Corresponding T-stub force, $F = 235,524.63 \text{ N}$ (OK in tension, compression and shear)

Therefore, applied moment, $M = F \times h = 235,524.63 \times 190.55 = 44,879,218.2 \text{ Nmm}$

Calculate rotation due to column web in tension:

$$\theta_{wt} = \left(\frac{N}{EA_t} \right) \left(\frac{d}{h_t} \right) = \left(\frac{235,524.63}{210,000 \times 2375.25} \right) \times \left(\frac{160.8}{190.55} \right) = 0.413 \text{ mrad}$$

Calculate rotation due to column web in compression:

$$\theta_{wt} = \left(\frac{N}{EA_t} \right) \left(\frac{d}{h_t} \right) = \left(\frac{235,524.63}{210,000 \times 2680.05} \right) \times \left(\frac{160.8}{245.1} \right) = 0.284 \text{ mrad}$$

Calculate rotation due to column web in shear:

$$\theta_s = \frac{Q}{GA_v} = \frac{235,524.63}{(80,769.23 \times 3105.45)} = 0.973 \text{ mrad}$$

Determine Total Rotation:

$$\theta = \theta_t + \theta_s + \theta_{wc} + \theta_{wt} = 45.25 + 0.973 + 0.284 + 0.413 = 46.862 \text{ mrad}$$

Therefore, the moment-rotation points calculated are:

Point 1: (3.323 mrad, 9.00 kNm)

Point 2: (9.901 mrad, 25.10 kNm)

Point 3: (46.862 mrad, 44.88 kNm)

These are shown, along with the full predicted moment rotation curve in figure C.3.

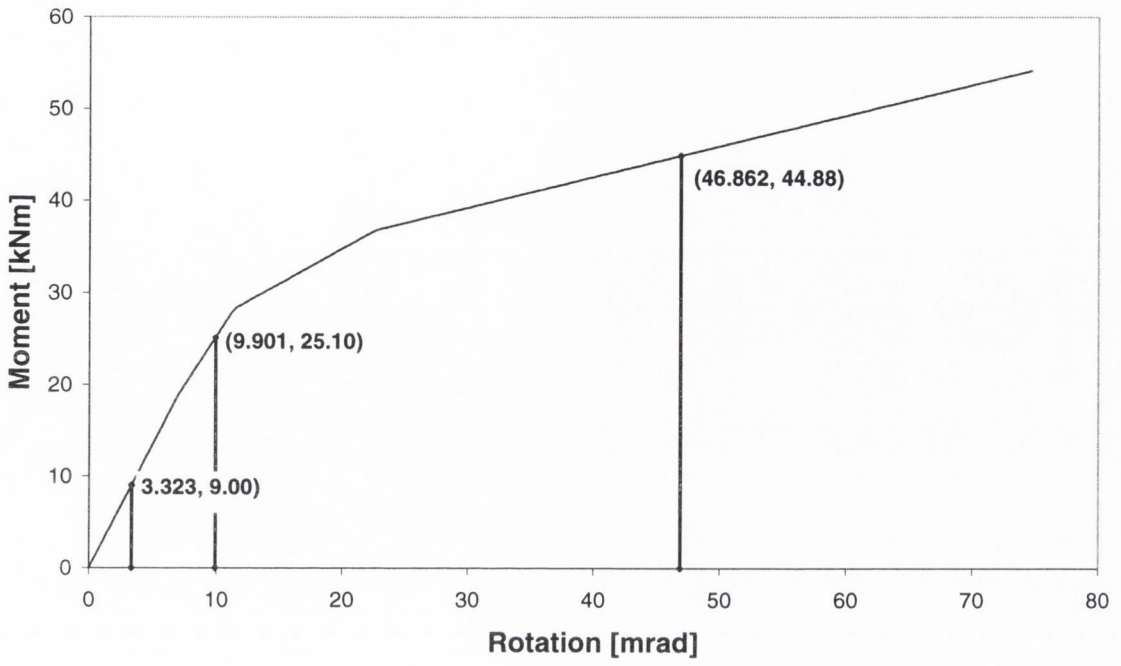


Figure C.3: Predicted moment-rotation curve

Appendix D

Frame Design Specifications

D.1 Case Study 1

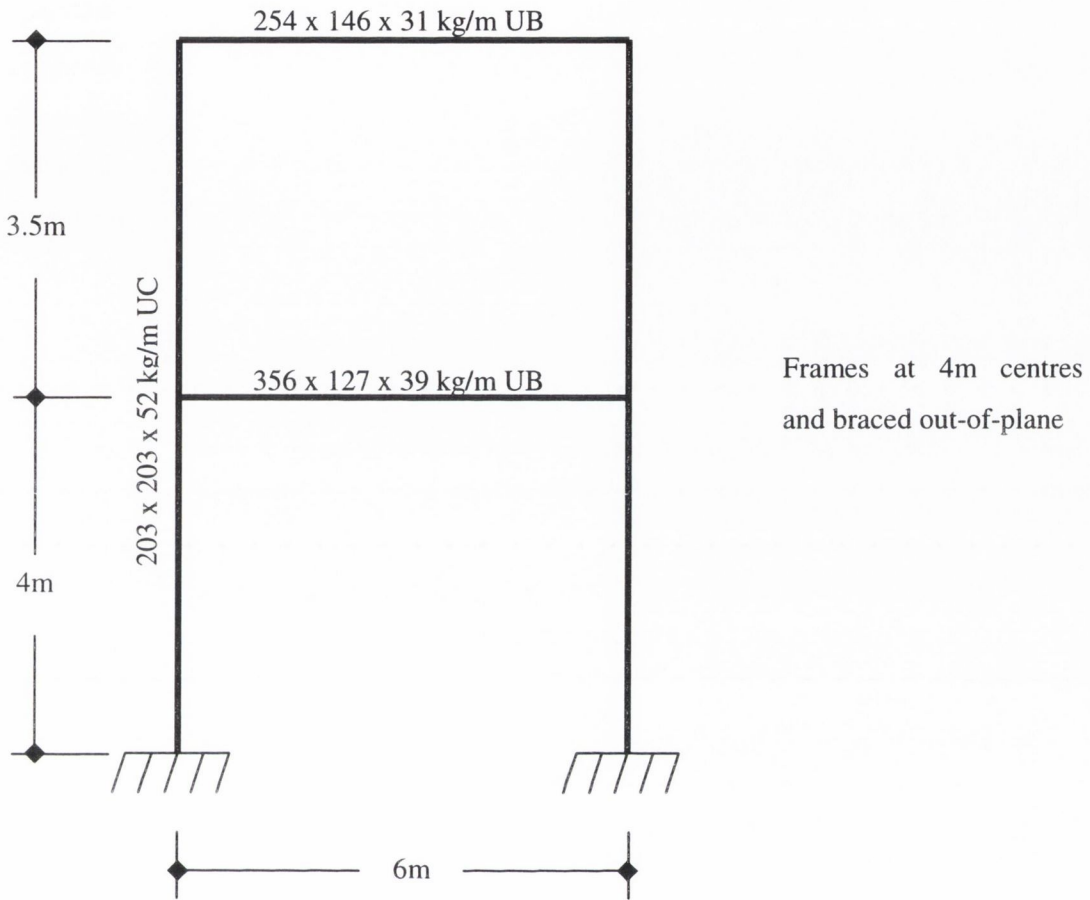


Figure D.1: Case study 1 – 2-Storey, 1-bay frame

Roof Loading	Dead:	14.4 kN/m
	Imposed:	3.0 kN/m
Floor Loading	Dead:	16.8 kN/m
	Imposed:	12.0 kN/m
Wind Loading	Floor:	11.8 kN
	Roof:	10.3 kN

Bending Moment Diagrams for Case Study 1

Sample bending moment diagrams are shown for the proposed Faella et al/Shi et al model for the four loadcases required for the wind-moment design method and seismic design. Loadcase 4 is for a load factor of 25. These are illustrated for the mode 2 joints only (Frame M2-1). Similar diagrams were obtained for all of the joint failure modes and frames. Moment values have been shown at selected locations. These locations are the mid-span of the beams, the joints and the column base. Also illustrated is the first mode shape as determined by the eigenvalue analysis.

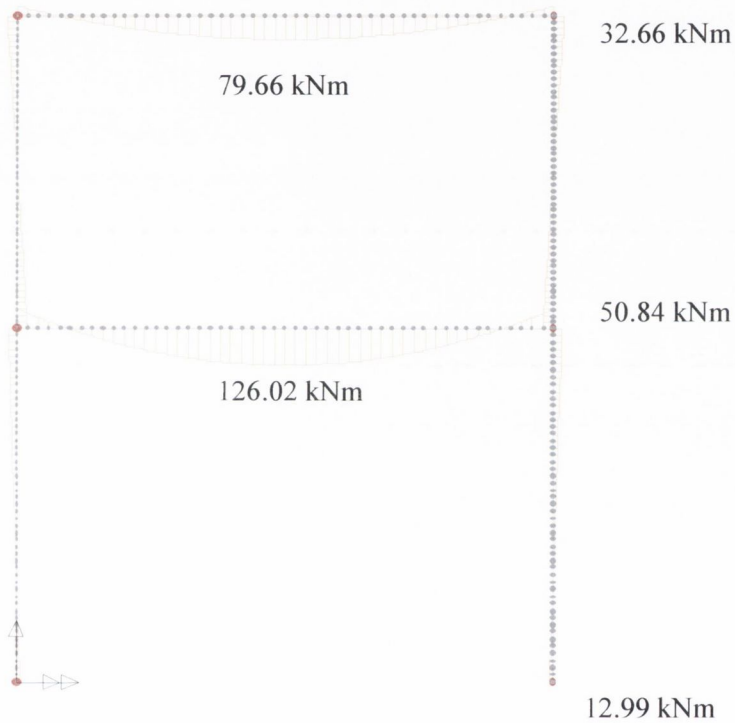


Figure D.2: Case study 1 – BMD for loadcase 1

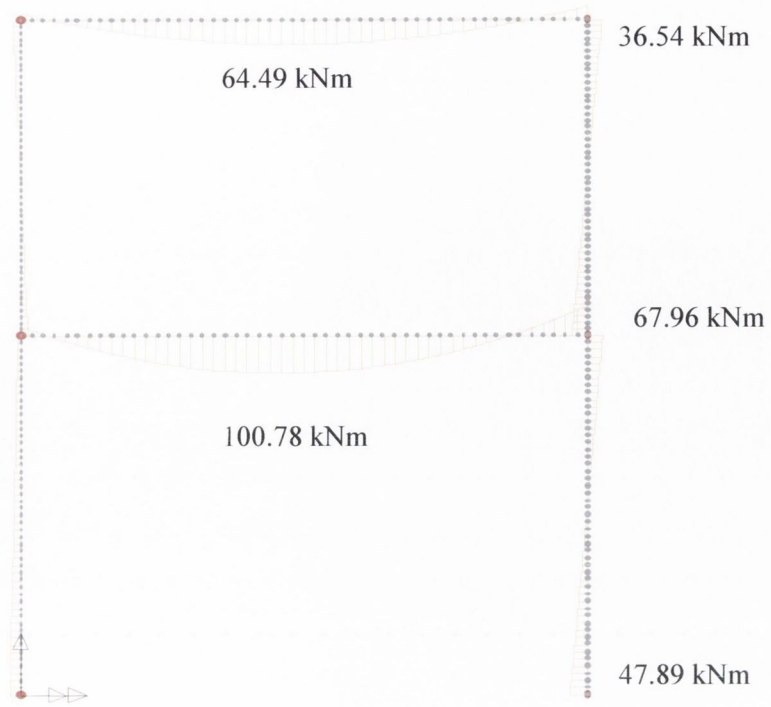


Figure D.3: Case study 1 – BMD for loadcase 2

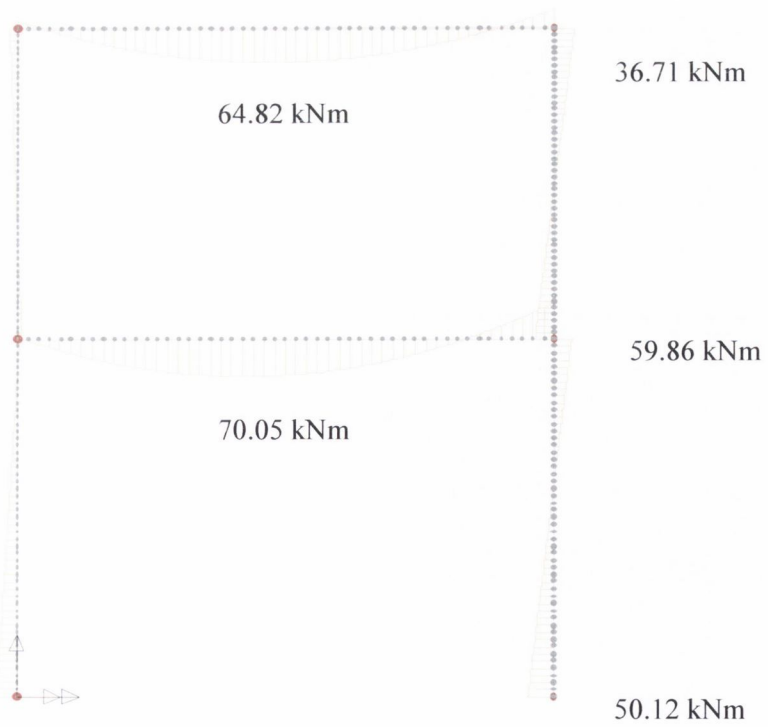


Figure D.4: Case study 1 – BMD for loadcase 3

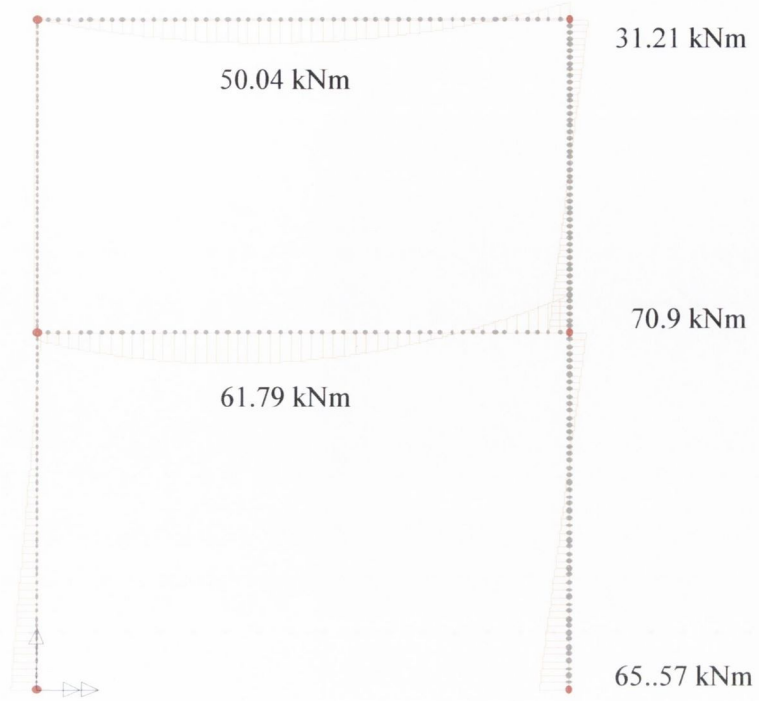


Figure D.5: Case study 1 – BMD for loadcase 4 (Seismic Load Factor = 25)

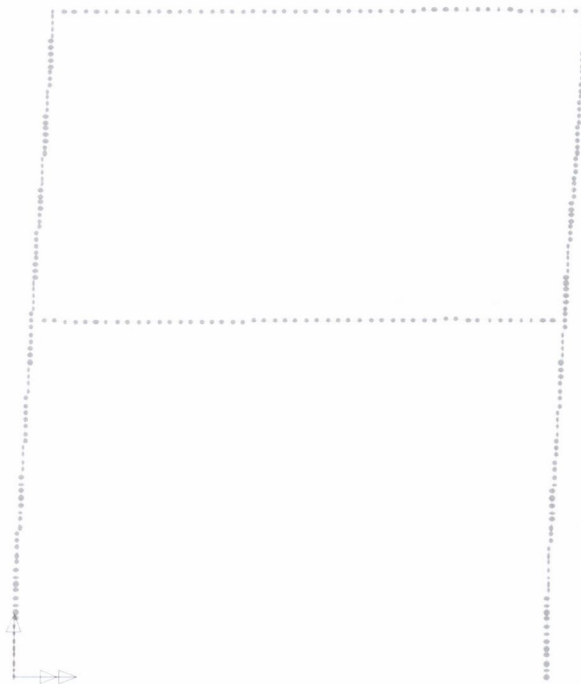


Figure D.6: Case study 1 – 1st mode shape

D.2 Case Study 2

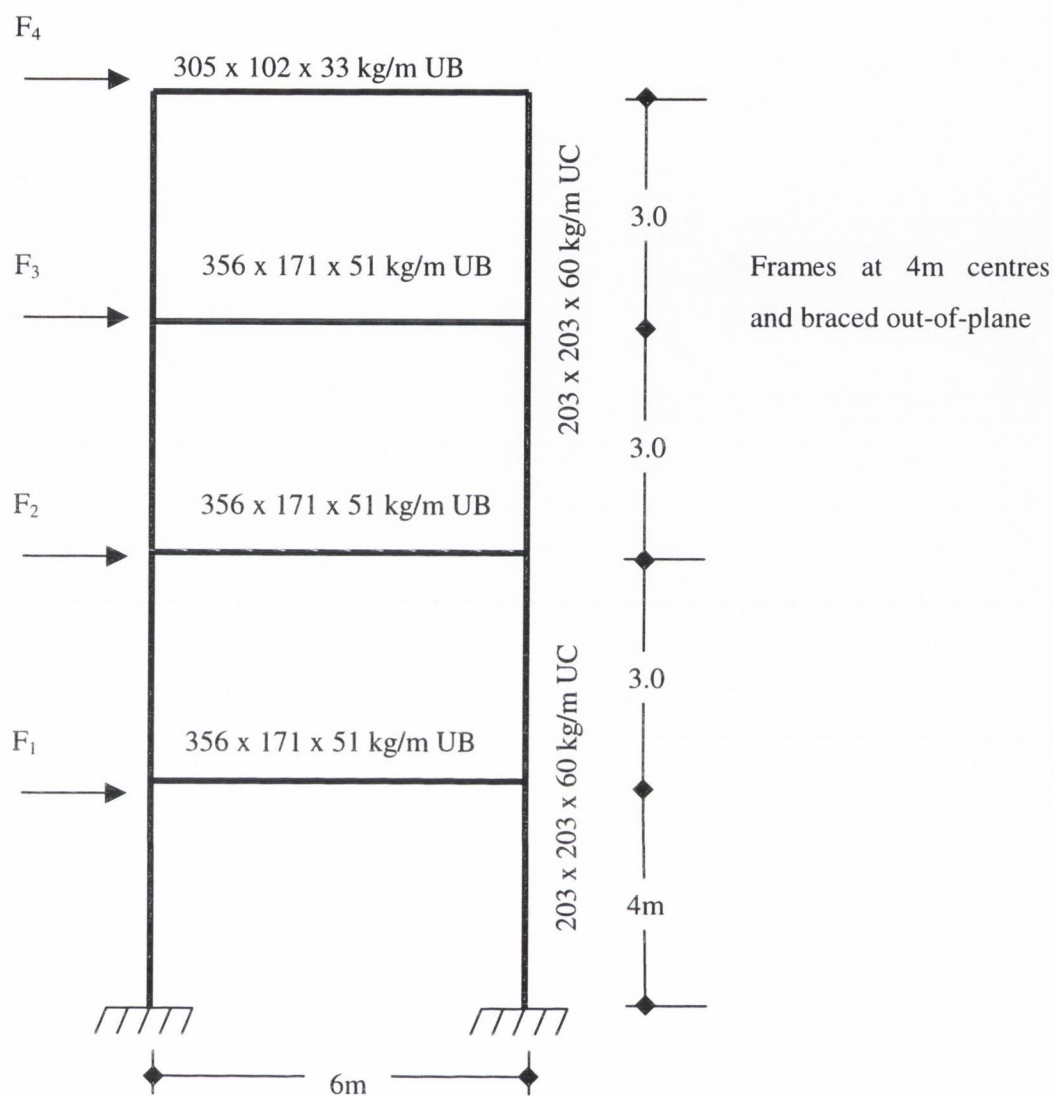
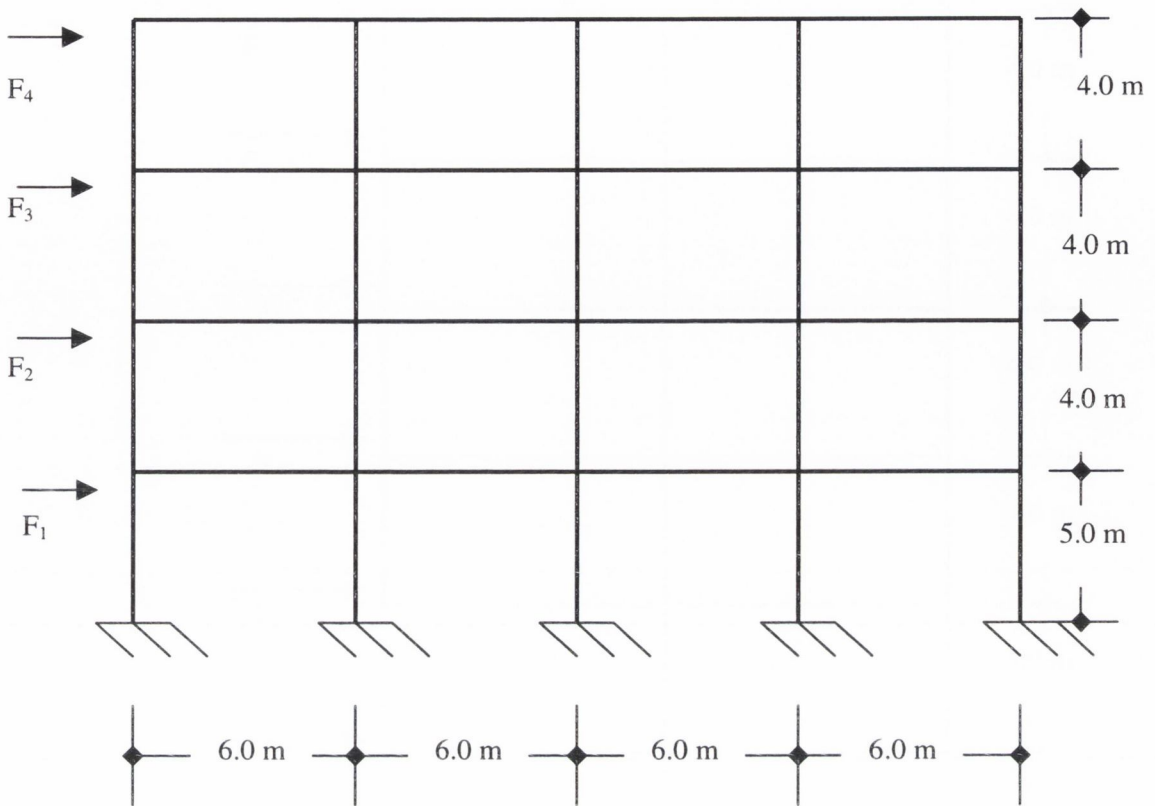


Figure D.7: Case study 2 – 4-Storey, 1-bay frame

Roof Loading	Dead:	16.8 kN/m
	Imposed:	3.0 kN/m
Floor Loading	Dead:	16.8 kN/m
	Imposed:	12.0 kN/m
Wind Loading	F_1 :	11.8 kN
	F_2 :	8.8 kN
	F_3 :	10.6 kN
	F_4 :	10.6 kN

D.3 Case Study 3



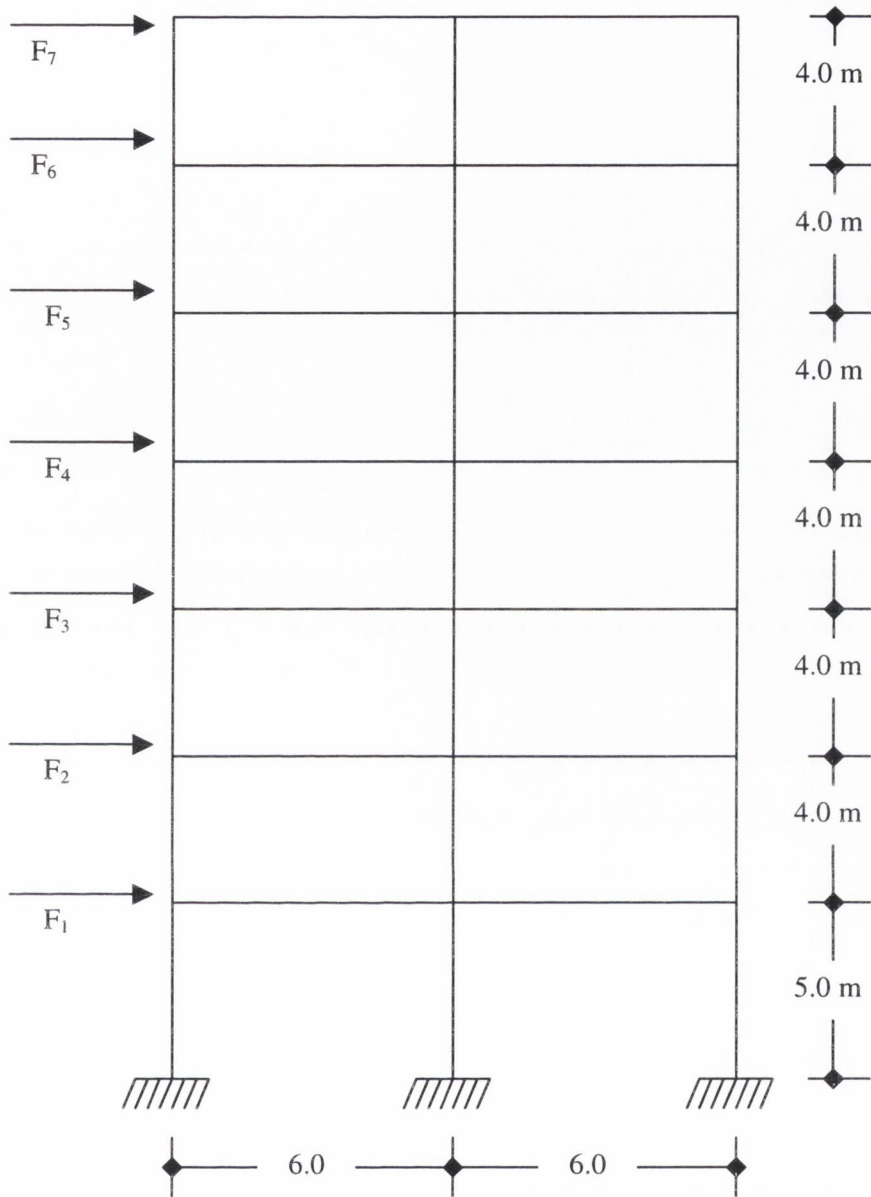
Roof Beam:		305 x 165 x 54 kg/m UB
Floor Beams:		406 x 178 x 74 kg/m UB
Internal Columns:	(Ground-to-2 nd Floor):	254 x 254 x 89 kg/m UC
	(2 nd Floor-to-Roof):	203 x 203 x 52 kg/m UC
External Columns:	(Ground-to-2 nd Floor):	203 x 203 x 71 kg/m UC
	(2 nd Floor-to-Roof):	203 x 203 x 52 kg/m UC

Frames at 6m centres
and braced out-of-plane

Figure D.8: Case study 3 – 4-Storey, 4-bay frame

Roof Loading	Dead:	24.0 kN/m	Wind Loading	F ₁ :	16.6 kN
	Imposed:	9.0 kN/m		F ₂ :	17.0 kN
Floor Loading	Dead:	27.0 kN/m	F ₃ :	14.2 kN	
	Imposed:	30.0 kN/m	F ₄ :	13.0 kN	

D.4 Case Study 4



1 st Floor Beam:	457 x 191 x 82 kg/m UB
2 nd – 6 th Floor Beam:	356 x 171 x 51 kg/m UB
Roof Beam:	305 x 102 x 33 kg/m UB
External Column:	(Ground-to-4 th Floor): 203 x 203 x 86 kg/m UC
	(4 th Floor-to-Roof): 203 x 203 x 52 kg/m UC
Internal Column:	(Ground-to-4 th Floor): 254 x 254 x 107 kg/m UC
	(4 th Floor-to-Roof): 203 x 203 x 52 kg/m UC

Figure D.9: Case study 4 – 7-Storey, 2-bay frame

Roof Loading Dead: 14.4 kN/m
Imposed: 3.0 kN/m

Wind Loading F₁: 8.43kN
F₂: 8.43 kN
F₃: 8.43 kN
F₄: 8.67 kN
F₅: 9.51 kN
F₆: 10.23 kN
F₇: 10.86 kN

Floor Loading Dead: 19.2 kN/m
Imposed: 12.0 kN/m